

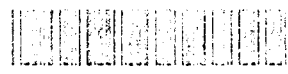
2

USDA REPORT 140 (Vol 5)

Copy

SUBALLOID MEMORANDUM

531694-13827



6

HANDBOOK OF SUPERSONIC AERODYNAMICS

SECTION 20

WIND TUNNEL INSTRUMENTATION AND OPERATION

By

R. J. YOLLUZ

Ordinance Aerophysics Laboratory
Daingerfield, Texas

Accession For	
NTIS	CRA&I
DTIC	TAB
Unannounced	
Justification	
By	
Distribution /	
Availability Co	
Dist	Avail and / c Special
A-1	

Produced and edited by the Aerodynamics Handbook Staff of The Johns Hopkins University Applied Physics Laboratory, Silver Spring, Maryland, under Contract NO. 7386 with the Bureau of Ordnance, Department of the Navy. The selection and technical review of this material were functions of a Laboratory Reviewing Committee consisting of Lester L. Cronvich and Ione D. V. Faro.

For sale by the Superintendent of Documents
U.S. Government Printing Office
Washington 25, D.C.
Price \$1

JANUARY 1961

SERIES CONTENTS

<u>Section</u>	<u>Publication Status</u>
Volume 1	
1 Symbols and Nomenclature	1950
2 Fundamental Equations and Formulae	1950
3 General Atmospheric Data	1950
4 Mechanics and Thermodynamics of Steady One- Dimensional Gas Flow	1950
Volume 2	
5 Compressible Flow Tables and Graphs	1953
Volume 3	
6 Two-Dimensional Airfoils	1957
7 Three-Dimensional Airfoils	1958
8 Bodies of Revolution	In process
Volume 4	
9 Mutual Interference Phenomena, by Cornell Aeronautical Laboratory	In process
10 Stability and Control Analysis Techniques, by R. S. Swanson	In process
11 Stability and Control Parameters, by R. S. Swanson	In process
12 Aeroelastic Phenomena	1952
Volume 5	
13 Viscosity Effects, by R. E. Wilson	In process
14 Heat Transfer Effects, by R. E. Wilson	In process
15 Properties of Gases	1953
16 Mechanics of Rarefied Gases, by S. A. Schaaf and L. Talbot	1959
Volume 6	
17 Ducts, Nozzles, and Diffusers, by C. L. Dailey	In process
18 Shock Tubes, by I. I. Glass and J. G. Hall	1959
19 Wind Tunnel Design, by A. Pope	In process
20 Wind Tunnel Instrumentation and Operation, by R. J. Volluz	1961
21 Ballistic Ranges	No statement

PREFACE

The preface appearing in Volume 1 of the Handbook of Supersonic Aerodynamics defines the Handbook's purpose and also traces the sequence of events leading to its undertaking. In accordance with the criteria established at that time, the subject matter of the Handbook is selected on the basis of anticipated usefulness to all who are actively concerned with the design and performance of supersonic vehicles. Essential to this subject matter are the properties of fluids in which a vehicle operates or is tested and the flight characteristics of the vehicle itself. Each section of the Handbook therefore presents appropriate theory and relevant data which are basic to supersonic aerodynamics and which conform to the practical requirements imposed by the criteria.

A complete list of Handbook sections and their status appears on the facing page. The unpublished sections, now being prepared by individual authors and the Handbook Staff, will be published separately as they become available.

Volume 6 of the Handbook series is devoted to the design, construction, and operation of test facilities such as free jets, shock tubes, and wind tunnels from which a great deal of aerodynamic data is obtained. Section 18, "Shock Tubes," is already available. Section 17, "Ducts, Nozzles and Diffusers," and Section 19, "Wind-Tunnel Design," are being prepared for publication. Section 20, "Wind Tunnel Instrumentation and Operation," is published herewith.

Section 20 was prepared by R. J. Volluz, who at the time of contract award was Chief of the Wind Tunnel Division, Ordnance Aerophysics Laboratory, Daingerfield, Texas. The manuscript was reviewed in its entirety by E. A. Bonney and H. P. Liepman. Specific sections were reviewed by F. S. Billig, D. E. Harrison, H. H. Hart, F. K. Hill, A. I. Mahan, F. F. Mobley, G. J. Pietrangeli, and others on the staff of the Applied Physics Laboratory. Much of the excellent advice offered by these reviewers has been incorporated in the final revision.

The subject matter appearing in the Handbook is selected and reviewed by the Technical Reviewing Committee at the Applied Physics Laboratory, headed by M. L. Cronvich. Constructive criticism or recommendations relating to the inclusion of suitable material in the Handbook should be directed to:

Editor, Aerodynamics Handbook Project
Applied Physics Laboratory
The Johns Hopkins University
8621 Georgia Avenue
Silver Spring, Maryland

The Handbook is printed and distributed by the Bureau of Naval Weapons, Department of the Navy. It is available for public sale (see Title Page) and is also distributed without charge to an approved list

of facilities and institutions actively engaged in national defense research and development. Correspondence relating to the distribution of the Handbook should be directed to:

Chief, Bureau of Naval Weapons
Department of the Navy
Washington 25, D. C.

Improvements in the format, adopted for Section 18 and consisting for the most part of a more concise running head and consecutively numbered pages, are continued herein. It has been judged that these changes enhance the usefulness of the sections and offset any sacrifice to uniformity in the whole series.

The Handbook of Supersonic Aerodynamics is edited and produced by the Handbook Staff, which includes Mrs. Doris Rupertus, reproduction copy typist; Thomas Timer, Mathematical Assistant; and Anthony Strank, Associate Editor.

Ione D. V. Faro, Editor

ACKNOWLEDGEMENT

The assistance of many individuals who contributed information for this Section of the Handbook is gratefully acknowledged. Among those who warrant special mention are Robert C. Dean, Jr., of the Gas Turbine Laboratory, Massachusetts Institute of Technology, and the members of the Supersonic Tunnel Association, listed below.

- H. E. Maloy and T. L. Smith of the Ballistics Research Laboratory, Aberdeen Proving Ground (BRL)
- R. Jackson, M. R. Mulkey, and J. D. Whitfield of the Gas Dynamics Facility, Arnold Engineering Development Center (AEDC GDF)
- H. Ramm and H. E. Gardenier of the Propulsion Wind Tunnel Facility, Arnold Engineering Development Center (AEDC PWT)
- R. G. Peters and J. H. Russell of the Seattle Division, Boeing Airplane Company (BAC)
- H. M. Schurmeier and W. R. Howard of the Jet Propulsion Laboratory, California Institute of Technology (JPL)
- R. C. McWherter of Chance Vought Aircraft (CVA)
- K. D. Bird of the Cornell Aeronautical Laboratory (CAL)
- R. T. Patterson, S. de los Santos, and J. B. Hippler of the Aerodynamics Laboratory, David Taylor Model Basin (DTMB)
- R. W. Bratt and J. F. L. Aldrich of the El Segundo Division, Douglas Aircraft Company (DAC)
- D. H. Ross and J. R. Baron of the Naval Supersonic Laboratory, Massachusetts Institute of Technology (MIT)
- K. Orlik-Ruckemann of the National Aeronautical Establishment, Ottawa, Ontario, Canada (NAE)
- I. M. Nestingen, F. J. DeMeritte, and B. D. Gilbert of the Naval Ordnance Laboratory (NOL)
- R. H. Spangler of North American Aviation, Inc. (NAA)
- J. D. Lee of Ohio State University (OSU)
- S. M. Bogdonoff of the Gas Dynamics Laboratory, Princeton University
- E. B. May and J. W. Clark of the Army Ballistic Missile Agency, Redstone Arsenal (ABMA)
- A. Pope of the Sandia Corporation
- P. F. Keller of the Southern California Cooperative Wind Tunnel, California Institute of Technology (CWT)

I. Twomey and E. C. Chapin of the Research Department, United Aircraft Corporation (UAC)

H. P. Liepman of the Aeronautical Engineering Laboratory, University of Michigan (U Mich)

J. H. Carrington of the Aeronautic Laboratories Department, University of Southern California (NAMTC/ATD)

P. P. Antonatos and J. B. D'Andrea of the Wright Air Development Center (WADC)

The Staff of the Ordnance Aerophysics Laboratory, Convair, Daingerfield, Texas (OAL)

Gratitude is also expressed to Miss J. Carlson and Mrs. M. Guy of the General Motors Corporation Research Staff for their assistance in typing the author's draft of the manuscript.

Section 20 of the Handbook of Supersonic Aerodynamics is hopefully dedicated to the challenge of rapid advance demanded of wind tunnels and their instrumentation and operation.

R. J. Volluz

CONTENTS

	<u>Page</u>
List of Tables	xiii
List of Figures	xiv
Symbols	xxv
1. Introduction	1
1.1 Objectives	2
1.2 Organization.	2
2. Pressure Measurement	3
2.1 Static Pressure Measurement	4
2.1.1 Inherent Errors	4
2.1.2 Tap Errors	5
2.1.3 Mach Number Effects	6
2.1.4 Effect of Turbulence	8
2.1.5 Effect of Non-Steady Pressures	9
2.1.6 Effect of Probe Misalignment	9
2.1.7 Effect of Velocity Gradients	9
2.1.8 Reynolds Number Effects	10
2.1.9 Other Means of Static Pressure Measurement	10
2.2 Stagnation Pressure Measurement	11
2.2.1 Supersonic Mach Number Effects	11
2.2.2 Effect of Yaw.	12
2.2.3 Shrouded Stagnation Probe.	12
2.2.4 Effects of Viscosity	12
2.2.5 Minimum Spacing for Total Pressure Probes.	13
2.2.6 Effect of Transverse Velocity Gradients	13
2.2.7 Stagnation Pressure Measurement Near a Wall	15
2.2.8 Turbulence Effects	18
2.2.9 Effect of Periodic Pressure Pulsations	19
2.2.10 Low Density Effects	20
2.2.11 Effect of Entrained Particles.	20
2.3 Pressure-Indicating Instruments	21
2.3.1 Hydrostatic Pressure Indication	21
2.3.1.1 Common Manometers	21
2.3.1.2 Manometer Fluids, Fittings, and Leads	23
2.3.1.3 Accuracy of Simple Manometer Systems.	27
2.3.1.4 Precision Manometers.	31
2.3.2 Mechanical Pressure Indicators	35
2.3.2.1 Bourdon Gage.	35
2.3.2.2 Bellows or Diaphragm Gages	36
2.3.3 Pressure Transducers	36
2.3.3.1 WADC Pressure Transducer.	37
2.3.3.2 OSU Pressure Transducer	40
2.3.3.3 Hagan Transducer.	40
2.3.3.4 Use of Transducers in an Arc-Heated Blow-down Tunnel.	41

	<u>Page</u>
2.3.4 Free-Molecule Probe	41
2.3.5 Mass-Flow Probe	42
2.3.6 System Response Time Lags.	43
2.3.6.1 Optimum Capillary Size	44
2.3.6.2 Limitations	45
2.3.6.3 Criteria for Minimum Response Time	45
2.3.6.4 Criteria for Slip Flow and Free-Molecule Flow	46
2.3.6.5 Working Charts	47
2.4 Mach Number Determination	49
2.4.1 Mach Number from Free-Stream Static Pressure Measurements	49
2.4.2 Mach Number from Stagnation Pressure Measurements	50
2.4.3 Mach Number by Means of Conical Probes	50
2.4.3.1 Sensitivity of Conical Probes	50
2.4.3.2 Machine Computation from Cone Pressures	51
2.4.3.3 Five-Orifice Truncated-Cone Probe	53
2.4.4 Mach Number by Means of Wedge-Face Static Pressure	54
2.4.5 Visual Methods of Determining Mach Number.	55
2.5 Nozzle Calibration Equipment.	55
2.5.1 Linear Actuators	55
2.5.2 Equipment for Calibration of a Flexible Nozzle	56
2.6 Measurement of Internal Flow Characteristics.	58
2.6.1 Design and Operation of a Force and Pressure Support	58
2.6.1.1 Design Modification for a Pressure Support	60
2.6.2 Reduction of Diffuser Inlet Data	60
2.6.3 Effect of Model Scale on Diffuser Characteristics	62
2.6.4 Probe Position in a Circular Duct.	64
2.7 Pressure Measurements on the External Surfaces of Models	65
2.7.1 Pressure Surveys on Bodies of Revolution	65
2.7.2 Pressure Surveys on Thin Surfaces.	66
2.7.3 Correct Angle-of-Attack Determination for Pressure Models	67
2.7.4 Pressure Model Supports	67
2.7.4.1 Roll-Indexing Support	67
2.7.4.2 Diffuser Inlet Pressure Support	68
Tables and Figures (See pp. xiii and xiv for list)	69
3. Force Measurement.	117
3.1 Strain Gages.	119
3.1.1 Application, Moisture-proofing, and Testing	122
3.1.2 Associated Instrumentation for Strain Gage Measurements	123

	Page
3.1.2.1 Some Theoretical and Practical Considerations of the Wheatstone Bridge.	123
3.1.2.2 Some Typical Strain-Gage Circuits . . .	129
3.1.3 Errors Associated with Strain Gages . . .	130
3.1.3.1 Thermal Coefficient of Resistance . . .	130
3.1.3.2 Temperature Differences in a Bridge . . .	133
3.1.3.3 Unequal Expansion Effects . . .	133
3.1.3.4 Error Due to Gage Factor Mismatch Within a Bridge . . .	134
3.1.3.5 Error Due to Strain-Gage Creep . . .	134
3.1.4 Strain-Gage Use at High Temperatures . . .	135
3.2 Design of Conventional Strain-Gage Balances . . .	135
3.2.1 Basic Two-Moment Strain-Gage System . . .	137
3.2.2 Direct Measurement of Normal Force . . .	138
3.2.3 Use of Composite Bridge . . .	140
3.2.4 Design Considerations for Strain-Gage Balances	141
3.2.4.1 Materials . . .	143
3.2.4.2 Effect of Section Size and Indicator Sensitivity on Repeatability. . .	144
3.2.4.3 Mounting the Model on the Internal Balance . . .	145
3.2.5 Rolling Moment Measurement . . .	145
3.2.6 Axial Force Measurement . . .	147
3.2.6.1 Strain-Gage Techniques for Measurement of Axial Force . . .	147
3.2.6.2 Induced Boundary-Layer Transition . . .	151
3.2.7 Interference Effects on Force Measurements . . .	151
3.2.7.1 Mechanical Interference . . .	151
3.2.7.2 Aerodynamic Interference. . .	153
3.2.8 Calibration of Strain-Gage Balances . . .	157
3.2.8.1 Basic Loading Systems . . .	158
3.2.8.2 Readout System . . .	159
3.2.8.3 Loading Process . . .	159
3.2.8.4 Derivation of Interaction Equations . . .	161
3.2.8.5 Sources of Interactions and Methods of Elimination . . .	165
3.2.8.6 Deflection Calibration . . .	167
3.2.8.7 Roll Orientation Calibration. . .	169
3.3 External Balances . . .	171
3.3.1 Six-Component Hydraulic Balance . . .	172
3.3.1.1 Advantages of the External Balance . . .	173
3.3.1.2 Operational Performance, Range, and Accuracy. . .	174
3.3.2 Reflection-Plane Technique . . .	175
3.3.2.1 Side-Wall Balance . . .	177
3.3.2.2 Flexure-Pivot Wall Balance . . .	177
3.4 Hinge-Moment Balances . . .	178
3.4.1 Sting-Mounted Hinge-Moment Models. . .	179
3.4.2 Calibration of Hinge-Moment Balances . . .	180
3.5 Special-Purpose Balances and Supports . . .	180

	<u>Page</u>
3.5.1 Remote Roll-Indexing and Drag Supports	181
3.5.2 High Angle-of-Attack Device	181
3.5.3 Combined Force and Pressure Balance	182
3.5.4 Micro-Balance.	183
3.5.5 Skin-Friction Balance.	184
3.6 Dynamic Stability Measurements	184
3.6.1 Dynamic Pitch Measurement.	188
3.6.1.1 Half-Model Techniques	188
3.6.1.2 Three-Dimensional Model Techniques	190
3.6.2 Dynamic Roll Measurement	191
3.6.3 Measurement of Cross Derivatives	193
3.6.4 Magnus Forces.	194
3.6.5 Oltronix Dampometer	195
3.7 Analog-to-Digital Converters.	196
3.7.1 Electro-Mechanical Analog-to-Digital Converters	196
3.7.2 Electronic Analog-to-Digital Converters	197
3.7.2.1 Operational Principles	197
3.7.2.2 Description of Components	198
3.7.2.3 Advantages	200
3.8 Automatic Data Plotting	200
3.8.1 Digital Data Plotting.	201
3.8.2 Analog Computers	202
3.9 Potentiometers	203
Tables and Figures (See pp. xiii and xvi for list)	205
4. Temperature Measurement	279
4.1 Effect of Stem Conduction on Probe Temperatures	282
4.2 Effect of Radiant Heat Transfer on Probe Temperature.	282
4.3 Effect of Turbulence, Secondary Flow, and Non-Steady Measurements on Probe Temperatures	283
4.4 Design of Temperature Probes.	284
4.5 Thermo-Electric Thermometry	287
4.5.1 Indicating Instruments for Use with Thermo- couples	288
4.6 Supplementary Techniques for Measuring Gas Tem- peratures	288
4.7 Application of Temperature-Measuring Techniques	289
4.7.1 Steady-State Heat Transfer	290
4.7.2 Transient Heat Transfer	290
4.7.3 Temperature Distribution in the Boundary Layer	291
Tables and Figures (See pp. xiii and xx for list).	293
5. Flow Visualization	303
5.1 Shadowgraph	304
5.1.1 Light Source	306
5.2 Schlieren Systems	307
5.2.1 Variations of the Simple Schlieren System.	309

	Page
5.2.1.1 Single-Mirror System.	309
5.2.1.2 Double-Mirror System.	310
5.2.1.3 Multiple-Source System.	311
5.2.1.4 Grating-Screen Method.	312
5.2.2 Components of the Schlieren System.	312
5.2.2.1 Light Source.	312
5.2.2.2 Condenser Lens.	313
5.2.2.3 Field Mirrors.	314
5.2.2.4 Test-Section Windows.	314
5.2.2.5 Camera.	315
5.2.3 Sensitivity of the Schlieren System.	316
5.2.4 Color Schlieren.	318
5.2.4.1 Light Source.	319
5.2.4.2 Sensitivity Control Slit.	319
5.2.4.3 Effective Light Source.	320
5.2.4.4 Condenser Lens.	320
5.2.4.5 Photographic Film.	321
5.2.4.6 Simple Color Schlieren System.	321
5.3 Interferometry.	322
5.3.1 Mach-Zehnder Interferometer.	322
5.3.2 Design of an Interferometer.	323
5.3.2.1 Light Source.	323
5.3.2.2 Splitter Plates, Mirrors, Windows, and Compensating Cell.	324
5.3.2.3 Mounting the Interferometer.	324
5.3.3 Adjustment of the Interferometer.	325
5.3.4 Evaluation of Interferograms.	326
5.3.4.1 Accuracy of Density Calculations.	327
5.3.5 Interferometric Photography.	328
5.3.6 Applications of Interferometry.	329
5.4 Electrical Discharge and Afterglow Methods of Flow Visualization.	329
5.5 Vapor Screen Method of Flow Visualization.	330
5.5.1 Light Sources.	331
5.5.2 Dew Point.	332
5.6 Visualization of Boundary-Layer Transition.	332
5.6.1 Optical Methods.	332
5.6.2 China Clay Method.	333
5.6.3 Liquid-Film Methods.	334
Figures (See p. xxi for list).	337
6. Turbulence.	351
6.1 Effect on Wind-Tunnel Measurements.	351
6.2 Measurement of Turbulence.	352
6.2.1 Indirect Methods of Measurement.	352
6.2.2 Measurement of Turbulent Velocity Fluctuations.	353
6.2.2.1 Hot-Wire Anemometer.	354
6.2.2.2 Corona Anemometer.	356
6.3 Minimizing Turbulence Effects.	357

	Page
6.4 Fixing Boundary-Layer Transition on Models	357
Figures (See p. xxii for list)	359
7. Tunnel Blockage	363
7.1 Inadequate Compression Ratio.	363
7.2 Excessive Humidity	363
7.2.1 Humidity Indicating Instruments	363
7.3 Model Size	364
Figures (See p. xxii for list)	367
8. Model Design	371
8.1 Shock-Wave Reflection	371
8.2 Aerodynamic Loads Imposed by Starting and Stopping Flow.	372
8.3 Model Construction Techniques	374
8.3.1 Joining Body Sections.	375
8.3.2 Mounting Aerodynamic Surfaces.	375
8.3.3 Surfacing and Fillers.	376
Figures (See p. xxii for list)	377
9. Typical Force Measuring Systems	405
9.1 Data Taking, Reduction, and Plotting Techniques	405
9.1.1 Damping Device	408
9.1.2 Measuring Bridges.	408
9.2 Analog-to-Digital Conversion.	408
Figures (See p. xxiv for list)	411
10. Pressure Measuring Systems	421
10.1 Pressure Transducer Systems	421
10.1.1 Switches Used in Conjunction with Pressure Transducers	422
10.1.2 Performance Characteristics of Pressure Transducer Systems	423
10.1.3 Unique Features in Pressure Transducer Systems	424
10.1.3.1 Automatic Zero Balancing.	424
10.1.3.2 Cathode-Ray Manometer Simulator	425
10.1.3.3 Internal Manometer	425
10.2 Automatic Digital Recording Manometers	425
Figures (See p. xxiv for list)	429
References	437
Index	457
Appendix A: Supplemental Bibliography	A-1

LIST OF TABLES

<u>Table</u>		<u>Page</u>
2-1	Properties of common manometer fluids	69
2-2	Sample cases showing lag effect.	70
2-3	Shock angles for cones as a function of Mach Number.	71
2-4	Probe distances from center for equal-area spacing .	72
3-1	Change in indicator count due to a temperature rise of 72°F for various gages of 2-in. lengths of copper and nickel wire	205
3-2	Loading schedule for balance calibration	206
3-3	Characteristics of OAL supports.	207
4-1	Recovery factors measured under various conditions .	293
4-2	Temperature limits and uncertainty intervals for Leeds and Northrup thermocouples	294

LIST OF FIGURES

<u>Figure</u>		<u>Page</u>
2-1	Inherent probe errors on stream-pressure measurements in subsonic flow	73
2-2	Effect of orifice edge form on static pressure measurements	73
2-3	Effect of hole size on stream-pressure measurements for air or water ($M = 0$) for square-edged hole	74
2-4	Change in flow parameters through a normal shock in air	75
2-5	Comparison of static pressure on a 5-deg cone and on a specially designed probe.	76
2-6	Error in stream-pressure and stagnation-pressure measurements due to isotropic turbulence	76
2-7	Stagnation-pressure error vs angle of yaw at constant Mach number for flat and round-nosed probes at supersonic speeds	77
2-8	Stagnation-pressure error vs angle of yaw at constant Mach number for flat and round-nosed probes at subsonic speeds	77
2-9	Stagnation-pressure error vs angle of yaw at constant Mach number for flat-nosed probes with internal bevel	78
2-10	Stagnation-pressure error vs angle of yaw at constant Mach number for truncated-cone probes	78
2-11	Stagnation pressure error vs angle of attack for shrouded stagnation-pressure probes	79
2-12	Viscous effects in a stagnation-pressure tube	79
2-13	Effective position vs mouth opening for Stanton's boundary-layer probe	80
2-14	Effective position vs velocity for Fage and Falkner boundary-layer probe	80
2-15	Probe contact as shown by pitot pressure survey.	81
2-16	Manometer board and associated hardware.	81
2-17	Specific gravity characteristics of Merriam Unity Oil	82
2-18	Specific gravity characteristics of tetrobromoethane	82

<u>Figure</u>		<u>Page</u>
2-19	Manometer sliding valve and porting.	83
2-20	Schematic of commercial micromanometer	84
2-21	NACA micromanometer.	84
2-22	Exploded view of pressure transducer	85
2-23	Operational details of pressure transducer	85
2-24	Diagram of wire probe and flat plate	86
2-25	Slip-flow correction factor for glass and copper tubing	86
2-26	Plot of $1 + \frac{v_2}{v_1} (1 + \frac{1}{K})$ vs $\frac{d_2}{d_1}$ for various values of $\frac{l_2}{l_1}$	87
2-27	Plot of $\frac{2}{K}$ vs $\frac{l_2}{l_1}$ for various values of $\frac{d_2}{d_1}$	88
2-28	Values of $F_v \left[1 + \frac{v_2}{v_1} (1 + \frac{1}{K}) + \frac{2}{K} \frac{v_m}{v_1} \right]^{-1}$ for $\epsilon = 0.05, 0.025, 0.01, \text{ and } 0.005$	89
2-29	Values of $F_d \left(\frac{2}{K} \frac{v_d}{v_1} \right)^{-1}$ for $\epsilon = 0.05, 0.25, 0.01, \text{ and } 0.005$	90
2-30	Plot of $\frac{0.111 \mu (l_1/d_1)^2}{p_f}$ vs $\frac{l_1}{d_1}$ for various values of p_f	91
2-31	Eleven-probe total head rake mounted in tunnel	92
2-32	Cruciform inclinometer mounted in tunnel	93
2-33	Cone sensitivity vs Mach number.	94
2-34	Ratio of average cone pressure to free-stream total pressure vs free-stream Mach number	95
2-35	Details of 10-deg half-angle cone and truncated-cone probes	96
2-36	Experimental and theoretical flow inclination parameters for sharp-cone and truncated-cone probes	96
2-37	Fifteen-degree half-angle cone probe with total-pressure orifice	97
2-38	Typical pressure wedge installation.	98

<u>Figure</u>		<u>Page</u>
2-39	OAL linear actuator.	99
2-40	OAL-32 linear actuator support	100
2-41	OAL-35 linear actuator support	101
2-42	Simulated axial actuator with horizontal total head rake and 15-deg half-angle conical forebody at zero angle of attack; Mach number 1.25	102
2-43	Simulated axial actuator with horizontal total head rake and a 10-caliber ogive forebody at zero angle of attack; Mach number 1.25.	103
2-44	OAL-22 force and pressure support	104
2-45	Variation of minimum A_p/A_1 value (swallowed shock) with free-stream Mach number for various values of pressure recovery	105
2-46	Details of mounting end of model configuration for OAL-22 force and pressure support.	106
2-47	Disassembled OAL-22 force and pressure support	107
2-48	OAL-39 pressure support.	108
2-49	OAL-41 pressure support.	109
2-50	Error in capture-area ratio due to errors in free- stream Mach numbers	110
2-51	Geometric comparison of two ramjet diffuser inlet models	111
2-52	Diffuser characteristics of two ramjet diffuser inlet models	111
2-53	Peripheral pressure locations on body of revolution.	112
2-54	Sketch of probe configuration for an airfoil of 3% thickness	113
2-55	Comparison of pressure distributions obtained from probes and interferograms.	113
2-56	OAL-21 roll-indexing support	114
2-57	OAL-42 pressure support.	115
3-1	Graphic reference for basic measurement terms	208
3-2	Effect of jumper location on temperature compensa- tion of strain-gage bridge	208
3-3	Effect on C_h when strain gages are protected from air blast.	209

<u>Figure</u>		<u>Page</u>
3-4	Effect on C_N vs C_D when strain gages are protected from air blast	210
3-5	Effects of time on output of complete bridge bonded to test element, constant applied load	211
3-6	Temperature-controlled strain-gage balance and model	212
3-7	Calibration constant, K , vs gage temperature; temperature-controlled balance	213
3-8	Method of reducing moment data	214
3-9	Schematic diagram of differential moment (direct normal force) bridge, showing method for wiring electrical strain-gage circuits	215
3-10	Schematic diagram of differential moment (direct normal force) bridge, showing method for wiring electrical strain-gage circuits	216
3-11	Gage location and wiring diagram; composite bridge .	216
3-12	Errors due to strain-gage location	217
3-13	Typical internal balance, showing standard taper seat	217
3-14	Internal balance-support connection, showing tapered seat method	218
3-15	Cannon plug, showing base pressure lead.	219
3-16	Tapered-seat connection for support-adaptor with base pressure lead	219
3-17	Typical internal balances	220
3-18	Typical two-component roll-indexing support. . . .	221
3-19	Typical balance evaluation data.	222
3-20	Simple internal drag beam used at ABMA	223
3-21	Air-bearing drag balance	223
3-22	Models used in windshield-and-sting interference tests.	224
3-23	Variation of afterbody pressure with windshield distance for a 20-deg half-angle windshield at Mach number 1.50 and at zero angle of attack	225
3-24	Distance from model base at which windshield affects model base pressures at Mach 1.50.	226
3-25	Effect of windshield lip diameter on slopes of the normal force; stability curves at Mach number 2.00	227

<u>Figure</u>		<u>Page</u>
3-26	Effect of windshield clearance on aerodynamic characteristics; Mach number 1.73.	227
3-27	Normal force distribution along exposed portion of the internal balance, using a typical cruciform body-tail configuration at a free-stream Mach number of 1.73	228
3-28	Typical fixture for calibrating internal sting-supported balances	228
3-29	Dead-weight calibration loading system	229
3-30	Dead-weight calibration loading system utilizing shot	229
3-31	Semi-automatic shot loader	230
3-32	Dead-weight calibration system utilizing long-arm fixtures	231
3-33	Calibration system utilizing jack and load cell.	231
3-34	Roller box	232
3-35	Method of measuring one load in the presence of another	233
3-36	Typical calibration data plot	233
3-37	Typical six-component, wire strain-gage balance.	234
3-38	Internal balance calibration fixture	234
3-39	Rolling-moment calibration rig	235
3-40	Axial-force calibration rig.	236
3-41	Axial-force measuring section	236
3-42	JPL balance and suspension system	237
3-43	JPL six-component external balance	238
3-44	Schematic diagram of JPL hydraulic system	239
3-45	Automatic weighing beams and digitizers.	240
3-46	Typical reflection plate mounted in steel window	241
3-47	Five-component side-wall balance	242
3-48	Side view of five-component side-wall balance	243
3-49	Internal balance for five-component side-wall balance	243
3-50	Cross-section of half-model mounted on five-component side-wall balance	244

<u>Figure</u>		<u>Page</u>
3-51	Flexure-pivot wall-mounted support system, access hatch open	245
3-52	Wing model mounted on flexure-pivot support. . .	246
3-53	Maximum allowable lift and drag load for flexure-pivot wall-mounted support	247
3-54	Typical three-dimensional hinge-moment model . .	247
3-55	Method for measuring wing hinge moment	248
3-56	Typical installation for measuring flipper hinge moment	249
3-57	Typical hinge-moment models; integrated wing and tail, four active panels (body cover plates removed), and wing alone, two active panels. . .	250
3-58	Arrangement for measuring hinge moment	250
3-59	Tail hinge-moment model, integral with the internal balance	251
3-60	Wing hinge-moment internal balance, showing integral gaged beam and surface, and installation in balance	252
3-61	Balance arrangement in test section.	253
3-62	Characteristics of OAL extensions, spacers, and support bases.	254
3-63	OAL-23 two-component roll-indexing support. . .	255
3-64	Roll angle indexing control panel	256
3-65	Side view of OAL-24 two-component roll-indexing support, showing rolling moment flexure arm and axial-force flexure arm	256
3-66	Operating principle of the OAL E-10 extension . .	257
3-67	OAL-37 9-deg offset roll-indexing support . . .	258
3-68	OAL-36 17-deg offset manual-indexing support . .	258
3-69	Pilot model of focused-flexure balance	259
3-70	Skin-friction balance floating element and micrometer installed in the plate	260
3-71	Schaevitz differential transformer	261
3-72	Block diagram of free oscillation with feedback excitation	261
3-73	Test rig for oscillation in pitch	262

<u>Figure</u>		<u>Page</u>
3-74	Typical results of oscillation-in-pitch tests on half models	263
3-75	Pitch-damping balance, reflection plate, and model .	264
3-76	Model, sting, and shaker system.	265
3-77	Damping-in-pitch balance and model	266
3-78	Dynamic steady-roll balance support.	266
3-79	Dynamic steady-roll balance support, with internal details	267
3-80	Schematic drawing of rpm counter for dynamic steady-roll balance	268
3-81	Arrangement of dynamic roll balance and associated equipment.	268
3-82	NAE test rig for oscillation in roll	269
3-83	High-speed air turbine balance and model	270
3-84	Oltronix dampometer.	271
3-85	Typical calibrated slotted discs and principle of dampometer operation	272
3-86	Wiring diagram of wind-tunnel indicators	273
3-87	Pilot model of analog-to-digital high-speed electronic converter	274
3-88	Block diagram of the ADHEC	275
3-89	Correlation of ADHEC data with existing indicator data	275
3-90	Model 205G vari-plotter and model 17-31A digi-verter	276
3-91	Basic standard scale for conventional three-component data	277
3-92	Basic standard scale for other general data. . .	278
4-1	Difference between stagnation temperature and stream temperature vs velocity for air at atmospheric pressure	295
4-2	Thermal conductivity of air vs temperature . . .	296
4-3	Viscosity and Prandtl number of air vs temperature .	296
4-4	Effect of radiant heat transfer on shielded and bare thermocouples	297

<u>Figure</u>		<u>Page</u>
4-5	Sensitivity and recovery factor of Pratt and Whitney probe.	297
4-6	Variation of probe temperature recovery factor with free-stream Reynolds number at various free-stream Mach numbers	298
4-7	Variation of probe temperature recovery factor with free-stream Reynolds number at three different stagnation temperatures for a free-stream Mach number of 4.90	298
4-8	Variation of probe performance with vent-to-entrance-area ratio	299
4-9	Summary of calibration data for five probes.	299
4-10	Typical traversing pitot thermocouple	300
4-11	Details of pitot-tube traversing gear	301
5-1	Comparison of shadowgraph, schlieren, and interferometer optical techniques	337
5-2	Typical schlieren of a sting-mounted, hemispherical-nosed cylinder; Mach number 1.25, 6-deg angle of attack	338
5-3	OAI optical system	339
5-4	Three-way optical system designed for maximum flexibility	340
5-5	Focusing effect of multiple-source schlieren	340
5-6	Optical system for NAA color schlieren	341
5-7	Effect of prism on light path	342
5-8	Ten-inch Mach-Zehnder interferometer and schlieren system for WADC 6 × 6-in. supersonic wind tunnel	343
5-9	Interferograms illustrating superposition for evaluating band displacement	344
5-10	Dependence of depth of field on ratio w/f_1	345
5-11	Glow-flow visualization system	345
5-12	Typical air afterglow of bow shocks and boundary layer on a wedge and flat plate; Mach number 3.0, static pressure of 90 microns.	346
5-13	Flow pattern, vapor-screen technique	347
5-14	Isometric sketch of vapor-screen technique	347

<u>Figure</u>		<u>Page</u>
5-15	OAL vapor screen technique	348
5-16	Light source with inspection door open	349
5-17	Portable vapor-screen light source mounted on tripod	350
6-1	Effect of stilling chamber screens on model stability and axial force characteristics in the OAL Mach 1.73 nozzle	359
6-2	Variation of body-alone (RM-10) axial force coefficient with angle of attack; Mach number 1.73, Reynolds number 6.66×10^{-6}	359
6-3	Comparison of transition Reynolds number on 5- and 10-deg cones observed at several facilities . . .	360
6-4	Typical plot of drag coefficient vs roughness height	361
6-5	Effect of Mach number on critical roughness height .	362
7-1	Minimum operating compression ratio for supersonic wind tunnels	367
7-2	Saturation weight of water vapor in air.	368
7-3	Lower limit of dew point as a function of Mach number for various errors in static pressure; $T_0 = 500^\circ\text{F}$ and 100°F	369
7-4	Upper limit of model area to test section area as a function of Mach number	370
8-1	Bow waves from conical and hemispherical noses, Mach number 1.25	377
8-2	Bow waves from conical and hemispherical noses, Mach number 1.73	378
8-3	Bow waves from ducted model inlet with no flow through duct	379
8-4	Bow waves from conical and hemispherical noses; Mach number 1.5, $\alpha = 0$ deg.	380
8-5	Bow waves from conical and hemispherical noses; Mach number 1.5, $\alpha = 15$ deg	381
8-6	Bow waves from conical and hemispherical noses; Mach number 1.5, $\alpha = 30$ deg	382
8-7	Bow waves from conical and hemispherical noses; Mach number 2.0, $\alpha = 0$ deg.	383

<u>Figure</u>		<u>Page</u>
8-8	Bow waves from conical and hemispherical noses; Mach number 2.0, $\alpha = 15$ deg	384
8-9	Bow waves from conical and hemispherical noses; Mach number 2.0, $\alpha = 30$ deg	385
8-10	Bow waves from conical and hemispherical noses; Mach number 2.5, $\alpha = 0$ deg.	386
8-11	Bow waves from conical and hemispherical noses; Mach number 2.5, $\alpha = 15$ deg	387
8-12	Bow waves from conical and hemispherical noses; Mach number 2.5, $\alpha = 30$ deg	388
8-13	Bow waves from conical and hemispherical noses; Mach number 3.0, $\alpha = 0$ deg.	389
8-14	Bow waves from conical and hemispherical noses; Mach number 3.0, $\alpha = 15$ deg	390
8-15	Bow waves from conical and hemispherical noses; Mach number 3.0, $\alpha = 30$ deg	391
8-16	Bow waves from conical and hemispherical noses; Mach number 4.0, $\alpha = 0$ deg.	392
8-17	Bow waves from conical and hemispherical noses; Mach number 4.0, $\alpha = 15$ deg	393
8-18	Bow waves from conical and hemispherical noses; Mach number 4.0, $\alpha = 30$ deg	394
8-19	Bow waves from conical and hemispherical noses; Mach number 5.0, $\alpha = 0$ deg.	395
8-20	Bow waves from conical and hemispherical noses; Mach number 5.0, $\alpha = 15$ deg	396
8-21	Bow waves from conical and hemispherical noses; Mach number 5.0, $\alpha = 30$ deg	397
8-22	Maximum normal force loads experienced during wind-tunnel starting and stopping	398
8-23	Maximum axial force loads experienced during wind-tunnel starting and stopping	399
8-24	Details of screw-joint and slip-joint methods for joining model sections	400
8-25	Details of left and right-hand thread in screw-type joint.	400
8-26	Model sections joined by means of a tie rod.	401
8-27	Details of base for surface with fixed attitude.	401

<u>Figure</u>		<u>Page</u>
8-28	Model with incidence pins installed.	402
8-29	Methods for setting incidence on surfaces	403
8-30	Fixed incidence tail and retaining ring.	404
9-1	Typical stability data at constant roll attitude	411
9-2	Typical force data for various constant angles of attack	412
9-3	Wiring diagram of a-c bridge	413
9-4	Wiring diagram of d-c bridge	414
9-5	Digital converter (Dayton Instrument Model No. DI-4-54)	415
9-6	OAL automatic data system	416
9-7	One channel of BRL converter servo system	417
9-8	Schematic of BRL analog-to-digital converter	418
9-9	Block diagram of high-speed wind-tunnel data system.	419
10-1	OAL pressure transducer console.	429
10-2	Flow diagram of WADC 98-channel pressure recording system	430
10-3	WADC 98-channel automatic pressure recording system.	431
10-4	OAL pressure data recording system	432
10-5	Boeing 12-point pressure selector valve wafer assembly	433
10-6	Boeing 12-point pressure selector switch assembly	433
10-7	Two-tube automatic digital recording manometer (ADRMAN)	434
10-8	ADRMAN meniscus transducer	435
10-9	ADRMAN counting head	435
10-10	Block diagram of digital recording manometer	436

SYMBOLS

A	area, axial force
a	speed of sound: $\sqrt{\gamma RT}$
C	coefficient
C_p	pressure coefficient
c_p	specific heat at constant pressure
c_v	specific heat at constant volume
D	diameter (also d)
E	voltage; elasticity; error
F	force; stream thrust = $A_p (1 + \gamma M^2)$
f	focal length
h	convective heat transfer coefficient
I	moment of inertia; intensity of light
K	Gladstone-Dale constant
k	local coefficient of thermal conductivity
l	length
M	Mach number; pitching moment
m	mass
Pr	Prandtl number
p	pressure
q	dynamic pressure: $1/2 \rho U^2 = \gamma/2 p M^2$
R	universal gas constant = $1715 \text{ ft}^2/\text{sec}^2 \text{ }^\circ\text{F}$ for air; resistance
r	recovery
Re	Reynolds number, $\frac{\rho U l}{\mu}$
S	stress
T	temperature
t	time
U	velocity

u, v, w	turbulent velocities in the three coordinate directions
V	volume; voltage
x	distance
x, y, z	rectangular coordinates; distances along these axes
α	angle of attack
γ	isentropic exponent: $\frac{c_p}{c_v}$
δ	boundary layer thickness
ϵ	emissivity
λ	wave length
μ	viscosity, 3.8×10^{-7} slugs/ft at 80°F for air
ρ	density
σ	Stefan-Boltzmann constant

Subscripts

A	axial force
C	cross-wind force
i	indicated
L	lift
M	pitching moment
N	normal force
o	free stream or reference condition
t	stagnation
w	wall conditions
∞	static, undisturbed stream

Superscripts

$'$	rms value; indicates value is taken behind shock wave
$-$	average

WIND TUNNEL INSTRUMENTATION AND OPERATION

1. Introduction

The use of special test equipment to investigate the characteristics of aerodynamic surfaces can be traced to a period beginning about 1870, when Wenham of England, Irminger and Vogt of Denmark, and A. J. Wells of the United States used wind tunnels to measure the lifting effect of plane surfaces at various angles of attack. Within this period also, Horatio Phillips and Sir Hiram Maxim of England used wind tunnels to investigate the aerodynamic characteristics of curved air foils. Other prominent experimenters during this period included Lilienthal of Germany and Langley of the United States, both of whom used the "whirling arm" to investigate lifting surfaces.

Basic information relating to lifting surfaces, controls, and effective test procedures, however, was largely unknown or speculative when the Wright Brothers began their serious study and experimentation in 1899. Much of their success therefore can be attributed to the investigative techniques, including wind-tunnel instrumentation, which they evolved. In experiments conducted with their first wind tunnel during late 1901, they employed a balance which measured lift and drag. Although this balance introduced an error of 10% in direction and velocity of the flowing air, the technique was so successful that they went on to build larger and more accurate equipment.

With their second wind tunnel, the Wright Brothers employed a wire mesh and a honeycomb of sheet iron to control turbulence and to improve the quality of the air flow. In their first series of tests with this arrangement, they tested more than 100 plane and curved surfaces at 0 to 90-deg angle of attack. Their techniques improved as their investigations continued, and they compiled much useful data on airfoils and flow phenomena. They were the first to achieve wind-tunnel test results accurate enough for the design of successful aircraft. These results were applied first to their gliders and then to the powered aircraft they flew for the first time in December 1903.

The entire technology of flight has experienced a systematic and relatively rapid advance since the early days of flying. Wind-tunnel instrumentation, particularly, has become varied, specialized, and highly accurate, and the modern wind tunnel facility has become large and complex.

The engineering problems which arise during development of the modern wind-tunnel facility are much like those encountered with high-performance airplanes and missiles. Increasing speed capabilities are invariably associated with increasingly complex instrumentation and operational techniques. The development and construction time needed for a new facility may exceed six years or more. Additional problems are introduced by a consistently changing "state of the art" and by the always disturbing knowledge that future research problems cannot always be anticipated.

In addition to the changing conditions implied by a changing state of the art, wind-tunnel facilities are confronted by special problems of instrumentation. The design of new components, for example, is generally compromised by existing instrumentation that is still useful

and by the unique operational limitation at each facility. In many cases, even before a given component has become operational, more sophisticated instrumentation is devised. New operational procedures are also frequently imposed upon a test facility by the extremes in testing environment (e.g., temperature, pressure, blow time) which the higher altitude and velocity capabilities of new vehicle development demand. Any attempt, therefore, to treat the broad field of wind-tunnel instrumentation in a work such as this must adhere closely to an operational point of view.

1.1 Objective

The objective of this Handbook Section is to provide a compendium of useful rules and techniques for wind-tunnel operation rather than a completely organized guide to optimum solutions. This approach is particularly appropriate for subject matter which is not easily presented in conventional handbook style because of a changing state of the art and a wide range of instrumentation requirements and techniques. The material therefore relies heavily on the practical experience accumulated at some of the prominent tunnel facilities of the past decade. Even though the rapid rate of change may cause some of these techniques to become obsolescent within a relatively short time after publication of this Handbook Section, most of them should prove useful as long as wind-tunnel technology retains its present character.

1.2 Organization

In view of the diversity of subject matter in this Section, an explanation of its organization may prove useful to the reader. The material is arranged in two major categories of Instrumentation and Operation and is supplemented by references to the source material used. The subsections dealing with Instrumentation are further subdivided into topics dealing with pressure, force, and temperature measurements, and with optical measurement techniques. Each topic in turn then treats the design and construction of the basic elements of the instrumentation, their use and operation, and the manner in which the data may be read or recorded and analyzed. The basic physical principles and relevant equations as well as the references from which details of their derivation may be obtained are also included.

The second major category deals with integrated systems and presents some account of how the elements of instruments described in the first category are used in conjunction with one another. Included also are appropriate examples of extant systems.

It was not possible in many cases to provide source references for the material presented because the information is not readily available in published literature. A significant part of such unpublished information was drawn from the informal proceedings of the Supersonic Tunnel Association whose members are listed in the Acknowledgment. To supplement the cited references, an extensive bibliography has been extracted from Ref. 1 and included as Appendix A.

2. Pressure Measurement

Pressure is one of the significant properties of a fluid and is critically associated with aerodynamic measurement (Ref. 1). Pressure is characterized by a compressive stress exerted uniformly in all directions. It may be regarded as a potential force because in theory its compressive work can be completely recovered. The basic principles which govern the measurement of pressure state that pressure acts normal to a surface and that pressure is proportional to the kinetic energy of the random molecular motion per unit volume. Pressure can therefore be defined as the force per unit area ($ML^{-1}T^{-2}$) which a fluid or a gas exerts on a restraining surface.

To define completely the state of a perfect gas, it is necessary to determine the pressure and one other independent property of the gas. Pressure, density, and absolute temperature of a perfect gas are related by

$$p = \rho RT \quad (2-1)$$

where

p = pressure

ρ = density

T = absolute temperature

R = constant for the gas = $1715 \text{ ft}^2/\text{sec}^2\text{°F}$ for air*

The steady-flow energy equation for reversible adiabatic flow gives the relationship between the stagnation pressure and the static pressure for the compressible perfect gas,

$$\frac{p_t}{p_\infty} = \left[1 + \frac{\gamma - 1}{2} M^2 \right]^{\frac{\gamma}{\gamma - 1}} \quad \text{or} \quad M = \sqrt{\frac{2}{\gamma - 1} \left[\left(\frac{p_t}{p_\infty} \right)^{\frac{\gamma - 1}{\gamma}} - 1 \right]} \quad (2-2)$$

This equation gives the Mach number directly from the ratio p_t/p_∞ . However, since $(p_t - p_\infty)$ is often measured instead of the absolute values of p_t and p_∞ , the equation can be written

$$\begin{aligned} \frac{\Delta p}{q} = \frac{p_t - p_\infty}{\frac{1}{2} \rho U^2} &= \left\{ \left[1 + \frac{\gamma - 1}{2} M^2 \right]^{\frac{\gamma}{\gamma - 1}} - 1 \right\} \frac{2}{\gamma M^2} \\ &= 1 + \frac{M^2}{2 \cdot 2!} + \frac{2 - \gamma}{2^2 \cdot 3!} M^4 + \dots \end{aligned} \quad (2-3)$$

* Unless otherwise defined in the text or in the list of symbols, all letter symbols used herein conform to the American Standards Association Letter Symbols for Aeronautical Sciences (ASA V10.7), ASME, 1954.

For the incompressible case only the first term of the series need be considered. This term is accurate to within 1% error in $(p_t - p_\infty)$ up to Mach 0.2. The first two terms of the series can be used to Mach 0.8 with the same error, and the first three terms are accurate to Mach 1.0 with less than 0.2% error.

Approximations of the foregoing equation for speeds above Mach 1 are relatively valueless for purposes of measurement because it is impossible to measure p_t directly without a normal shock in front of the probe. Such a shock is non-isentropic and will change the measured stagnation pressure, thus requiring a different relation (Subsec. 2.2.1). By definition the relation represents the true difference between the local stream and stagnation pressures under any conditions, even if the value cannot be measured.

2.1 Static Pressure Measurement

Measurement of the static or stream pressure, p_∞ , requires that testing conditions be so arranged that the stream cannot sense or otherwise recognize the presence of the probe. Thus, if a probe which does not distort the flow streamlines can be inserted in the region of the pressure measurement, the stream pressure can be measured.

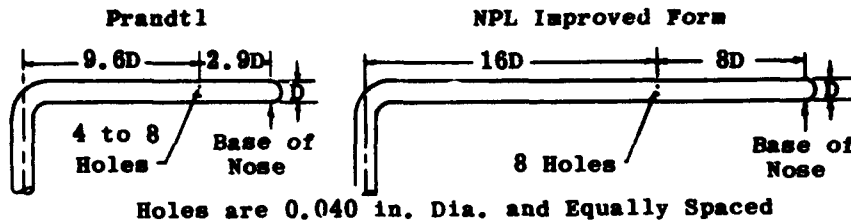
2.1.1 Inherent Errors in Static Pressure Measurement

A measuring instrument, even though it will always disturb the streamlines to some extent, can be so designed that the stream pressure is measured at some point on the probe where initial disturbances have subsided and the streamlines are once more parallel to those of the main flow. For all stream pressure measurements it is essential that this condition be met or that the flow be distorted in a predictable manner in order to facilitate calculation and calibration of the ratio between indicated stream pressure at the tap, p'_∞ , and the pressure in the undisturbed flow. A pressure tap on a flat wall parallel to the stream gives accurate static pressure measurements where the influence of the tap is negligible (Subsec. 2.1.2).

The disturbance produced by any given probe (hence, the accuracy of its stream-pressure measurement) is a function of probe geometry. The head and stem cause the streamlines to curve with consequent changes in local stream pressure, which are sensed many probe diameters downstream. Eventually the streamlines tend to return to their original direction. It is theoretically impossible to employ a probe of sufficient length to ensure completely undistorted flow about the pressure taps. However, this flow field may be calculated for an ideal gas by potential theory (Ref. 2), and the errors in measurement predicted. Measurements (Ref. 2) of the local stream pressure on long cylinders aligned with the flow are presented in Fig. 2-1.

Most common stream-pressure probes have a supporting stem not far removed from the pressure taps. The presence of the stem is sensed upstream and produces a local variation from true stream pressure. This effect is shown in Fig. 2-1 for a cylindrical stem of the same diameter as the head. Although attempts have been made to streamline the stem in order to reduce its disturbing effect, a better solution lies in locating the pressure taps far enough upstream to avoid the effect.

Prandtl optimized the opposing effects of head and stem, cancelling one error with the other, thereby producing a compact probe which reads stream pressure with a high degree of accuracy. This probe is illustrated below.



If stem effects are significant at the tap location, care must be exercised to maintain the stem effects uniformly about the probe or to place the pressure taps only on that side of the probe from which the stem emerges. If pressure taps are distributed around the probe at a given section, an asymmetric pressure distribution can produce internal flow in the probe. This flow governs the indicated pressure and is itself a function of internal geometry.

2.1.2 Tap Errors in Static Pressure Measurement

Another phenomenon which will cause a pressure tap to indicate an erroneous stream pressure is the effect of the hole itself upon the flow. This error is often ignored in aerodynamic measurements. Extensive work (Refs. 3 to 7) upon water and gas flows indicates significant errors due to hole effects. Previous investigators have discussed the possible errors in gas flows, but Ref. 8 appears to contain the only measured data. Considered in Ref. 8 are holes normal to the streamlines, holes inclined upstream and downstream, the effect of mouth configurations, the effect of external and internal burrs, and the effect of boundary-layer thickness.

These phenomena arise because of the fact that any finite hole in the retaining wall will produce some curvature of the streamlines due to removal of the constraining boundary. The magnitude of the effect obviously diminishes with the size of the hole. The streamlines will dip into a hole producing a centrifugal force field which raises the tap pressure above stream pressure. The magnitude of the excess depends upon the flow velocity and the geometry of the hole. In some cases separation of the flow from the leading edge of the hole will produce local tap pressures below stream pressure.

Any hole will sense a pressure gradient (across the hole and in the direction of flow) arising from different flow phenomena and different curvatures of the streamlines at various points inside the hole. The hole integrates the pressure across its entry, giving the indicated pressure, p'_∞ . Pressure taps can be made self-compensating by proper design, as indicated in Ref. 8.

Figures 2-2 and 2-3 show the errors associated with common tap configurations. It was concluded that a hole 0.020 to 0.040 in. in diameter, countersunk a half diameter to eliminate burred orifices, will substantially eliminate tap errors.

2.1.3 Mach Number Effects on Static Pressure Measurement

Up to Mach numbers of about 0.7 the stream-pressure tube (Subsec. 2.1.1) measures the stream-pressure subject only to the previously mentioned errors. However, at Mach numbers above 0.7 the situation changes; at some Mach number between 0.7 and 1.0, local shocks will stand on the probe, altering the local stream-pressure. This phenomenon was noted early in the investigation of the pitot-static tube (Ref. 9) as a random error of significant magnitude when the stream approached Mach 1.0. Under these conditions the indicated pressure depends on the location of the shock and may be subject to errors of the order of 6% of the difference ($p_t - p_\infty$).

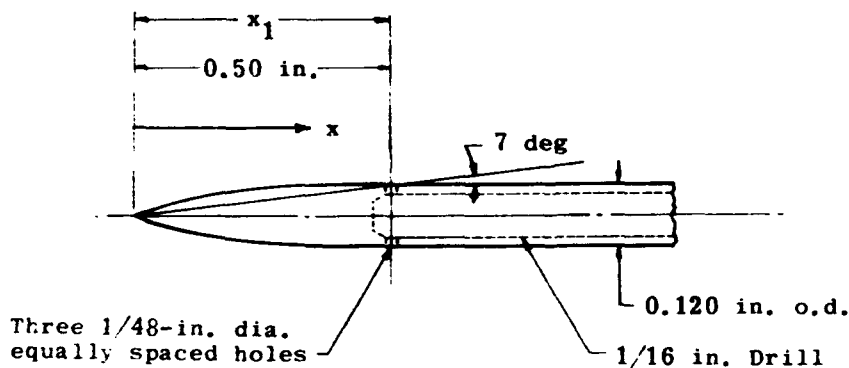
Above a Mach number of 1.0 the shock passes ahead of the tube and stands before the nose as a detached bow wave. The shock is substantially normal immediately adjacent to the tube, allowing use of the normal shock relations to predict the difference between the stream pressure immediately after the shock and the true stream pressure ahead of the shock.

$$\frac{p'_\infty}{p_\infty} = \frac{2\gamma}{\gamma + 1} M^2 - \frac{\gamma - 1}{\gamma + 1} \quad (2-4)$$

This relation is plotted in Fig. 2-4, which illustrates the error involved in the assumption that $p'_\infty = p_\infty$ above Mach 1.0

As the stream-pressure taps are moved downstream away from the shock, the indicated stream-pressure approaches the free-stream value ahead of the shock. Since the shock is a local disturbance, the stream-pressure must ultimately return to the free-stream value.

Using slender-body theory, it is possible to shape the nose of a pressure probe so that it measures free-stream static pressure independently of Mach number at supersonic speeds (Ref. 10). The pressure orifices can be placed far enough forward that the effects of the boundary layer are insignificant.



For the probe shown previously, slender-body theory gives the following pressure coefficient:

$$C_p(x) = \left[p(x) - p_\infty \right] / \frac{1}{2} \rho U^2 \quad (2-5)$$

$$= \frac{1}{\pi} \left\{ S''(x)_{x=0} \ln x + S''(x) \ln \left[2/R(x) \sqrt{M^2 - 1} \right] + \int_0^x \ln(x-t) dS''(t) \right\} - [R'(x)]^2$$

where

p_∞ = static pressure in the undisturbed stream

$R(x)$ = body radius at a distance x from the nose

$S(x) = \pi [R(x)]^2$, the body cross-sectional area

S'' = second derivative of S with respect to x

It can be seen that $C_p(x_1)$ becomes independent of M if the orifices are drilled at the point x_1 when $S''(x_1) = 0$. The other terms in $C_p(x_1)$ can be made to vanish by a suitable choice of $S(x)$ over the interval $0 < x < x_1$. For example, $S(x)$ can be expressed as a fourth-degree polynomial in x and the coefficients chosen so as to make $C_p(x_1) = 0$. The result is

$$R(x) = (\delta/\sqrt{\pi}) \sqrt{x^2 - 0.968 x^3 + 0.317 x^4} \quad (2-6)$$

where δ is a thickness parameter which can be chosen freely and x has been non-dimensionalized by dividing by x_1 . The resulting probe contour is shown in the previous sketch. Slender-body theory shows that the mean pressure in three holes drilled at x_1 , 120 deg apart around the circumference of the probe will be the same for a probe at an angle of yaw or aligned with the stream. (This is true only when the holes are not manifolded into a common plenum in the probe, in which case there is inflow and outflow through the orifices. This will affect the resultant measurement; see Subsec. 2.1.6).

Experimental results for the above probe are compared with the calculated error for a 5-deg conically tipped probe in Fig. 2-5, where the static pressure error is plotted versus Mach number. The calculated error includes the uncertainty due to machining errors up to 0.001 in. The results show an almost constant error over the Mach number range, which may be due to imperfections in the probe contour.

Another static pressure probe (whose configuration details are classified) shows considerably less error than the standard cone-cylinder probe and something less than half the error shown in Fig. 2-5.

2.1.4 Effect of Turbulence on Static Pressure Measurement

The scale of turbulence and the magnitude of the turbulent velocities vary from time to time at any location in a given stream. However, any given stream will possess at any one location an average scale of turbulence and rms values of the turbulent velocity components.

Even though the macroscopic streamlines of a flow appear to be straight and parallel over a pressure tap, a microscopic examination of the flow will reveal turbulent velocity components normal to the streamlines of the main flow. These components will cause a stream-pressure tap to read slightly above the local stream pressure. This effect was noted (Ref. 9) as an error of about 4% in velocity for pitot-static tubes. It has been theoretically analyzed (Ref. 11) and experimentally investigated (Ref. 12) in greater detail.

The pressure indicated by a pressure tap, $p_{\infty i}$, is the pressure of the stagnated gas inside the taphole. If the stream flows smoothly over the hole, this pressure will be equal to the stream pressure, p_{∞} , as discussed before; but if there are turbulent velocity components directed into the hole, $p_{\infty i}$ would undoubtedly be equal to a stagnation-pressure resulting from the local stream-pressure, p_{∞} , and the component of velocity directed into the hole.

The indicated stream pressure is given by

$$p_{\infty i} = \bar{p}'_{\infty} + \frac{1}{2} \rho (u')^2 \quad (2-7)$$

where

$p_{\infty i}$ = indicated stream pressure in the turbulent flow

\bar{p}'_{∞} = average stream-pressure in the turbulent flow

u' = mean turbulent velocity

The non-dimensional error, $\frac{p_{\infty i} - p_{\infty}}{\frac{1}{2} \rho U^2}$, is plotted as a function of the turbulent intensity, u'/U , in Fig. 2-6.

The results from Refs. 13 and 14 indicate turbulence levels as high as 10% may be encountered behind obstacles, depending on Reynolds number, flow configuration, and position downstream of the obstacle. It is probably safe to state that turbulence levels as high as 10% are a common occurrence, which according to Fig. 2-6 would indicate an error of approximately 1% in pressures measured in turbulent regions.

2.1.5 Effect of Non-Steady Pressures on Static Pressure Measurement

It is often necessary to measure stream and stagnation pressures that are pulsating or otherwise unsteady. Such measurements at best can offer only an average value of the fluctuating pressures and velocities in the generally disturbed flow. The reading will depend not only upon the variation in stream conditions, but also upon the characteristics of the instruments and the time response of lines and pressure sensing devices.

2.1.6 Effect of Probe Misalignment on Static Pressure Measurements

If the probe axis deviates from the true stream direction, the streamlines will be distorted along the entire probe (see Subsec. 2.1.3). Such distortion will of course produce local stream pressures differing from that of the undisturbed flow. If the deviation is large enough the flow will separate on the downstream surface of the probe and will produce pressure gradients around the circumference of the probe. If the probe is equipped with pressure taps around its circumference and is vented into a common duct the pressure gradients will produce internal flow, causing the indicated pressure to depend partly on the internal geometry. It is therefore difficult to predict how a misaligned stream-pressure tube will behave in any actual case, although it can be said that all such devices are very sensitive to yaw or pitch. In cases where it is necessary to measure the stream pressure in a flow of unknown angularity, the probe must be calibrated in a flow of known angularity as a function of inclination to the flow. The use of a conical probe with four separate orifices is recommended for such cases.

2.1.7 Effect of Velocity Gradients on Static Pressure Measurements

When a stream-pressure probe is standing in a transverse velocity gradient, the effects of the probe head and stem can be separated. For the case of a long cylindrical probe aligned with the stream, for example, no gradient in stream pressure can exist if the streamlines are straight and parallel. However, there is a gradient in velocity which results in a gradient in stagnation pressure. The fluid which is stagnated by the nose of the probe will therefore be subject to a pressure gradient increasing toward the region of higher velocity. The resulting surface pressure gradient will cause a flow in the boundary layer which results in a slight downwash of the stream in the vicinity of the probe. In addition, viscous forces along the tube surface are of greater strength in the region of higher velocity. This effect will also contribute to the downwash in the direction of the region of lower velocity. The effect of downwash on a stream-pressure measurement is probably similar to a slight yaw of the probe in a uniform stream.

The probe's stem may also exert an influence in the vicinity of the pressure taps. In a velocity gradient the leading edge of the stem will sense a stagnation-pressure gradient which increases toward the region of higher velocity. A downwash of fluid appears along the leading edge of the stem toward the region of lower velocity. This stem downwash may distort the streamlines about the pressure taps and thus introduce an error in measurement. This source of error is best eliminated by locating the pressure taps far enough away that they are not influenced by the stem. The 16 diameters between stem and taps employed on the "improved" probe shown in Subsec. 2.1.1 are probably sufficient.

In boundary-layer measurements, the near presence of a wall will constrain the downwash and alter its effects upon the measurement. For this and other reasons stream-pressure probes are not recommended for boundary-layer measurements. The wall tap or stagnation-pressure probe is usually employed with satisfactory results for boundary-layer measurements.

2.1.8 Reynolds Number Effects on Static Pressure Measurements

Reynolds number is proportional to the ratio of dynamic and viscous forces acting on a gas flow. The viscous forces set up velocity gradients on the probe, but as long as the gradients are symmetric no variation in indicated stream-pressure with Reynolds number would be expected. At extremely low densities, i.e., low Reynolds numbers, the gas enters a region of free molecular flow. Under these conditions an erroneous stream pressure indication might be expected due to molecular velocity components directed into the pressure tap. An analysis similar to that employed in dealing with turbulence should predict the magnitude of the error (Ref. 15).

2.1.9 Other Means of Static Pressure Measurement

Attempts have been made (Ref. 16) to construct self-aligning instruments in order to eliminate errors due to yaw and pitch in subsonic and supersonic streams. These devices consist of either a tube or a flat plate in gimbals with one or two degrees of freedom. Such instruments are usually considerably larger than a simple probe, and their use in many cases is therefore restricted.

The use of uncalibrated cones and wedges is reported in Refs. 17 and 18. The stream pressure at the pressure taps is calculated by two- or three-dimensional compressible-flow theory (see Subsec. 2.4). This method is quite accurate but offers little advantage in subsonic flow over the simple cylindrical probe.

One interesting development of a static pressure probe for subsonic speeds that is relatively insensitive to deviations in flow direction is reported in Ref. 19 and is commercially available. It consists of a small 1/8-in. diameter sphere supported by a thin stem placed downstream of the sphere. The pressure measured by a ring of minute holes just behind the sphere proved to be essentially independent of airstream direction for a large range of pitch and yaw angles. This wake pressure was found to be below true static pressure by an amount $K(p_t - p_\infty)$, where K was a function of the Mach and Reynolds numbers and of turbulence level. A pair of separation rings added to the sphere fixed the character of the wake and reduced the dependence of K on Reynolds number and Mach number for the subsonic flow. The stem support configuration was chosen to maximize insensitivity to pitch and to place the zero-pitch angle in the center of the usable range. The probe permits determination of time-average static pressure with an error of less than 2% of velocity head, despite flow direction deviation of ± 45 deg in yaw or -17 to $+35$ deg in pitch at 450 fps. At any other velocity between 100 to 1000 fps, angle ranges are comparable but slightly reduced. Its one disadvantage is that it requires an auxiliary reading of total head (e.g., with a standard kiel probe, see Subsec. 2.2.2).

The development of a method for measuring pressure on oscillating wings using a thin pressure-sensitive probe traversing the wing in a chordwise direction but not in contact with it is treated in Ref. 20.

2.2 Stagnation Pressure Measurement

The stagnation pressure, p_t , is often called the "total," the "impact," or the "pitot" pressure. More accurately the impact and pitot pressures are measured behind a normal shock and corrected to the stagnation pressure by means of the Rayleigh formula.

Stagnation pressure is measured by means of a tap at the stagnation point of a body inserted into the stream. This immersed body may have any shape, although a simple cylindrical tube with axis aligned to the flow direction has advantages. It is assumed that stagnation of the flow takes place with such rapidity that heat transfer and frictional effects are negligible. This assumption has been experimentally checked (Ref. 9) and appears to be true within 0.2% error to Mach number 1.0. In the absence of a transverse velocity gradient, the downstream probe geometry has no measurable effect (Ref. 2), even with the stem at the leading edge (see Subsec. 2.2.5). In the usual range of investigations, the stagnation-pressure tube is insensitive to tube geometry, Mach and Reynolds number effects, and considerable misalignment. A summary of pertinent information for the designer and user may be found in Ref. 21.

2.2.1 Supersonic Mach Number Effects on Stagnation Pressure Measurement

The relation between p_t , p_∞ , and the velocity or Mach number given in Eq. 2-3 holds up to Mach 1.0. Above Mach 1.0 the measurement is affected by a detached shock. Since the streamline entering the pressure orifice passes through the bow shock at normal incidence and the fluid is then brought to rest from a subsonic velocity, the stagnation pressure probe will measure the stagnation pressure downstream of the normal shock which differs from the value upstream. The magnitude of the difference depends upon the strength of the shock, a function of Mach number, and the ratio of specific heats, γ . This relation, commonly called the Rayleigh formula, is given for $M > 1.0$ by

$$\frac{p_t}{p_t'} = \left[\frac{2\gamma}{\gamma+1} M^2 - \frac{\gamma-1}{\gamma+1} \right]^{\frac{1}{\gamma-1}} \left[\frac{(\gamma-1) M^2 + 2}{(\gamma+1) M^2} \right]^{\frac{\gamma}{\gamma-1}} \quad (2-8)$$

where

p_t = stagnation pressure before the shock

p_t' = stagnation pressure after the shock

M = free-stream Mach number.

Figure 2-4, in which the Rayleigh formula is plotted, illustrates the error in assuming $p_t' = p_t$ for the supersonic flow of air.

2.2.2 Effect of Yaw on Stagnation Pressure Measurement

In most experiments the stream direction is only approximately known or else is to be determined. It is necessary to know the error due to a probable yaw of the stagnation probe or, better, to use a tube which is insensitive to large angles of yaw.

The common cylindrical tube with square leading edge possesses sufficient yaw insensitivity for most applications. The characteristics of this probe are presented in Figs. 2-7 to 2-10. A fairly complete design criteria for predicting the yaw sensitivity of stagnation-pressure probes in subsonic and supersonic flows is presented in a series of NACA reports (Refs. 22 to 25) which resulted from extensive experimental investigation. The data in these reports are presented in terms of a given probe's "critical angle," i.e., the angle of attack at which the

error in reading p_t reaches $\pm 1\%$ of the indicated dynamic head, $(\frac{\rho U^2}{2})$.

The least sensitive probes are the venturi-shrouded or Kiel probes whose configuration and performance are shown in Fig. 2-11. Of the simple probes, those with cylindrical heads are less sensitive to yaw than those with conical heads, which in turn are less sensitive than ogival heads. The least sensitive tubes were those having the largest pressure orifice for their size, the sharpest leading edges, and the smallest internal and external bevels. Figures 2-7 to 2-10 show their effects. It can be seen that all simple tubes have critical angles approximating ± 15 deg in subsonic flow, while in supersonic flow the critical angle is usually larger by 4 to 10 deg. For example, at Mach number 1.50, Ref. 26 indicates that the measured stagnation pressure, p_t , is constant up to an inclination of 22.4 deg and shows a 1% error at 28 deg.

2.2.3 Shrouded Stagnation Probe

Using a flow visualization technique, Kiel (Ref. 27) demonstrated that a yawed venturi tube maintained its internal streamlines parallel to the venturi axis up to angles of about ± 40 deg yaw. By Fuler's equation, the stagnation pressure is shown to be constant along a streamline in frictionless flow; thus a stagnation pressure tube placed inside the venturi should read the correct value. At yaw angles greater than 40 deg, flow separation occurs at the mouth of the venturi and causes errors that increase rapidly with yaw angle. In spite of many modifications (Refs. 28 and 29) to Kiel's original design, little improvement has been realized through any geometric change except rounding the mouth. This modification delays leading edge separation and permits about 20 deg more yaw with an error of less than $\pm 1\%$ of the dynamic head. Kiel's probe, its best modification, and their performance are illustrated in Fig. 2-11. These probes are commercially available.

2.2.4 Effects of Viscosity on Stagnation Pressure Measurement

At very low velocities it might be expected that viscous forces would cause the deceleration of the fluid to deviate from an isentropic process. This effect can be anticipated from the low Reynolds number and the fact that stagnation is no longer an instantaneous process as assumed previously.

The first direct investigation of the stagnation pressure tube at low Reynolds number was carried out in water (Ref. 30). Evidence from subsequent investigations (Refs. 31 to 34) appears to corroborate the initial work, which indicates that the stagnation pressure is correctly given down to a Reynolds number of 30 (based on the radius of the pressure orifice). Below this Reynolds number a viscous effect causes the indicated stagnation pressure, p_t' , to be higher than its true value.

The Stokes solution for flow about a sphere at low Reynolds numbers has been applied to explain experimental results for a tube which probably had a hemispherical leading edge. The derived relationship (Ref. 30) is

$$\frac{p_t' - p_\infty}{\frac{1}{2} \rho U^2} = 1 + \frac{3}{Re} \quad (2-9)$$

where

$$Re = \frac{\rho U r}{\mu} < 30$$

r = radius of the stagnation pressure orifice.

The extra term represents an error which increases with decreasing velocity. From a more precise measurement (Ref. 34) a similar criterion for the critical Reynolds number was found; here it was indicated that the last term of the above equation should be $5.6/Re$. Figure 2-12 illustrates this effect and the corresponding error. These results are recommended as the best data available.

Reynolds numbers of the order of 30 (corresponding to a velocity of 12 fps in atmospheric air using a tube of 0.010-in. diameter) are rarely encountered except in exploration of the boundary layer and at low densities (Subsec. 2.2.10). Boundary-layer explorations also suffer from effects of steep velocity gradients (Subsec. 2.2.6) which in combination with the viscous phenomena above can produce serious errors in stagnation-pressure measurements.

2.2.5 Minimum Spacing for Total Pressure Probes

Wind tunnel tests were conducted (Ref. 35) to determine the minimum critical spacing between total pressure probes for a Mach number range of approximately 1.9 through 3.7. The results of these tests indicated that no significant interference effects occurred at any spacing up to and including contact for two cylindrical probes tested in the free stream. Results of measurements in the boundary layer were not as conclusive. The pressure profiles measured by a blunt-edged wedge rake having zero-length probes were in error; however, indications were that useful approximations could be obtained from them.

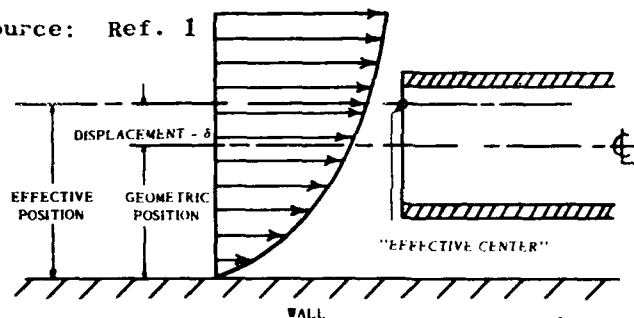
2.2.6 Effect of Transverse Velocity Gradients on Stagnation Pressure Measurement

All probes must have a pressure orifice of finite size. This size is governed by manufacturing tolerances and allowable response time. Most small probes use cylindrical square-ended hypodermic tubing

which is available in many sizes down to 0.004-in. o.d. To obtain a reasonable response time and yet maintain a very small tip it is desirable to employ fairly large tubing drawn down to a small orifice and flattened. Reference 36 describes a technique for manufacturing a probe having a pressure orifice 0.001-in. high by 0.010-in. wide which when used with optimum line length came to equilibrium about 7 sec after a pressure change of 21 in. Hg was applied. Reference 37 presents a method of manufacturing extremely small tubes by electro-deposition of metals on nylon fibers.

The pressure orifice should be made as small as possible in the direction of any existing velocity gradients. If the stream pressure, p_∞ , is constant across the mouth of the tube and the transverse velocity gradient is $\partial U/\partial y$, there will exist a gradient in stagnation pressure. The stagnation-pressure tube in general will not integrate this pressure gradient to give an indicated pressure, p'_t , representative of the velocity at the geometric center of the orifice. This is due to two effects: 1) The stagnation pressure is proportional to the square of the velocity and, when averaged by equal areas across the orifice, it will have a higher value than the stagnation pressure calculated from the square of the velocity at the geometric center of the orifice; and 2) the presence of the probe in a velocity gradient causes deflection of the streamlines toward the region of lower velocity. This deflection causes the probe to indicate a stagnation pressure that is higher than that which exists at the same location when there is no probe. Both of these effects diminish with decreasing probe diameter.

Source: Ref. 1



$$U' = \text{Velocity Corresponding to } p'_t - p_\infty = \frac{1}{2} \rho (U')^2$$

Reference 38 shows experimentally that the total effect could be expressed, as illustrated above, as a displacement of the "effective center" of the tube (i.e., the point at which the local velocity corresponds to the indicated pressure, p'_t) from its geometric center toward the region of higher velocities by an amount δ , given by

$$\delta = 0.131 D_o + 0.082 D_i \quad (2-10)$$

where

D_o = external diameter of the tube

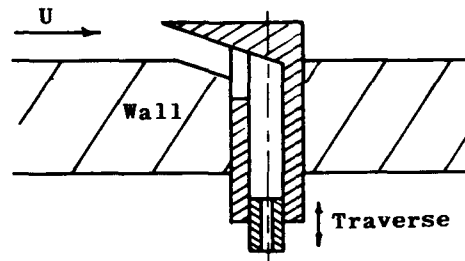
D_i = internal diameter of the tube

This is shown to be true in the range $0.1 < (D/q) (dq/dy) < 1.2$. Other experimenters have found that a rectangular, 0.050 by 0.015-in. orifice behaved as a circular orifice with a diameter equal to the dimension in the direction of the gradient. It should be mentioned that the results of both investigations were obtained in the wake of an airfoil. Turbulent effects discussed below may be a source of error in the data. The results may also be erroneous in a velocity gradient near a wall due to other boundary-layer effects discussed below.

2.2.7 Stagnation Pressure Measurement near a Wall

In boundary-layer studies, it is frequently desirable to make velocity measurements extremely close to a wall. The resultant combination of small probes and low velocities leads to viscous effects complicated by a velocity gradient, turbulence, and wall interference. Unfortunately, very little quantitative work is available for interpretation of results under these circumstances.

A surface probe designed by Stanton (Ref. 39) was calibrated by traversing the known velocity gradient in the laminar flow through a pipe of radius a . A one-sided rectangular tube was used, the bottom surface of which was formed by the wall of the pipe. The position of the outer lip could be adjusted as indicated below.



From the observed response of the instrument in a known laminar profile, the "effective position" of the tube was plotted against the "opening" of the tube, as shown in Fig. 2-13, and this plot was used as a calibration curve to interpret measurements near the wall in turbulent profiles. A finite reading was indicated as the tube opening approached zero. The displacement of the effective position from the centerline of the tube was not constant, but decreased as the opening increased. For small openings at low velocities, the effective position of the tube was actually outside the outer lip of the tube. One curve was faired through data taken at three velocities, but there is a definite indication of a velocity (or Reynolds number) effect.

These results are discussed in Ref. 30 and are shown to be predictable. Using Stokes' formula for creeping flow, the pressure on the nose of a sphere of radius r in a stream of velocity U is

$$p_t = \frac{3}{2} \frac{\mu U}{r} \quad (2-11)$$

For the parabolic velocity profile (Ref. 39) in a pipe of radius a , with centerline velocity U_c , the velocity at the center of a sphere in contact

with the wall (velocity at a distance r from the wall) is

$$U = U_c \left(\frac{2r}{a} - \frac{r^2}{a^2} \right) \quad (2-12)$$

Combining these two equations and letting r approach zero, the pressure close to the wall would be given by

$$p'_t = \frac{3\mu U_c}{a} \quad (2-13)$$

The corresponding effective probe opening, d' , at the wall is

$$d' = \sqrt{\frac{3\mu a}{2\rho U_c}} \quad (2-14)$$

In Stanton's experiment, $a = 0.1345$ cm; $U_c = 1910, 1140$, and 740 cm/sec; and $\mu/\rho = 0.148$. Inserting these values in Eq. 2-14 gives a value of d' corresponding to each of the given velocities. These points are plotted in Fig. 2-13. Stanton gives an average curve from his three sets of results at different velocities. Actually, at least two lines could have been drawn, which would indicate the velocity effect shown in Eq. 2-12. Since the stagnation tube is assumed to behave as a sphere and the velocity gradient and wall interference are neglected, the good agreement is probably fortuitous.

The same technique was employed with similar results in Ref. 40, and the data obtained for the effective displacement for a boundary-layer probe are presented in Fig. 2-14. Use of this method provided data on airfoil skin friction which in turn was used to compute stagnation-pressure loss. The values thus obtained agreed with those obtained from a survey of the wake.

In both investigations the assumption was made that the effective displacement, δ , was equal in the calculated laminar boundary layer and in the measured turbulent layer. The common assumption of a laminar sub-layer would substantiate the above procedure; but Ref. 41 shows (using the hot-wire anemometer) that the free-stream turbulence level may actually be magnified by a factor of the order of two in the turbulent boundary layer beyond the transition point. None of these matters have been resolved; many problems will arise if pressure measurements must be undertaken to determine boundary-layer velocities. Small changes in surface roughness, e.g., dust accumulations, may radically change the entire flow pattern.

At the present time the actual measurement-location can only be estimated, and the estimate is based upon the velocity gradient and Reynolds number corrections mentioned above. A probable turbulence error can be estimated from Fig. 2-6 if there is some knowledge of free-stream turbulence.

Current practice with velocity profiles involves the use of the velocity gradient correction given in the preceding subsection and neglects viscous and wall effects. In some cases, as indicated by Ref. 34, substantial errors due to Reynolds number effects may be hidden in published data. The technique utilized in Ref. 42 consists of measuring laminar velocity profiles and adjusting the effective position of the probe when it is in contact with the wall until the profiles extrapolated smoothly to the wall, and friction coefficients computed from velocity gradients agreed with those calculated from the momentum integral theorem. The same displacement was applied to turbulent profiles measured with the same probe. This appears satisfactory so long as probes are kept large enough to make viscous effects negligible ($Re_r > 30$, where r , the characteristic length, is the probe radius). In measurements made on a porous surface, the displacement of the effective center from the geometric center, δ , appeared to be about 0.3 diameter, a somewhat different value than that indicated for the solid wall.

The effect of probe shape on turbulent boundary-layer profiles obtained on a flat plate in a supersonic stream is indicated in Ref. 43. The same turbulent boundary-layer profile was traversed with an impact probe made of razor blades and also with the same probe equipped with a close-fitting rectangular shroud to increase the nose area. The two configurations registered the same pressure, within the accuracy of the measurements, except when the larger probe approached the wall closer than twice the probe height. This experience was consistent with that of Wilson and Young (DRL, University of Texas) although the former probes were of rectangular rather than circular cross-section.

Several methods of manufacturing a fast-response total head probe have been investigated (Ref. 44), and the following was found to be the most satisfactory.

Select a piece of 0.032-in. diameter brass tubing several inches in length. Heat the tubing and draw it until it fractures. The diameter will be reduced considerably at the fracture point, but the wall thickness may still be thicker than necessary. This thickness should be reduced to approximately 0.003 in., which can be accomplished by etching in a dilute copper sulphate solution (1 part copper sulphate, 2 parts distilled water). Next, slightly flatten the small end of the tubing and insert a very thin (0.001 in.) piece of steel shim stock 1/4 in. into the end of the probe. (If 0.001-in. stock is not available, thicker stock can be selected and then etched with a solution of 34% concentrated sulphuric acid, 42% ortho-phosphoric acid, and 24% distilled water.) Then flatten approximately 1/10 in. of the brass tube about the steel insert. Polish the surface of the probe with a fine whetstone and withdraw the steel insert. View the probe under a suitable microscope to verify the dimensions and smoothness of its surfaces. After the size and smoothness of the tip have been checked, the response time should then be determined. This step can be effected easily on a bench by using a U-tube with the probe connected in series with one leg and a pressure (or vacuum) source with the other leg. If the response time is not satisfactory, the tip probably was flattened too much. In order to reduce the length of passage, clip about 1/64 in. off the end of the tube, which should then be re-opened by filing or stoning. (In order to prevent clogging of the opening by filings, it is advisable to connect a pressure line to the probe during the re-opening operation. As soon as the orifice begins to open, the escaping air will prevent filings from entering the passage.) The clipping

procedure should be repeated until the response time is satisfactory.

The response time typical of probes made in this manner and used with optimum lead length is of the order of 5 to 7 sec for a 21-in. Hg pressure change.

Among the other methods that were tried during the developmental period was the drawing of glass tubing. However, the brittleness of glass tubes and the difficulty of shaping the tip accurately made their use impractical.

An interesting method of detecting contact between the probe body and the wall (Ref. 43) is shown in Fig. 2-15. When contact is first made the direction of motion of the orifice is reversed and the observed impact pressure begins to increase. The four profiles shown were obtained at different stagnation pressures at a Mach number of about 4.5; they exhibit the repeatability of the probe positioning mechanism that was used. The distance from the probe entrance to the wall was taken as half the separation of the probe from its reflection in the highly polished plate surface as determined with a cathetometer (Wild NIII precision level, manufactured by Henry Wild Surveying Instruments Supply Co., Ltd., Heerbrugg, Switzerland).

2.2.8 Turbulence Effects in Stagnation Pressure Measurement

Little has been published on the effect of turbulence on stagnation pressure readings. Kumbruch (Ref. 45) found by traversing a pitot-static tube in a channel behind a turbulence generator and integrating to get the total flow that the instruments read 3 to 5% high, depending upon design. This was attributed to the same factors that govern the behavior of a pitot-static tube in yaw, the turbulent fluctuations being considered primarily as variations in the direction of the main stream. For such an effect to be significant, it would appear that the scale of turbulence would have to be large compared with the dimensions of the stagnation tube.

Goldstein, using a different approach, integrated the equation of motion along a streamline in turbulent flow and showed that a stagnation tube should indicate

$$p'_t = p_\infty + \frac{1}{2} \rho U^2 + \frac{1}{2} \rho (u')^2 \quad (2-15)$$

where

U = mean stream velocity

u' = root-mean-square value of the axial turbulent velocity

This same equation can be obtained by assuming that the stagnation tube correctly reads the average total pressure corresponding to the mean velocity, U , and the parallel component of fluctuating velocity, u . Thus,

$$p'_t - p_\infty = \frac{1}{2} \rho (U + u)^2 = \frac{1}{2} \rho (U^2 + 2 Uu + u^2) \quad (2-16)$$

Since the time average of $U \cdot u$ is zero and the time average of u^2 is the square of the rms value, u' , both equations are the same.

The error involved in neglecting the last term of Eq. 2-15 is presented in Fig. 2-6. In order for this error to amount to 4% of q , the mean dynamic head, the intensity of turbulence, u'/U , must equal 20%. Since the error due to isotropic turbulence is the same for both p_t and p_x , the ratio of these quantities, as found by means of a pitot-static tube, should be independent of turbulence errors. It does not appear then that Kumbruch's results can be explained on the basis of isotropic turbulence.

Birdwell (Ref. 46) applies Eq. 2-15 to stagnation pressure measurements in turbulent boundary layer and finds that the correction is significant in some circumstances for calculating friction by the momentum theorem.

2.2.9 Effect of Periodic Pressure Pulsations on Stagnation Pressure Measurements

When a total pressure probe in a compressible medium is subjected to a fluctuating pressure, the manometer to which it is connected may not represent the time-weighted average of the applied total pressure because of certain nonlinear effects. The probe behavior can be predicted reasonably well within the limitations enumerated below.

1. The entrance tube (length L) should open into a tube of much larger diameter (e.g., four to eight times).
2. The flow across the ends of the tube should always be sub-critical.
3. The period of fluctuation, T , should be much smaller than the time constant, τ_o , of the probe and associated system and much larger than the time, τ_1 , required for a pressure disturbance to be propagated along the probe's entrance tube. If the speed of the pressure disturbance is taken as the speed of sound under ambient conditions, a , then

$$\tau_1 = \frac{L}{a} \quad (2-17)$$

The preceding limitations can be expressed by the inequality

$$2\pi \tau_o \gg T \gg \frac{L}{a} \quad (2-18)$$

4. The flow within the probe should be either laminar over a complete cycle or turbulent over a complete cycle. (It is possible to have laminar flow over one part of the cycle and turbulent over the other part.) Good agreement between the analytical method and experiment have been obtained if the Reynolds number

$$\begin{array}{ccc} 8000 > Re > 20,000 & & (2-19) \\ \text{laminar} & & \text{turbulent} \end{array}$$

Reference 47 gives all the necessary details for the method of correcting the pressure as averaged by the probe in the presence of oscillating flow and calculating a time-weighted average pressure. The averaging characteristics are a function of the wave shape of the pressure oscillation, the gas properties, the probe geometry, and the magnitude of pressures involved. Tests showed good agreement with the theoretical results when the maximum Reynolds number of the probe was less than 8000. The averaging error is minimized when the inside diameter of the probe's entrance tube is made as small as possible and its length as great as possible, consistent with an acceptable response time.

2.2.10 Low Density Effects in Stagnation Pressure Measurement

Recent research in flows at very low pressures has aroused interest in the response of stagnation tubes under such circumstances. Tsien (Ref. 48) discusses this problem for the case of pressures in the transition region between continuum flow and free-molecule flow, and he indicates that at low pressures viscous effects become important even at high velocities. This is a Reynolds number effect; for subsonic flow, the discussion of Subsec. 2.2.4 applies.

When impact and static pressure probes are used at low pressures, where the molecular mean-free-path becomes large compared with the tube diameter, flow conditions become more complicated and statistical methods may be needed for calculations. Under such conditions the effect of viscosity and the internal geometry require special attention. The viscosity effect perturbs the pressure and causes changes from its ideal value, and the internal geometry, if not handled with care, can cause response times that are too long to be usable. References 31 and 49 analyze the probability of a molecule escaping from the manometer reservoir through the pitot tube and conclude that the probability and hence the pressure in the manometer reservoir would depend strongly on the length-to-diameter ratio of the stagnation tube and leads. These calculations imply a pressure in the system low enough everywhere that the assumption of free molecule flow is valid. The University of California Institute of Engineering Research has contributed a considerable amount of work in this field, and this work is briefly treated in Refs. 15 and 50 to 56.

2.2.11 Effect of Entrained Particles on Stagnation Pressure Measurement

The presence of liquid or solid particles in a gas stream will cause a stagnation-pressure probe to indicate a pressure between the stagnation pressure of the gas and that of the gas-particle mixture. The magnitude of the difference between these two pressures depends on the mass of particles present in each unit volume of gas and upon the probability of the particles entering or bypassing the probe. Small particles tend to follow the gas flow and bypass the probe entrance; larger particles have a greater tendency to enter the probe and induce an erroneous reading. When liquid droplets are embedded in the flowing gas, they may be partially or completely evaporated by the rising pressure and temperature due to stagnating flow (Refs. 57 and 58).

No proven means of measuring the gas stagnation pressure in a heavily laden stream is available, although research along these lines

is underway. Reference 59 indicates that both the pitot pressure and the Mach number obtained from the ratio p_t'/p_t in a supersonic stream are virtually independent of the presence of condensation. However, the flowing gas should be dried whenever possible to obviate the effect of condensation on the static pressure (Ref. 60).

2.3 Pressure-Indicating Instruments

After an appropriate pressure-sensing probe is chosen and its performance evaluated, it is then necessary to select an adequate indicating instrument and pressure hookup. There are many pressure indicators of varying accuracy for use under different conditions. These indicators will be taken up under three headings:

1. Hydrostatic instruments, which depend upon the relative displacement of the surface of a fluid and are the most versatile low-pressure indicators.
2. Mechanical instruments, such as the Bourdon gage, which depend upon a pressure differential deflecting the walls of a metallic chamber. These mechanical indicators are used for moderately high pressures and are readily adaptable to use with recording or controlling devices.
3. Transducers, which translate pressure differentials into voltage outputs which may be recorded or used in connection with digital or analog computers.

The discussion under each heading will include the general physics of the devices, their ranges of operation (with appropriate instruments for each range), and an evaluation of the accuracy attainable under industrial and laboratory conditions.

It is important to realize that all pressure indicators measure a differential pressure, either between two pressures associated with the flow or between a flow pressure and some reference pressure source such as the atmosphere. If pressure data are referenced to atmospheric pressure, an accurate barometer must be utilized to measure this value so that the pressure differentials can be reduced to absolute pressure.

2.3.1 Hydrostatic Pressure Indication

The simplest form of hydrostatic pressure indicator is the U-tube manometer. Its elementary principle of operation affords much opportunity for ingenuity in design and construction to improve operating capabilities. Under steady conditions the difference between the pressures applied to the two vertical arms of the glass U-tube is indicated by the difference in height of two columns of liquid contained in the tube.

2.3.1.1 Common Manometers

Multimanometers.--The two readings that are required to measure a pressure differential in the U-tube are reduced to a single reading if one limb is made of a cross section sufficiently large that the

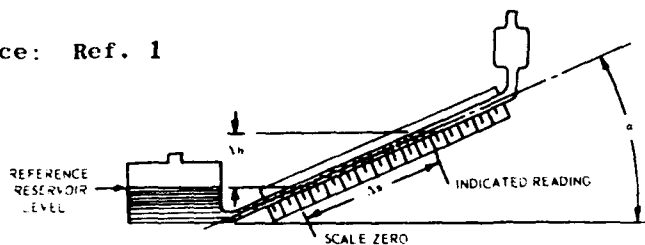
level of the fluid is virtually unchanged. Such an arrangement is used in the multimanometer shown in Fig. 2-16. The number of tubes in such a bank depends on the number of pressures expected to be measured at any one time, and the height of the tubes is chosen to include the maximum anticipated pressure differential. When a bank consists of a large number of tubes, it is customary to reserve the two outer tubes to read the reference or "zero" pressure. This reference level may be readily changed by raising or lowering the fluid reservoir which must be large enough in relation to the number of tubes so that the level may remain constant. It is wise to adjust the reference level to a pressure of the same order as the anticipated pressure since the accuracy increases as the pressure differential decreases. Overflow reservoirs should be attached to the ends of the tubes to preclude the possibility of blowing manometer fluid into the pressure lines in case the pressure limit of the system is exceeded. In some cases application of a dynamic pressure variation, such as experienced during start of the flow in a supersonic nozzle, justifies the use of a guillotine or clamp between the orifice and the manometer. The pressure lead is then opened after steady-state flow conditions are established, and clamped off again before the flow is stopped.

Frequent pinching of plastic tubing by the conventional guillotine method of clamping sometimes results in the tube sticking to itself when the guillotine pressure is removed. The staff of the Army Ballistic Missile Agency has tried a novel solution to this problem by inserting a solid bar inside the plastic tube. The application of high pressure all over the outside of the tube squeezes it over the core and prevents the tube from sticking to itself. When a large number of plastic pressure tubes are passed between the high-pressure rubber hose and the steel knife-edge of the conventional guillotine, there is some probability that all of the tubes will not be clamped off when the pressure valve is actuated. This probability can be reduced substantially by passing each pressure lead through the guillotine twice. A device known as the Boeing Pressure Valve (available commercially from the General Design Company, 631 30th St., San Diego, Calif.) can also be used as a pressure clamp. This device is discussed in Subsec. 10.1.1.

A cleverly-devised Australian multimanometer (Ref. 61) cuts off the liquid rather than the pressure air, and is claimed to be more accurate.

Inclined Manometers.--The sensitivity of a single-tube or multi-tube manometer may be increased many times by inclining the manometer at an angle to the horizontal.

Source: Ref. 1



From the sketch it may be seen that

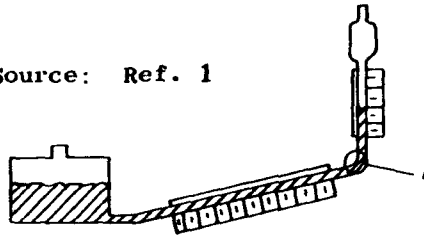
$$\Delta p = p_1 - p_2 = \Delta h \rho = \rho \Delta S \sin \alpha \quad (2-20)$$

and that the sensitivity increases as α decreases. Unfortunately, it is necessary to calibrate inclined manometers since small errors in the curvature or in the bore of the tube may produce appreciable errors in the displacement of the fluid. Manometers with slopes of 1/4 and 1/10 are available commercially with ranges of 3 in. of water and 1 in. of water, respectively. The instruments are very sensitive to levelling and are usually fitted with a pre-set spirit level.

These instruments are built to withstand average pressures up to about 100 psi, although the common instruments are intended for atmospheric pressures. They are rugged and suitable for industrial and laboratory purposes.

A combined form of U-tube which allows accurate readings at low pressure differentials is shown below. No accurate reading is possible at the knee of the tube, region A.

Source: Ref. 1



2.3.1.2 Manometer Fluids, Fittings, and Leads

U-tube manometers are available for reading differential surface heights from a few inches to 15 or 20 ft. With liquids of different densities, the range covers differential pressures from 0.03 psi (with alcohol) to about 120 psi (with mercury). The range of a given manometer can be calculated from the specific gravity of the available manometer fluids given in Table 2-1. In selecting the most suitable fluid, it may be helpful to remember that for each psi of pressure differential the displacement is roughly 2 in. for mercury, 9.1 in. for TBE, 27.2 in. for water, and 34 in. for oil. The properties of the more common manometer fluids, some discussion of the type of fittings to use with each fluid, and the precautions necessary for their use and handling (Ref. 62) follow.

Mercury.--This is by far the most commonly used fluid in manometry, and special care is necessary to avoid mercury vapor poisoning caused by inhalation and from contact with the skin. The use of a mercury vapor detector in the area where mercury is used is advisable. No brass or copper fittings should be used in contact with mercury, since these materials amalgamate with mercury. Iron fittings tend to cause scale and rust, which contaminate the mercury and clog the tubes.

Therefore, stainless steel fittings should be used whenever possible. The mercury should be cleaned at intervals in order to eliminate the contamination and foreign matter which may clog the tubes and reduce pressure-measuring accuracy.

Merriam Unity Oil.--This fluid is also commonly used. The effect of temperature on its specific gravity is shown in Fig. 2-17. Since this fluid attacks nearly all rubber compounds, only metal or glass fittings should be used. The gaskets may be made of neoprene. Naphtha or white gasoline in a well-ventilated room is recommended as an agent for removing unity oil from manometer tubes and other fittings. The fluid is toxic on prolonged contact with the body, and care should be exercised to prevent excessive spillage and continuous exposure to the fluid. Toxic action is evidenced by development of a form of acne which does not generally appear until after months of continuous exposure. Short or infrequent exposures and ordinary use of the fluid produce no toxic effects. Washing all exposed parts of the body with mild soap and water after contact is recommended.

Tetrabromoethane.--This fluid (known as TBE and acetylene tetrabromide) is soluble in alcohol or ether, but insoluble in water. It can be purified by rectification (fractionation). Its specific gravity is 2.98 to 3.00, and the variation with temperature is shown in Fig. 2-18. Moisture and ultraviolet light will promote decomposition of the fluid. Tests on small animals have shown insignificant toxic effects on breathing in a saturated TBE atmosphere for up to two hours exposure. Repeated exposures of 15 min a day also showed no ill effects. No data on its effect on humans are available, but it is expected that in a room with normal ventilation the concentration would be well under the saturation point and the health hazard very small. Skin irritations and blisters result from spilling on the skin. Washing with soap and water immediately after exposure will greatly reduce skin effects. Glass, stainless steel, or brass fittings are satisfactory for use with TBE, but rubber and most plastics will deteriorate rapidly. A material called Resisto-Flex (Resisto-Flex Corp., Belleville, N.J.) has been used satisfactorily where flexible tubing is required; however, Resisto-Flex is soluble in water.

Glass Tubes.--Glass tubing which will withstand average pressures of several hundred pounds per square inch is commercially available. Since all manometers have a definite maximum pressure limit, care must be exercised so that this limit is not exceeded at any point in the instrument. Manometer explosions are a common source of eye injury and mercury poisoning. The bursting pressures (Ref. 63) in atmospheres of German soda-glass tubing are tabulated below.

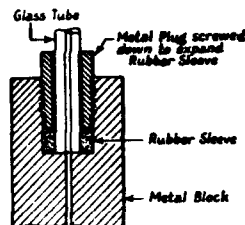
Bursting Pressures (atm) of German Soda-Glass Tubing

Wall Thickness (mm)	Tube Bore (mm)						
	1	2	3	4	5	6	7
1	---	310	280	230	220	150	140
2	570	---	340	---	330	240	220
3	560	420	460	400	---	---	230
4	---	450	---	400	310	320	280

It is advisable to apply a factor of safety of not less than two and to shield the tube by a cover plate of transparent plastic to protect the observer in the event of failure.

Attachment.--An arrangement (Ref. 64) for attaching a glass tube to the metal lead from a manometer is shown below.

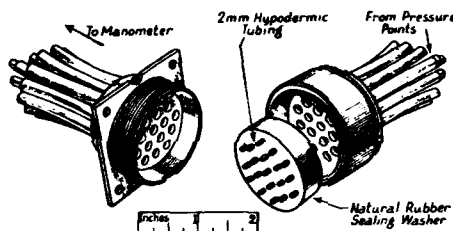
Source: Ref. 64



This method was found to be satisfactory (at NPL) for internal pressures up to 25 atm. At this pressure no trouble was experienced with the use of rubber or grease in the joints, but it should be noted that it is dangerous to use these materials in compressed oxygen systems. A similar arrangement, but substituting a teflon sealing gasket in place of the rubber sleeve, has been used at OAL.

A convenient method for connecting pressure leads to a multi-tube manometer has been developed at the Royal Aeronautical Establishment (Ref. 65). With this method the manometer leads are permanently attached to the rear of the socket, as shown in the sketch below.

Source: Ref. 64



The leads from the model are attached to the rear of a plug which fits into the socket, and the plug is located by a key and held in place by a threaded cover. A rubber washer fitted with a number of short lengths of hypodermic tubing is placed between the plug and the socket to prevent leaks. The one disadvantage of this method is that all leads have to be broken and re-connected if only one lead is found to have a leak in the connection.

Manometer Leads.--In the past, rubber tubing has been the most common means of connecting the manometer to the pressure orifice. The tubing is forced over the appropriate nipples, which may be greased with petroleum jelly, or (for low pressures) with one of the high-vacuum greases which are commercially available. Tubing which comes into contact with mercury should be free from sulphur in order to avoid contamination of the mercury.

Commercial plastic tubing has a number of advantages over rubber. It does not deteriorate and is resistant to many chemicals. The transparent variety has obvious incidental advantages. The tubing

is available in a wide range of sizes and in multi-tube strips, some already color-coded for ease in making extensive pressure hookups. Nevertheless, for some purposes the natural properties of rubber are indispensable.

If the internal pressure is to exceed that of the atmosphere, the tube should be bound to the nipple with safety wire. Rubber is often inconvenient for long leads, and it is then usually preferable to employ copper or brass tubing with rubber attachments at the ends. The soft metal tubing is convenient because it is easy to bend, retains its shape, and is easy to solder. Although reinforced rubber tubing which can withstand any internal pressure likely to be encountered in aerodynamic testing is available, copper or brass leads with soldered joints for internal pressures in excess of about three atmospheres are generally preferred. If stainless-steel tubing is to be used in any pressure system, it should be pressure checked before actual use because small cracks sometimes exist in the material when it is delivered.

The tendency for a rubber lead to collapse under sub-atmospheric internal pressures may be avoided by inserting a metal spring into the interior of the tube, but for very low pressures it is advisable to keep the length of rubber tubing in the leads to a minimum. Outgassing in plastic tubing is critical at the low pressures encountered at high Mach numbers. According to Kendall of NOL, Saran tubing is the only plastic tubing that is almost as good as metal; but it also has the disadvantage of being nearly as stiff as metal.

The leads should be so arranged that they can be rapidly identified along their whole length. With rubber or plastic leads, care must be taken to prevent the formation of kinks, particularly at corners. These suggestions are especially pertinent for the use of multi-tube manometers since much time may be saved by an orderly layout, particularly when a leak is being sought.

Suitable fluid traps must be installed close to the pressure taps of a system measuring pressures in moist or droplet-laden gas. The entrapped fluid should not, and cannot, be properly removed by blowing with the mouth or compressed air. First, water is introduced by condensation and second, much of the fluid is merely smeared along the inner hose walls, ready to re-collect later. The best procedure is to hang the hose up for draining. Later, it should be internally washed with an appropriate solvent if the manometer fluid is non-volatile.

Actual fluid pressures always oscillate slightly. This effect can become severe if the fluid column has a natural frequency close to the driving pressure frequency. A short length of capillary tubing or a tubing clamp on the pressure lines can be manually adjusted to give critical damping and a minimum variation in the indicated reading.

Leaks.--All pressure lines and connections must be tight because slight leaks in systems with small pressure orifices or small-diameter tubing can introduce sizable fixed errors which are difficult to detect in the final data. All connections should be made with a soft and a hard material, with a properly clamped or safe joint of at least two tube diameters in length. Metal-to-metal couplings are acceptable if great care is employed in installation, and periodic pressure checks are effected. For high pressures, where plastic or rubber tubing will

be overstressed, a well-designed glass-to-metal joint can suffice if a rubber or teflon O-ring or gasket is incorporated. Rubber tubing is often porous and will split with time when under tension at the joints. Further assurance against leakage can be realized by painting joints carefully with a hardening material such as glyptal paint.

For the best leakage test the system should be pressurized to a pressure which exceeds that to be measured, and the pressure system should subsequently be sealed. The indicating instruments should then be observed for the system's rate of pressure decline. As a guide, the leakage of the sealed, pressurized system should be compared with the rate of pressure decline in the same system (same initial pressure level) with the pressure taps open. If the sealed system's pressure-decline rate is one-tenth that of the open system's rate, significant errors may be anticipated. The pressurized system may be checked by painting all joints and other suspected parts with a soap solution. This check will usually reveal any leaks.

Sometimes it is difficult to apply a positive pressure to the system. If a variable pressure can be applied to the sump of a multiple-tube manometer, either by raising or lowering the level of the sump, the fluid in the manometer tubes can be raised to a high level on the board. Next, the orifices can be sealed off with scotch tape and the sump level lowered, and system leaks can then be detected by a sag in the level of any of the tubes. Leak detection by this method, i.e., applying a suction on the line, is not as foolproof as a positive pressure because a small leak may seal itself against entrance of higher-pressure external air and yet readily leak under a positive internal pressure.

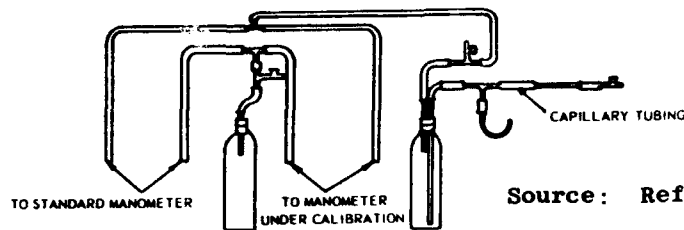
Good testing practice for any but the most simple pressure system requires: 1) A complete pressure check of the system prior to testing; 2) at least one check, and possibly more, during an extended test program; and 3) a final check at the end of the test. To enhance the confidence level of test data, the repair of leaking or plugged pressure leads must be carefully documented.

2.3.1.3 Accuracy of Simple Manometer Systems

The error introduced by the indicating equipment is often larger than that associated with the probe. These errors are often fixed errors which are not revealed by scatter in the final data.

Suspected or non-standard instruments should be calibrated over their full range against an instrument of known accuracy. However, the accuracy of the calibrated instrument should not be taken as that of the standard instrument (which is often done) because such practice can lead to errors larger than anticipated. That is, the calibrated instrument may possess normal repeatability, reading, or zero-shift errors which are larger than those of the calibrating instrument and which are hidden during a careful calibration. Once calibrated, the instrument should be assigned a probable error, depending upon its design.

The apparatus (Ref. 66) illustrated in the next sketch is recommended for calibration. This apparatus eliminates atmospheric pressure fluctuations and reduces thermal effects by evacuating instead of pressurizing the reference reservoir.



Source: Ref. 1

The accuracy of a manometer depends upon the factors discussed below.

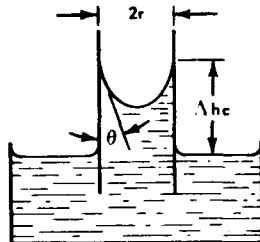
Uniformity of the Bore.--Except for the inclined manometer, any small variation in the bore of the tubes does not appreciably affect the differential height. In the case of long, large-bore tubes it may have a slight effect on the zero level.

Meniscus-Capillary Errors.--The shape of the surface of separation between two fluids at rest is a function of the relative magnitude of the gravity forces, the forces of cohesion between the fluid molecules, and the forces of adhesion between the fluid molecules and those of the container walls. The shape of the wall-boundary of the fluid depends predominantly upon the last two phenomena, while gravity and cohesive (surface tension) forces govern the shape of that part of the surface at a distance from the walls.

The governing attractive force in a fluid is usually described by the tendency of the fluid to wet its container walls. If the fluid wets the wall, the meniscus is concave upwards and adhesive forces predominate. If the fluid does not wet the wall, the meniscus is concave downward and cohesive effects predominate.

Water, alcohol, kerosene, and many other fluids wet the container; mercury and some others do not. Detergents and other wetting agents are often added to water to minimize the meniscus error. If the meniscus always retained the same shape, its existence would introduce no error. However, sticking of the meniscus as the fluid moves up or down the tube changes its configuration, introducing random errors in the determination of the column height. To minimize this error, the height of the column is taken at the center of the meniscus. The shape of the meniscus is also a function of the tube diameter; the error decreases with increasing tube diameter. Tubes of 3/8-in. or larger bore are recommended, if this error is to be minimized.

Capillary forces not only produce a meniscus, but cause an elevation or depression of the entire column. This effect is also a function of tube diameter.



A useful approximate relation for small tubes such as shown in the sketch is

$$\Delta h_c = \frac{2i \cos \theta}{\rho r} \quad (2-21)$$

where

Δh_c = maximum capillary elevation

r = inside tube radius

i = surface tension

θ = fluid angle at the wall

ρ = fluid density

(all in consistent units)

When the fluid wets the tube, θ is zero and Δh_c becomes $\frac{2i}{\rho r}$. Values of $\frac{2i}{\rho}$ are given in Table 2-1 for many different fluids. The angle θ depends not only on the fluid, but also on the surface material, roughness, and whether the wall is wet or dry as the meniscus passes over it. Since θ is usually quite small, the tabulated values of $\Delta h_c r$ in

Table 2-1 are a fair approximation for the general case. The surface of a tube in which the fluid is falling is wetted, and one where it is rising is not wetted; hence one source of error is lessened if the levels are allowed to oscillate before coming to equilibrium. This equation should therefore be regarded only as an indication of the uncertainty interval due to capillarity and not as a correction factor.

Source: Ref. 1



The meniscus is elongated in the inclined manometer, as shown above, the distortion increasing with the slope angle. The capillary uncertainty interval from Table 2-1 should be applied to the reading in vertical inches of fluid. Thus, there is a minimum angle below which increased sensitivity is trivial in comparison to the capillary error. A slope of 10:1 is probably the practical limit.

Density Gradients.--Temperature gradients are the only phenomena which will produce significant density gradients in a manometer. Variation of fluid density with pressure is negligible up to pressures of many hundred psi. If a temperature gradient is known to exist along the manometer, a correction can be calculated from the coefficients of thermal expansion given in Table 2-1. This effect is usually negligible in the simple manometer, but may become significant for very long manometers or in the micromanometers to be discussed later. Instruments with expected errors of the order of 0.001 in. of water or less must be shielded from thermal effects (drafts and direct sunlight) by

an appropriate zone box or agitated liquid bath. Thermal expansion of the fluid in an instrument with an inadequate reservoir will cause a shift in zero, but this is easily corrected with a shift of scale or reservoir level.

Scales.--Common scales can be read to 0.05 in., which is a smaller value than the probable error of a simple manometer. Cross hairs, microscopes, illuminated fields, and fluid coloring are often used to make the meniscus more visible and to eliminate parallax. Useful coloring agents are presented in Table 2-1. Thermal elongation of scales is negligible compared to fluid expansion errors.

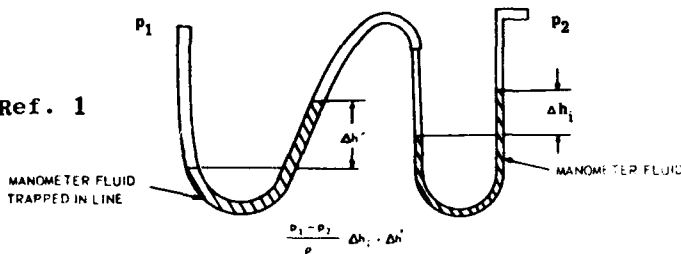
Service Conditions.--Evaporation and mixing of the fluid or fluids will change the fluid density and instrument calibration, and will shift the instrument zero, which is easily compensated by periodic scale adjustments. Changes of density often occur where two fluids are in contact and diffuse into one another. This problem occurs when the bi-fluid U-tube is used. Some fluids are mixtures and may be subject to density changes through selective distillation. In any event, periodic checks should be made of fluid density.

Dirt on the walls of the manometer tubes not only obscures the reading, but also causes random changes in meniscus shape and capillary elevation as the fluid traverses the tube. Proper cleaning reduces the error; some fluids are solvents and tend to be self-cleaning (Table 2-1; also see Subsec. 2.3.1.2).

On multi-tube manometers (such as that shown in Fig. 2-16) using mercury as the fluid, a simple feature of manometer design can markedly decrease the frequency of board disassembly and tube cleaning. The mercury well at the base of the tubes is sloped at an angle of approximately 6 deg. The well is made of stainless steel, and the stainless steel nipples are inserted into the common well so that the opening is well below the top of the mercury filled well. The last nipple at the upper end of the well does not penetrate the mercury and is attached to a tube of much larger bore. Since dirt and most contaminants float on mercury, the debris does not enter any of the working tubes, but floats along the well to the last nipple and deposits on the walls of the larger-bore "scavenging" tube.

Pressure hookups should be open, free of leaks, and free of liquid. If fluid is accidentally blown into the pressure lines, great care must be exercised to remove all the fluid from the lines. Any fluid accumulation which does not lie in a perfectly horizontal line will produce an error. This type of error is illustrated in the sketch below, where Δh_i is the indicated reading and $\Delta h'$ is the error due to fluid in the hose connection. This is a common and often sizable fixed error which is difficult to detect in the final data.

Source: Ref. 1



2.3.1.4 Precision Manometers (Micromanometers)

Many devices have been designed to increase the sensitivity of the manometer by reducing one or more of the sources of error. Null-reading instruments in which the liquid-gas surface is stationary reduce the inherent capillary errors. Optical instruments may reduce scale reading errors. A manometer with an accuracy of less than 0.01 in. of water is commonly called a micromanometer. Various forms of micromanometers are described below.

Coles' Low-Pressure Multimanometer.--This manometer (Ref. 43) was designed to measure a number of very low pressures under the handicap of a very high upper limit on the pressures. A conventional manometer using a light fluid and low reference pressure was deemed most suitable for the anticipated pressures in the range of 2 to 15 mm Hg.

As a compromise for the desirable properties of low viscosity, low volatility, and uniform wetting characteristics, one of the silicone fluids (DC-200 fluid, manufactured by Dow Corning Corporation, Midland, Mich.) with a viscosity of about 10 centistokes appeared to be quite satisfactory. The specific gravity of the fluid was measured under the conditions of use.

Each of the 40 tubes in the manometer was provided at the top with a two-way sliding valve, shown in Fig. 2-19, so that any tube could be connected either to the reference vacuum (equalized position) or to the tunnel pressure (reading position). The sliding valves could be operated by remote control through individual pneumatic pistons, which were supplied with air at 125 psig through a solenoid valve. The sliding valves were spring-loaded to assume the equalized position when the actuating air pressure was less than about 80 psig, and the valves could also be operated manually and locked in either position when desired.

Experience with low-pressure manometers suggests several precautions for preventing damage to the manometer in case one or more of the tubes is exposed to a pressure higher than the range of the instrument, in the present instance 110 mm Hg abs.

Banks of ten tubes were manifolded together to a single fluid reservoir and the four reservoirs were, in turn, interconnected through a system of valves. The manifolds, however, were slanted at about 45 deg and were placed at the rear of the manometer at a position well above the lowest point of the individual tubes. Thus, if air entered the manifolding system under pressure through a tunnel line, the manometer fluid would be forced into the reservoir and the tubes would be by-passed. After all tubes of the manometer are equalized, the reference vacuum may be restored and the manometer made ready for use in about half an hour. It is essential to provide adequate drainage into the reservoir or glass tubes for the valve system passages, since dissolved air may occasionally carry liquid into the valve block when the manometer is being evacuated.

The manometer also has provisions for connecting any one of the model pressure lines to an auxiliary vacuum pump or to a source of pressure through an auxiliary passage in the valve block, so that model lines may be checked for leakage or identified.

Under steady conditions and when reasonable care is exercised, the difference in pressure between the reference vacuum and a given model orifice can be read with an accuracy of about 0.3 mm of silicone fluid, or 0.02 mm Hg. For pressures greater than 10 mm Hg the reference pressure of 20 microns can usually be neglected, and the manometer thus becomes an absolute pressure instrument. However, when pressures are measured in this lower range, care should be taken to establish equilibrium between the pressures at the manometer and at the model. The time required to reach equilibrium may be of the order of ten minutes, and since two or three minutes are sufficient to read the manometer fluid levels visually, it appears that photographic recording of data at low pressures is not always advantageous and may even involve a sacrifice in accuracy without a compensating saving in time.

McLeod Gage.--The McLeod gage is a primary standard for measuring very low absolute pressures (Ref. 67), i.e., 0.001 to 1 mm Hg. A special McLeod gage (Ref. 68), developed for the University of California Low Density Wind Tunnel, is unique in that it has a low, flat, stainless-steel reservoir to contain the mercury; a large glass compression volume; and long, relatively large diameter, precision bore capillaries. This combination of features has resulted in an instrument capable of measuring pressures from a small fraction of a micron of mercury to 2.38 psf (850 microns) with an accuracy of approximately 0.2% in the range from 35 to 850 microns (0.096 to 2.38 psf). A precise mechanism to measure the differential heights of the mercury columns has also been provided. Optical elements, one fixed at the top level of the closed capillary and one mounted on a translating nut, are used to view enlarged images of the menisci. The nut is positioned by a hand-driven precision screw. The differential height is automatically indicated by a five-digit Veeder-Root counter connected to the precision screw with approximate gearing, the least count being 0.001 in.

Precision Oil Manometer.--The precision oil manometer (Ref. 69), capable of measuring pressures up to 5.5 psf (20 mm Hg), can be used whenever rapid and continuous (as opposed to sampling) measurements are desired. Special design features include the large-bore glass tubing instead of the usual capillary tubing and the large-size valves in the manifold block. Precision screws, hand-driven and with suitable gearing, control the level of the optical elements used to view the menisci. To avoid errors, a mechanical differential is geared directly to the screws, with the output shaft connected to a mechanical counter. The gearing and screw characteristics are such that the counter registers directly in thousandths of an inch. The differential height can be determined immediately by the operator.

Precision Mercury Manometer.--For measuring stagnation pressures in a low-density wind tunnel (Ref. 67), a mercury manometer can be built to follow conventional wind-tunnel design procedure with a large, glass, mercury reservoir, which can be connected to the pressure being measured, and a single vertical tube connected to a very low reference pressure. An optical element is used to view the enlarged image of the meniscus, with a motor-driven, precision screw controlling the level of the optics mounting platform. The height of the column is indicated by a five-place mechanical counter connected directly to the screw. Cold traps are used to isolate the mercury reservoir and column from the reference pressure and tunnel areas. This precaution is taken to prevent the migration of mercury vapor.

Precision Thermistor Manometer.--The desire to measure local model pressures with some degree of accuracy at very low densities has led to the development of a special temperature-controlled precision thermistor manometer. This instrument (Ref. 70) makes use of a small-volume heat conductivity or Pirani-type gage. By reason of its small size and electrical operation, this sensitive element can be located within the tunnel shell (open-jet with enclosing chamber), thereby reducing the time response of the gage system, or for a given time constant, permitting a much smaller sensing orifice (Ref. 71).

Flow Corporation Micromanometer.--This commercially available micromanometer (Ref. 19) is designed to measure small pressure differences with an accuracy of ± 0.0002 in. of manometer fluid over its 2-in. operating range. This tolerance corresponds to a pressure difference of six millionths of one psi with the manometer fluid supplied. The unit, shown schematically in Fig. 2-20, operates on a simple principle first proposed by Prandtl. Its basic function is to measure the unknown pressure difference between two points. To achieve this measurement (referring to the schematic) the first point is connected by tubing to Tap 1 (the "static" tap) and the other point to Tap 2. The zero of the instrument is then determined by turning Valve 2 to "zero" (placing the static pressure at both points A and B) and adjusting micrometer-screw C until the meniscus coincides with the hairlines viewed through the optical eyepiece. This micrometer reading is the zero value. The unknown pressure difference is placed between points A and B by turning Valve 2 to the "on" position and adjusting the micrometer screw until the meniscus again coincides with the hairline. This reading minus the zero value is the desired pressure difference in inches of manometer fluid. Valve 1 permits observation of any of the pressures at Taps 1, 2, 3, and 4 independently against a closed reservoir.

NACA Micromanometer.--This industrial and laboratory instrument employs an inclined tube connected by flexible tubing to a large reservoir (Fig. 2-21). The inclined tube, with a slope of about 20:1, is raised and lowered by an accurate screw. The reference level is set at zero pressure differential by elevation of the reservoir until the axial point of the meniscus coincides with a mark scribed on the inclined tube. After application of the pressure differential, the null is re-established by raising the inclined tube until the axial point of the meniscus again coincides with the mark on the tube. The value of Δh is then read by noting rotations and fractions of rotations of the screw on a suitably calibrated dial. The meniscus should always approach the null mark in the same direction, maintaining the meniscus shape as constant as possible. Alcohol, kerosene, or alcohol-water mixtures (2:1) minimize capillary distortion.

The screw should be accurate within 0.005 in. in lead to reduce mechanical errors. The reservoir cross-section should be at least 40 times the area of the connecting hose to minimize changes in reservoir level due to variations in hose diameter. Since the length of the fluid column is constant, there is no fluid outflow from the reservoir to cause error.

The normal accuracy of this instrument has been determined experimentally to be 0.001 in. of water. Within this limitation, it may be taken as a pressure standard without further calibration. Its advantage is a range of 10 in. or more, combined with rugged construction.

This manometer has also been fitted with a Chattock-type bubble indicator and microscope as described in Ref. 1, giving accuracies of the order of 0.0001 in. of water with a very accurate lead screw or suitable calibration. Such modification introduces the same practical limitations as other bubble-indicating equipment.

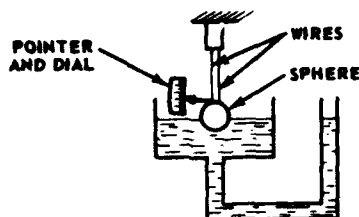
Foxboro Micromanometer.--Most micromanometers are limited to operation close to atmospheric pressure by strength considerations. There is a demand in research for an accurate micromanometer which will withstand average pressures of 100 psi or more. The Foxboro Company's simple hydrostatic U-tube manometer fitted with a sensitive electrical level-indicator fulfills this requirement. This instrument employs large glass tubes (2 in. i.d.) of accurate bore to minimize capillary and meniscus errors. The tubes are supported in an enclosing heavy steel frame which reduces high pressure deflection errors. The level of the liquid (water with a wetting agent) is indicated by a special brass float guided up one tube with little friction. The position of the float is determined by a center-tapped induction-coil traversed and nulled on the float by a micrometer which then indicates the fluid level above the zero position. The split coil forms two branches of a phase-sensitive impedance-bridge which is balanced at only one fixed position of the float, relative to the coil. Balance of the bridge is noted by a suitable galvanometer operating through a modified SR-4 strain-indicator.

The instrument has the advantage of a range of 6 in. or more, with good accuracy at average pressures of 0 to 100 psig. The device is rugged enough for industrial use and is adaptable to automatic control and/or recording service. It may be regarded as a standard within its accuracy limitations.

Reference 72 shows an experimental determination of the inherent accuracy of this instrument. An uncertainty interval of 1×10^{-3} in. of water at 20:1 odds over the full scale was reported. A human error uncertainty-interval based on 20:1 odds of approximately 0.4×10^{-3} in. of water was also reported. Above 20 psig, zero-differential readings are necessary at the required average pressure level to eliminate zero-shift errors due to frame deflection, etc. Thermal effects require zero-differential readings at frequent intervals.

Concentric Tube Manometer.--Another micromanometer for measurement of differential pressures greater than 10^{-4} in. of water with tolerable accuracy is reported in Ref. 73. The instrument uses concentric tubes to form fluid passages and provides for remote indication of the level in the central tube by means of a mirrored float and telescope and scale arrangement. The greatest instrument sensitivity obtained was 3.15×10^{-5} in. of water applied pressure per millimeter of scale reading. Greater sensitivities are reportedly possible.

Spherical Float Micromanometer.--This Italian micromanometer (Ref. 74) consists of a spherical float suspended from two wires and floating in the fluid as shown in the next sketch. A very slight change in fluid level rotates the sphere markedly.



"Barn Gate" Micro-Pressure Gage.--The "Barn Gate" micro-pressure gage developed by the GALCIT hypersonic tunnel staff has a maximum measurement range of one inch of silicone oil with an accuracy of 0.001 in. The glass tube which was fashioned in the shape of a barn gate was pivoted at one end, and the other end was raised or lowered by a micrometer. A very fine wire located in the tube opposite the pivot showed the balance point when it penetrated the liquid. The point of penetration was observed by means of a microscope.

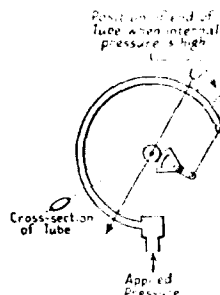
Single-Tube Micromanometer.--This single-tube micromanometer (manufactured by the Ideal Tool Co., Cheyenne, Wyo.) has been used successfully at the AEDC Gas Dynamics Facility when protected against slight temperature changes. The unit, obtainable in 30- and 80-in. heights, has a fluid height accuracy of ± 0.001 in. The inner bore of the tube is approximately 1 in. in diameter. A readout system consisting of two photo-cells mounted on a lead screw to trace the meniscus can be provided. The lead-screw motion is digitized by a Coleman digitizer.

2.3.2 Mechanical Pressure Indicators

Pressures greater than about three atmospheres are often measured by mechanical gages (on a pressure-indicating dial), usually as the excess of the pressure over the ambient atmospheric pressure. Most of the industrial gages currently in use are adaptations of the simple principle of the Bourdon gage.

2.3.2.1 Bourdon Gage

The common mechanical-deflection instrument is the Bourdon gage. In this instrument, illustrated below, a circular metal tube is deflected by the differential between internal and external (usually atmospheric) pressure.



Source: Ref. 64

The Bourdon-tube deflection is communicated through a rack-and-pinion or helical-cam mechanism to a pointer. The range of this type of gage extends from about 1 in. Hg to thousands of psi. The instruments are subject to frictional sticking and should be rapped or vibrated for accurate readings. The smallest gage division usually indicates the order of the error in a new instrument. For accurate data, the gages must be periodically calibrated on a dead-weight tester over the entire scale-range. At the same time, instrument repeatability should be investigated in order to determine the likely error from frictional sticking. Manufacturers supply data on the approximate accuracy of new gages. Further information on Bourdon gages is given in Refs. 75 and 76.

2.3.2.2 Bellows or Diaphragm Gages

Instruments which rely upon the deflection of a sylphon bellows or metallic diaphragm are available for accurate indication of differential pressures as low as 0.01 in. of water. Such a mechanism is commonly employed in recording pressure indicators and in barometers. These devices are readily adaptable to automatic control, but are delicate and unsuited for experimental work in general. Manufacturer's catalogs (e.g., Ref. 77) may be consulted for detailed specifications of the various types.

2.3.3 Pressure Transducers

Automatic recording of pressures is obviously needed to avoid excessive time delays between test and evaluation, to reduce human errors, and to make pressure testing competitive with force testing in terms of time. As a result, there has been rather extensive developmental work in the field of pressure transducers of various types. Transducers, in general, used as pressure-measuring devices have a voltage output which can be recorded on any proven analog-to-digital recorder. Such outputs can also be amplified and operated on in digital or analog form to produce the desired coefficients or ratios. The main problems with transducers involve 1) accuracy of reference pressures, 2) effects of temperature, and 3) size of transducer, i.e., small enough to mount inside the model to minimize lag and leakage problems.

Pressure indicators employing unbonded strain gages to measure the deflection of a metallic diaphragm have been developed into commercial instruments. These gages offer the advantage of electrical recording and/or control. They will accurately measure non-steady pressures with a frequency up to about 300 cps, depending on the particular gage. The use of an unbonded strain gage reduces the mass attached to the diaphragm, giving the gage a higher natural frequency than that of common pressure-indicators. If the pressure-indicator is attached to a pressure probe and a pressure hookup, a dynamic evaluation of the indicated pressure output must include the system characteristics as well as those of the diaphragm-strain element. These gages are commercially available with an accuracy of 1% of full range and a sensitivity of 0.1% of full range. The available ranges run from 0 to 0.5 psi, to 0 to 10,000 psi (Ref. 78) differential or "gage" pressure. However, these instruments are relatively expensive compared to the simple hydrostatic or mechanical displacement instruments. Most commercially available transducers of the strain-gage type are temperature sensitive in that the zero drifts as the ambient temperature of the instrument varies. This may be controlled by locating the transducer in a controlled temperature environment. In some such transducers, carbon resistors have

been added to the circuitry to adjust the gage factor to a specified value, and it has been found that removal of this resistor minimizes the sensitivity to temperature.

Below is a partial listing of manufacturers from whom pressure transducers are commercially available.

1. Consolidated Electrodynamics Corp. (CEC), 300 N. Sierra Madre Villa, Pasadena, Calif.
2. Electronic Engineering Associates, Ltd., 778 El Camino, San Carlos, Calif.
3. Statham Laboratories, 12401 W. Olympic Blvd., Los Angeles, Calif.
4. Wiancko Engineering Co., 2670 N. Fair Oaks, Altadena, Calif.

Pressure transducers of the "home-made" type are used at some facilities. These include:

1. NACA miniature pressure pickup (described in NACA TN 2659).
2. NACA capsule and digital recorder (described in NACA TN 2880).
3. NOL pressure gage (described in NAVORD 3630).
4. University of Michigan capsule. Uses pre-stretched flat diaphragm with Schaevitz transformer with maximum error less than ± 0.125 mm Hg (described in Report UMM-59).

It is generally agreed that knowledge of the static pressure to about $\pm 1\%$ is sufficiently accurate for most pressure tests below Mach number 5. On this basis, probes and recording instruments should be accurate to ± 0.1 to 0.25% . Experience at North American Supersonic Aerodynamic Laboratory indicates measurement accuracies of ± 0.003 and ± 0.008 in. Hg for static and total pressures, respectively, with Wiancko transducers. Total head errors are in general two to three times those of static pressure errors.

At the Co-operative Wind Tunnel it was observed that Statham and CEC differential pressure transducers have a 2% difference in gage factor for negative and positive pressure differences due to unequal diaphragm end effects.

2.3.3.1 WADC Pressure Transducer

This instrument (patent pending) was designed and constructed for application in a multiple pressure-measuring device suitable for automatic pressure-distribution measurements on wind-tunnel models. The transducer is also intended for use in all applications where a high-accuracy instrument is required for absolute and differential pressure measurements.

It has been found that accuracies of 0.1% of applied load can be obtained with strain-gage-type force-measuring devices if certain

precautions are taken in respect to the load member design, strain-gage application procedure, and instrumentation. Based on this experience, the pressure transducer is designed around a bonded strain-gage-type sensing element.

The pressure to be measured is applied to a bellows which is restrained by the strain-gage flexure system. In order to keep the instrument dimensions small, a bellows diameter of 1-1/2 in. was selected. Figure 2-22 shows various details and the external configuration of such an instrument.

Due to the small bellows diameter the forces transmitted to the flexure system are small; therefore, a tension compression-type flexure was impractical and a suitable bending-type flexure had to be developed. Extensive experimental work showed that this type of flexure fulfills several essential requirements. First, since it wraps around the bellows, it requires a minimum of space, which keeps the volume of the transducer small. Second, it provides ample space for the application of strain gages. Third, it approximates closely the movement of a parallelogram, which results in turn in a rigid guidance of the bellows close to its longitudinal axis under applied load as shown in Fig. 2-23.

The bellows is rigidly attached to the flexure at one end; the other end is bolted to a steel base plate to which the flexure is also mounted.

Great care should be taken to install the bellows so that it is stress free in the flexure assembly in order to avoid a condition which would result in calibration errors. If a maladjustment were present, the bellows would act as a pre-stressed spring which would enforce the movement of the flexure in one direction and restrain it in the other direction, resulting in a change in the calibration constant. It is obvious that in order to maintain the same stress-free relationship between flexure and bellows under varying temperatures, the temperature expansion coefficient for bellows and flexure should be the same. This condition has been met closely by using a stainless-steel bellows and a steel flexure assembly. A secondary purpose of the utilization of stainless steel is the prevention of corrosion within the instrument. The bellows is welded pressure tight to its steel flanges.

The pressure seals consist of rubber O-rings, the housing is aluminum, and all other parts are made of steel. The pressure connections to the bellows and housing are silver soldered, and the electrical leads are cemented in position.

Over a period of at least 24 hr before the calibration starts, the strain-gage bridge should be temperature compensated and checked for drift. (During operation the calibration room should be air conditioned, the room temperature should not vary more than $\pm 2^\circ\text{F}$, and the instrument should not be subject to vibration.) Furthermore, the transducer should be pressurized and evacuated through the full load range at least 10 times. In case of excessive zero shifts, excessive hysteresis, or drifting, new gages should be applied and the procedure repeated. The bridges are temperature compensated for less than 0.22-mv drift for a 70°F temperature change. The slight amount of hysteresis observed is credited to the strain gages and not the bellows. This is probably

correct because temperature changes affect Young's modulus, which changes the gage factor.

The calibration requires at least 10 steps over the pressure and vacuum range, with the vacuum and pressure applied either to the bellows or the housing. In all calibrations, pressure application to either bellows or housing should show identical results.

With the procedures outlined above, accuracies of 0.1% can be obtained from 20 to 100% of the load range with the 1-atm model, and 0.25% with the 1/4-atm model. Hysteresis, zero return, and drift should stay within the accuracy limits.

Since the operating stress in the flexure is only about 7000 psi, flexures are made of normalized steel. (Values to 12,000 psi have been used, but the accuracy suffers.) The flexure (Fig. 2-23) is by far the most expensive part to manufacture and represents approximately 50% of the total transducer cost. Investigations are being made to explore the possibility of casting the flexure and machine finishing only the gaging surfaces and further reducing the size of the instrument. The transducer characteristics are summarized below.

Pressure range (Existing models)	1 atm, 1/4 atm
Excitation voltage	12 v d-c
Bridge resistance	240 ohms
Current rating	50 ma
Gage type	SR-4 ABD 7(8 gages) or AB 7-1 (4 gages)
Insulation resistance	20 megohms or better
Output	Approx 8 mv for max pressure
Maximum working stress	7000 psi
Linearity	0.1% of reading down to 20% of full scale
Hysteresis	Within accuracy

The largest contributing factor to inaccuracy is the flexure design. The bellows are quite consistent in their mechanical properties.

The sensitivity, K , of a bonded strain-gage pressure transducer may be computed from the expression

$$K = \frac{SG}{E_p} \times 10^3 \text{ mv/v/psf} \quad (2-21a)$$

where

s = stress at the gage section when full design pressure is applied, psi

G = gage factor, dimensionless

E = elastic modulus of the flexure material, psi

p = design pressure, psf

For a one-atmosphere transducer, assuming $G = 2$ and a design pressure of 2000 psf,

$$\kappa = \frac{(10,000)(2)(10^3)}{(3)(10^7)(2000)} = 0.00033 \text{ mv/v/psf} \quad (2-21b)$$

Since heat dissipation in the gage limits the usable gage current to about 25 ma or 50 ma for a four-arm bridge, the maximum output signal is obtained when a voltage equal to 1/20 (bridge resistance) is applied to the transducer. Thus 12 v may be applied to the transducer, causing a full-scale output of $(0.00033)(12)(2000) = 8 \text{ mv}$.

2.3.3.2 OSU Pressure Transducer

The pressure-measurement range at the Ohio State University hypersonic tunnel is 500 to 5000 microns. Liquid manometers are preferred here instead of bellows-type transducers. A glass U-tube with mercury as the fluid is used. The core of a Schaevitz transformer is floated on small wooden pegs on top of the mercury in both legs of the U-tube. The transformers are hooked up in series, and a voltage divider is used to provide adequate sensitivity over a 150- to 5000-micron range of pressures. The output is transferred to a Brown strip-chart recorder by balancing the voltage in the Brown transformer so that no voltage exists when balance is reached. A vibrator is used on the recorder to eliminate instrument friction effects. A 50-micron spread in repeatability was initially reported for tubes of constant diameter, but a new float design reduced the errors to less than + 2 microns. The U-tube must be completely isolated from vibration, and both legs of the manometer must be at the same temperature within 0.01°F, or large errors result. A zero is obtained by exposing both legs of the tube to the same pressure. Approximately two minutes is required for the system to reach equilibrium when a step in pressure is encountered, and the system has to be hooked to a high vacuum source between runs to prevent outgassing.

Lower pressures could be attained by using lower density silicone oil. However, the range would be limited by the linear range of the transformers.

2.3.3.3 Hagan Transducer

With this transducer the pressure is balanced by the force exerted on a d-c coil by a permanent-magnet field. The displacement of the pressure bellows is detected by use of a differential transformer,

amplified and rectified to control an amplifier which provides the proper coil current to balance the pressure. The current passes through a manganin resistor in series with the coil, thus giving a voltage output proportional to the pressure. The voltage is read with a digital voltmeter.

2.3.3.4 Use of Transducers in an Arc-Heated Blowdown Tunnel

The arc-heated blowdown tunnel, commonly referred to as the "hot shot" tunnel at AEDC, differs from conventional tunnels in several respects. The run times are extremely short and the supply air is energized by arc heating. Air is initially charged into the pressure reservoir at moderate pressures and room temperature and is isolated from the nozzle by a frangible diaphragm of thin plastic across the throat. The electrical energy is stored in a large bank of electrical condensers. This energy is discharged across the arc chamber or reservoir. Pressures in the order of 20,000 psi have been measured, once the energy was transmitted to the air. From these pressures, temperatures up to 8000°K have been estimated. The sudden pressure ruptures the diaphragm and the expansion proceeds down the nozzle. The total run time of the hypersonic flow varies from 20 to 40 msec, which represents an order of magnitude longer than the available testing time in a shock tube. The heat-transfer rates at the nozzle are about three orders of magnitude greater than any calculated rates of heat transfer for bodies re-entering the earth's atmosphere. With this heat-transfer rate the nozzle throat begins to melt in 1 msec or less.

Many kinds of instrumentation, including conventional shock-tube instrumentation, proved unsuccessful for such operation. The longer run time appeared to be responsible for failure of some of the shock-tube equipment. The failure of the electrical transducers was attributed primarily to the arc driving source. Instrumentation that did work was for the most part the kind used in short-duration conventional tunnels. Stagnation static pressure was successfully measured by Fotocon FM-type transducers designed for blast. A Consolidated Engineering Company 1-127, 20-kc carrier amplifier system worked. Ultra-Dyne pressure transducers were used inside the model.

2.3.4 Free-Molecule Probe

The free-molecule probe is an instrument unique to the low-density field which has been developed at the University of California (Ref. 71) to study the nature of the shock wave and boundary-layer regions near the leading edge of a thin flat plate in two-dimensional low-density flow. The basic feature is that the temperature recovery factor and the heat transfer coefficient for a cylinder in free-molecule flow, both of which are sensitive functions of the local Mach number, can be predicted accurately. Measurement of a wire temperature, which is a function of the local velocity and temperature, has enabled a qualitative picture of a flow field to be obtained at Reynolds numbers less than 1000 in the Mach 2 to 4 range (Ref. 79). To obtain reliable measurements, it is necessary to select a wire diameter, d_w , that is small when compared to the mean free path, λ , of the molecule (i.e., the Knudsen number of the wire should be greater than 5. $K_n = \lambda/d_w > 5$). A tungsten wire probe of 0.00025-in. diameter with a current of 0.25 ma was used successfully to determine the resistance across a central

1/2 in. part of the wire and hence the temperature of the wire by measuring the voltage through a pair of potential leads of the same material (Fig. 2-24). The current was sufficiently small to have a negligible heating effect on the wire. The wire temperature can be found by measuring the resistance of the measuring element and by using the manufacturer's value for the temperature coefficient of resistance. The potential across the measuring element can be read to within 0.005 mv, corresponding approximately to an error of 0.06% in the resistance measurement, and hence also in the temperature of the wire. If the fixed current through the wire is held to an accuracy of 0.1%, the estimated error in wire temperature will be approximately 0.13%.

2.3.5 Mass-Flow Probe

The relationship between velocity and temperature in real fluids is a matter of fundamental importance in high-speed aerodynamics; consequently, several instruments have been proposed to assist in measurement of this relationship. Conspicuous among these instruments is the stagnation temperature probe, which has been used with various degrees of success by Spivack, Wegener, Monaghan and Cooke, and many others. The most obvious check on the accuracy of such an instrument is verification of the fact that the total energy in the flow must remain constant for steady flow without heat transfer to the wall.

$$\int_0^{\delta+} \rho u (T'_0 - T_0) dy = 0 \quad (2-22)$$

where

T_0 = free-stream or reservoir stagnation temperature

T'_0 = local stagnation temperature in the boundary layer

δ = boundary-layer thickness

u = velocity

ρ = density

In considering obvious difficulties in the determination of local specific energy in high-speed airflows, it appeared (Ref. 43) that measurement of mass-flow rate serves the same purpose as measurement of local stagnation temperature. Consider that the impact and static pressure together determine the local Mach number and therefore the local dynamic pressure,

$$\rho u^2 = \gamma p_\infty M^2 \quad (2-23)$$

independently of the relationship between velocity and temperature. If the local mass flow rate,

$$\rho u = \frac{dm/dt}{A} \quad (2-24)$$

could be determined for a stream tube of area A , the velocity and density, and hence the static and stagnation temperatures, could be calculated immediately.

If the flow is supersonic, one may visualize a sharp-edged hollow probe with a sufficiently low internal pressure so that an attached shock system exists at the entrance. The nose area, A , then defines the stream tube being studied, and the mass-flow rate may be measured at leisure further downstream. Closing off the internal passage converts the instrument to a conventional impact probe and thus allows the necessary measurements to be carried out at precisely the same point in the flow.

The development of a mass-flow impact probe was undertaken at JPL (Ref. 43). In the final analysis the performance of the instrument in a boundary layer was found to be unsatisfactory. Nevertheless, there is sufficient promise for the technique, and the experience (Refs. 43 and 80) has been made available to others working in the field.

2.3.6 System Response-Time Lags

Calculated and experimental data (Ref. 81) are in reasonable agreement in showing that response time in a pressure-measuring system incorporating capillaries is a function of the orifice pressure, the initial pressure differential, and the system volume. It is directly proportional to capillary length and to the viscosity of the gas in the capillary, and is inversely proportional to the fourth power of the capillary inside diameter. The response time increases as the orifice pressure decreases. An orifice in a capillary system has little effect on response time when its diameter is greater than about 0.25 of the internal diameter of the capillary to which it is attached.

The response time, t , for a pressure-measuring device to reach a pressure, p , for an initial pressure, p_0 at $t = 0$, and an orifice pressure, p_1 , is

$$t = \frac{128 \mu \ell_e}{\pi d^4} \left[\frac{v_1}{p_1} \ln \frac{(p_0 - p_1)(p + p_1)}{(p - p_1)(p_0 + p_1)} + \frac{3v_d}{(p_0 - p_1)} \ln \frac{(p_0 + p_1)}{(p + p_1)} + \frac{v_d}{(p_0 - p_1)} \ln \frac{(p_0 - p_1)}{(p - p_1)} \right] \quad (2-25)$$

where

v_1 = entire air volume of system from orifice to and including measuring device at $p = p_1$ (i.e., $t = \infty$), ft^3

v_d = volume displaced by motion of manometer fluid or by deflection of capsule walls, ft^3

d = common diameter for a set of connected capillaries
(see below), ft

l_e = length of capillary of diameter d which is equivalent in flow resistance to total resistance of all series-connected capillaries in the system (see below), ft

μ = coefficient of viscosity of air in system, lb-sec/ft²

A value of l_e , based on a common diameter, d , for a set of connected capillaries in a series-connected system (designated by subscripts 1, 2, 3 ..., n), is determined by finding the equivalent lengths of each and adding the resulting lengths to that of the capillary of diameter d . If d_1 is chosen arbitrarily as the basic diameter,

$$d = d_1$$

$$l_e = l_1 + l_2 \frac{d^4}{d_2^4} + l_3 \frac{d^4}{d_3^4} + \dots + l_n \frac{d^4}{d_n^4} \quad (2-26)$$

2.3.6.1 Optimum Capillary Size

Obviously the greatest gain in reducing the time lag of a pressure-measuring system is achieved by increasing the bore of the smaller capillaries, consistent with space, structural limitations, and an orifice size small enough to minimize disturbances in the flow in the neighborhood of the orifice, or by replacing as large a portion of the smaller capillaries as possible with larger tubing.

System volume, which has a direct relation to response time, is influenced by the capillary volumes, and for the larger capillaries an optimum exists between the large bore with its large volume and the small bore with its greater flow resistance. For a system incorporating only two sizes of capillaries, the problem of determining the optimum is relatively simple, but such a system is rarely found in practice. In the case of a wind-tunnel model installation, a system can usually be divided into two groups of capillaries: those in the model and support system, the sizes of which are determined principally by space limitations and are usually the greatest source of time lag, and those which connect them to the pressure-measuring device and on which no space limitations are imposed. By resolving the former group into an equivalent length, l'_e , of a single capillary of diameter d , the system becomes a two-capillary one.

Then the equivalent length is

$$l_e = l'_e + l_x \frac{d^4}{d_x^4} \quad \text{and} \quad V_1 = V'_1 + l_x \frac{\pi}{4} d_x^2 \quad (2-27)$$

where the subscript x refers to the capillary whose optimum diameter is sought. If the volume V'_1 is known and the two displacement terms

in Eq. 2-25 are neglected, then in the practical case, where

$$\left[\frac{l_x d^4}{3 l_e'} \right]^3$$

is negligible compared to

$$\left[\frac{4V_1' d^4}{\pi l_e'} \right]^2$$

the optimum diameter is

$$d_x \approx \sqrt[3]{\frac{8 V_1' d^4}{\pi l_e'}} \quad (2-28)$$

which shows that for practical purposes the optimum diameter of the capillary is independent of length.

2.3.6.2 Limitations

In spite of the exact nature of the equations, the response times obtained are accurate only to an order of magnitude in many instances because the exact geometry of the system and the initial and final pressures imposed may be difficult to ascertain. Some of the probable causes for discrepancy are:

1. Inaccuracies in measurement and constancy of capillary diameter
2. Unknown system volume
3. Unknown capillary length (particularly, the smallest)
4. Elasticity of flexible tubing
5. Porosity of capillaries (particularly, flexible tubing)
6. Effect of distributed volume
7. Effect of orifices and capillary junctions
8. Kinks or bends which reduce considerably the cross-sectional area of the capillary.

2.3.6.3 Criteria for Minimum Response Time (Ref. 82)

The criteria for minimum response time are:

1. Orifice diameter should not be less than one-half the model-tubing diameter, with slight advantage to be gained as the orifice diameter approaches the tubing diameter.

2. Model tubing should be as short as possible, incorporating the largest feasible inside diameter.
3. Connecting tubing should be short, with the inside diameter between 1.25 and 1.50 times the inner diameter of the model tubing.
4. Volume of the sensing-unit reservoir should be minimized.
5. Pumping the initial reservoir and line pressure to a value close to the model-surface pressure offers scant advantage unless the initial pressure approaches the equilibrium pressure to within 1 mm Hg.

2.3.6.4 Criteria for Slip Flow and Free-Molecule Flow (Ref. 82)

Equation 2-25 is based on the assumption that the coefficient of viscosity, μ , is a constant (i.e., proportional to the temperature which is constant in an isothermal process) and that the condition of no-slip at the tube wall is valid. The assumption of constant μ at moderate and high pressures is predicted by kinetic theory. However, the failure of Eq. 2-25 is explained by the failure of the no-slip condition rather than on the basis of variable viscosity.

Under very low pressure conditions the no-slip at the wall condition is violated, since μ becomes a function of the pressure. If slip-flow conditions exist in the capillary system (i.e., the mean-free path of the molecules is of the same order as the capillary inner diameter), the time response obtained from Eq. 2-25 may be divided by a correction factor, F , shown in Fig. 2-25 as a function of H , where

$$H = \frac{\mu}{p_m a(\rho_1)^{1/2}} = \frac{2\mu}{p_m d(\rho_1)^{1/2}} = \frac{8.20}{p_m d}$$

$$p_m = \text{mean pressure, } \frac{p_0 + p_1}{2}, \text{ in microns of Hg}$$

d = tube diameter in centimeters

ρ = gas density at one micron Hg, mass

μ = gas viscosity at atmospheric pressure

and 1 micron = 0.001 mm Hg

Hence, for air, $\frac{\mu}{\sqrt{\rho_1}} = 4.10$

Rigorously, this correction is true only if p_0 and p_1 are both in the range where slip flow occurs. If not, a numerical integration over the pressure range will be required for an accurate estimate of response time.

At extremely low pressures the internal friction of the fluid becomes very small because the mean-free path of the molecules becomes large compared to the tubing inner diameter (free-molecule flow), and the collisions between molecules are infrequent and may be neglected. This assumption is valid if the mean pressure in microns (10^{-3} mm Hg abs) is less than the reciprocal of the tubing diameter in inches,

$$p_m = \frac{p_o + p_1}{2} < \frac{1}{d} \quad (2-29)$$

For the normal case of supersonic wind-tunnel testing, where the mean pressure might be as low as 5000 microns and the tubing inside diameter may be as small as 0.020 in., it is readily seen that free-molecule flow is not approached:

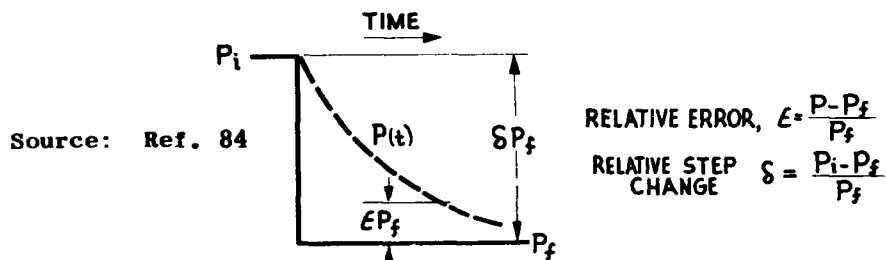
$$p_m = 5000 \gg \frac{1}{d} 50$$

More recent work on this subject is presented in Ref. 83.

2.3.6.5 Working Charts

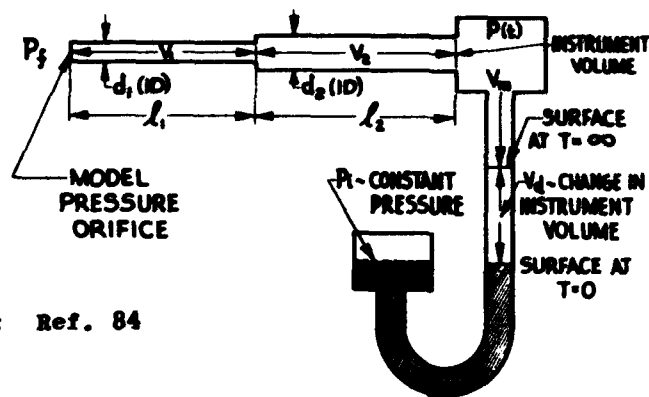
Working charts (Figs. 2-26 to 2-30) have been prepared (Ref. 84) to allow quick calculation of the necessary delay times for a given pressure-measuring system incorporating capillaries so that the indicated pressure will not be in error from the true pressure by more than a given per cent. Effects of various parameters on time lag are also presented. These charts are based on the work of Ref. 85, which is in more general agreement with experimental time lags than Ref. 81.

The step pressure history and some of the associated nomenclature used in the charts and in the equations which follow are presented below.



The solid line shows the orifice pressure history, while the dashed line shows the pressure at the instrument end of the pressure tubing. This instrument may be a manometer or a pressure transducer. The error at any time is expressed as a fraction of the final or true pressure.

Illustrated in the following sketch are the significant components of the pressure tubing or capillary system and the indicating instrument.



Source: Ref. 84

A two-element capillary system is considered which reduces to a single element system when $V_2 = 0$ or $l_2 = 0$. A manometer is shown as a general pressure-indicating instrument having an air volume, V_m , at $t = \infty$ and a volume, $V_d + V_m$, at $t = 0$. Dynamics of the manometer fluid are not considered in this problem. A pressure transducer is a special case of the general indicating instrument where $V_d = 0$, i.e., the total instrument volume is constant and equal to V_m . Usually the internal volume of a transducer is considerably less than a manometer, and the lag effects decrease with decreasing volume.

The general case of a step pressure change has been solved in Ref. 62 which presents experimental verification of the theory and shows agreement of lag times within 10 to 20%. The resulting solution for a step pressure change of the time, t , in seconds required for the instrument pressure, p_1 , to come within $(100\epsilon)\%$ of p_f (psi) is

$$t = \frac{0.111 \mu (\ell_1/d_1)^2}{p_f} (F_v + F_d) \quad (2-30)$$

where

$$F_v = \left[1 + \frac{V_2}{V_1} \left(1 + \frac{1}{K} \right) + \frac{2}{K} \frac{V_m}{V_1} \right] \ln \left[\frac{(\epsilon + 2)/(\delta + 2)}{\epsilon/\delta} \right] \quad (2-31)$$

$$F_d = \frac{2}{K} \frac{V_d}{V_1} \left[\frac{(\epsilon + 2)^{\frac{\delta+3}{\delta}}}{(\delta + 2)} \frac{\delta-1}{(\epsilon)} \right] \quad (2-32)$$

$$\frac{1}{K} = 1 + \frac{\ell_2/\ell_1}{(d_2/d_1)^4} \quad (2-33)$$

and

$$\epsilon = \frac{P - P_f}{P_f}$$

$$\delta = \frac{P_1 - P_f}{P_f}$$

μ = viscosity of air, 3.8×10^{-7} slugs/ft-sec at 80°F

(For additional symbols see previous sketches)

Figures 2-26 to 2-30 may be used for computing the lag times of any given final error. Some typical cases are tabulated in Table 2-2 to illustrate various effects of the system variables. The lag time increases approximately linearly with tube length, approximately inversely with the fourth power of the tubing diameter, and approximately inversely with the final pressure. These effects are modified slightly by the presence of an instrument volume and a second tube. Cases 4 and 5 show that for a given total length of tubing to the instrument and a given Tube 1, there exists an optimum diameter for Tube 2. Instrument volume increases the lag time more markedly when it is the predominant volume. Increasing the allowable error decreases the lag time slightly. It can be seen that for an intermittent wind-tunnel run time of the order of 30 to 40 sec, the response times of pressure-measuring systems can become a serious problem. Operating efficiency can be increased by optimizing the tubing sizes, allowing the run to be as short as possible, repumping the storage tanks faster, and reducing the interval between runs.

2.4 Mach Number Determination

Several pressure measuring instruments have been used with varying degrees of success to determine free-stream Mach number in a supersonic airstream. A brief discussion of each follows.

2.4.1 Mach Number Obtained from Free-Stream Static Pressure Measurements

Free-stream static pressure as determined from wall orifices or orifices in a tube axially located on the nozzle centerline used in conjunction with the stilling chamber pressure (assumed to be the stagnation pressure) is the simplest method of obtaining the Mach number variation along the nozzle. However, this technique results in a rather crude calibration because the flow conditions at the wall, for example, are a relatively poor indication of those in the region of the test section where the model is usually mounted. Some efforts have been made to utilize a static pressure probe (see Subsec. 2.1.3). However, more consistent results are obtainable from the stagnation pressure probe and the cone-face static pressure methods.

2.4.2 Mach Number Obtained from Stagnation-Pressure Measurements

Stagnation pressure behind a normal shock has been used quite successfully in conjunction with stilling chamber pressure to determine local Mach number. One of the main attributes of this technique is the relative insensitivity of the pitot probe to local flow inclinations. A rather large number of stagnation-pressure probes which will allow surveys of fairly large areas of the test section simultaneously can be mounted on a planar or cruciform rake as shown in Fig. 2-31.

2.4.3 Mach Number Determined by Means of Conical Probes

Consistent values of free-stream Mach number are obtained when the static pressure on the face of a cone is used in conjunction with conical flow theory and stilling chamber pressure. Pressure measurements at four circumferential locations spaced 90 deg apart on each of several probes mounted in a cruciform rake as shown in Fig. 2-32 provide a rapid means of surveying the model test area in the test section. This technique has an added advantage in that flow inclination in the vertical and horizontal planes can be determined concurrently with the Mach number distribution, if the pressures at each of the four orifices on each cone probe are measured and recorded individually. The probes must be sufficiently far apart so that the shock wave from the tip of each probe does not affect the static pressure measurements on the adjacent probes. Since the pressure rise from an incident shock on the probe can propagate forward through the boundary layer, thus affecting the static pressure measurement on the cone face, it is good practice to assure that the nose shock from the adjacent probe does not strike the cylindrical barrel of the probe closer than two probe diameters from the cone shoulder.

2.4.3.1 Sensitivity of Conical Probes

A measure of the sensitivity of a cone probe at a given Mach number is the ratio of the difference between the top and bottom static pressures to the free-stream total pressure per degree of angle of attack. This ratio has been obtained by the method of Ref. 86 and is presented graphically in Fig. 2-33 for a series of cone half-angles of 10 to 30 deg. It is apparent that cones of larger half-angles should be used at high Mach numbers. The ratio of mean static pressure from the four orifices on the cone-face to free-stream stagnation pressure is also shown in Fig. 2-34. Reference 87 gives an experimental evaluation of a 20-deg half-angle cone.

In order to obtain consistent results with conical probes, considerable care should be taken in their manufacture. Reference 88 indicates that the cone angle should be held to within ± 2 min of the design-value half-angle. Consequently, the conical tips must be precision ground, and care should be taken with the proper alignment of the conical tip and the cylindrical afterbody. It was also indicated (Ref. 88) that the spacing of the four taps on the surface of the conical tip should be held to the same tolerance of ± 2 min and that the taps should be drilled perpendicular to the conical surface with great precision to yield a probe free from the effects of asymmetry. Examination of the orifice under a microscope should disclose no burrs or other defects. Since the sharp tip of the cone is quite fragile (running a finger lightly over the tip can destroy the sharp point), it is

advisable to provide a lucite shroud, sufficiently relieved that it cannot touch the tip, for protection when the probe is not actually in use in the wind tunnel. Each probe should be calibrated in the wind tunnel by placing its tip at the center of rotation of the angle-of-attack actuator and taking readings through an angle-of-attack range and also with the probe rotated 90 deg, 180 deg, and 270 deg at zero angle of attack to check for asymmetry.

2.4.3.2 Machine Computation of Mach Number from Cone Pressures

Relations between cone-surface pressure and free-stream conditions have been calculated from Taylor-Maccoll theory and tabulated in Ref. 86 for a large number of half-cone angles.

It is apparent that much time must be devoted to reference tables during a routine calibration of a supersonic wind tunnel. Even with the aid of digital computing equipment, much time is required to match the pressure ratios with master decks to obtain the related Mach number. The use of approximation equations allows the unknown to be found quickly in an IBM 650 or other similar calculator. Ninth-degree equations for determining Mach number from 10- and 15-deg half-angle conical probes have been developed by Blanchard and Kennedy at OAL, and these equations are available as Master Decks 343 and 344. The approximations were derived using the Gram-Tschebysheff method, and enough equations are presented to obtain a Mach number when either of the following pressure ratios is known:

1. Cone-surface static pressure to free-stream total pressure (p_s/p_t)
2. Cone-surface static pressure to total pressure behind the normal shock (p_s/p'_t).

Reference 86 was used to determine the pressure ratios for given Mach numbers. These were checked by two independent methods and plotted for each of the two conical probes. Equations to approximate p_s/p_t from given Mach numbers were developed from values read from these plots. The equations were developed to include Mach number values from 1.200 to 3.000 in 0.001 intervals. From the values obtained by these equations, similar plots and equations were developed to approximate Mach numbers when either p_s/p_t or p_s/p'_t is known.

Parameters for Approximation Equations 2-34 to 2-39

θ_s (deg)	(x)	f(x)	Maximum Error	Equation No.
10	M	p_s/p_t	0.0002	2-34
15	M	p_s/p_t	0.0006	2-35
10	p_s/p_t	M	0.002	2-36
15	p_s/p_t	M	0.003	2-37
10	p_s/p'_t	M	0.005	2-38
15	p_s/p'_t	M	0.002	2-39

These parameters are applied to the approximation equations (Eqs. 2-34 to 2-39) when p_s is the average of the cone-surface static pressures measured at the four circumferentially spaced static pressure orifices on the surface of the probe and θ_s is one-half the included angle of the cone.

Range $1.200 < M < 3.000$; $\theta_s = 10$ deg

$$\begin{aligned} p_s/p_t = & 0.47479 - 1.03755 x + 0.99380 x^2 - 1.82739 x^3 \\ & + 8.90837 x^4 - 26.22983 x^5 + 43.66978 x^6 \\ & - 41.81075 x^7 + 21.50732 x^8 - 4.60614 x^9 \quad (2-34) \end{aligned}$$

where

$$x = 0.55556 M - 0.66667$$

Range $1.200 < M < 3.018$; $\theta_s = 15$ deg

$$\begin{aligned} p_s/p_t = & 0.53990 - 1.23762 x + 2.20559 x^2 - 7.17425 x^3 \\ & + 20.67758 x^4 - 34.34499 x^5 + 28.18875 x^6 \\ & - 5.11288 x^7 - 7.10368 x^8 + 3.41782 x^9 \quad (2-35) \end{aligned}$$

where

$$x = 0.55006 M - 0.66007$$

Range $0.0428 < p_s/p_t < 0.4748$; $\theta_s = 10$ deg

$$\begin{aligned} M = & 1.19987 + 0.42386 x - 0.72659 x^2 + 4.56220 x^3 \\ & - 12.71877 x^4 + 19.82626 x^5 - 18.05403 x^6 \\ & + 9.56761 x^7 - 2.73458 x^8 + 0.32670 x^9 \quad (2-36) \end{aligned}$$

where

$$x = -4.62962 (p_s/p_t) + 2.19840$$

Range $0.0575 < p_s/p_t < 0.5399$; $\theta_s = 15$ deg

$$\begin{aligned} M = & 1.19998 + 0.73956 x - 0.41043 x^2 + 10.33126 x^3 \\ & - 59.10989 x^4 + 188.67195 x^5 - 352.88729 x^6 \\ & + 387.49722 x^7 - 231.20630 x^8 + 58.17087 x^9 \quad (2-37) \end{aligned}$$

where

$$x = - 2.07297 (p_s/p_t) + 1.11920$$

$$\text{Range } 0.1290 < p_s/p_t' < 0.4782; \theta_s = 10 \text{ deg}$$

$$\begin{aligned} M = & 1.19997 + 0.68905 x - 0.13574 x^2 + 2.40341 x^3 \\ & - 4.04847 x^4 + 0.81891 x^5 + 10.33433 x^6 \\ & - 16.45154 x^7 + 10.11700 x^8 - 1.92393 x^9 \end{aligned} \quad (2-38)$$

where

$$x = - 2.86369 (p_s/p_t') + 1.36942$$

$$\text{Range } 0.1748 < p_s/p_t' < 0.5438; \theta_s = 15 \text{ deg}$$

$$\begin{aligned} M = & 1.19999 + 0.58974 x + 0.39513 x^2 + 0.59601 x^3 \\ & - 3.19487 x^4 + 16.42127 x^5 - 44.28010 x^6 \\ & + 65.16608 x^7 - 48.38444 x^8 + 14.48614 x^9 \end{aligned} \quad (2-39)$$

where

$$x = - 2.71003 (p_s/p_t') + 1.47371$$

2.4.3.3 Five-Orifice Truncated-Cone Probe

The results of an investigation of the performance of a truncated-cone probe as a nozzle calibration instrument is presented in Ref. 89. Tests were made over the Mach number range 1.25 to 2.50

at free-stream Reynolds numbers in the order of $0.6 \times 10^6/\text{in}$. The test probe (Fig. 2-35) was a 10-deg half-angle cone-frustum incorporating four static pressure orifices spaced equally around the periphery of the conical face and one orifice in the blunt tip. The ratio of the diameters of the tip and the base was 0.0945. The static pressure orifices were located 17 tip diameters aft of the blunt tip.

Data obtained by use of the truncated-cone probe were compared with that obtained with a conventional sharp-tipped conical probe of the same size and design. It was shown that the truncated-cone probe was equal in performance to the conventional probe in the test Mach number range and furthermore, that the flow inclination of the free stream may be determined simultaneously with its Mach number, a distinct advantage.

The most important geometric parameter to be considered in the design of a conventional low-angle truncated-cone probe is the ratio of the distance between the probe tip and the static orifices to the diameter of the blunt tip. It was found that if this ratio is less than approximately 15, then significant differences between experimental

and theoretical cone surface pressures are in evidence.

In Fig. 2-36 the average flow inclination parameter for each probe is plotted as a function of Mach number and compared with the Taylor-Maccoll theory (Ref. 86). The agreement between theory and experiment is quite good, with the exception of the data taken at Mach 1.73, which were influenced by the presence of tunnel disturbances. The truncated-probe performance is seen to be equal to that of the true cone through the test Mach number range.

The average repeatability within a run was largest at Mach 1.25, and amounted to ± 0.016 deg in flow inclination and ± 0.002 in Mach number. Corresponding repeatability of data between runs was one order of magnitude larger than the values quoted above.

A set of two 15-deg half-angle conical probes, as shown in Fig. 2-37, were also evaluated at Mach 1.50 and 2.00 to establish the accuracy of Mach number determination by the three possible methods and the accuracy of flow inclination determination. A conventional pitot tube was provided on the test rig to give an independent check on Mach number. Mach number was obtained from the rake by the three possible methods:

1. Ratio of average static pressure on the cone surface (p_s) to total pressure measured at the apex of the cone (p_t')
2. Ratio of p_s to stagnation pressure (p_t) in the free stream
3. Ratio of p_t' to p_t .

The effects of inclination of the probes to the flow was also investigated.

The tests indicated that all three methods agreed within 0.03 in Mach number up to flow inclinations of ± 6 deg. The Mach number obtained from the ratio of pitot pressure to free-stream total pressure was essentially constant up to a flow inclination of 15 deg. It was characteristic at both test Mach numbers that the first method resulted in the lowest indicated Mach number, the second in an intermediate value, and the third in the highest value.

The calibration also indicated that the use of the theoretical slope of the static pressure differential from diametrically opposed orifices to free-stream stagnation pressure ratio versus angle of attack to obtain flow inclination is valid over a range of ± 10 deg.

2.4.4 Determination of Mach Number by Means of Wedge-Face Static Pressure

The static pressure on the face of a wedge can be used in conjunction with two-dimensional oblique shock theory and stilling chamber pressure to determine local Mach number (Ref. 90). A typical wedge installation is shown in Fig. 2-38. The disadvantage of this technique is that the Mach number determined is not truly a local Mach number since the static pressure measured at the orifice, which must necessarily be located a finite distance aft of the leading edge, is affected

by any static pressure variation in the area bounded by the Mach lines between the leading edge of the wedge and the orifice. A preliminary investigation has been made at OAL using a stagnation-pressure probe mounted just above and parallel to the wedge face and located so that its region of influence is well away from the static taps. The advantage of this method is that "local" Mach number may be determined independently of stilling chamber pressure. However, only a limited amount of data has been obtained and no conclusion as to its relative merit can be drawn.

2.4.5 Visual Methods of Determining Mach Number

Although they are not as accurate as the methods mentioned above, it is possible to establish the Mach number in a supersonic stream by visual methods. If a wedge of semi-angle θ is placed at zero incidence in a supersonic airstream, the Mach number can be determined by observing the inclination, θ_w , of the attached bow wave to the direction of the undisturbed stream and by using the equation,

$$\frac{1}{M^2} = \sin^2 \theta_w - \frac{\gamma + 1}{2} \left(\frac{\sin \theta_w \sin \theta}{\cos (\theta_w - \theta)} \right) \quad (2-40)$$

A cone is sometimes used instead of a wedge. The relationship between M and the bow-wave angle for a cone of given semi-angle θ is shown in Table 2-3 for representative Mach numbers.

In some cases the Mach number may also be determined by measuring the inclination of very weak disturbances arising from scratches made in the surface of the tunnel wall or that of the model under test. These disturbances are assumed to approximate Mach lines, and the Mach number is then found from

$$\sin \theta_w = \frac{1}{M} \quad (2-41)$$

2.5 Nozzle Calibration Equipment

A wind tunnel must be calibrated to provide the user with a knowledge of local flow conditions, both Mach number variations and flow inclination. However, time spent in tunnel calibration does not provide usable experimental data on airplanes or missiles and is therefore not considered productive. For this reason, any method which helps reduce the time required to provide a reasonable flow calibration should be of interest.

2.5.1 Linear Actuators

The simplest and most obvious method of speeding up nozzle calibrations is by providing a suitable, remotely-controlled linear actuator to drive the multi-probe rakes mentioned in Subsec. 2.4.

The linear actuator (Ref. 91) shown in Fig. 2-39 is designed to operate various pressure probes mounted on any of several bodies of revolution, but it may easily be adapted to hold a calibration rake. The actuator shaft, which is supported by the nose, is attached to a lead screw and is capable of travelling approximately six inches in the axial direction. The body of revolution is mounted on the forward bulkhead with quickly removable set screws. Pressure and electrical leads are secured to the inside of the actuator to prevent unnecessary motion during axial movement of the shaft. The leads pass through a 3/8-in. diameter hole at the base. It is advisable to place all pressure and electrical lead connections inside the actuator, which is provided with a quick-access inspection door on the cylindrical barrel. Limit switches installed on the front and middle bulkhead will prevent any damage that might occur through over-travel of the shaft. A micro-switch and a multi-lobe cam are used in conjunction with an electronic counter device to record the axial position of the shaft. The device is powered with a Globe Moto-Mite miniature 24-v d-c motor.

A heavy-duty linear actuator support such as the one shown in Fig. 2-40 is suitable for large planar or cruciform rakes and has the advantage of being more rigid and less susceptible to angular errors at large extensions than the lighter actuator. The main structure of the actuator supports the internal mechanism and is enclosed in a rotatable case. As the case is rotated, inspection holes in the case expose the internal mechanism of the actuator. A Thompson ball-bushing is mounted on the forward end of the actuator and allows the 1.0-in. i.d. main shaft to move axially. The aft end of the shaft is mounted in a bracket which is moved axially by means of two lead screws. Power from the d-c motor in the aft end of the actuator is transmitted to these screws through a series of gears. As before, electrical impulses from a micro-switch, actuated by a multi-lobe cam, are converted by an electronic device to inches of axial movement. The maximum axial movement of the main shaft is 10 in., and micro-switches are provided to prevent any movement of the shaft beyond the prescribed limits. The design normal force is 250 lb with the main shaft fully extended.

A smaller diameter support with basically the same internal mechanism is shown in Fig. 2-41. One feature of particular interest in this actuator is its ogival forebody, which is required to prevent the support from blocking the tunnel. Considerable experimentation was required to determine the maximum diameter (needed for rigidity) that could be used without choking the tunnel at $M=1.25$. This investigation proved that the choking characteristics at low supersonic speeds are not only dependent on the geometrical cross-sectional area of the support, but that they are also a strong function of the support forebody contour. A comparison of Figs. 2-42 and 2-43 shows the marked effect of substituting a 10-caliber ogive for a 15-deg half-angle conical forebody on cylindrical supports of the same maximum diameter, 3.375 in. The expansion at the sharp corner in high subsonic flow apparently causes a region of disturbance which effectively increases the cross-sectional area and prevents the normal shock from swallowing.

2.5.2 Equipment for Calibration of a Flexible Nozzle

A unique solution to the calibration and correction of the 20-in. supersonic wind tunnel at the CIT Jet Propulsion Laboratory is reported in Ref. 92. The calibration of a flexible nozzle presents

two problems: 1) Determination of the quality of the existing flow field, and 2) necessary changes to improve it. The process is an iterative one, each adjustment giving an improvement on the preceding distribution, within the limits of plate thickness and jack spacing. The adjustments are of two types: symmetrical adjustments to change the centerline Mach number or static pressure distribution, and asymmetrical corrections to change the centerline flow inclinations. These corrections may be made separately, as one does not affect the other.

The first step in calibration is to find at what tunnel stations in the region of the test rhombus the first and second reflections from each jack, downstream of the throat, occur as a function of Mach number. For this the centerline axial total head probe is used. The total head ratio behind a normal shock is an explicit function of the Mach number, which in turn defines the static pressure ratio. If this information is immediately obtainable with the use of an automatic plotter and remote axial actuation of the probe, it is then possible to adjust the jack positions experimentally with a great saving in time.

Such a plotter was developed at the Jet Propulsion Laboratory, where a total head tube rather than static pressure orifices on a calibration wedge is used because the technique speeds the procedure to the point where there is no longer a great advantage in taking one pair of readings and computing both flow inclination and static pressure variation from them. Experience shows that the static pressure reading and total pressure readings do not define the same Mach number in the order of 0.02. This difference is ascribed to the local slope of the boundary layer at the static pressure orifice on the wedge, giving a different virtual wedge angle. The total head probe does not require this additional correction; it provides a larger change in absolute value of pressure for a given change in Mach number.

The outputs from two Statham pressure transducers, one measuring p_t , the other p'_t , are fed through two readouts to opposite ends of a mechanical differential gear whose output corresponds to p_t/p'_t , if p_t does not vary more than a few per cent. Stops are provided to keep within the linear range. The readout sensitivities are set to the total pressure ratio for the nominal Mach number so that any change in p_t which is reflected by a corresponding change in p'_t does not move the pen on the flat-bed plotter.

The sensitivities can be computed for both readouts as a function of Mach number in terms of p_t so that the total pressure ratio at the beginning of a run can be read from two manometers. A centimeter line is then chosen to represent the nearest 0.001 in total pressure ratio, and the pen zero-shifted to read correctly. Two points on each pass (preferably extremes in pressure ratio) are read on manometers and the computed points added to the plots as a scale check.

For flow-inclination measurements a 4-deg half-angle wedge with static orifices at top and bottom is used. The pressure difference between top and bottom orifices for a given wedge is directly proportional to the flow inclination for a given Mach number and total pressure. The wedge is remotely actuated, and the pressure difference is sensed with a pressure transducer and calibrated with a micromanometer

teed into the line. The wedge is run both upright and inverted to determine the aerodynamic zero. The scale is set in advance to be 0.1-deg flow inclination per centimeter. Then, for each Mach number to be calibrated, the readout sensitivity is computed in ohms as a constant times the supply pressure in centimeters of mercury. Since flow inclination is not as sensitive to supply-pressure fluctuations, some variation in supply pressure during a run is allowable. A calibration resistor allows the setting to be checked periodically by comparing the calibration swing of the pen with the computed excursion. As before, the maximum and minimum points should be read on a micromanometer, and then computed and plotted on the same graph to give a final check on the scale setting.

The results of such a calibration in the JPL 20-in. tunnel gave static pressure variation of less than $\pm 1.5\%$ at all Mach numbers, and centerline flow inclinations of 0 ± 0.1 deg. Vertical traverses which were taken every 4 in. from ceiling to floor through the centerline gave inclinations in the order of ± 0.2 deg.

2.6 Measurement of Internal-Flow Characteristics

Most of the internal-flow testing in the supersonic wind tunnel, aside from nozzle calibrations, is the testing of inlet diffusers for turbojets or ramjets. One of the prime necessities for this purpose is a well-designed force and balance support. It is usually designed for testing axially symmetric nose inlets, but can readily be adapted for the testing of two-dimensional inlet sections.

2.6.1 Design and Operation of a Force and Pressure Support

The force and pressure support shown in Fig. 2-44 was developed to measure the over-all axial force of a diffuser model as well as the pressures needed to compute the following:

1. Pressure recovery of the diffuser
2. Capture area ratio (or mass-flow ratio)
3. Velocity distribution at the rake
4. Static-pressure amplitude and frequency at the location of the rake under buzz conditions
5. External pressure distribution on the model, if pressure orifices and leads are provided in the model.

With the above information, it is possible to compute the external force acting on the diffuser cowl.

The support consists of three concentric shells as shown in Fig. 2-44. The inner shell provides the duct contour and supports the rake, the middle shell is attached to the diffuser duct section or nose to be tested and acts on instrumented cantilever beams when a force is applied, and the outer shell provides support for the internal mechanism and also acts as a windshield. The inner and outer shells are rigidly fastened together. The middle shell is supported between the inner and

outer shells by means of bearings which allow it to move fore and aft as axial loads are applied. Electric strain-gages, wired as two complete bridges, are mounted on two cantilever beams which restrain the motion of the middle shell. The strain-gage beams may be remotely disengaged from contact with the middle shell. This enables the operator to relieve the strain gages from shock loads that are encountered during starting and stopping of the tunnel and during violent buzz conditions. It also enables the operator to check the zero-load readings on the strain gages so that any shift in the output may be detected while the test is in progress. It is especially important that the solenoid be energized to disengage the beams under buzz conditions, since experience has shown that the strain gage itself will fail due to fatigue after a few hours exposure to such conditions.

A throttle located behind the rake can be moved axially to vary the exit area and pressure in the plenum chamber and thereby simulate the pressures encountered during burning in the ramjet combustor. A micro-switch and multi-lobe cam are used in conjunction with a counting device to record the throttle position. Pressure amplitude and frequency during buzz is obtained with a Sheffield reluctance-type static pressure pickup which is mounted in the shell near the total head rake. The output from this pickup is recorded by means of an oscillograph.

The maximum diffuser inlet size can be obtained by using Fig. 2-45. The ratio of the exit area to the inlet area (A_n/A_i), which will allow the normal shock to swallow at the design Mach number, is plotted as a function of Mach number and pressure recovery. To be conservative it is recommended that, by means of a curve such as this, an inlet size should be chosen corresponding to the lowest Mach number at which tests are to be run. A value of 80% of the maximum allowable exit area is recommended for A_n in the calculation to allow for the possibility that the pressure recovery will be lower than predicted and to allow for the attainment of several swallowed shock data points. A set of curves for converting the area ratio to the recommended design inlet diameter based on the above statements is also included in Fig. 2-45 for several OAL pressure supports which will be mentioned later.

Figure 2-46 illustrates the mounting end of the model which is attached to the OAL-22 support. As will be noted, the pressure leads from the model should be recessed and should come out of the mounting end of the model in the position shown so that they can be led out through the external channels around the internal mechanism and back into the support at the base, where they can be threaded out through the tunnel crossarm. The number of metal pressure leads that may be brought from the model is limited by the dimensions shown. These dimensions take into consideration the distance between the windshield and the retainer ring. Any binding that may occur between the pressure leads and the force-measuring support can of course influence the strain gage readings. Therefore, it is advisable to keep the number of pressure leads to a minimum and also to have a minimum number of bends in the leads as they pass from the mounting end of the model to the pressure lead channel. The gap between the mounting end of the model and the windshield can be varied to keep the leakage from the balance plenum chamber to a minimum by means of a labyrinth seal.

A disassembled view of the OAL-22 support with a typical test configuration is shown in Fig. 2-47. Two sets of cantilever beams equipped with strain gages are shown with one set installed. One of these sets is designed for a 200-lb axial force and the other for 400 lb (at a stress under the bridge of 30,000 psi). The strain-gaged beams can be removed and replaced through access plates while the balance is installed in the tunnel. In some cases, when one of the bridges failed, the test was continued quite successfully on the remaining link.

2.6.1.1 Design Modifications for a Pressure Support

Two diffuser supports of much simpler design are shown in Figs. 2-48 and 2-49. The OAL-39 support is designed to take the same diffuser models as the OAL-22 (Fig. 2-44) and can also be mounted from a crossarm at the rear or on a strut extending from the floor or wall of the tunnel. The OAL-41 support is capable of taking larger model inlets than the OAL-39. Remote control of the throttle as well as position indication are incorporated in both supports.

2.6.2 Reduction of Diffuser Inlet Data

As mentioned above, the diffuser model is attached to a floating member in the support which is restrained from fore and aft motion by two cantilever beams fitted with strain gages to measure the resultant force acting parallel to the model centerline. Base pressure is measured to correct the axial force to free-stream base pressure. A total pressure rake with 33 total pressure probes located on equal areas (see Subsec. 2.6.4) is located at the exit of the diffuser model from which total pressure recovery is obtained. The throttle, for varying back-pressure, consists of an axisymmetric nozzle with a remotely controlled plug that moves into the nozzle to vary the exit area. The exit area for the different throttle settings has been determined by calibration tests with normal shock inlets where capture area ratio was known to be 100%.

Capture area ratio is computed from

$$A_o/A_i = (A_n/A_i) (p_{tr}/p_{to}) (A/A^*)_o \quad (2-42)$$

where

A_o = capture area

p_{tr} = stagnation pressure at the rake

p_{to} = stagnation pressure in the free stream

and

$$\frac{A}{A^*} = \frac{1}{M} \left[\frac{2 + (\gamma - 1) M^2}{\gamma + 1} \right]^{\frac{\gamma + 1}{2(\gamma - 1)}} \quad (2-43)$$

Equation 2-42 is derived from the following assumptions:

1. The mass flow at all stations is equal.
2. There is no loss in total temperature in the diffuser duct.
3. There is no total pressure loss between the rake and the throttle.
4. Flow in the throttle is at sonic velocity.

When the duct area at the rake station and the exit area are known, the Mach number at the rake may be obtained. The capture area ratio is very sensitive to the Mach number at the inlet due to its functional relationship in the $(A/A^*)_o$ factor. Figure 2-50 shows the percentage error in capture-area ratio for a 1% error and also for constant error of 0.01 in Mach number. The internal axial force on the diffuser model may now be calculated from

$$C_{AI} = \frac{(F_r - F_o) + (A_o p_o - A_r p_r)}{q_o A_R} \quad (2-44)$$

where

$$F = \text{stream thrust} = A p (1 + \gamma M^2)$$

$$q = \text{dynamic head} = \frac{1}{2} \rho U^2 = \frac{\gamma}{2} p M^2$$

A_R = any reference area.

The external axial force is given by

$$C_{AE} = C_{A \text{ ind}} - C_{AI} - C_{AB} \quad (2-45)$$

where subscripts

A = axial force

B = base

o = total isentropic stagnation conditions

ind = indicated

Since C_{AI} and C_{AB} are usually large compared with C_{AE} , a 1% error in either of the former will give an error of several per cent in the latter.

The static pressure is measured in the duct just aft of the rake by a transducer and read out on analog-to-digital indicators during the test. A plot of the ratio of this pressure to the local total

pressure as a function of throttle setting constructed at the time of calibration is helpful in the data reduction. It is also desirable to make a plot of P_{tr}/P_{to} versus A_o/A_i during the run so that there will be a sufficient number of data points to define a curve. This is particularly important in the region of critical total pressure.

From eight tests (consisting of 126 runs), during which the flow conditions were maintained as constant as possible, average values of the parameters were obtained. The following table gives an indication of the repeatability of such diffuser tests.

Parameter	± Deviation from Average	
	Mean	Maximum
A_o/A_i	0.0007	0.0060
P_{tr}/P_{to}	0.0007	0.0045
C_{AE}	0.0014	0.0079
Axial Force (lb)	0.34	1.94*

*One point out of 126 runs.

2.6.3 Effect of Model Scale on Diffuser Characteristics

The question of the relative accuracy between identical models of greatly different scale in regard to supersonic inlet diffusers has frequently been raised. In general, it can be stated that pressure recovery and mass-flow ratio are relatively unaffected by large differences in model scale so long as the smaller models are adequately instrumented to measure these parameters and the change in Re is not critical. Oscillatory flow (buzz) conditions are not independent of model scale, however, since the length and volume of the flow channel which generally cannot be scaled, play a part in the buzz frequency and amplitude. For example, buzz frequencies encountered in a full-scale diffuser were of the order of 50 cps, whereas those in a 1/5-scale model were 150 to 250 cps under similar flow conditions. Usually the buzz-free range of mass-flow ratios is greater for the full-scale model than for a small-scale model, but one instance on a particular diffuser type for a ramjet in which the reverse was true has been experienced. Hence, this cannot be considered an axiom.

To indicate the comparative effects of scale on pressure recovery and mass flow, data were obtained for two different scale-model diffusers of the same full-scale configuration. The two models shown in Fig. 2-51 are essentially the same internally except for the rake position with respect to the cowl lip. The external contours are comparable for several inlet diameters aft of the cowl lip. As indicated in Fig. 2-51 there are two items which are not reduced in true scale: 1) Each model was built to the same tolerance in the critical regions (± 0.001 in.) and 2) each model has the same physical lip thickness of 0.005 in. (Note that the ratio of the inlet areas of these models is 5 to 1.) The rake used for measuring pressure recovery of the large

model utilizes 33 total pressure probes located on an equal area basis, while that for the small model uses nine total pressures, also spaced on equal areas.

Figure 2-52 shows the diffuser characteristics obtained for each of these models at four Mach numbers. In general, the agreement between the two models is good. The differences between the maximum capture area ratios are 0.013 at Mach 1.73 and 0.008 at Mach 2.23, increasing to 0.025 at Mach 2.50 and decreasing to 0.010 at Mach 2.77. There is little difference in the maximum pressure recovery obtained at 1.73, and a difference of about 0.015 at Mach 2.23, which is the same order of magnitude as observed at Mach 2.50 and 2.77. It is probably fortuitous that the buzz starts at about the same capture-area ratio for both models at Mach 2.23. Flagged points indicate that buzz is occurring; the reliability of the data at any flagged point is therefore questionable.

At each Mach number, except 2.77, the large model was run three times. The points from every run are plotted. No attempt to differentiate between the runs has been made because the points are crowded. Many of the data points were identical between runs and therefore a single point may represent two data points. All of these points were plotted in order to indicate the repeatability of the measuring apparatus (Fig. 2-44) which was utilized with the large model only. For the small model, the average repeatability within a run was ± 0.001 of both pressure recovery and capture-area ratio.

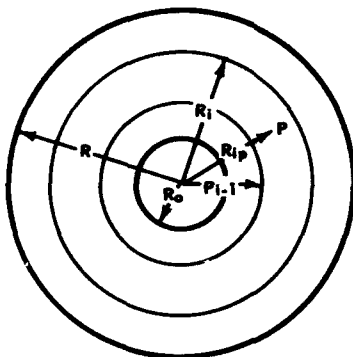
An analysis of the data reduction procedures indicates that if the Mach number at the inlets had been interpolated to the estimated values of free-stream Mach number to the thousandth place instead of the hundredth, the difference between maximum capture-area ratios would have been reduced from 0.013 to 0.011 at nominal Mach 1.73 and from 0.008 to 0.004 at nominal Mach 2.23. This had no effect upon pressure recovery, however.

An examination of the large model innerbody disclosed that from tip to lip the vast majority of stations were 0.001 in. under design contour. This is a condition tending to increase capture, but only in the order of 0.001 in A_0/A_1 , if previous test data may be interpolated to values this small. A similar examination of the small innerbody showed that the first 70% from tip to lip was consistently 0.001 in. under size, and the last 30% was 0.001 in. oversize. Previous test data indicate that slightly larger changes than this in the compressing surface do not change the maximum capture-area ratio, though the peak pressure recovery is affected.

It may be stated that reasonably accurate diffuser data may be obtained from very small models and that a fabrication tolerance of ± 0.001 in. in critical regions is sufficient for Mach numbers less than 4. The above information is a confirmation of earlier tests of full-scale, 1/3-scale, and 1/5-scale diffusers, from which comparable results in capture area, pressure recovery, and external cowl drag (including additive drag) were obtained.

2.6.4 Probe Positions in a Circular Duct

An average pressure or an integrated pressure over the cross section of a circular duct is very easily obtained if the pressure probes are so distributed that each is at the center of an equal area. Pressures are usually measured by means of a rake consisting of a rectilinear array of probes which span the duct. The positions of the probes may be calculated by the following method for the most general case of a duct with an inner body.



Let there be n equal areas in the duct annulus whose limiting radii are R and R_o . P_i is any probe, $0 \leq i \leq n$. R_i and R_{i-1} are the radii of the annulus served by P_i . Then

$$R_i^2 - R_{i-1}^2 = \frac{1}{n} (R^2 - R_o^2),$$

from which one may obtain

$$R_i = \sqrt{R_o^2 + \frac{1}{n} (R^2 - R_o^2)}$$

Similarly, since P_i is centrally located in its annulus,

$$R_i^2 - R_{ip}^2 = R_{ip}^2 - R_{i-1}^2$$

giving

$$R_{ip} = \sqrt{\frac{2i-1}{2n} (R^2 - R_o^2) + R_o^2}$$

When there is no central body, $R_o = 0$ and these equations reduce to

$$R_i = \sqrt{\frac{i}{n}} \cdot R$$

and

$$R_{1p} = \sqrt{\frac{2i-1}{2n}} \cdot R$$

The number of probes on a rake is usually $2n$ since it spans the diameter rather than the radius. Occasionally a cruciform rake may be used with $4n$ probes.

Asymmetric effects may be determined by the rotation of the rake. Directions for the placement of pressure orifices on bodies of revolution given in Subsec. 2.7.1 will also apply to the rotation of the duct rake.

The probe positions for a duct of radius R may be easily determined from Table 2-4.

2.7 Pressure Measurements on the External Surfaces of Models

Pressure distributions on the external surfaces of wind-tunnel models are frequently required to establish the load distribution on the airframe components in the structural design phase. In certain instances where fundamental flow problems (e.g., wing-body or wing-tail interference) are being investigated, pressure measurements are useful for a basic understanding of the phenomena. Because a great deal of time, both in actual testing as well as in data reductions, is required to integrate pressure distributions to give forces and moments, it is better to obtain the latter directly from force tests. The objective of a pressure distribution test should be carefully assessed beforehand so that the test may be accomplished with the least number of pressure orifices and leads, since a great proportion of the test time is taken up by installation, pressure checking, and elimination of leaks. On the other hand, a knowledge of pressure distribution is often used to explain anomalies that occur in force tests.

Several pressure distribution techniques are discussed below.

2.7.1 Pressure Surveys on Bodies of Revolution

Assuming that peripheral and axial pressure distributions are desired on a body of revolution, three pressure orifices located strategically in the same lateral plane around the model can yield a maximum of 46 pressures and two known slopes around the periphery when the model is run through equal positive and negative angle-of-attack ranges at each of four roll orientations. The orifices, however, must be carefully located. They must not be placed at 120-deg intervals, with one orifice on top. Instead, the orifices should be placed at $\theta = 5, 100,$ and 285 deg when the model is at zero roll-orientation ($\phi = 0$). If the model is run through the angle-of-attack range at $\phi = -15, 0, 15,$ and 30 deg, a total of 46 individual pressures are obtained by imaging each pressure about the vertical plane of symmetry (see Fig. 2-53). Although no actual pressures are obtained at $\theta = 0$ and 180 deg, by symmetry it is known that the slope due to angle of attack must be zero at these two points. It is also observed that only four 15-deg gaps exist between adjacent pressures, and these can be moved around to other areas by judicious selection of ϕ 's.

The axial location of the pressure orifices is largely dependent upon the model shape. In the regions of continuous curvature, such as an ogival nose or boattail, close spacing of the orifices is desirable in contrast to the spacing required on cylindrical sections, where the pressures are not expected to vary appreciably. If axial force is of primary interest, the data reduction may be simplified by placing the orifices at centers of equal incremental area, when viewed from the front, in much the same manner as described in Subsec. 2.6.4. A similar approach can be taken if normal force and pitching moment are of primary interest. The initial and final axial orifices should be located as close to the tip and base of the model as is physically possible.

Even though flow irregularities of ± 0.01 in Mach number may be tolerated in force tests, they may produce unwanted anomalies in pressure data. Hence, if the tunnel is not free from flow disturbances, every effort should be made to place the model in a region of the tunnel where the disturbances are fewest. If they cannot be avoided entirely, they may often be allowed to occur in the regions of least interest on the body.

2.7.2 Pressure Surveys on Thin Surfaces

The installation of static pressure orifices on a thin-wing surface is frequently required. In some cases, where pressures are to be measured on one surface of the wing only, it is possible to drill the orifices completely through the wing and to make a soldered connection to conventional metal capillary tubing on the opposite surface of the wing. The tubes can then be run along this surface (provided that they are tacked securely to the surface so that they do not tear loose during operation) and led out of the tunnel through the sting support or wall support device.

If pressures are to be measured on both sides of a wing surface, or if disturbances from external tubing cannot be tolerated, grooves may be machined in the wing surface and the metal tubing soldered into the grooves. After the grooves are filled and faired flush with the original surface, the pressure orifice can then be drilled perpendicular to the surface into the tube. If the surface is sufficiently thick, it can be manufactured in three layers composed of the top and bottom surfaces and an intermediate layer which has machined grooves routed to the desired orifice locations. The orifices can be drilled through the top and bottom surfaces to intersect the appropriate grooves. It is usually good practice to leave sufficient material on the top and bottom surfaces so that the wing may be ground to final dimensions after the three layers are fastened together.

Surface pressures on two-dimensional bodies of small thickness ratio have been measured by traversing the surface with a conventional static pressure probe (Ref. 93). The method may be applied to thin bodies that are difficult to instrument with conventional surface pressure taps. Surface pressures on thin bodies can be measured precisely with probes at points slightly off the surface, since viscosity provides a boundary layer through which the static pressure is constant in a direction normal to the body surface when the curvature is small. This is true only for flows which are irrotational outside the boundary layer. Figure 2-54 shows a pair of slender static-pressure probes aligned with

the chord of a thin two-dimensional airfoil that was used to obtain surface pressure distributions at transonic speeds and small angles of attack. The ratio of probe diameter to airfoil thickness was of the order of one-half, and the probes were held together by a loop of wire approximately two diameters from the tips. The wire loop also made the probe boundary layer turbulent, an important factor in measuring steep pressure gradients. The agreement between interferometer and probe measurements was good except in the vicinity of the airfoil leading edge, as shown in Fig. 2-55; the bow shock was attached in one instance and detached in the other.

2.7.3 Correct Angle-of-Attack Determination for Pressure Models

Since the model support system will deflect to some extent under air loads, the true angle of attack will differ from the indicated angle of attack. In most instances it is necessary to correct for this deflection. The simple technique of taking a spark photograph of the model and some reference line on the wind tunnel window and then reading the angular difference between the reference and the silhouette of the model on a comparator does not give accurate or repeatable results, even when the prints are read when still wet to diminish the effects of paper distortion. A preferred method is to mount strain gages on the support and to calibrate the strain outputs against angle of attack (see Subsec. 3.2.8.6). Experiments at David Taylor Model Basin (Ref. 94) have shown that mounting a single bridge at one particular axial location on a given sting support (determined by experiment) will give an output that is uniquely a function of angle of attack due to support deflection. This bridge cannot correct for angular deflections or slop in the mechanism behind the gages, and deflections in this area must be accounted for in some other manner.

2.7.4 Pressure Model Supports

There are so many ways of mounting pressure models from the wall or floor of the wind tunnel, each dependent on the model configuration, the test section design, and the measurements to be made, that only a few sting-type supports with certain unique features will be described here. Although remotely-controlled variable features in pressure supports are of advantage predominantly in continuous-flow wind tunnels, they also have certain applications in blowdown tunnels, if the blow time is long enough to obtain several sets of data in one run.

2.7.4.1 Roll-Indexing Support

The roll-indexing support shown in Fig. 2-56 was designed for remote control of the roll of sting-mounted pressure models carrying a relatively large number of pressure leads. The case, made of three parts which screw together, has provisions for adding spacers or extensions to vary the axial location of the model in the tunnel. The main shaft (0.75-in. i.d.) is supported by two ball bearings and is roll-indexed by a d-c motor, offset from the centerline of the support so that it will not interfere with the pressure leads. Pressure connections can be made inside the support and are accessible by unscrewing the aft section of the support. If there are only a few pressure connections to be made, they can be made in the area at the forward end of the shaft where provisions have been made for the installation of a cannon plug in the event that it is desired to convert the unit to

support an internal force balance. A wiper mounted on the shaft and the slide wire mounted on the shell indicate the roll attitude of the model. It is possible to rotate the shaft through an included roll-angle range of only 300 deg due to the single-turn, slide-wire limitation, but the model can be oriented at any initial angle with respect to the shaft to give the desired range of investigation. The offset motor housing was resorted to in order that the frontal area could be kept small enough to permit operation at Mach number 1.25 in the OAL closed-wall tunnel.

2.7.4.2 Diffuser Inlet Pressure Support

This pressure support is designed for measuring pressure recovery and mass flow of diffuser inlet models when they are in the presence of a wing or wing-body model. Figure 2-57 shows a sketch of this support carrying a simulated model mounted ahead of the diffuser inlet. The model is mounted on a sting that is supported on the mounting base (Section A-A) which can be moved laterally or vertically to adjust the model position in relation to the diffuser inlet. Any model or engine inlet design may be used with this support within certain physical limits. A total head rake and static pressure orifices at the rake are used to make the measurements required for computing pressure recovery and mass-flow ratio by the method indicated in Subsec. 2.6.2. The range of maximum diffuser inlet sizes that can be used with this support is given in Fig. 2-45.

Table 2-1

Properties of common manometer fluids

Manometer Fluid	Density (lb/ft ³)	Specific Gravity (at 60°F)	Coefficient of Thermal Expansion (1/°F)	$\Delta h_c r = \frac{2i}{p}$ (in. ²)	Chemical Formula	Color*	Water Solubility	Remarks
Distilled Water	62.3623	1.000	--	0.0227	H ₂ O	Colorless	--	Corrodes iron and steel
Ethyl Alcohol	49.55	0.7944	1.12×10^{-3} (68°F)	0.0091	C ₂ H ₅ OH	Colorless	Yes	Corrodes iron and steel
Methyl Alcohol	49.69	0.7969	1.199×10^{-3}	0.0088	CH ₃ OH	Colorless	Yes	Corrodes iron and steel; poisonous and toxic
Ethyl Alcohol- Water Mixture (2:1 by weight)	--	0.880	--	--	--	Colorless	Yes	Corrodes iron and steel
Methyl Alcohol- Water Mixture (2:1 by weight)	--	0.883	--	--	--	Colorless	Yes	Corrodes iron and steel; poisonous and toxic
Acetylene Tetrabromide (Merriam No. 3)	184.83	2.9638 (68°F)	1.067×10^{-3} (55-100°F)	--	CHBr ₂ CHBr ₂	Yellow (red for commercial use)	No	Corrodes iron and steel, weakens synthetic en- amels and plasticized rubber; poisonous
Ellison Draft Gage Oil	52.083	0.834	3.66×10^{-4} (30-112°F)	--	Mineral Oil	Red	No	Non-corrosive; poisonous
Merriam Red Oil	51.646	0.827	3.73×10^{-4} (30-105°F)	--	Mineral Oil	Red	No	Non-corrosive; poisonous
Merriam Unity Oil	63.291	1.047	3.875×10^{-4} (30-110°F)	--	Mineral Oil and Hollowax	Red	No	Non-corrosive; poisonous
Kerosene	51.21	0.820	0.45×10^{-3} (approx)	0.0008	--	Colorless	No	Non-corrosive; poisonous and toxic
Mercury	846.26	13.570	1.819×10^{-4} (68°F)	0.0113	Hg	Silver	No	Combines with brass and copper; poisonous and toxic

* Coloring agent: Pontamine for red, Fluorescein for green.

Note: Boiling and melting points at 1 atm for Acetylene Tetrabromide are 462°F and 32°F; for mercury, they are 675°F and -37.8°F.

Table 2-2

Sample cases showing lag effect

Case	Tube No. 1 l_1 (in.) d_1 (in.)	Tube No. 2 l_2 (in.) d_2 (in.)	Instrument Volume (in. ³) V_m V_d	Final Pressure P_f (psi)	δ	ϵ	Effect Shown	Time (sec)
1	60 0.03	0 --	0.3 0	7.35	1	0.01	Basic	1.5
2	600 0.03	0 --	0.3 0	7.35	1	0.01	Length	23
3	600 0.06	0 --	0.3 0	7.35	1	0.01	Diameter	3.3
4	60 0.03	540 0.054*	0.3 0	7.35	1	0.01	Optimum d_2	11
5	60 0.06	540 0.09*	0.3 0	7.35	1	0.01	Optimum d_2	2.0
6	60 0.06	540 0.10*	6.0 -0.3	7.35	1	0.01	Instrument Volume	2.4
7	60 0.06	540 0.10*	6.0 -0.5	1.47	9	0.01	Final Pressure	14
8	60 0.06	540 0.10*	6.0 -0.5	1.47	9	0.05	Allowable Error	10

* Optimum

Table 2-3

Shock angles for cones as a function of Mach number
(θ = nose semi-angle)

Mach No.	Shock Wave Angles					
	$\theta = 5$	10	15	20	25	30
1.05	72.4	--	--	Detached Bow-Wave		
1.1	65.6	67.0	--			
1.2	56.4	57.5	60.6	72.5	--	--
1.3	50.5	51.4	53.4	58.0	--	--
1.4	45.5	46.3	48.3	52.8	59.3	--
1.6	39.0	39.4	41.6	46.2	52.2	59.1
1.8	34.0	34.6	37.1	41.6	46.7	52.6
2.0	30.1	31.3	33.7	38.0	43.0	48.3
2.5	23.8	24.8	27.8	32.2	37.1	42.6
3.0	20.0	21.3	24.7	29.3	34.2	39.5
3.5	16.9	19.4	23.4	27.7	32.7	38.3
4.0	14.8	17.5	22.0	26.5	31.5	37.2
4.5	13.4	16.5	21.9	25.6	30.9	36.5
5.0	12.4	15.5	20.0	24.9	30.2	35.8
5.5	11.5	14.9	19.3	24.4	29.8	35.2
6.0	10.7	14.4	18.9	24.0	29.4	34.8
6.5	10.1	14.0	18.5	23.6	29.1	34.5
7.0	9.5	13.5	18.2	23.3	28.9	34.3
7.5	9.0	13.2	18.0	23.0	28.7	34.1
8.0	8.5	13.0	17.8	22.8	28.5	34.0

Table 2-4
Probe distances from center for equal-area spacing

$\frac{1}{n}$	Position Factor, F									
	1	2	3	4	5	6	7	8	9	10
2	0.500	0.866								
3	0.409	0.707	0.913							
4	0.354	0.612	0.791	0.941						
5	0.316	0.548	0.707	0.837	0.949					
6	0.289	0.500	0.646	0.763	0.866	0.957				
7	0.267	0.463	0.597	0.707	0.801	0.886	0.963			
8	0.250	0.433	0.559	0.661	0.750	0.830	0.902	0.968		
9	0.236	0.409	0.527	0.623	0.707	0.782	0.850	0.913	0.972	
10	0.224	0.387	0.500	0.592	0.671	0.742	0.806	0.866	0.922	0.975

Note: Distance of probe from center of circular duct = FR , where R = duct radius.

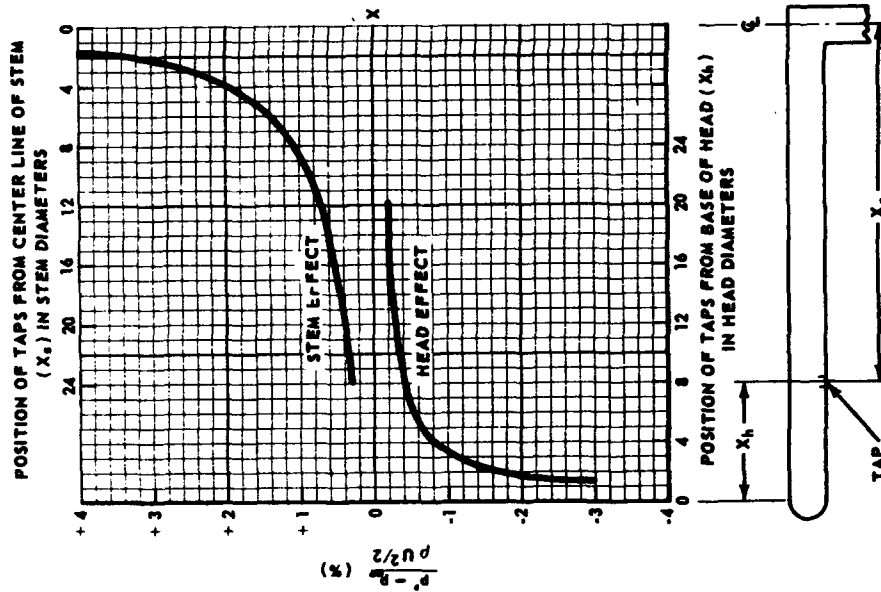


Fig. 2-1. Inherent probe errors on stream-pressure measurements in subsonic flow.

Source: Ref. 8

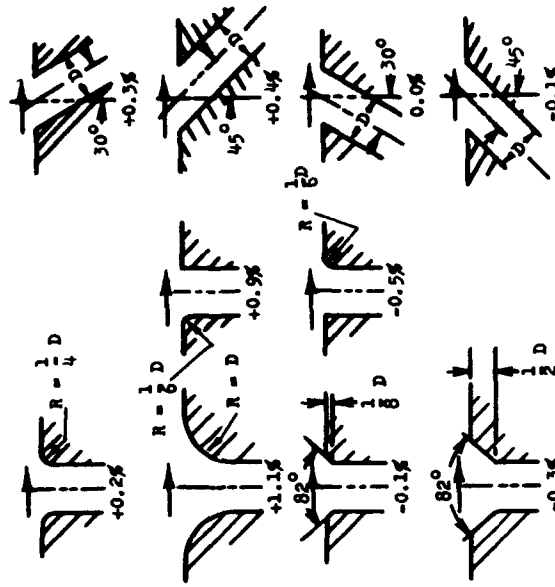


Fig. 2-2. Effect of orifice edge form on static pressure measurements (Correction for values in Fig. 2-3).

Source: Ref. 8

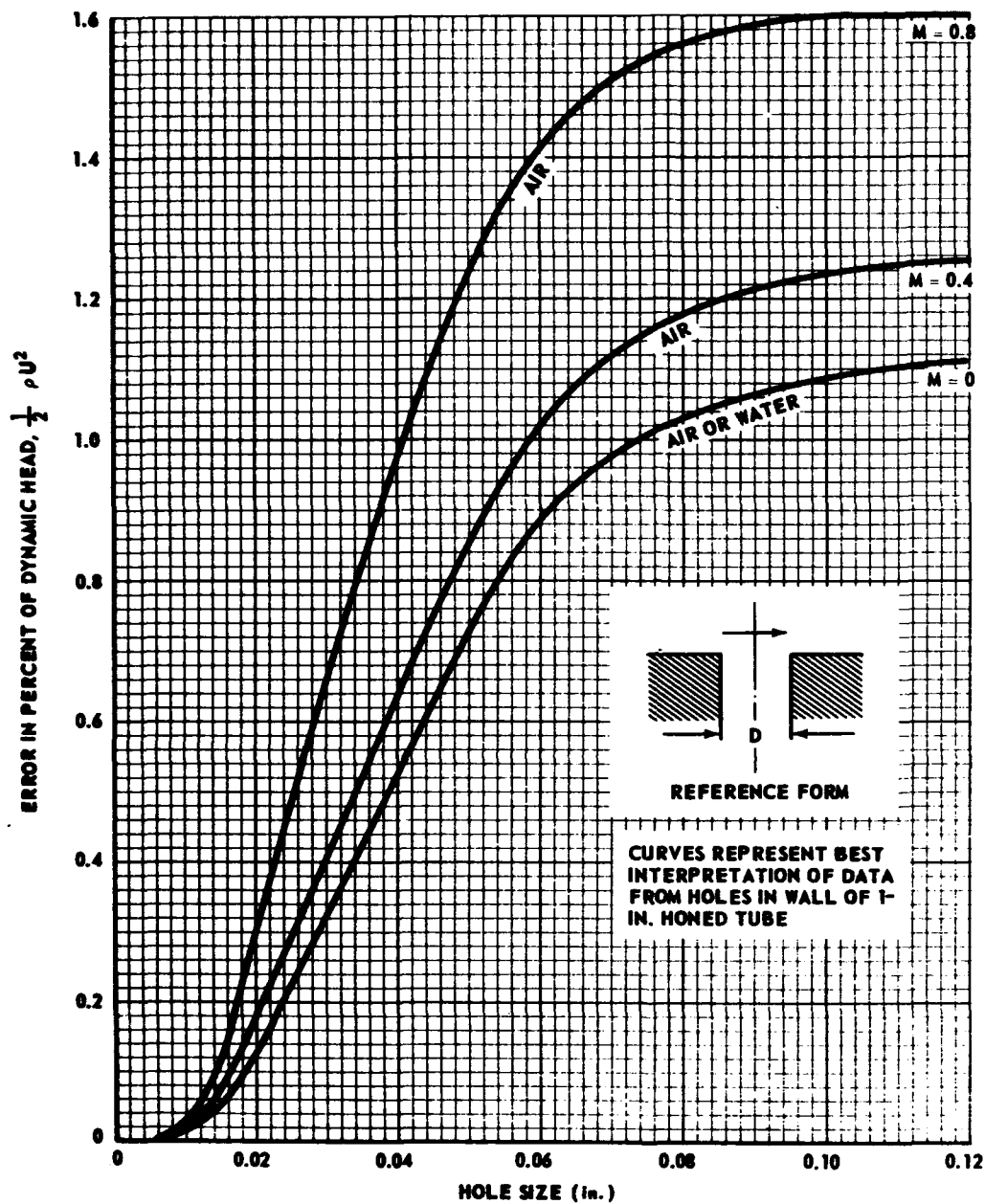


Fig. 2-3. Effect of hole size on stream-pressure measurements for air or water ($M = 0$) for square-edged hole.

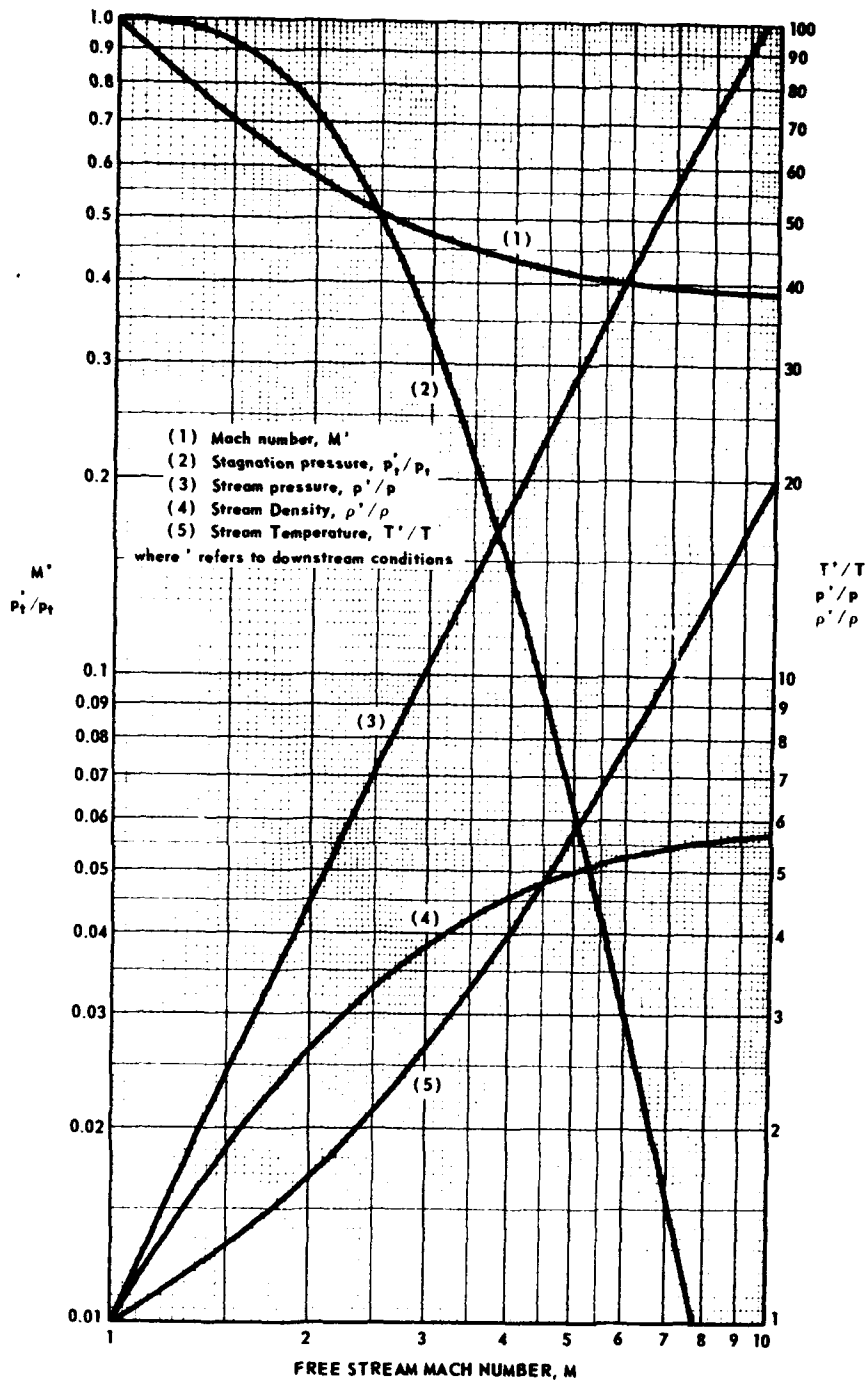


Fig. 2-4. Change in flow parameters through a normal shock in air.

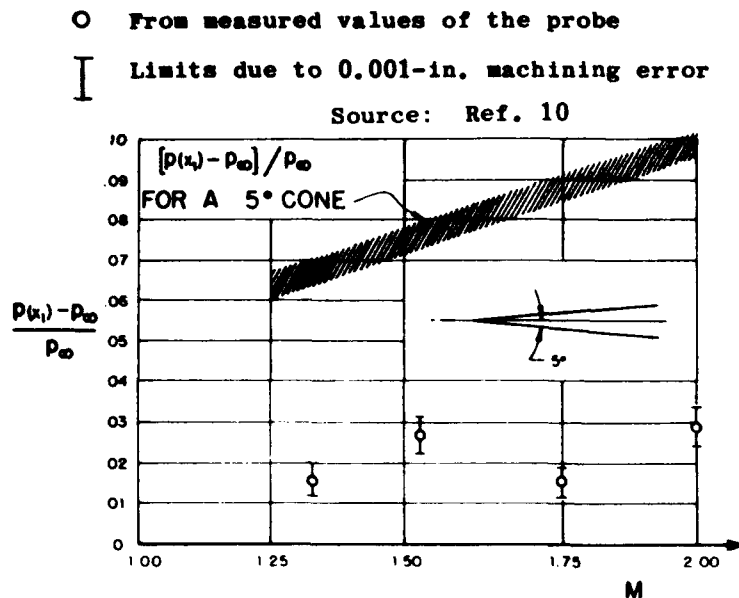


Fig. 2-5. Comparison of static pressure on a 5-deg cone and on a specially designed probe.

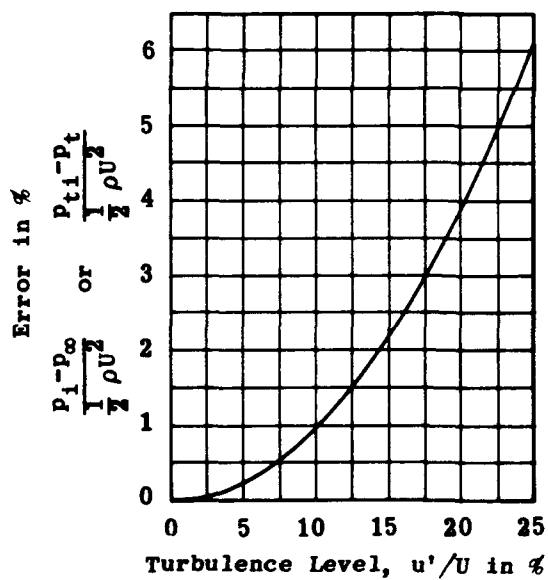


Fig. 2-6. Error in stream-pressure and stagnation-pressure measurements due to isotropic turbulence.

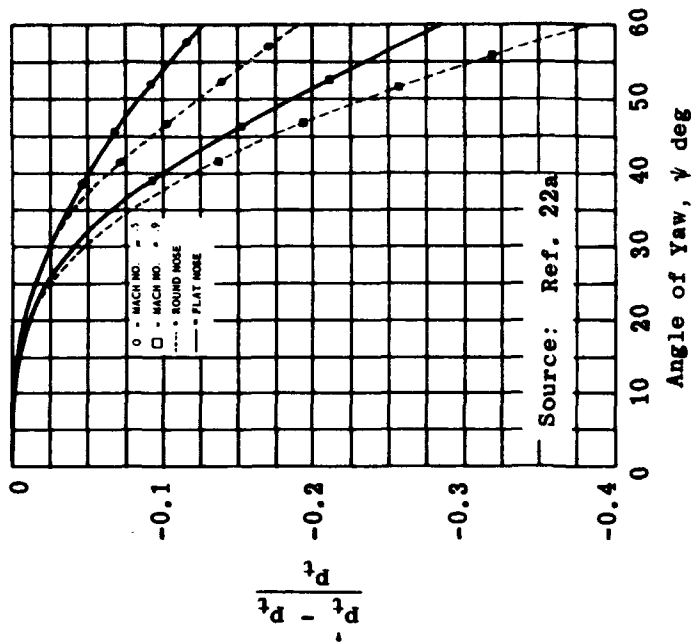


Fig. 2-8. Stagnation-pressure error vs angle of yaw at constant Mach number for flat and round-nosed probes at subsonic speeds.

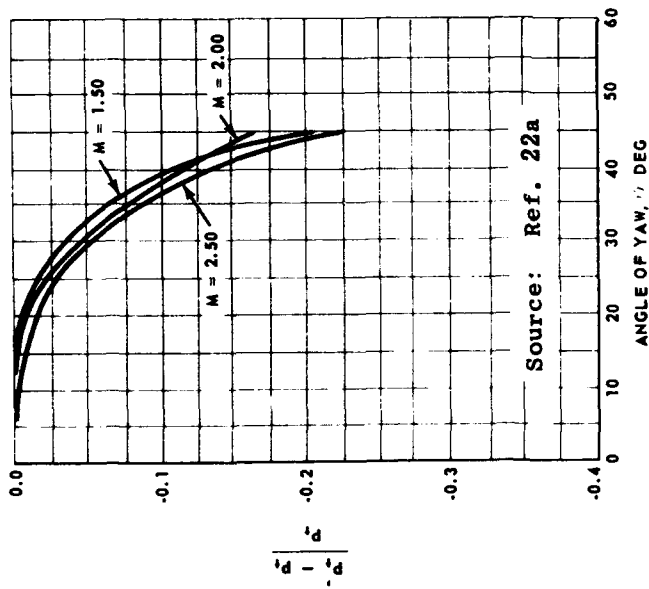


Fig. 2-7. Stagnation-pressure error vs angle of yaw at constant Mach number for flat and round-nosed probes at supersonic speeds.

Source: Refs. 23 and 24

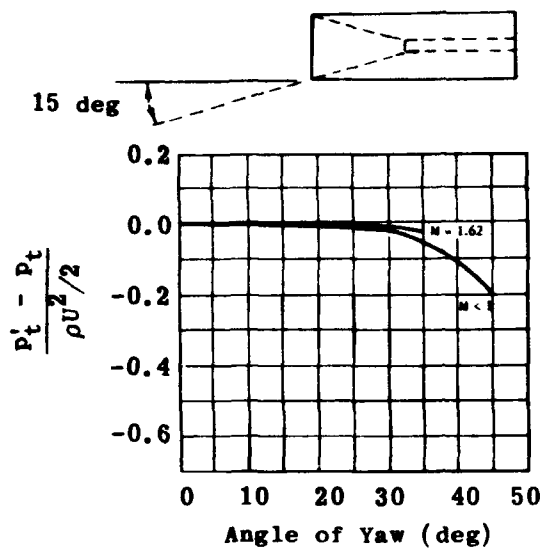


Fig. 2-9. Stagnation-pressure error vs angle of yaw at constant Mach number for flat-nosed probes with internal bevel.

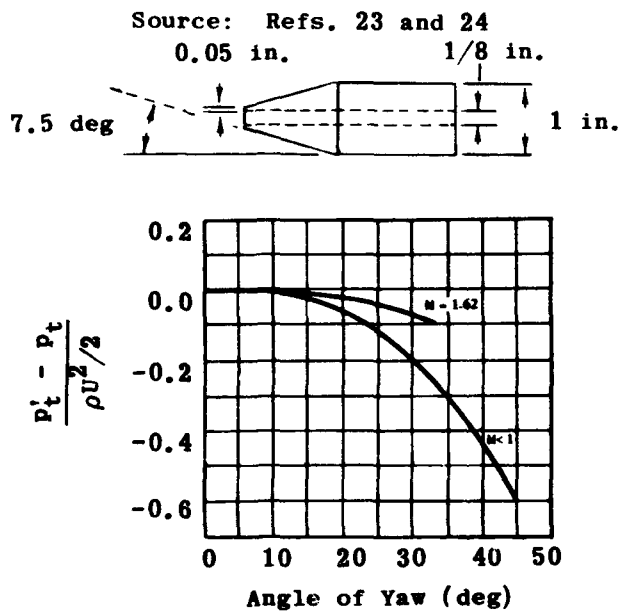


Fig. 2-10. Stagnation-pressure error vs angle of yaw at constant Mach number for truncated-cone probes.

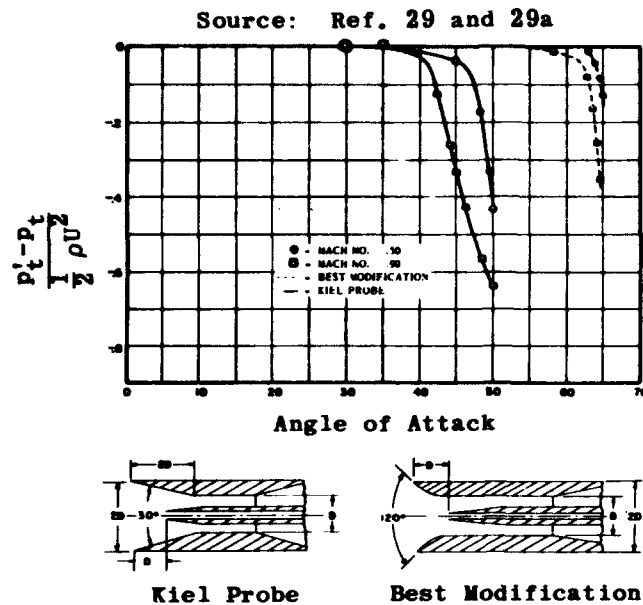
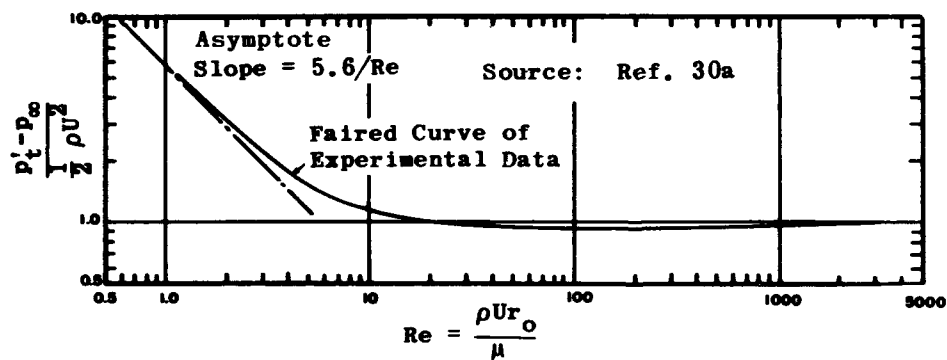


Fig. 2-11. Stagnation pressure error vs angle of attack for shrouded stagnation-pressure probes.



(r_o is the outside radius of a thin-walled tube)

Fig. 2-12. Viscous effects in a stagnation-pressure tube.

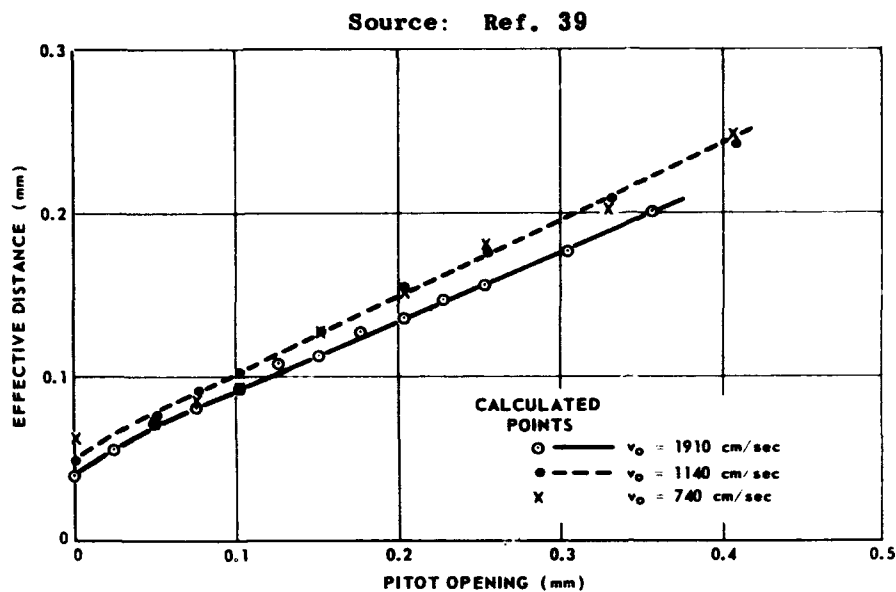


Fig. 2-13. Effective position vs mouth opening for Stanton's boundary-layer probe.

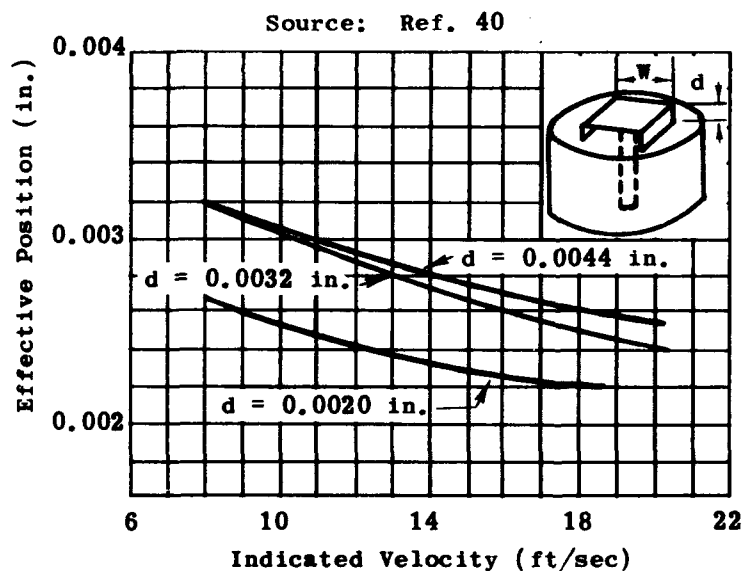


Fig. 2-14. Effective position vs velocity for Fage and Falkner boundary-layer probe.

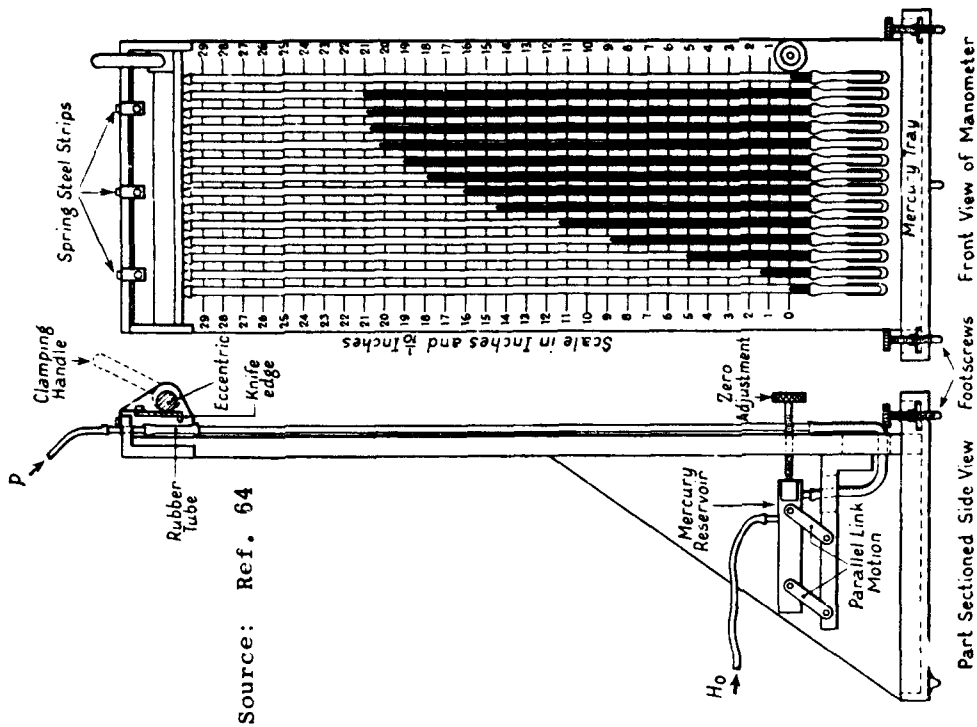


Fig. 2-16. Manometer board and associated hardware.

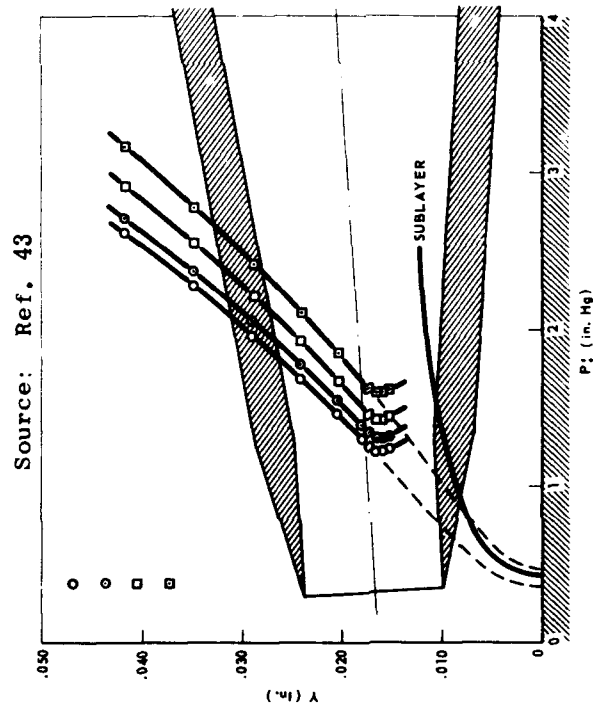


Fig. 2-15. Probe contact as shown by pitot pressure survey.

Source: OAL

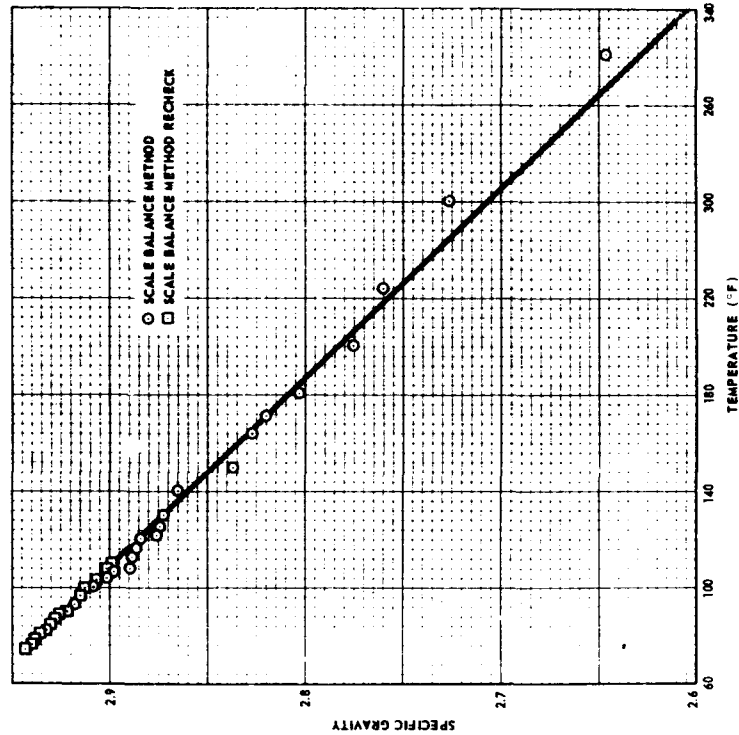


Fig. 2-18. Specific gravity characteristics of tetrobromoethane.

Source: OAL

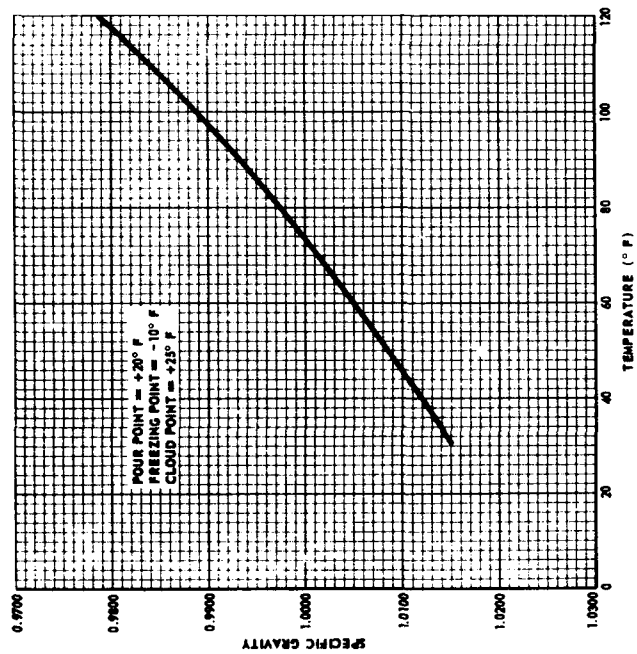


Fig. 2-17. Specific gravity characteristics of Merriam Unity Oil.

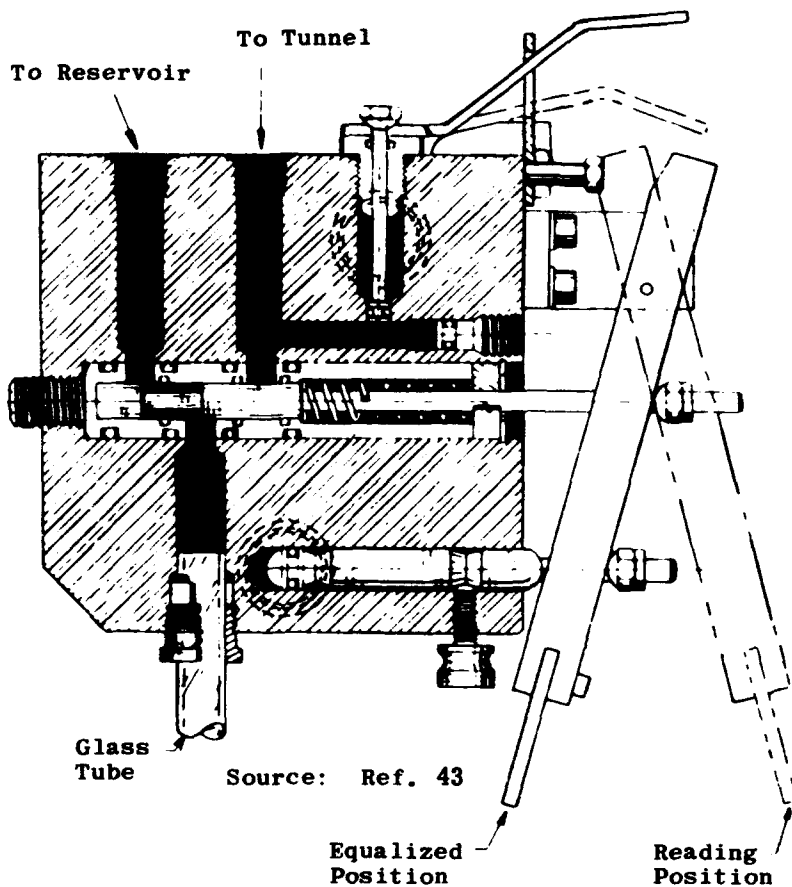


Fig. 2-19. Manometer sliding valve and porting.

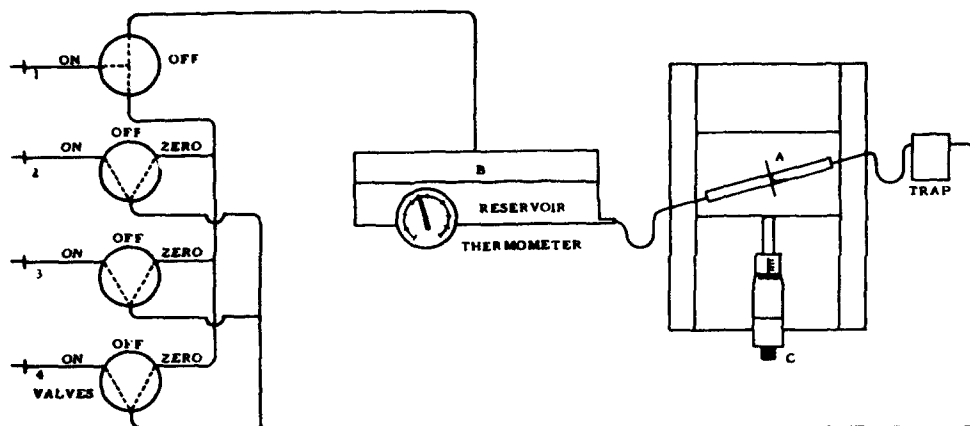


Fig. 2-20. Schematic of commercial micromanometer.
(Flow Corp., Mod. MM-2)

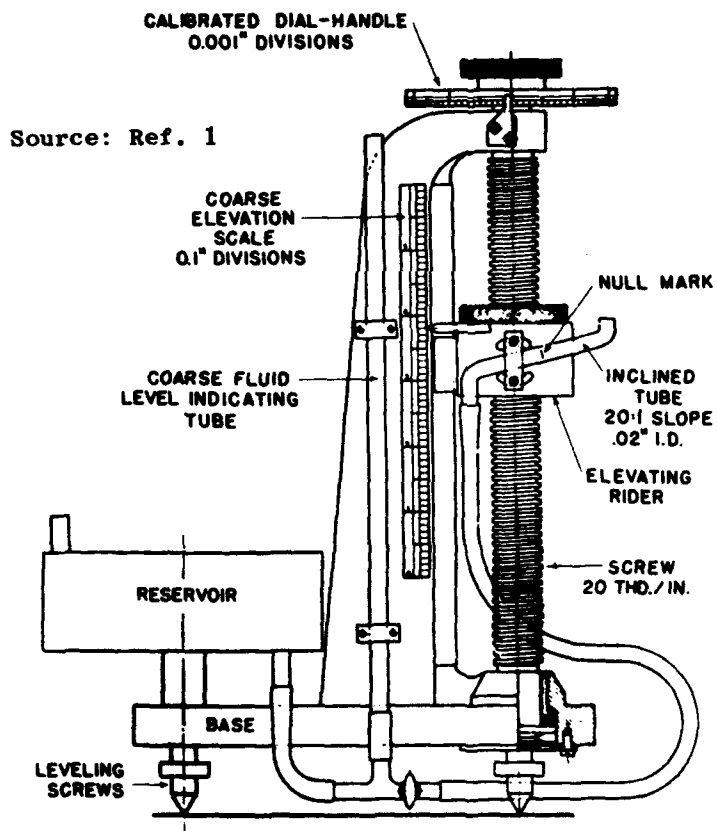


Fig. 2-21. NACA micromanometer.

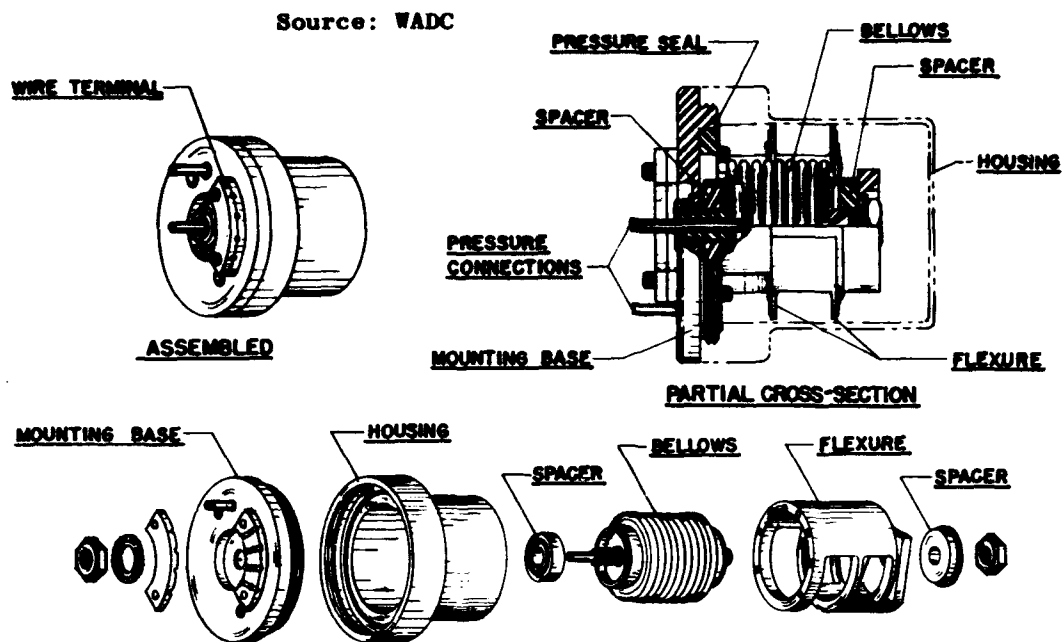


Fig. 2-22. Exploded view of pressure transducer.

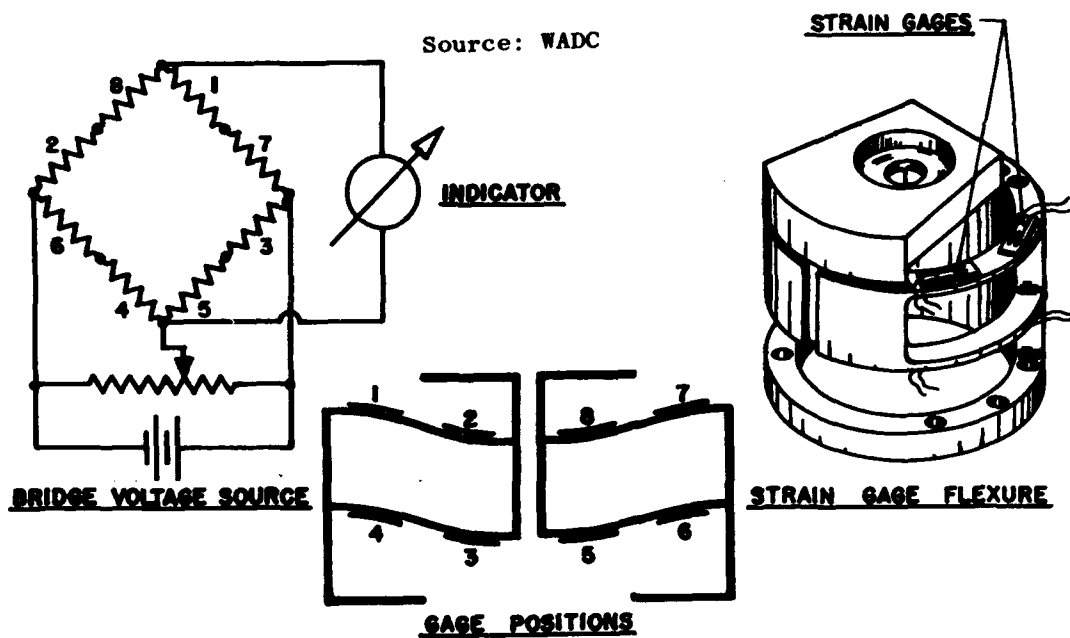


Fig. 2-23. Operational details of pressure transducer.

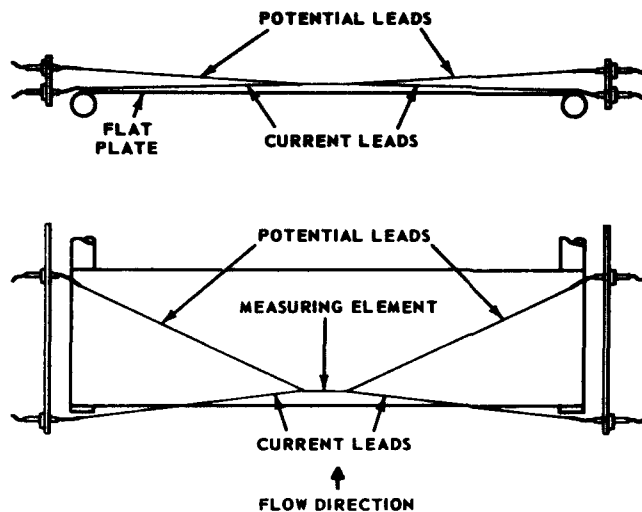


Fig. 2-24. Diagram of wire probe and flat plate.

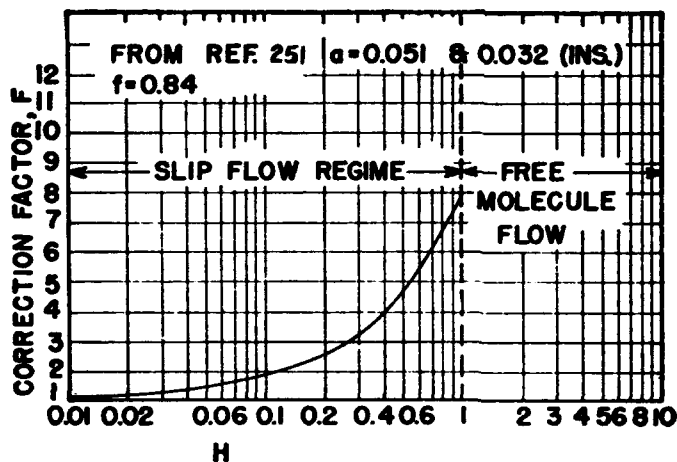


Fig. 2-25. Slip-flow correction factor for glass and copper tubing.

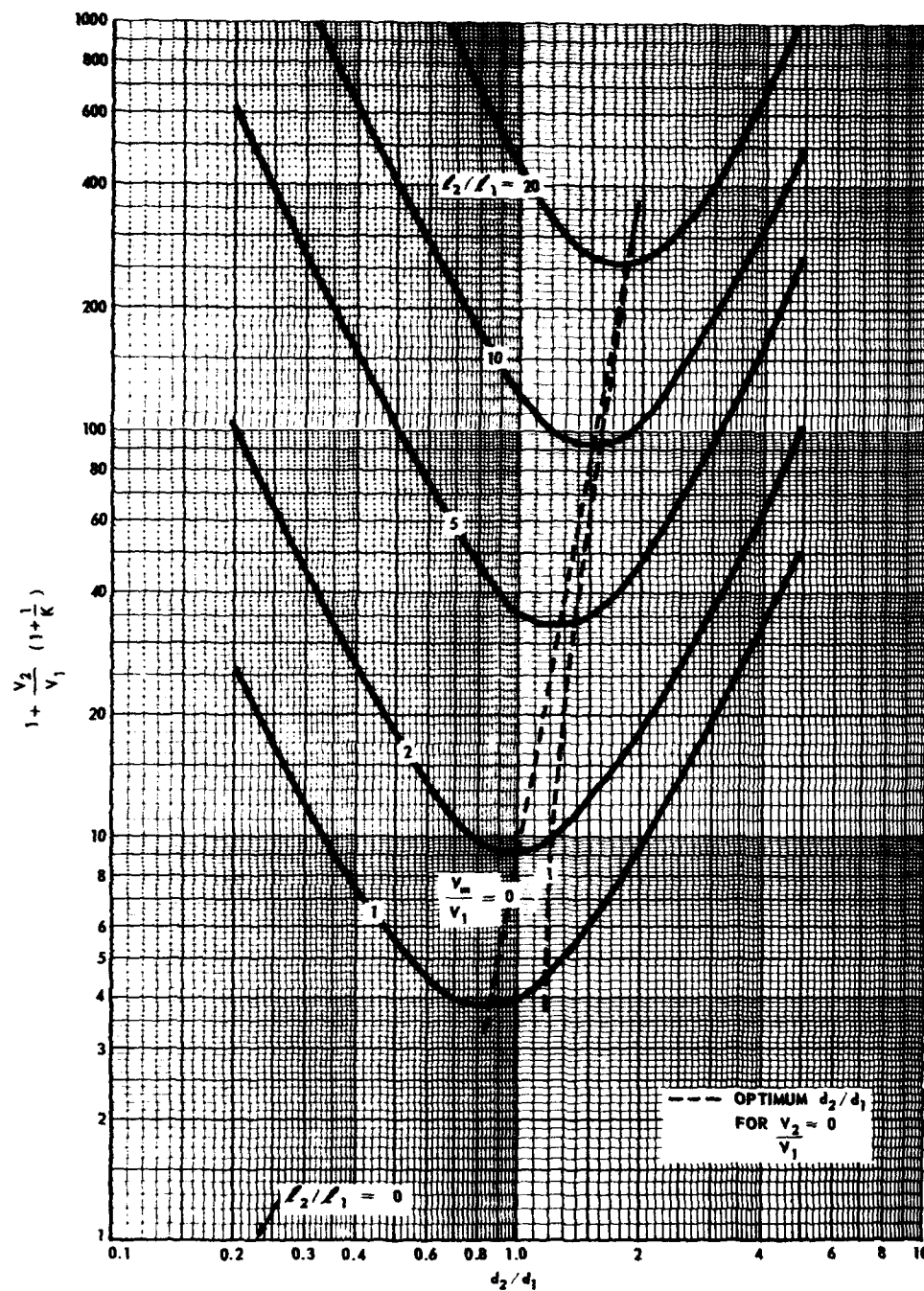


Fig. 2-26. Plot of $1 + \frac{v_2}{v_1} \left(1 + \frac{1}{K}\right)$ vs $\frac{d_2}{d_1}$ for various values of $\frac{l_2}{l_1}$ (Eq. 2-31).

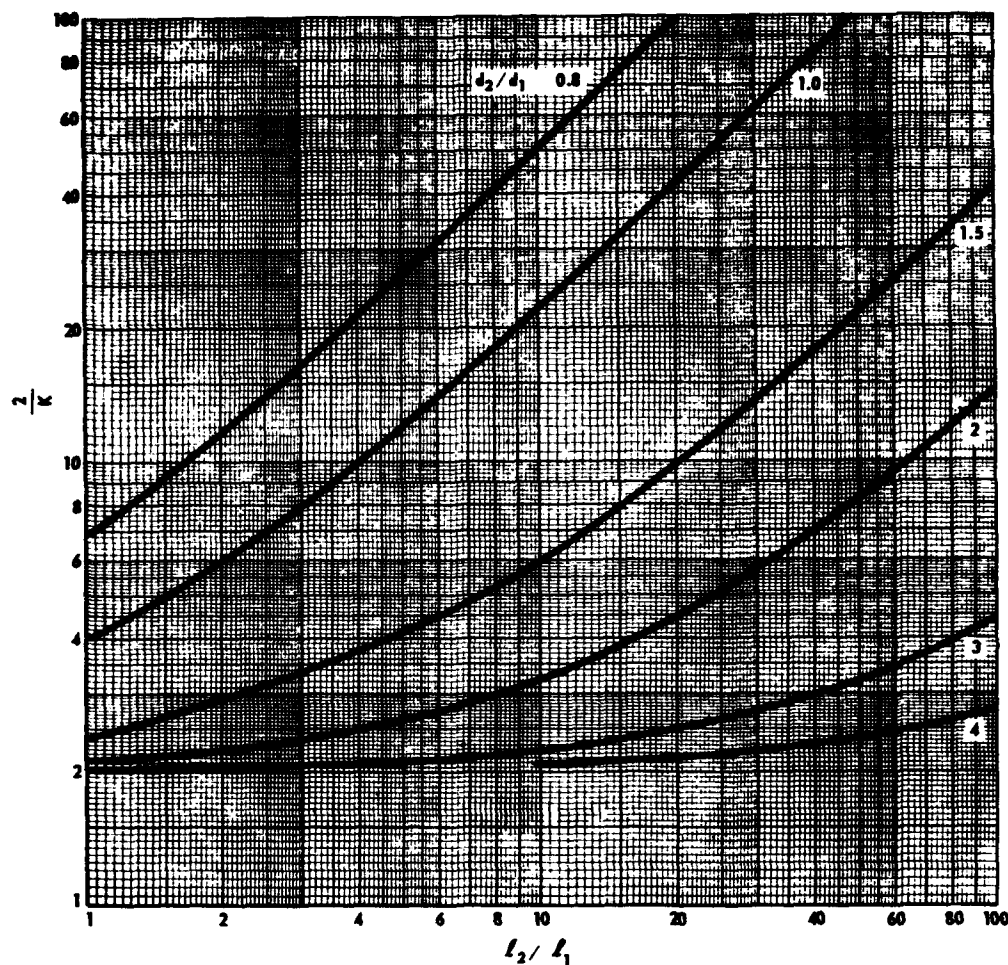


Fig. 2-27. Plot of $\frac{2}{K}$ vs $\frac{l_2}{l_1}$ for various values of $\frac{d_2}{d_1}$
(Eq. 2-31).

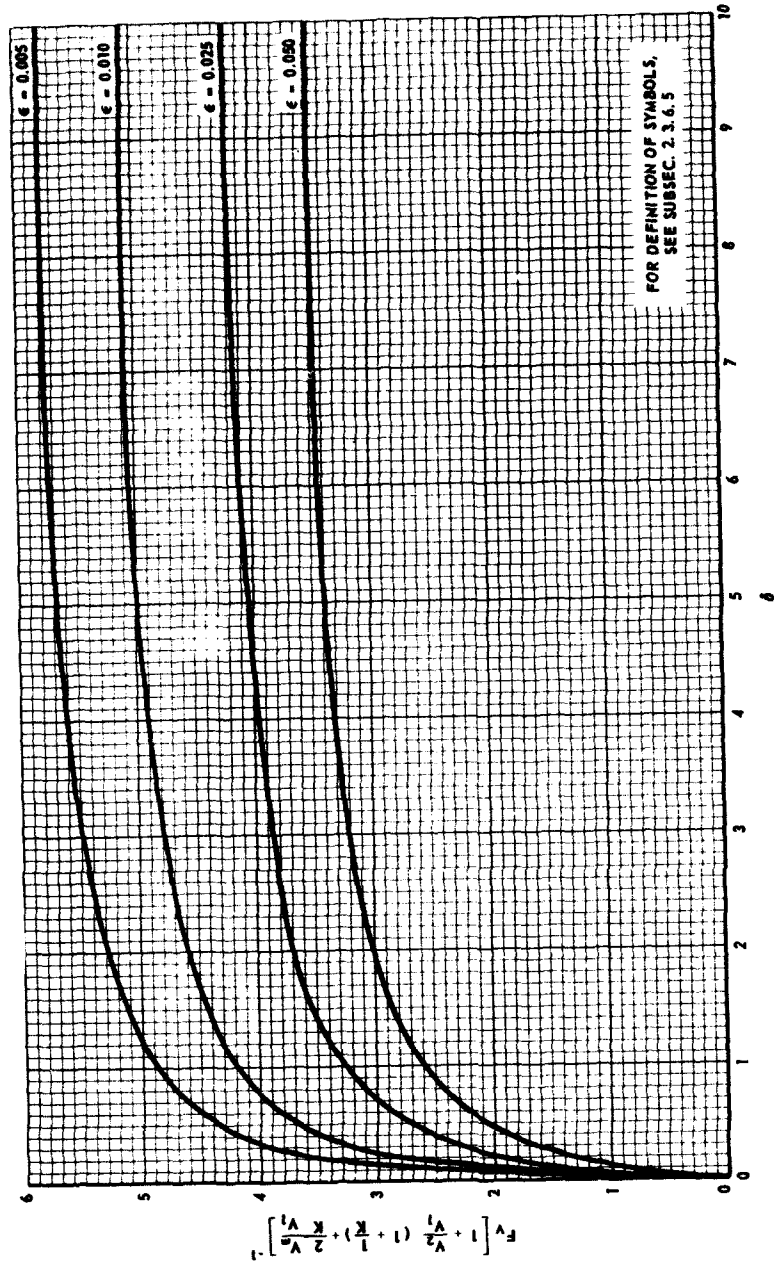


Fig. 2-28. Values of $F_v \left[1 + \frac{V_2}{V_1} \left(1 + \frac{1}{k} \right) + \frac{2}{k} \frac{V_2}{V_1} \right]^{-1}$ for $\epsilon = 0.05, 0.025, 0.01, \text{ and } 0.005$ (Eq. 2-31).

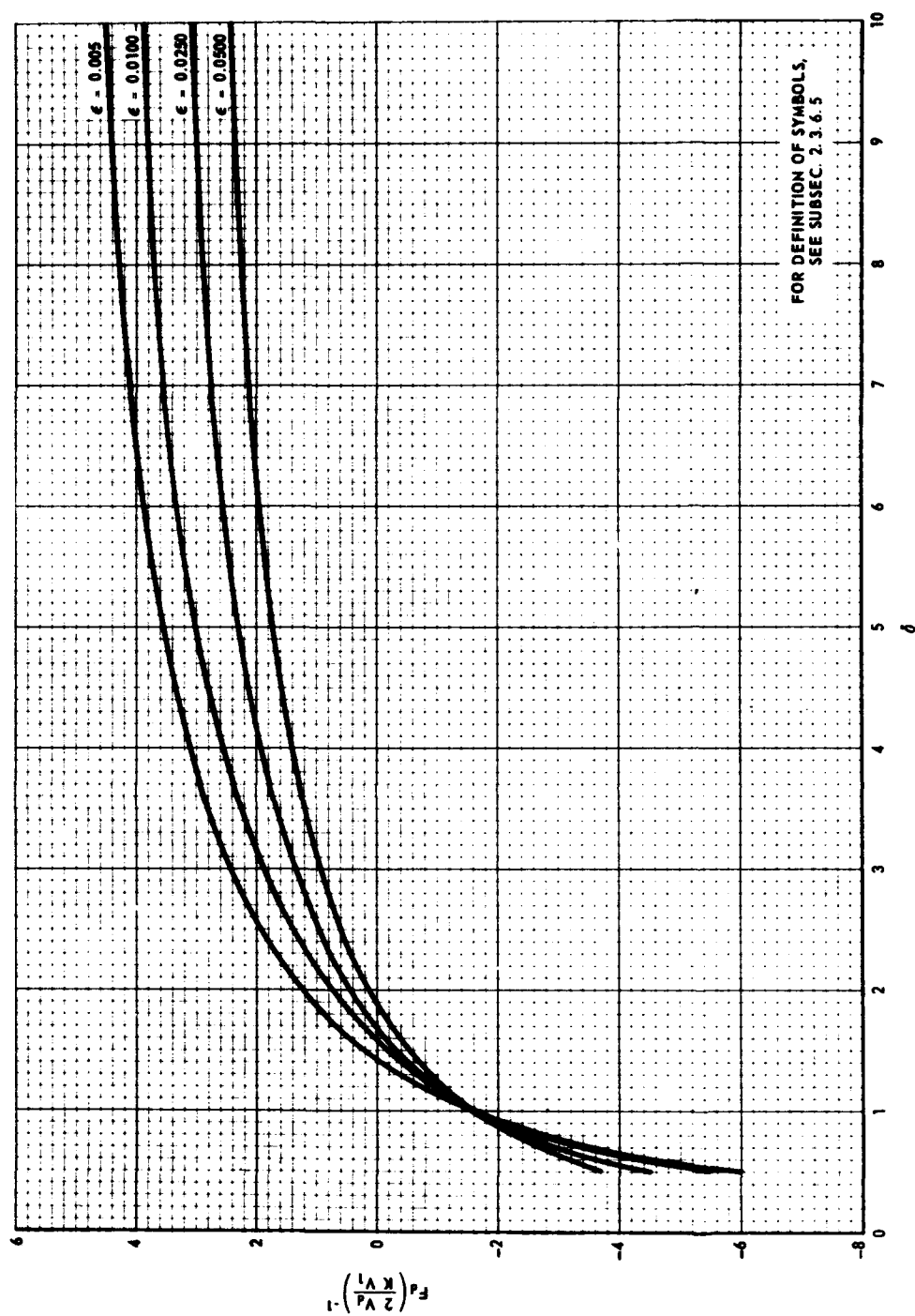


Fig. 2-29. Values of $F_d \left(\frac{2 V_d}{K V_1} \right)^{-1}$ for $\epsilon = 0.05, 0.025, 0.01$, and 0.005 (Eq. 2-32).

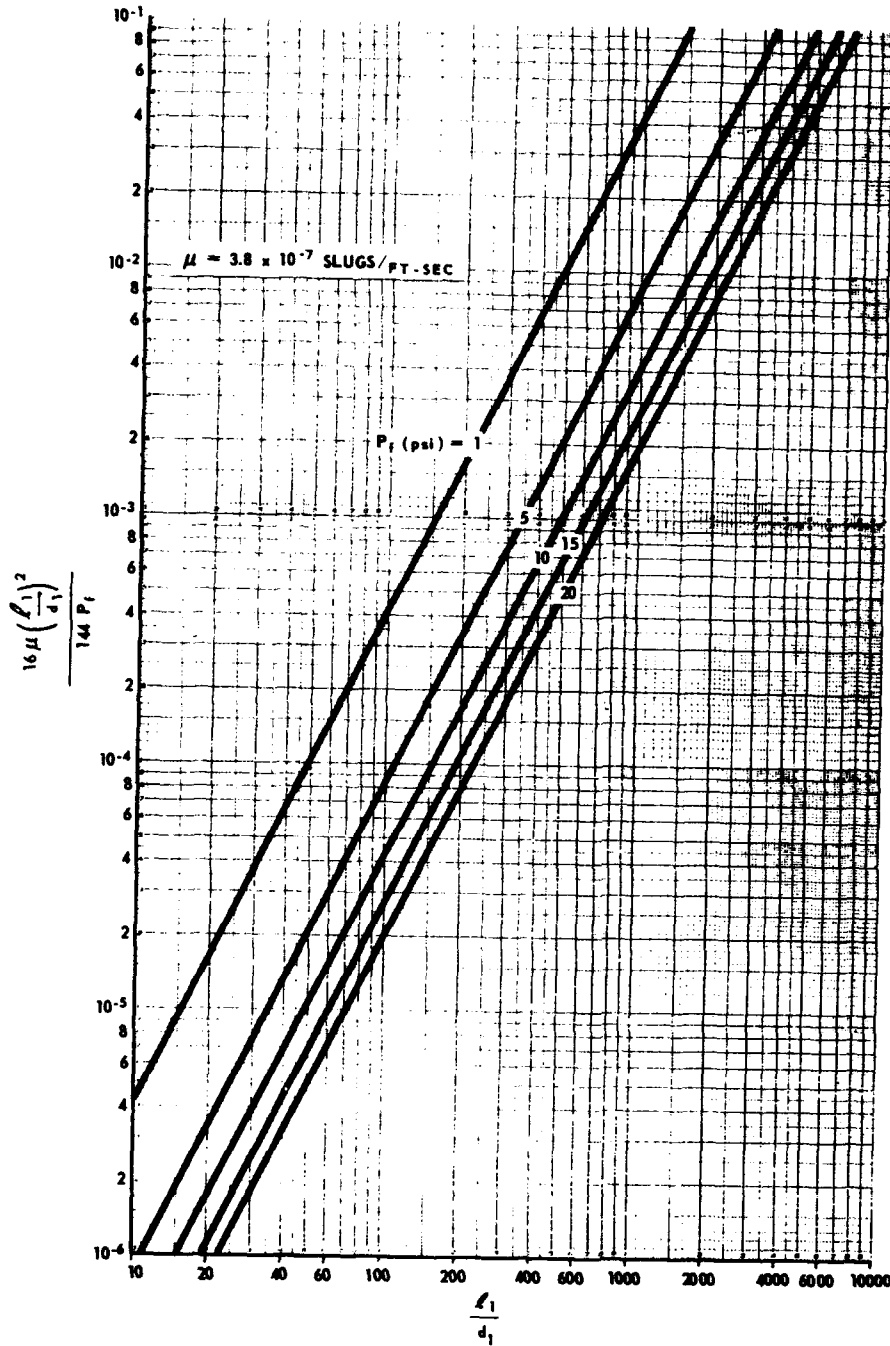


Fig. 2-30. Plot of $\frac{0.111 \mu (\ell_1/d_1)^2}{p_f}$ vs $\frac{\ell_1}{d_1}$ for various values of p_f (Eq. 2-30).

Source: OAL

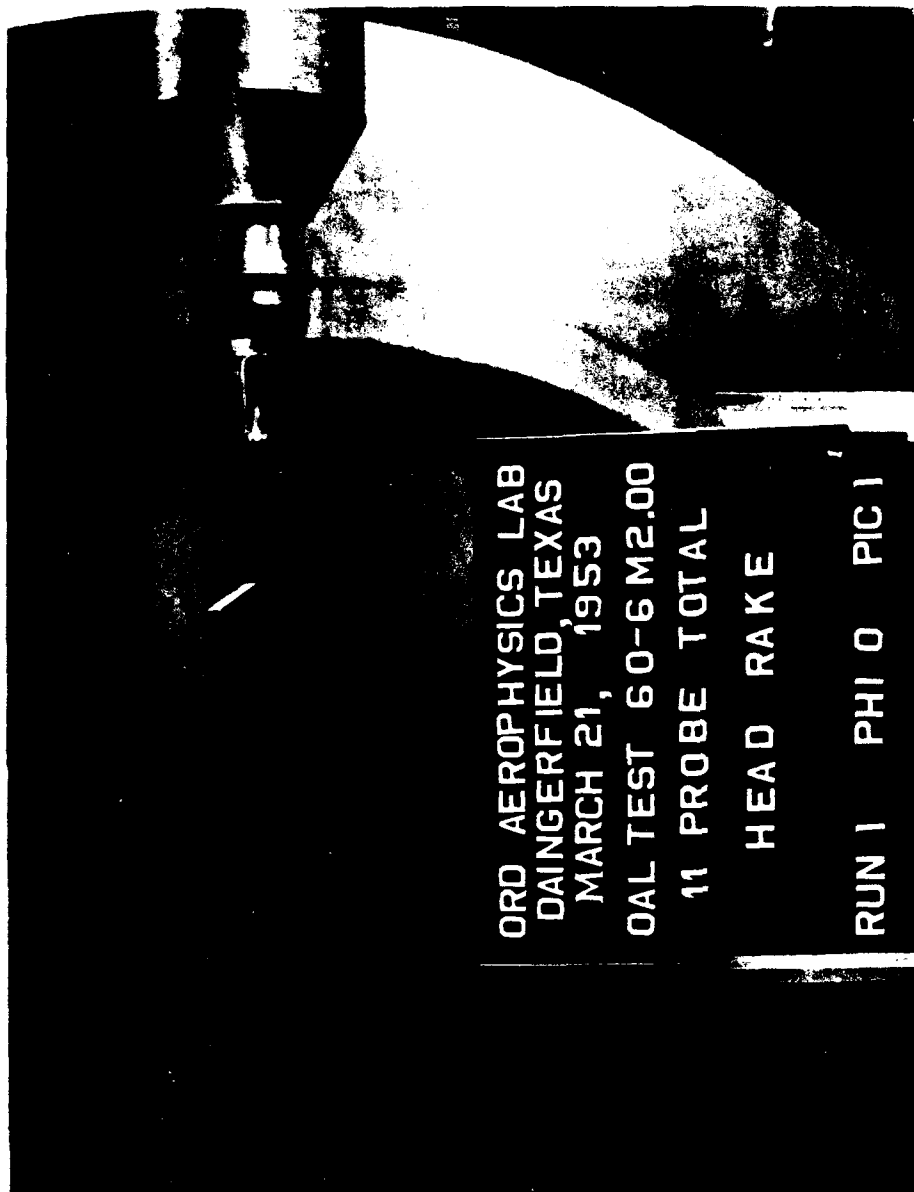


Fig. 2-31. Eleven-probe total head rake mounted in tunnel.

Source: OAL



Fig. 2-32. Cruciform inclinometer mounted in tunnel.

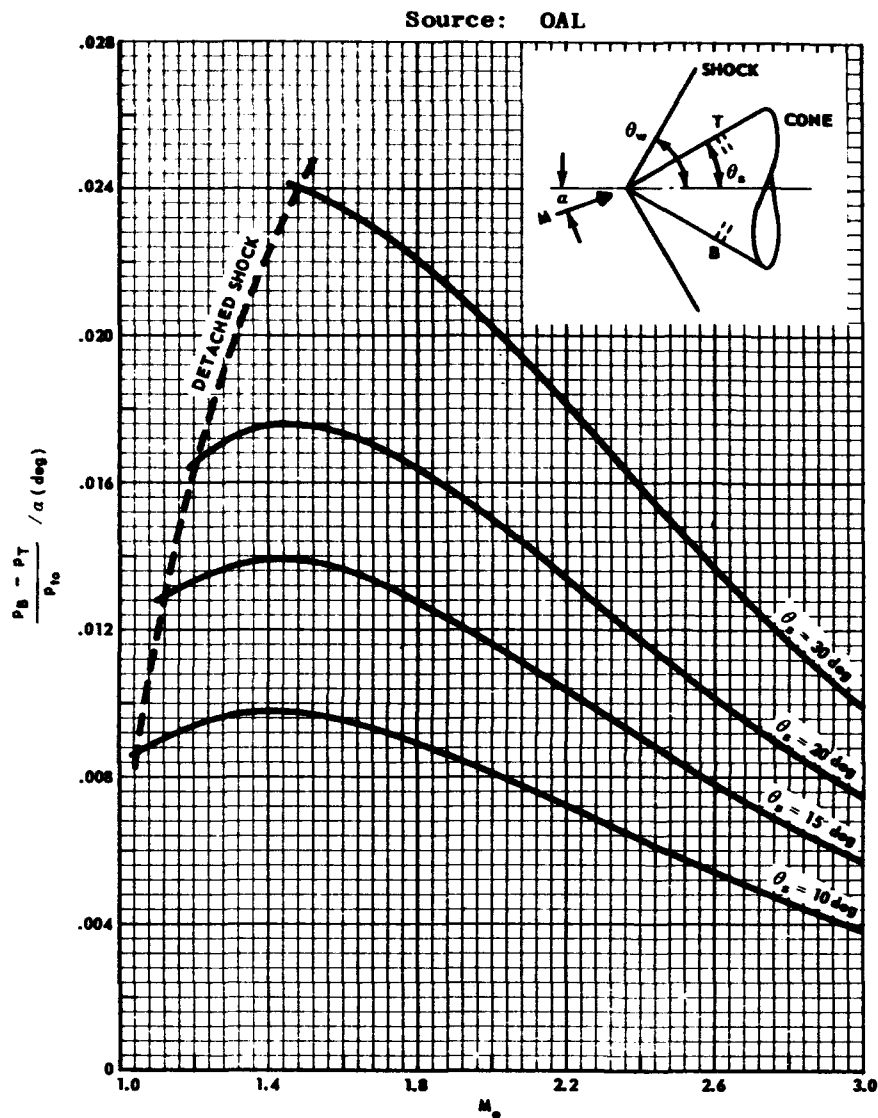


Fig. 2-33. Cone sensitivity vs Mach number.

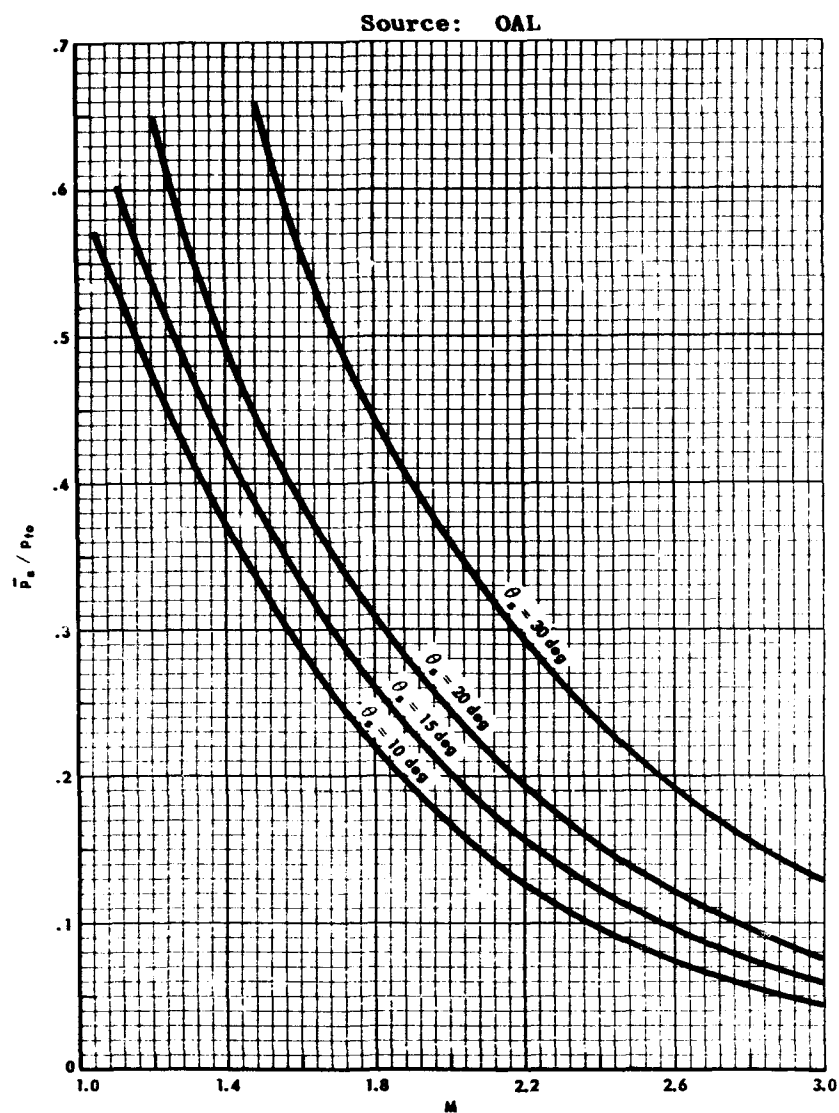
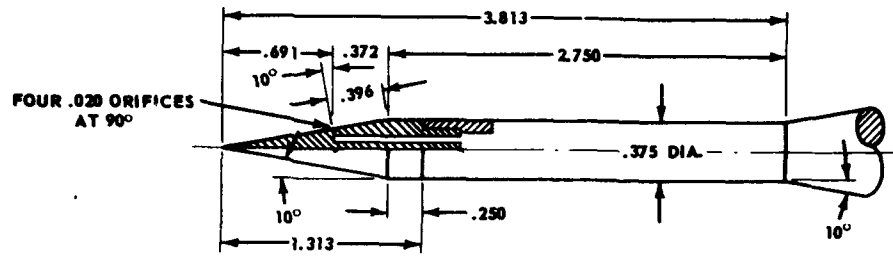


Fig. 2-34. Ratio of average cone pressure to free-stream total pressure vs free-stream Mach number.



Source: OAL

NOTE: DIMENSIONS ARE IN INCHES

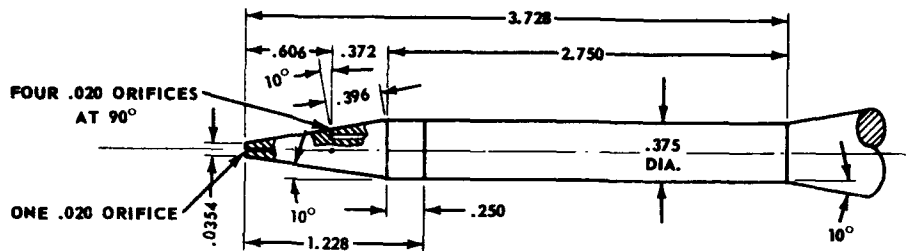


Fig. 2-35. Details of 10-deg half-angle cone and truncated-cone probes.

Source: OAL

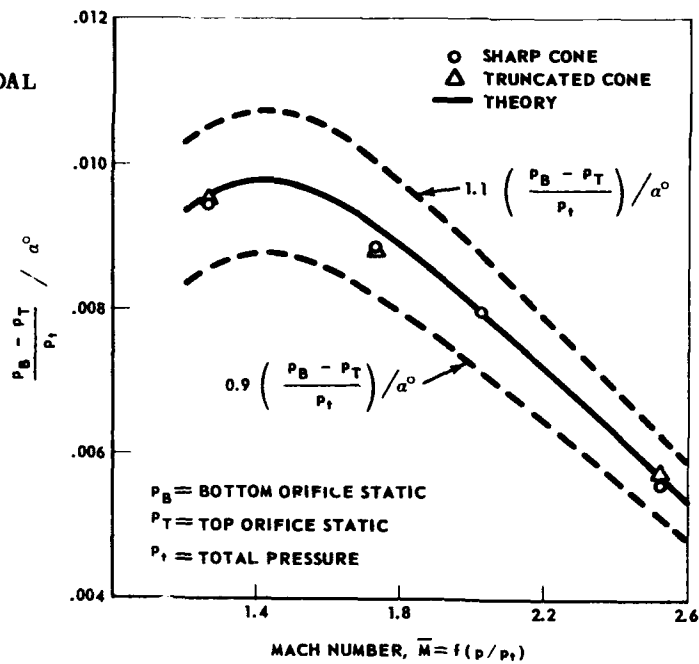


Fig. 2-36. Experimental and theoretical flow inclination parameters for sharp-cone and truncated-cone probes.

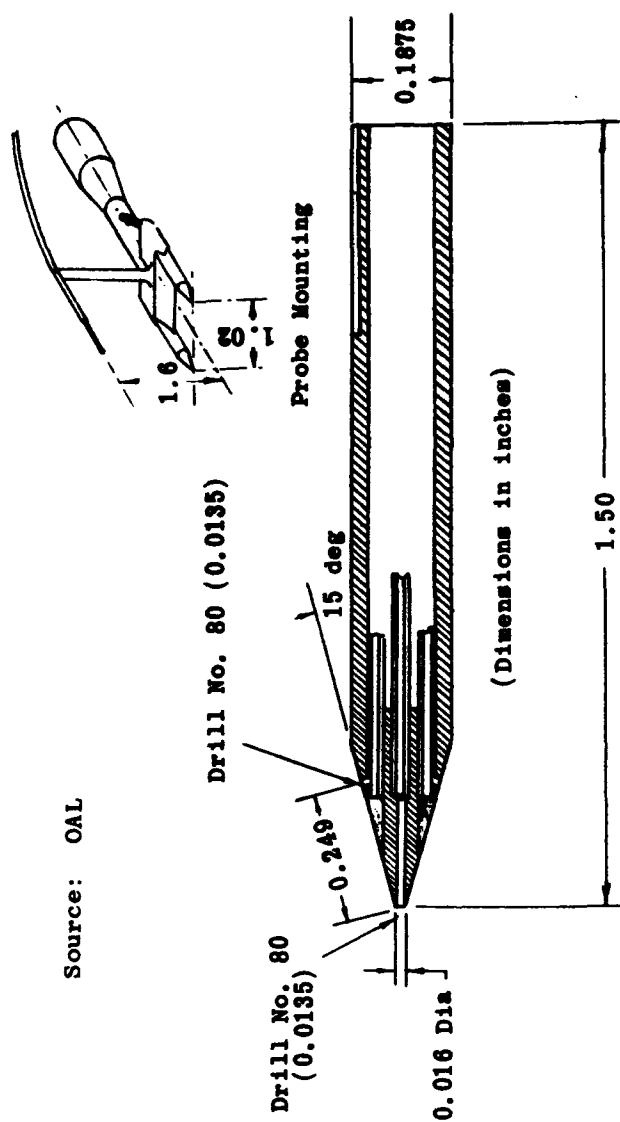


Fig. 2-37. Fifteen-degree half-angle cone probe with total-pressure orifice.

Source: OAL



Fig. 2-38. Typical pressure wedge installation.

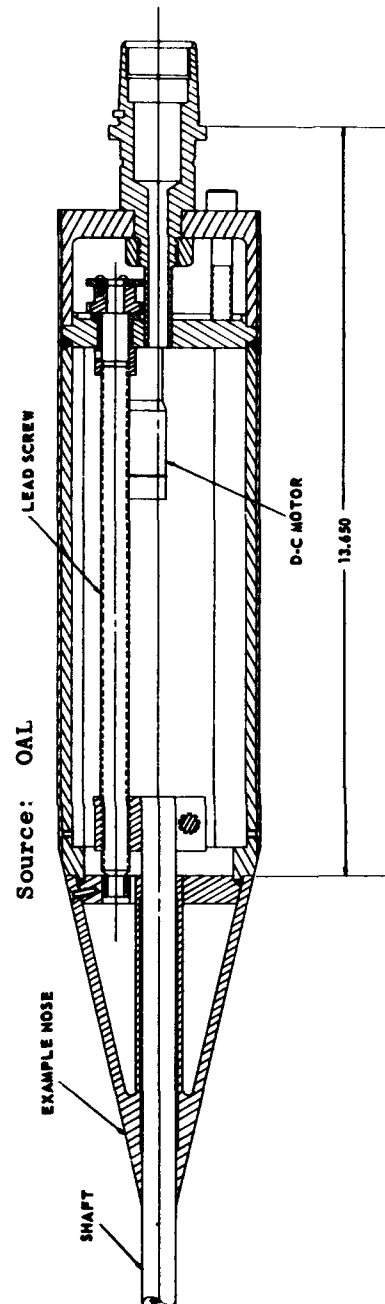
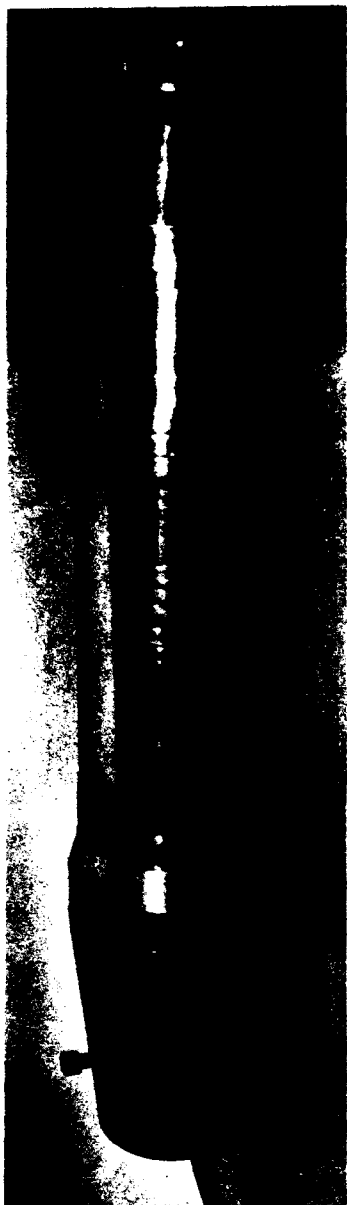


Fig. 2-39. OAL linear actuator.



Outer Sleeve Rotates about Inner Shell to Provide Access

Source: OAL

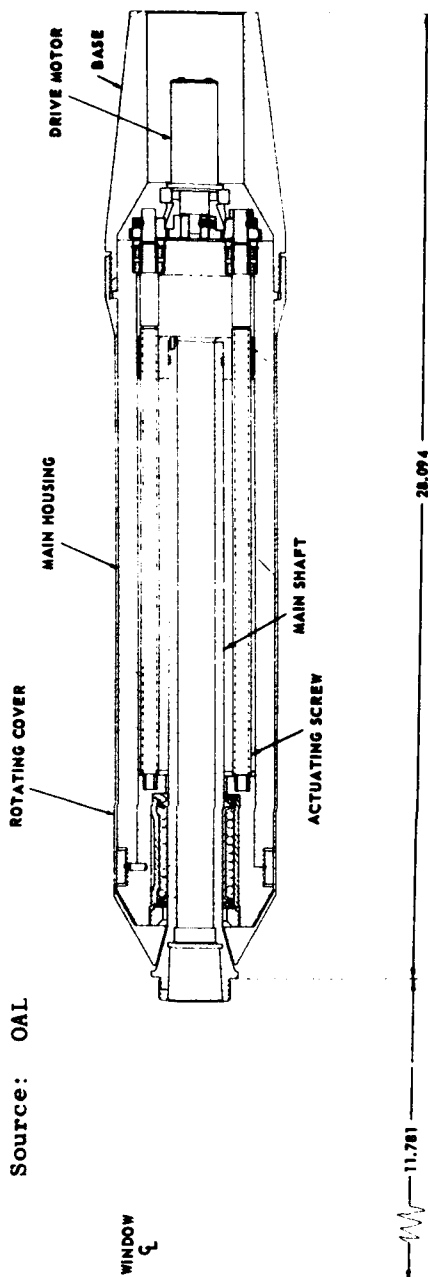


Fig. 2-40. OAL-32 linear actuator support.

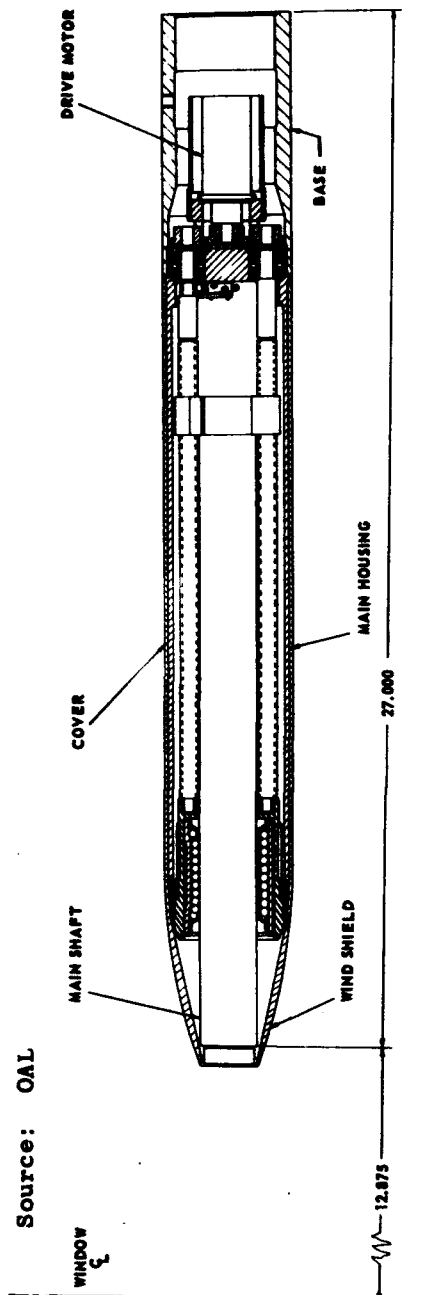


Fig. 2-41. OAL-35 linear actuator support.

Source: OAL

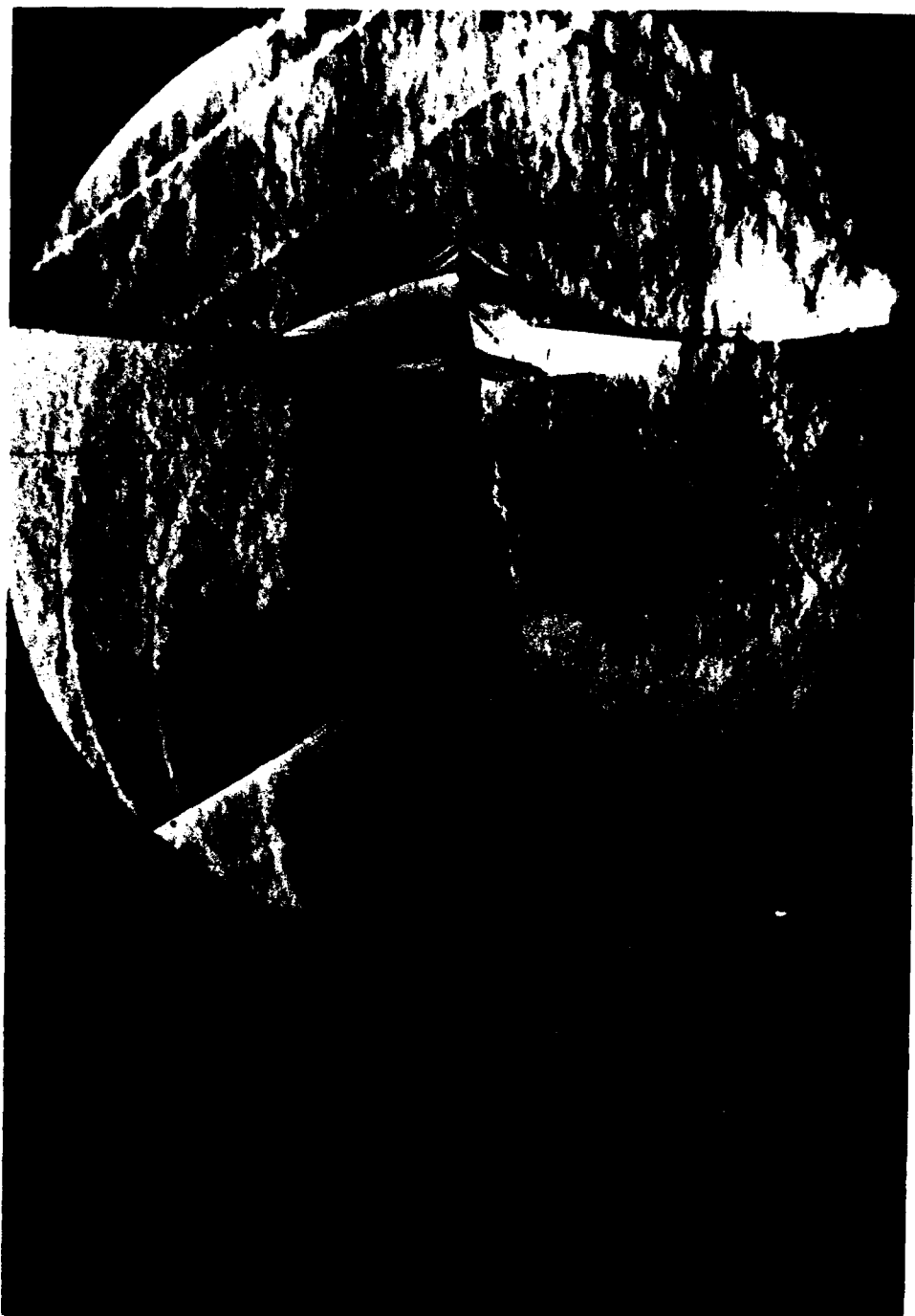


Fig. 2-42. Simulated axial actuator with horizontal total head rake and 15-deg half-angle conical forebody at zero angle of attack; Mach number 1.25.

Source. OAI



Fig. 2-43. Simulated axial actuator with horizontal total head rake and a 10-caliber ogive forebody at zero angle of attack; Mach number 1.25.

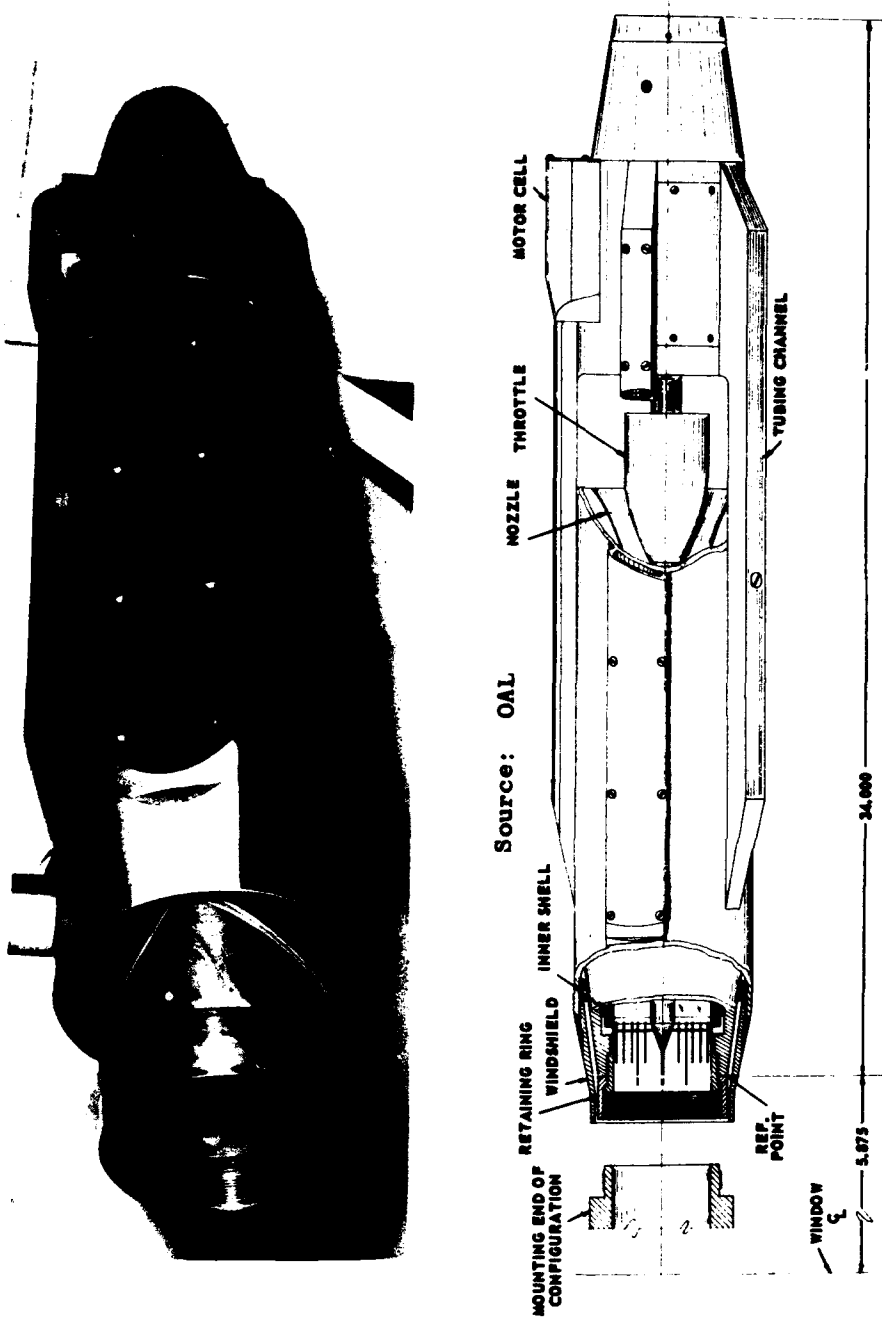


Fig. 2-44. OAL-22 force and pressure support.

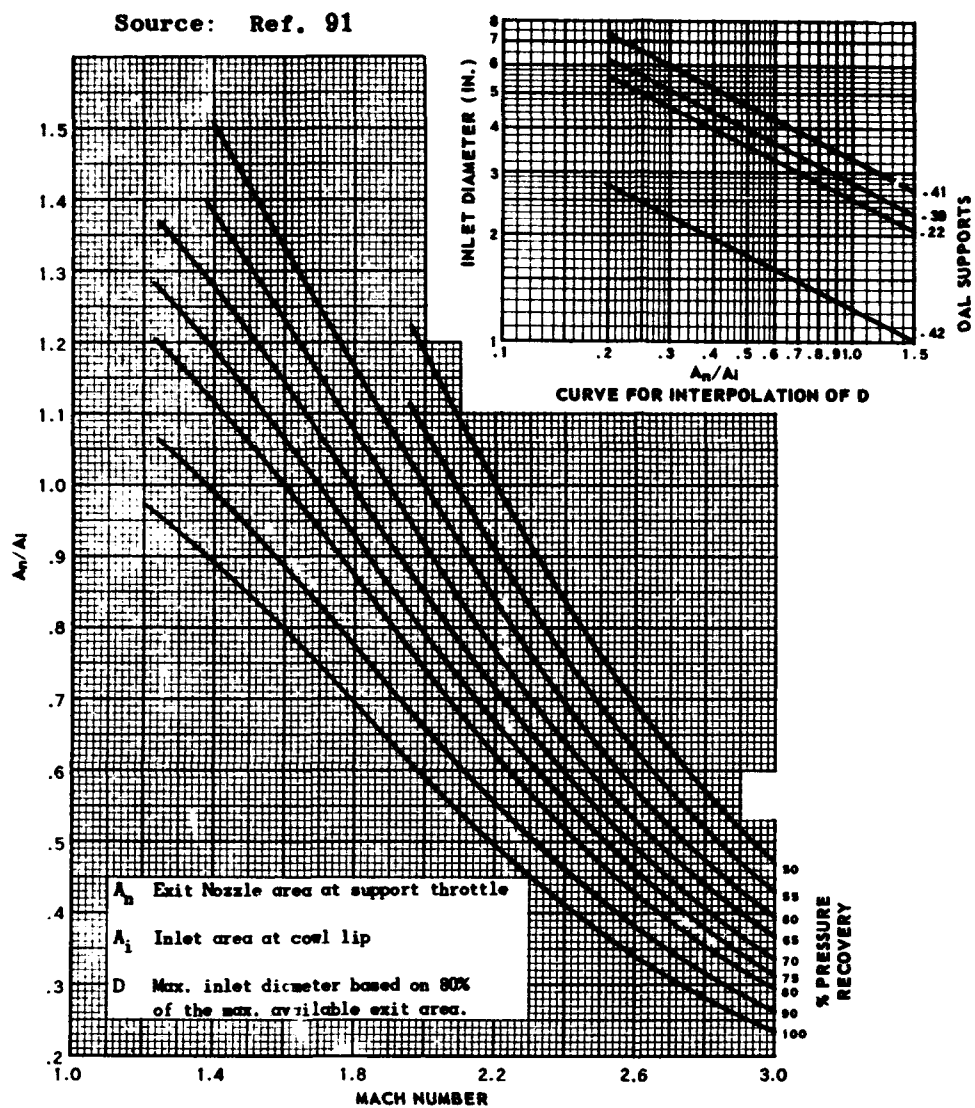


Fig. 2-45. Variation of minimum A_n/A_i value (swallowed shock) with free-stream Mach number for various values of pressure recovery.

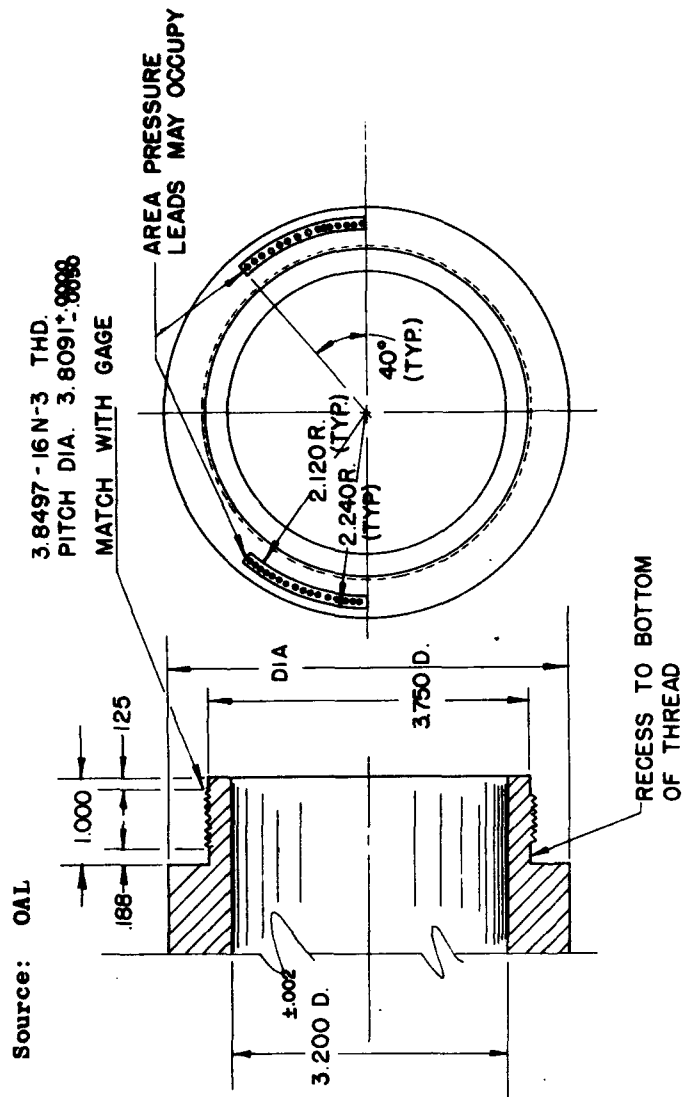


Fig. 2-46. Details of mounting end of model configuration for
OAL-22 force and pressure support.

Source: OAL

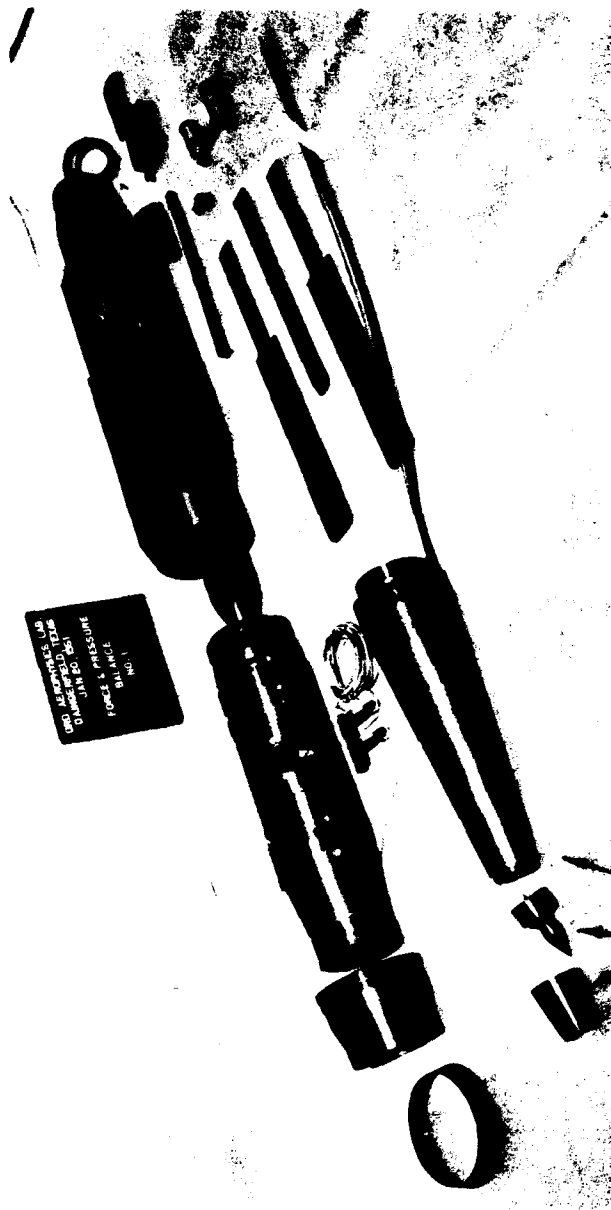
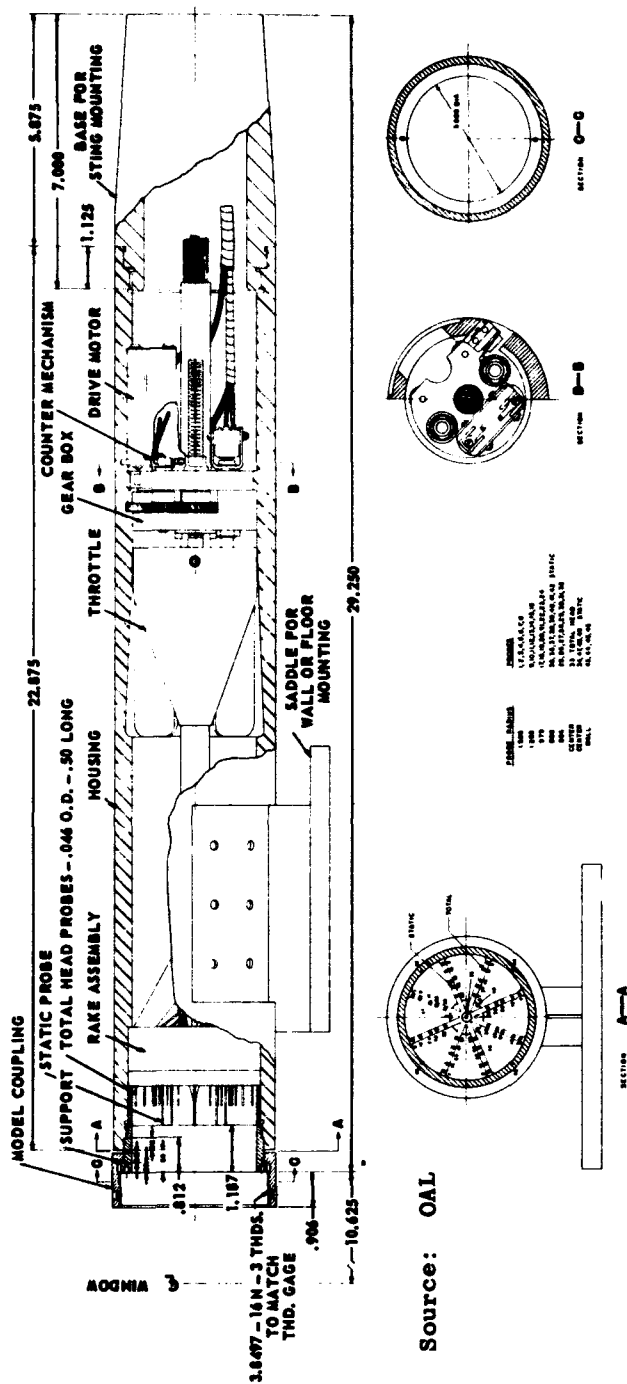


Fig. 2-47. Disassembled OAL-22 force and pressure support.



Source: OAL

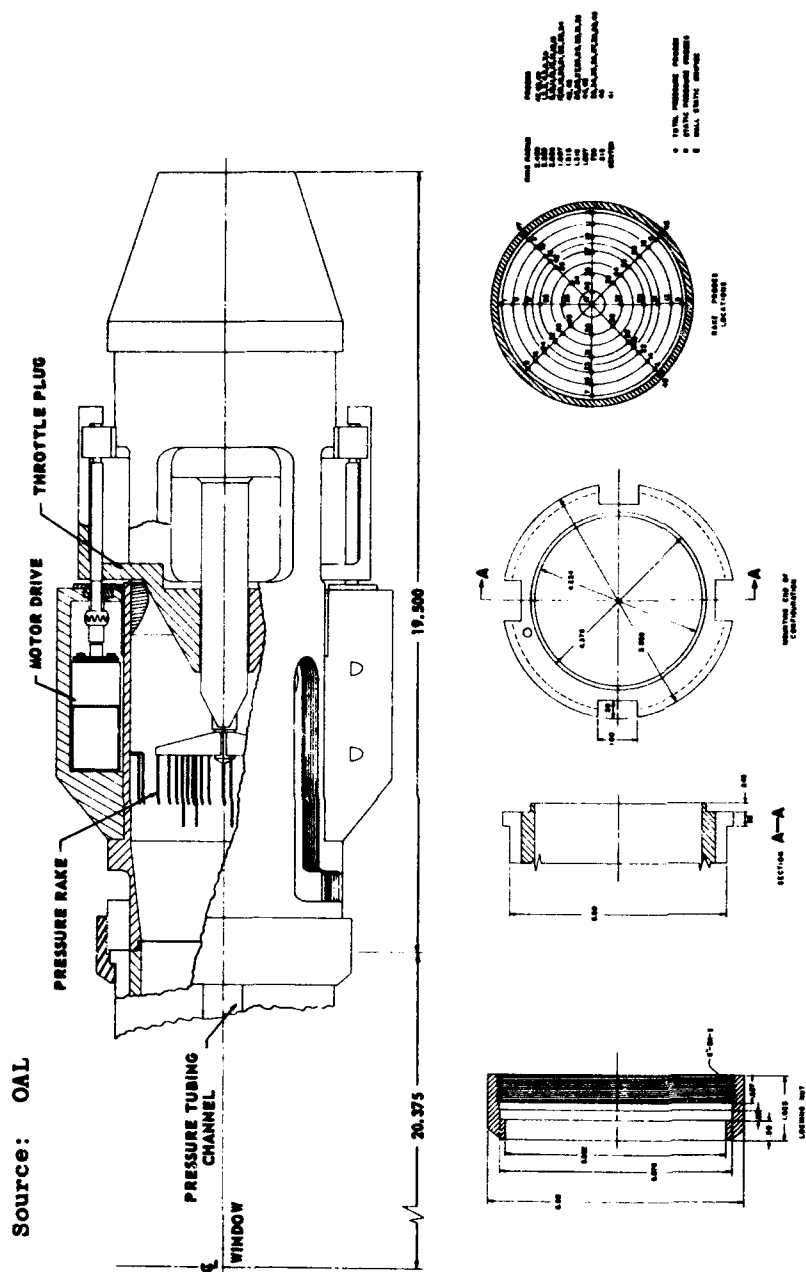


Fig. 2-49. OAL-41 pressure support.

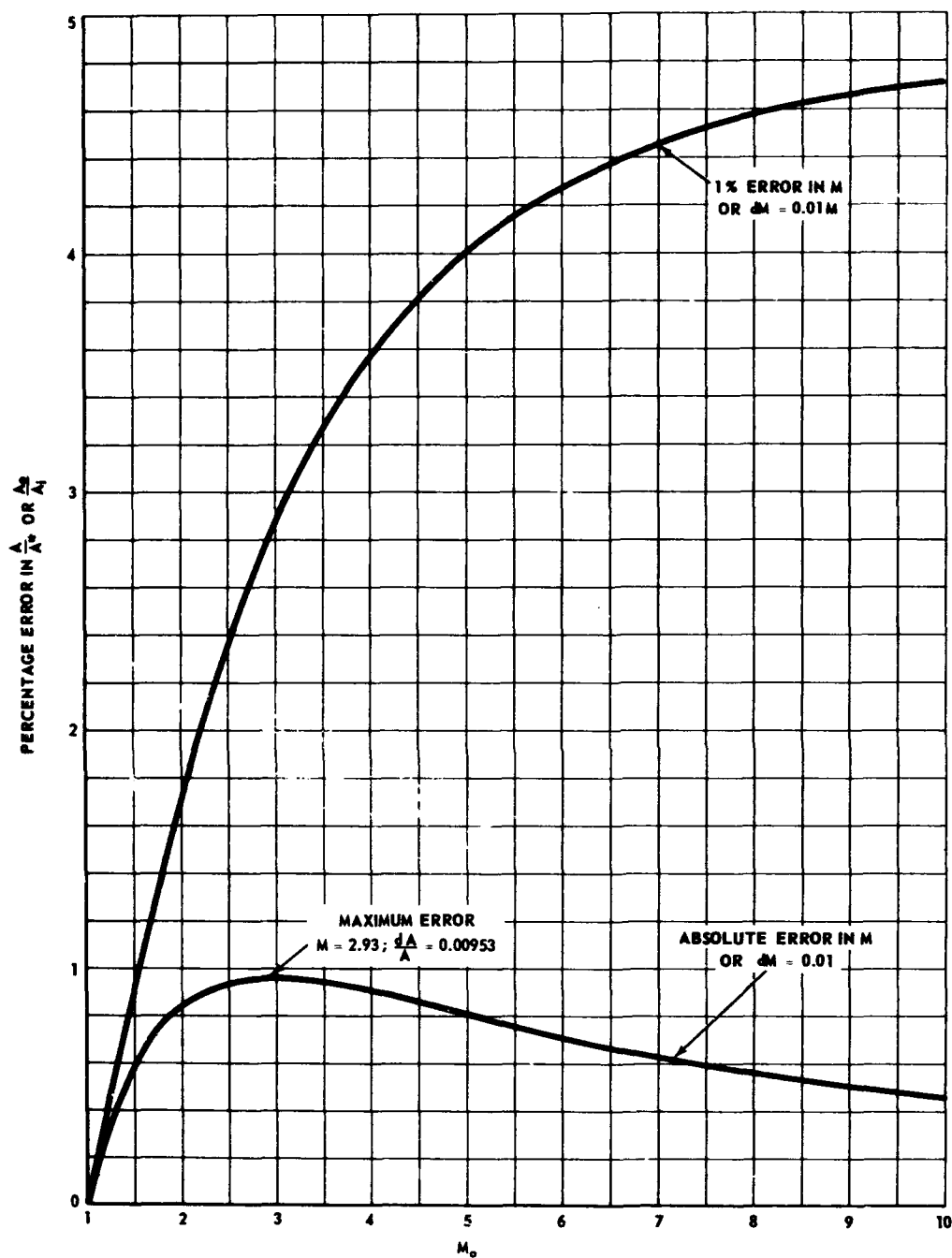
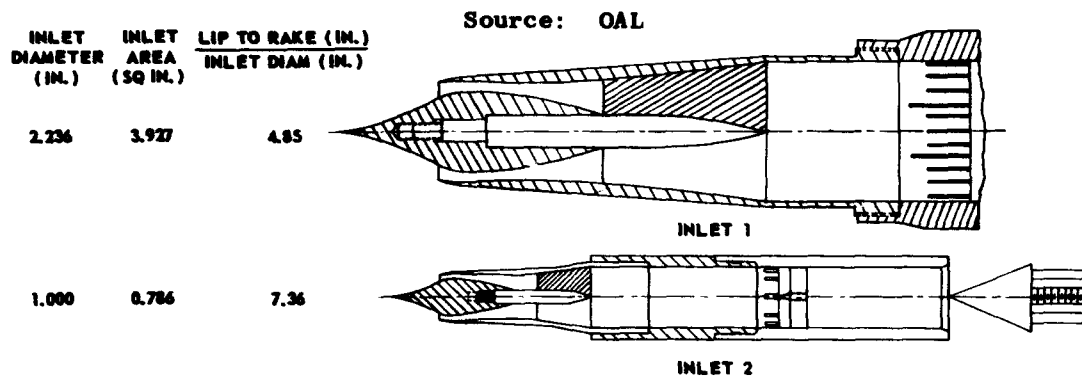


Fig. 2-50. Error in capture-area ratio due to errors in free-stream Mach numbers.



Note: For both models, tolerance of $+0.001$ in. is held for innerbodies and internal cowl surfaces, and initial cowl thickness is 0.005 in.

Fig. 2-51. Geometric comparison of two ramjet diffuser inlet models (of different scale).

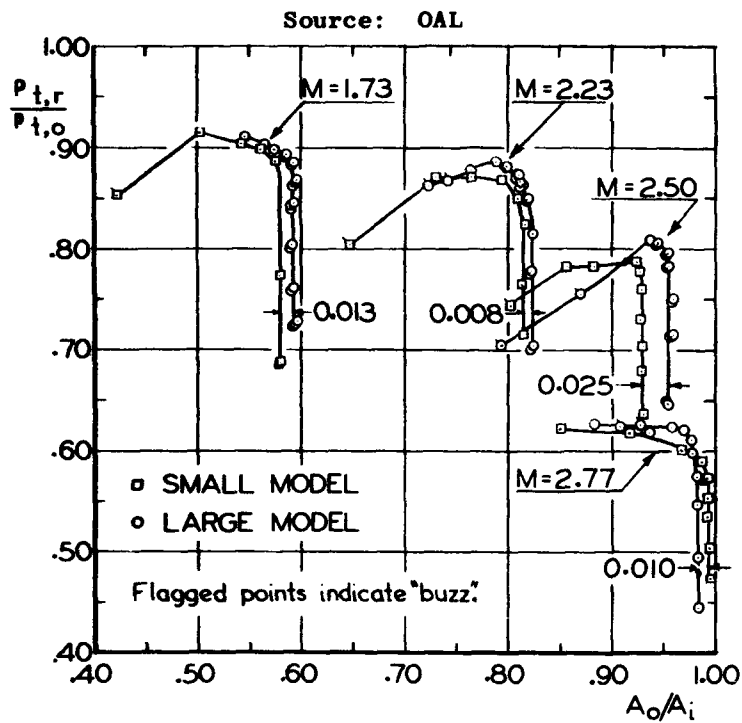
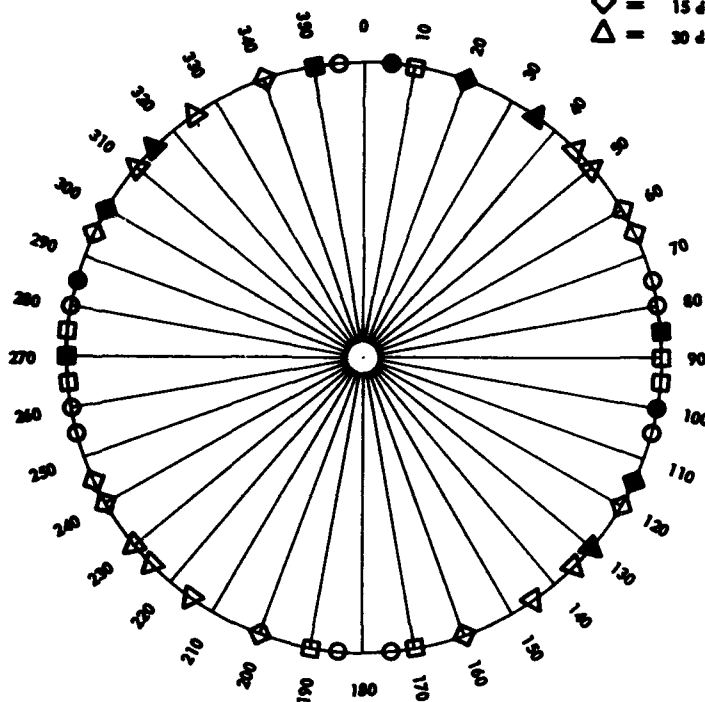


Fig. 2-52. Diffuser characteristics of two ramjet diffuser inlet models (shown in Fig. 2-51).

Source: OAL

MODEL ROTATION (ϕ)

- = 0 deg
- = -15 deg
- ◇ = 15 deg
- △ = 30 deg



NOTE: SOLID SYMBOLS INDICATE ACTUAL ORIFICE POSITIONS
WHEN $\phi = 0$ POSITIONS ARE 5 DEG, 100 DEG, AND 285 DEG.

Fig. 2-53. Peripheral pressure locations on body of revolution.

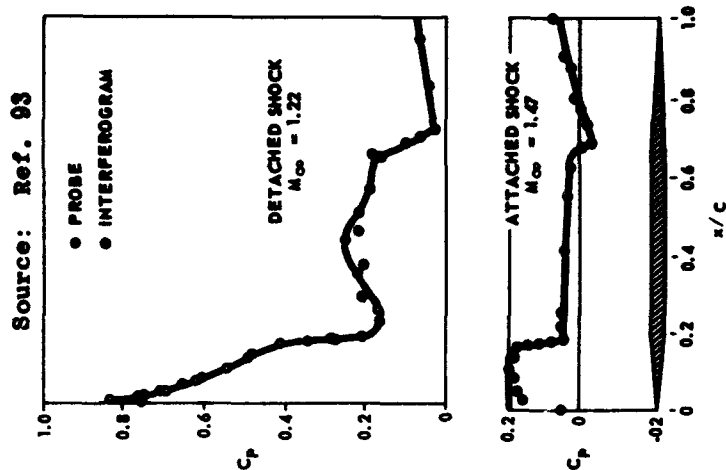


Fig. 2-55. Comparison of pressure distributions obtained from probes and interferograms.

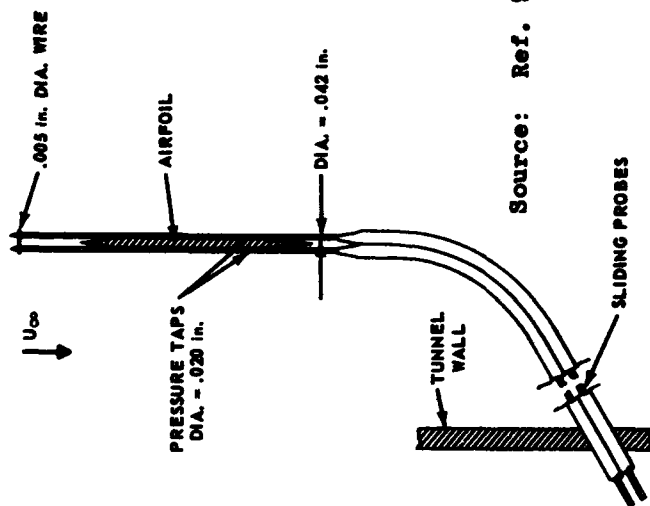


Fig. 2-54. Sketch of probe configuration for an airfoil of $\frac{3}{8}$ thickness.



Source: OAL

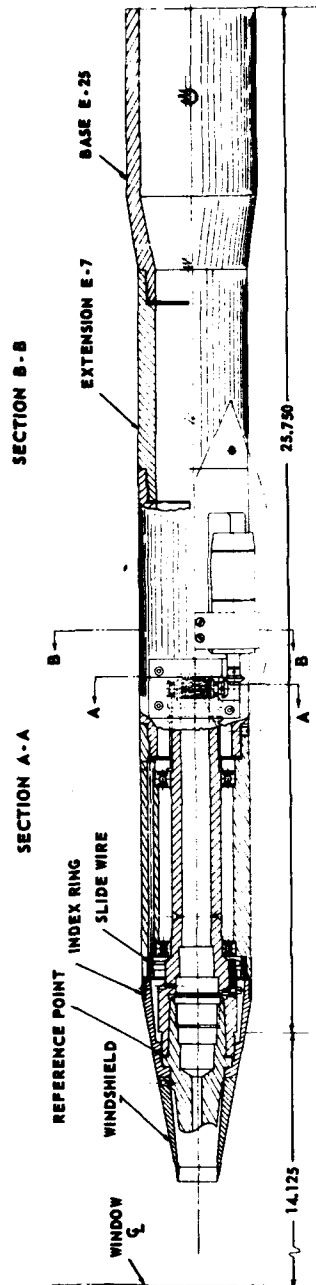
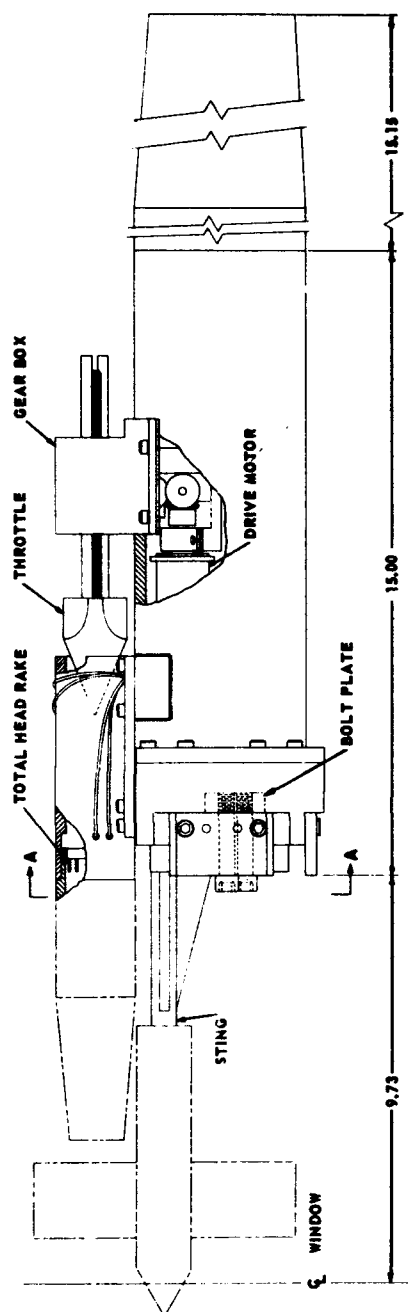


Fig. 2-56. OAL-21 roll-indexing support.



Source: OAL

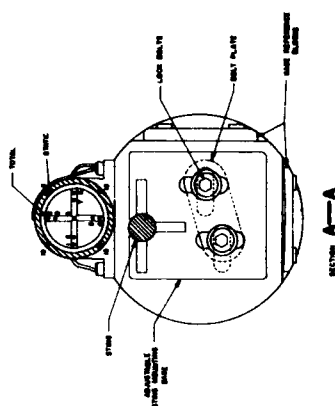


Fig. 2-57. OAL-42 pressure support (carrying simulated model).

3. Force Measurement

Before going on to the discussion of force measurement, it may be worthwhile to review briefly the basic terms (Fig. 3-1) and definitions that apply to the measurement of forces (Ref. 265).

Accuracy is the degree of correctness with which a measuring means yields the "true" value of a measured quantity. The true value refers to accepted engineering standards, such as the standard meter, gram, etc. It is assumed that a true value always exists even though it may be impossible to determine.

Precision is the degree of reproducibility among several independent measurements of the same true value with one set of instruments under specified conditions. This is frequently referred to as "repeatability." It is usually expressed in terms of deviation in measurement.

Error is the algebraic difference between a value which results from measurement and the corresponding true value. A positive error denotes that the measured value is algebraically greater than the true value. Error is usually expressed in the units of the measured quantity, or as a fraction (or per cent) of the full scale value, or of the actual value.

Deviation is a statistical number representing the randomness among independent measurements of the same true value. Deviation is variously expressed as 1) the difference between any measurement and the mean value of two or more; 2) the average of several independent variations from the mean (i.e., the Average Deviation); 3) the root-mean-square value computed from several individual deviations (i.e., the Standard Deviation); or 4) the ratio of 1), 2), or 3) to the mean. In any case the number of observations should be stated.

Sensitivity is the ratio of output response to a specified change in the measured variable. For example, an automatic-temperature controller having a net output pressure of 15 psi and a full scale range of 0 to 150°F would have a sensitivity of 0.1 psi/°F. Where nonlinear relationships are involved, the point or points at which the sensitivity is given should be stated.

Resolution sensitivity is the minimum change in the measured variable which produces an effective response of the instrument or automatic controller. Resolution sensitivity may be expressed in units of the measured variable, as a fraction or per cent of the full scale value, or as a fraction or per cent of the actual value.

Threshold sensitivity is the lowest level of the measured variable which produces effective response of the instrument or automatic controller.

Dead band is the range of values through which the measured variable can be varied without initiating effective response.

Bridge is a four-terminal network capable of being balanced.

Bridge arm is the portion of a bridge network between two adjacent terminals.

Bridge input is the voltage applied to the bridge.

Bridge output is the current or voltage of the detector branch of the bridge network.

Balance is the condition existing in a bridge when the magnitude of the (d-c) resistances or (a-c) impedances are such that a zero output voltage or current results. When this condition is obtained, the values of the resistances or impedances satisfy the bridge equation which has been derived on the assumption of zero output.

Unbalance occurs when the arm impedances do not have the proper magnitudes to satisfy the bridge equation (i.e., the bridge is unbalanced). Some bridges are deliberately operated unbalanced, and the variations in output voltage or current are used as a measure of the change in magnitude of a particular bridge element.

Resistance (or resistive) balance is the condition existing in an a-c bridge when the resistance elements are of the proper magnitude to satisfy the conditions of the bridge equation. An a-c bridge that has both resistance and reactance elements cannot be adjusted to balance unless both the resistance and reactance elements have the proper values simultaneously. If the capacitive reactance elements are not adjusted to the proper value for balance and the resistance elements are being varied, the detector will indicate a minimum for some value of the variable. The values of arm resistance for which this minimum occurs do not satisfy the basic bridge equation except in the equal arm bridge. However, the adjusting of the resistances to this minimum is often referred to as "obtaining a resistance balance." The general procedure for obtaining balance in an a-c bridge is to successively adjust the resistance and reactance to smaller and smaller minima until a zero detector indication is obtained.

Capacitive balance is the condition existing in an a-c bridge when the capacitance elements are of the proper magnitude to satisfy the conditions of the bridge equation. It has similar limiting conditions to those just enumerated for the resistance balance defined above.

Bridge resistance or impedance is the resistance or impedance between the output terminals when the source terminals are shorted.

Per cent unbalance is the percentage by which the impedance or resistance of the arm being varied deviates from that value which would balance the bridge (assuming only one arm is being varied). If two or four opposite arms are being varied simultaneously (most frequently done in supersonic wind-tunnel balances), the per cent unbalance is the sum of the per cent unbalances of the two or four arms.

Contamination in a bridge refers to any output not due to bridge unbalance.

Sixty-cycle contamination is the appearance in the output of a bridge of a 60-cycle voltage or current when the bridge elements or detector are either electrostatically or electromagnetically coupled to the 60-cycle power system.

Detector is the device sensitive to voltages or currents used to determine the magnitude of the bridge output. The bridge is considered balanced when the detector indication is zero.

Precision (or sensitivity) of balance is the degree to which a given combination of source, bridge, and detector can be adjusted for balance. It can be expressed in a number of ways, such as the per cent magnitude change in a particular bridge element which gives the minimum observable detector output for a given applied voltage. Note that it is dependent on all three items: source voltage, minimum observable detector input, and the per cent change in the bridge element or elements.

Noise is the existence in a detector of a randomly varying output without a corresponding bridge input. This detector characteristic limits the precision of balance because when the bridge output voltage or current produces a detector indication of comparable magnitude to the noise indication, it becomes difficult to separate the output from the noise.

Capacitive contamination, a term usually applied to resistance bridges, is a bridge output caused by small stray capacitances between bridge elements or capacitances within a bridge element. These produce a capacitive unbalance even though the resistive elements may be balanced.

3.1 Strain Gages

The ultimate in strain-measuring devices at the present time is the resistance-type strain gage (Ref. 95). Its construction and operation are very simple, but it is so precise that strains on the order of 0.1% may be measured. The gage is about the size of a postage stamp and only slightly heavier. It consists of a metallic wire or strip whose electrical resistance varies with its linear variation. The gage is securely bonded to the member to be strained so that any strain in the member is transmitted to the wire. Hundreds of types of strain gages are commercially available, each having been developed in response to a demand for a gage to meet a specific condition. An explanation of the differences between the gage types (see Ref. 96 for more detailed treatment) will indicate the nature of the application for which each is suited.

The most fundamental part of the gage is the wire itself (Ref. 97). The resistance increase of a wire when it is stretched is due in part to an increase in length and a decrease in cross section, and in part to an actual change in specific resistance. The gage factor is defined as the ratio of resistance change to length change:

$$G = \frac{\Delta R/R}{\Delta L/L} \quad (3-1)$$

If this were due entirely to dimensional change, it would be expected, from Poisson's ratio, that the gage factor of any wire would be approximately 1.7. However, materials vary widely in this respect, and some actually have a negative gage factor. The gage factor differs for different materials: from -12 for nickel to +6 for platinum. Unfortunately, materials with a high gage factor also exhibit a high temperature effect on the coefficient of resistance (Ref. 98). The two

materials most widely used in strain gages are a copper-nickel alloy known as advance, copel, or constantan, which has a gage factor of approximately 2, and an iso-elastic alloy of nickel, chromium, iron, and molybdenum, which has a gage factor of 3.5. When strains are to be held at a constant value for a period of time and changes of strain applied as step functions, it is desirable to use the constantan filament gages which, while having the lower sensitivity, also have a low temperature sensitivity. In investigations where the rate of change of strain is high, it is better to use the more sensitive iso-elastic filament in spite of its greater temperature sensitivity.

The second variation in the gage type is the actual construction of the grid. The bonded strain gage usually consists of about 5 in. of 1-mil wire formed into a series of long parallel loops. For strain gages of 3/8 in. or less in length, the wire is often wound around a cylindrical paper core in the form of a close-wound helix. The core is then flattened. In the newer foil gages the strain-sensitive element is composed of metallic foil on which the grid pattern is printed with an acid-resistant ink. The unprinted portion is then etched away. Foil gages are usually made of constantan or nichrome. For convenience in measuring strains in different directions, gages known as "rosettes" were developed. These gages have three or four separate grids with various angular orientations and can be cemented to the part with no particular attention being paid to the over-all grid orientation. The resultant strains on each of the grids can be recorded, and the true magnitudes and directions of the significant surface strains in the part can be calculated from these data. The nominal gage resistance is 120 ohms, but standard gages are also made with resistances of 60, 75, 240, 300, 350, 500, 1000, and 2000 ohms.

The third factor that may vary in the gage construction is the base or carrier which is used for the filament wire. For most applications, this carrier is a rag bond paper which provides a very sturdy and satisfactory gage. In many strain-gage applications, however, ease of application and fast drying time are factors. Hence, a base was developed in which a special thin paper is used instead of the rag bond paper. This type of carrier permits quicker evaporation of the cement solvent; it also makes for remarkably easy and fast installation on flat or curved surfaces. On some strain gages a protective layer of felt is used to cover the top side of the gage.

Temperature considerations led to still a third type of base. This type utilizes paper impregnated with bakelite. The sensitive element is baked under pressure between two layers of this impregnated paper, with the result that the filament is firmly imbedded in a bakelite wafer. These gages will stand continuous operation at 300°F, and will give limited service up to 500°F.

The foil strain gages are not mounted in paper but in a very thin lacquer having excellent mechanical and electrical properties. This is said to improve the transmission of strain from the test surface to the grid, and hence to improve gage performance and stability. The rectangular cross-section of the conductor gives greater surface area for a given cross-sectional area, providing better adhesion between gage and test surface. The extreme flexibility of foil gages permits application to fillets and other curved surfaces without pre-forming.

The cements used to attach the gages may also vary. In the past nitro-cellulose or phenol-resin adhesives have been used. However, new bonding agents are being produced with superior properties and

shorter drying times. Manufacturers of gages usually supply a suitable cement with each type of gage. Foil gages may be obtained with strippable backing.

The last variable to be considered in gage construction is the type of connection between the lead wire and the filament of the gage. Bonded gages may have round or flat larger-diameter leads welded or soldered to the ends of the grid wire. These are satisfactory for ordinary stress analysis under static or varying loads. In this field, each gage is subjected to a relatively small number of stress changes of moderate magnitude. When, however, gages are used for fatigue study, fatigue failure of the filament wire is sometimes experienced, in many cases early in the test. Similarly, when large strains are involved, hysteresis becomes noticeable and premature failure may occur. The dual-lead wire strain-gage which has wire of intermediate size introduced between the lead wire and the grid wire was developed to meet this situation. By distributing the stress concentration between two joints instead of one, it effectively increases fatigue life and markedly decreases hysteresis at high strains. Foil gages are usually supplied without lead wires or ribbons. After the gage has been installed, connections are made by soldering the lead wires directly to large tab-like extensions of the grid.

Printed-circuit wiring strips are now commercially available. These strips are etched out of a glass-epoxy-copper laminate about 0.006 in. thick and are used in connection with fine-strand solid wire in certain types of gage installation. They are particularly useful for multiple installations because they provide soldering points for inter-gage wiring and securely anchor the heavier lead-out wires.

Since the designs of strain gages are constantly being improved and new features are being developed, the manufacturers' catalogs should be studied before a gage is selected for a particular purpose. Such information is readily available from:

Baldwin-Lima-Hamilton
Electronics and Instrumentation Division
Waltham 54, Massachusetts

Tatnall Measuring Systems Company
Phoenixville, Pennsylvania

High Temperature Instruments Corporation
Bala-Cynwyd, Pennsylvania

A gage manufactured in Europe has also been used successfully for balance applications. This gage (the TEPIC) has a high gage factor, is highly moisture proof, and is easy to apply. It is available with a transparent, plastic body (Type BL) or paper mounted (Type BP). Two types of cement, one for air drying and the other for heat curing, are also available. The manufacturer's address is:

Huggenberger
Ackersteinstr. 119
Zurich 10/49
Switzerland
(Cable address: Tenso Zurich)

Because information relating to this gage may not be readily available, specifications for the Type BL gage are presented in the following tabulation.

Type BL Gage Specifications

Type	Active Length (in.)	Active Width (in.)	Total Length (in.)	Total Width (in.)	Resistance (ohms)	Gage Factor
BL 1/2/120	0.20	0.14	0.47	0.40	120	2.50
BL 1/120	0.40	0.06	0.67	0.40	120	2.50
BL 2/120	0.83	0.02	1.10	0.40	120	2.50
BL 2/350	0.83	0.10	1.10	0.40	350	2.50
BL 2/500	0.83	0.14	1.10	0.40	500	2.50
BL 2/1000	0.83	--	--	0.40	1000	2.50
BL 3/350	1.22	0.06	1.50	0.40	350	2.50
BL 6/350	2.40	0.02	2.70	0.40	350	2.50

3.1.1 Application, Moisture-proofing, and Testing of Strain Gages

To get the maximum accuracy from strain gages, it is essential that they be installed with utmost care and in accordance with the instructions which manufacturers will include with every order of strain gages. Because new bonding techniques and new cements are constantly being produced, and because complete application kits and specific instructions are readily available (e.g., see Ref. 99), this subject will be given only a general treatment here.

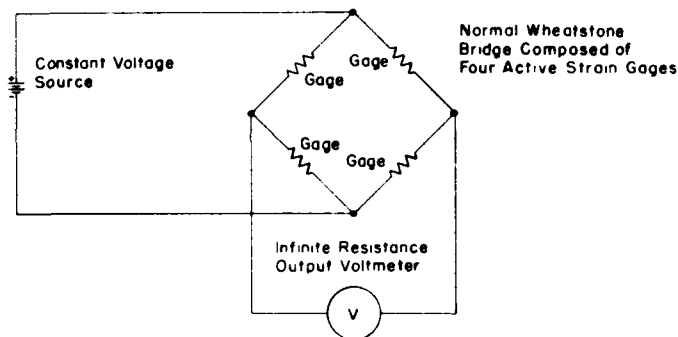
Application.--The surface to which the gage will be applied must be clean and even. Rust, scale, grease, etc., must be removed and pits or unevenness must be ground out. Highly polished surfaces should be roughened. Solvents (toluol, acetone, and carbon tetrachloride) may be applied with a swab, and the surface should not be touched after it is clean. When the cement (which comes with the gages) is properly applied, it will ooze out around the periphery of the gage. Clamping should be done with weights or spring-loaded clamps. (C-clamps, because they do not give constant pressure over the complete drying cycle, should be avoided.) The gages may then be heat dried. Specifications for the drying cycle of any particular gage are available in the instruction manual which comes with the gage (e.g., Ref. 99 for Baldwin SR-4 gage). Progress of the drying may be tested by checking the electrical resistance from gage to metal or by removing a gage and testing for the smell of solvent. (Note: Carbon tetrachloride is toxic.)

Moisture-proofing.--Since resistance stability is essential in strain-gage measurement and the principal cause of instability is moisture (other causes are a matter of technique and are not treated here), gages must be moisture-proofed when conditions and requirements demand. (That is, short run-time measurements in dry air may not call for moisture-proofing while continuous operation in humid air would.) Moisture has two effects: 1) dimensional changes, and 2) moisture absorption; both cause a change in resistance, the first through a change in strain, the second by a change in conductivity. Grease, wax, or Neoprene may be used to coat the gage and surrounding area. The coating depends upon the conditions under which the gage will be used. The cement must be completely cured and the gage must be dry before it is moisture-proofed. Specific instructions may be obtained from the manual which comes with the gage (e.g., see Ref. 99).

Testing.--Resistance tests may be made with any ohmmeter. There may be danger of ruining the gage by insulation breakdown if the voltage used is too high (e.g., 22-1/2 v for Baldwin gages). The test for leakage resistance (from gage to metal) is made after the cement has dried or cured and the gage has cooled. It is preferable to perform this test before the gage is put into the circuit so that the measured leakage is that of the gage and not the circuit. Leakage due to moisture may be corrected by heating the gage and re-moisture-proofing. Specific information can be found in full detail in the instruction manual which can be obtained with the gage (e.g., see Ref. 99).

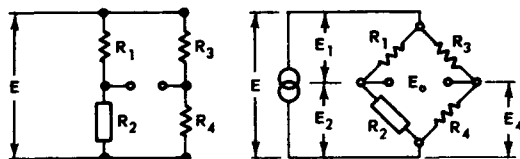
3.1.2 Associated Instrumentation for Strain-Gage Measurements

After the strain gage has been applied to a surface, it must be connected to instruments capable of measuring and recording or at least indicating small changes in resistance. These instruments may be both complex and expensive, particularly for those applications where it is desired to record simultaneously the output of a large number of strain gages. In the case of few gages and for static or incremental strains, the instrumentation can be both simple and inexpensive. The gaging circuits can be of two kinds, either potentiometer type or bridge type. The Wheatstone bridge may be considered as two parallel potentiometer circuits; as such it is inherently insensitive to supply-voltage fluctuations. The simplicity and broad frequency accommodation as well as the capability for measuring changes in resistance as small as 0.001 ohm have justified the almost exclusive use of the Wheatstone bridge. A simple circuit is shown below and will be briefly reviewed in following paragraphs.



3.1.2.1 Some Theoretical and Practical Considerations of the Wheatstone Bridge

The following analysis (Ref. 100) establishes the resulting changes, E_o , in the output voltage when the resistance in arm R_2 , a strain gage, changes by a small amount, ΔR_2 .



For an initially "balanced" bridge, $E_4 = E_2$. When R_2 becomes $(R_2 + \Delta R_2)$, E_2 becomes $(E_2 + \Delta E_2)$. Hence,

$$E_o = (E_2 + \Delta E_2) - E_4 = \Delta E_2$$

Since

$$E_2 = \frac{E}{R_1 + R_2} \cdot R_2$$

then

$$E_o = \Delta E_2 = E \left[\frac{R_2 + \Delta R_2}{R_1 + R_2 + \Delta R_2} - \frac{R_2}{R_1 + R_2} \right]$$

Let

$$R_1 + R_2 = R$$

and

$$E_o = E \frac{R_1 \Delta R_2}{R^2} \left[1 + \frac{\Delta R_2}{R} \right]^{-1}$$

i.e.,

$$E_o = E \frac{R_1 \Delta R_2}{R^2} \left[1 - \frac{\Delta R_2}{R} + \left(\frac{\Delta R_2}{R} \right)^2 - \left(\frac{\Delta R_2}{R} \right)^3 + \dots \right] \quad (3-2)$$

For the usual case, $R_1 = R_2$, i.e., $R = 2R_2$, and

$$E_o = \frac{E}{4} \cdot \frac{\Delta R_2}{R_2} \left[1 - \frac{\Delta R_2}{2R_2} + \frac{1}{2^2} \left(\frac{\Delta R_2}{R_2} \right)^2 - \frac{1}{2^3} \left(\frac{\Delta R_2}{R_2} \right)^3 + \dots \right] \text{ etc.} \quad (3-3)$$

By neglecting the quantity in the bracket,

$$E_o \cong \frac{E}{4} \cdot \frac{\Delta R_2}{R_2} \quad (\text{single-arm output}) \quad (3-4)$$

If the strain in arm R_2 is 1%, i.e., $\frac{\Delta L}{L} = 0.01$, a gage factor of $G = 2$ will give $\Delta R/R = 0.02$. The quantity represented by the bracket in Eq. 3-3 then becomes

$$[] = 1 - \frac{1}{2} (0.02) + \frac{1}{4} (0.0004) - \frac{1}{8} (0.000008) + \dots \approx 0.99$$

Hence, Eq. 3-4 is in error by approximately 1% for strains of 1%.

Consider a two-arm bridge with tension acting on leg R_2 and compression on R_1 such that $\Delta R_2 = -\Delta R_1$. Under strain, R_1 becomes $R_1 - \Delta R_1$ and R_2 becomes $R_2 + \Delta R_2$. Then

$$E_o = \Delta E_2 = E \left[\frac{R_2 + \Delta R_2}{R_1 - \Delta R_1 + R_2 + \Delta R_2} - \frac{R_2}{R_1 + R_2} \right] = E \left[\frac{\Delta R_2}{R_1 + R_2} \right] \quad (3-5)$$

and for the usual instance of $R_1 = R_2$,

$$E_o = \frac{E}{2} \cdot \frac{\Delta R_2}{R_2} \quad \text{exactly (two-arm output)} \quad (3-6)$$

By superposition, for a four-active-arm bridge with all resistance changes additive,

$$E_o = E \frac{\Delta R_2}{R_2} \quad \text{exactly (four-arm output)} \quad (3-7)$$

The strain equation (Eq. 3-1) may be written as

$$\Delta R = GR(\Delta L/L)$$

If the strains, $\Delta L/L$, imposed on each arm of a bridge are equal, then the factor GR must be held fixed to achieve matched resistance changes in each arm. In practice this means using gages of matched gage factor and resistance. In this case Eqs. 3-1, 3-6, and 3-7 may be combined to give

$$E_o = \frac{GENS}{4} \quad (3-8)$$

where

N = number of active matched gages

and

$$S = \frac{\Delta L}{L}$$

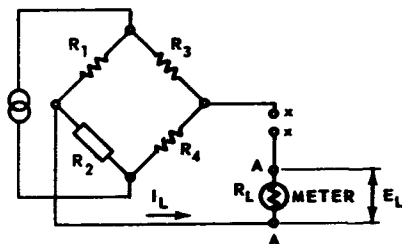
Temperature Compensation.--The use of two- or four-active-arm bridges is effective for increasing the output and also securing complete temperature compensation. Assume that gages of matched resistance and temperature coefficient are mounted on the same material and exposed to the same temperature environment. Then, with temperature change, each gage will exhibit an equal change, ΔR_T , in resistance. The net resultant change in bridge output is zero; thus temperature compensation is achieved, i.e.,

$$\Delta E_T = E \left[\frac{R_2 + \Delta R_T}{R_1 + \Delta R_T + R_2 + \Delta R_T} - \frac{R_2}{R_1 + R_2} \right] \quad (3-9)$$

When $R_1 = R_2$,

$$\Delta E_T = E \left[\frac{R_2 + \Delta R_T}{2(R_2 + \Delta R_T)} - \frac{R_2}{2R_2} \right] = 0 \quad (3-10)$$

Equation 3-8 gives only the open-circuit voltage of the bridge. When a meter or amplifier whose impedance is not much higher than the bridge impedance is connected across the output terminals, the following calculations apply:



The impedance of this network as measured at x-x is

Z_{xx} = load resistance + effective bridge resistance

$$Z_{xx} = R_L + \frac{(R_1 + R_3)(R_2 + R_4)}{R_1 + R_2 + R_3 + R_4} \quad (3-11)$$

(When bridge arms and load are pure resistances, an ohmmeter across x-x will give the impedance.) When x-x is shorted, the current through the load (by Thevenin's Theorem) is

$$I_L = \frac{E_O}{Z_{xx}} \quad \text{and} \quad E_L = I_L R_L = \frac{E_O R_L}{Z_{xx}} \quad (3-12)$$

For equal resistance legs, $R_1 = R_2 = R_3 = R_4 = R$. Then, after strain,

$$Z_{xx} = R_L + R$$

$$E_L = \frac{R_L}{R_L + R} E_O \quad (3-13)$$

$$I_L = \frac{1}{R_L + R} E_O$$

where

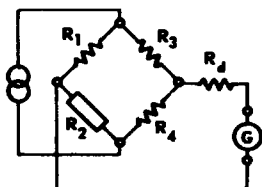
E_L = potential across meter, volts

I_L = current through the meter, amperes

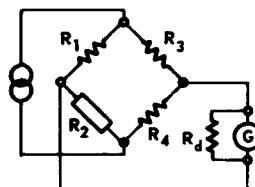
E_O = bridge open-circuit output, volts

R, R_L = resistance defined above, ohms

It should be noted that the resistance "seen" by the meter at terminals A-A is the bridge resistance, R . In the case of magnetically damped galvanometers, the damping resistance into which the meter must "look" is defined by the manufacturer, and the defined value must be held within $\pm 2\%$ if the correct value of damping is to be achieved.



If $R_D > R$,
then $R_d = R_D - R$



If $R_D < R$,
then $R_d = \frac{R R_D}{R - R_D}$

where

R_D = damping resistance specified by manufacturer, ohms

R = effective bridge resistance, ohms

R_d = shunt or series resistor to be added, ohms

The maximum voltage (Ref. 100) to be applied to a bridge may be calculated from $E = \sqrt{WR}$ volts,

where

W = permissible wattage, varying between $1/4$ and 1 w, depending on thermal inertia and cooling

R = bridge input resistance, ohms

The minimum voltage is fixed by the sensitivity of the measuring instrument used and maximum amount of strain expected. If the permissible bridge output is insufficient to drive the measuring instrument directly, then amplification is required.

Practical Considerations (Ref. 101).--No d-c bridge is balanced unless its output is zero. In some a-c bridges having non-sinusoidal input voltages or nonlinear arm impedances, harmonic voltages of considerable magnitude may appear in the output. These harmonic voltages and currents remain even though the bridge is balanced for the fundamental frequency. The usual technique of adjusting for minimum voltage output or for zero average output in these bridges is dangerous. The only true measure of balance is a zero fundamental frequency component in the output. Bridges which do not readily adjust to balance should have their output waveform examined to make sure the cause is harmonics and not contamination.

The most sensitive resistance bridge is always the one with four equal arms, if the detector has a high resistance and is voltage sensitive. (This also assumes that the allowable power dissipation of all arms is the same. If two arms, R_1 and R_3 , can have a greater power dissipation than R_2 and R_4 , the use of an increased voltage and larger values for R_1 and R_3 will increase the output.)

The output of a bridge is directly proportional to the input. Doubling the input voltage doubles the output current or voltage.

Less contamination will occur with a-c bridges if no output transformer is used to couple the bridge to the detector.

Contamination in any form impairs sensitivity and linearity of the bridge output versus unbalance curve.

Matching of bridge impedance and detector impedance is not usually required for the average bridge.

Sixty-cycle bridge input voltages are to be avoided, because the bridge may have 60-cycle contamination which cannot be detected or eliminated.

A-c bridges having very low bridge arm impedances (10 ohms or less) should be avoided. The same is true of arms over 10,000 ohms.

The power dissipation of the various bridge arms should be kept to a minimum, i.e., the lowest input voltage consistent with adequate sensitivity should be used.

3.1.2.2 Some Typical Strain-Gage Circuits

The simplest circuit that may be used for strain-gage measurements requires four gages, a battery, and a galvanometer. The long period of the galvanometer limits this circuit to static measurements; its requirement for a level position and freedom from shocks and vibrations adds to the difficulties of its use in field testing. The use of a d-c supply has the advantage of eliminating the influence of cable capacitances and allows very long cables to be used.

To eliminate the use of sensitive galvanometers, the d-c supply may be replaced by an alternating voltage, in which case the output of the bridge is placed into an amplifier with a rectifier, and an ammeter is used to indicate the off-balance. Strain indicators for such circuits are commercially available for both the null method and the direct-indication method. In the latter case, the amplifier and the supply oscillator have to meet higher requirements of accuracy and stability.

When an a-c powered bridge is followed by an amplifier, some circuit for indicating the phase between oscillator voltage and the bridge unbalance voltage must be provided in order to show the sign of the strain. When static strains are being measured, a direct coupled amplifier may be used; for the simultaneous indication of static and dynamic strains, its use is a necessity. This type of amplifier has poor stability, and its zero drifts with time. It is also difficult to adjust, and hence it is not often incorporated in commercially available units.

A carrier system is less critical to construct and more versatile in operation than a d-c amplifier. The carrier frequency should be from 4 to 10 times higher than the modulating frequency or else a gate or filter should be used to make the circuit insensitive to the carrier frequency. Thus, in the case of dynamic measurements, the highest frequency that can be measured is determined by the carrier frequency of the measuring apparatus, and this is chosen such that cable capacitances are no longer important. The amplifier should be designed to pass a limited band of frequencies since the noise level is determined by the bandwidth.

It is usual to record the output signal by means of a cathode-ray oscilloscope with an electron beam or else a magnetic oscillograph.

Although complete strain-gage systems are commercially available, it is often desirable to build them. For such cases, the information in Refs. 102 and 103 will prove very useful.

3.1.3 Errors Associated with Strain Gages

The use of electrical-resistance strain gages to measure aerodynamic loads in wind-tunnel balances has proved so successful that refinements have been carried to the point where a high precision of measurement is expected (Ref. 104). This has necessitated a critical examination of the characteristics of the strain gage itself as well as the consideration of the accuracy of the equipment used to indicate the resistance of the gage. This subsection is concerned with the former problem (Refs. 102, 104, and 105).

Aerodynamic loads are usually measured by means of four-arm strain-gage bridges mounted on cantilever beams or stings. The gages are subjected to the effect of the ambient stream conditions both directly and indirectly through the supporting sting. These effects often vary with time. Errors in indicated strains are mainly attributable to variation in temperature. The effect of this variation may be demonstrated by placing the sting in an oil bath and measuring the change in bridge output as it varies with temperature while the sting is in a no-load condition. By means of several hot and cold oil baths with temperatures up to 150°F, a specific bridge arrangement may be calibrated for temperature effect in about 15 min, whereas the same procedure in a heated air stream might take several hours. The oil may be cleaned from the unit by use of carbon tetrachloride (toxic).

3.1.3.1 Thermal Coefficient of Resistance

The major source of strain-gage error is the fact that the resistance of most wires changes with temperature. The variation is not only a function of the change in temperature but may also be a function of the number of heating cycles to which the gage has been subjected and of the time elapsed between cycles. Theoretically, temperature compensation may easily be accomplished by installing a second strain gage, often known as a dummy gage on an unstrained piece of the same metal as that to which the active gage is bonded. If the two pieces are subjected to the same temperatures during testing, both gages will experience identical thermal resistance changes and will allow correction to be made to the gage under load. The dummy gage may be so connected in the bridge that it may also measure strain, provided that they measure in opposite directions. This method represents a very effective device for significantly increasing the strain sensitivity and simultaneously securing temperature compensation. For applications where space will not permit the use of additional gages, a temperature-compensated strain gage has been designed. The gage grid is constructed of two different wire materials in series, the lengths of which are so proportioned that the total increase in resistance due to temperature in the one is cancelled by a decrease in the other. The temperature range over which this is even theoretically true is limited. The use of this gage is also limited by the fact that there is an uncanceled resistance change in the lead wire, whereas in the dummy gage application this change is covered.

In actual practice, temperature compensation is not easily achieved, since there is also a random scatter, even in gages of the same resistance, gage factor, and lot number. It is found that wire taken from various sections of one spool may show a slightly varying temperature coefficient of resistance. The coefficient for constantan wire (which is essentially the same as that used in strain gages) may

vary from -30 to +20 parts per million (ppm) per degree Fahrenheit. In terms of equivalent stress, two gages having these extremes of the coefficient would indicate 420 psi compression and 250 psi tension for each 1°F change from the reference temperature. It is apparent that production gages are seldom if ever found having these extremes. In a tunnel operating at a stagnation temperature of 150°F they would cause temperature drifts equivalent to as much as 60,000 psi stress. References 106, 107, and 108 present data on the change of resistance with temperature of various types of strain gages, as determined by the Bureau of Standards. These data indicate large variations among the various types of gages tested. Reference 108 contains data for gages that indicate a maximum difference between two gages of 0.63 ppm/°F. Reference 109, published ten years later than the aforementioned references, gives a more optimistic picture.

Development of new alloys and new bonding cements as well as improved manufacturing techniques and stepped-up quality control are doing much to reduce the temperature errors. The use of 0.001-in. Karma wire and either Quigley No. 1925 (Quigley Co., New York, N.Y.) or Brimor U529 bonding cement (Morganite, Inc., Long Island, N.Y.) will allow the construction of a strain gage with a temperature coefficient of resistance of 2.5 ppm/°F over a temperature range of 80 to 800°F. Reference 109 also gives temperature-compensation calibration curves for nichrome-V foil gages bonded to any base metal for which the thermal coefficient of expansion is known.

In view of the random error in gages, it is wise in any one application to use gages from the same lot, and to place the compensating gages as close together as possible.

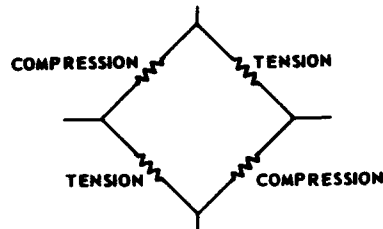
A second useful method would be to determine the coefficient of the gages and then to match them in bridges. This would require a temporary (removable) cement which would withstand the stagnation temperature to which it must be subjected. A completely satisfactory one is yet to be found. This method holds the best promise for installations where clearances are very small and compensating wire cannot be accommodated.

The third possibility, used at several facilities, consists of inserting compensating wire in the arms of the bridge. This compensating wire has a relatively high temperature drift, and when the correct length is inserted in the proper arm it will counter-balance the drift of the gages. This method requires at least two and possibly three heat checks: the first to find the gage drift, the second to check the effect of the compensating wire, and perhaps a third if the first attempt at correction does not work. This method is simple but time-consuming. In some cases there may be difficulty with the extra wire if the installation is cramped for space.

The resistance of the jumper wires will increase with increasing temperature, and this factor should be considered in wiring the bridge. There are essentially three possible arrangements, as shown in Fig. 3-2. If the bridge is wired as shown in Fig. 3-2(c), an output of from 200 to 400 psi for an 80°F change can result, depending on the jumper length. Substantiation of this has been obtained experimentally in several instances where jumpers were used in all combinations shown, and these results were of the same order of magnitude as predicted theoretically.

Since the circuits in Fig. 3-2(b) and (c) are known to have an error or temperature drift, it is more reasonable to employ the circuit shown in Fig. 3-2(a). The jumper lengths should be the same, where practicable. The unbalances, shown in Fig. 3-2(b) and (c), may be resorted to as a means of compensation for small-order drifts which may occur from mismatched gages when wired to give no jumper error. The sign of the correction can be made positive or negative by proper wiring; thus it can be used to cancel drifts of about 200 to 400 psi.

The mechanics of compensation can be described (Ref. 110) by referring to the sketch below.



This is a four-arm bridge in which the strains have been identified for each arm. It is assumed that a positive load on the member will result in strains as shown. It can now be shown that an increase in resistance with temperature of a single gage can result in either a positive or negative output from the indicator. If the bad gage is in either of the arms marked compression, its increase in resistance with temperature will be opposite to the resistance change caused by the positive load, and a negative output will result.

Since the great majority of gages show a resistance increase with temperature, the direction of indicator drift can be used to deduce the location of the drifting gage. If the drift is in the same direction as results from a positive load (positive output), the tension gages are drifting. If a negative output occurs, the compression gages are drifting. This logic similarly indicates the location for the compensating wire.

Both nickel and copper wire have positive changes in resistance with increasing temperature, resulting in increased resistance. Thus, if the compensating wire is placed in a tension arm (or arms), a positive indicator drift will result. Similarly, if it is placed in one or both of the compression arms, a negative indicator drift will result. Compensation is merely this application of extra wire in the bridge to counterbalance the resistance changes of the gages with temperature.

Two kinds of wire frequently used for compensating are nickel and copper. The temperature coefficient of resistivity of these is 0.0033 and 0.0022/°F, respectively. Thus, nickel has an advantage over copper in that it will give more resistance change per inch of wire than copper. Similarly, nickel has a greater resistivity than copper, and a given length of wire of a certain gage will result in several times the resistance change of a similar piece of copper wire. However, copper is easier to handle and to solder, and also is available in a wider variety of sizes, coverings, and strand combinations.

Table 3-1 gives a short summary for various lengths and gages of wire in terms of indicator counts (where each count is equivalent to 6.55 psi). These are theoretical values and hence will not be exact

for practical applications. They will serve only as a rough guide and a starting place for empirical work.

3.1.3.2 Temperature Differences in a Bridge

The above compensation technique is effective only when the gages and compensation wires are all at the same temperature. Any temperature difference between components in a full bridge will result in an output error. A slight breeze or a ray of sunlight playing on any one part has been known to cause a worse temperature drift than that of the uncompensated bridge.

Care must be exercised to maintain all components of the bridge at the same temperature by insulation or some other means. An example of this difficulty was experienced with an internal strain-gage balance in a nose-inlet ducted model, in which serious shifts in strain-gage readings for air-on conditions occurred because compensation wire was exposed to the air flowing through the model. The same effect was also noted during wing hinge-moment tests of the same model. The effect is illustrated in Figs. 3-3 and 3-4, where serious discrepancies between right and left panel data are noted in the upper curve. The data should be coincident since the model was symmetrical. The middle curves show that the data are brought into close agreement by plugging the duct so that no airflow was possible over the gages. The bottom curves show test data which were obtained after the forward hinge-moment gages were insulated and the model sealed internally to reduce air leakage in the gaged beam section to a minimum. The aft gages were only covered with Duco cement, which may explain the small discrepancy between right and left panel hinge moments. Subsequent tests of this model, in which all gages were covered with insulation, produced excellent agreement.

Calculations have been made to show the effect of a 1°C temperature differential; the resulting error was found to be negligible. It is believed that temperature differentials on a sting, after thermal equilibrium is attained, during testing are not normally large enough to introduce appreciable errors.

3.1.3.3 Unequal Expansion Effects

A further source of strain-gage error stems from the fact that the thermal coefficients of expansion of the strain-gage wire is different from that of the member to which it is bonded. If a gage were constructed completely free of temperature errors when bonded to steel, it would be greatly in error if it were bonded to some other metal having a different coefficient of expansion. Compensating gages reading equal strains but in opposite directions will also compensate for this expansion error. Standard self-temperature-compensated gages are made for bonding on specific surfaces and are available for annealed mild steel, quartz, titanium, and duraluminum. Any other surface would require a custom-made gage. Since the coefficient of linear expansion of quartz is nearly zero, gages which are temperature compensated for this material are frequently used in determining the coefficient of expansion of other materials.

3.1.3.4 Error Due to Gage Factor Mismatch Within a Bridge

Strain gages supplied by the manufacturer have their gage factor specified with a tolerance of $\pm 1\%$. It is generally accepted that most gages actually vary less than 1% and are appreciably more accurate than guaranteed. However, the maximum error which might occur has been computed using the $\pm 1\%$ figure.

As noted previously, there are two changes in gage resistance which are caused by temperature changes. The first effect is the temperature coefficient of resistivity which is a random effect that may be considered as independent of the gage factor. The second effect is the difference in linear expansion between the gage and the member on which it is mounted. This latter effect is one in which the gage factor is significant.

Assuming a homogeneous metal member, the differential expansion will induce the same strain in all four gages of a full bridge. The resistance change in any individual gage will be its gage factor times the strain times the gage resistance. Since each gage has the same strain and resistance, the resistance changes will be different in each arm of the bridge if the gage factors are different. The maximum output which can result from a gage factor mismatch is computed to be about 100 psi. It is therefore desirable to match gages for gage factor, but a mismatch of 0.01 or 0.02 is probably acceptable as long as the resistance and lot numbers are the same.

3.1.3.5 Error Due to Strain-Gage Creep

Experiments (Ref. 111) have shown that if a test element instrumented with bonded strain gages is subjected to a load suddenly applied, the strain-gage bridge output decreases with time from an initial value. The rate of decrease is relatively large for the first few seconds and decreases thereafter so that the output approaches a constant value as an asymptote. This phenomenon is known as creep effect. The magnitude of the total change with time has been found to be approximately proportional to the unit strain of the material to which the gage is bonded when subjected to the applied load. Typical creep curves are plotted in Fig. 3-5.

The creep effect is apparently the result of a partial relaxation of the bonding material, such relaxation occurring as a plastic type of flow. Generally speaking, the amount of creep will be greater for the cases in which the ratio of gage length to cement thickness is small, and smaller for cases in which this ratio is large. The typical curves shown in Fig. 3-5 indicate that there is a very large difference in the creep effect between paper-backed gages and bakelite gages. Since no methods have yet been discovered by which the creep effect can be reduced or completely eliminated, the use of paper-backed gages for instrumentation purposes where accuracies within 1% are desired is not recommended. Also, in consideration of this effect, investigations with regard to other factors have been concerned primarily with bakelite gages.

The use of plastic bags over strain-gage beams, with vacuum drawn on the bag and pressure applied external to the bag during the curing process, has been of great help in diminishing the creep problem. It also facilitates easy alignment of strain gages on the beams. The entire element may be placed inside a transparent plastic bag. The bag

is then evacuated and collapsed to the surface of the element, thus holding the gages in place under approximately atmospheric pressure. Since the bag is transparent and pliable it is possible to make a final check on gage location and, if necessary, to make adjustments with the clamping pressure applied.

The instrumented element is then placed in an oven for a curing process. A special oven which may be pressurized to 100 lb psi is used in conjunction with the evacuated bag in order to provide high uniform pressures during the baking cycle. The primary factor in a baking or curing cycle is to avoid gassing of the bakelite cement and consequent formation of bubbles. Such bubbles, it has been found, not only affect the thermal response characteristics of the gage but also promote the formation of fatigue cracks, with ultimate destruction of the gage bond. A satisfactory cycle consists of baking at 150°F for two hours, followed by 200°F for two hours, followed by 250°F for two hours, followed by 300°F for one hour.

It has also been noted that gage stability is improved by cycling the gage to its maximum load several times. This stability is lost if the gage is left without load for a few days or if the sign of the load is reversed. Creep in the foil-type strain gage may be reduced by using an end loop much wider than the grid line itself.

3.1.4 Strain-Gage Use at High Temperatures

The use of hypersonic wind tunnels having temperatures up to 1500°F brings new problems in strain-gage measurements. Heretofore, strain gages were commercially manufactured for use up to about 250°F, but recently a great deal of work has been done to produce gages with stable characteristics up to 2000°F. A great deal of information on high temperature operation and research is to be found in Refs. 109, 112, and 113, as well as in the current bulletins issued by the manufacturers listed in Subsec. 3.1. It should be noted that the state of the art is advancing rapidly, and therefore the material presented at this time (i.e., in 1960) may quickly grow obsolete. Current research is being concerned with new methods of bonding, particularly with ceramic bonding and also with the production of new alloys whose temperature characteristics are stable enough to allow calibration.

One practical way (Fig. 3-6) of using available bakelite gages and bonding techniques has been tried successfully at 1000°F on a 3/8-in. diameter strain-gage balance mounted inside a closed-nose body of revolution (Ref. 114). Cooling water was passed through the entire length of the balance and the model nose at the rate of about one-half gallon per minute, and satisfactory measurements (Fig. 3-7) were made despite the high temperature of the air passing over the model (see also Ref. 115 for more details). This technique would probably fail if the hot air passed directly over the gages, as it would in the ducted model.

3.2 Design of Conventional Strain-Gage Balances

A general method for the measurement of stability, control, and drag parameters of supersonic wind-tunnel models as well as several variations of the basic method are presented in Ref. 116. The systems described, when properly tailored to the load ranges of the model under test, have proved very reliable and can be installed and operated at reasonable cost by relatively inexperienced personnel.

The requirements of wind-tunnel testing call for a balance system capable of accurately measuring the force and moment components associated with static longitudinal and lateral stability and control of a model. (The axial force, or drag, is usually required as well. However, since its measurement is somewhat unique, a detailed discussion is needed. This appears in Subsec. 3.2.6.) The problem is often complicated in supersonic testing by the requirement that the model be mounted on a relatively long and slender sting protruding from the aft end of the model to eliminate the interference usually associated with side-mounted models. This means that the moment reference point of the model may have an appreciable movement due to structural deflection of the model support system. Therefore, when a balance system external to the model is used, suitable moment transfers must be applied to account for the fact that the moment reference point of the model is not fixed relative to the balance.

When a sting mounting is used in conjunction with an external balance, either some means of evaluating the tare due to air loads on the exposed sting must be provided or a windshield must be used. The evaluation of tare forces by methods such as images or split stings is tedious; but these forces can be a major factor in the accuracy of the data. Windshields are objectionable because they must be larger than the bare sting and because they increase the possibility of aerodynamic interference between the support system and the model.

The problems of movement of the moment reference and aerodynamic tares can be avoided by using a balance system internal to the model; this system is preferred by a vast majority of users. To be of practical value an internal balance must offer:

1. Adaptability to a variety of model configurations, generally with very severe restrictions on available space inside the model.
2. Accuracy over widely varying load ranges.
3. Reasonably direct indication of the forces and moments acting on the model for ease of data reduction.
4. Relatively simple, yet fast installation in the wind tunnel.
5. Ruggedness enough to withstand normal handling with minimum maintenance.

In order to satisfy the first two requirements, it is often preferable to tailor the balance to fit each specific model rather than to use standard balances; and in cases where a model is to be tested over a large range of velocities and/or densities, it may be desirable to provide several balances having different load ranges in order to obtain higher accuracy. Thus it becomes advantageous to have a balance that is relatively inexpensive and easy to construct. In large wind tunnels, where the test-section dimensions are measured in feet instead of inches, models are large enough to allow the use of one or more standardized, six-component, internal balances in most of the force models tested. Because most readers are probably concerned with smaller wind tunnels, most of the discussion will be directed to these tunnels; however, the comments apply equally well to large wind tunnels. Each has been written about strain-gage balances; the reader is particularly directed to Refs. 114 and 117 to 122.

Important factors in the selection of an internal balance, where space is limited, are the number of electrical leads required and the number and arrangement of the strain gages.

3.2.1 Basic Two-Moment Strain-Gage System

The simplest of strain-gage measuring systems consists of a beam extending into the base of the model, as shown in Fig. 3-8, on which resistance-wire gages are mounted to measure the bending moment at two points. Each moment bridge is wired as shown in Fig. 3-9. From the moment diagram in Fig. 3-8, it is apparent that the normal force, N , is

$$N = \frac{M_b - M_a}{X} \quad (3-14)$$

and the pitching moment, M_o , at the center of gravity is

$$M_o = M_a - Nx_a = M_a - \frac{x_a}{X} (M_b - M_a) \quad (3-15)$$

Strain gages mounted on the beam at 90 deg to a and b measure the side force, Y , and the yawing moment, M_y .

Since the voltage output of the bridge is measured in terms of $\frac{\Delta V}{V_o}$ (note change in nomenclature to allow use of E = modulus of elasticity), Eqs. 3-14 and 3-15 can be written,

$$N = \frac{1}{G_b X} \left(\frac{\Delta V}{V_o} \right)_b - \frac{1}{G_a X} \left(\frac{\Delta V}{V_o} \right)_a \quad (3-16)$$

$$M_o = \frac{\left(1 + \frac{x_a}{X} \right)}{G_a} \left(\frac{\Delta V}{V_o} \right)_a - \frac{x_a}{G_b X} \left(\frac{\Delta V}{V_o} \right)_b \quad (3-17)$$

where G is the gage factor, which, from Eq. 3-1, may be written

$$G_a = \frac{\left(\frac{\Delta V}{V_o} \right)_a}{M_a} \quad \text{and} \quad G_b = \frac{\left(\frac{\Delta V}{V_o} \right)_b}{M_b}$$

To measure all four forces and moments, a total of 16 strain gages and 10 electrical leads would be required, assuming four active gages are used per bridge and a common power supply is used for all bridges. If separate power were used for each bridge, a total of 16 electrical leads would be required. If space is extremely limited and operating temperatures are not too high or too low, a bridge having

only two active gages (commonly referred to as a half-bridge) could be used, in which case only 8 strain gages and 6 electrical leads would be required. The use of a full bridge is recommended wherever possible since the full bridge has better accuracy, less temperature effect, and greater stability.

Most strain-gage installations are merely variations of this basic system.

3.2.2 Direct Measurement of Normal Force

A bridge circuit such as shown in Fig. 3-10 has been used successfully to obtain a single reading proportional to the normal force. In this case, a differential circuit is used instead of the standard strain-gage bridge generally used for moments in which all gage outputs are additive.

From basic strain-gage considerations,

$$\frac{\Delta L}{L} = \delta = \frac{Mc}{EI} \quad (3-18)$$

where

M = moment

E = modulus of elasticity

$\frac{I}{c}$ = section modulus

Thus, Eq. 3-1 becomes

$$G = \frac{\Delta R/R_G}{\delta}$$

For a half-bridge, Eq. 3-6 gives,

$$\frac{\Delta V}{V_o} = \frac{1}{2} \frac{\Delta R}{R_G} \frac{V_G}{V_o}$$

and these equations combine to give

$$M = \frac{E}{G} \frac{I}{c} \frac{\Delta R}{R_G} = \frac{2E}{G} \frac{I}{c} \frac{V_o}{V_G} \frac{\Delta V}{V_o} = \frac{\Delta V/V_o}{\alpha} \quad (3-19)$$

where

$$\alpha = \frac{G}{2E} \frac{c}{I} \frac{V_G}{V_o} \quad (3-20)$$

Physically, α represents the gage sensitivity for a half bridge. For a full bridge connected differentially as shown in Fig. 3-10, the net voltage output is the difference of the outputs of the two half-bridges.

$$\left(\frac{\Delta V}{V_o}\right)_{\text{net}} = \left(\frac{\Delta V}{V_o}\right)_a - \left(\frac{\Delta V}{V_o}\right)_b \quad (3-21)$$

Considering the moment diagram of Fig. 3-8 and Eqs. 3-14 and 3-19,

$$N = \frac{M_b - M_a}{X} = \frac{1}{X\alpha_b} \left(\frac{\Delta V}{V_o}\right)_b - \frac{1}{X\alpha_a} \left(\frac{\Delta V}{V_o}\right)_a \quad (3-22)$$

Then, if

$$\alpha_a = \alpha_b \quad (3-23)$$

$$N = \frac{1}{X\alpha_a} \left(\frac{\Delta V}{V_o}\right)_N = \frac{1}{\beta_N} \left(\frac{\Delta V}{V_o}\right)_N \quad (3-24)$$

Therefore, if Eq. 3-23 is satisfied, the normal force is a direct function of the voltage output of the combined bridge. The condition may be stated as

$$\frac{\alpha_a}{\alpha_b} = \frac{G_a}{G_b} \frac{E_b}{E_a} \frac{(I/c)_b}{(I/c)_a} \frac{(V_G/V_o)_a}{(V_G/V_o)_b} = 1 \quad (3-25)$$

The sensitivity of the combined bridge can be expressed as

$$\beta_N = X\alpha_a = \frac{X}{2} \frac{G_a}{E_a} \left(\frac{c}{I}\right)_a \left(\frac{V_G}{V_o}\right)_a \quad (3-26)$$

It is evident that by proper manipulation of the ratios of gage factor (G_a/G_b), modulus of elasticity (E_b/E_a), section modulus $(I/c)_b/(I/c)_a$, and gage voltage $(V_G/V_o)_a/(V_G/V_o)_b$, the conditions of Eq. 3-25 can be met. Each of these factors is discussed below.

Gage Factor.--Commercially available strain gages range in gage factor (see Subsec. 3.1) from 1.75 to 3.5, giving a possible ratio of two. However, care should be exercised if gages having the higher gage factor are selected since these gages may have undesirable temperature effects (see Subsec. 3.1).

Modulus of Elasticity.--It would be possible, although perhaps not practical, to use a beam of composite material in which, for instance, the portion under gages "a" was dural and the portion under gages "b" was steel. This would produce a value of this ratio of about three.

Section Modulus.--This, an easily varied parameter, is merely a function of the size and shape of the beam used. In general it is limited only by strength and rigidity considerations of the design.

Gage Voltage.--This is another, rather easily varied parameter which can be varied by the method shown in Fig. 3-11 by inserting appropriate resistances at either R_a and R'_a or R_b and R'_b . Gages for which the gage voltage ratio was changed as much as 15% to 20% by attaching matched lengths of fine constantan wire in series with the gages in one half of the bridge circuit have been used successfully. For large changes in the gage voltage ratio, a voltage reducing network is recommended.

3.2.3 Use of Composite Bridge

In order to obtain a four-component balance having the fewest possible number of gages and leads while still retaining the desirable characteristics achieved with full strain-gage bridges, the composite bridge shown in Fig. 3-11 can be used.

In this system, Gages 1, 2, 5, and 6 make up a direct-reading normal-force bridge with either R_a and R'_a or R_b and R'_b inserted as required for compensation. At the same time Gages 1, 2, 3, and 4 form a bridge which indicates the moment in the beam at a point approximately half way between Gages 1 and 2, and Gages 3 and 4. Since R_a and R'_a are either zero or of small magnitude, their effect on the sensitivity of the moment-measuring bridge is generally negligible.

Since the moment must be analytically transferred to the moment reference point, it is advantageous to place the moment-measuring bridge as close to the moment reference point as possible in order to reduce the transfer distance, thus reducing the resulting errors in the moment.

Care must be exercised in the selection of the indicating system used with this composite bridge to avoid interaction between the normal force and moment outputs. If a single indicator is to be switched from bridge to bridge, no problem should be encountered as long as the zero-balance networks commonly used are properly located. Simultaneous recording of moment and normal force has been successfully accomplished with automatic null-balancing systems and can be done with Brown electronic potentiometers or other similar instruments as long as sufficient damping is present to prevent the indicators from "hunting" due to their mutual interaction.

From practical considerations the direct normal force or composite bridge types are normally avoided, unless it is necessary to measure dynamic forces such as those imposed during starting or stopping of a supersonic tunnel or unless it is necessary to reduce data by hand methods to coefficient form. When high-speed, digital, data-processing equipment is available, it is much more practical to use the operationally more simple, two-moment system.

3.2.4 Design Considerations for Strain-Gage Balances

In the design of beams used in the foregoing systems, it is generally assumed that the maximum stress under any gage should not exceed 30,000 psi for steel (although stresses up to 75,000 psi have been used under certain conditions). With the maximum stress set and the design loads determined, the analysis of the beam then reduces to a matter of obtaining the maximum sensitivity of each component in the space available.

The optimum placement of the bridges can be approached in a logical manner. Consider the simple strain-gage system shown in Fig. 3-12, which measures the magnitude, F , and the location, Y , of the unknown force. Then

$$M_1 = FY$$

and

$$M_2 = F(Y - X)$$

giving

$$F = \frac{M_1 - M_2}{X} \quad (3-27)$$

and

$$Y = \frac{M_1}{M_1 - M_2} \cdot X$$

$$M_{cg} = M_2 + F(X - Z) = M_1 - FZ$$

Now assume that an instrumentation error exists in the measurement of M_1 and M_2 of magnitude ϵ_1 and ϵ_2 , respectively, such that the indicated, \bar{M} , and the true values of the moments are related as follows:

$$\bar{M}_1 = M_1 + \epsilon_1 \quad (3-28)$$

$$\bar{M}_2 = M_2 + \epsilon_2$$

where

$$|\epsilon_1| \leq |\epsilon_{1 \max}|, \quad |\epsilon_2| \leq |\epsilon_{2 \max}| \quad (3-29)$$

The indicated force is

$$\bar{F} = \frac{(M_1 + \epsilon_1) - (M_2 + \epsilon_2)}{X} = F + \frac{\epsilon_1}{X} - \frac{\epsilon_2}{X} \quad (3-30)$$

and the error is

$$E = \bar{F} - F = \frac{\epsilon_1 - \epsilon_2}{X} \quad (3-31)$$

By inspection, the maximum error, E, in the force, F, occurs when

$$\epsilon_1 = \epsilon_1 \text{ max} ; \quad \epsilon_2 = -\epsilon_2 \text{ max}$$

or

$$\epsilon_1 = -\epsilon_1 \text{ max} ; \quad \epsilon_2 = \epsilon_2 \text{ max} \quad (3-32)$$

Conversely, no error in the force, F, occurs when

$$\epsilon_1 = \epsilon_2 \quad (3-33)$$

If $\epsilon_1 \text{ max}$ and $\epsilon_2 \text{ max}$ remain constant and independent of the magnitude of the moments M_1 and M_2 , respectively, then the maximum error, E, in the force, F, would be independent of Y for any given value of X, and E could be diminished by making X very large. However, practice shows that ϵ is directly proportional to the magnitude, M, of the corresponding moment. Hence, equal errors ϵ_1 and ϵ_2 would be most likely to occur when $M_1 = M_2$ (i.e., when $Y = \frac{X}{2}$; i.e., when the gages are equally distant on opposite sides of the center of pressure). The magnitude of X is proportional to I/c , and hence X is limited by practical values of I/c for the maximum expected moments.

Actually the desired moment accuracy at the reference point (i.e., the center of gravity) places more stringent limitations on the bridge locations than do force considerations. Referring to the lower part of Fig. 3-12, it may be seen that if Z is greater than X, M_{cg} can take values a through e, of which only c is the correct moment (i.e., $\epsilon_1 = \epsilon_2 = 0$). It is obvious that the error in the moment at the center of gravity would be a minimum for

$$\frac{Z}{X} = \frac{1}{2} , \quad \text{if} \quad \epsilon_1 \text{ max} = \epsilon_2 \text{ max} \quad (3-34)$$

or

$$\frac{Z}{X} = 1, \quad \text{if } \epsilon_{1 \max} \gg \epsilon_{2 \max} \quad (3-35)$$

In practice, the bridges can rarely be located in such a manner as to minimize errors in force and moment simultaneously. Therefore, primary importance should be given to minimizing the moment errors.

In the practical problem of gage location, such factors as minimum size of beam for gage application, uncertainty or movement of the center of pressure, and rigidity of the model support system must be considered and compromised with gage sensitivity.

The problem of providing an easy and rapid method of installation in the wind tunnel can be solved by the use of a precision-ground taper joint as shown in Figs. 3-13 and 3-14. This joint incorporates a 17-pin Cannon plug which is automatically mated as the taper is seated. In addition, one pressure connection for the measurement of base or cavity pressure has been incorporated as shown in Figs. 3-15 and 3-16. This pressure connection is accomplished by means of a specially designed spring-loaded probe.

Typical internal strain-gage balances designed in accordance with this concept are shown in Fig. 3-17.

3.2.4.1 Materials (Ref. 123)

Although steel is generally used for the manufacture of most strain-gage balances because it lends itself readily to machining and grinding operations, can be heat treated, and has high strength and toughness properties (6150 steel heat-treated to Rockwell C35-37 is a good example), the singular properties of other metals can occasionally be used to advantage. For example, the high thermal conductivity, machinability, and mass-inertia characteristics of aluminum might have some advantages over steel in some balance applications. Constants for elastic solids and the conventional stress-strain relations may be used to design aluminum beams with performance characteristics having the same reliability as steel beams.

An internal balance may be represented by a cantilever beam of length L , with a concentrated load, P , at the end. The deflection, y , of the end of the beam is then given by

$$y = PL^3/3EI \quad (3-36)$$

where, in consistent units,

E = modulus of elasticity

I = section moment of inertia

This expression holds for all homogeneous beams regardless of section geometry. Since the modulus of elasticity of steel is approximately three times that of aluminum, an aluminum beam will need a moment of inertia three times that of steel if it is desired that both beams be of equivalent strain (or deflection). On this basis, a square aluminum beam will be 1.316 times as thick as the equivalent-strain steel beam ($I = x^4/12$). By using the stress relationship given in Eq. 3-18,

$$s = Mc/I \quad (3-37)$$

it can be shown that fiber stress in aluminum will be 0.439 times that in the strain-equivalent steel beams.

In summary, strain-equivalent and stress-equivalent beams of aluminum have the following relationships to steel beams (where steel parameters are considered unity in all cases):

Parameter	Aluminum Beam	
	Strain-Equivalent	Stress-Equivalent
Local Bending Moment	1.000	1.000
Section Dimensions	1.316	1.000
Cross-Section Area	1.732	1.000
Local Surface Stress	0.439	1.000
Unit Deformation	1.000	3.000

An experimental check of these theoretical figures was made using SAE 4130 steel and 24S-T3 aluminum alloy. The average deflection ratio for the stress-equivalent beams was 2.8 (instead of 3.0) in both planes, and the average deflection ratio for the strain-equivalent beams was 1.0 in both planes. These values are in reasonable agreement with the theoretical predictions in view of the fact that the modulus of elasticity may vary somewhat for a given material, depending on its composition and hardening process.

3.2.4.2 Effect of Section Size and Indicator Sensitivity on Repeatability

The repeatability of strain-gage measurements is a factor of importance to the experimenter. He must be assured that the indicator of any system will always show a value proportional to the stress applied to the gage and not be affected by the manner of application. Referring to Eq. 3-37 the stress is a function of the moment and the section modulus. In order to give repeatable measurements, the system should be insensitive to the variations in the factors that make up the stress and should be affected only by changes in the product.

An analysis of a large number of data points taken in the same tunnel where all other test parameters were controlled have shown that:

1. The section modulus (or size) has very little effect on the data repeatability in the normal range of stresses for which the system is designed. Increasing the stress level above the normal range increases the scatter in the data in rough proportion to the stress increase.
2. The repeatability of data in terms of moment in inch-pounds is a linear function of the internal-balance section modulus at the bridge station.
3. Increasing the indicator sensitivity gives a proportional increase in the repeatability of the data in terms of moment.

3.2.4.3 Mounting the Model on the Internal Balance

Since the model may be removed from the internal balance several times during calibration and test, it is essential that it be re-attached to the balance with great accuracy in order to assure that the distance between the electrical centers of the strain-gage bridges and the moment reference remains constant. This can be accomplished most conveniently by grinding a shallow (2 or 3-deg) taper on the balance end as shown in Figs. 3-13 and 3-14, and by fitting it to a mating female taper in the model. Experience has shown that the model can be replaced repeatedly on the balance within an accuracy of ± 0.002 in., which is as close as it is possible to establish the location of the gage by experimental calibration techniques.

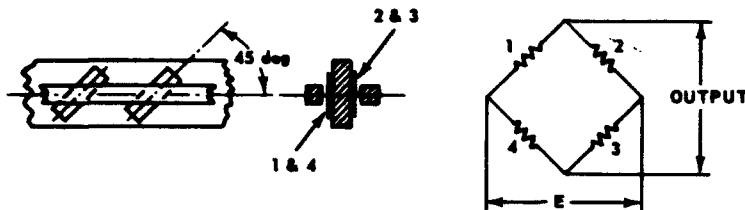
The model can be oriented in roll on the balance by using a height gage. The internal balance is positioned on its support in the tunnel, the power hooked up to the gages, and a weight hung on the end of the balance. The balance is then rotated until the output from the side-moment bridge which was zeroed during the calibration returns to zero. Next, the model is rotated until two opposing wing or tail surfaces are level, at which time the taper is pulled tight. After the angle of attack is zeroed, perhaps also with a height gage, the model is then ready for testing.

3.2.5 Rolling Moment Measurement

In addition to the pitching and yawing moments, one other moment is needed to define completely all of the moments acting on the model in the wind tunnel. This is the rolling moment about the longitudinal axis. Unlike the other two moments, which must be measured internally at or near the moment reference point to avoid errors induced by the mathematics of transferring to some remote position, the rolling moment can be measured either externally or internally without loss of accuracy.

Although it is possible to mount a strain-gage bridge with the gage axes at 45 deg to the longitudinal axis of an internal balance

without changing the cross section of the member, the beam is usually far too stiff in torsion to give the desired sensitivity. The section may be machined to some cruciform section as shown below.



It is obvious that this arrangement will weaken the internal balance and will allow it to bend more on application of a normal force or side force; consequently, the cruciform section should be located at or near the anticipated center of pressure of such forces. If it is located at some distance from the center of pressure, the internal balance will deflect excessively and cause binding between the model base and the internal balance even under moderate loads. The major advantages of the cruciform rolling moment section are its compactness, ease of manufacture, and the simplicity of mounting and wiring the strain-gage bridge. The bridge can be wired in such a manner that interaction effects of loads applied normal to the longitudinal axis can be minimized. For example, when a pure torsion moment is applied, Gages 1 and 3 are in compression when 2 and 4 are in tension, thus magnifying the bridge output. On the other hand, a pitching moment induced by the normal force puts Gages 1 and 4 in tension and Gages 3 and 2 in compression, with no resulting output from the bridge. Similarly, a yawing moment would be cancelled out. In reality, it is impossible to construct such a device so that it is entirely free of interaction (see Subsec. 3.2.8).

Some of the disadvantages of the internal method are that it increases the complexity of the internal balance, increases flexibility, and makes it virtually necessary to tailor individual internal balances for each model.

These disadvantages can be avoided by measuring the rolling moment external to the model. As shown in Fig. 3-18, the four-component internal balance taper fits into a shaft which is mounted on ball bearings and restrained in roll by a cantilever on which the strain-gage bridge is mounted. The unique advantage of this system is that a small d-c motor driving through a worm and gear attached to the other end of the rolling moment cantilever provides a simple way for remotely driving the model to any desired roll attitude without shutting down the tunnel. (Note: A slide wire or selsyn system should be provided ahead of the roll cantilever, instead of behind as shown in Fig. 3-18, to provide external indication of roll position.) This particular balance support restrains the shaft from axial movement by means of a second cantilever similar to that used to measure rolling moment. These two cantilevers are easily replaced to allow for the different loads which are anticipated from a wide variety of models or from variation of the dynamic pressure. To minimize friction, the outer shell and shaft act as the outer and inner races of the ball bearings which are held in place by a brass cylinder with holes evenly spaced around the periphery of the shaft. These cylindrical bearing retainers are free to float up

against the machined shoulders at the ends of the shaft. To minimize the resulting friction, three piano wire springs are soldered to the ends of the bearing retainers in order to hold the retainer away from the shoulders. The shaft and balance support case must be hardened steel (6150, Rockwell C-57). Low-friction bearings mounted on the ends of the cantilever beams and fitted with very close tolerances in the forked members which transmit the loads from the floating shaft are required for trouble-free operation.

One of the outstanding advantages of this external means of measuring rolling moment, aside from its versatility, is its virtual freedom from interaction caused by combined loadings on the model. In order to realize this advantage, however, the longitudinal axes of the shaft and the internal balance must be perfectly aligned.

3.2.6 Axial Force Measurement

The measurement of axial force is the sixth and last component needed to define completely the over-all force characteristics of an aircraft. In many ways, it is the most difficult component to measure because of its susceptibility to interaction from all forces and moments, other than the rolling moment. The interaction difficulties can be lessened to some extent at the expense of added pressure corrections if the force is measured external to the model.

3.2.6.1 Strain-Gage Techniques for Measurement of Axial Force

That approach by which the basic drag balance is incorporated in a sting-support positioned between the model and angle-of-attack mechanism of the wind tunnel is considered the most satisfactory method for measuring axial force. As shown in Fig. 3-18, the model is supported by a central shaft mounted in the ball bearings within the balance housing and the balance base, which is attached rigidly to the angle-of-attack mechanism. The central balance shaft is free to rotate and translate except for the restraint imposed by cantilever beams between the balance housing and aft portion of the shaft. Strain gages mounted on these beams transmit indications of applied rotational and axial loads to appropriate recording devices. Roll orientation of the shaft is controlled and recorded remotely. It is necessary to measure the model base pressure and the static pressure inside the balance support. It is therefore essential to seal the support at the base to prevent airflow through the support so that the internal static pressure acting on the shaft cross-sectional area at the windshield lip completely defines the unwanted force or tare inside the support case which is measured by the cantilever. Experimental evidence has shown that it is virtually impossible to obtain a base pressure on a wind-tunnel model with a practical sting-windshield combination that will truly represent the free-flight base pressure at supersonic speeds. Consequently, the base pressure acting on the model base area (less the sting area, which has already been accounted for) must be corrected to the free-stream static pressure or some other common reference pressure. In this manner, base pressure anticipated in free flight, along with Reynolds number corrections to skin friction drag, can be applied to the wind-tunnel data to obtain realistic drag values for free-flight conditions.

In all cases where the axial force is measured external to the model, the supporting member between the model base and the windshield lip must be cylindrical in order that the pressure drag on the

member remains negligible. Skin-friction drag on a cylindrical supporting member of practical length has been calculated to be negligible as it is well within the drag-measuring accuracy of most systems in current use. It is conceivable, however, that this skin-friction drag may become significant in cases where small absolute values of drag are to be measured, and therefore it must be evaluated in order to correct the drag measurements.

The roll and drag cantilever beams may be changed as needed to give the required sensitivity for a particular installation. Interaction of applied normal loads, not exceeding the balance design load, on the two-balance components of roll and drag are usually negligible.

The repeatability of balance-data components obtained from diverse models under actual test conditions over a long period of usage is indicative of balance performance. Representative values obtained by use of a balance of the type shown in Fig. 3-18 are tabulated below.

Number of Repeat Points	Normal Force (lb)	Axial Force (lb)	Rolling Moment (in.-lb)	Average Repeatability	
				Axial Force (lb)	Rolling Moment (in.-lb)
674	0-150	--	0-24	--	± 0.04
1177	0-150	2-26	--	± 0.10	---

A systematic balance evaluation program consists of an experimental study of the performance of the primary support balances operating within their design load ranges. Tests conducted at the same Mach number, using the same models and configurations with all balances, provide a good comparison of the performance of the various balances. Typical data, shown in Fig. 3-19, were obtained with the balances operating under a varying normal and axial force. Figure 3-19 shows a comparison of experimental and theoretical axial-force coefficients for a typical test model consisting of a cylindrical body with conical noses of various apex angles.

A balance of the type described above has been used to test an NACA standard model (RM-10), and the axial-force measurements have been compared with those obtained in several NACA wind tunnels operating at comparable free-stream conditions (Ref. 125). The results show an average difference in axial force of ± 0.03 lb, with a maximum axial force of 2.5 lb.

Six-component internal balances incorporating an internal drag link based on the flexure principle have also been constructed. The maximum interaction of normal load on the axial component of two typical units is 3% and 9% of the applied normal load. The average repeatability of axial force is ± 0.07 lb for axial loads of the order of 4 lb where the normal force varies from 0 to 160 lb.

The most commonly used type of balance at the Boeing Wind Tunnel is an internal strain-gage, six-component, temperature-compensated balance. The experience at Boeing, in common with that elsewhere,

is that axial force is the most difficult component to measure. Part of the reason for this is that the drag cage must carry all of the other comparatively large loads while measuring the relatively small drag load. Recent Boeing designs place the drag cage at approximately the model's center of lift; thus, this problem is somewhat alleviated because the moments imposed on the drag cage are greatly reduced.

During the "warming up" period of a continuous-flow tunnel, there exists a transient heat flow from the model and balance to the model support system. This heat flow induces erroneous readings in the balance even though the balance is properly temperature-compensated. It is therefore good practice to allow a 5 to 10-min period for temperatures to come to equilibrium before data is taken. This procedure allows the model, balance, and support system to assume an approximately equal temperature, thereby eliminating the heat flow.

One of the more recent Boeing strain-gage balances (the 636) is characterized by low interactions and a relatively large capacity for its size, which is 6.10 in. in length and 0.656 in. in diameter. The capacities of the various components are: normal force, 150 lb; pitching moment, 200 in.-lb; side force, 75 lb; yawing moment, 130 in.-lb; rolling moment, 50 in.-lb; and chord force, 15 lb. A main feature of this balance is what may be described as an "inside-out" construction. In a conventional drag cage design, the main supporting structure is generally on the top and bottom, with the flexures in between. In the 636 balance, the structure is in the form of a pair of T sections (one inverted), with the flexures running between the crosses of the T's.

The Naval Ordnance Laboratory has evaluated the performance of a highly sensitive one-component internal drag balance. The construction of this balance is conventional in that applied model loads are resisted by a flexure-pivot arrangement. Its unique feature is the detection of a small axial displacement of the model by a Schaevitz variable-reluctance transformer which may be calibrated in terms of applied axial force. The capacity of the existing balance is approximately 135 lb normal force and 36 lb axial force. The maximum diameter is approximately 0.5 in. Experimental results are characterized by interactions of extremely small magnitude and by small variations of this magnitude with normal-load axial location.

Figure 3-20 shows a version of a recent drag-beam design used at the Army Ballistic Missile Agency. The calibration indicated almost negligible (approximately 1%) interaction effect with normal drag sensitivity. Failure has been experienced when the weld bead was ground too thin. Fabrication is relatively simple.

Friction in bearing-supported balances can sometimes introduce sizeable errors in axial force measurements on low-drag configurations, especially in the absence of vibration. An air-bearing balance (patent pending, File 674262) has been designed at the ABMA wind tunnel for such measurements and is shown in Fig. 3-21. The upper view represents the arrangement initially tried. Air is supplied to Chamber A until the model moves forward. The pressure in the supply line to Chamber A is increased and observed. It can be related to the drag force. A more sophisticated version is pictured in the partial cross-section on the left. The motion between the model shell and the balance is resiliently restrained. The displacement due to a drag load is sensed by a differential transformer-type transducer.

Some air-bearing experiments conducted at David Taylor Model Basin indicate that this technique may be successful for very small diameter internal drag balances.

Measurement of axial force is complicated by the interference effects of the sting and windshield on the base pressure. A unique method of circumventing this problem has been developed at DTMB by supporting the model from the front or upstream direction. A drag balance is mounted in the downstream end of a cylindrical tube positioned on the longitudinal axis of a wind-tunnel nozzle. The tube begins in the tunnel stilling chamber, extends downstream through the effusor and nozzle, and ends with its base in the test section. The tube is supported only in the stilling chamber and effusor in such a manner that the influence of the supporting structure is not detectable in the test section. Test configurations are attached at the downstream end to a strain-gage balance enclosed within the tube. Cylindrical bodies are mounted concentric with the tube, and the pressure on the forward face of these bodies is measured in order to make drag corrections. Pressure and electrical leads are conducted forward in the tube and taken out through the stilling chamber. Base pressure measurements are made by means of an auxiliary probe. This technique has the following advantages:

1. It permits the measurement of afterbody drag characteristics which are free of support interference.
2. Transonic testing may be conducted without the usual choking or blocking problems caused by sting and windshield.
3. Larger scale afterbodies may be tested for a given supersonic shock reflection or subsonic wall correction condition.
4. The effect of protuberances and their influence on base drag may be evaluated.
5. Data accuracy is improved because afterbody drag is measured directly, larger scale models may be used, and problems associated with measuring drag and several other components simultaneously are eliminated.
6. By measuring both base-pressure drag and total afterbody drag, the contribution of wave drag plus skin-friction drag may be readily assessed.
7. It offers a potential means for investigating the effects of a jet emanating from the base.

The primary disadvantage is that data are obtained only at zero pitch or yaw attitude. It has been determined experimentally that the effect of the axial tube on supersonic flow in the test section is to increase the Mach number according to area ratio theory and to create a positive Mach number gradient (0.5%/in. at $M = 1.875$). It is expected to have no effect on subsonic or transonic test-section flow.

Another solution to the base-flow interference problem has been demonstrated by a French tunnel that has vertical flow from top to bottom. The model is fired upward into the flow with just enough energy to enter the test section and fall back into a catcher. Data were obtained photographically during the model's excursion into the test section. High-speed schlieren movies were taken at the instant the model floated at rest.

3.2.6.2 Induced Boundary-Layer Transition

The problem of measuring the drag of wind-tunnel models is complicated by the transition from laminar to turbulent boundary-layer flow on the model (Ref. 126). Because Reynolds number in full-scale free flight is usually much larger than for a small-scale model in the wind tunnel, the transition point in free flight is generally near the leading edges. On a model, transition may occur at various points, depending upon many factors, with a resulting change in the measured drag level. One means of overcoming this problem is to deliberately trip the boundary layer on the model so that turbulent flow over the complete model is assured. A common method for achieving this is to use roughness or trip wires near the leading edges of the model surfaces. Caution is needed, however, to trip the boundary layer without creating a disturbance large enough to produce additional wave drag. A systematic program (Ref. 127) was conducted to determine the critical size and location of grit or trip wires, and various sizes of grit applied near the nose tip were tested through a range of Mach and Reynolds numbers. A comparison of grit and a single wire shows that grit is considerably more effective as a tripping element.

If a positive means of assuring completely turbulent or completely laminar boundary layer over the entire model is not possible, it is necessary to establish the location of boundary-layer transition in order that appropriate corrections to the axial force can be made for the skin-friction drag. This subject is covered more extensively in Subsec. 5.6.

3.2.7 Interference Effects on Force Measurements

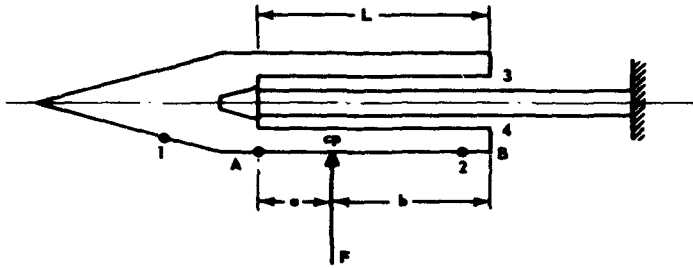
No discussion of force measurement is complete without some mention of sting and windshield interference effects. The ideal situation calls for a sting of zero diameter and for an infinite distance from the model base to the windshield lip.

3.2.7.1 Mechanical Interference

In wind tunnels where the dynamic pressure and the resulting loads on the model are high, practical considerations frequently prevent the use of long slender stings. Since the slenderness might give rise to excessive deviation with consequent interference, and too long a length may produce over-stressing, an optimum length and diameter must be determined for each type of application.

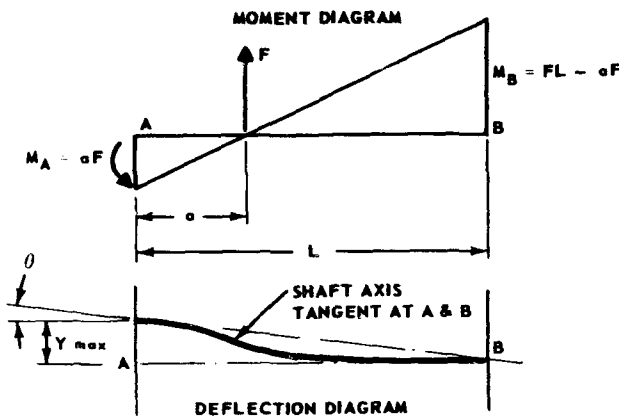
It is sometimes possible to eliminate mechanical interference (or grounding) with the model base, first by proper positioning of the internal taper connection between the model and sting, and second by varying the sting cross-section so that the internal portion of the sting takes an "S" shape under load, with no relative motion of the sting at the model base. This problem has a simple analytic solution and an even simpler experimental solution.

For the analytic solution (Ref. 128), the designer usually is given the external shape of the specified model and the approximate center-of-pressure location for the critical configurations to be tested. The problem is to place the internal balance in such a manner as to prevent grounding under load.



From the sketch, a load, F , applied at Points 1 or 2 will cause the clearance to decrease at Points 3 or 4, respectively. It is reasonable, then, that the application of the load at some point, preferably at the center of pressure, will result in no change in clearance at the model base. Hence, the dimension L is sought with the dimension b known.

For simplicity, assume that the theoretical internal balance is of constant section and therefore has a constant moment of inertia, I , along its length within the model. The appropriate moment and deflection diagrams follow.



It is obvious from the deflection diagram that the clearance at the model base will remain unchanged if the slope of the deflection curve at Point A extended passes through Point B. This condition is fulfilled if $y_{\max}/L = \theta$, in radians. Hence, independent equations for θ and y_{\max}/L as $f(a, L)$ are sought.

From the area-moment method of determining beam deflections, the angle, θ , between the tangents to the elastic curve of a beam at any two points, A and B, is equivalent to the area under the moment

diagram between the two points divided by EI . Hence,

$$\theta = \frac{FL^2}{2EI} - \frac{aFL}{EI} \quad (3-38)$$

Also, the displacement, y_{\max} in this case, of Point A from the tangent to the elastic curve at B equals the moment (about Point A) of the area under the bending moment diagram between A and B divided by EI . Therefore,

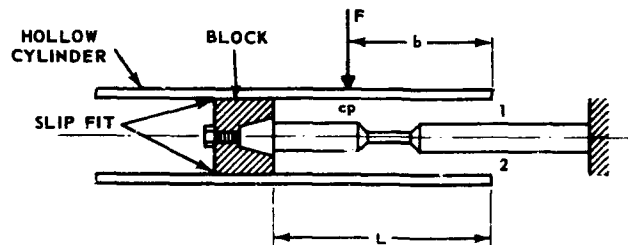
$$\frac{y_{\max}}{L} = \frac{FL^2}{3EI} - \frac{aFL}{2EI} \quad (3-39)$$

Equating Eqs. 3-38 and 3-39 and solving for L in terms of a ,

$$L = 3a \quad (3-40)$$

It is concluded for this case, therefore, that the internal balance should be so located that the center of pressure is two-thirds of the distance from the model base to the attachment point. Further, the location of the balance attachment point is independent of the load, F , the modulus of elasticity, E (for a homogeneous balance), or in this special case, the moment of inertia, I . For the practical case, however, the local moment of inertia of the internal balance will vary within the model cavity and will influence the solution to some extent.

For an existing internal balance and a known inner-body diameter and center of pressure, it is a simple matter to determine experimentally the distance, L , by hanging a weight at a distance, b , from the base of a hollow cylinder with known inner diameter and sliding it back and forth on a cylindrical block attached to the internal balance until the position is found where the clearance at 1 and 2 (below) does not change when the weight is removed. The distance L is then found by direct measurement.



3.2.7.2 Aerodynamic Interference

Aside from structural considerations, the internal balance should be designed so as to keep aerodynamic interferences to a minimum.

A few of the factors which may set up interferences are discussed briefly below.

Ratio of Internal-Balance Diameter to Model Diameter, d/D .-- This factor is of little consequence when the model is not boattailed, or when the model is boattailed and the boundary layer in the boattailed region is fully turbulent. When the boundary layer at the tail of a boattailed model is laminar, the presence of a large internal balance may cause premature separation of flow in the boattailed region and thereby cause erroneous measurements. Tests were conducted at the ABMA wind tunnel for the laminar boundary-layer condition at Mach numbers 1.99, 2.44, 2.98, 3.26, and 3.89, and Reynolds numbers between 1.9 and 0.8×10^6 on a cone-cylinder model. Base-pressure data for laminar boundary layer were obtained at zero angle of attack for various sting diameters and adapter locations. Based on these tests, it is concluded that there is 1) a negligible effect on base pressure at all Mach numbers for a ratio of sting size to model base diameter of 0.40 or smaller (in fair agreement with NACA data at $M = 2.00$), but that larger sting diameters have a noticeable effect on base pressure, particularly at the lower supersonic Mach numbers; and 2) a critical distance between the model base and adapter (windshield) location, within which the base pressure is greatly affected by an abrupt change in sting diameter, the distance varying with Mach number. (L/D values greater than 2 at $M = 1.99$, increasing to 3 at $M = 3.26$, are apparently free of sting effects.)

Windshield Interference.--One of the major problems associated with the measurement of axial force in a wind tunnel is that of windshield interference. A systematic study of windshield and support interference was run for the purpose of providing specific criteria for the design of model support systems which are free from interference effects. (Note: Criteria may be different for different wind tunnels.) The three configurations employed are shown in Fig. 3-22. Pressure taps were provided on the side of the model near the base as well as on the base of the model. The base and afterbody pressures were measured at angles of attack up to 15 deg. Data were obtained using windshield half-angles of 10, 20, and 30 deg with four sting diameters ranging from 0.33 to 0.83 of the maximum body diameter. Distance between the windshield and model base was varied from zero to six maximum body diameters. It was anticipated that windshield interference would be most critical for the non-boattailed body; however, the boattailed configuration was tested to verify the hypothesis. Figure 3-23 presents the primary results of the test at Mach number 1.50. Here the static pressure ratio at the extreme end of the body is plotted versus the ratio of the base-to-windshield distance to the maximum body diameter for the zero angle-of-attack condition. These pressure orifices were on top of the body, as close to the base as possible. The solid lines represent the interference-free condition, i.e., no further pressure variation with L/D . The non-boattailed body requires the greatest windshield distance to establish an interference-free condition and is therefore the most critical case. It should be mentioned that zero angle of attack also proved to be more critical than higher angles. A summary of the data obtained is given in Fig. 3-24. The results of base-pressure measurements corresponded quite closely with the data in Fig. 3-23. The critical distance is independent of windshield half-angles equal to or less than 20 deg. A geometrically similar model was extensively investigated by Whitfield in the 12-in. E-1 tunnel at AEDC's Gas Dynamic Facility. His results showed a strong dependence on Reynolds number in that the critical value of L/D increased as Reynolds number diminished at Mach numbers 3 and 4. He also showed measurable errors in

over-all axial force (less base pressure drag) when windshield interference existed with boattailed bodies.

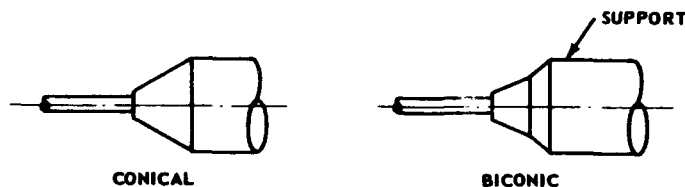
Bogdonoff (of Princeton) pointed out that sting interference is still a big problem at Mach numbers over 12 in helium where a sting length of 20 body diameters proved insufficient. He conjectured that 100 diameters might be required to assure measurements that are completely free of sting interference. The problem seems dependent on the presence of reflected shocks. Base-pressure measurements free of sting effects are very difficult if not impossible to measure. Because of the thick boundary layer on the sting, pressures creep forward and affect the base pressures and even cause separation forward on the model.

It is difficult to distinguish between laminar and turbulent boundary layers in helium at Mach numbers greater than ten. The boundary layer looks laminar at a Reynolds number per inch of 10×10^6 at Mach 15. Very close inspection shows the boundary layer to consist of a laminar sublayer of normal thickness covered by a very thin turbulent layer obeying a twelfth power law. Wake closure is another severe problem at these Mach numbers. Thin struts leave wakes which reduce the stagnation pressure by 100:1 and do not readily close.

It is obvious that such interference data cannot be considered entirely independent of the facility in which experiments are run; hence, it is necessary to run similar evaluations in each individual wind tunnel.

The windshield lip diameter must be larger than that of the sting in order that mechanical interference will not compromise the force measurements made in the external support. Figure 3-25 shows that $dC_N/d\alpha$ and dC_m/dC_N are functions of the windshield distance behind the model base when the windshield lip diameter becomes larger than the model base diameter. These data were obtained at Mach 2.00 in the OAL tunnel. The effect of windshield clearance on the slopes of the normal force, pitching moment, and stability curves and axial force at Mach 1.73 in the same wind tunnel is shown in Fig. 3-26. Here again it appears that an L/D of 1.5 or greater is sufficient for a finned, boattailed model when the windshield lip diameter is less than the model base diameter.

The use of small-diameter sting supports will minimize the windshield interference effects when the windshield distance from the base must be smaller than 4.0 model-body diameters. This allows conical windshields of smaller cone angles to be used. Although simple conical windshields are most commonly used, biconic windshields can sometimes minimize windshield interference when large diameter supports are used.



Interestingly enough, sometimes an ogival-shaped windshield provides less interference than conical windshields do at the low supersonic Mach numbers (1.25 or thereabouts), even though the leading-edge angle of the former is considerably greater than the equivalent length cone (see Subsec. 2.5.1).

Another phenomena occasionally encountered in supersonic wind-tunnel testing is "windshield buzz." This is nothing more than the oscillatory swallowing and regurgitating of the shock that is frequently encountered in inlet diffusers for engines when the mass flow is restricted past the point of maximum pressure recovery and an unstable shock pattern exists. In the case of the windshield that is screening the external drag balance, it is readily understood that an oscillating pressure within the support would effectively prevent this tare evaluation, making the axial force measurement worthless. If the amplitude and frequency of the buzz combine in an undesirable manner, it is probable that the voltage output from the drag-measuring strain-gage bridge will be prohibitively oscillatory and could reach such an extreme as to cause the strain gages to fail due to fatigue. Windshield buzz can be easily overcome by changing the inlet geometry, i.e., providing a larger or smaller inlet diameter, thus moving away from the critical buzz condition.

Still another phenomena that is unpredictable and infrequently encountered, but which is serious when it does, is high-amplitude model vibration. Occasionally, the combination of a particular model, internal balance, external support, and wind tunnel may result in a particular mass-moment of inertia and natural frequency that will amplify an excitation due to buffeting (unsteady flow from forward surfaces striking aft surfaces) or tunnel vibration at the same or a harmonic frequency of the system's natural frequency. Sometimes this may be encountered at a unique model orientation with an airstream. At higher or lower angles of attack, for instance, it may disappear entirely. However, when such a vibration is encountered, it must be stopped immediately, or the model may be destroyed. The condition may be halted either by changing the model's angle of attack or roll orientation, or by shutting down the wind tunnel. In practice, susceptibility to such vibration can most simply be avoided by changing the system's mass moment of inertia (e.g., by replacing the nose of a steel model with an identical nose made of aluminum). A change in mass at the extreme forward end of the model is most effective because its moment arm to the tunnel support attachment is the greatest.

Measuring the axial force internal to the model eliminates to a large extent many of the aerodynamic interferences mentioned above, but at the same time it introduces many other forms of interference. Most balance configurations involve an asymmetric geometry that is susceptible to relatively large and frequently nonlinear interactions of normal and side force on the axial force measurement. The interaction from a normal force differs from that obtained with a side force. This is especially undesirable in a system where the model and internal balance can be remotely rolled about its longitudinal axis while the tunnel is operating, since interaction calibrations must be made beforehand for every balance orientation that is to be used in the test. Further complications are encountered in the data reduction, especially when high-speed digital calculators are used.

The use of internal drag balances is most practical in large wind tunnels with reasonably low dynamic pressure. In this case the models are generally large enough for one six-component balance to be

used for a great number of models. The small models used in small wind tunnels, especially those with high dynamic operating pressures, usually necessitate a re-design of the internal balance to fit each particular model, assuming that the balance can be miniaturized satisfactorily. This is not economical because adding the capability of measuring axial force more than doubles the cost of building a conventional five-component balance. (It is usually desirable to provide a standby duplicate balance in order to diminish the possibility that a test program, which is confined to a rigid time schedule, will be aborted.)

Another disadvantage of the internal drag balance is that it must be isolated from any airflow through or around the balance such as might be encountered in a model of a ramjet-propelled missile with a nose inlet. Admittedly, the task of evaluating the drag due to internal flow through the model is difficult when the axial force is being measured externally, but it is well-nigh impossible on an internal balance.

Exposed Length of Internal Balance.--When both the balance diameter and the exposed length are large, measurable air loads will be experienced on the exposed part of the balance at very high angles of attack (see Fig. 3-27). If strain gages are used on the balance aft of this region, their reading will be influenced by these loads. Therefore, strain gages mounted on the balance for measuring forces and moment (with the exception of rolling moment and axial force) should be located within the model cavity whenever possible.

3.2.8 Calibration of Strain-Gage Balances

Any device that is to be used for measurement must be calibrated so that the output can be converted to conventional units of measurement. Of all the phases that a balance goes through in the process of preparation for tunnel use, the calibration phase is probably the most important, for the wind-tunnel force data obtained are seldom, if ever, better than the calibration. Since calibration techniques vary widely from facility to facility, the method outlined below may have many modifications.

In contrast with large balances external to the wind tunnel, internal balances are rarely entirely free of interactions of one component of load on the measurement of other components. In the design of strain-gage balances, emphasis should be placed on eliminating sources of non-repeatable or indeterminate errors. As a result of this policy and the space limitations usually encountered, internal balances will sometimes have what appears to be a large number of interactions. However, these interactions can be determined and are repeatable, so that the balance data can be corrected with acceptable accuracy. The major purpose of the procedure covered here is to determine these interactions. The procedure also serves other important purposes:

1. To proof-load the balance
2. To check the gaging and wiring
3. To determine hysteresis and repeatability
4. To determine component sensitivity

5. To determine deflections under load
6. To determine accuracy.

Improper or incomplete procedures at this time can very easily nullify most of the benefits gained from careful design and meticulous workmanship in the balance fabrication. For this reason the importance of proper testing in this phase cannot be overemphasized (Ref. 129). It is important that the balance be calibrated over the entire anticipated load and center-of-pressure ranges and that sufficient points be taken to assure an accurate and repeatable calibration. (It is suggested that the data obtained be reduced by the least squares method, preferably on a digital calculator.)

3.2.8.1 Basic Loading Systems

In order to load a balance accurately it is first necessary to construct a fixture which simulates the model to be tested and which will transmit loads to the balance in the same manner as the model will transmit the loads in tunnel testing. It should be attached as the model will be attached and should have reference surfaces which will remain fixed with respect to the balance reference surface as the balance is being loaded. To achieve this it is convenient (and necessary) to have an accurately machined surface or surfaces on the balance, close to its mounting surface, which can be used as a reference for both the calibration fixture and the model.

Figure 3-28 shows a typical fixture used in calibrating internal sting-supported balances. It is an accurately machined box with precisely located V-shaped grooves in which the loads are applied during evaluation. It is important that both the calibration fixture and the model be aligned with the balance in exactly the same manner. All fixtures are made as light and as stiff as possible.

Loads applied to the balance components are considered to be absolute loads. Therefore, the weight of the calibration fixture and even parts of the balance must be considered as applied load. It is sometimes necessary to consider the angular shifting of the weight vector with respect to balance measuring sections as the system deflects under load.

The attitude adjustments shown in Fig. 3-29 are used to set the original attitude of the calibration fixtures.

In addition to the loading systems mentioned below, several research organizations are now working on systems which more or less automatically load the balances. If they work as expected, they will make all the necessary loadings in less than four days as compared with the four weeks required with existing systems.

The type of basic loading system, either the dead weight or the jack and load-measuring cell, determines the actual shape of the fixture.

Dead-Weight Loading System.--When the dead-weight system is employed, the weights are applied in the form of cast-iron disks (accurate to 0.1%) hanging on a weight pan supported on a double set of knife edges as shown in Fig. 3-29. The weight also may consist of

lead shot in a bucket (Fig. 3-30), which in turn is supported on an accurate strain-gage load-measuring cell hanging on a pair of knife edges. The latter is used for loads of 500 to 3000 lb. Figure 3-31 shows bucket details.

In one variation of the dead-weight system, moments are applied by moving small weights to the end of long, accurately located arms mounted on the balance fixture as shown in Fig. 3-32. With this technique it is possible to maintain a constant force while varying the moment, which simplifies the data-reduction process. In addition, it also reduces the amount of weight to be handled.

It is usually necessary to apply forces normal to a calibration-fixture surface. In order to make this possible, an attitude-adjusting system as shown in Fig. 3-29 is provided. The position is maintained through the use of precision levels to within 15 sec of level position.

Jack and Load-Cell Loading System.--In the second type of loading system, shown in Fig. 3-33, the loads are applied by means of a hydraulic jack in series with a load-measuring cell of 0.1% accuracy, two pairs of knife edges, and a push rod. This system is used only when dead-weight systems become impractical from the standpoint of handling the weights, because of space limitations, or for safety reasons. With this technique, leveling is impractical. As a result, the push rod must be kept normal to the reference surface of the calibration fixture by accurate clinometer readings and a roller box as shown in Fig. 3-34. The roller box minimizes the possibility of applying undesired side loads.

3.2.8.2 Readout System

The readout system used during calibration should be either the exact system intended for use in the tunnel or its electrical equivalent. This statement is particularly true if the balance being evaluated has comparatively high stresses under the gages of one component due to the loading of other components (interactive stresses).

To measure the effect of load "A" in the presence of load "B", illustrated in Fig. 3-35, the strain gages are wired as shown in (b) of the figure. It will also be seen that load "B" causes an equal compressive (or tensile) stress in all the gages, which should result in no bridge output, provided that the gage factor of each gage is the same. Usually a circuit similar to Fig. 3-35(c) is used for the purpose of zero adjustment. When a null-balance load-indicating system is used, the circuit shown in Fig. 3-35(d) is typical. It can be seen that unless special care is taken in choosing the external circuits the effective relative gage factor of each arm is no longer the same, and an interaction of component B on component A results. Similarly, it can be shown that even though the same readout system is used during the balance evaluation period it is possible for the position of the zero-adjusting potentiometer to affect data collected during tests unless special precautions are taken.

3.2.8.3 Loading Process

The purpose of the procedure for determining load interactions on a six-component balance is to furnish data from which equations may be derived to represent the response of the balance to loads

likely to be encountered in tunnel testing. That is,

$$\text{Normal Force} = \frac{\text{normal-force reading}}{\text{sensitivity constant}}$$

$$- (K_1 \times \text{side force} - K_2 \times \text{pitch} \times \text{yaw} + \dots) \quad (3-41)$$

Investigators (at the Langley Laboratory) have not encountered any terms for these equations which are higher than the second order, although many load combinations have been made which would reveal many third-order terms if they were present.

The 26 first-order and second-order interaction terms possible per component in any six-component balance, plus the one sensitivity term, are tabulated below.

Linear (First Order)	Nonlinear (Second Order)
N	N ²
A	A ² NA
C	C ² NC AC
m	m ² Nm Am Cm
n	n ² Nn An Cn mn
l	l ² Nl Al Cl ml nl

For the sake of discussion, the interaction terms are classified as either linear or nonlinear. The linear terms result from such things as construction errors, improperly positioned gages, variation in gage factor, and, as brought out earlier, electrical circuits. The nonlinear terms are attributed to deflections.

Table 3-2 lists the loadings made and the terms revealed by those loadings when a balance with a system like that in Fig. 3-32 is evaluated. The forces applied at the end of the long arms are approximately one-tenth of the design force in that direction.

It will be noted that the loads are classed as primary and secondary loads. The primary load is one which is changed incrementally and which loads only one component on the balance. Only one primary load is used for any one load combination. The magnitude, position, and alignment of this load must be accurately known in order that the effect of the incremental changes on the balance may be accurately determined. The secondary load is one which remains constant during the period the primary load is being changed. It may load one or more balance components at a time with one or more loads, the magnitude, position, and alignment of which need not be known as accurately as those of the primary load but which must be maintained constant. For this reason the use of pulleys in making these loadings is acceptable. Pulley loads are properly aligned with the reference surface of the

calibration fixture by means of optical devices and squares.

As mentioned earlier, the loadings to determine the effects of force are each made at the moment center ($x = y = z = 0$).

The loadings to determine the effects of the moments are each made by applying the required small force at the moment center before zeroing the indicators and then transferring this load in increments to the end of the proper loading arm. This procedure results in a variation of moment only, the small force remaining constant throughout the loading.

The outputs of the various components are plotted as functions of the component which is varied in each case. The result is in a pattern of curves similar to that shown in Fig. 3-36. These plots are usually made as soon as possible to serve as a quick check on balance characteristics. The smoothness of the curves, repeatability of points, discontinuities, etc., are all indications of the balance qualities. From this evaluation it is usually possible to decide whether or not certain components of the balance are acceptable, whether certain loadings should be repeated because of unexplainable data, or even whether certain gages should be replaced because of poor bond or re-located because of bad interactions.

With some experience, it is also possible to check the plotted data and roughly approximate the interactions present. Then, it should be possible through analysis to determine the sources of the interaction terms which are present. After this is done, it can be decided whether a reasonable balance alteration will decrease the interaction and whether the alteration is worthwhile.

3.2.8.4 Derivation of Interaction Equations

To illustrate the manner in which balance interactions are reduced to equation form, it is assumed that only pitching moment, m , and normal force, N , have interactions on the component in question (plotted in Fig. 3-36). The addition of other components merely increases the number of possible interaction terms and the operations required to determine them. The terms and operations illustrated below are typical.

The meter deflection, θ , of the component in question in terms of N and m can be described by the following equation:

$$\theta = K_1' N + K_2' m + K_3' N^2 + K_4' m^2 + K_5' Nm \quad (3-42)$$

By substituting the values of the end points as determined from the curves (having due regard for sign) into the simple equation below, values of the individual constants of the general equation may be obtained.

$$\theta_{\Delta N} = K_1' \Delta N = \frac{A - A_1}{2} \quad (3-43)$$

$$\theta_{\Delta m} = K'_2 \Delta m = \frac{(B_1 + B_2) - (B_3 + B_4)}{4} \quad (3-44)$$

$$\theta_{(\Delta N)^2} = K'_3 (\Delta N)^2 = \frac{A + A_1}{2} \quad (3-45)$$

$$\theta_{(\Delta m)^2} = K'_4 (\Delta m)^2 = \frac{(B_1 + B_2) + (B_3 + B_4)}{4} \quad (3-46)$$

$$\theta_{N\Delta m} = K'_5 N\Delta m = \frac{(C_1 - C_2) + (C_3 - C_4)}{4} \quad (3-47)$$

In this method the values of K'_2 and K'_4 are obtained from average values of B_1 and B_2 , and B_3 and B_4 . Values could have been derived from B_1 and B_3 , or B_2 and B_4 .

The symbols ΔN and Δm represent the total changes in those loads from the time the zero readings were taken to the end-point conditions. The symbols N and m represent the total magnitudes of the components present (including the weight of fixtures, levels, balance parts, etc.) which are supported by the component being interacted upon.

The interaction-equation constants (K'_1 , K'_2 , K'_3 , etc.) as just determined are all expressed in units of meter deflection per unit interactive load. In order to free this interaction equation from the particular readout system used during the calibration, the constants are each divided by the sensitivity constant of the component being interacted upon (expressed in meter deflection per unit load). The result is an interaction equation which yields a correction in units of apparent load on the component due to the "interactive" loading:

$$\text{Correction} = K_1 N + K_2 m + K_3 N^2 + K_4 m^2 + K_5 Nm \quad (3-48)$$

Extreme care must be exercised to make sure that the interaction terms are not derived to fit faulty data. There should be a feasible explanation for the existence of every interaction term, which would tie in directly with the sources of linear and nonlinear interactions as brought out earlier.

After the interaction terms have been derived, several six-component loadings are made with known forces at known locations. Using the derived equations, the forces and their positions are then calculated to check these equations.

A typical six-component wire strain-gage balance of 3/4-in. diameter (Fig. 3-37), used in testing external stores in an NACA supersonic wind tunnel, was designed to measure any combination of the following load ranges:

Normal Force, lb	0 to \pm 40
Axial Force, lb	0 to \pm 7
Side Force, lb	0 to \pm 20
Pitching Moment, in.-lb	0 to \pm 85
Yawing Moment, in.-lb	0 to \pm 60
Rolling Moment, in.-lb	0 to \pm 15

The interaction equations for the balance follow. (Note that the value listed after each interaction-equation term is the size of the term in per cent of full-scale output of the component being interacted on when the components in the term are equal to their design values. Also, the constants for the terms are in units of apparent load on the component due to interaction loading.)

$$\text{Normal Force} = \frac{\text{normal-force meter deflection}}{\text{normal-force sensitivity constant}} - \epsilon_N$$

where

	Value (%)
$\epsilon_N = 0.00348 \times m$	0.7
$-0.00105 \times Cl$	0.7
$-0.000137 \times nl$	0.3

$$\text{Axial Force} = \frac{\text{axial-force meter deflection}}{\text{axial-force sensitivity constant}} - \epsilon_A$$

where

	Value (%)
$\epsilon_A = 0.00367 \times N$	2.1
$-0.00141 \times m$	1.7
$+0.00375 \times l$	0.8
$-0.00213 \times n$	1.8
$+0.00328 \times C$	0.9
$+0.000334 \times NA$	1.3
$+0.00000991 \times n^2$	0.5
$-0.000152 \times nl$	1.9
$-0.000257 \times C^2$	1.4
$+0.000156 \times Cl$	0.6
$+0.00000696 \times m^2$	0.7

$$\text{Pitching Moment} = \frac{\text{pitching-moment meter deflection}}{\text{pitching-moment sensitivity constant}} - \epsilon_m$$

where

	value (%)
$\epsilon_m = 0.0224 \times N$	0.5
$+0.134 \times l$	1.2

$$\text{Rolling Moment} = \frac{\text{rolling-moment meter deflection}}{\text{rolling-moment sensitivity constant}} - \epsilon_l$$

where

	Value (%)
$\epsilon_l = -0.00146 \times m$	0.7
$-0.0000264 \times nm$	0.5

$$\text{Yawing Moment} = \frac{\text{yawing-moment meter deflection}}{\text{yawing-moment sensitivity constant}} - \epsilon_n$$

where

	Value (%)
$\epsilon_n = -0.0400 \times m$	5.5
$-0.0630 \times l$	1.5
$+0.0248 \times C$	0.8
$-0.000373 \times Nl$	0.4
$+0.000444 \times ml$	0.9

$$\text{Side Force} = \frac{\text{side-force meter deflection}}{\text{side-force sensitivity constant}} - \epsilon_C$$

where

	Value (%)
$\epsilon_C = 0.00448 \times N$	0.9
$-0.00284 \times m$	1.2
$+0.0145 \times n$	4.3
$+0.0131 \times l$	0.9
$+0.000507 \times Nl$	1.5
$+0.000437 \times ml$	2.8

Although all the interaction terms down through 0.3% are listed because they may be required for certain tests, it is frequently possible to eliminate many and sometimes all of the interaction terms because they may be negligible under the test conditions expected.

The interaction equations will differ for every balance, but they may be similar for similarly designed balances. At OAL it was found in general that the linear variations were:

$$\epsilon_N \text{ and } \epsilon_C \rightarrow 0$$

$$\epsilon_A = f(N, C, m, n)$$

$$\epsilon_l = f(N, C, m, n)$$

$$\epsilon_m = f(C, n)$$

$$\epsilon_n = f(N, m)$$

Figures 3-38, 3-39, and 3-40 show simplified calibration equipment used at OAL.

3.2.8.5 Sources of Interactions and Methods of Elimination

As an illustration of the sources of interactions, several terms listed in the preceding set of interaction equations will be discussed. The first term listed is a pitching-moment interaction on normal force which, if the pitching moment reaches its design value of 85 in.-lb, will amount to 0.7% of full-scale normal force. The balance design is such that there is an undesired stress under the normal-force gages which is proportional to the pitching moment. This particular interaction could be caused by:

1. Variations in the cross-sectional area of the normal-force beams in the vicinity of the normal-force gage grids.
2. Gage-factor variations in the normal-force gages.
3. Variations in gage placement.

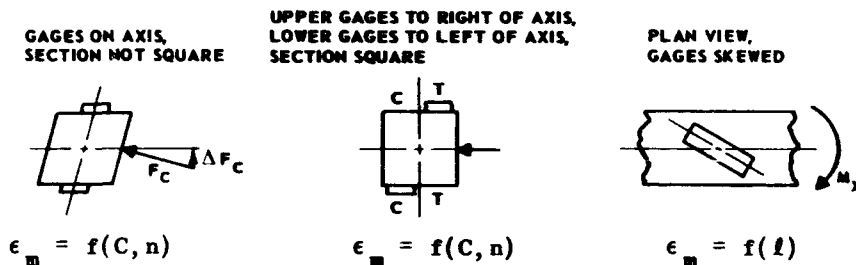
All three causes would result in the same varied responses of the normal-force gages to pitching moment, which more than likely would not cancel each other.

The side-force-times-rolling-moment interaction on normal force can be explained from a deflection standpoint. As a rolling moment is applied to the balance, the model rotates with respect to the axis of the balance normal-force section. If a side force is then applied to the model it will apply a force component to the normal-force beams. This interaction component is therefore proportional to side force and to the sine of the rotation angle or, since the angle is small, to the angle or rolling moment.

The normal-force-times-axial-force interaction on the axial-force component is an example of another type of nonlinear interaction. This can best be illustrated by Fig. 3-41. The axial-force section deflects as shown when an axial load is applied. If a normal force is applied at the same time, it increases the flexure stress being measured by the axial-force gages and as a result has an interacting effect.

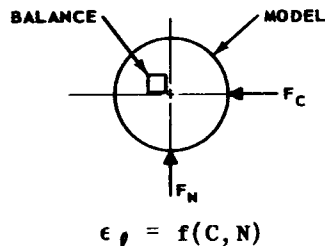
An example of interaction introduced by gage-location error is the side-force interaction on the yawing-moment component. The beams on which the yawing-moment gages are mounted bend in an S-shaped fashion when side force is applied. The effective grid centers of the yawing-moment gages were placed with extreme care at the point of inflection of that bending pattern. However, the tabulated interaction indicated that this point was missed by several thousandths of an inch. The fact that there was a 5.5% interaction of pitching moment on yawing moment indicates that the gages were probably also misplaced in the transverse direction.

If the cross section of the internal balance is not perfectly symmetrical or laterally displaced from the true longitudinal axis, a side load applied to the balance will result in an interaction on the pitching-moment gages. If the pitching-moment gages are skewed slightly with respect to the balance longitudinal axis, they will be sensitive to an applied rolling moment. However, reasonable care on gage alignment will usually make this interaction negligible.



Similar statements apply to the side force and yawing moment, since the principle of measurement is identical to that of normal force and pitching moment.

The major source of rolling moment interactions is derived when the electrical center of the bridge is not exactly at the model centerline. From the sketch below, it is apparent that either or both N and C will result in an output from the rolling-moment bridge, except in the singular case when the resultant force passes through the model and balance axes.



It is obvious that the longitudinal location, as well as magnitude, of N and C would affect the rolling moment if the balance and model axes were skewed with respect to each other. Hence,

$$\epsilon_l = f(N, C, m, n)$$

It is important to note that the model (instead of a calibration bar) should be used for an accurate rolling-moment interaction calibration, because the relationship between the model and balance axes may differ from that between the calibration bar and balance axis. Further, if such interactions do exist, it is essential that model and balance

orientation in roll be accurately re-established if they are separated prior to the test. Otherwise, the interaction calibration will be worthless.

If the rolling moment is measured external to the model, as shown in Fig. 3-18, it is essential that the balance shaft be perfectly straight. If the shaft is out of line by only a few thousandths of an inch, the rolling-moment error will increase rapidly with angle of attack. Rolling-moment data taken at two roll orientations can easily establish, by simple trigonometric relations, which way and by how much the shaft is bent.

It is possible to decrease or even to eliminate many of the linear interactions by one or more of the following approaches:

1. Re-machining
2. Changing some of the gages
3. Altering effective gage factors with series and shunt resistors
4. Taking a fraction of the output of one interacting component and adding it to the output of the component being interacted with, in such a fashion as to cancel its effect. If this system is used and sequential readout is not permissible, an additional isolated signal is required from the interacting component.

Although these techniques are possible, they are usually not necessary, especially if automatic computers are used in the reduction of the wind-tunnel data.

It is obvious in the normal force expression, for example, that N includes components which have in themselves interactions from other components; the solution therefore will not be an exact one. This being the case, the order in which the components are corrected will have an effect on the accuracy obtained and also may determine whether or not iteration is required to obtain the desired accuracy.

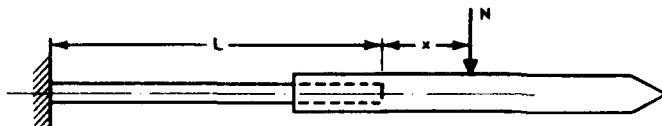
The loads applied to a balance during the evaluation process are absolute loads and include the weights of the various fixtures involved in the loading. Since the interaction terms are based on absolute loads, it is necessary that this fact be considered when the balance is used for force measurements in the wind tunnel. Particular caution should be exercised if nonlinear interaction terms are large or if comparatively heavy models are to be tested on the balance. Under these conditions the initial loads on the balance caused by model weight must often be considered in reducing the data in order to make proper nonlinear interaction corrections.

3.2.8.6 Deflection Calibration (Ref. 130)

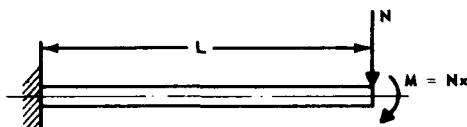
It is a simple matter, with a pre-test deflection calibration, to ascertain the incremental angle of attack or sideslip that is induced by air loads on the model when these loads are measured, as in the conventional force test. However, occasions will arise when the over-all loads on the model, and hence the deflection, will not be obtainable

in this fashion. Such a case is encountered when the model is instrumented to measure only the forces on the model surfaces when mounted on the body (commonly referred to as a hinge-moment test).

If it is assumed that the model itself does not bend, the angular deflection of the tangent to the centerline of the cantilever beam (or model support) at the free end (taper section) is equal to the angular deflection of the model centerline. To find the angular deflection, α , of the model, consider the sketch below:



The force, N , can be represented as shown below with no change in deflection.



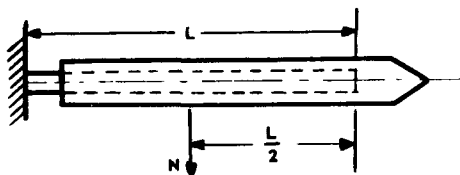
Then

$$\alpha = \frac{NL^2}{2EI} + \frac{ML}{EI} = \frac{NL^2 + 2NxL}{2EI} \quad (3-49)$$

The position at which the model should be placed so that there is no deflection will be given by

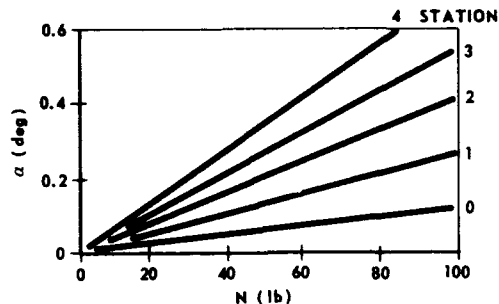
$$NL^2 + 2NxL = 0, \quad \text{or} \quad x = -\frac{L}{2} \quad (3-50)$$

That is, the center of pressure should be over the center of the support as shown in the next sketch.

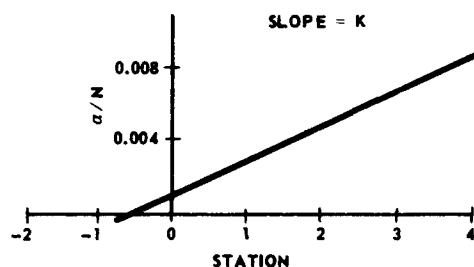


Since any loading condition may be represented by a force and a moment about Station $L/2$, the above expression shows that the deflection is a function only of the moment at that station. In actual practice this positioning of the model on the beam is achieved by calibration rather than by calculation.

The usual practice in calibrating deflection of a complete model-balance system is to hang the normal-force loads, N , on the model at different stations and to measure the angle, α , through which the model deflects. This deflection angle is measured on the model so that deflection of the complete system, including the mounting arc, is taken into account. Angles of deflection are then plotted against normal force as shown below.



Slopes of the above curves are then plotted against station or distance. This results in one linear curve which defines the model deflection in terms of normal force, N , as shown below.



If a strain-gage bridge is mounted at the location where $\alpha/N = 0$, then the angular deflection is a unique function of the moment at that station ($\alpha = KM$), and the constant K is determined from the calibration. This calibration must be carried out in both the pitch and yaw planes of the model.

A situation could arise wherein it is not possible to mount a strain gage at the unique station on the member. In this case it might be noted that an error in angular deflection of small magnitude may be acceptable if the strain gage is mounted as near as possible to the desired point. In one typical example (Ref. 130), an error of 0.03 deg at 100-lb normal load resulted when the gage was mounted 1.0 in. from the desired point.

3.2.8.7 Roll Orientation Calibration

Experience has shown that large residual side forces and yawing moments may be caused by relatively small errors in the model's surface alignment or roll attitude. An error of less than 1 deg in roll setting gives residuals much greater than the normal statistical expectation.

Data may be corrected for some misalignments if the amount is known accurately, but the best approach is to reduce the number of possible misalignments, if mechanically practical.

Misalignments may occur in many ways. The entire balance system can be misaligned in yaw, the model can be set at an angle on the internal balance, or the individual aerodynamic surfaces of the model can be set incorrectly due to an error in the incidence-setting device. Eccentricity of the internal balance, which is seldom checked unless rolling-moment data looks peculiar, can cause residuals. These errors may be caused by 1) misalignment of the model in roll on the internal balance, 2) an incorrectly "zeroed" internal balance, or 3) an inexact roll-attitude setting. Calibration errors in gage factors, distances, or interactions can create indications of residual forces and moments, depending upon the magnitude of the errors.

For automatic roll-indexing supports (Subsec. 3.5), the accuracy with which models are positioned in roll is dependent on the following factors:

1. Repeatability of the automatic roll-indexing system
2. "Slop" between the roll slide-wire and the shaft which supports the internal balance
3. Deflection of roll-links in roll and drag supports.

These factors are discussed and evaluated below.

Repeatability of Roll-Indexing System.--The roll-indexing system considered herein consists of a conventional single-turn, potentiometer slide-wire in the support, a variable multi-turn potentiometer with a 1000-count dial, a unit which senses an electrical unbalance between the balance slide-wire and the potentiometer, and a galvanometer that registers such an unbalance.

The first step in making a roll-index calibration is to adjust the system to an electrical balance with the support shaft at zero-roll attitude ($\phi = 0$) and the variable potentiometer at a predetermined value. The next step is to adjust the potentiometer to obtain an electrical balance at each roll angle, and then to record the potentiometer dial reading at each roll angle.

The potentiometer dial settings used to position models during tests are values obtained by averaging dial readings from two or more calibrations. The maximum deviation of individual calibration dial readings from average values used during tests are tabulated below for several typical remote roll supports used at OAL.

Support Designation	-19A	-20	-21	-23	-24	-33	-38
Number of Calibrations	5	9	5	10	14	2	2
Maximum Deviation (deg)	0.64	0.72	0.51	0.93	0.60	0.32	0.27
Average Max Deviation (deg)	0.32	0.36	0.23	0.50	0.30	0.13	0.03

The first four supports have small-diameter slide wires whereas the -24 and -38 supports have a much larger diameter slide wire of

the same type. Each of the slide-wires has a resolution of approximately 3.0 counts/deg rotation.

It is believed that the average maximum deviation is a good estimate of the probable errors in the automatic roll-indexing system. However, since the maximum deviation is expected to increase as the number of calibrations increase or as the amount of use increases (due to slide-wire wear, etc.), the data for supports having the greater number of calibrations should be more indicative of the operational magnitude of probable errors in the system. On this basis, probable errors in this particular automatic roll-indexing system are believed to be about ± 0.3 to ± 0.5 deg for small diameter supports, and ± 0.1 to ± 0.3 deg for the larger diameter supports. (The -24 and -38 have the same diameter slide wires, but the -24 had seen considerably more actual service than the -38 at the time of these investigations.)

"Slop" Between Roll Slide-Wire and Shaft.--The only place in the roll and drag measuring supports where slop exists and can contribute to roll indexing inaccuracy is at the connection of the bearing end of the roll link to the forward balance shaft. A minimum clearance should be allowed between the outer bearing race and the yoke attached to the forward balance shaft. In the OAL supports the clearance is 0.002 in., and the slop within the roll-link bearing is approximately the same. The total slop creates an error in roll of approximately 0.17 deg. The slide wires should be at the forward end of the supports, between the model and the roll drive linkages. It is virtually impossible to reduce the error due to slop and still allow the shaft sufficient axial freedom to prevent degradation of the drag measurements.

Deflection of Roll Links.--The deflection of the rolling-moment measuring link is dependent upon the load capacity or size of the link. A deflection calibration should be made with applied rolling moment as the variable. The calibration may be accomplished by electrically balancing the automatic roll-indexing system with an inclinometer attached to the forward end of the balance shaft. The system should then be zeroed with an applied rolling moment equal to the design load limit of the beam. The rolling moment should be reduced in suitable increments, and after each change the balance should be driven until the automatic roll-indexing system indicates that the slide wire has returned to the initial position. The angular deflection of the forward balance shaft with respect to the slide wire is then measured by means of an inclinometer. Some scatter in roll-attitude measurements (~ 0.25 deg) is to be expected since it is not possible to position the slide wire with absolute precision.

The roll-attitude resolution of the system may be improved by replacing the single-turn slide wire with high-precision synchros (Norden Ketay synchros are reported to have resolution accuracies of 3 min of arc). A multi-turn potentiometer would also improve the resolution of the system (see Subsec. 3.9). However, the size of such a unit does not lend itself readily to installation in roll-indexing supports of this size.

3.3 External Balances

An arbitrary distinction (Ref. 131) is made between external balances, which are fixed with respect to the ground, and internal balances, which are not. The external balance, having ample space, resolves its forces and moments into individual components at a fixed

point. However, there are numerous sources of relative motion between this fixed point and the model which must be accounted for in correcting the data. By reducing the size, the internal balance may be arranged so that it rotates with, and is directly attached to, the model. Therefore, the relative motion between the model and balance can usually be neglected. However, the internal balance is usually unable to resolve directly all the forces and moments to individual components. The individual components must be computed by means of a set of simultaneous linear equations, which include the various interactions between gages. The number of components which can be resolved is equal to the number of independent bridges, regardless of their arrangement in the balance. However, the usual design has no more than two important components on any one bridge. The same basic equations can be used for all balance data reductions for either type of balance; but certain steps can be omitted, depending on whether the balance is internal or external. In an internal strain-gage balance, deflections are often neglected, while interactions are not; in an external balance, interactions are neglected, but deflections are not. There are occasional exceptions to the foregoing assumptions.

3.3.1 Six-Component Hydraulic Balance

A cutaway drawing and a photograph of a six-component external hydraulic balance system (designed by Sandberg and Serrell, Pasadena, Calif.) for a 20-in. supersonic wind tunnel is shown in Figs. 3-42 and 3-43. The total system consists of two major parts: 1) The model suspension system (built by Taller and Cooper, Brooklyn, N.Y.), and 2) the balance system (built by Boller and Chivins, Pasadena, Calif.).

The model's suspension system assembly is mounted on top of the balance moment table, with the center of rotation of the crescent-shaped sector on the tunnel centerline. In order to eliminate air loads on the suspension system, the entire assembly is protected by a windshield extending to the model base. The total pitch-angle range of the crescent is mechanically limited to 29 deg. Aerodynamic forces on the model are transmitted through the suspension system to the force and moment tables.

The balance system is basically a two-table assembly consisting of a moment table and a force table. Pitching, rolling, and yawing moments are separated at the moment table, and the lift, drag, and side forces at the force table. The point about which the moments are measured is the focal point of the pyramidal flexure arrangement and is coincident with the center of rotation of the model suspension system.

Each force and moment component is converted to a hydraulic pressure by a force-sensing element called a load cell. The output of the load cell is piped to a weighing beam, where a servo-driven poise weight balances the hydraulic pressure, and the position of the poise weight is subsequently digitized as the final output. A schematic diagram of the hydraulic system is shown in Fig. 3-44. The six weighing beams are shown in Fig. 3-45.

The operation of the external balance involves testing techniques and special requirements which are usually unnecessary for six-component, internal strain-gage balance systems. For example, it is necessary to ensure that there is no air flow in or out of the annulus between the model sting mount and the windshield leading edge during a

run. The technique used at present to prevent this annulus flow is to adjust the pressure inside the windshield or balance tank so that it is equal to the model base pressure. A large vacuum pump attached to the balance tank is used for this purpose. Since the base pressure may vary with the model attitude, an operator must monitor and control the windshield pressure.

In order to minimize the aerodynamic interference effects of the model support system, the sting and windshield should be made as small as possible. The clearance annulus between the windshield and sting is often as small as $1/32$ in., which means that the sting-windshield tracking servo system must be maintained in the best possible operating condition. Experience indicates that the balance can be damaged as a result of mechanical interference between the windshield and sting. Therefore, it may be necessary to provide a safety system to protect the balance against fouling.

It is wise to recalibrate the balance once a year. The time required for calibration is relatively long because extreme care must be exercised in order to give the required accuracy. The precision required in the rigging of the loading wires, for example, is determined by the capability of the balance to establish with accuracy the point of application of the load. In the JPL balance it was necessary to determine the point of application to within 0.02 in. for a load of 20 lb.

One of the persistent problems associated with the balance involves the model. Each contractor must design and fabricate his model so that it can be mounted successfully on the balance suspension system without access to the actual balance prior to test. During a typical pre-test setup week, the model is fitted to a mockup which represents the actual balance sting and windshield mounts. At this time, bench calibrations are made to determine the sting deflection constants and the physical relationship between the model and the sting centerline for the data reduction procedure.

3.3.1.1 Advantages of the External Balance

As a measuring instrument the external balance offers three major advantages. The first of these advantages is a capability for measuring relatively large forces and moments to an exceptionally high degree of accuracy. Its pitching-moment component, for example, can determine the center of pressure for a body-alone model with $L/D = 10$ within one-tenth of a caliber. One of its best characteristics, however, is its capability to obtain an adequate measure of the small axial force simultaneously with a highly accurate measure of large lift and drag forces. This capability helps to solve the problem of obtaining accurate minimum drag (axial) forces with a balance designed to measure much larger loads. Measurement of the axial force is one of the major problems of wind-tunnel testing, since the error in the axial force is often of the same magnitude as the force itself. An external balance having a repeatability of 0.2% is adequate for most purposes. Comparison of free-flight and wind-tunnel drag data for several missiles reveals that both sets of data have about the same scatter. When wind-tunnel results are corrected for base pressure and boundary-layer transition, they agree with the free-flight data to within $\pm 5\%$. (Methods of determining the position of boundary-layer transition are treated in Subsec. 6.4.

The rolling-moment sensitivity or accuracy of the balance in general is sufficient for airplane models. However, the balance is not accurate enough to measure the small induced rolling moment of a typical missile model. This inaccuracy can be attributed to interaction effects, which may be obviated by placing a separate roll balance in the model sting.

The second major advantage of the external balance is that the model may be mounted at any desired location with respect to the moment center of the balance. The full-scale center of gravity of the model is usually made coincident with the moment center of the balance in order to eliminate the errors incurred in transferring moments. This is particularly advantageous for very thin configurations such as delta wings, within which it would be impossible to store a strain-gage balance system. Other models in this category are very short, odd-shaped bodies or extremely thin models such as a missile-plus-booster configuration. It should also be noted that the basic configuration models or "build-up" study models used with the external balance may be manufactured quickly and inexpensively as discussed further in Subsec. 8.3.1.

The last and perhaps the greatest advantage of the external balance is that the space inside a typical airplane or missile model remains available for other purposes. The number of pressure orifices that can be accommodated is limited only by the number of leads that the internal diameter of the sting support will carry. Models often carry such components as a remote-control drive and position indicator, which make it possible to measure control-surface effectiveness directly by varying the control-surface angle during the run. The aerodynamic forces and moments applied to control and lifting surfaces are often measured internally. One may thus obtain such additional component data simultaneously with the external balance data.

3.3.1.2 Operational Performance, Range, and Accuracy of the External Balance

The operational performance presented below is that of the JPL balance system that has been in almost constant use for several years.

Load Ranges

Load	High Range	Low Range
Lift (lb)	300 to -200	30 to -20
Drag (lb)	300 to -200	30 to -20
Side Force (lb)	100 to -100	10 to -10
Pitching Moment (in.-lb)	2000 to -2000	200 to -200
Rolling Moment (in.-lb)	1000 to -1000	100 to -100
Yawing Moment (in.-lb)	1000 to -1000	100 to -100

**Bench Calibration Accuracy and Air-on*
Repeatability in any Run**

	High Range	Low Range
Force (lb)	± 0.1	± 0.02
Moment (in.-lb)	± 1.0	± 0.2
Accuracy (%)	0.1	0.2

*Exception: Pitching moment drifts approximately 1% of low range during first half-hour run after overnight shutdown.

**Air-on Accuracy Between Runs
(from 5 identical runs)**

	High Range	Low Range
Force (lb)	± 0.1	± 0.03
Moment (in.-lb)	± 1.0	± 0.3
Accuracy (%)	0.1	0.3

Interactions.--All linear and less than 1% of balance range on any component under full load conditions. Average of all interactions is 1/3%.

Deflections.--All linear and repeatable to 0.005 in.

3.3.2 Reflection-Plane Technique

"Reflection-plane" or "half-model" testing are terms applied to the general field of wind-tunnel testing that makes use of a model divided at its plane of symmetry. The half-model may be mounted on the tunnel sidewall or on a splitter plate. In the former the model is attached directly to the tunnel wall (with or without a boundary-layer spacer), while in the latter the model is attached to a splitter plate or reflection plane that is mounted at some distance from the tunnel wall in order to avoid the effects of the tunnel-wall boundary layer.

The splitter plate is merely a flat surface used in conjunction with a wall-mounted balance. It is usually mounted on a steel frame that is interchangeable with the test-section window (Fig. 3-46). The leading and trailing edges at the plate centerline are supported by a wedge-shaped island that is just wide enough to accommodate the model support shaft. The contours under the plate must be carefully established to avoid choking flow and a resultant detached shock wave ahead of the plate. This may be accomplished by filling the frame with lead and re-fairing the contours until satisfactory flow characteristics are attained.

The plate leading edge should be swept at an angle that assures a supersonic leading edge at the minimum Mach number and should

be beveled on the under-surface to a sharp leading edge. Experience shows that the flat surface of the plate should be ground to a tolerance of ± 0.001 in. before the leading-edge under-surface is beveled. Then, if the leading edge should curl due to residual stress relief, the sharpness can be restored by a final grinding cut. The plate should be fabricated of stainless steel to eliminate corrosion, and a protective metal cover should be provided to prevent scratches, nicks, and dents from marring the surface when the plate is not in actual use.

There are many advantages to the reflection-plane technique. In the first place it may be used to obviate the sting effect on pointed afterbodies. For transonic and supersonic testing, such models are sting mounted, requiring that the pointed afterbody be modified to receive the sting and the resultant data corrected in some manner to account for this modification. A half model may be tested without any aerodynamic modification. The conventional subsonic strut support in wings or fuselage is not acceptable for supersonic testing. High loads would demand large struts which would produce unwanted interference effects. Tests made at NAE (Ref. 132) with half-models and full-scale models of various sized bodies of revolution have shown that the frictional drag may be accurately determined by means of the reflection-plane technique. Fair agreement in normal-force and pitching-moment measurements at low angles of attack on half and on complete winged-cone-cylinder models was found at OAL for roll angles up to 45 deg.

Another advantage in this technique is that in general it allows the use of larger scale models. Full scale tests of a missile wing of 16-in. chord and span were successfully run in a 19×27.5 -in. test section at a Mach number of 2 and a dynamic pressure of 12 psi.

Investigations of hinge moments and control-surface effectiveness have used the reflection-plate technique to great advantage. The Jet Propulsion Laboratory has conducted a large number of tests using half models of missile configurations with boundary-layer spacers to determine control-surface effectiveness and hinge moments. Comparison of these results with sting-mounted, complete-model tests and flight-test data has been quite good and has shown that fore-shortening the body or varying the boundary-layer spacer thickness has little effect on the results. The balance used in these investigations was a four-component (no side force or yawing moment), orthogonal, strain-gage type with the roll axis about four inches from the model axis. The balance rotated in pitch with the model, and measured body-axis forces.

Half-model tests have also proved most useful in inlet studies.

One of the major problems in the use of reflection plates is that of the size of the gap between the half-model and the plate or the tunnel wall. The boundary-layer spacer effect for sidewall-mounted models has been checked (Ref. 133) at David Taylor Model Basin. It was found that, for spacers between 1 and 2 tunnel-wall boundary-layer displacement thicknesses, the pressure distribution over the model for moderate angles of attack agrees with those for a complete sting-mounted model to within $\pm 1\%$.

For high angle-of-attack testing, DTMB constructed a wall balance on which half-models on a circular face-plate are mounted. This faceplate is flush with the tunnel wall and is a part of the balance. Tare data are obtained by mounting the half-model adjacent to, but not touching, the balance faceplate. Results showed that the magnitude of the gap between the half-model and the faceplate did not affect the tare-data results. Measurements on the half-model indicated

that wall-balance half-model data agreed well with full-model sting-balance data when the shim between half-model and faceplate was two-ninths of the total boundary-layer thickness. This value agreed reasonably well with the NAE value (Ref. 132). The balance is described in detail in Ref. 134. British and French efforts in this field are given in Refs. 117 and 118.

3.3.2.1 Side-Wall Balance

Figure 3-47 shows a side-wall balance that is essentially a cantilever beam mounted in bearings and restrained from rotation (pitching for the model) by a strain-gage beam that measures the model pitching moment. The internal balance, with model attached, may be rotated about the beam axis by means of a worm gear drive to any predetermined angle of attack (up to $+90^\circ$) by use of a commercial machine index plate, which is shown in Fig. 3-48. The aft end of the model support spindle is standardized to fit the balance, and the front or model end may be designed to suit individual model requirements as shown in Figs. 3-49 and 3-50. This balance is particularly versatile since the main shaft is readily interchangeable with other shafts which are designed for the air loads anticipated on the model. Four strain-gage bridges mounted on the model spindle and one bridge mounted on the pitching moment cantilever beam give the aerodynamic forces and moments for the entire model configuration. The spindle or internal balance is usually made weaker in the axial force than the normal force direction to improve sensitivity in measuring axial force, which is usually a fraction of the normal force. The amount that the beam can be weakened is governed by deflection rather than load, because the axial force and resulting yawing moment of the model tends to make the base of the model bind against the reflection plate or tunnel wall when the clearance between model and reflection plane is as small as desired (see Subsec. 3.3.2).

3.3.2.2 Flexure-Pivot Wall Balance

The heavy-duty balance shown in Fig. 3-51 is designed on the flexure-pivot principle and used to measure components of lift, drag, pitching moment, yawing moment, and rolling moment in wind axes. It has been used with and without a boundary-layer or splitter plate. When used with the boundary-layer plate, the balance and the plate mount on an adapter that fits into one of the test-section windows. This requires that model changes be made through the opposite window. When models are mounted on the wall of the tunnel, it is possible to swing the support from the tunnel wall to expose the model.

The model is mounted on a spindle (Fig. 3-52), in the center of the support, which is rotated to vary the angle of attack of the model. A vernier protractor mounted on the end of the spindle registers the angle of attack. The spindle is supported by a series of prestressed links on which resistance strain gages are mounted.

The maximum forces to which the balance can be subjected are mainly a function of the net-load location and the stresses under the strain gages. The maximum allowable lift and drag loads for this balance are shown in Fig. 3-53. In order to assure repeatable results, it is advisable to limit the loads in order that the net-load location never travels more than 1.8 in. from the hinge line. The maximum design pitching moment is 1600 in.-lb and the lift load is 900 lb. If

several traverses of the angle-of-attack range are made and if the support is used within the limitations quoted, the scatter of the data will be in the order of ± 2 lb for drag, ± 5 lb for lift, and ± 10 in.-lb for pitching moment.

3.4 Hinge-Moment Balances

One of the most exacting requirements in wind-tunnel testing is that of obtaining hinge moments of variable-incidence surfaces in the interference flow field of other components of the total configuration. It is relatively simple to obtain wing panel loads and hinge moments of isolated surfaces to the desired accuracy on external balances such as those described in Subsec. 3.3.2. On the other hand the problem of measuring individual panel loads on a three-dimensional model such as that shown in Fig. 3-54 may be very difficult. Most of the difficulty stems from the fact that, in order to accommodate the total configuration in the average sized supersonic wind tunnel, the wing must be of much smaller scale than it is for a wing-alone test. In the first place the reduced size has inadequate space for the necessary control and measurement instrumentation. In the second place, the hinge moment varies as the cube of the scale factor. If the hinge moment of a full-scale surface is 100 in.-lb, that of a one-tenth scale model would be reduced to 0.1 in.-lb. The difficulty of making accurate hinge-moment measurements is also increased by the fact that the hinge line, in most practical cases, is placed as close to the center of pressure as is possible in order to minimize the absolute value of the hinge moment and thereby minimize the servo power requirements of the missile.

Figures 3-55 and 3-56 show a hinge-moment balance in which the pure torsional moment on the shaft from the wing is resisted by a cantilever beam and knife-edge support, and measured by strain gages mounted on the cantilever. Normal force may be calculated by dividing the difference of the hinge moments recorded at two hinge-line locations by the distance between the hinge lines. This not only involves running the model in two positions with respect to the shaft but requires a careful determination of the angle of inclination of the panel to the air flow. Correction must be made for the difference in deflection with the change in load. If the cantilever beam is fixed to the shaft, the incidence of the aerodynamic surface may be changed by varying the height of the knife-edge support. Some designs may restrict the use of this method for changing incidence, and it may be necessary to change the incidence by clamping the cantilever beam to the shaft after the incidence of the surface is set. One disadvantage, however, of this form of balance is that the shaft from the surface passes through oilite bronze bearings and is subjected to some frictional forces due to the bearings. Most of this friction could be eliminated if a ball bearing or needle bearing were used. However, in some cases the dimensional geometry of the model may prohibit the use of low-friction bearings.

Three-component panel loads (normal force, hinge moment, and bending moment about the root chord) can be measured by using the system shown in Figs. 3-57 and 3-58. The advantage of this system is that no frictional forces are present in the system and that normal force can be measured directly when a fully instrumented cantilever beam is used. The cantilever beam is mounted parallel to the geometric chord of the wing when it is at zero incidence and is so designed that incidence pins can be inserted to change the surface incidence. The

hinge moment is computed as a function of the normal force, the moment at the forward hinge-moment bridge, and the distance from the bridge to the hinge centerline. Gages mounted 45 deg to the centerline of the beam and at 90 deg to each other measure the torsional moment in the beam (panel bending moment). The panel bending moment about some spanwise reference point is computed as a function of the normal force, the torsional moment, and the distance from the centerline of the cantilever beam to the reference point, usually taken as the panel root chord.

The wing-alone model in the lower part of Fig. 3-57 was designed to measure three-component data on each of two wing panels that are identical to those in the upper photo. In this case, the wing was made integral with the instrumented beams. In order to prevent undesirable air loads on the beams, a windshield was provided. Severe buzzing observed at the windshield lip was eliminated by adding the vent holes shown. Some flow passed through the windshield, but a comparison of data showed reasonably good correlation with that taken from the integrated model with the body at zero angle of attack and the wing incidence varied.

Another example of this technique is shown in Fig. 3-59, where the extreme boattail angle did not permit insertion of the incidence pins in the retracted position. The thumb screw shown is used only to withdraw the instrumented beam from the model by rotating about the internal hinge mounted forward in the model. This screw is removed during test.

One undesirable feature of the cantilever beam arrangements shown in Figs. 3-57 and 3-59 is the inherent errors in measured hinge moment introduced by the fact that both strain-gage bridges must be located on the same side and at some distance from the hinge line about which the measurements are desired (see Subsec. 3.2.4). At an increase in model expense and required testing time, it is possible to circumvent this problem by making the surface and the instrumented beam out of a single piece as shown in Fig. 3-60. Separate components must be made for each unique incidence setting required; however, it is possible to locate the strain-gage bridges in such a manner as to straddle the hinge line. One other attribute of this particular technique is that the wing panel and instrumented beam are absolutely fixed in relation to each other. Once an accurate calibration is made, no errors can result from a change in the relative location of the two components. A similar technique is described in Ref. 117.

3.4.1 Sting-Mounted Hinge-Moment Models

In large wind tunnels, where larger models are used, it is quite feasible to obtain surface hinge moment and load data at the same time that the conventional six-component over-all force data are measured. However, in the intermediate and smaller wind tunnels this is usually not the case. The one exception in the latter case is the 20-in. JPL tunnel where the external six-component balance described in Subsec. 3.3.1 lends itself admirably to such combined measurements, since the model interior is available for hinge-moment instrumentation and, in some instances, for remote incidence changing devices.

In each of the hinge-moment models shown in Figs. 3-57, 3-59, and 3-60, the sting mount is an integral part of the model when the unit is assembled. The cantilever beams are mounted rigidly to the model or sting and are shielded from air loads by a body shell that

slips over them. Sufficient clearance is provided in the body shell around the wing hubs to prevent mechanical interference under load. Great care should be taken to minimize airflow through the aperture in the body shell so that spurious air loads on the instrumented beam are negligible and temperature gradient difficulties described in Subsec. 3.1.3 are avoided. Although such sting mounts are considerably more rigid than the conventional internal balance, some angular deflection in angle of attack is experienced due to the over-all air loads on the model, and the true angle of attack must be established in the manner described in Subsec. 3.2.8.6.

One unique design feature of the system shown in Fig. 3-60 is that the airflow was required through the model in sufficient quantity to prevent a normal shock from forming ahead of the nose-inlet diffuser. This was accomplished by splitting the flow just downstream of the inlet into four quadrants. The instrumented hinge-moment beams were embedded in the horizontal arms of the resulting plus-shaped section. Two dummy, or uninstrumented, wing panels were mounted in the vertical arm of the plus-shaped section.

3.4.2 Calibration of Hinge-Moment Balances

Figure 3-59 shows a typical hinge-moment calibration panel mounted on the model. The panel is used to determine all interactions, bending-moment and hinge-moment gage factors, and gage locations. The panel has holes drilled at precise distances for the purpose of locating the calibrating weights accurately. To simplify the calibration, it is important that these holes be drilled in rows that are absolutely parallel and perpendicular to the beam to be calibrated. If errors in rectilinearity do exist, the moments recorded must be corrected before the raw calibration data can be used. Necessary reference dimensions for locating gages with respect to the calibration panel must be recorded. The calibration procedure consists of hanging varying loads at consecutive stations. The weight hanger consists of a C-shaped piece of metal having a conical peg mounted on the under side of the upper leg. The cone is inserted into the holes of the calibration panel, one after the other, and the varying weights are hung from the lower leg of the hanger.

When the wing panel and the beam are made in a single piece, as shown in Fig. 3-60, the calibration holes are drilled in the wing panel itself and filled with duratite or some other filler material prior to testing.

In evaluating hinge-moment data from models of this type, it is important to note that the forces and moments measured are referenced to the body axes which are coincident with the wing-panel axes only at zero incidence. At incidences other than zero it is not possible to transfer the hinge moment to an arbitrary hinge line by use of the normal force alone since the axial force makes a contribution which is not measured. If one of the moment bridges is mounted directly on the desired moment reference line, the need for moment transfer is obviated and the source of error eliminated.

3.5 Special-Purpose Balances and Supports

The task of instrumenting and operating any specific wind tunnel to obtain force data for a diversity of models and parametric

variables demands a large array of specialized balances and supports. In estimating the loads (see Table 3-3) to which models are subjected, it is necessary to account for the temperature and pressure conditions under which the tests will be made. For a tunnel whose test section is shown in Fig. 3-61 a descriptive list of balances and supports is presented in Table 3-3 and Fig. 3-62. Some of these devices will be described briefly here.

3.5.1 Remote Roll-Indexing and Drag Supports

The remote roll-indexing supports may be instrumented internally to measure rolling moment and axial force as described in Subsecs. 3.2.5 and 3.2.6. When used in conjunction with a four-component internal balance, six-component data can be obtained. The ruggedness of the support may be increased by increasing the over-all diameter.

The case (Fig. 3-63) which supports the internal mechanism is made of two parts which are fastened and sealed together by a tapered joint. The forward end of the case supports the main shaft. Thompson ball bushings, used in the forepart of the support, allow free axial movement of the shaft. This motion is restrained by a strain-gage-equipped cantilever beam. Two ball bearings support each of the ball bushings, thereby providing the shaft with freedom to roll. The ball bushings may be replaced by individual balls retained in a perforated brass cage as described in Subsec. 3.2.5. The shaft is restrained in roll by an instrumented cantilever beam. This beam is resisted by a yoke mounted to the main shaft and transmits power from the driving mechanism to the main shaft to roll the model remotely.

Remote indexing is achieved by means of a series of shafts and gears that transmit power from a small 24-v motor to the main support beam. The resistance slide wire and wiper creates a variable resistor in the indicating circuit which is proportional to the roll-angle range of the support. A known resistance for a particular roll angle is set in an automatic electronic device (Fig. 3-64), housed in the control room, which feeds power to the motor and rotates the main shaft until the voltage drop in the indicating circuit is zero. The main shaft and model will then be at the desired roll angle, and the ammeter will give a visual confirmation of a null. The roll attitude range of the support is restricted to an included angle of 315 deg, but the model can be oriented with respect to the internal balance to give the desired initial roll attitude. The support case and wind-shield are sealed except for the opening for the internal balance, thus eliminating uncertain corrections for pressure differential along the support.

The case which supports the internal mechanism may be constructed of three sections, designed so that the internal mechanism is exposed when the forward section is removed, as shown in Fig. 3-65. A cutaway sketch is shown in Fig. 3-18 and its axial-force repeatability in Fig. 3-19. A manually operated brake may be added to make it possible to hold the main shaft in any position for model installation.

3.5.2 High Angle-of-Attack Devices

The angle of attack of a model may be limited by the loads which the model can withstand or which the balance can measure. It is more usual, however, for it to be limited by simple geometric considerations of the total length of the model and balance arm, and the height

of the test section. The available arc travel in the OAL balance section shown in Fig. 3-61 is physically limited to ± 14 -deg angle of attack. This balance has no provisions for varying the yaw or sideslip angle.

The E-10 extension shown in Fig. 3-66 is designed for use with a support system to test models through an angle of attack range at a constant angle of sideslip or yaw. The spud on the extension is mounted at an angle of 6 deg with the tunnel centerline and is offset in such a manner that the center of rotation of the model is normally on the tunnel centerline. When the extension and support system are rolled as a unit (zero angle of attack of the crossarm), the model will always lie in a plane canted 6 deg with respect to the tunnel axis. Angles of sideslip up to ± 6 deg may be obtained by various combinations of the roll angle of the support and extension, and the pitch angle of the model. Predetermined angles may be repeated accurately if matching holes in the extension and the crossarm are aligned with the aid of an indexing pin. Also, when the model is rolled 90 deg, the model can be tested through an angle-of-sideslip range at a constant indicated angle of attack. When the extension is used in the vertical plane of the tunnel, the available angle-of-attack range is -8 to $+18$ deg. The positive angle-of-attack range is limited by the fact that the extension strikes the floor of the tunnel before the angular limit of the crossarm is reached.

The 9-deg offset roll-indexing support shown in Fig. 3-67 is designed to provide remote roll indexing and to give an angle-of-attack range of -5 to $+23$ deg. The support case is made of two sections, aft and forward, connected by means of a slip joint and spanner nut. Two ball bearings mounted in the forward section support the main shaft which is remotely indexed in roll by a d-c motor system working through a universal joint and a gear train. A movable scale for roll attitude is scribed externally on the main shaft, thus enabling operating personnel to read the roll attitude of the model directly from the support. By removing the electrical cable and cannon plug used for force tests, this support can be easily modified to accommodate pressure-measuring equipment if only a small number of pressure leads are required.

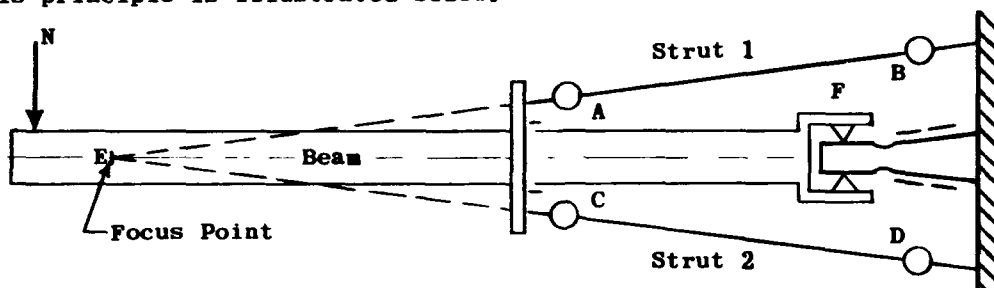
At low Mach numbers, where choking may be a problem, it may be necessary to sacrifice the remote roll-indexing device and to streamline the offset support. Such a design is shown in Fig. 3-68. The position of the model in roll is accomplished manually and held by means of index pins.

3.5.3 Combined Force and Pressure Balance

The usual technique for obtaining experimental aerodynamic characteristics of an aircraft powered by an air-breathing engine is to separate the external (force data on the over-all configuration) and internal (diffuser development) aerodynamics by running independent test programs. However, when the engine inlet is located in such a manner that mutual interference effects play a prominent part, it may be desirable to obtain both sets of data simultaneously on the same model.

A combined force and pressure balance was designed (Refs. 135 and 136) for a single-engine, ramjet missile. The balance proper consists of a focused, flexure-pivot, pyramidal six-component balance so designed that a duct is provided to capture the full mass-flow of the

model. The duct is provided with pressure-measuring orifices, and a remotely controlled throttle varies the mass flow through the duct during the test. The throttle is actuated by a gear train and electric motor. Since the internal flow characteristics are duplicated, it is necessary to measure all force components from a position aft of the model. Experience in force measurement has shown that all components except pitching and yawing moments can be measured with acceptable accuracy in a strain gage balance external to the model. Pitching and yawing moments, however, are subject to significant degradation in accuracy where a large moment transfer is required for conventional sting-type strain-gage balances. Hence, the focused-flexure principle, frequently used in subsonic wind tunnel external balances, was applied. This principle is illustrated below.



The struts, 1 and 2, are focused at Point E and include flexure pivots A, B, C, and D. The flexure pivots provide essentially frictionless ball and socket action. When a normal load is applied to the beam, it will tend to rotate with E as a center. If the beam supports a model whose center of gravity coincides with E, the pitching moment at E can be measured by the restraint required at F to maintain equilibrium. Yawing and rolling moments may be similarly measured by changing the location of the restraining beams and strain gages. A bench model of such a balance, shown in Fig. 3-69, was constructed and tested to establish the relation between the pitching moments, whose arms were mounted well aft of the model base and just aft of the model moment reference point. The experiment proved that the output of the aft-mounted bridge represented the moment applied about the flexure-focus point as anticipated. A similar application of the focused-flexure principle is given in Ref. 112.

3.5.4 Micro-Balance

The measurement of lift and drag forces, of about 100 mg, acting upon a model mounted in a supersonic, low-density free jet has been achieved through the use of a sensitive micro-balance (Ref. 137). This unit may be described as a beam-type, crossed flexure balance.

In operation, the balance is used as a null-type instrument with the null position indicated by a linear variable differential transformer. The force required to maintain the model at its null position is applied by means of a quartz spring, whose extension is controlled by a micrometer screw and travelling nut. Measurement of the spring extension, together with a knowledge of the spring characteristics and the model sting and balance arm distances, permits measurement of the force acting on the model. The micro-balance repeatability has been recorded as ± 0.02 mg, using a quartz spring constant of 1 mg/mm.

3.5.5 Skin-Friction Balance

The floating-surface, skin-friction instrument described in Ref. 43 is similar in principle to the floating-element mechanism of Liepmann and Dhawan. The most important difference, aside from size and range, is the use of the null technique in measuring applied forces.

The basic components of the instrument are shown in Fig. 3-70. The inner flexure system, consisting of the table, two flexlinks, and the ring, allows a deflection of the floating element under an applied load. The deflection is measured indirectly, i.e., in terms of the displacement which must be given to the table in order to return the element to a standard null position with respect to the surrounding structure. Motion of the upper table is effected by means of a precision micrometer, acting through a piano wire push rod clamped at both ends, and is constrained by the second or outer flexure system shown.

The null position of the floating element is detected by a Schaevitz variable reluctance transformer (Fig. 3-71) whose coil is fixed on the instrument structure and whose core is attached to the element ring, so that no physical contact between the gage and element is present to interfere with measurement of the small forces involved. Two dashpots provided for damping in the inner flexure system are constructed with sufficiently small clearances so that capillary attraction prevents loss of fluid when the instrument is turned upside down.

The skin-friction instrument, including the flexure systems, damping device, and Schaevitz gage, is assembled on a stainless-steel disc 4 in. in diameter and 5/16 in. thick. Installation in the flat plate for wind-tunnel tests is accomplished by means of 16 leveling screws which are alternately tapped into the disc and into the plate. Experience has shown that the discontinuity in surface level at the 4-in. parting circle can be reduced to less than 0.00005 in. without difficulty, and that a standard dial test indicator is adequate for measurement of the discrepancy. It follows that one skin-friction instrument can be exchanged for another in a relatively short time and that repairs need not involve serious interruption to a particular wind-tunnel experiment.

To lock the floating element during lapping, the gap may be filled with glyptal (glyptal clear varnish or red enamel, General Electric Co., Schenectady, N.Y.). The glyptal is allowed to harden before lapping and is removed with acetone or other solvents after a smooth flush surface has been obtained. It is believed that this technique, one of several that were tried, avoids possible elastic deformations in the flexlink structure, which could lead to serious misalignment when the element is released.

The balance chamber must be sealed with extreme care. For the instrument discussed in Ref. 43, satisfactory sealing was achieved with solid rubber compression seals which were installed in grooves beneath the various cover plates.

3.6 Dynamic Stability Measurements

Wind-tunnel measurements of dynamic stability derivatives require techniques in which the model is rigidly restricted in one or more of the basic degrees of freedom (Ref. 138). In fact, in most cases the model is free to move in one degree of freedom only, thus involving

only one equation of motion. The analysis of test results is thus simpler and, in principle, more accurate. Since other factors such as scale effects and wind-tunnel and model-support interference affect the accuracy of results, the accuracy will vary from case to case.

The dynamic stability derivatives can be determined from wind-tunnel tests using models which describe a rotational or oscillatory motion in relation to a parallel air stream. This motion occurs when models rotate or oscillate in a parallel air flow in a straight test section and when models are rigidly fixed in a test section with a curved flow or a rotating flow. The measurements follow two main principles, namely measurement of moments and forces when the relative motion between model and air stream is given, or measurement of the relative motion when forcing moments and forces are given. This technique is summarized below.

Methods of Determining Dynamic Stability Derivatives

For a Model Moving in the Test Section	For a Model Fixed in the Test Section
Measure Forces and Moments with:	
1. Rigidly forced oscillation 2. Self-exciting oscillations with constant amplitude 3. Rigidly forced continuous rotation	1. Rotating flow 2. Curved flow 3. Parallel flow over dis- torted model
Measure Motion with:	
1. Free oscillation 2. Elastically forced oscillation 3. Forced oscillation around two axes 4. Continuous rotation	1. Rotating flow 2. Curved flow

Model Moving in the Test Section.--The most general method for measurement of dynamic stability is that of "rigidly forced oscillation." A harmonic motion, angular or translational, is imparted to a model, and forces and moments between the model and the forcing part of the rig are measured and divided into the in-phase and out-of-phase components. Theoretically, all dynamic derivatives can be obtained by this method. In practice, however, there are many difficulties, the most important of which is the need to balance out large responses due to inertia of the model. A further difficulty is encountered in the measurement of the small-valued cross responses, such as C_{n_p} and C_{l_r}

which require balance flexures of relatively high flexibility in one degree of freedom, whereas at the same time much more stiffness is required in the direction of the forcing moment or force.

A method which can be successfully used for determining all the derivatives except cross derivatives is the method of "self-exciting oscillation" with constant amplitude. A feedback system connects the displacement transducers on the model suspension with driving coils of an electromagnetic oscillator and also includes provisions for a 90-deg

phase shift and a device to keep the amplitude constant. Oscillatory damping derivatives such as $(C_{m\dot{q}} + C_{m\dot{\alpha}})$, $(C_{n\dot{r}} - C_{n\dot{\beta}})$, and $C_{l\dot{p}}$ are obtainable from measurements of the energy required to keep the oscillation at a constant amplitude, and aerodynamic stiffness derivatives such as $C_{m\alpha}$ and $C_{n\beta}$ are obtainable from frequency measurements. The method can easily be applied at both low and high speeds and at a large range of frequencies. The feedback system automatically provides for the frequency setting at resonance, thus eliminating the need for manual tuning of frequency during the test.

A convenient method for determining derivatives due to rolling (such as $C_{l\dot{p}}$, $C_{n\dot{p}}$, $C_{Y\dot{p}}$) is the method of "rigidly forced rotation."

This method is quite similar to that of rigidly forced oscillation, except that it avoids difficulties with inertia effects, which is a great advantage. The measurement of small cross-responses is also somewhat less serious because the stiffness-in-roll requirements are no longer as critical. The roll response (damping in roll) can be measured between the driving motor and the model, or between the whole apparatus and the wind-tunnel structure. The differences in results of tests with continuous rolling or with oscillation in roll, which are due to different time histories of the motion in the two cases, are usually small. Both types of motion are of interest, however, the continuous one in connection with rolling performance and the oscillating one in connection with stability analysis.

The method of "free oscillation" is usually considered to be the simplest and most straightforward one for the determination of the oscillatory damping derivatives, such as $(C_{m\dot{q}} + C_{m\dot{\alpha}})$, and aerodynamic

stability derivatives, such as $C_{m\alpha}$. This method consists simply of the evaluation of decaying oscillation performed by an elastically constrained model following an initial disturbance. With modern instrumentation, damping derivatives determined by this method have an accuracy that is often considered higher than that achieved by any other method because of the straightforward type of analysis. The accuracy of frequency measurements, however, is about the same as it is with other methods. The initial disturbance usually has the form of an abrupt release from a deflection, but at higher experimental frequencies it can be conveniently replaced by an excited oscillation of a desired amplitude, sometimes in connection with a feedback system which automatically secures the frequency setting at resonance value. For high accuracy the model suspension should be completely elastic, avoiding any friction effects.

It is often argued that the free oscillation methods are inferior to forced oscillation methods because they give results representative of an amplitude range rather than of a discrete value of amplitude. This may be an advantage (Ref. 138) rather than a disadvantage. Since the motion of an aircraft, subsequent to a disturbance, covers a whole range of amplitudes, it can be described better by equations of motion that contain constants representative of this range rather than of a single value of amplitude. Both methods (with the use of modern instrumentation) are suitable for obtaining results as a function of amplitude; but in the case of a single value to be used, this value is more representative if it is obtained by the free oscillation method than by a constant amplitude method.

In the method of "elastically forced oscillation" the harmonic motion is imparted to the model through a linear spring. The oscillatory damping derivatives can be determined from the amplitude ratio at resonance between the forcing and the forced motions and the value of the resonance frequency. The same result can be obtained by another method of analysis from measurements of the resonance frequency and the frequency for which the ratio of forced amplitude to its value at resonance is equal to $\sqrt{2}/2$.

Another method which can be applied if the resonance conditions are difficult to maintain requires measurement of the amplitude ratio between the forcing and the forced motion at any frequency, the value of this frequency, and in addition, the phase angle between the forcing and the forced motion. The advantage of this method lies in the fact that the aerodynamic stability derivatives can also be obtained from the measurements.

If a harmonic motion is imparted to a model in one degree of freedom and the "model response in a second degree of freedom" is measured, the appropriate cross derivative can be determined from such a measurement. A particularly simple analysis can be used if the frequency of the forcing motion is tuned to the resonance frequency of the forced motion. The desired cross derivative (e.g., C_{n_p}) is then equal

to the amplitude ratio between the forced motion and the forcing motion times the oscillatory damping derivative for the forced motion (in that case, $C_{n_r} - C_{n_\beta}$), which has to be determined from other tests. This

approach uses the forced motion's maximum obtainable amplitude, which facilitates its measurement but on the other hand requires an exact tuning of the forcing frequency, in contrast to the difficulties mentioned in connection with the method of rigidly forced oscillation. A feedback system between the displacement of the forced motion and the excitation of the forcing motion is probably a good solution.

In contrast to the method of rigidly forced rotation is the method of "continuous rotation" forced by a known moment. Only the derivative C_{l_p} can be determined by this method. The known moment can

be given by an aileron deflection on the model itself or by a specially added forcing wing, and can be calibrated before the test. The steady roll rate is measured. If damping of the forcing wing occurs, it needs special calibration. Special corrections are needed if the rolling moments acting on the wings are dependent on the angle of bank, as may be the case where secondary flows in the test section disturb the rotational velocity of the model and introduce inertia effects.

Model Fixed in the Test Section.--By use of the methods mentioned below, the model can be fixed in the test section, and all measurements can be made on static balances of the usual type.

In a test section with "rotating flow," derivatives due to rolling (C_{l_p} , C_{n_p} , C_{y_p}) can be measured. The test conditions are somewhat different from those in which an aircraft (or model) is rolled because of the presence of a radial pressure gradient in the air due to the centrifugal force. If the flow could be considered a potential flow and the model were symmetrical (and symmetrically mounted), the total effect of such a gradient would be zero; but in cases of incidence or yaw and in the inevitable presence of model boundary layer, a correction would have to be applied to account for this effect.

Similar test conditions exist in a test section with "curved flow," where the derivatives due to pure yawing (such as C_{n_r} , C_{l_r} , C_{y_r}) and pure pitching (such as C_{m_q} , C_{L_q}) can be measured. Test sections with rotating or curved flows are used only for low-speed work.

Instead of placing a model in a curved or rotating flow it is possible to use a "parallel flow" and a model "distorted" in such a way that pressures at different stations on the model are similar to what they would have been on an undistorted model in a curved or rotating flow (or in a rolling or yawing motion in the still air). A stationary wing model with linearly distributed asymmetrical twist, for example, gives approximately the same pressure distribution over the wing as the pressure distribution over a wing performing a rolling motion. Although the method has the advantage of measuring dynamic derivatives on fixed models using static balances, it also involves complex and costly models, a great disadvantage, and is therefore mainly of academic interest.

3.6.1 Dynamic Pitch Measurement

Although the development of techniques for measuring dynamic pitch has lagged behind other wind-tunnel techniques, several facilities have nevertheless made such measurements in the past several years. These techniques fall into two general categories which utilize 1) a reflection plane or half-model (Subsec. 3.3.2), and 2) a three-dimensional model.

3.6.1.1 Half-Model Techniques

Half-models have been oscillated in pitch at the NAE 30 x 16 in. tunnel with an apparatus (Ref. 138) shown schematically in Fig. 3-72. This apparatus consists of 1) an elastic suspension for the model with displacement transducers attached to the spring element, 2) Oltronix Dampometer, 3) phase-shift device, 4) limiter, 5) Krohn-Hite power amplifier, and 6) electromagnetic oscillator. As indicated in Fig. 3-72, the components of the apparatus form a closed loop system, which includes both electrical and mechanical connections.

The model suspension and the electromagnetic oscillator are built as one unit (Fig. 3-73) to give "free oscillation with feedback excitation." The model is clamped to one end of a cruciform spring whose other end is rigidly attached to a frame mounted on the wind-tunnel wall. Strain gages are mounted near the root end of the spring and are connected to a full bridge. A transverse arm carrying fork coil holders in each end is mounted on the model end of the spring. The arm and the coil holders are made of aluminum. The square coils were wound on temporary bobbins of cerrobend, which were melted away afterwards. The coils are structurally stiffened with araldite baked between and around the layers of enamelled copper wire. The coils can oscillate in the gap of a permanent magnet system, each moving in a direction opposite to the other and thereby causing the model to oscillate in pitch. Depending on the power used, amplitudes as large as + 7 deg can be obtained. Frequencies of the order of 100 cps can normally be used, the exact value depending on the inertia of the model and the dimensions of the spring, several of which are provided.

The signal from the strain-gage bridge is fed into an Oltronix Dampometer, from which the logarithmic decrement and frequency of oscillation are obtained (from readings on two electronic counters). The Dampometer, described in Subsec. 3.6.5, is stressed here because it permits the full exploitation of the free oscillation test method and eliminates the tedious evaluation of time-history oscillograms. It also permits greater accuracy in the measurement of the logarithmic decrement and frequency by dividing every period of oscillation into a large number of equal parts. (At high damping, for instance, instead of having one or two oscillation peaks for calculating the logarithmic decrement, a two- or even three-digit number which is inversely proportional to the decrement is available for this purpose.) The improved accuracy of primary data in turn enhances the accuracy of secondary data (such as $C_{L_q} + C_{L_\alpha}$).

The exciting voltage for the coils of the electromagnetic oscillator is taken from the amplifiers of the Dampometer and passed through a phase-shifting device (to set a 90-deg phase shift in relation to the displacement pickup), to an amplitude-limiting device, and finally to the power amplifier. From the power amplifier the exciting voltage is fed through a manual switch into the coils, which are mechanically connected with the model and the displacement transducers, thus completing the feedback loop.

The manual switch closes and opens the feedback loop. When the loop closes, oscillation builds up to a pre-set amplitude, at which the Dampometer counters automatically are set to zero. (Some small mechanical or electrical vibration is always present in the system to initiate the oscillation.) When the loop opens, the oscillation decays and the counters register two four-digit decimal numbers, which are inversely proportional to the logarithmic decrement and frequency of oscillation. Three to six complete measurements are usually made during one 15-sec wind-tunnel run, depending on the value of damping (i.e., the pre-set fraction of the original amplitude that is desired).

It is to be noted that no frequency adjustment is necessary during the course of measurements, as feedback keeps the frequency of oscillation automatically at the resonance value of the system.

The oscillatory damping derivative, $C_{m_q} + C_{m_\alpha}$, is proportional to the difference between the products of logarithmic decrement and frequency in the air-on and the air-off conditions. The aerodynamic stability derivative, C_{m_α} , is proportional to the differences between the squares of the frequency with air-off and with air-on.

From the difference between $C_{m_q} + C_{m_\alpha}$ for two axis positions and C_{m_α} for one axis position, the derivative, $C_{L_q} + C_{L_\alpha}$, of the lift force due to pitching is calculated. From the difference between C_{m_α} for two axis positions the static lift curve slope, C_{L_α} , is calculated.

The system can also be used for negative damping. In this case the electromagnetic oscillator becomes a brake when the coil circuits are shorted. The counters then have to be zeroed manually.

Some results obtained for three delta wing-body configurations by this method are presented in Fig. 3-74. The total scatter in the results from about 20 measurements are shown by the vertical lines on the upper diagram.

The simple free-oscillation device shown in Fig. 3-75 can be utilized to fulfill the unusual requirement of obtaining the average damping in pitch of half-bodies through an amplitude of ± 180 deg in angle of attack. This technique requires the use of a side-wall balance, such as described in Subsec. 3.3.2.1. The instrumented shaft of the side-wall balance, however, must be removed and replaced by a freely rotatable shaft mounted in precision ball bearings. During operation the output from a potentiometer mounted on the end of the shaft gives a trace of angle of attack versus time on an oscillograph, and the model must then be mass-balanced and tested a second time at another moment-reference station. The normal difficulties of obtaining the first and second time-derivatives of angle of attack are compounded by nonlinear damping over the large amplitude of oscillation. Better results can be obtained by mounting accelerometers in the model. The static force measurements can be obtained with the standard side-wall balance described in Subsec. 3.3.2.1. It should be noted that errors due to flow through the gap between the model and the reflection plane or wall (Subsec. 3.3.2) will be encountered.

3.6.1.2 Three-Dimensional Model Techniques for Dynamic Pitch Measurement

A forcing (as opposed to free oscillation) technique was developed (Ref. 139) in the MIT transonic blowdown wind tunnel to meet the need for a method by which the dynamic stability derivatives of conventional high-density (heavy) models normally used for static wind-tunnel tests could be measured. It was found that if a model of this type can be forced at its natural pitching frequency the inertial effect of the mass is cancelled, and the moment required to maintain the forced oscillation is the damping moment on the model.

A sting balance designed to accommodate some available, high-density models is shown in Fig. 3-76. A thin, flat flexure is machined near the upstream end of the balance, and the model's center of gravity is placed at the elastic center of this cantilever. At this point a load may be applied with no resultant angular deflection of the point, and a moment produces no linear deflection. The model is forced at a resonance by a flat spring, which is independent of the sting and is gaged near the elastic axis to measure the moment applied to the model. The motion of the model in pitch is indicated by the moment in the sting just upstream of the elastic axis. The downstream end of the forcing spring is attached to a forcing arm and electromagnetic shaker assembly. Inertial and stiffness terms are present in the sting, but only the moment required to maintain the forced oscillation is measured by the forcing spring.

The separation of the heave and pitch resonant frequencies creates the biggest problem in the balance design. The heave stiffness of the sting must be maintained as large as possible in order to minimize elastic coupling of the two modes when high-density models are used. Aerodynamic noise and vibrations of the plenum chamber and angle-of-attack support must also be minimized so that the signal-to-noise ratio of the accelerometers is acceptable. Much of the heave deflection could be eliminated by the application of less force at the shaker end of the system.

The Naval Ordnance Laboratory has designed a damping-in-pitch balance (Ref. 114) which allows a model to oscillate about a horizontal axis through its center of gravity and perpendicular to its longitudinal axis. Provisions are included for continuously measuring the angle of oscillation and the angular acceleration. The balance is shown schematically in Fig. 3-77. Crossed steel flexures in the damping balance effectively permit model oscillations about a point. By exchanging these flexures for others of different thickness, it is possible to vary the model's frequency of oscillation from 10 to 100 cps. Each set of these flexures is provided with strain gages which provide a continuous electrical signal proportional to the angular displacement. The zeroing mechanism applies a moment to the model in the direction opposite to the aerodynamic moment, thus keeping the model axis coincident with the balance axis at angles of attack. The magnitude of the moment is controlled by means of an electric motor. The tripping lever is extended by means of air operation to deflect the model. The lever is spring loaded and returns to neutral position when the air is suddenly shut off, thereby initiating model oscillations. The model is secured to the balance by an internal expanding collet built into the balance, which thus simplifies the adjustment and positioning of the model with respect to the balance center of rotation. Angular acceleration is measured by an accelerometer just forward of the collet arrangement. The sting is made of 4340 steel heat-treated to Rockwell C-37, and the flexures are fabricated from 6150 steel heat-treated to Rockwell C-45. Standard Baldwin AB-8 bakelite strain gages are used. The information from the strain gages is recorded on a Sanborn recorder, which produces a trace of angular displacement with respect to time from which the damping coefficient is obtained from the logarithmic decrement in the conventional manner. The Ballistics Research Laboratory has used the same technique for obtaining pitch damping (Ref. 119).

NOL has used another simple technique in which the model is fastened to a wire which spans the tunnel test section. The wire passes through the center of gravity of the model and leaves it free to oscillate in pitch. Micro-bearings installed in the model minimize friction. The damping moments at the low angles of attack measured by both techniques showed excellent correlation with results from the firing range, indicating that the interference effects from the suspension wires were negligible.

3.6.2 Dynamic Roll Measurement

A typical device for obtaining damping in roll by means of the forced steady-roll technique is shown in Figs. 3-78 and 3-79. The case which supports the internal mechanism also acts as a windshield to protect the internal mechanism. The shaft protrudes from the windshield and is driven through a planetary gear system by an electric motor mounted in the aft end of the support. The stationary ring gear mounted in the planetary gear system is restrained from rotation by an instrumented cantilever beam. The output of the strain gage is proportional to the torque required to drive the model. Three fine pieces of piano wire restrain the ring gear in axial movement but offer only small resistance to rotational movement.

The tachometer consists of a small Alnico magnet attached to the drive-motor shaft and in the field of a small pickup coil. The rotating magnet produces an alternating current in the pickup coil whose frequency is equal to the speed of the motor (see Fig. 3-80). This device produces a practically square wave, and "hash" is practically nonexistent.

In use, the output signal of the balance is connected to the vertical plates of a cathode ray oscilloscope. An audio oscillator is connected to the horizontal plates. An EPUT (events per unit time) meter is then connected to the audio oscillator to determine its exact frequency setting. To set a given model speed, the audio oscillator is set to the balance signal frequency corresponding to the required rotational speed. This setting is determined from calibration. The balance speed control is then advanced until a roughly square or circular figure appears on the screen of the oscilloscope. The figure will appear to rotate about opposite corners of the square when the balance speed approaches the desired speed. The balance should be adjusted so that the figure just stops rotating. The equipment setup is shown in Fig. 3-81. The gain of the vertical amplifier in the oscilloscope may require adjustment throughout the speed range to compensate for the variation of output voltage with rotational speed.

The balance is capable of rotational velocities of ± 1500 rpm under no-load conditions. The maximum rolling moment is limited by the torque output of the electric motor to 27 in.-lb, and the design normal force load for this support is 200 lb applied at the window centerline.

The balance is equipped with an air-actuated brake and a toggle system which operates a set of lead brake shoes. The brake consists of two double-acting cylinders connected in parallel to a compressed air supply. These cylinders are capable of exerting forces in excess of 50 lb with the brake connected to a 100-psi air supply. The brake control is a four-way valve mounted on the balance control chassis. Air is continually supplied to the brake either to hold it on or off. The brake is used to restrain the model in roll during wind-tunnel starting and stopping.

Cruciform models can be tested at angles of attack other than zero, but the large-amplitude, pulsating lift, load characteristics of a rolling mono-wing model poses severe operating conditions, especially if the frequency approaches the natural bending frequency of the system.

Rotational speeds in the order of 10,000 rpm are sometimes desired to simulate full-scale flight. Such speeds pose a difficult problem from a power standpoint if the use of electric motors is desired. For example, it is estimated that a 75-hp motor with a maximum diameter of 4 in. would be required to overcome the damping force of a typical model in the OAL tunnel. Such motors are available, but they are quite expensive and the cooling problems are a complicating factor. A simple and inexpensive technique was developed by the Naval Supersonic Laboratory at MIT which extracted the energy required from the supersonic airflow past the balance. The driving torque is delivered to the shaft by four rectangular wing surfaces mounted in cruciform fashion aft of the model on the support. The differential deflection of these surfaces is controlled remotely by a servo system which allows a braking action to be applied by reversing the differential deflection of the surfaces. The tunnel is started and stopped with the driving surfaces in the "feathered" position. The energy input to the shaft is measured by a conventional strain-gage bridge oriented to measure drive-shaft torque.

High rotational roll rates have also been obtained at NOL through the use of an air turbine (see Subsec. 3.6.4) housed within the model. The model is mounted on ball bearings which in turn are mounted on a non-rotating sting-type shaft. The model is brought up

to a high spin rate and the air supply is stopped instantaneously by a solenoid valve. The model is then allowed to damp freely to zero spin rate. Friction is evaluated as a tare by spinning the model in the air-off condition. Bodies of revolution or other configurations which do not have a large-amplitude pulsating normal force on the model can be tested at any angle of attack from 0 to 90 deg. The equations of motion are then used to reduce the data.

The method of free oscillation with feedback excitation is used for oscillation in roll (Ref. 138), as shown in Fig. 3-82. The model is mounted on a set of cantilever springs which together act as a torsion spring. The length of the springs is variable, thereby making it possible to change frequency. The output of the strain gages on the springs is proportional to the deflection in roll. The excitation unit consists of a rotor containing several small permanent magnets, which are radially spaced, and a stator consisting of a coil and an iron core, the ends of which are divided into several separate poles bent together to face the magnets of the rotor. An alternating current through the coil at the resonance frequency for the system brings the rotor (and the model) into oscillation. The rig operates at 200 to 400 cps, depending on the model inertia and spring length. The rig is mounted in the wind tunnel in such a way that a large angle-of-attack range can be covered.

3.6.3 Measurement of Cross Derivatives

A method for measuring the dynamic stability derivatives of a model airplane in the NACA wind tunnels is described in Ref. 140. The characteristic features of this system are that 1) single-degree-of-freedom oscillations were used to obtain combinations of rolling, yawing, and pitching motions; 2) the oscillations were excited and controlled by velocity feedback which permitted operation under conditions unfavorable for more conventional types of oscillatory testing; and 3) data processing was greatly simplified by using analog computer elements in the strain-gage circuitry.

The system is used primarily for measurement of the damping derivatives, C_{ℓ_p} (damping in roll), $C_{m_q} + C_{m_{\dot{\alpha}}}$ (damping in pitch), and $C_{n_r} - C_{n_{\dot{\beta}}}$ (damping in yaw); and the cross derivatives, $C_{\ell_r} - C_{\ell_{\dot{\beta}}}$ (rolling moment due to yawing) and C_{n_p} (yawing moment due to rolling). The method of testing also permits measurement under oscillatory conditions of the static derivatives of rolling moment due to sideslip, yawing moment due to sideslip, and pitching moment due to angle of attack. All these derivatives are of particular importance in estimating the short-period oscillatory motions of a rigid airplane.

In measuring the dynamic stability derivatives which apply to these motions there are certain advantages in employing oscillation methods, and most of the early measurements of damping in pitch were made from oscillation tests of a model in a wind tunnel. Damping in roll and damping in yaw have also been measured in this way, but experimental difficulties have generally prevented the wide application of this method to the lateral motions. This is particularly true in the case of the cross derivatives, yawing moment due to rolling, and rolling moment due to yawing, although in one recently developed method (Ref. 141) the yawing moment due to rolling has been successfully measured using a two-degree-of-freedom oscillatory technique.

3.6.4 Magnus Forces

The aerodynamic forces on a spinning body in a cross flow are commonly referred to as Magnus forces. These forces cause erratic trajectories of conventional rotating missiles flying in a cross wind. The rotational speed of spinning projectiles generally is very large. In simulating full-scale conditions with a scale model in the wind tunnel, the rotational speed has to be made even larger. The smaller the model is with respect to its full-scale counterpart, the higher the spin rate required for testing. Since electric motors of the required small size with sufficient torque are difficult to build and operate at 50,000 rpm and higher, air turbines have been designed and constructed for such use (Ref. 114).

Figure 3-83 shows a schematic drawing of the NOL balance for spinning models. The air turbine, of the impulse type, depends upon expansion of the gas through fixed nozzles, with no further expansion in the blades of the turbine wheel. When small size is desired and efficiency is relatively unimportant, this type offers certain advantages over the reaction type (where expansion takes place through the fixed nozzles or vanes and continues through the turbine blades). Some of these advantages are:

1. Design and construction of turbine blades is much less critical.
2. Clearance between blade periphery and housing is not critical, since no pressure gradient exists to encourage "spill over" from the high to the low pressure end.
3. The number of nozzles is not as critical as it is for the reaction turbine, which requires as many nozzles as blades to prevent leakage between blades.
4. The open area between blades is not critical, since there is no need for controlled fluid expansion through them.

The heart of the turbine is the gyro-rotor-bearing assembly. These bearings allow rotational speeds in the order of 120,000 rpm. The inner shaft of the bearing assembly connects the model to the impeller. The entire turbine and bearing assembly is mounted on a four-component, strain-gage balance which is designed for pitching loads up to 50 lb. Magnus moments which are in the order of one-twentieth of the pitching moments may be measured. The air supply which drives the turbine is fed through a center tube, through the nozzle box, across the impeller, and is exhausted through an annulus surrounding the center tube. Speed is measured by a tachometer unit built into the turbine and consisting of a permanent magnet ring (with north and south poles on opposite ends of a diameter) mounted on the turbine shaft and a soft-iron, wire-wound pole mounted to the housing near the ring. This combination acts as a generator, producing a sine wave with the same frequency as the turbine speed. The outputs of the strain gages and the tachometer are fed into a two-pen Leeds and Northrup Speedomax Recorder. The actual measurement of Magnus moment is accomplished in about 30 sec by accelerating the model through its range of spin rates, up to 80,000 rpm, at discrete angles of attack while the tunnel is blowing. In this way a graph of Magnus moments against rotational speed is obtained.

The balance is made of 4340 steel heat-treated to Rockwell C-37 with an RMS 32 flash nickel-plate finish. (The gyro-rotor-bearing-shaft assembly Q-36BD is manufactured by New Departure Division of General Motors, Bristol, Conn.) The impeller and nozzle box are fashioned from naval brass SAE 73, and the tachometer magnet is made of carbon steel SAE 1095 heat-treated to Rockwell C-55. The tachometer pole is made of Armco Iron (manufactured by American Rolling Mill Company, Middletown, Ohio). The strain gages used are type SR-4 AB-11 Baldwin gages.

Magnus measurements have been successfully measured at the Ballistics Research Laboratory on bodies of revolution at large angles of attack by means of an electric-motor drive mounted in the support behind the sting-mounted model. The strain-gage balance is mounted inside the model, and both the model and balance are rotated (as opposed to the NOL technique), making it necessary to record the strain-gage outputs on an oscillograph.

3.6.5 Oltronix Dampometer

Free-oscillation test results can be evaluated automatically by means of a Dampometer (Ref. 142), shown in Fig. 3-84. In this instrument, the damped oscillation is represented by a rotating vector on the screen of a cathode-ray tube, the rate of decrease of the length of the vector being a measure of damping. The screen of the cathode-ray tube is covered by a circular disc with a number of equally spaced radial slots, as seen in Fig. 3-85. When the head of the vector moves on a spiral path around the screen, it passes the slots of the disc and allows light pulses to reach a photocell. The number of pulses produced during the time the vector decreases from the outer to the inner radius of the slots is registered on an electronic counter, which gives the number directly in decimal digits. The logarithmic decrement is inversely proportional to this number. A second electronic counter is used to measure the number of oscillation periods of a crystal oscillator during a certain number of pulses, thus determining the frequency oscillation.

The Dampometer, which is commercially available (Ref. 142), provides several advantages: It eliminates the tedious evaluation of time-history oscillograms by providing a single digital reading at the time the amplitude of oscillation has decreased to some pre-set limit.

It increases the accuracy of measuring the logarithmic decrement and frequency by dividing every period of oscillation into a large number of equal parts (this number being equal to the number of slots in the disc). At high damping, for instance, instead of having one or two oscillation peaks for calculating the decrement, a two- or even three-digit number which is inversely proportional to the decrement is available for this purpose. The improvement in accuracy of primary data means that the static and dynamic aerodynamic derivatives can be computed with greater reliability.

It can be used to obtain amplitude effects. The resolving power is good enough to allow investigation so that a set of mean values of the logarithmic decrement can be obtained within a narrow amplitude range. As a result, it is possible for a derivative to be plotted as a function of amplitude.

It can be used in cases of negative damping, i.e., when amplitude increases with time.

Its automatic zero reset device resets the counters as soon as the radius on the screen exceeds a certain value, a handy provision for cases of high frequency and damping, when time may not be available to reset manually.

Its high-pass filter may be adjusted simultaneously with the phase-shifting network, thus permitting use of the cock-release method, as well as the continuous oscillation, where the damping starts when the power source is disconnected. Test of this device disclosed that the error introduced by it as a result of the distortion of the Fourier spectrum will be less than 3% at a logarithmic decrement of two. The error will be less at lower damping.

At the Sandia transonic wind tunnel, the Dampometer was modified so that it could be paralleled with a brush recorder or visicorder when a permanent trace was required to quantitatively evaluate cases of neutral stability or instability. The deflecting mechanism and dynamic free-oscillation rigs used in the 12-in. tunnel are programmed to obtain three releases (damping envelopes) during a 15- to 30-sec run. Two additional sets of readout counters were added to the Dampometer so that three values each of frequency and logarithmic decrement could be recorded during a run. The Dampometer reduces markedly the manhours expended in data reduction for dynamic tests and increases the accuracy in the calculations of the static and dynamic stability derivatives.

3.7 Analog-to-Digital Converters

No single piece of instrumentation has contributed as much to the automation of modern wind tunnels as the analog-to-digital converter. This device serves as the bridge between the voltage outputs from strain-gage balances, pressure transducers or thermocouples, and some form of digital data storage such as punched cards or magnetic or punched paper tape. It has also been used extensively as the digital data input to high-speed calculators which, when properly programmed, reduce the data concurrently with the test (frequently referred to as "on-line" data reduction).

Analog-to-digital converters (Ref. 143) fall into two main categories, electro-mechanical and electronic. Although a rather wide variety of converters are available commercially, only one example of each type will be discussed herein. Other systems will be mentioned briefly in Subsecs. 9 and 10. It should be pointed out that new developments are constantly being applied in this field, and more sophisticated equipment can therefore be expected.

3.7.1 Electro-Mechanical Analog-to-Digital Converters

The electro-mechanical analog-to-digital converter that was used operationally from 1949 to 1955 at the OAL supersonic wind tunnel is shown schematically in Fig. 3-86. The basic idea is credited to Dr. T. L. Smith of the Ballistics Research Laboratory.

Each indicator has four channels so that four individual voltage outputs can be read in sequence by a manual change of the gage selector. An additional channel is supplied to measure the output of a

standard bridge which serves as a calibration. The voltage output from the strain-gage bridge is amplified and used to drive a servo motor which is mechanically coupled to a large drum on which is mounted a 100-point slide wire. Rotation of this drum adds a resistance to the strain-gage circuit in such a manner as to null the voltage output from the bridge. If the voltage output is too great to be nulled by a single revolution of this drum, it proceeds to the end of its allowable travel and actuates a solenoid stepping switch which rotates a second drum equipped with 40 step-resistors, each of which is equivalent to the resistance of the 100-point slide wire on the first drum. A coarse balance is then obtained by the rotation of the second drum, and the fine balance is obtained by a final partial rotation of the first drum. When a null is reached, no voltage output from the strain-gage bridge remains to power the servo motor, and the two drums come to rest. Contacts are provided on the two drums to supply the digital output through an interlock system to an IBM card punch and tabulator, the first two digits being supplied by the second drum and the last two digits coming from the first drum. The unit is designed to read from 0 to 4000 counts, with the strain gage zeroed at 2000 counts to allow for plus and minus bridge outputs. If the maximum anticipated voltage output is exceeded, the indicator sensitivity may be halved by a manually operated switch, and an appropriate indication of this change is automatically recorded in the IBM punched card to assure that no errors are made in the subsequent data reduction.

This indicator (six of which were built) is capable of digitizing 24 outputs in sets of six at a time. Approximately 20 sec is required to cover the range and come to a balance for one set of six readings.

A more efficient and more flexible operation could be provided with all-electronic, single-channel indicators, which would allow simultaneous recording of more than six outputs with an attendant gain in data-taking speed.

3.7.2 Electronic Analog-to-Digital Converters

The electronic, analog-to-digital, high-speed converter shown in Fig. 3-87 is the ADHEC* (Ref. 144). It normally has a full-scale input of 10 to 75 mv ac, closed-circuit outputs for IBM data-processing machines, and visual numerical indication from 0000 to 9999. The digitizing requires 0.733 sec, and the IBM recording requires about 1.7 sec. A test parameter change, for example, in angle of attack, may usually be completed during the time needed for IBM recording, resulting in a cycle speed of about 24 points/min. The normal input is a bonded resistance-wire strain-gage (SR-4) bridge having four active arms and excited by 9 v ac rms. Thermocouple (d-c) inputs may be used by transposing connections to the chopper. The full-scale input may be increased by an external voltage divider. A programmer controls the data cycle, the model axis parameters, the ADHEC, and the IBM data machines.

3.7.2.1 Operational Principles of the Electronic Analog-to-Digital Converter

The ADHEC digitizer shown schematically in Fig. 3-88 takes the output voltage of a four-arm strain-gage bridge; amplifies and

* All rights reserved by the General Dynamics Corporation.

rectifies, and then compares it to known voltages. It then stores (for IBM readout) and visually displays the value of the known voltage that equals the bridge output. The amplification is achieved by an input transformer which isolates the digitizer from the bridge and the other digitizers, produces a working signal of larger magnitude, and makes the rectifier operate full wave. The rectifier, operating full wave, is a synchronous chopper charging a storage capacitor to a d-c voltage with polarity determined by the phase angle between input and chopper excitation, which may be either 0 deg or 180 deg. Full-wave operation reduces the ripple amplitude and increases the average charge on the storage capacitor. The time constant of the charging circuit is dependent upon the size of the storage capacitors. The time constant of 3/4-sec was selected to assure that several cycles of the randomly oscillating voltage output would be scanned before the result is digitized. However, too long a time constant will make the instrument excessively slow to rebalance. The second section of the rectifier (chopper) serves to reduce further the effects of ripple on the rectified input signal and also to reduce the effects of large signals on the amplifier. This is done by comparing the rectified input signal voltage and the known voltage (for only a short interval of time) shortly after the chopper has placed a fresh charge (if needed) on the condenser. The comparison, at full charge only, ignores the ripple caused by storage leakage. The brief interval of this error pulse is too short to block the amplifier, i.e., it is too short in relation to the time constants chosen in the amplifier which, if changed, would change the tube operating conditions and gain.

The actual comparison is an algebraic addition of the two voltages, the d-c input being virtually constant during the scanning period. The known voltage will change from less than the input to more than the input, the sum will change polarity, and the new polarity will be amplified and applied to the "And" gate, which has reference pulses on the other input. This coincidence of both positive pulses on the "And" gate causes an output pulse, which fires a thyatron, pulling in a relay and causing the number to be stored.

The sequence of scanning (steps of comparing) the known voltage is in the Arabic decimal system (because the IBM data machines require Arabic decimals). At the completion of the sequence four digits will be stored by four pulled-in relays, which (together) in the range resistor circuitry sum four voltages equal in magnitude to the input d-c voltage, and which (individually) close circuits in the appropriate columns for the IBM machines. Each sequence takes 0.733 sec. The method of decade counting makes possible a speed of measuring and storing that would be impossible by straight counting.

3.7.2.2 Description of the Components of the Electronic Analog-to-Digital Converter

The system consists of six different types of components, described below.

Digitizer unit.--There are 12 of these units in each ADHEC rack, and each consists of equipment and circuitry necessary to digitize one analog input when controlled by the common control equipment. (Consists of 1 and 3 to 8, below.)

Sequence control unit.--One of these units in each ADHEC rack contains the equipment and circuitry to control 12 ADHEC digitizers.

This includes the clock and reference pulse generators, the sequence counter, and the programmer. (Consists of 9 and 10, below.)

Calibration unit.--This unit includes the calibration standard transformer, the gage power transformer, the chopper power transformer, and a plugboard to simplify the routing of the various inputs to the 12 indicator units.

Regulated power supplies.--Four supplies furnish regulated d-c and a-c voltages to the various units. Each supply takes care of four indicator units or one control unit, and can supply 6.3 v a-c at 20 amp, 220 v d-c at 250 ma, 400 v d-c at 100 ma, and 105 v d-c (bias) at 40 ma.

Line voltage regulator.--A Sorensen regulator supplies all the a-c power for heaters, choppers, bridge supplies, etc.

Range resistor power supply.--A Sorensen 6.4 v d-c regulator supplies the voltage for the range resistor circuits.

In addition to these six types of units, the rack enclosure includes all the interconnecting wiring. Connectors are provided to tie the ADHEC into the associated equipment, the 117-v a-c power, and the 28-v d-c power. The rack also houses a blower and filter to maintain a slight internal pressure to prevent entry of dust.

The equipment consists basically of the following elements.

1. Input transformer to step up the voltage before rectifying.
2. Provisions to inject a standard voltage to calibrate the equipment.
3. Zero-balance circuitry to adjust bridge balance.
4. Two-section chopper to convert the a-c input voltage to an average d-c voltage (i.e., a synchronous rectifier with the dynamic component averaged out) and to supply the algebraic sum of the rectified bridge voltage and known voltage to the amplifier "And" gate in pulse form.
5. Three-stage amplifier for these pulses to make them capable of operating an "And" gate.
6. Reference-pulse generator and buffer for the other input to the "And" gate.
7. "And" gate to determine the phase (or polarity) of the signal applied from the amplifier and to control the operation of the thyatron and relay storage.
8. Source of known voltage obtained by a system of scanning and storage relays with range-adder resistors and range-multiplier resistors.
9. Clock pulse generator and sequence counter to control the scanning and storage relays.
10. Programmer to automatically control operation of ADHEC and associated equipment.

11. Power supplies to supply various regulated a-c and d-c voltages to the equipment.

When a large number of supposedly identical analog-to-digital converters are manufactured, the user should establish that each unit is in fact identical to the others in operation. Reference 145 discusses the manner in which 24 analog-to-digital converters (ADHEC) were checked for their linearity and uniformity.

3.7.2.3 Advantages of the Electronic Analog-to-Digital Converter

The ADHEC significantly reduces the complexity of data acquisition and markedly improves reliability. The results of a comparative check of the ADHEC with the multi-channel indicator under actual operating conditions in a wind-tunnel test are presented in Fig. 3-89 and show very good correlation. This test demonstrated that the effects of typical model vibration on the converter are negligible. Earlier controlled-frequency bench experiments, which showed less than 1% variation over a frequency spectrum of 10 to 200 cps of \pm 2000-count amplitude, had anticipated this result.

The ADHEC is considered superior to the multi-channel indicators (described in Subsec. 3.7.1) in the following ways:

1. Response time is reduced to 0.73 sec compared with 20 sec for a full-scale balance.
2. Resolution is 2-1/2 times greater for the same sensitivity setting.
3. Time delays associated with switching sensitivity are eliminated.
4. Use of sufficient number of single-channel ADHEC's eliminates the 30% increase in actual running time on tests that require a selector switching system when more than six simultaneous readings are desired.
5. Stability is greater with an oscillating signal input.
6. Maintenance is materially reduced because of fewer moving parts. Relays plug in as complete units, and the entire ADHEC can be replaced with a standby without a loss of test time for making repairs.
7. It is applicable to a wide variety of measurements which have an a-c or d-c voltage output within the design range.

3.8 Automatic Data Plotting

As the tempo of data-taking systems increases, it becomes increasingly important that wind-tunnel test data be assimilated more rapidly. This requires not only that the raw test data be reduced by a calculator, but also that it be plotted rapidly and in such a manner as to show graphically the variations in the test data due to model configuration and other parametric variables. The more rapidly the data are plotted, the sooner they can be examined, compared, and corrected should an error in data reduction or a fault in the equipment be evidenced.

The most direct means of automatic data plotting is the analog technique. With this method the voltage outputs from the measuring instruments are operated on in an analog computer and the corrected data are plotted instantaneously on a conventional x - y plotter. This system enables a test conductor to take a quick look at the data during the test, but it is not as accurate as the digital data.

3.8.1 Digital Data Plotting

A system of reducing test data concurrently with the wind-tunnel test should be complemented with a versatile and rapid plotting system. The plotting system described in Ref. 146 uses the conventional data plotter (Fig. 3-90) equipped with an automatic symbol head.

Punched cards are fed into an IBM 523 machine, which sends the digital information through the Digi-Verter to the Vari-Plotter, which is equipped with a symbol identification head rather than a pen so that the data may be identified by symbol. The symbol head automatically advances to the next symbol after receiving a pulse indicating a change of type of information in the cards. This feature permits the plotting of a great amount of comparative data on one sheet of graph paper in an identifiable manner. The symbol head is equipped with 16 different symbols. (A later model of the Vari-Plotter is equipped with circuitry which automatically advances the symbol head until the correct symbol, corresponding to a unique three-digit number from the IBM plotting card, is under the hammer. Although efficient utilization of the machine still requires that the cards be sorted by symbol prior to plotting, one misplaced card will not jumble the symbol order in the midst of a plot, as it can in the model being described herein.)

The OAL system (Fig. 3-90) is capable of plotting 19,200 points per 8-hr day (actual usage is 13,000 points). By substituting a 14-point clutch for the standard 7-point clutch on the IBM card punch, this speed can be increased by 70%. The Vari-Plotter board is large enough to accommodate two 11 x 17-1/2-in. sheets of graph paper, enabling the operator to position one while the other is being plotted.

Operational detail will vary with the type of machine employed, but efficient operation on any machine demands certain essentials. The first of these is that of a carefully planned program. The order of plotting and the parameters to be plotted must be scheduled and punched on master cards. The expected range of the parameters must also be known in order to prepare conversion cards that will be used in displaying the data most adequately on the graph paper. A great deal of time may be consumed by the manual setting of the origin and the required scales for any plot. This time may be reduced to a third if a fixed origin and a standard scale is used for all plots. OAL used the center of the paper as the origin and 1 in. (or 1 cm) as the scale unit. The translation or parallax of any specific "origin" should be set in the master card as a constant, and the scale factor adjusted to give the greatest plotting accuracy for the size of the paper. Figures 3-91 and 3-92 show basic scales and origins that have proved satisfactory for plotting the usual type of stability and control test data. Where a great deal of plotting is scheduled using the same scales, Van Dyke copies of the axes may be prepared beforehand. It is advisable to check at least one point per curve by manual calculation and plotting.

Other digital plotting devices are described in Ref. 147.

3.8.2 Analog Computers

An important advantage derived from use of the analog computer is that it enables wind-tunnel operators to use the "quick-look" method of examining test results. To fully utilize this advantage, operating personnel must be acquainted with the design and operation of the analog system.

The analog system designed and operated by the Boeing Company satisfies the design requirements originally established. These requirements called for a unit that required no programming or patch plugging, for all balance constants and calibration factors to be set into the computer on calibrated dials, and for freedom from zero-drift problems. The unit was also to be as simple as possible and constructed at minimum cost. In general, the computer was designed for an accuracy of 0.2% in the region of zero angle of attack, dropping to 1% or 2% at high angles.

To ensure freedom from the zero drifts, which have been troublesome in d-c analog computers, a 60-cps a-c current is used in the computing networks. Inputs to the computer are taken from low-impedance retransmitting slide wires mounted on the raw data indicators. Interactions between balance components are corrected by applying the best linear approximation of the interaction curve. This introduces some error in the case of balances having nonlinear interactions, but these errors have proved negligible. Data corrected to either wind axes or model axes may be presented. The angle-of-attack signal in the prototype unit was obtained from a Statham inclinometer located in the sting. The signal from this device goes to a standard raw-data indicator and appears on one of the retransmitting slide wires. The actual computation involved in wind-tunnel data reduction consists of applying scale factors to a number of terms and adding them all together. The unit uses an analog summing circuit to perform this addition, and the plotters are modified to act as self-balancing null-indicators.

One of the most difficult aspects in the design of the computer was the painstaking examination of the data processing equations to ensure that important factors were handled carefully, while factors which contributed little to the final result were omitted. For instance, when data from a simple model are converted to wind axes, the contribution of chord force to lift is very small while the computation (chord force times $\sin \alpha$) is somewhat cumbersome. This term was therefore eliminated from the computation.

The computer itself makes no provision for filtering the noise normally found on the signal from wind-tunnel balances. This does not usually present any problem in supersonic wind tunnels where the flow is relatively steady, but it is severe in transonic facilities. The filtering problem must be solved in all cases if random digital samples such as those taken by automatic data systems are to represent the forces and moments acting upon the model. In most transonic tunnels, however, considerable filtering will be required, and even then some unsteadiness will exist in the raw data signal. In such cases, the Boeing computer will indicate the existence of such a condition and, if a given test condition is maintained for a period of time, will indicate the magnitude of the disturbance by the pen excursion at the point on the plot. Fairing curves through such points is quite simple. If the disturbance is sufficiently great to make fairing of the final curves unreliable, it will indicate the need for correction of the situation.

The analog computer for the Boeing wind tunnel may be adjusted to perform any one of three operations: 1) It will present three-component data from the external balance system which is used for testing large models subsonically; 2) it will produce final plots of three-component pitch data taken from internal strain-gage balances; and 3) it will produce plots of raw data taken from internal strain-gage balances.

The cost of this special-purpose analog computer plus plotters is less than half the cost of a standard general-purpose analog computer requiring approximately 20 operational amplifiers to do the same job. While the latter computer would have greater versatility, it would require the use of trained personnel for setup and operation.

It is possible to eliminate the need for such an analog computer in the wind tunnel by resorting to on-line digital data reduction. However, the difficulty of programming digital computers materially increases the time required to get a test into operation; furthermore, some form of raw data storage is usually necessary for checking both the physical setup and the computation procedures.

Final data reduction at Boeing is done on an IBM 701 computer, which is shared with other organizations within the company. The wind tunnel requires less than one hour of 701 time per day for data reduction.

The Boeing analog computer can be set up and operated by any aerodynamicist, and practically no indoctrination is required. It presents final data plots that are reasonably accurate when compared with those obtained from the digital computer.

3.9 Potentiometers

The potentiometer, which is widely used in wind-tunnel testing, measures a potential difference without drawing any current from the circuit containing it. During operation this instrument balances a known voltage against an unknown voltage until there is no current flowing through a galvanometer in the circuit. In most potentiometers the known voltage is varied by means of a slide wire which makes contact along a single or coiled resistance wire. The unbalance of a galvanometer may be amplified mechanically, and the position of the slide wire moved to the point of balance either manually or by a motor-driven system of levers, pawls, and gears.

An improvement on this slide-wire type is the "continuous balance" potentiometer, which utilizes the same null balance circuit but converts the galvanometer unbalance to an alternating voltage and then amplifies it to provide the operating power for a rebalancing motor which maintains the null balance continuously. The sensitivity of measurement is increased, time is saved, and potentiometer life is longer, since fewer moving parts are required. Details of operating, installing, and maintaining the continuous-balance potentiometer may be found in Ref. 148.

In wind-tunnel testing, there is a constant demand for potentiometers of increased precision. For maximum accuracy and conformity of resolution, the variables encountered in the winding and fabrication of a wire-wound precision potentiometer (i.e., variations in resistance wire, spacing of turns, dimensions of card or mandrel, wiper contact, and distortion of winding during fabrication) should be controlled to the greatest possible extent.

There are only limited resistance ranges available in single and multi-turn units. The maximum resistance obtainable in single-turn styles is approximately 250 ohms, while in multi-turn units this maximum resistance value is approximately 250 ohms multiplied by the number of turns.

The use of a metal film as the resistance element is being investigated. The resistivity and the temperature coefficient of resistance of such films will probably be very different from those of wire. Reference 149 describes some experimental work on both metal and plastic films.

Table 3-1

Change in indicator count* due to a temperature rise of 72°F for various gages of 2-in. lengths of copper and nickel wire

Gage	Copper Wire	Nickel Wire
25	4	14
26	5	17.5
27	6.5	22
28	8.5	28
29	10.5	35.5
30	13	44.5
31	16.5	56
32	21	71
33	26.5	89.5
34	33	112.5
35	42	142

* 2.74 $\mu\text{v}/\text{count}$

Table 3-2

Loading schedule for balance calibration

Term being evaluated	Primary load added (5 increments)	Secondary load added (constant)	Number of loading setups
A, A ²	+A	None	1
C, C ²	+C	None	2
n, n ²	+n	$\pm \frac{C}{10}$	4
N, N ²	+N	None	2
m, m ²	+m	$\pm \frac{N}{10}$	4
l, l ²	+l	$\pm \frac{N}{10}$	4
mN	+m	+N	4
lN	+l	+N	4
ml	+m	$\pm l, \pm \frac{N}{10} (2)**$	8
NA	+N	+A*	2
mA	+m	+A*, $\pm \frac{N}{10}$	4
lA	+l	+A*, $\pm \frac{N}{10}$	4
lC	+l	+C	4
nC	+n	+C	4
nl	+n	$\pm l, \pm \frac{C}{10} (2)**$	8
CA	+C	+A*	2
nA	+n	+A*, $\pm \frac{C}{10}$	4
NC	+N	+C*	2
mC	+m	+C*, $\pm \frac{N}{10}$	4
Nn	+N	+C*, +n*	4
mn	+m	+C*, +n*, $\pm \frac{N}{10}$	8

Total 27

Total 83

Definitions: N = normal force or lift

m = pitching moment

A = axial force

n = yawing moment

C = side force

l = rolling moment

* Loading utilizing a pulley

** Two loads of $\frac{N}{10}$ or $\frac{C}{10}$ type

Table 3-3

Characteristics of OAL supports

OAL Support	Parameters Measured	Load Limits MAC* f A (lb) (in. lb) (lb)	Angle-of-Attack Range (deg)	Mach No. Range	Remarks
-10	f	200 80	+14	1.50 to 2.77	Remote roll indexing
-12	f	200 25	+14	1.50 to 2.77	Measure dynamic rolling moment
-13	N C A n n f	135 35 40	+14	1.50 to 2.77	Side force, 100-lb limit
-14	N C A n n	200 40	+14	1.50 to 2.77	
-16	p	200	+11 to -1 19 to -9	1.25 1.50 to 2.77	Support has 5-deg bend
-18	p	200	+6 +14	1.25 1.50 to 2.77	
-19A	A f	175 70 40	+6 +14	1.25 1.50 to 2.77	Remote roll indexing
-20	p	200	+23 to -5	1.50 to 2.77	Support has 9-deg offset; remote roll indexing
-21	p	200	+6 +14	1.25 1.50 to 2.77	Remote roll indexing
-22	A p	300 400	+14	1.50 to 2.77	Used for diffuser tests
-23	A f	150 150 100	+6 +14	1.25 1.50 to 2.77	Used principally for M = 1.25 tests; remote roll indexing
-24	A f	200 180 120	+14	1.50 to 2.77	Remote roll indexing
-25	Lift m n Drag	900 400	+35	1.25 to 2.77	Wall mounted; may be used with or without reflection plate
-26	p	200	+14	1.50 to 2.77	
-27	p	100	+14	1.50 to 2.77	Remote control linear actuator; remote axial movement
-28	p	150	+14	1.50 to 2.77	
-30	p	200	+6 +14	1.25 1.50 to 2.77	Linear position changed manually
-31	N A n n f		+90	1.25 to 2.77	Wall mounted; may be used with or without reflection plate
-32	p	250	+14	1.50 to 2.77	Linear actuator; remote axial movement
-33	—	125	+3 to 27	1.50 to 2.77	Remote roll indexing; 17-deg offset angle
-35	p	250	+7	1.25	Linear actuator; remote axial movement
-36	—	100 20	+9 to 23 +3 to 31	1.25 1.50 to 2.77	Index manually; 17-deg offset angle
-37	—	250	+23 to -5	1.50 to 2.77	Remote roll indexing; 9-deg offset angle
-38	A f	200 180 120	+14	1.50 to 2.77	
-39	p	200	+14	1.50 to 2.77	
-40	—	200	0 to 28	1.50 to 2.77	Remote roll indexing; 14-deg offset angle
-41	p	300	+14	1.50 to 2.77	
-42	p	200	+14	1.73 to 2.77	

* Normal and side force applied at window center

Note: Symbols are standard letter symbols used in text and defined in Table 3-2.

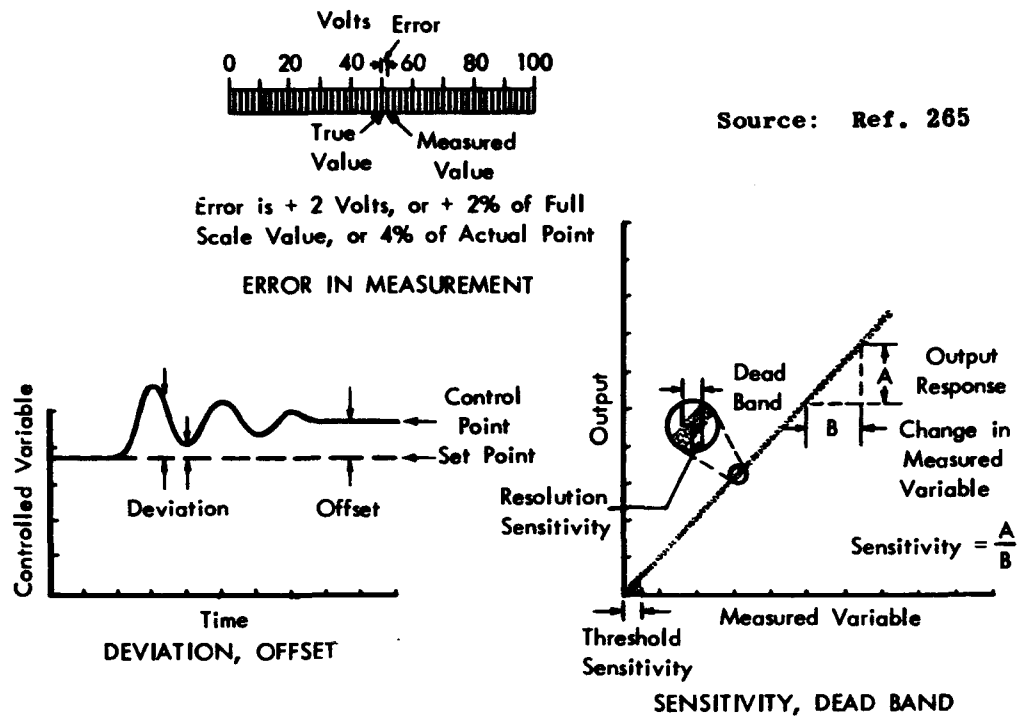


Fig. 3-1. Graphic reference for basic measurement terms.

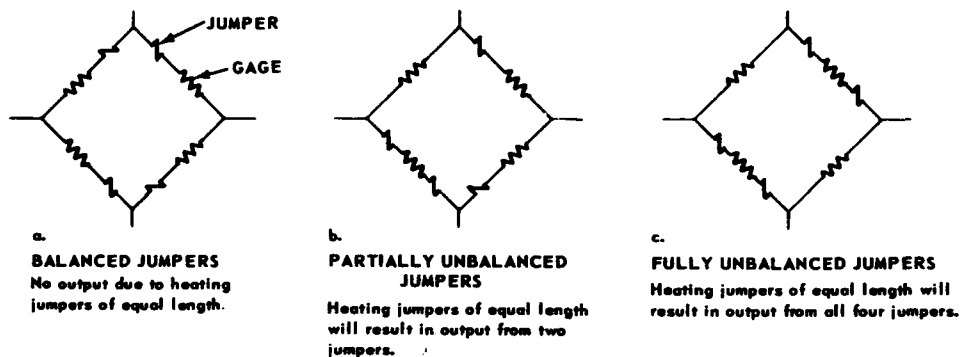
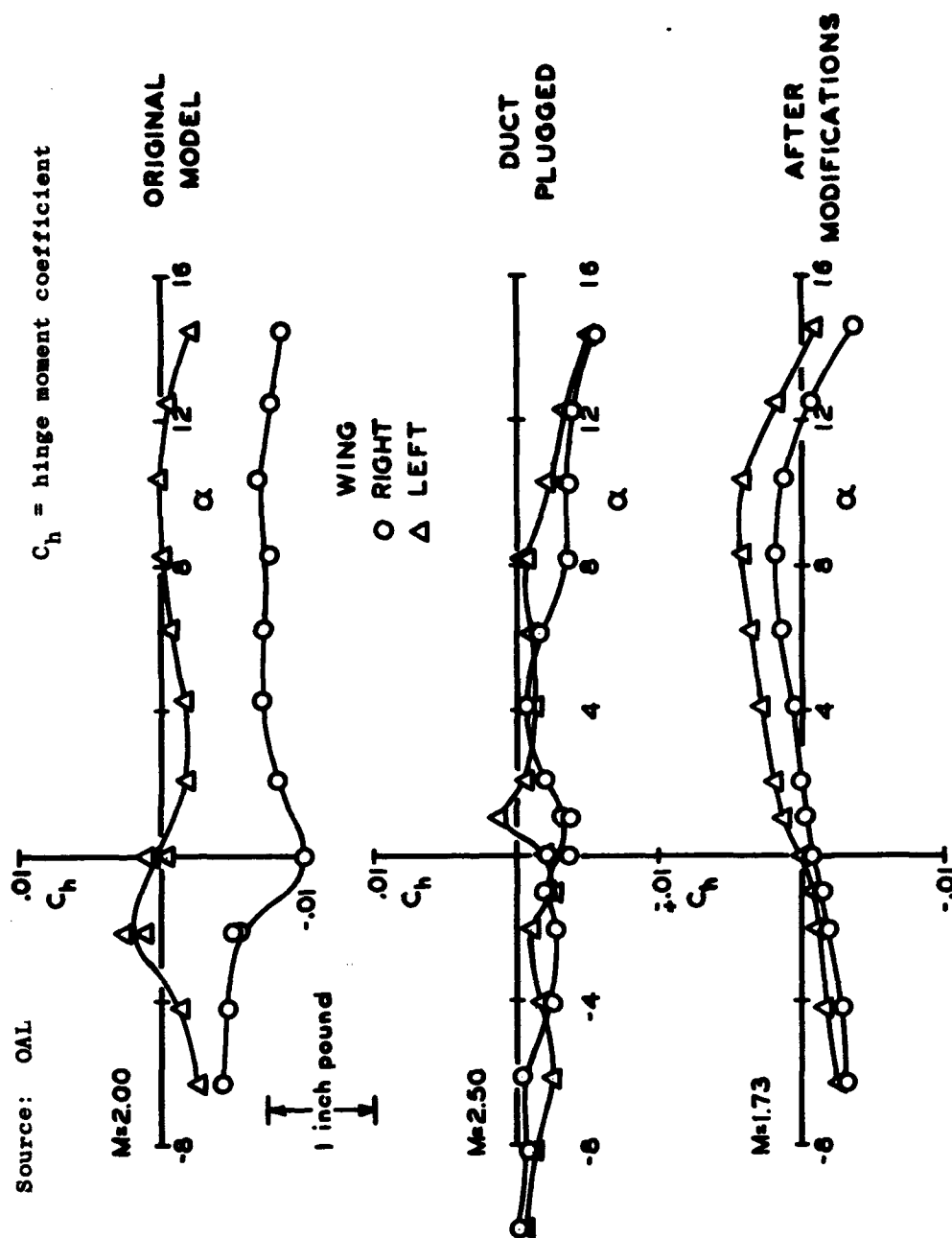
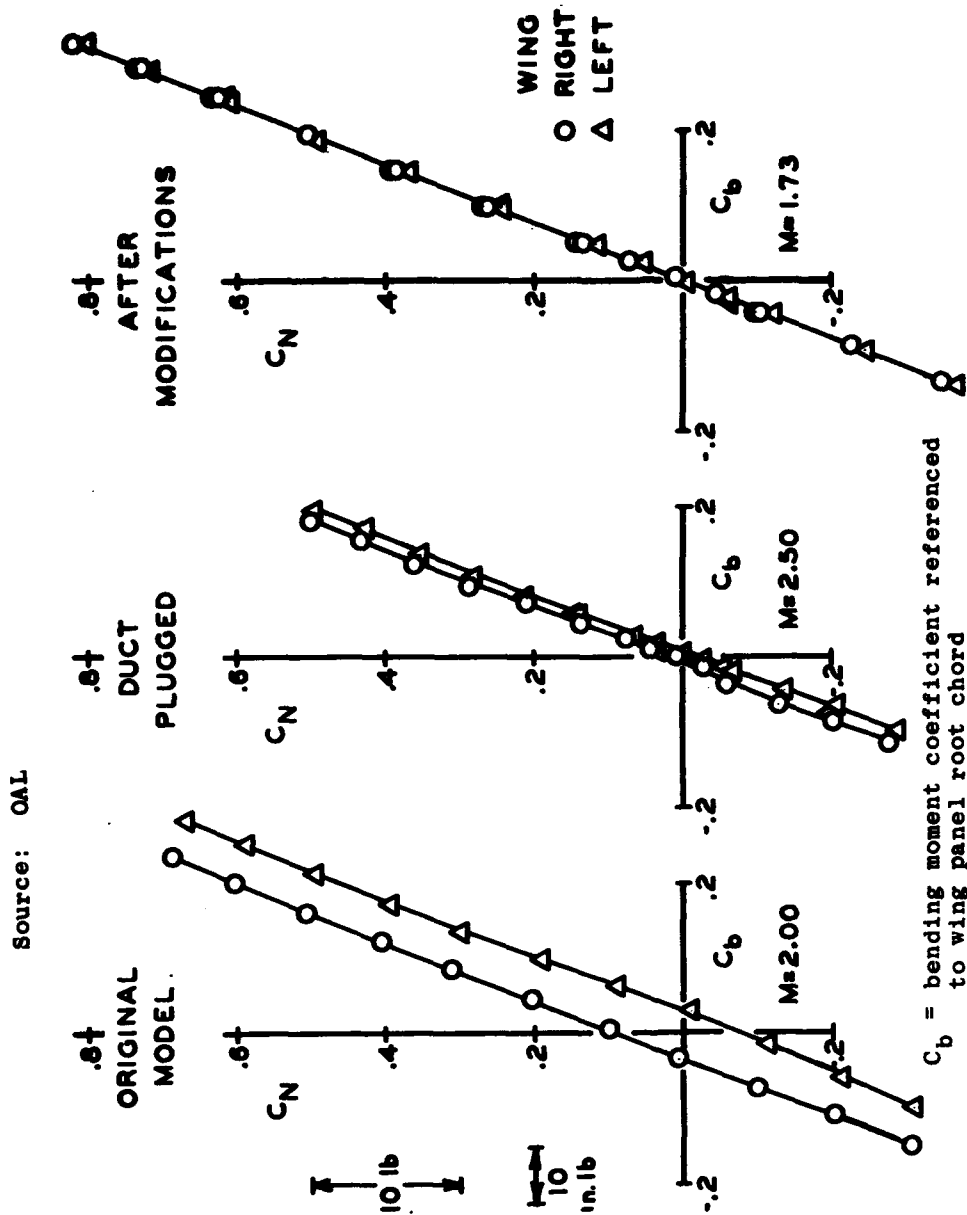


Fig. 3-2. Effect of jumper location on temperature compensation of strain-gage bridge.

Fig. 3-3. Effect on C_h when strain gages are protected from air blast.



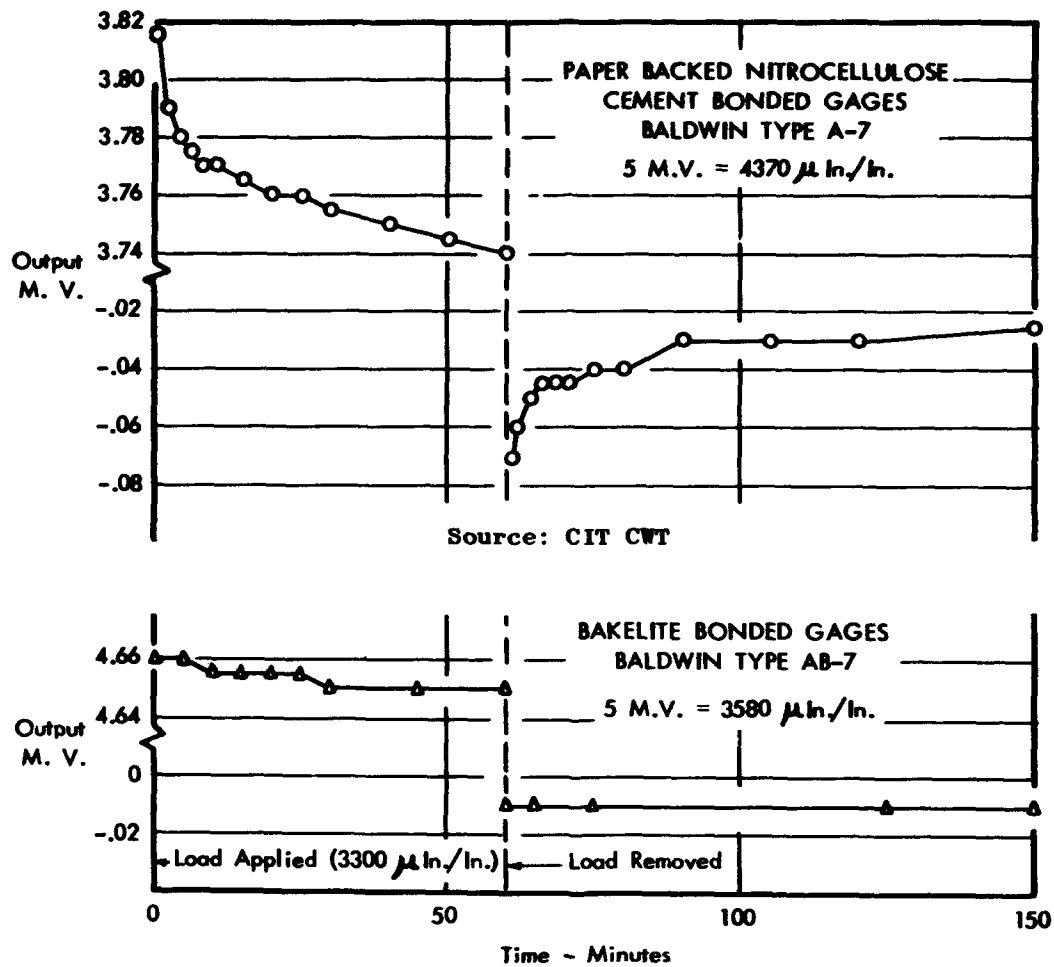


Fig. 3-5. Effects of time on output of complete bridge bonded to test element, constant applied load.

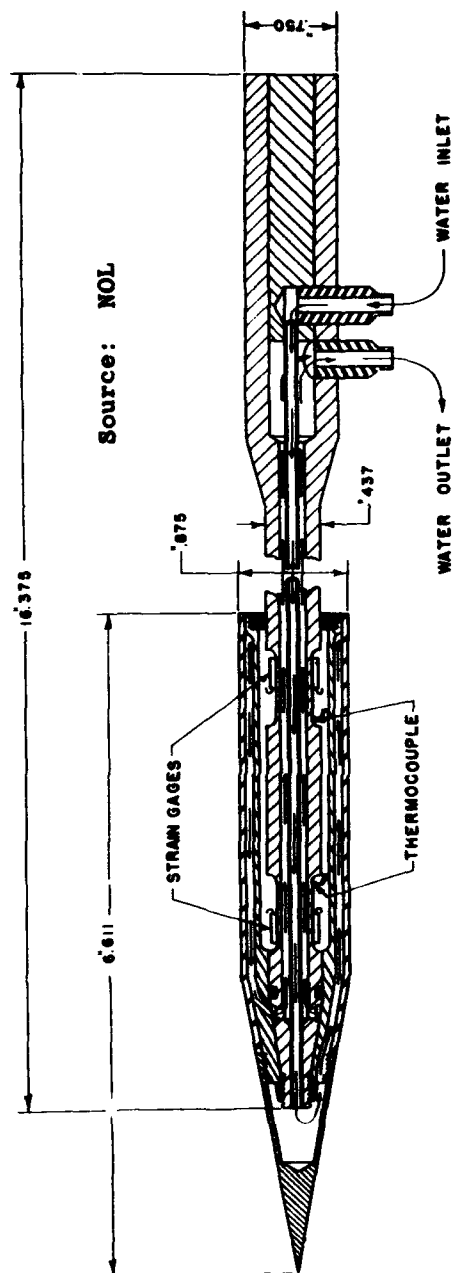


Fig. 3-6. Temperature-controlled strain-gage balance and model.

Source: NOL

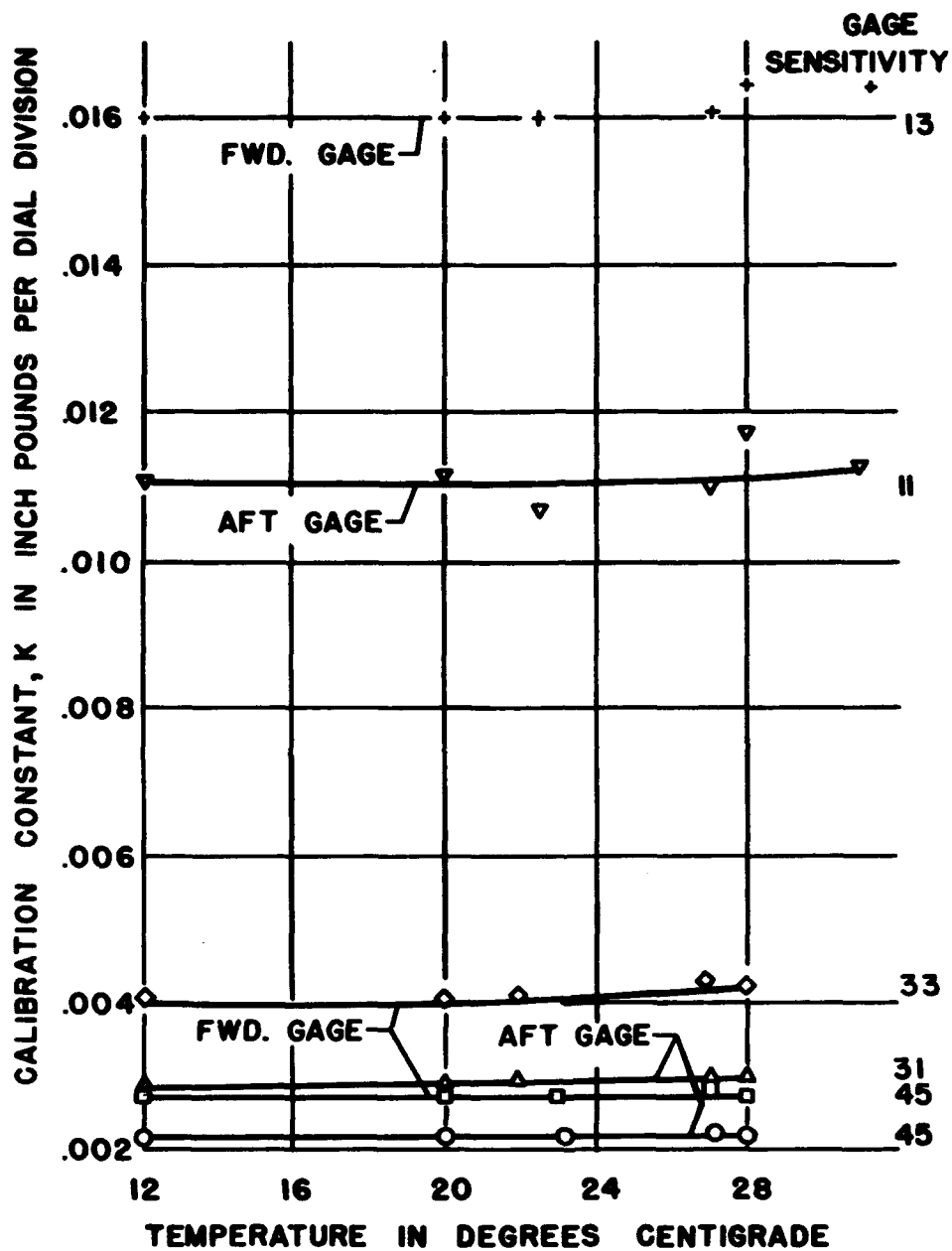


Fig. 3-7. Calibration constant, K, vs gage temperature; temperature-controlled balance.

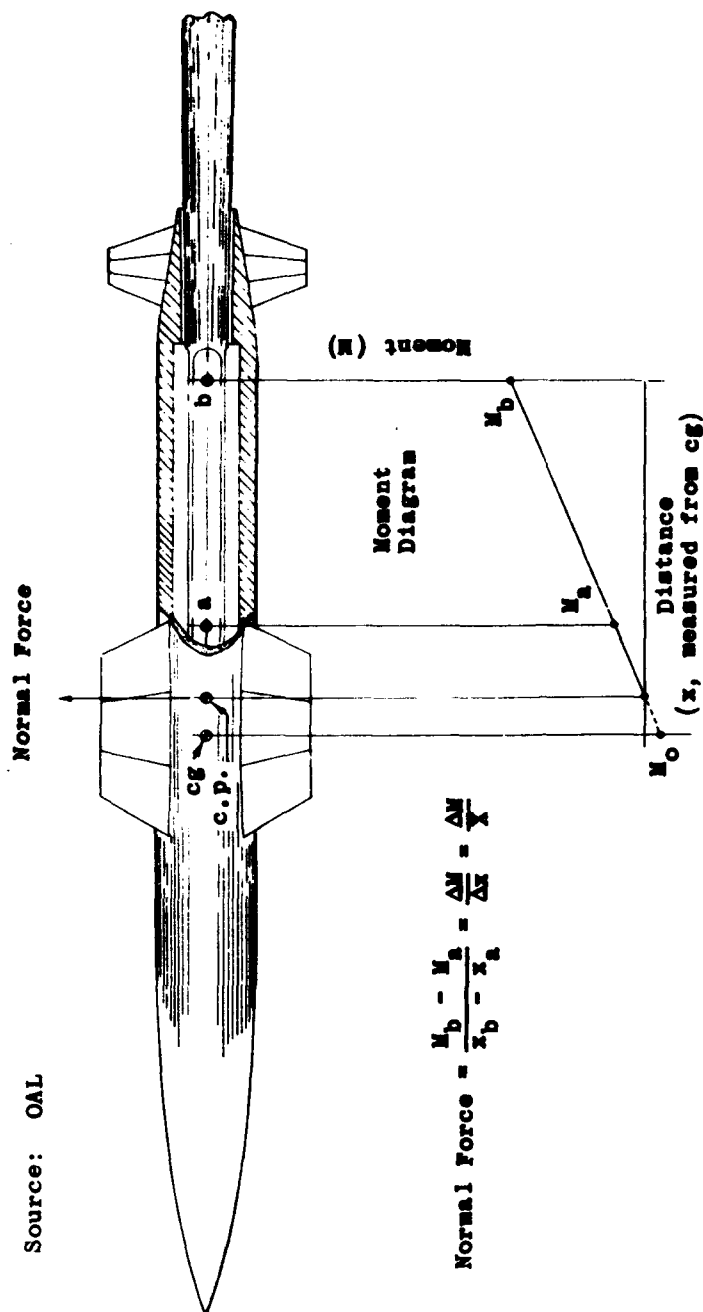


Fig. 3-8. Method of reducing moment data.

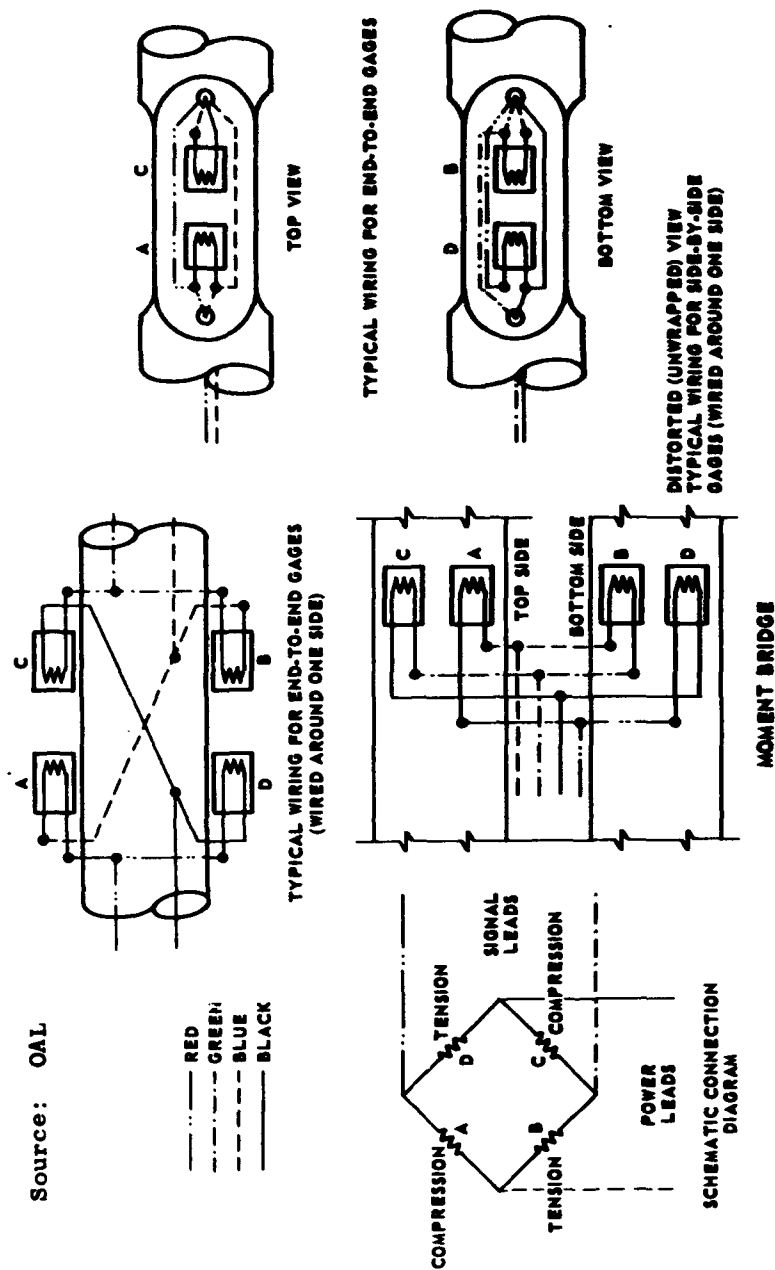


Fig. 3-9. Schematic diagram of differential moment (direct normal force) bridge, showing method for wiring electrical strain-gage circuits.

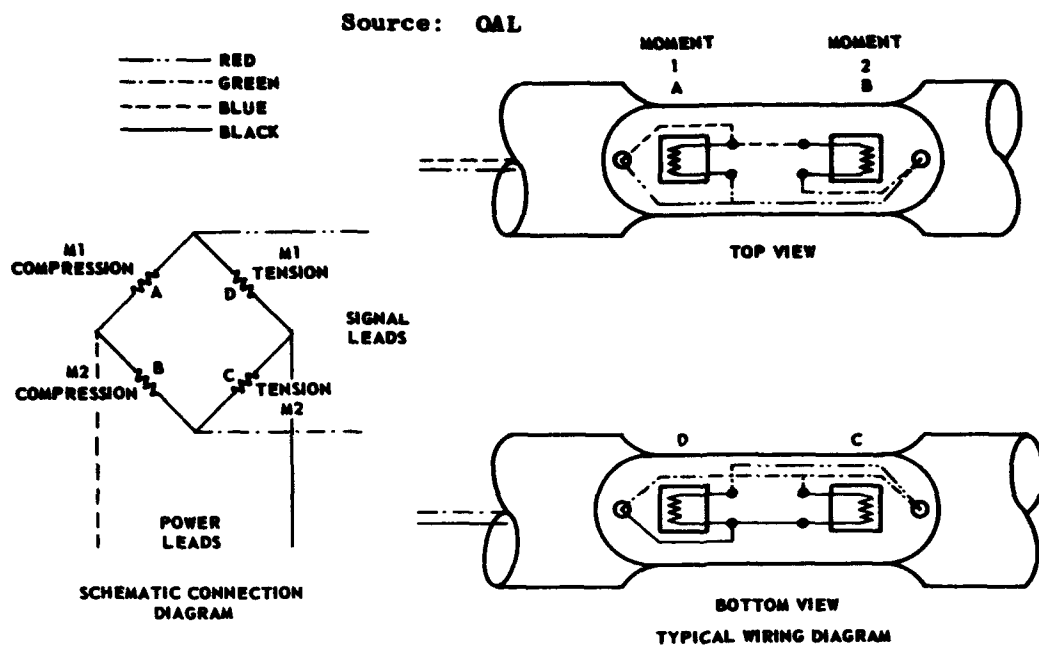


Fig. 3-10. Schematic diagram of differential moment (direct normal force) bridge, showing method for wiring electrical strain-gage circuits.

Source: OAL

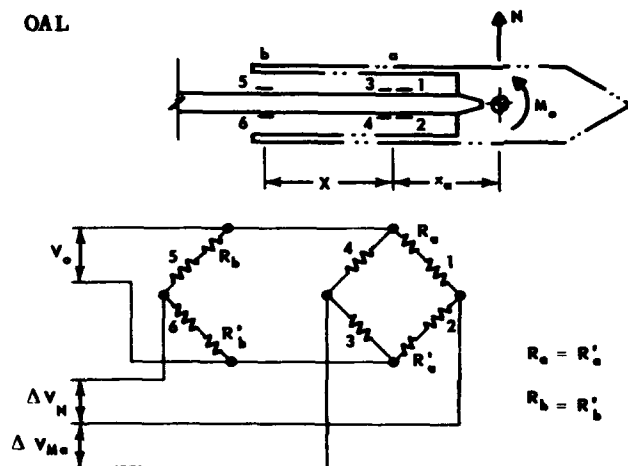
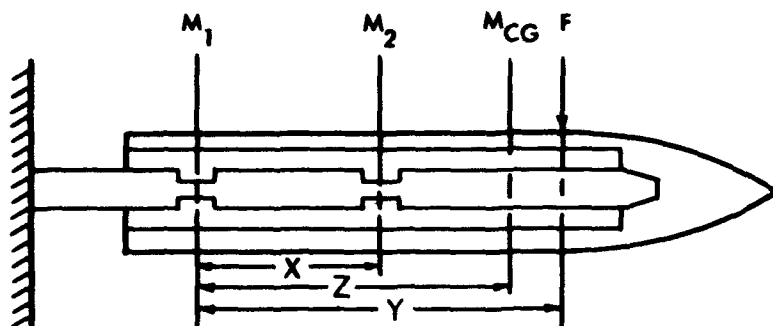


Fig. 3-11. Gage location and wiring diagram; composite bridge.



Source: OAL

Fig. 3-12. Errors due to strain-gage location.

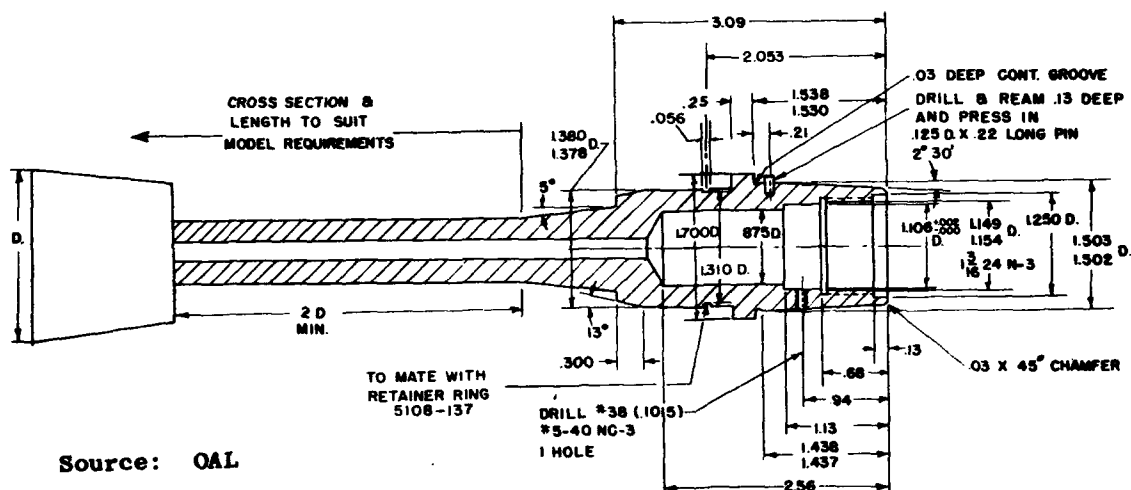


Fig. 3-13. Typical internal balance, showing standard taper seat.

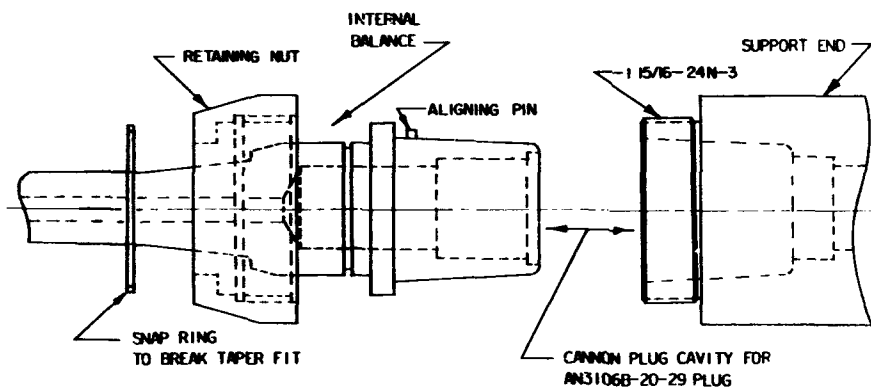
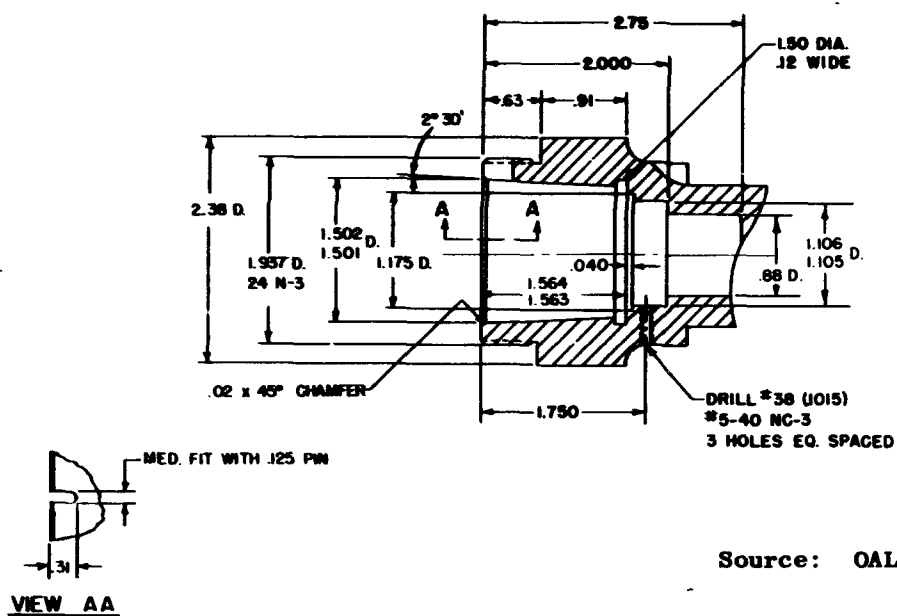
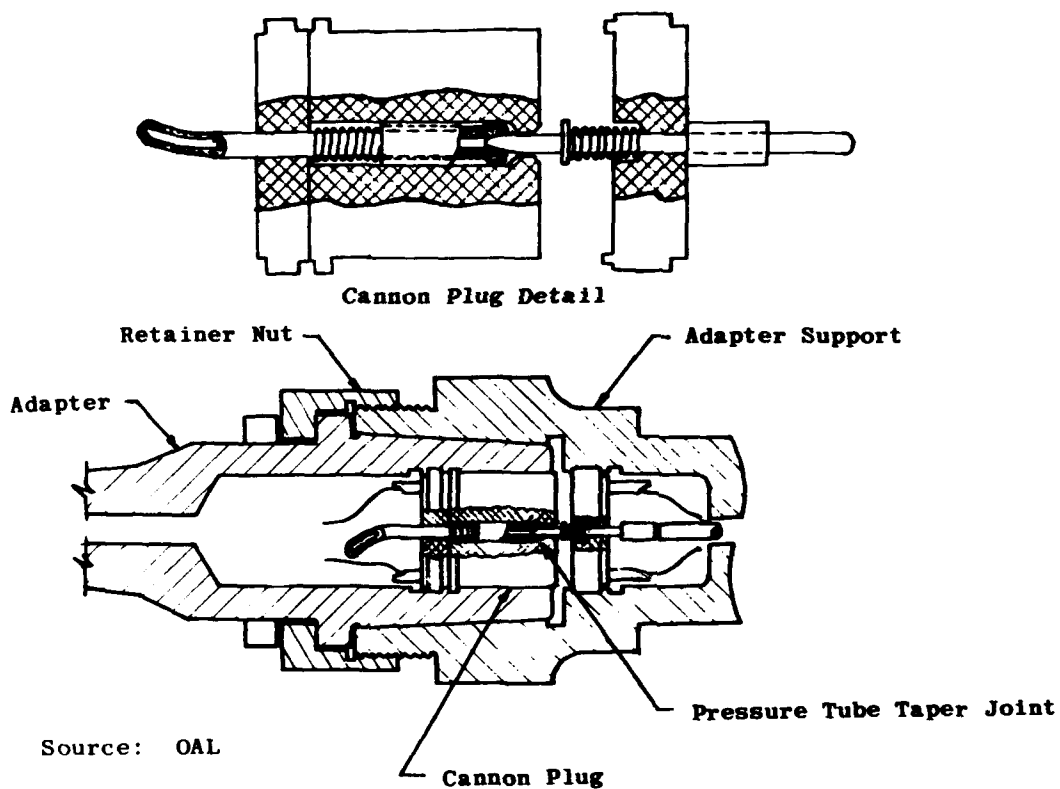


Fig. 3-14. Internal balance-support connection, showing tapered seat method.

Source: OAL



Fig. 3-15. Cannon plug, showing base pressure lead.



Source: OAL

Fig. 3-16. Tapered-seat connection for support-adaptor with base pressure lead.

Source: OAL

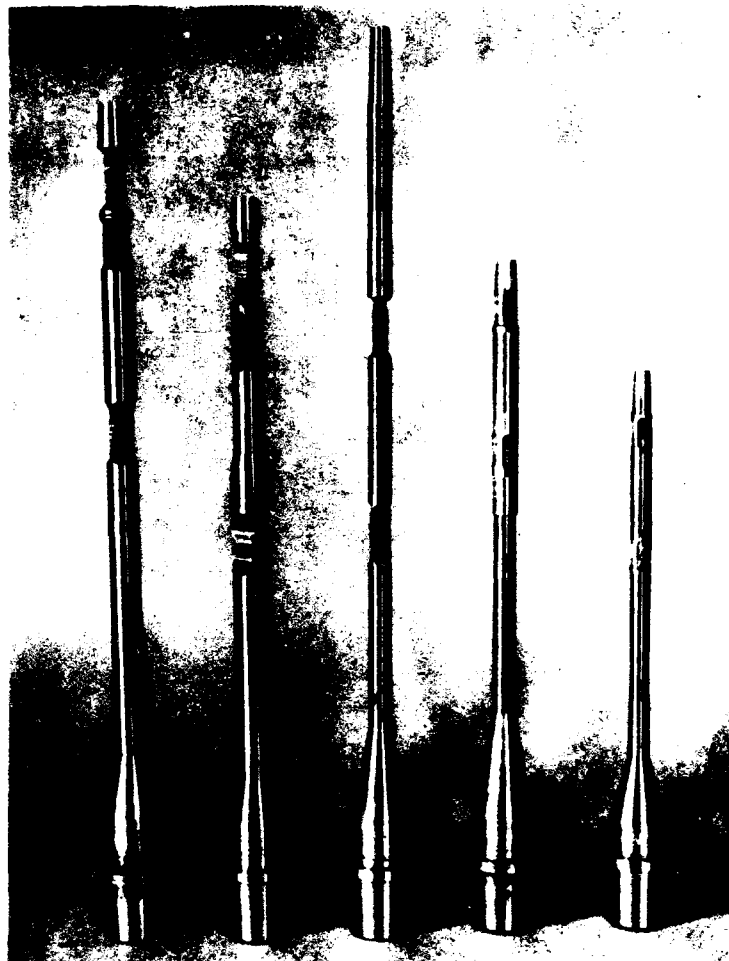
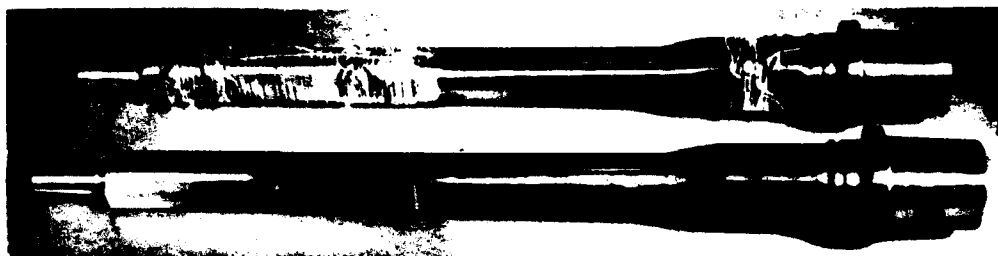


Fig. 3-17. Typical internal balances.

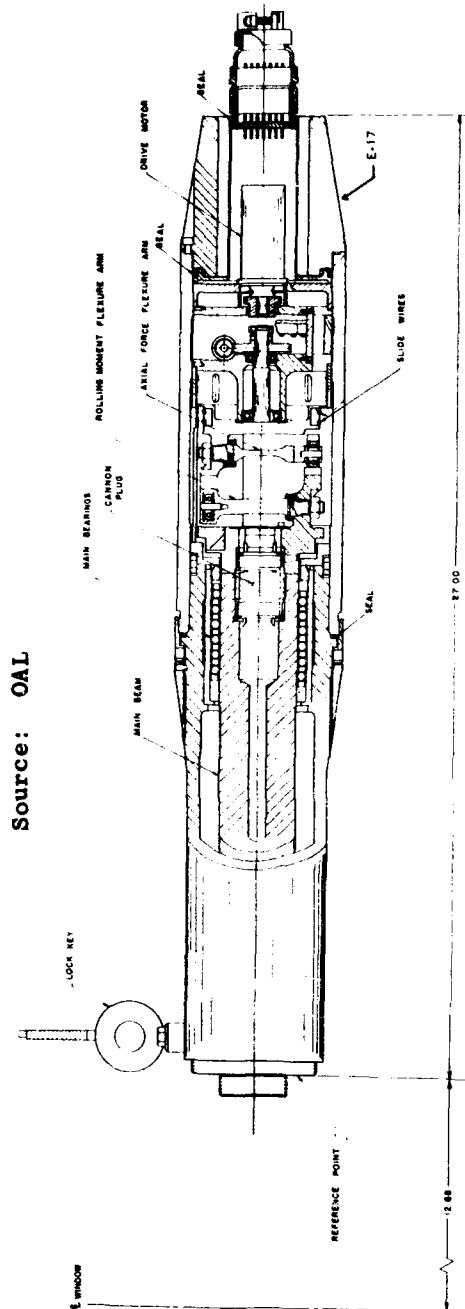


Fig. 3-18. Typical two-component roll-indexing support.

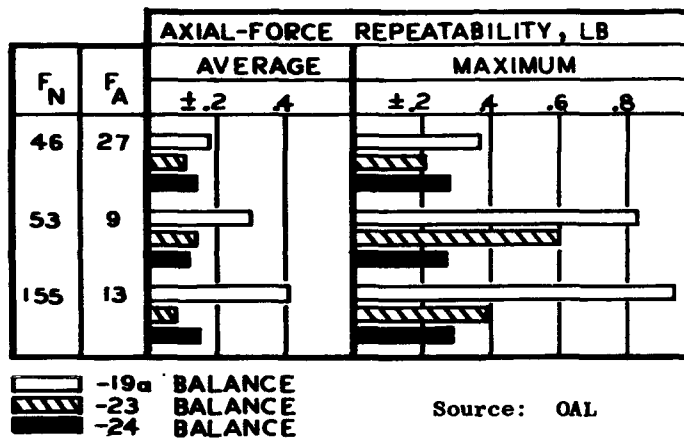
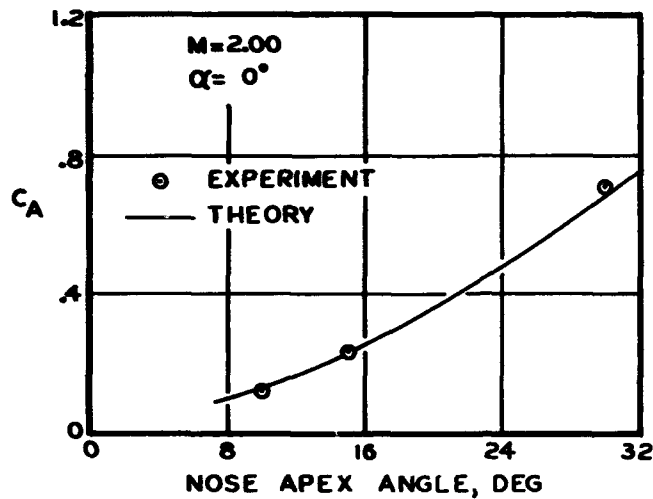


Fig. 3-19. Typical balance evaluation data.

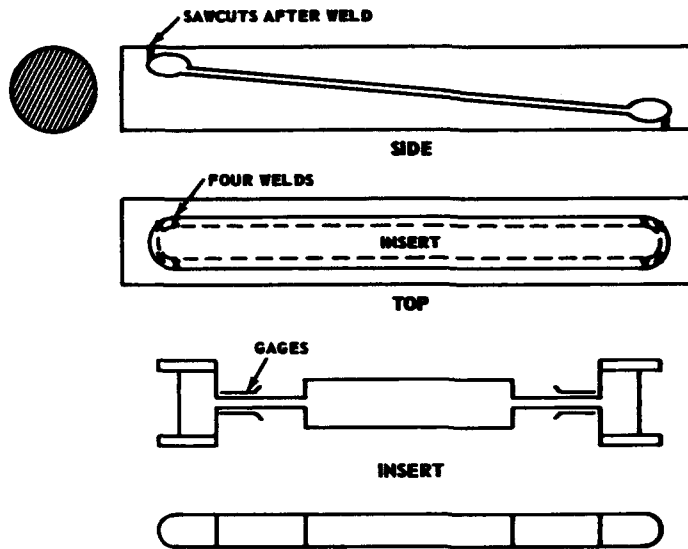


Fig. 3-20. Simple internal drag beam used at ABMA.

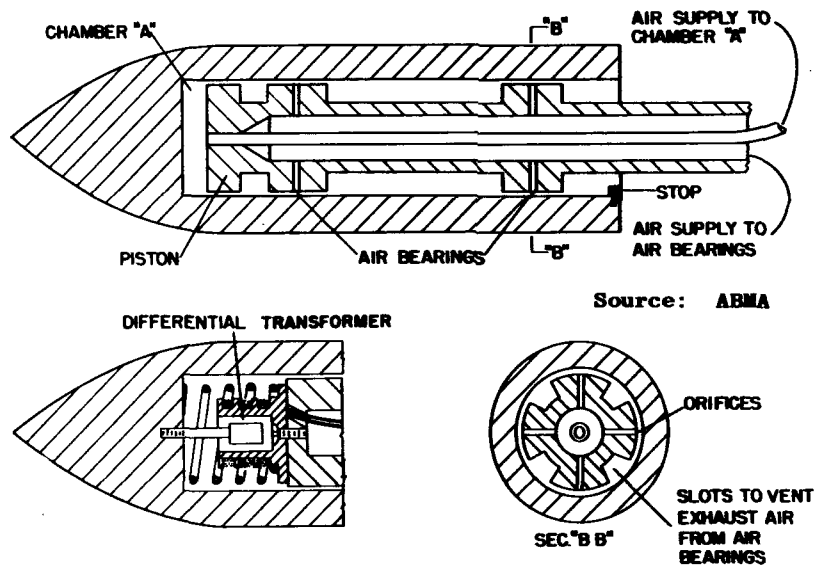
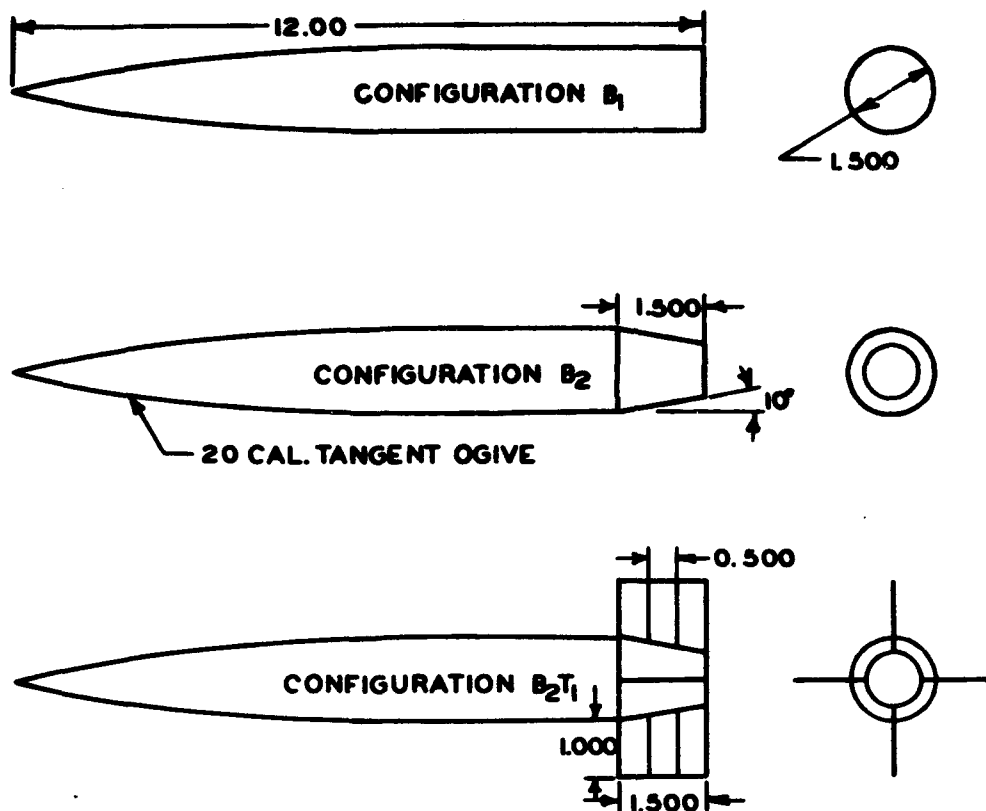


Fig. 3-21. Air-bearing drag balance.

Source: OAL



NOTE: TAIL SURFACES HAVE A SYMMETRICAL
DOUBLE WEDGE CROSS-SECTION WITH
A 6-PERCENT THICKNESS RATIO

Fig. 3-22. Models used in windshield-and-sting interference tests.

Source: OAL

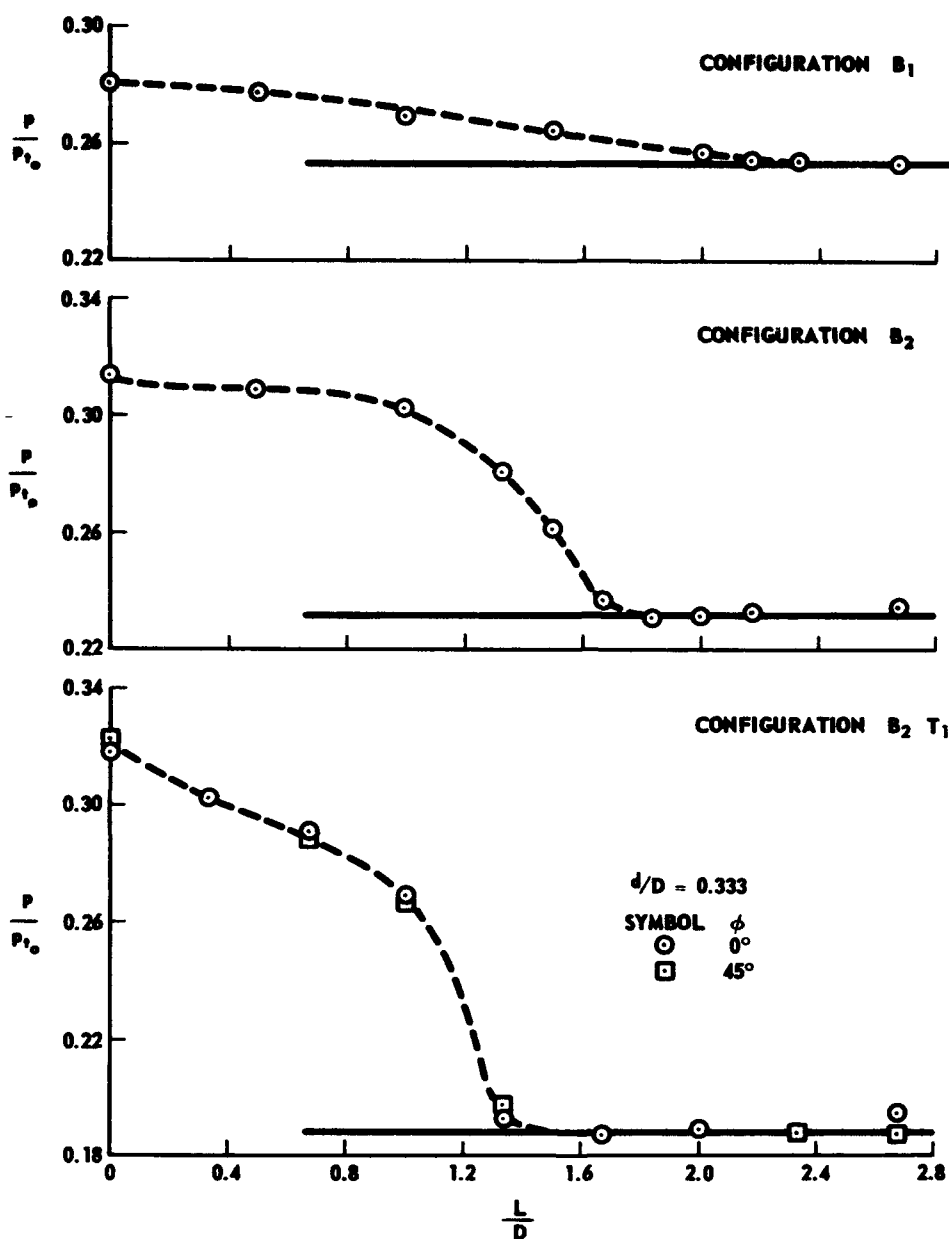


Fig. 3-23. Variation of afterbody pressure with windshield distance for a 20-deg half-angle windshield at Mach number 1.50 and at zero angle of attack.

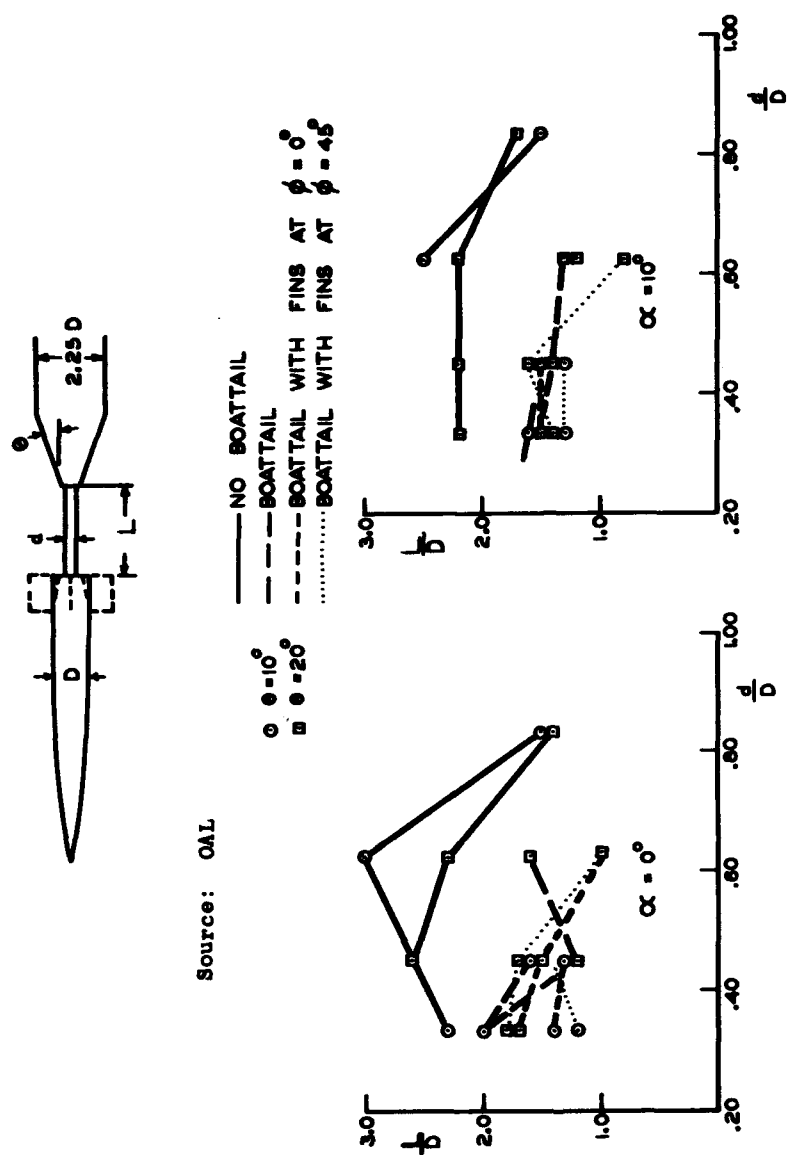
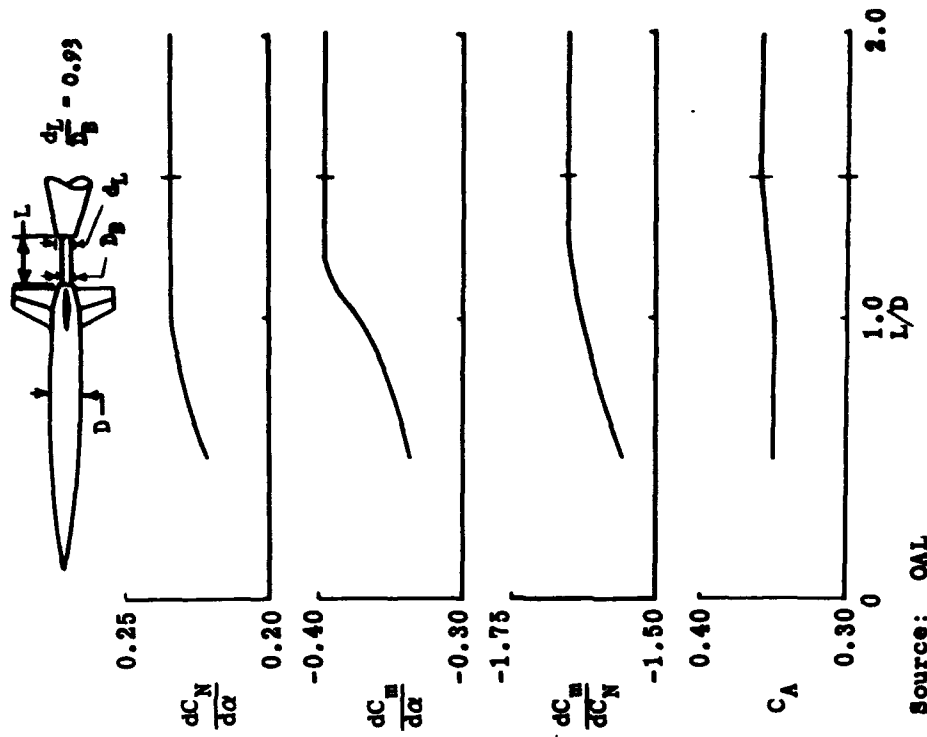
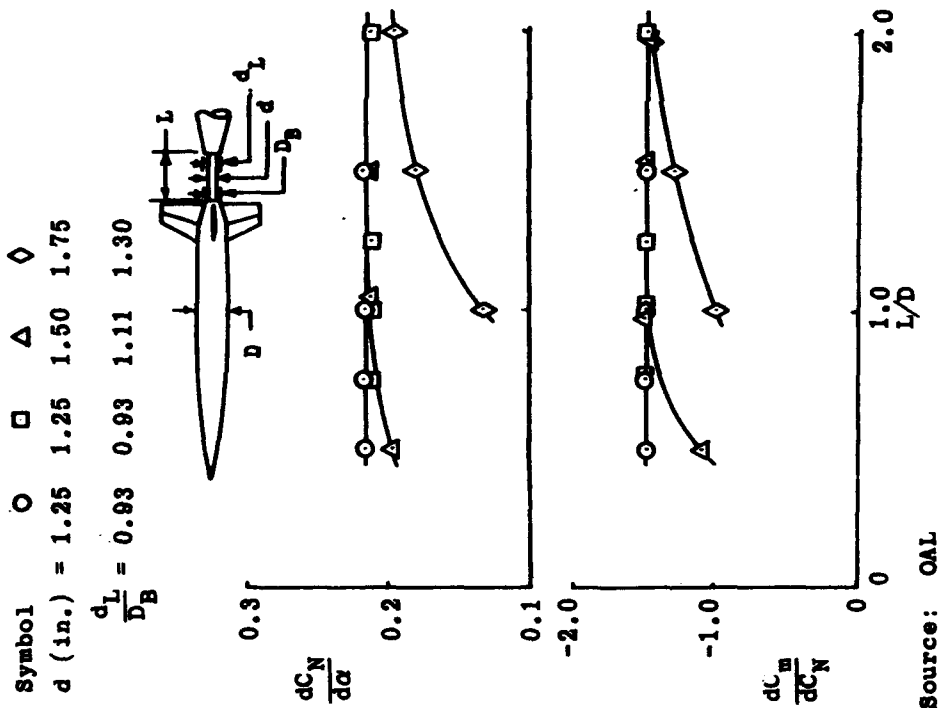


Fig. 3-24. Distance from model base at which windshield affects model base pressures at Mach 1.50.



Source: OAL

Fig. 3-26. Effect of windshield clearance on aerodynamic characteristics; Mach number 1.73.



Source: OAL

Fig. 3-25. Effect of windshield lip diameter on slopes of the normal force; stability curves at Mach number 2.00.

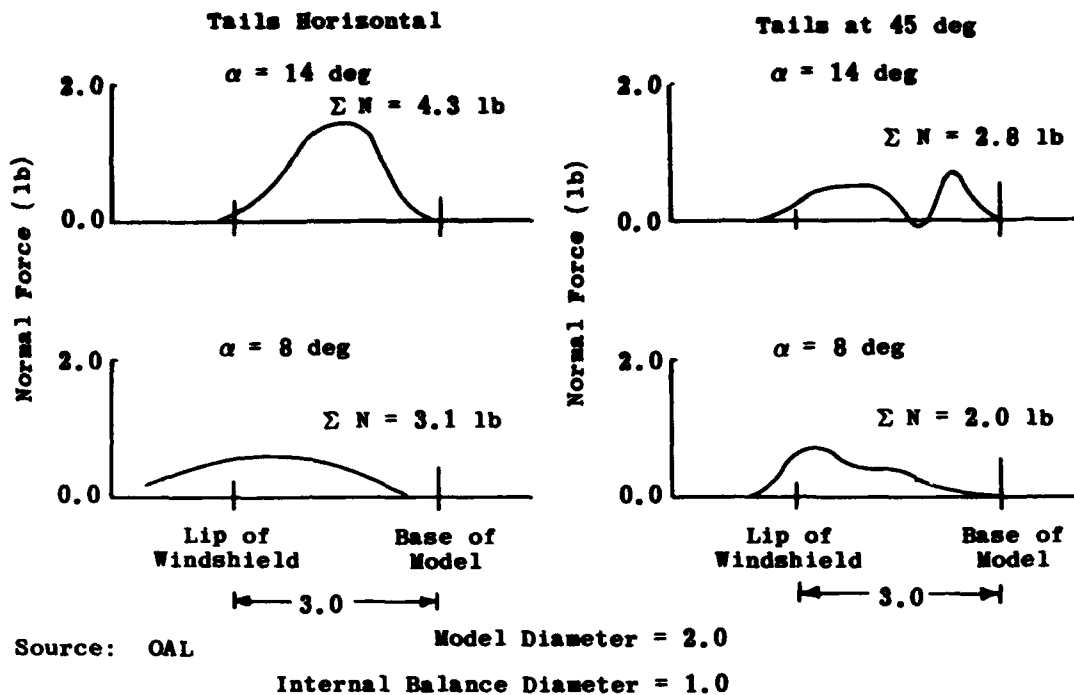
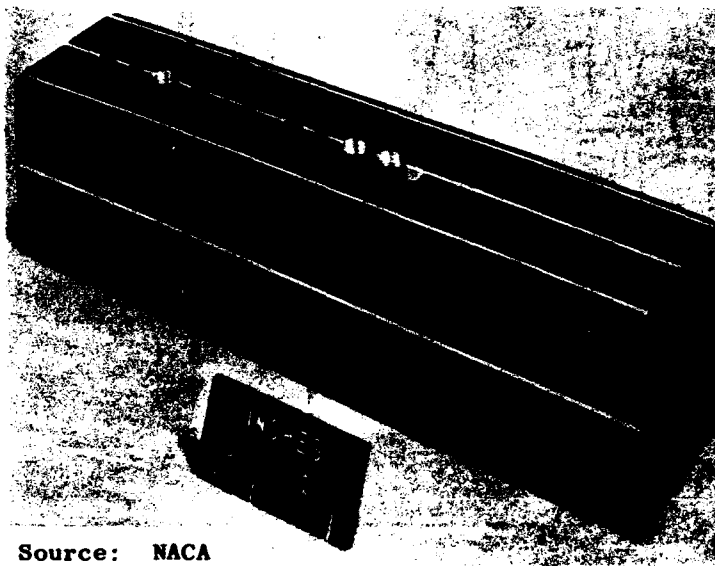


Fig. 3-27. Normal force distribution along exposed portion of the internal balance, using a typical cruciform body-tail configuration at a free-stream Mach number of 1.73.



Source: NACA

Fig. 3-28. Typical fixture for calibrating internal sting-supported balances.

Source: NACA

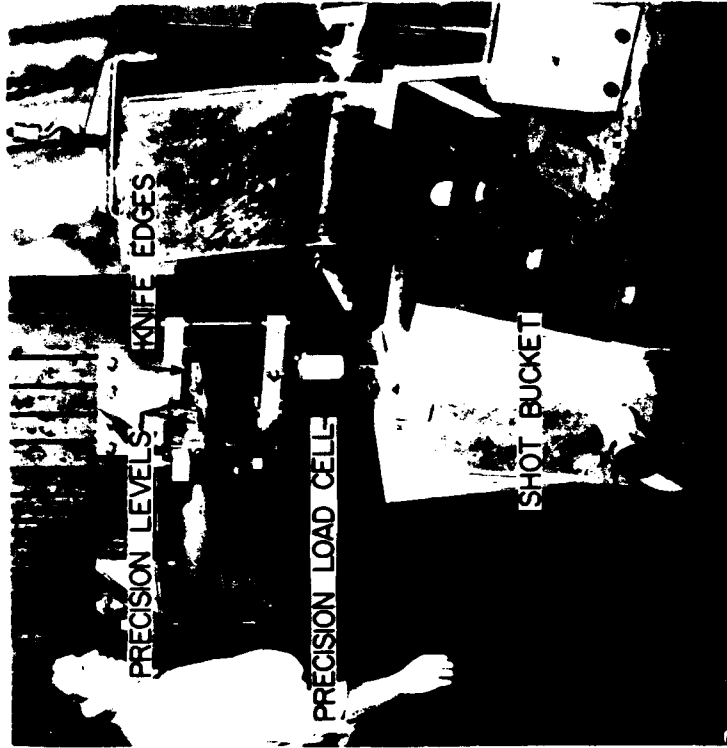


Fig. 3-30. Dead-weight calibration loading system utilizing shot.

Source: NACA

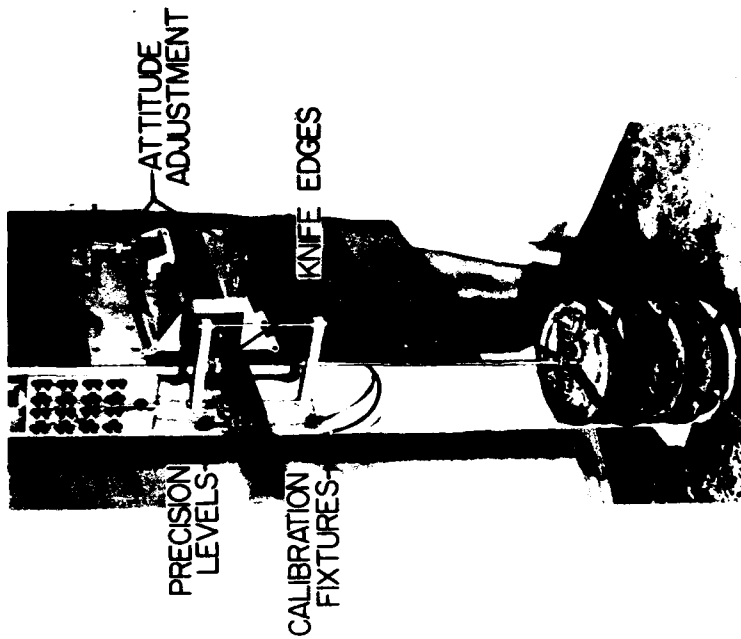


Fig. 3-29. Dead-weight calibration loading system.

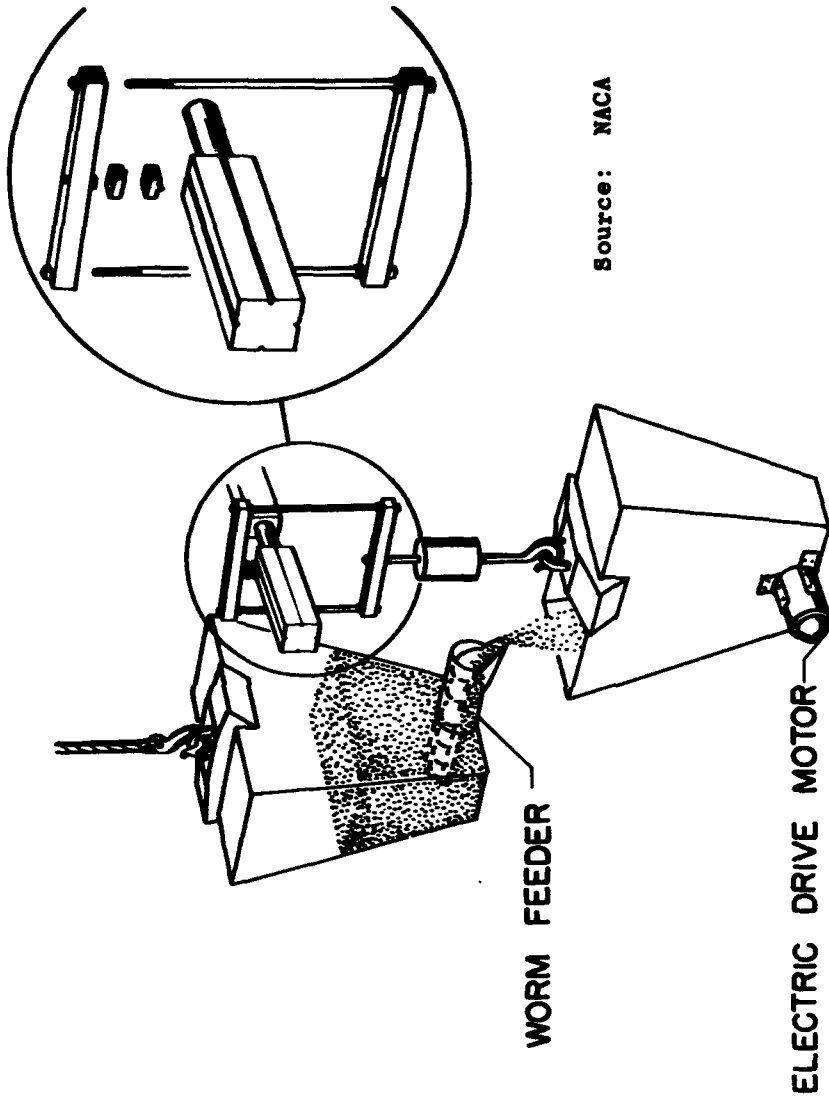


Fig. 3-31. Semi-automatic shot loader.

Source: NACA



Fig. 3-33. Calibration system utilizing jack and load cell.



Fig. 3-32. Dead-weight calibration system utilizing long-arm fixtures.

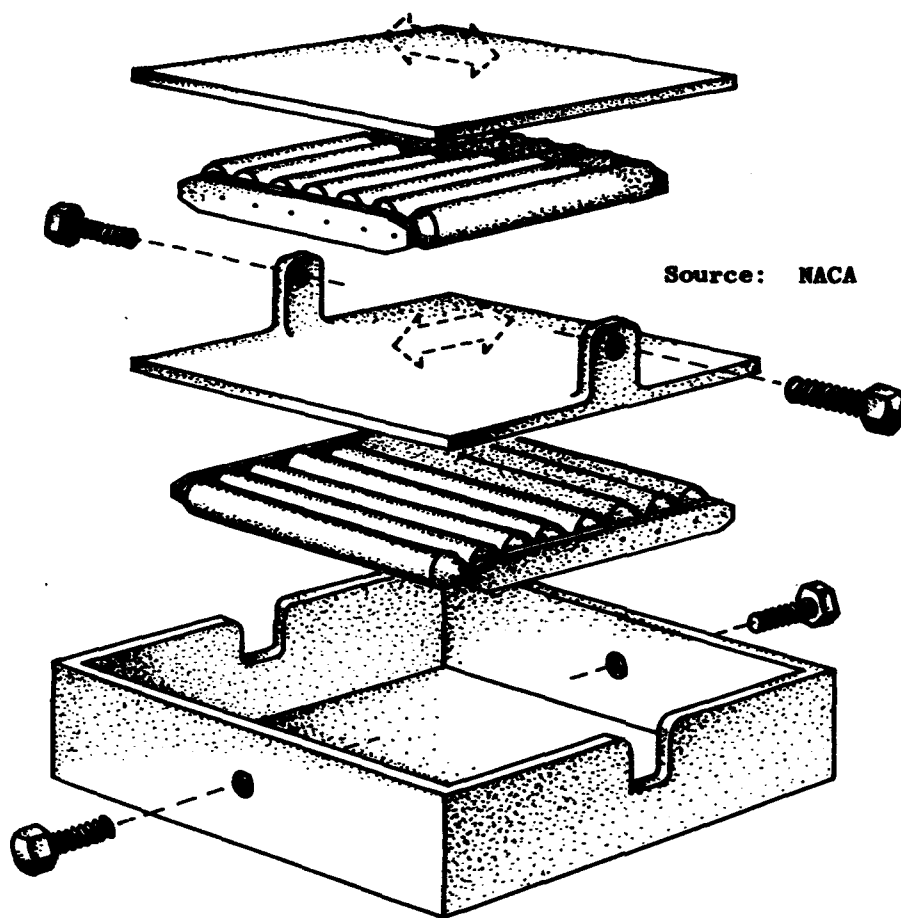


Fig. 3-34. Roller box.

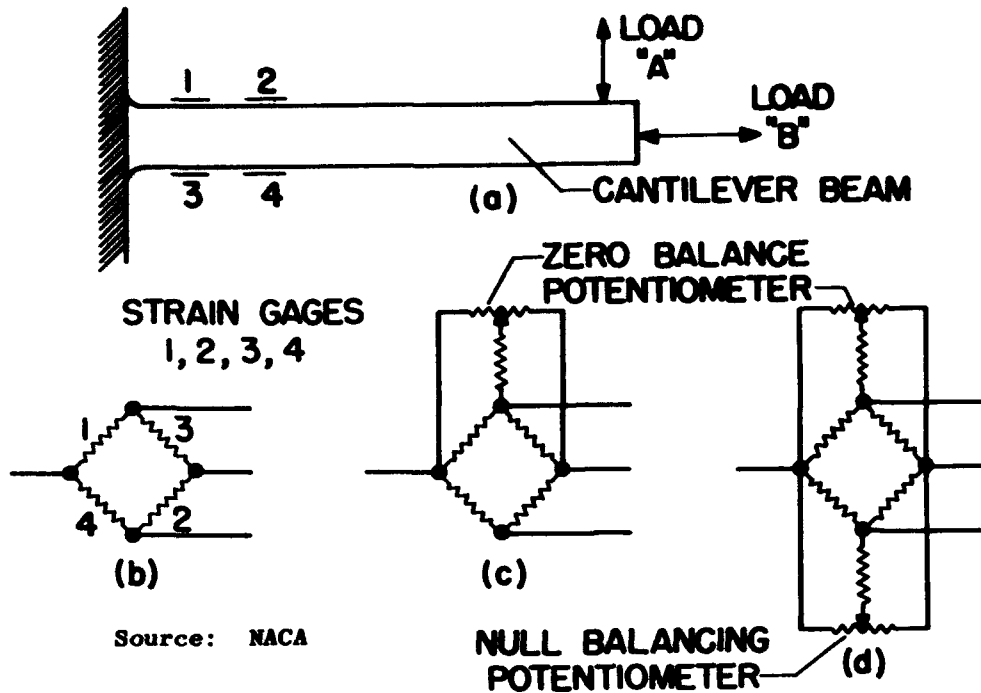


Fig. 3-35. Method of measuring one load in the presence of another.

- INCREMENTAL NORMAL FORCE (N) LOADINGS MADE AT $x=y=0$;
- △ INCREMENTAL PITCHING MOMENT (m) LOADINGS MADE BY MOVING ± 0.1 N FROM $x=0$ TO $x=(+)$;
- INCREMENTAL PITCHING MOMENT (m) LOADINGS MADE BY MOVING ± 0.1 N FROM $x=0$ TO $x=(-)$;
- ◆ INDICATES LOADING MADE IN PRESENCE OF FULL CONSTANT $\pm N$.

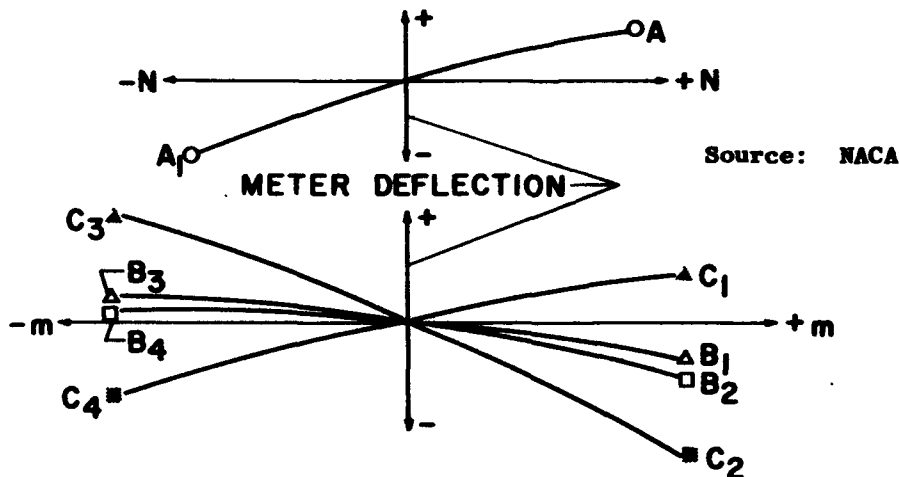


Fig. 3-36. Typical calibration data plot.

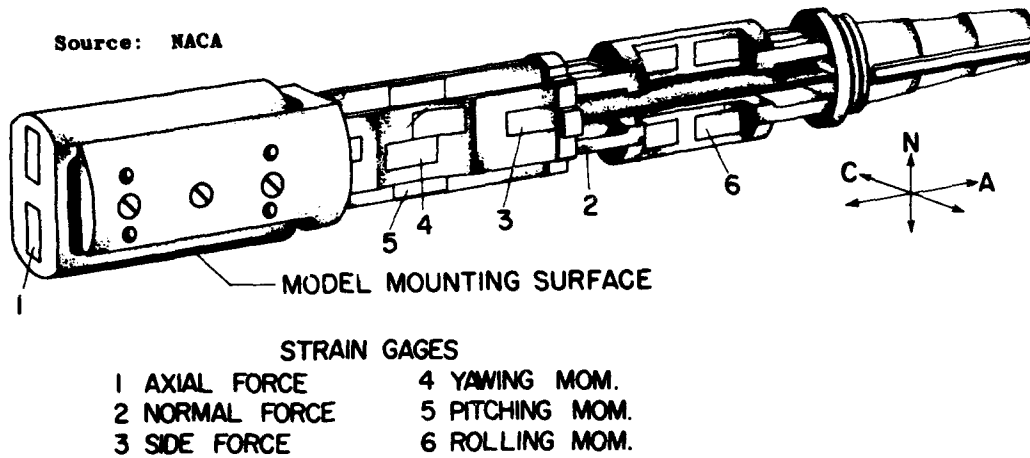


Fig. 3-37. Typical six-component, wire strain-gage balance.

Source: OAL

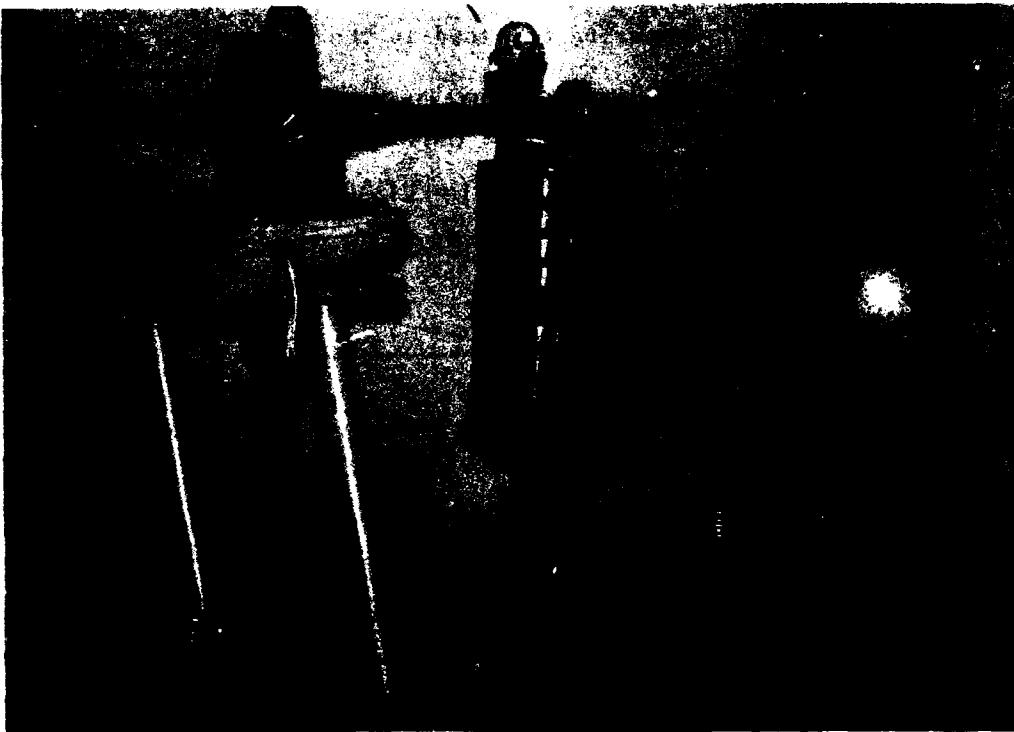


Fig. 3-38. Internal balance calibration fixture.

Source: OAL

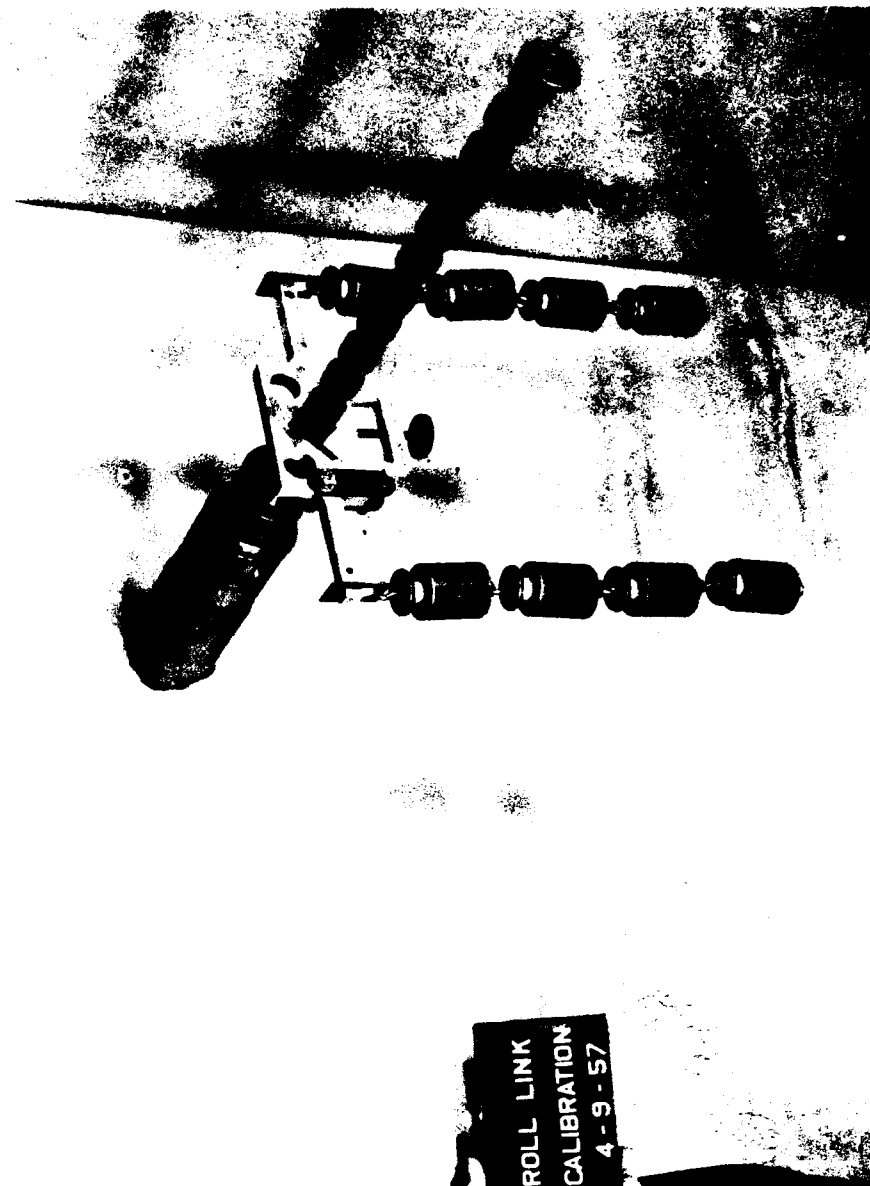


Fig. 3-39. Rolling-moment calibration rig.

Source: OAL

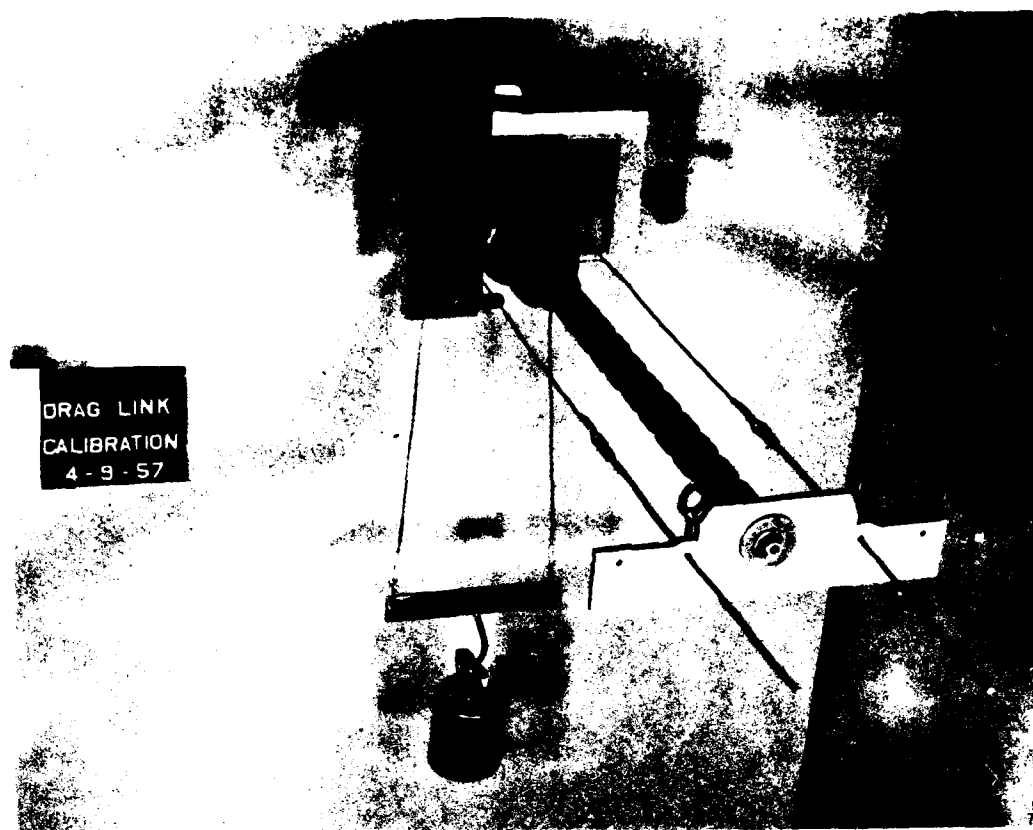
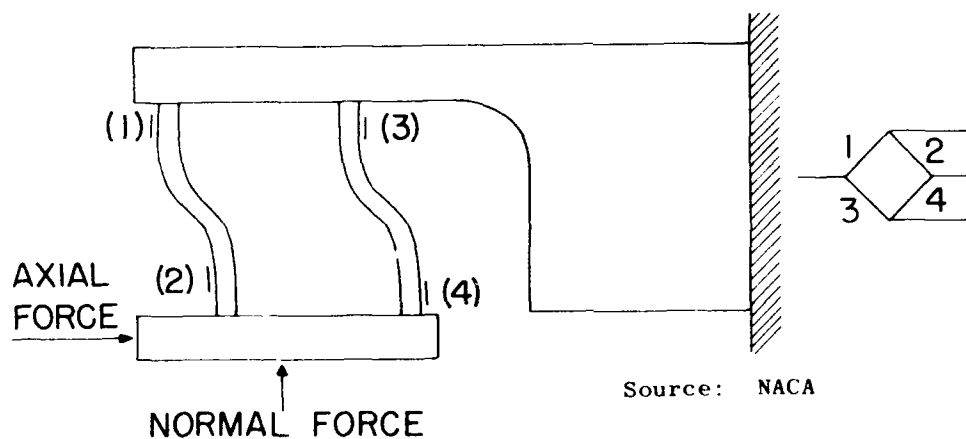


Fig. 3-40. Axial-force calibration rig.



Source: NACA

Fig. 3-41. Axial-force measuring section.

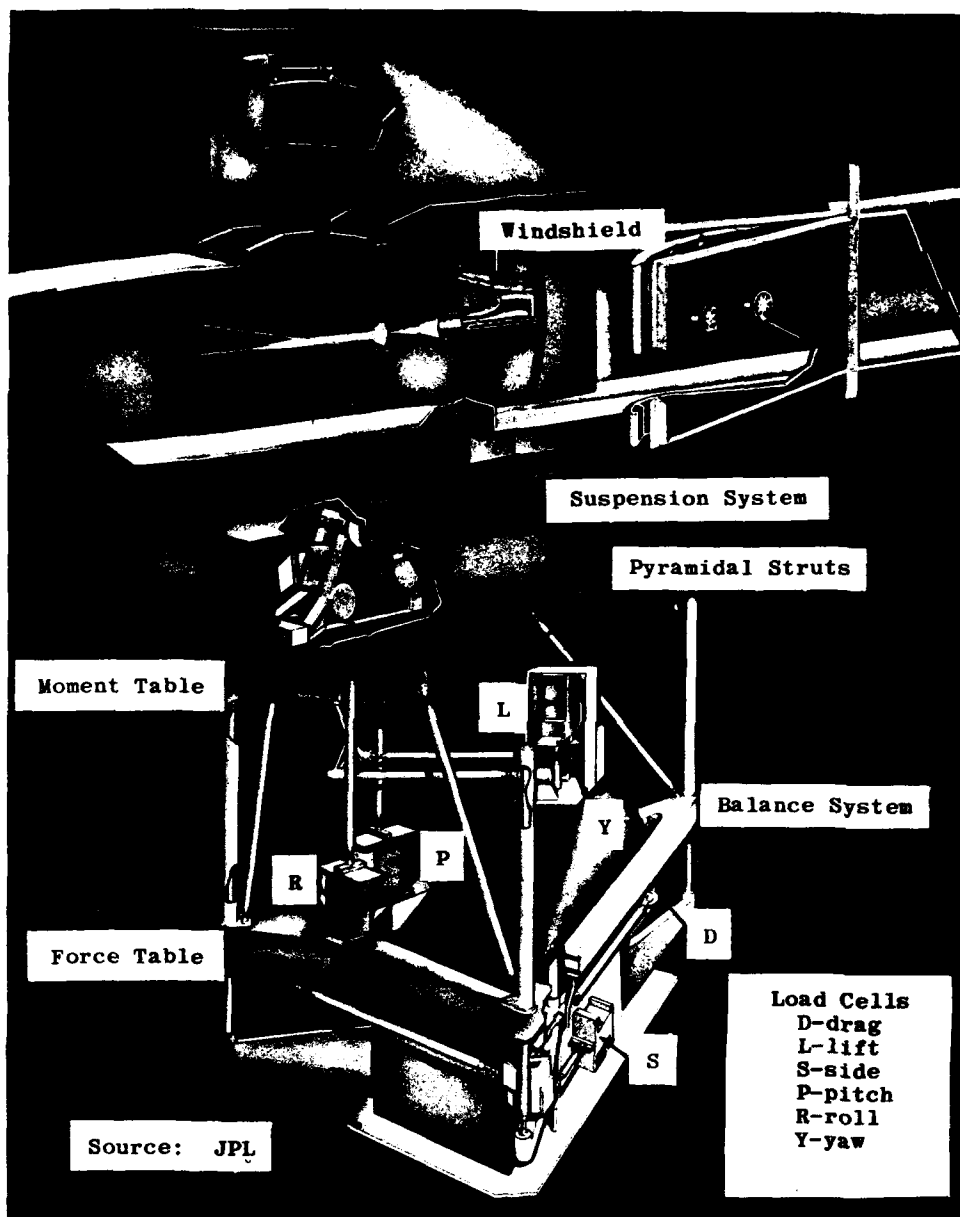


Fig. 3-42. JPL balance and suspension system.

Source: JPL

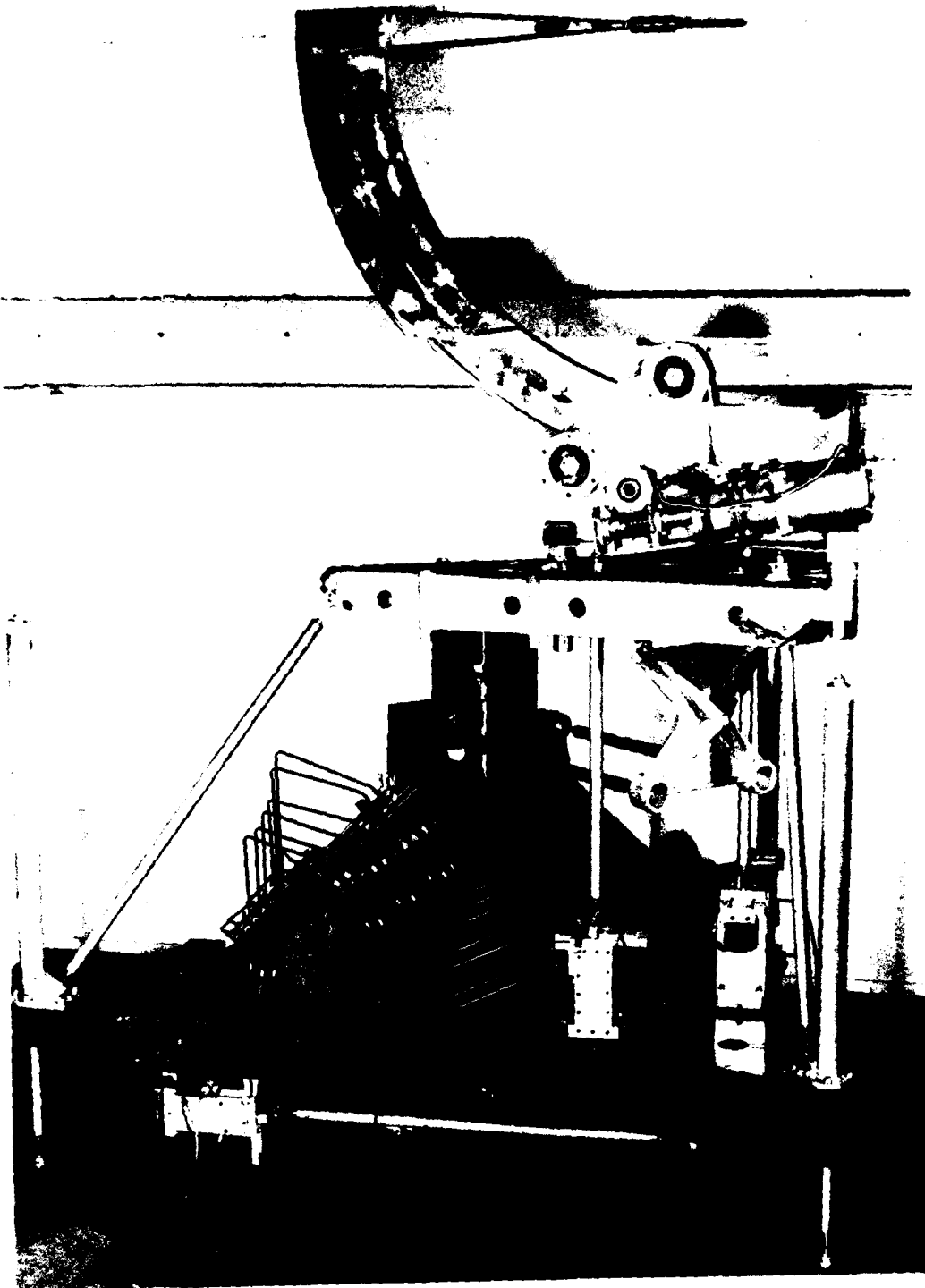


Fig. 3-43. JPL six-component external balance.

Source: JPL

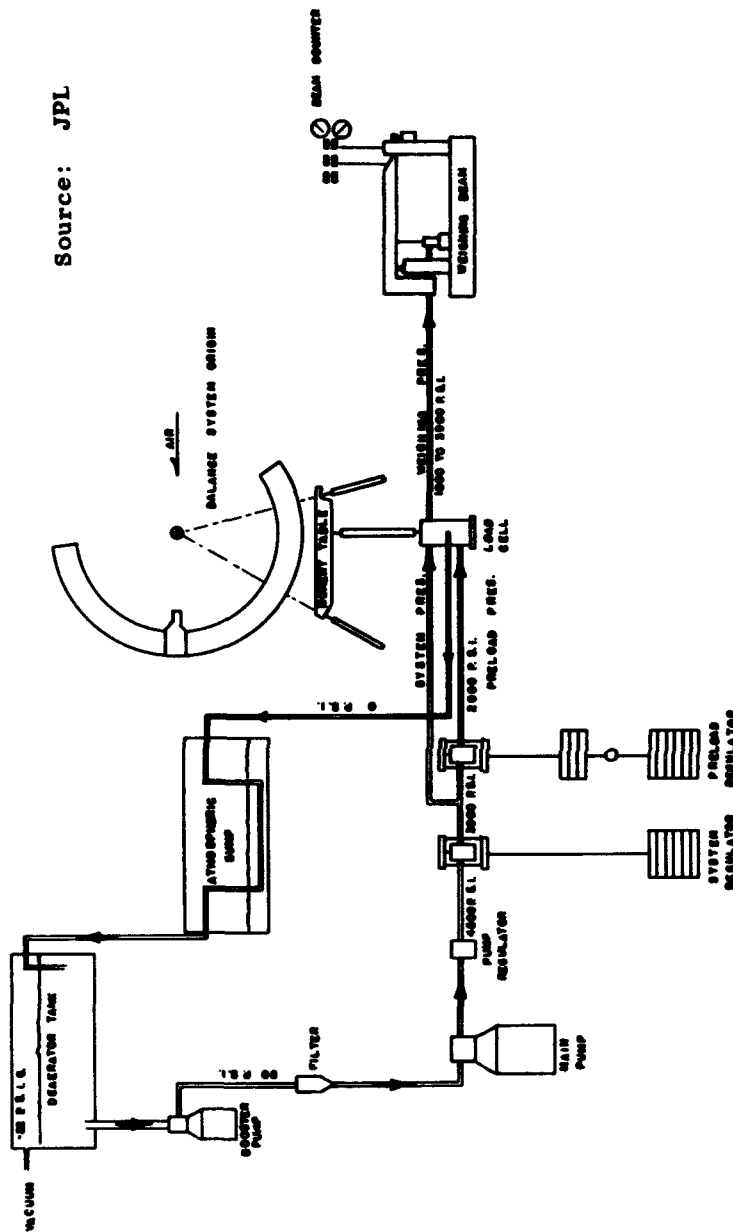
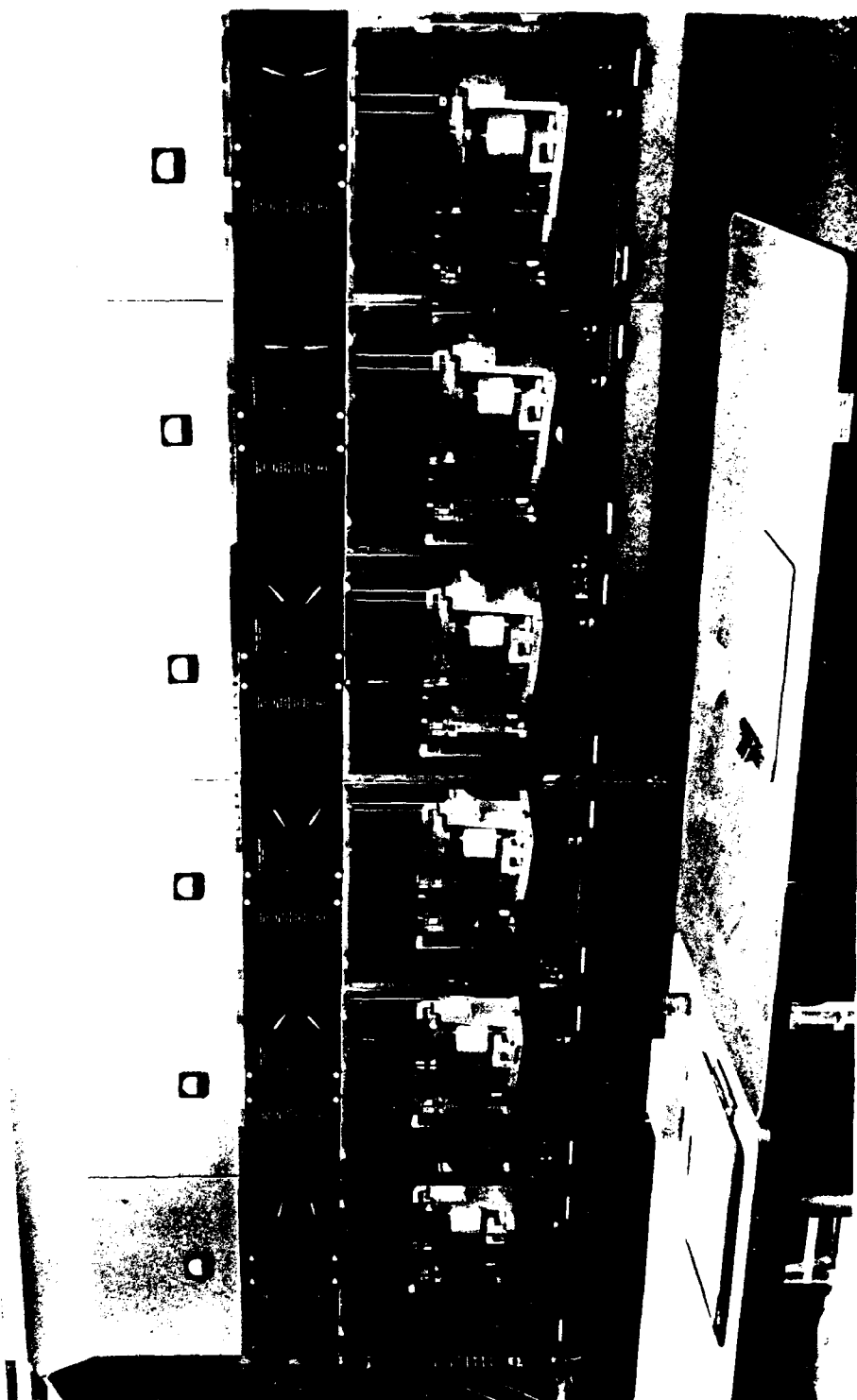
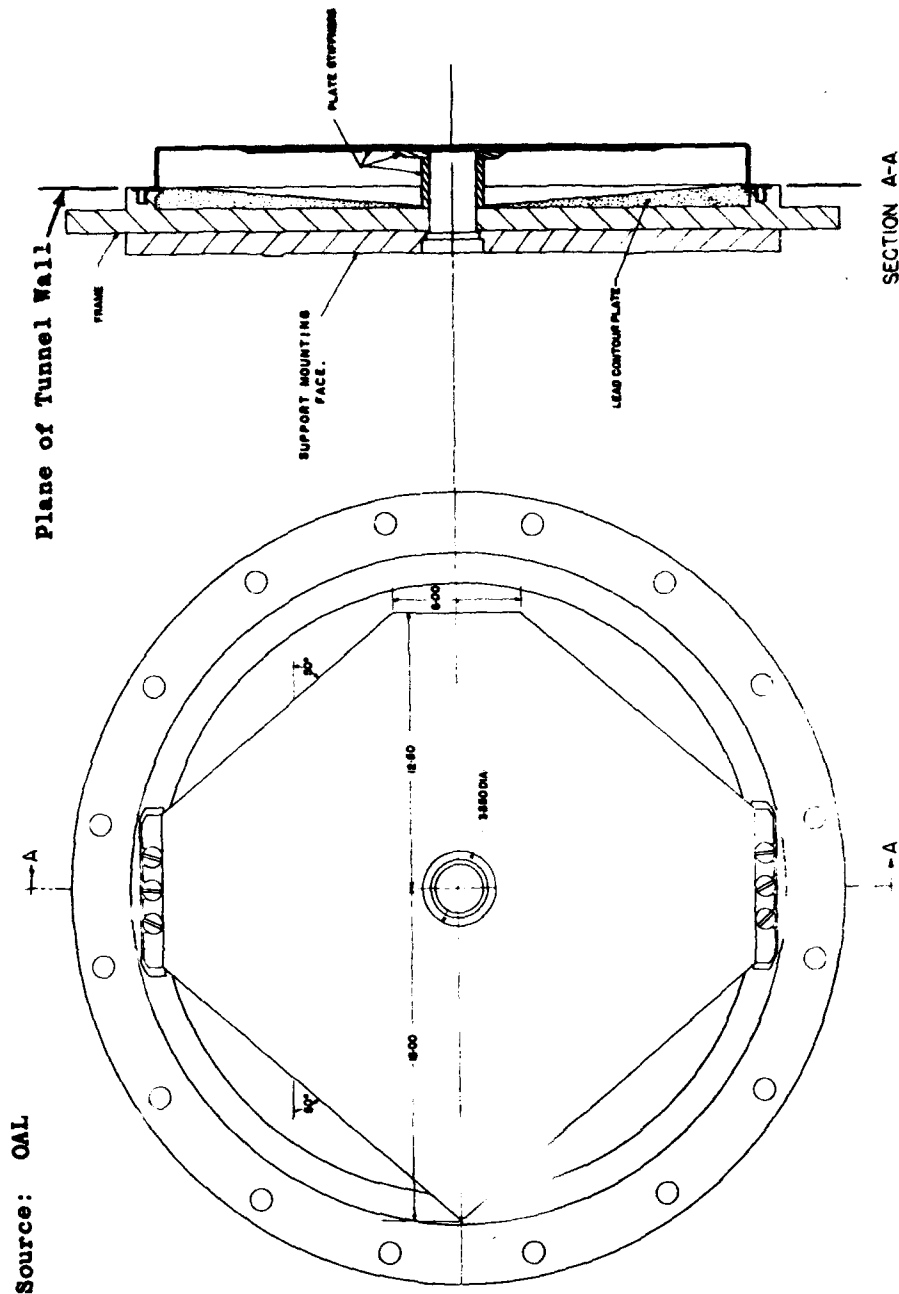


Fig. 3-44. Schematic diagram of JPL hydraulic system.





Source: OAL

Fig. 3-46. Typical reflection plate mounted in steel window.

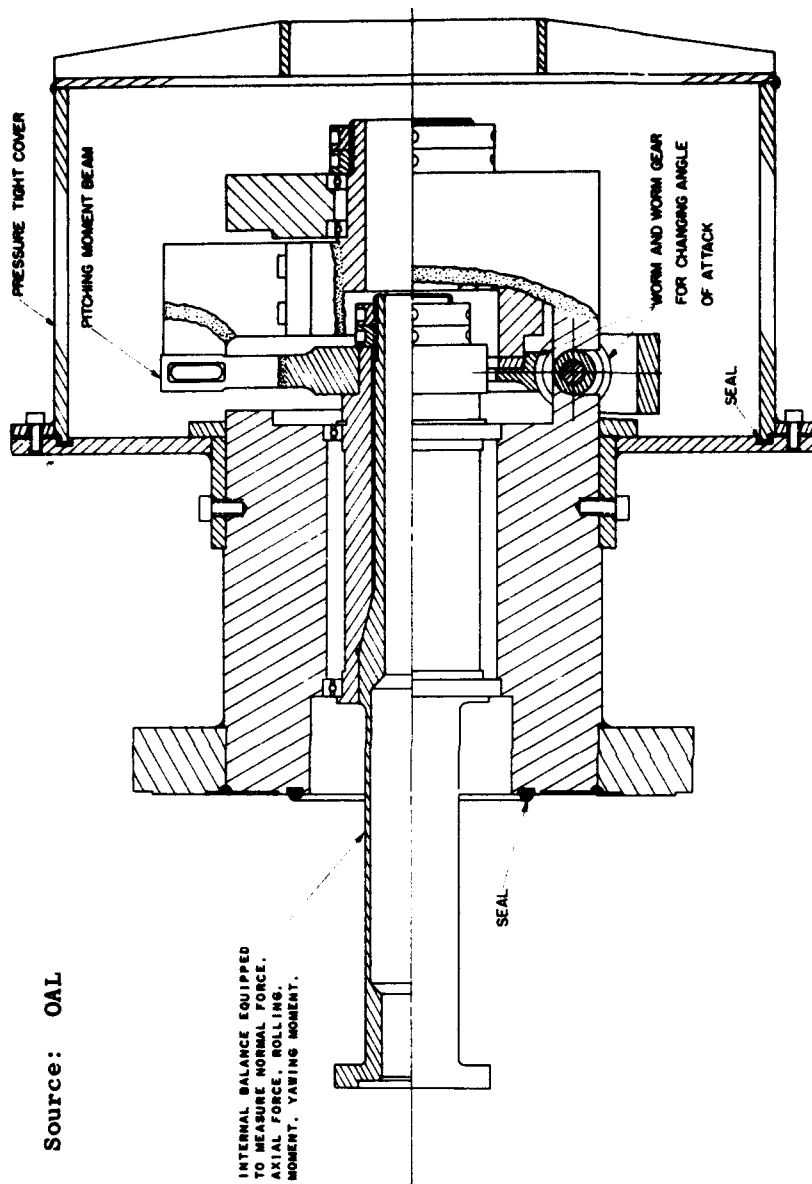


Fig. 3-47. Five-component side-wall balance.

Source: OAL

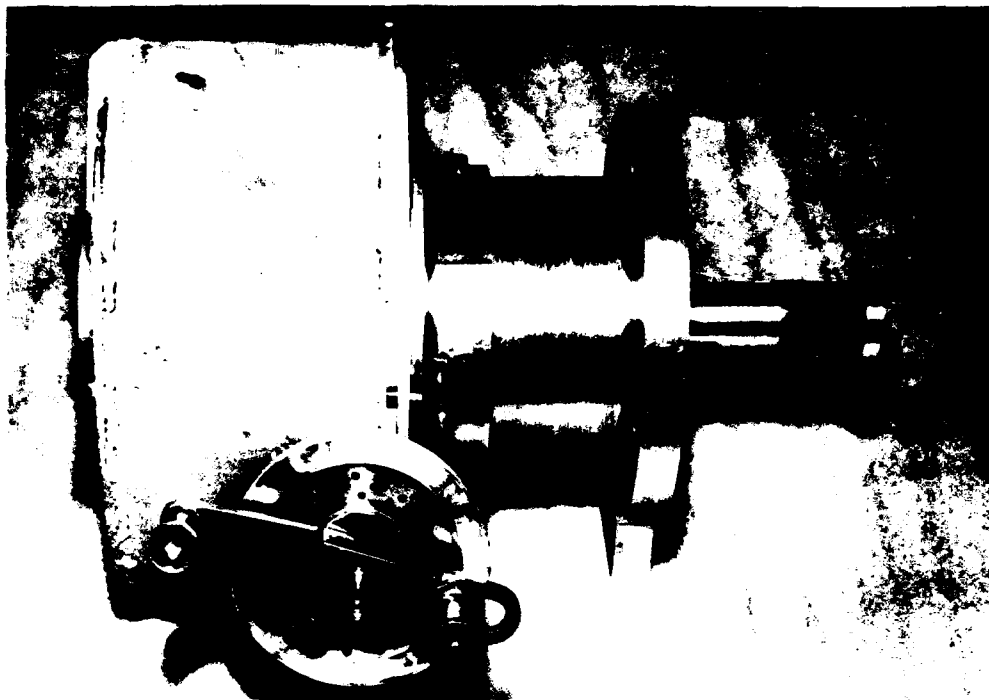


Fig. 3-48. Side view of five-component side-wall balance.

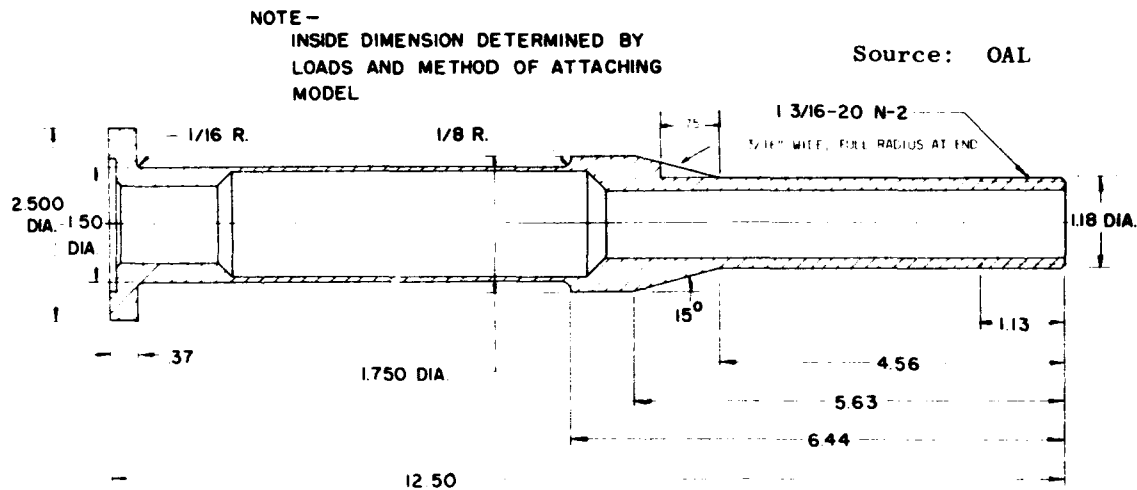


Fig. 3-49. Internal balance for five-component side-wall balance.

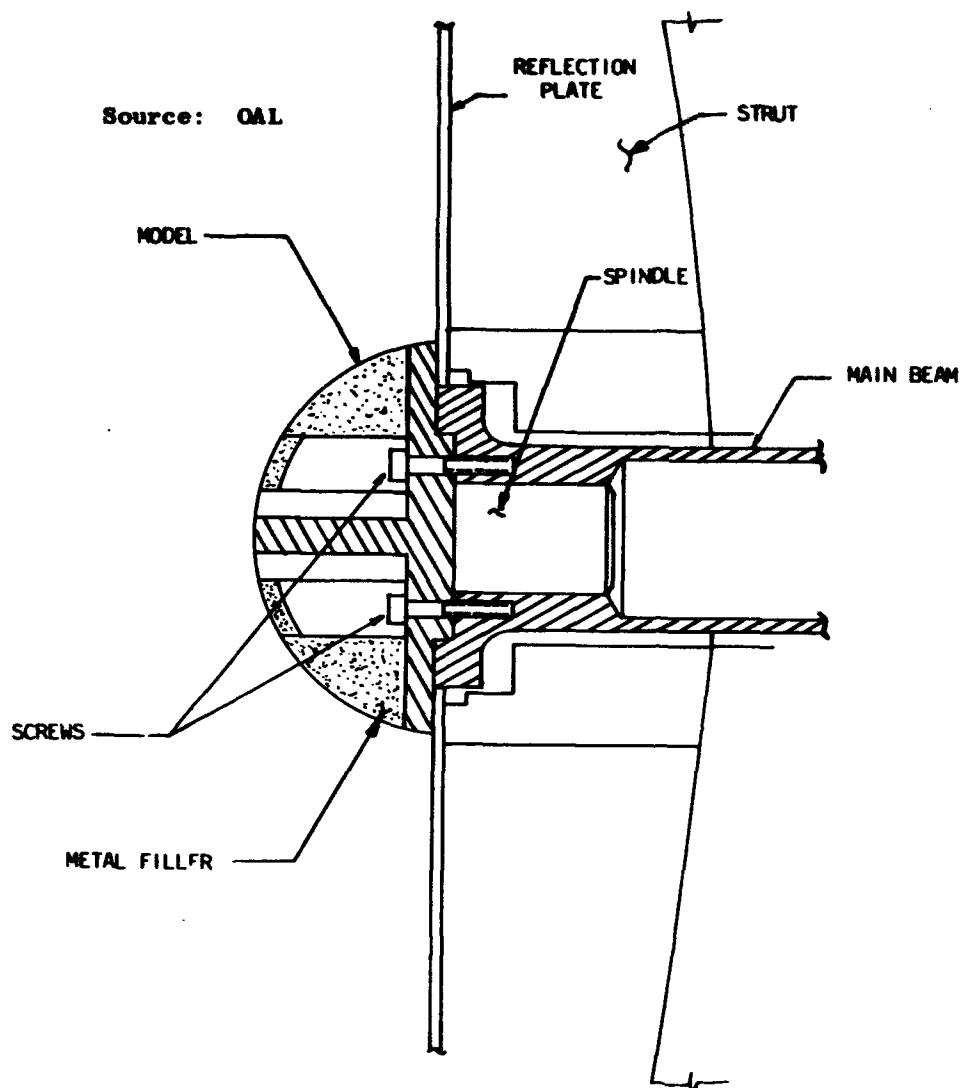


Fig. 3-50. Cross-section of half-model mounted on five-component side-wall balance.

Source: OAL



Fig. 3-51. Flexure-pivot wall-mounted support system, access hatch open.

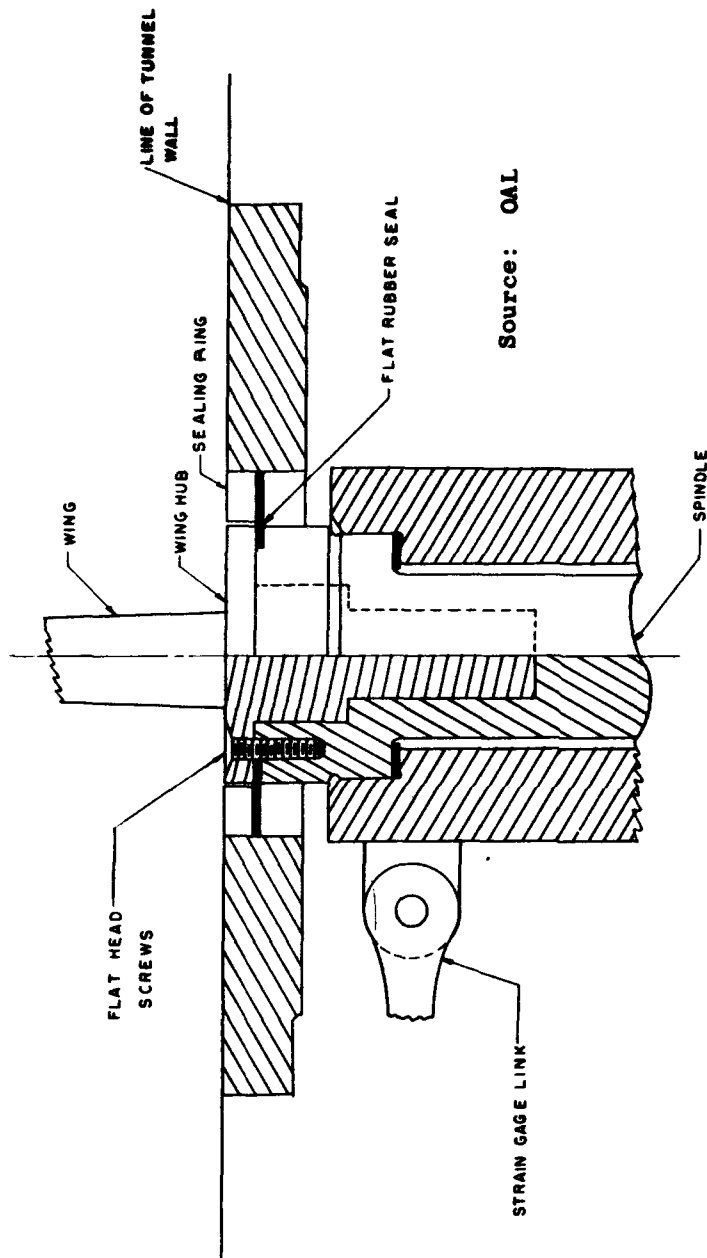
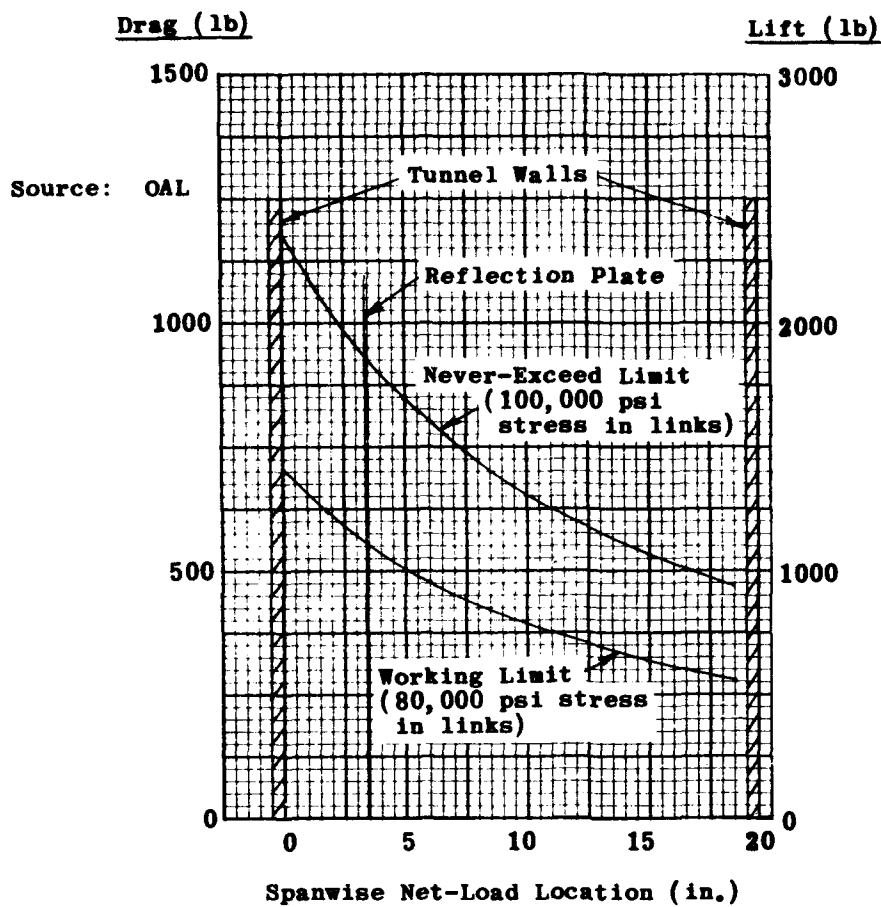


Fig. 3-52. Wing model mounted on flexure-pivot support.



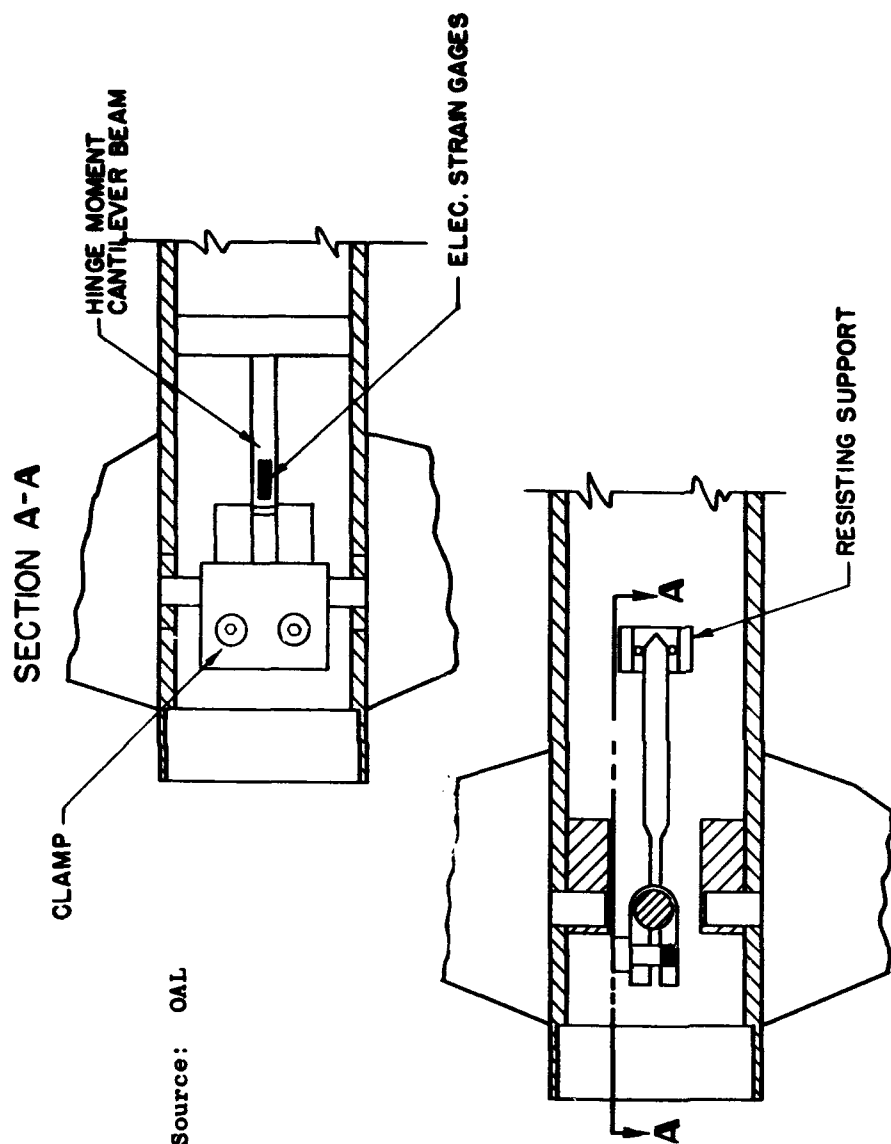
(Travel of chordwise net-load location is assumed less than 1.80 in. from hinge line)

Fig. 3-53. Maximum allowable lift and drag load for flexure-pivot wall-mounted support.

Source: OAL



Fig. 3-54. Typical three-dimensional hinge-moment model.



Source: OAL

Fig. 3-55. Method for measuring wing hinge moment.

Source: OAL

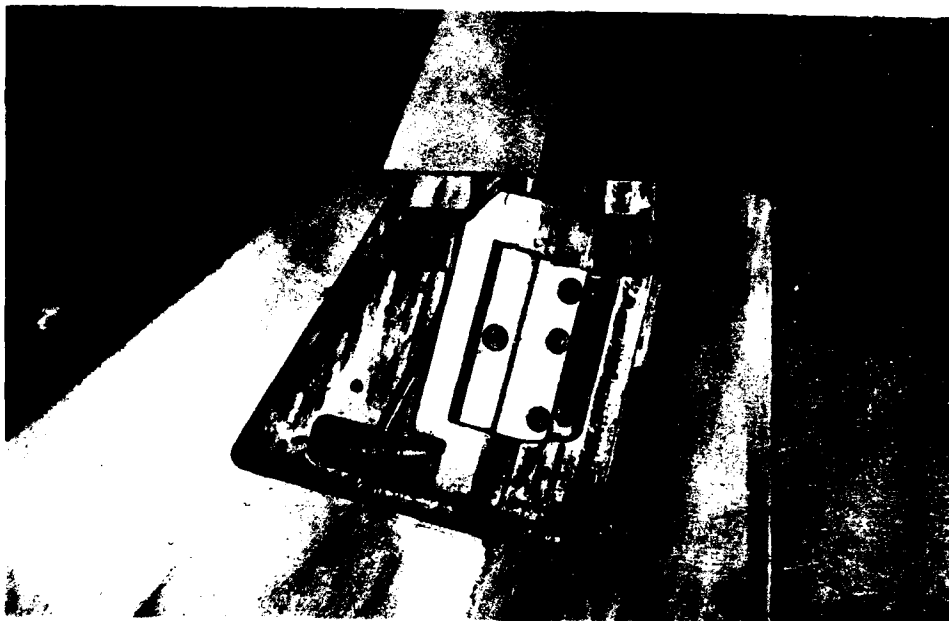
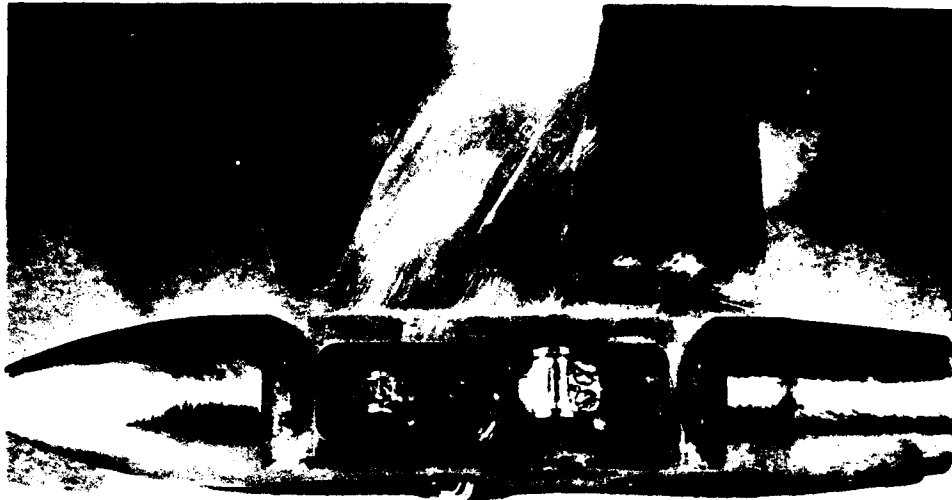


Fig. 3-56. Typical installation for measuring flipper hinge moment.

Source: OAL

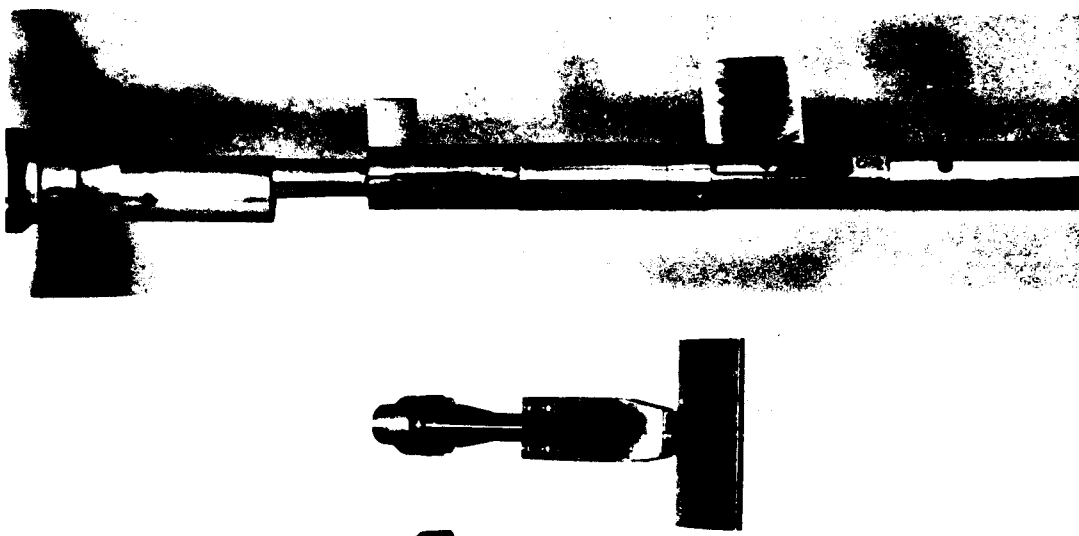
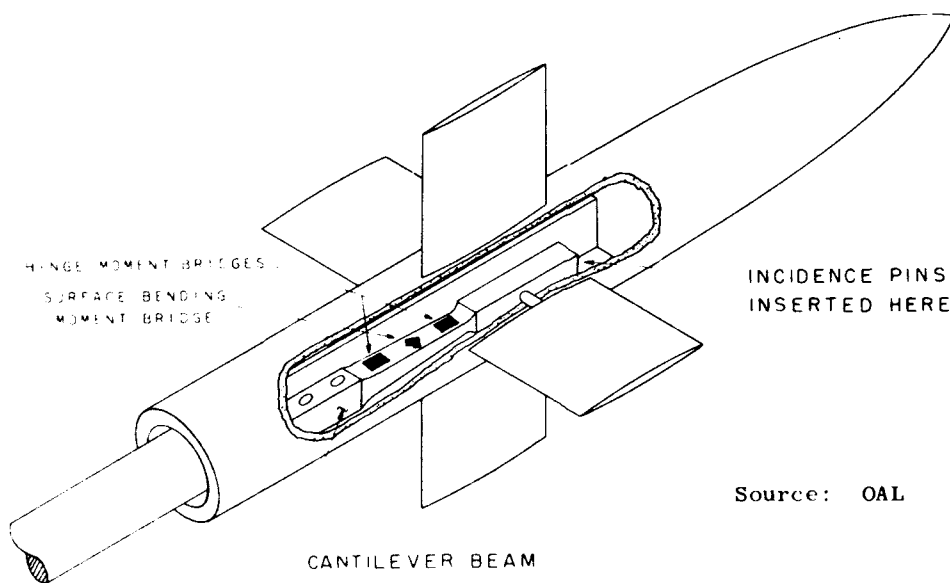


Fig. 3-57. Typical hinge-moment models; integrated wing and tail, four active panels (body cover plates removed), and wing alone, two active panels.



Source: OAL

Fig. 3-58. Arrangement for measuring hinge moment.

Source: OAL

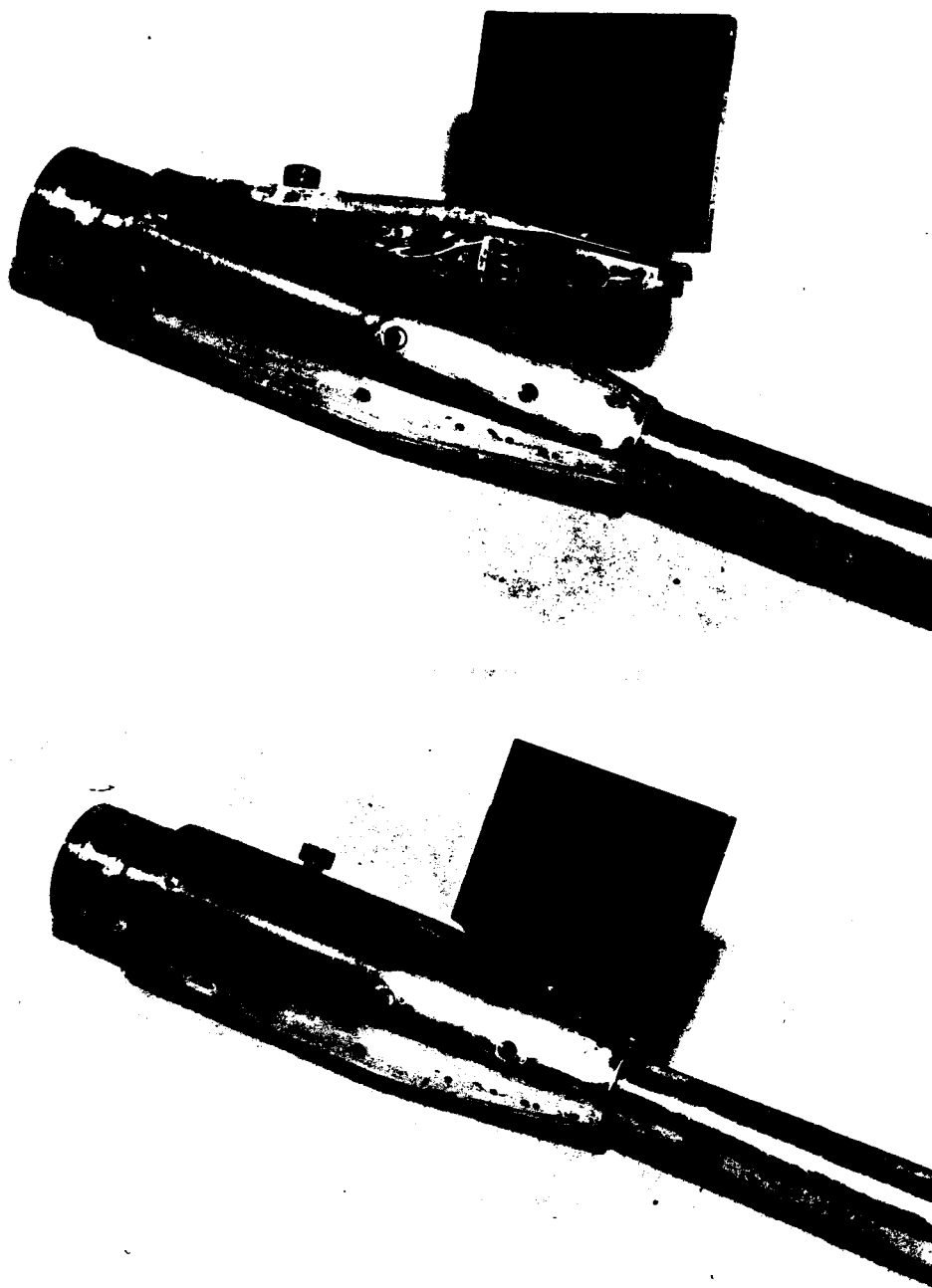


Fig. 3-59. Tail hinge-moment model, integral with the internal balance.

Source: OAL



Fig. 3-60. Wing hinge-moment internal balance, showing integral gaged beam and surface, and installation in balance.

Source: OAL

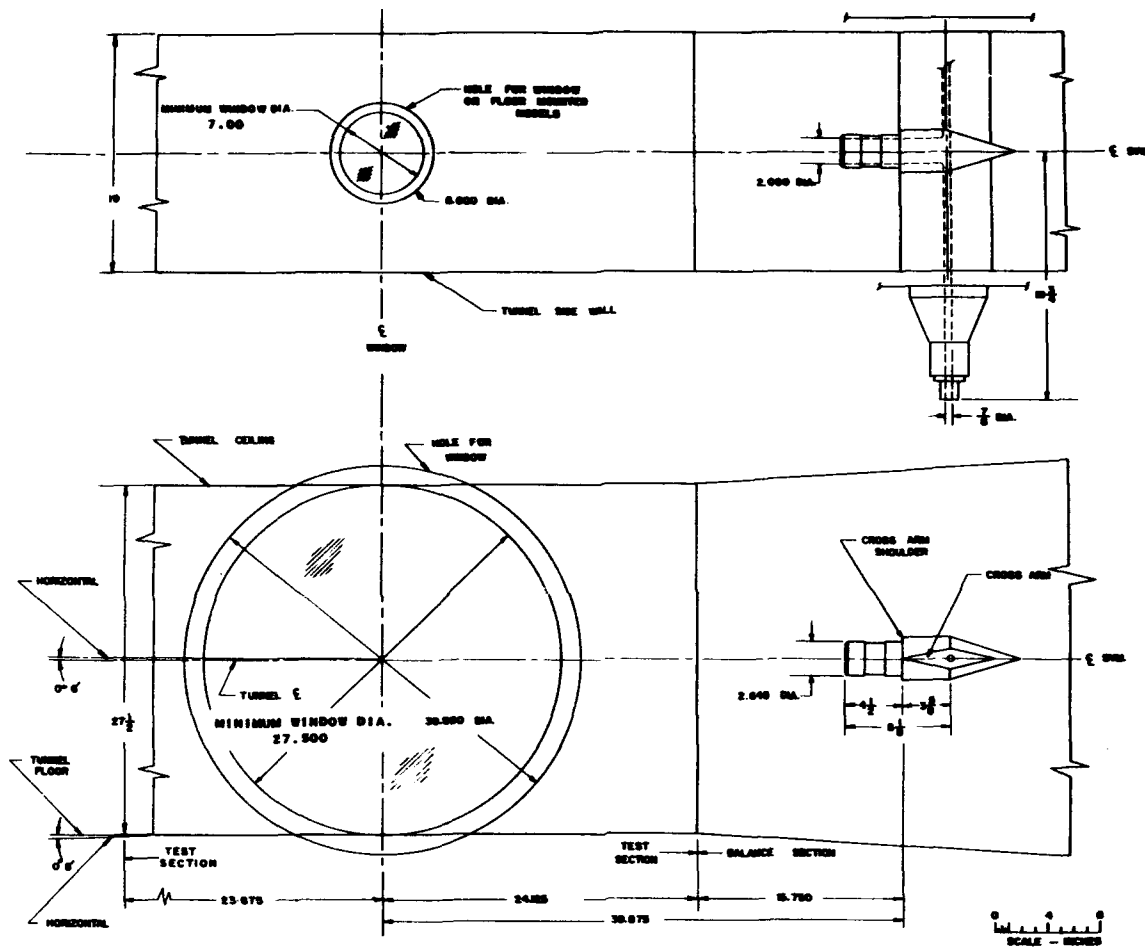
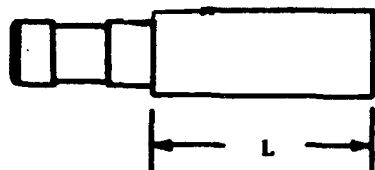


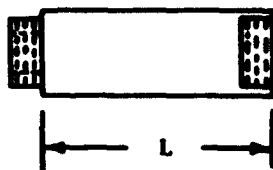
Fig. 3-61. Balance arrangement in OAL test section.

Source: OAL



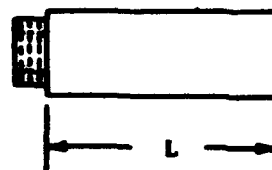
Straight Extension
(Fits any support)

E-4: $L = 12.979$
 E-5: $L = 4.988$
 E-6: $L = 5.000$
 E-13: $L = 7.500$
 E-14: $L = 16.000$
 E-16: $L = 8.000$



Spacer
(Fits -21 support)

E-37: $L = 2.00$
 E-7: $L = 5.00$
 E-8: $L = 7.00$
 E-9: $L = 9.00$



Base
(For -10 support)

E-1: $L = 4.438$
 E-2: $L = 12.435$
 E-3: $L = 8.425$

(For -19 support)

E-22: $L = 3.50$
 E-23: $L = 3.87$
 E-27: $L = 6.00$
 E-29: $L = 4.50$

(For -21 support)

E-24: $L = 5.380$
 E-25: $L = 6.630$

(For -23 support)

E-19: $L = 3.50$
 E-20: $L = 5.50$
 E-21: $L = 7.50$
 E-28: $L = 13.50$
 E-38: $L = 4.50$

(For -24 support)

E-17: $L = 3.87$
 E-18: $L = 5.87$
 E-26: $L = 8.00$
 E-39: $L = 4.87$

(For -32 support)

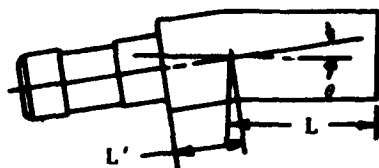
E-34: $L = 6.50$

(For -35 support)

E-35: $L = 7.00$

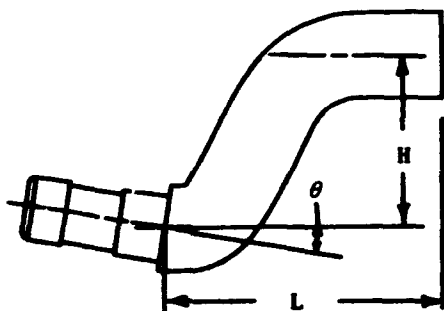
(For -38 support)

E-31: $L = 3.81$
 E-32: $L = 5.81$
 E-33: $L = 7.81$



Bent Extension
(Fits any support)

E-11: $L' = 1.375$, $L = 5.00$, $\theta = 16.75^\circ$
 E-12: $L' = 1.125$, $L = 5.40$, $\theta = 9.00^\circ$
 E-30: $L' = 0.875$, $L = 4.56$, $\theta = 5.00^\circ$



Offset Extension
(Fits any support)

E-36: $H = 3.873$, $L = 4.025$, $\theta = 6.00^\circ$
 E-10: $L = 2.680$, $\theta = 6.00^\circ$
 E-15: $H = 4.625$, $L = 9.688$, $\theta = 9.00^\circ$

Fig. 3-62. Characteristics of OAL extensions, spacers, and support bases.

Source: OAL

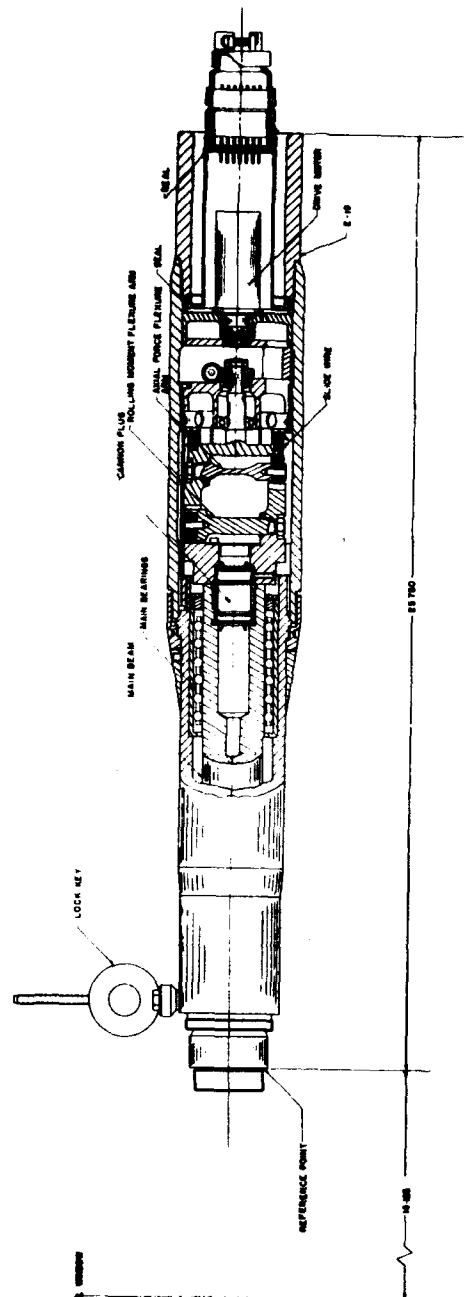


Fig. 3-63. OAL-23 two-component roll-indexing support.

Source: OAL

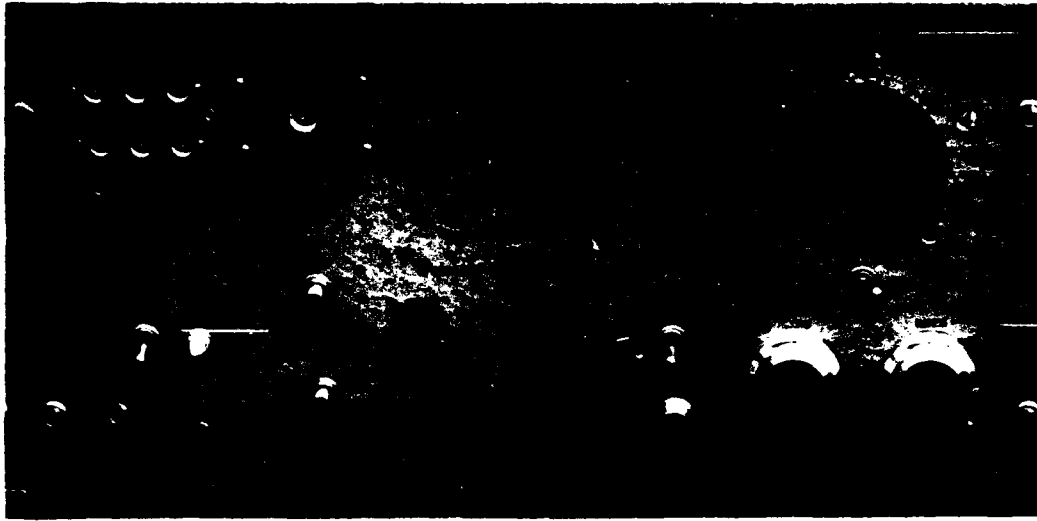


Fig. 3-64. Roll angle indexing control panel.

Source: OAL

Rolling Moment Flexure Arm



Axial Force Flexure Arm

Fig. 3-65. Side view of OAL-24 two-component roll-indexing support, showing rolling moment flexure arm and axial-force flexure arm.

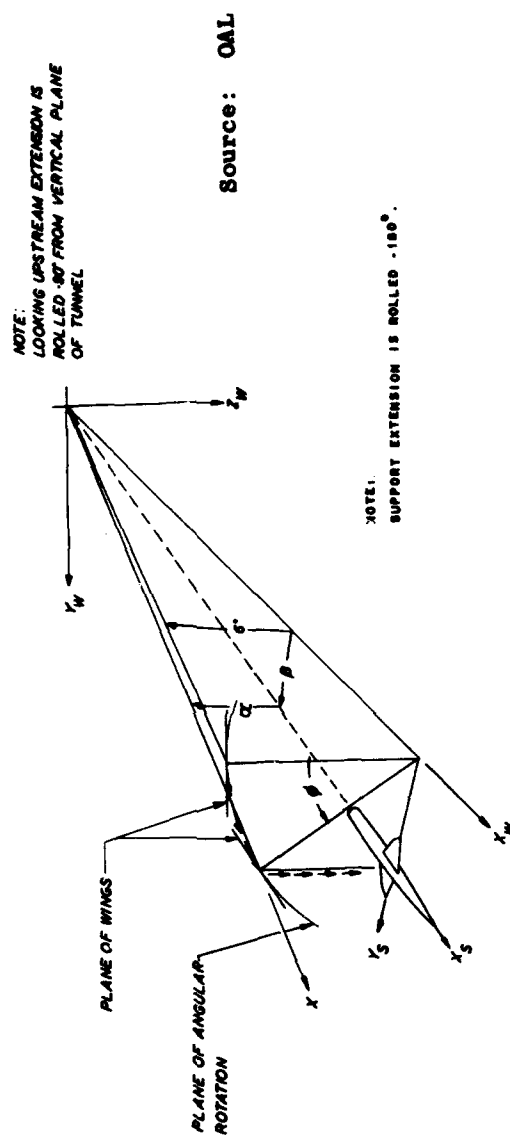
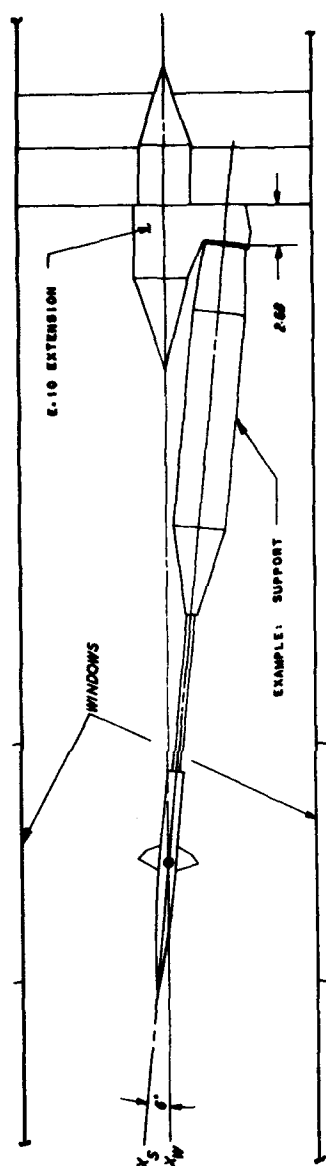


Fig. 3-66. Operating principle of the OAL E-10 extension.

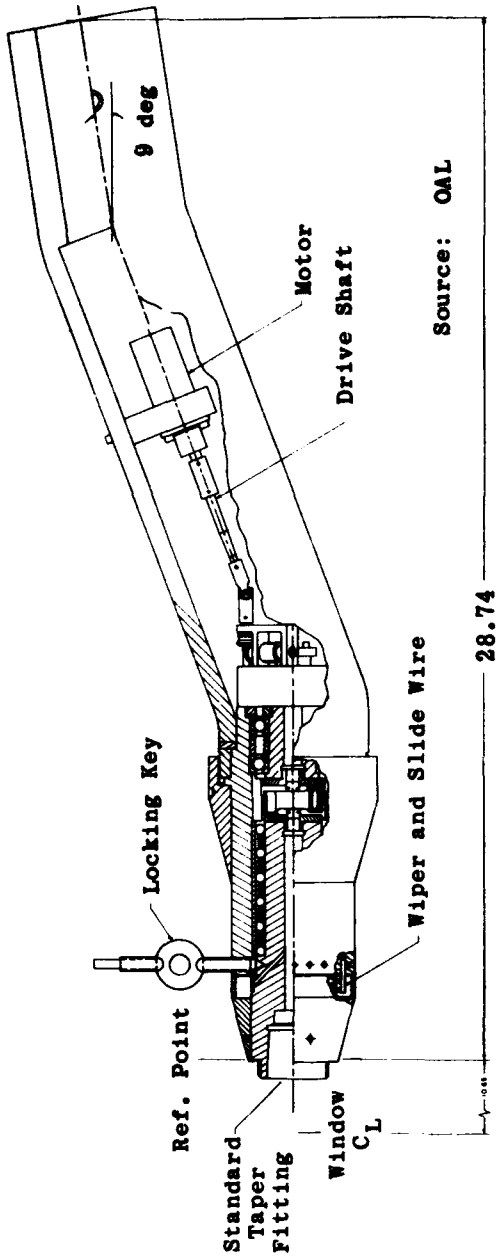
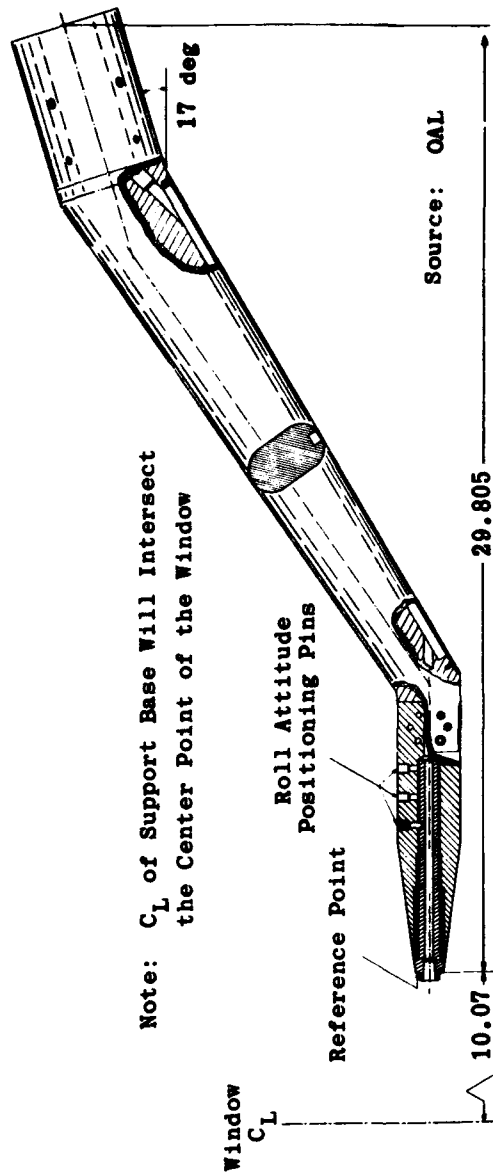


Fig. 3-67. OAL-37 9-deg offset roll-indexing support.



Note: C_L of Support Base Will Intersect the Center Point of the Window

Fig. 3-68. OAL-36 17-deg offset manual-indexing support.

Source: OAL

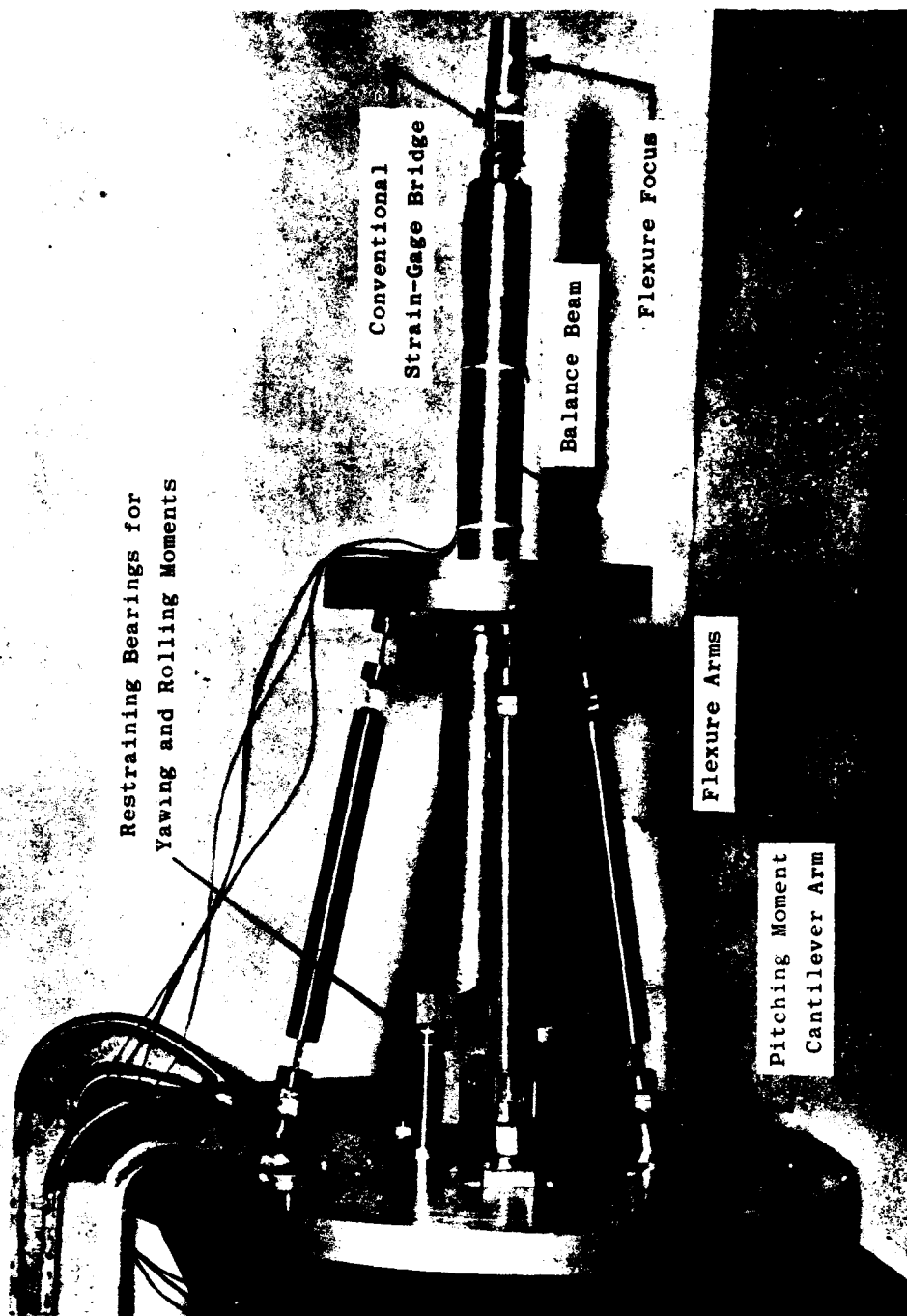


Fig. 3-69. Pilot model of focused-flexure balance.

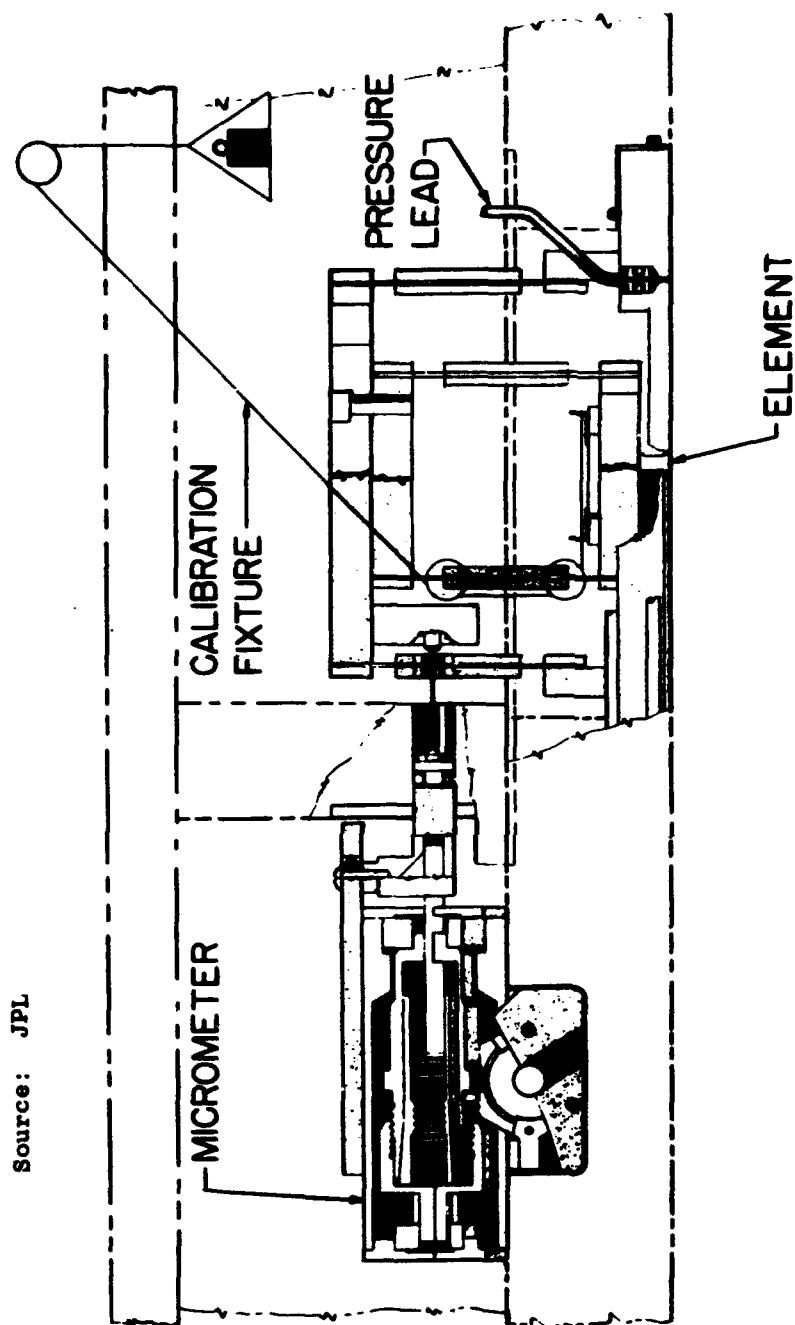


Fig. 3-70. Skin-friction balance floating element and micrometer installed in the plate.

Source: JPL

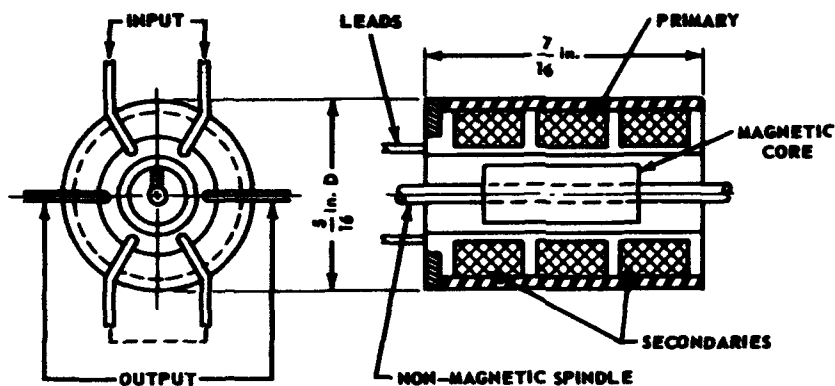


Fig. 3-71. Schaevitz differential transformer.

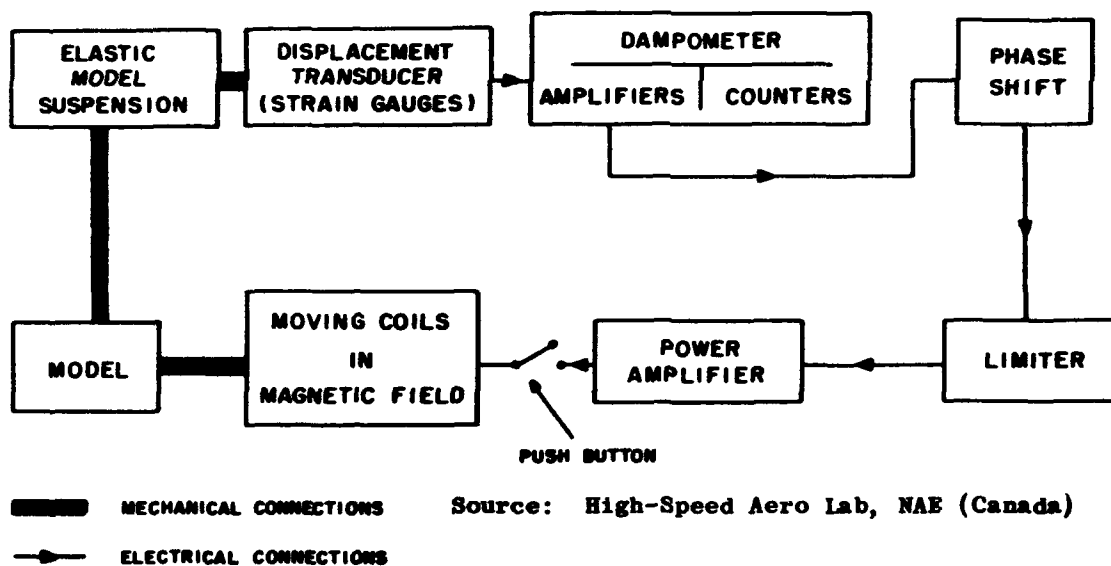


Fig. 3-72. Block diagram of free oscillation with feedback excitation.

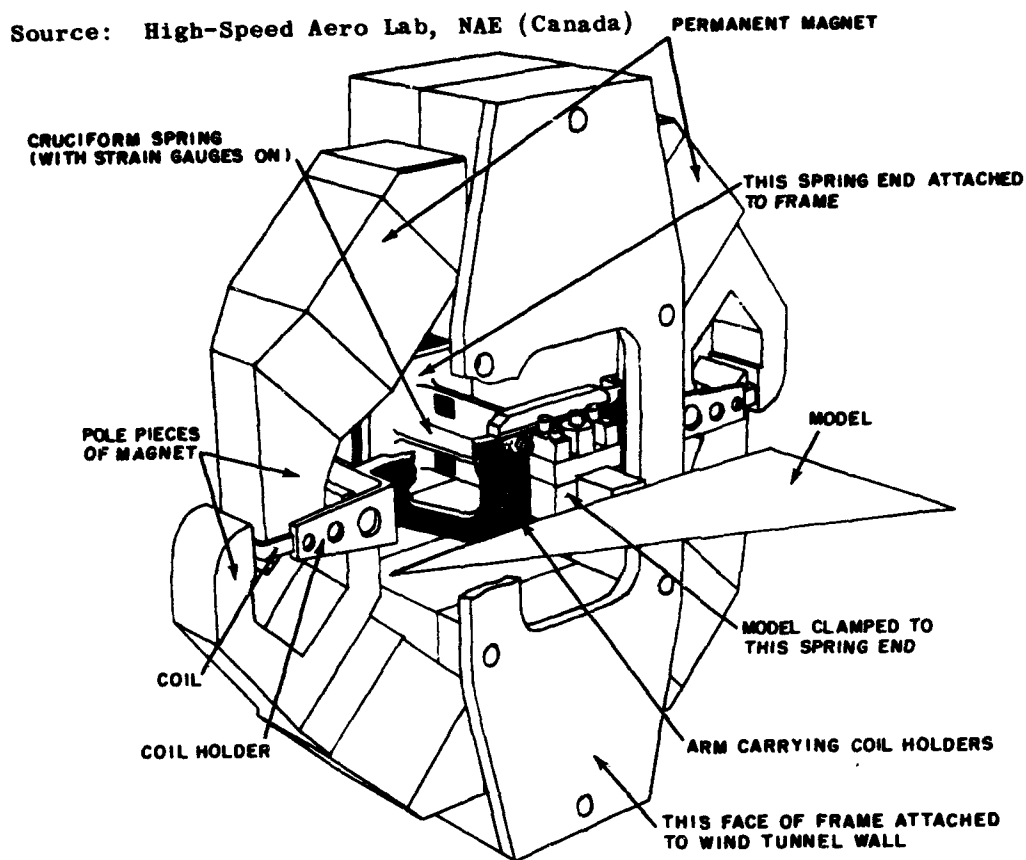
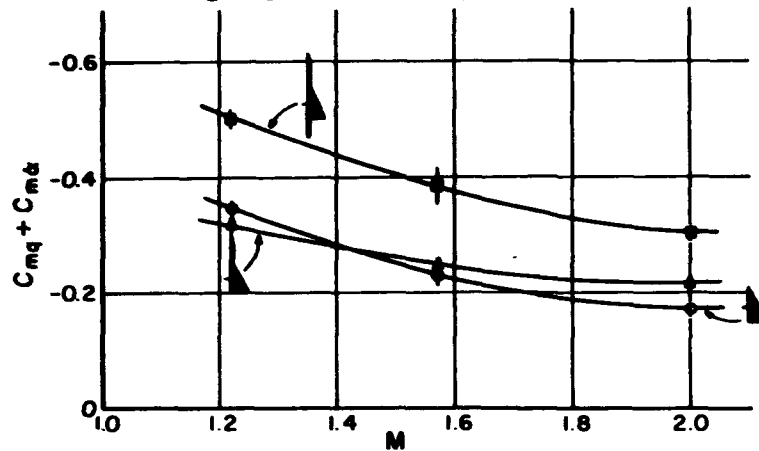


Fig. 3-73. Test rig for oscillation in pitch.

Source: High-Speed Aero Lab, NAE (Canada)



VERTICAL LINES REPRESENT TOTAL SCATTER IN 20 MEASUREMENTS
 AXIS POSITION 60 PERCENT OF WING ROOT CHORD

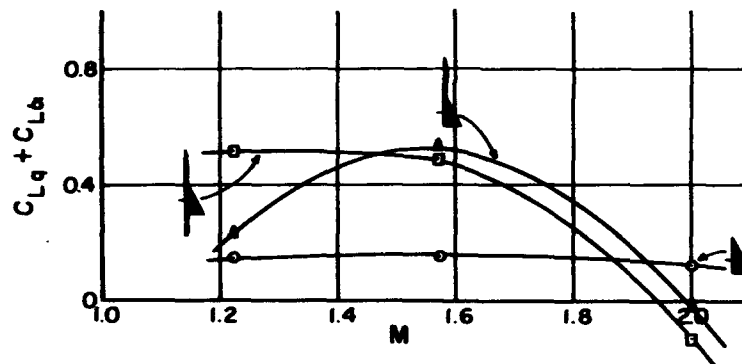


Fig. 3-74. Typical results of oscillation-in-pitch tests on half models.

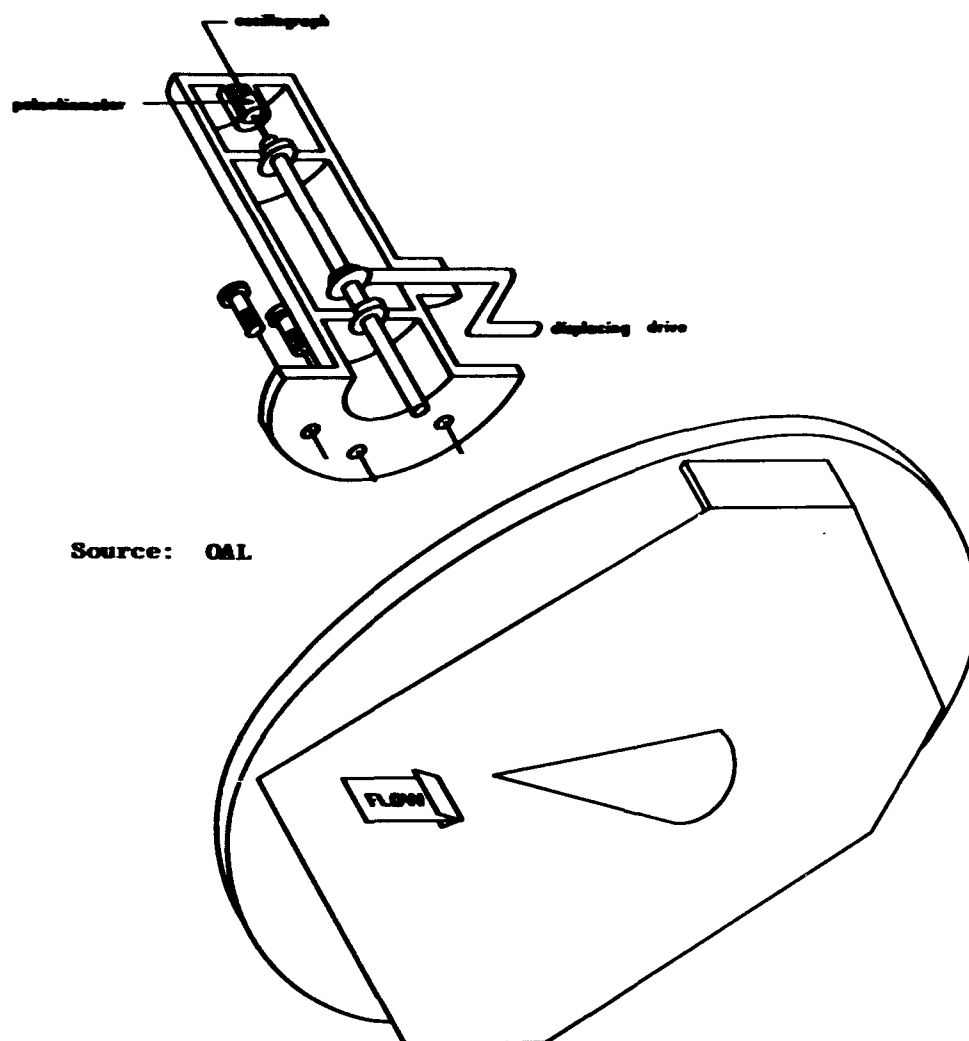
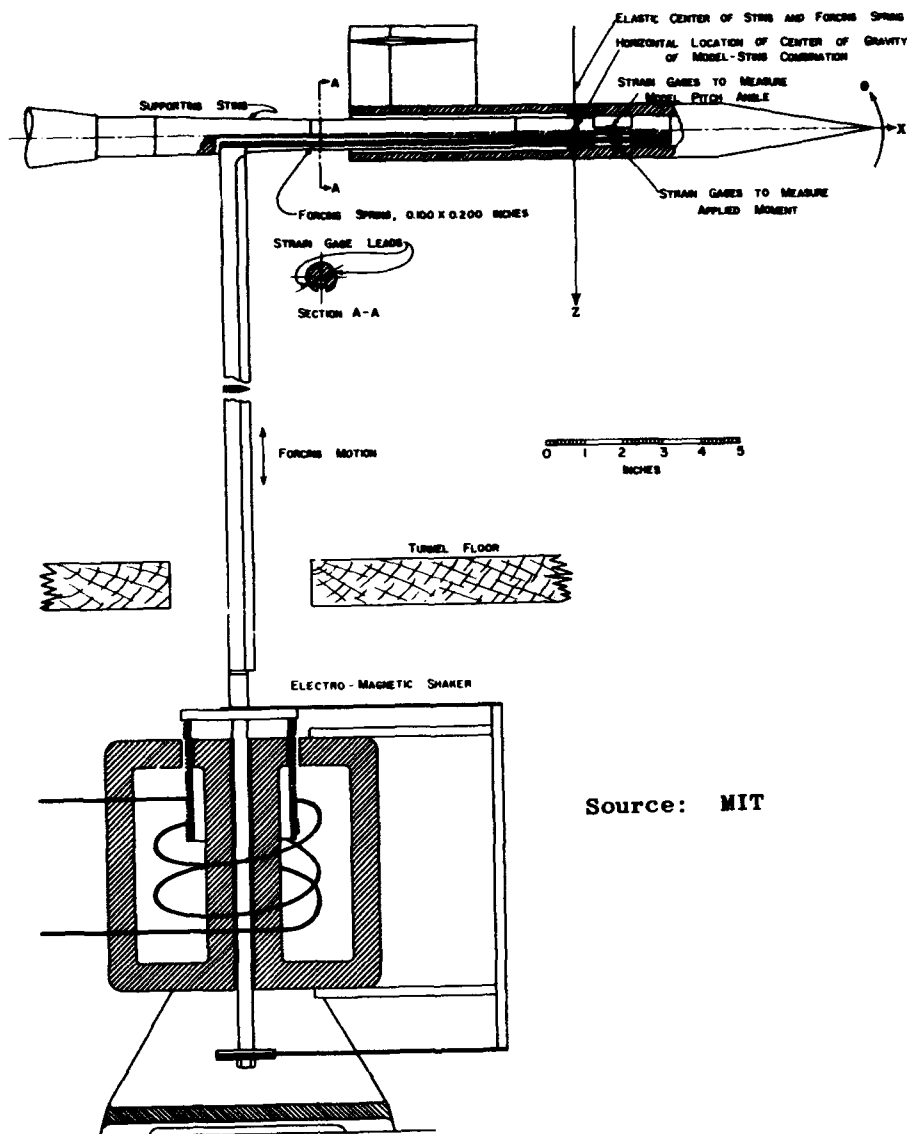


Fig. 3-75. Pitch-damping balance, reflection plate, and model.



Source: MIT

Fig. 3-76. Model, sting, and shaker system.

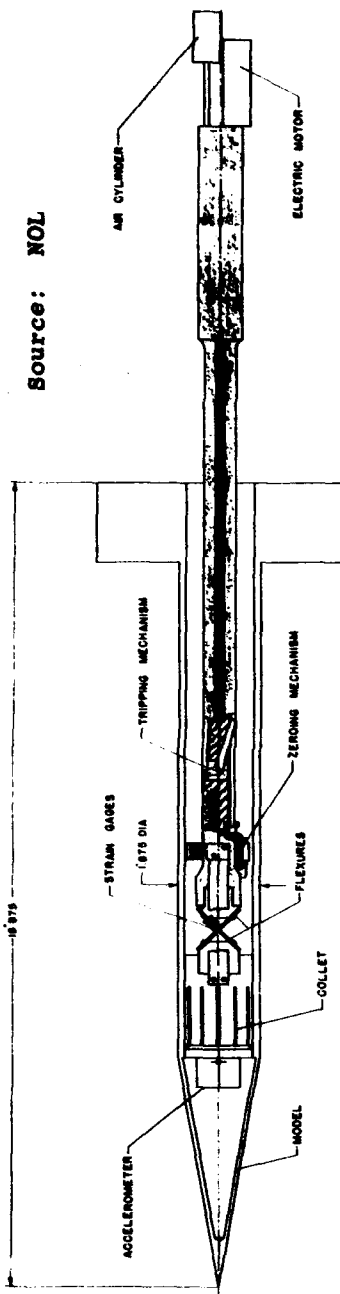


Fig. 3-77. Damping-in-pitch balance and model.

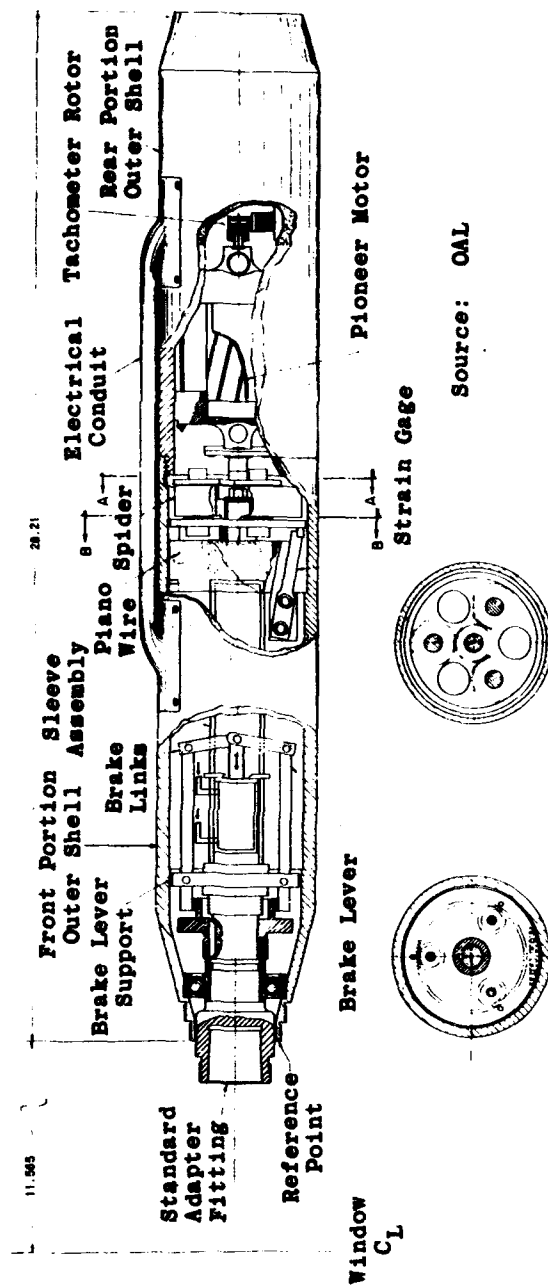


Fig. 3-78. Dynamic steady-roll balance support.

Source: OAL

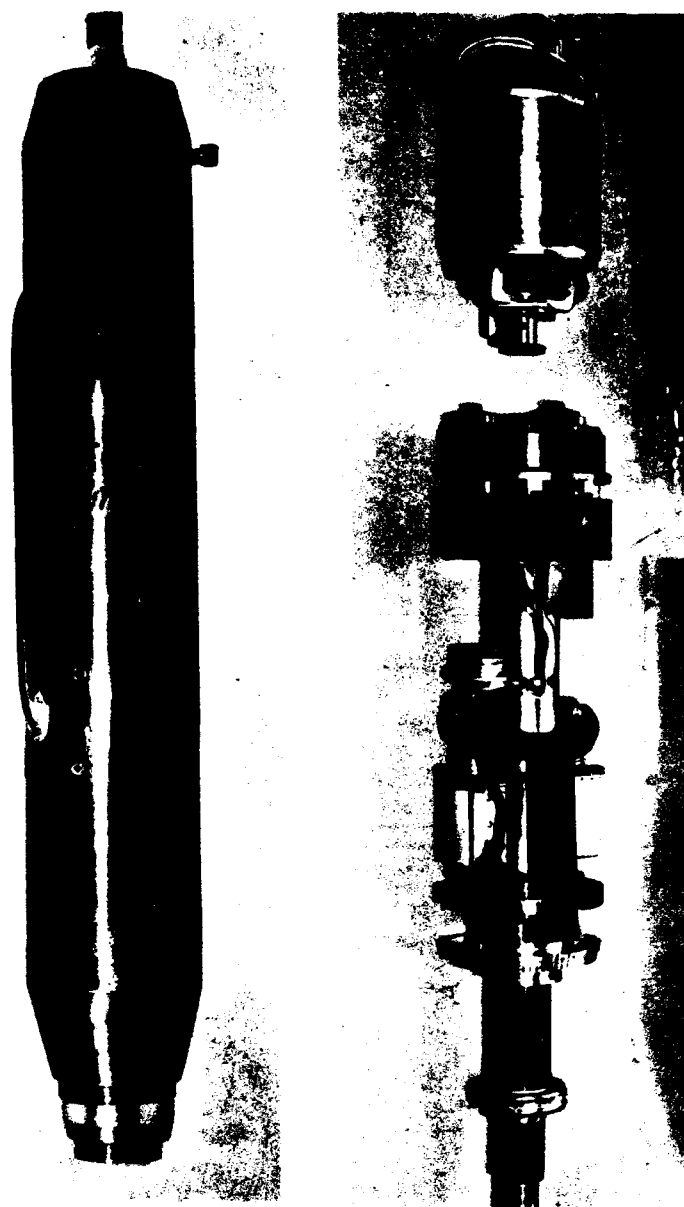


Fig. 3-79. Dynamic steady-roll balance support, with internal details.

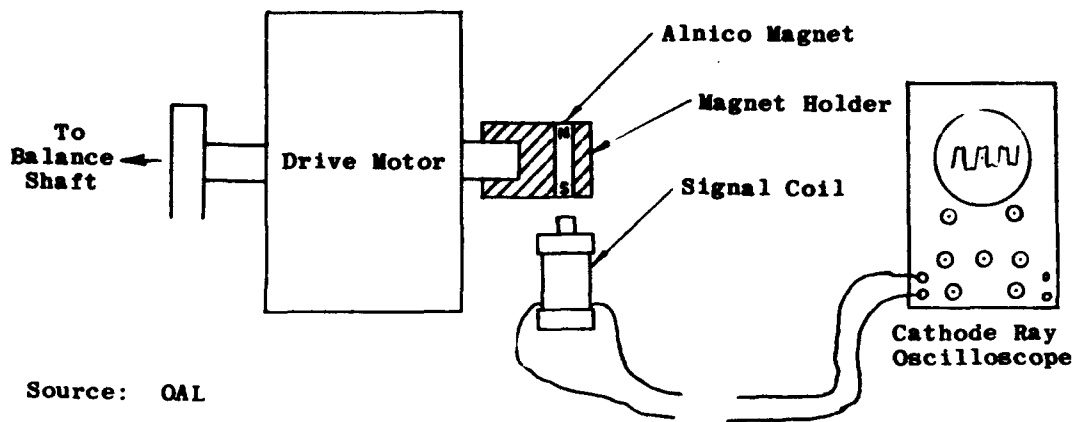


Fig. 3-80. Schematic drawing of rpm counter for dynamic steady-roll balance.

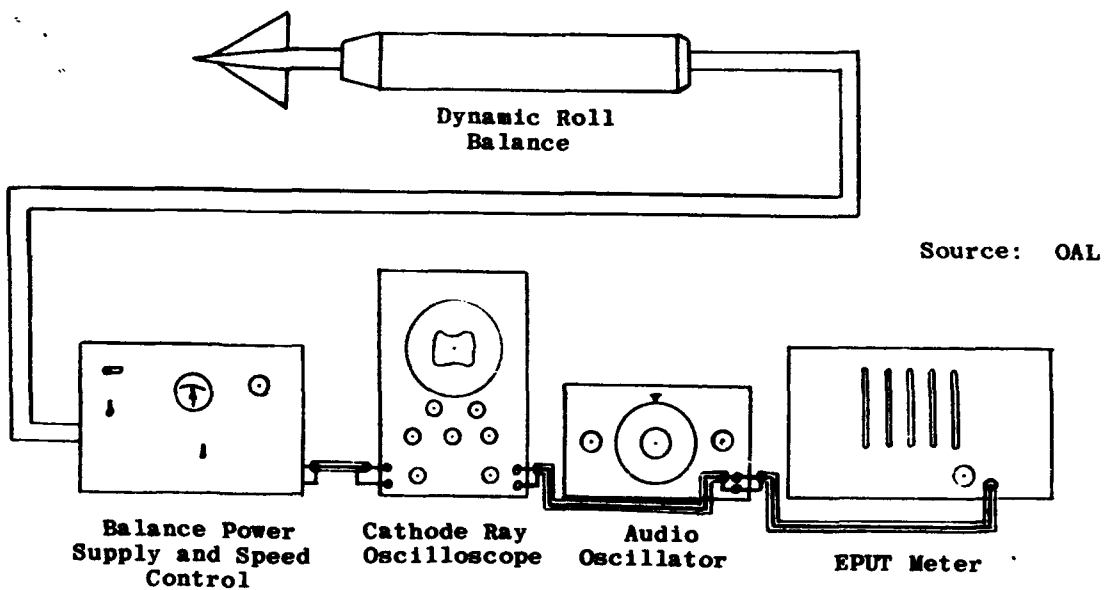


Fig. 3-81. Arrangement of dynamic roll balance and associated equipment.

Source: NAE

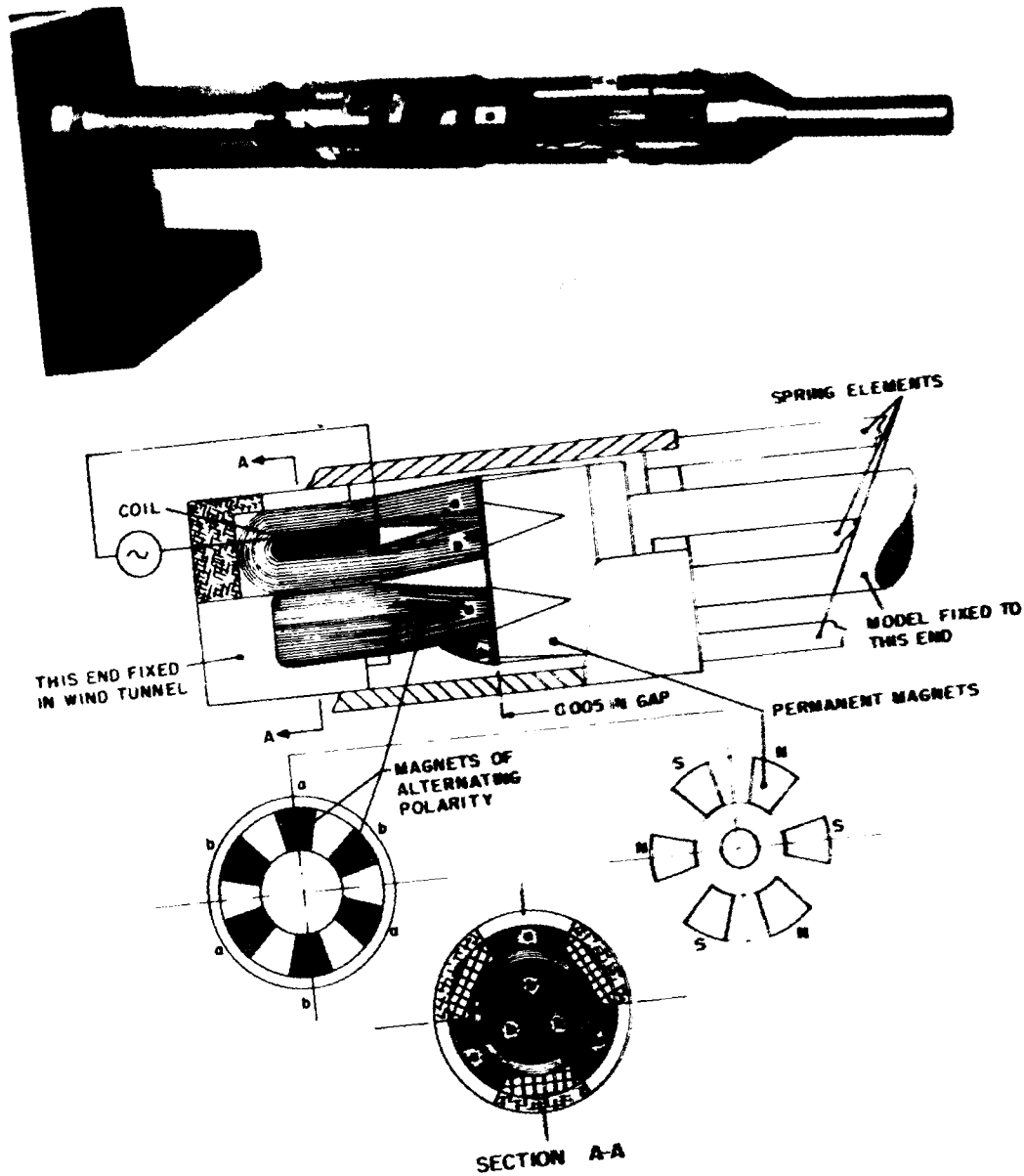


Fig. 3-82. NAE test rig for oscillation in roll.

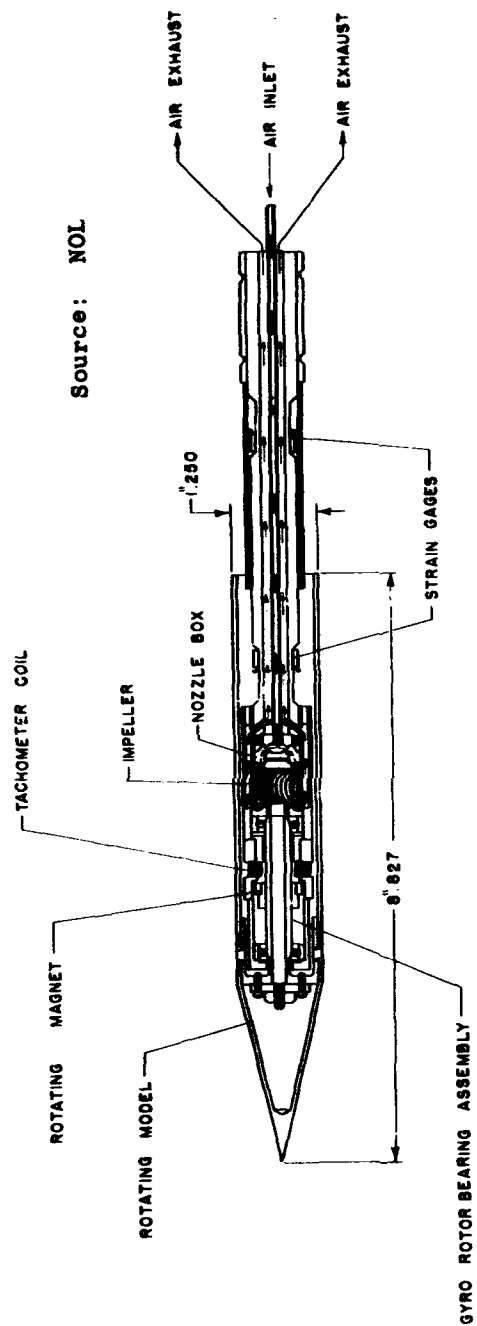


Fig. 3-83. High-speed air turbine balance and model.

Source: Oltronix

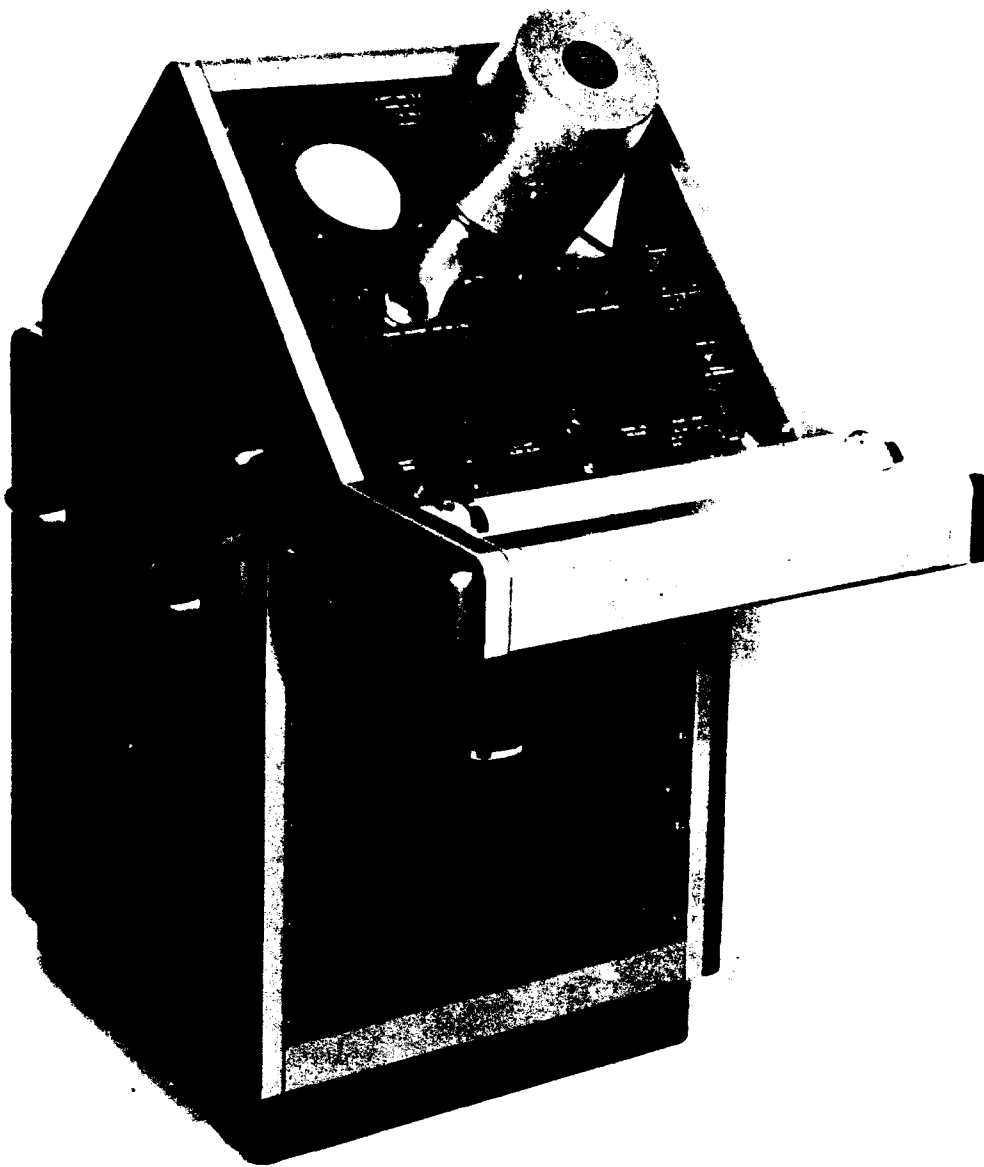


Fig. 3-84. Oltronix dampometer.

Source: Oltromix

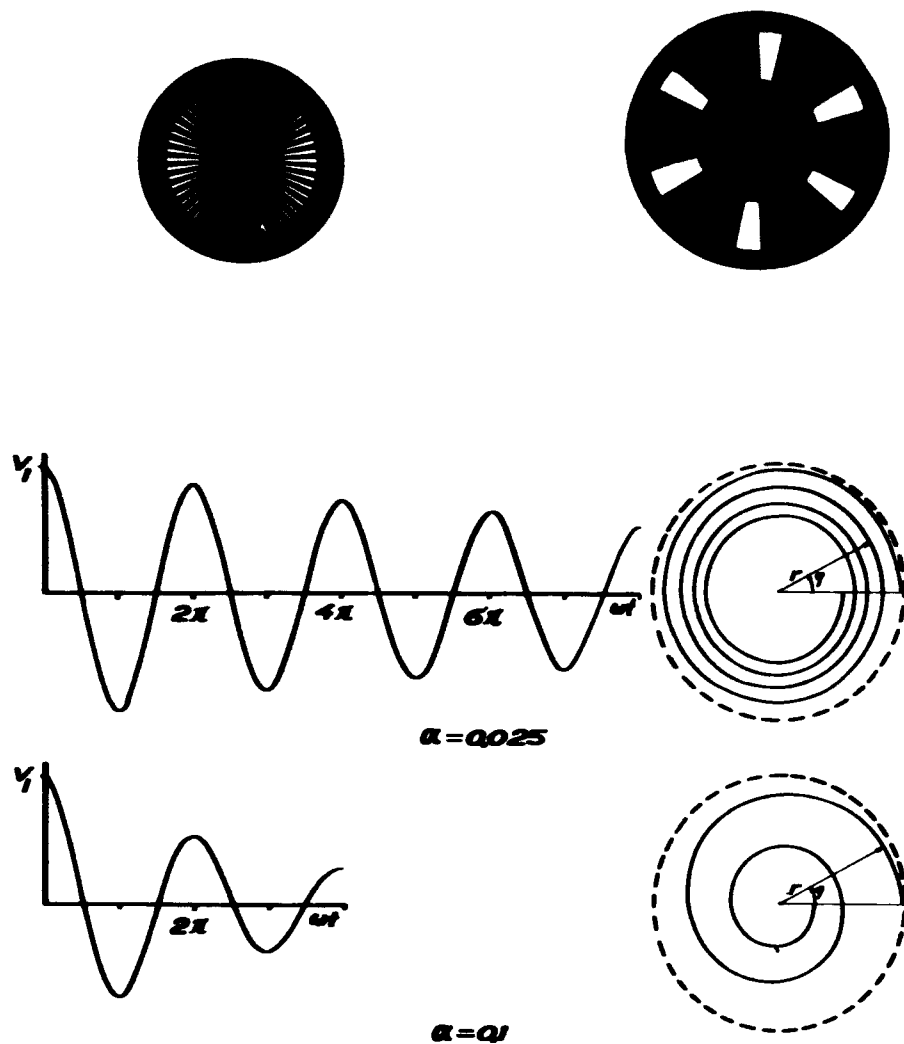


Fig. 3-85. Typical calibrated slotted discs and principle of dampometer operation.

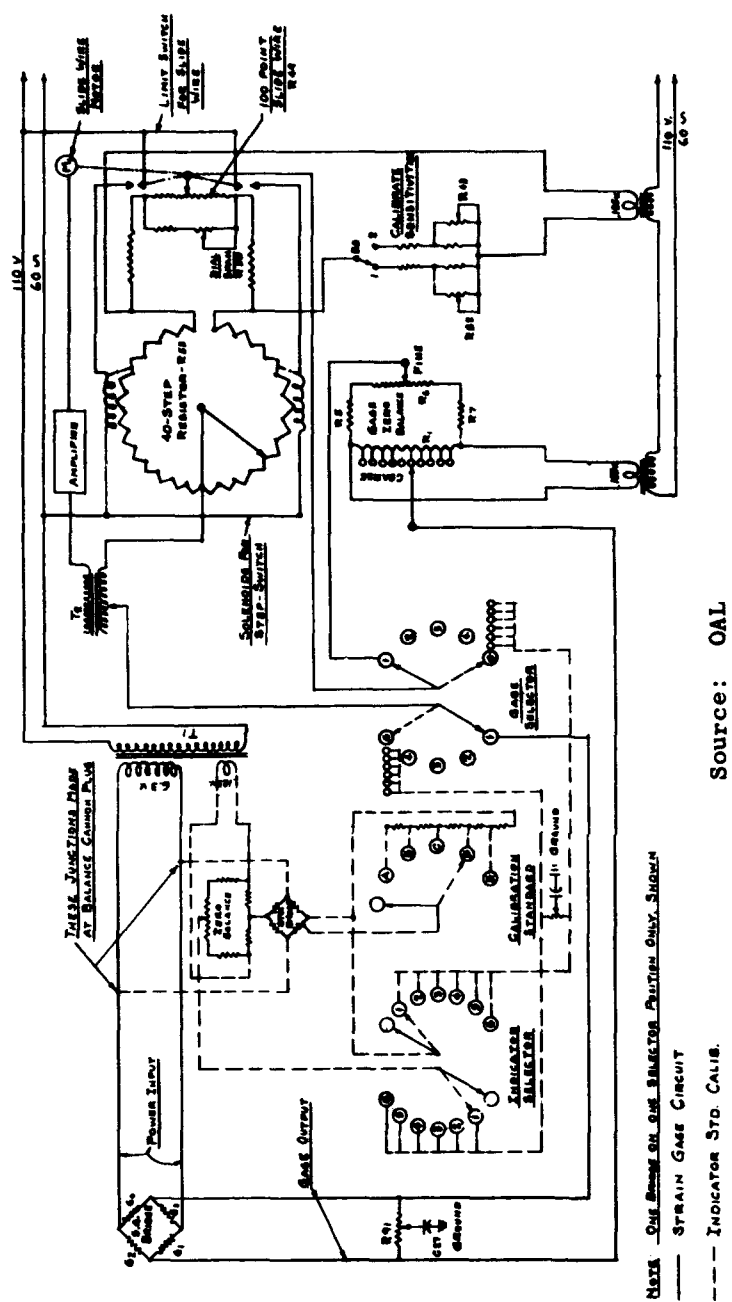


Fig. 3-86. Wiring diagram of wind-tunnel indicators.

Source: OAL

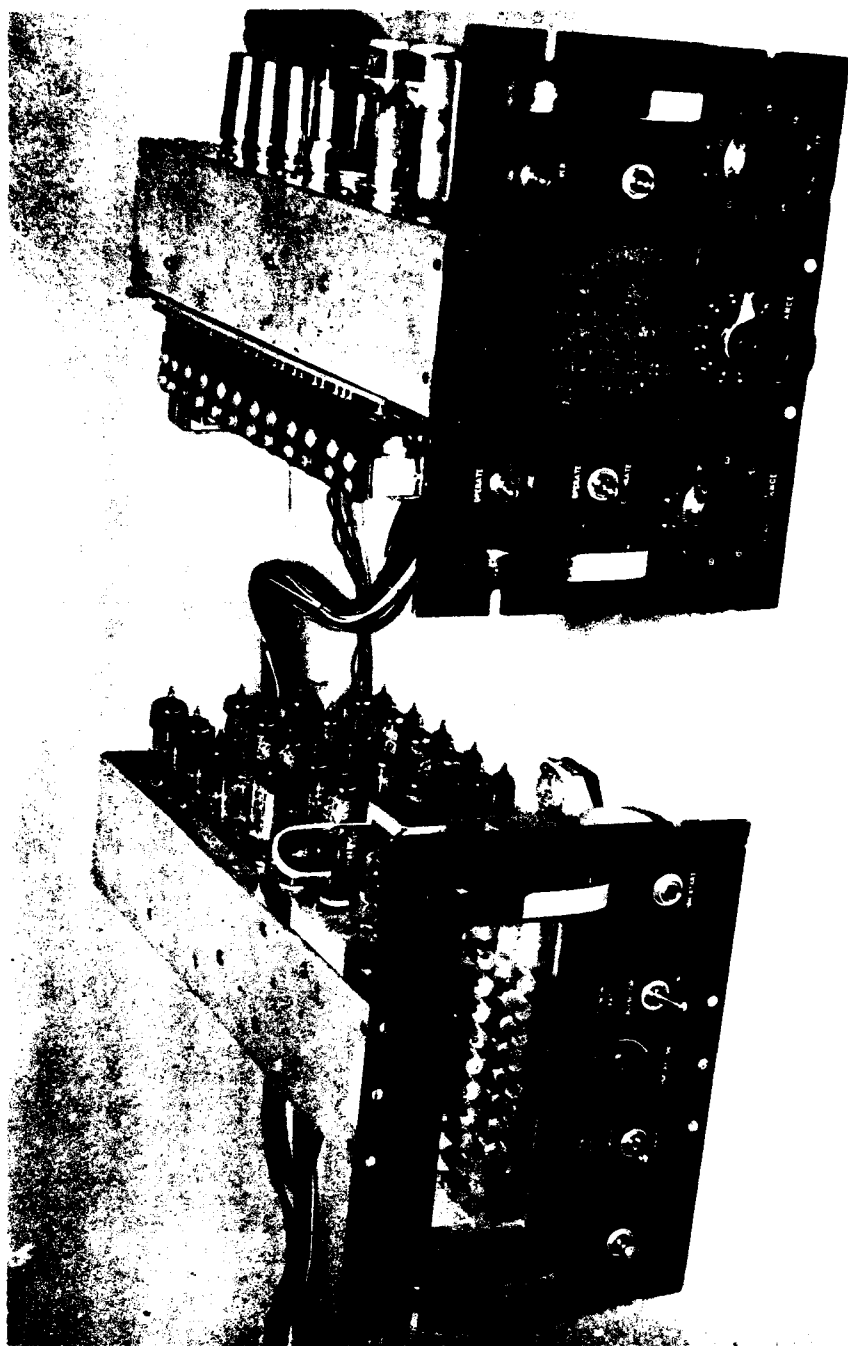


Fig. 3-87. Pilot model of analog-to-digital high-speed electronic converter (ADHEC).

Source: OAL

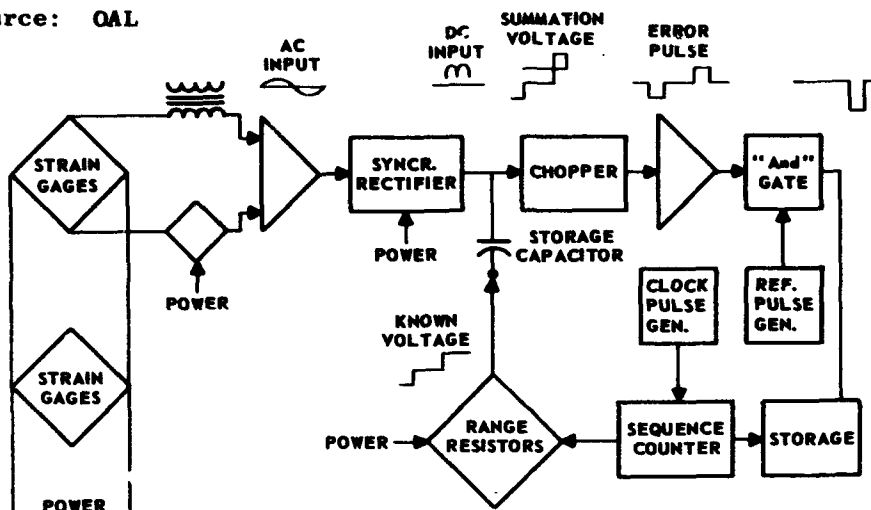


Fig. 3-88. Block diagram of the ADHEC.

 $\phi = 0$ α Varying in Positive Direction

Source: OAL

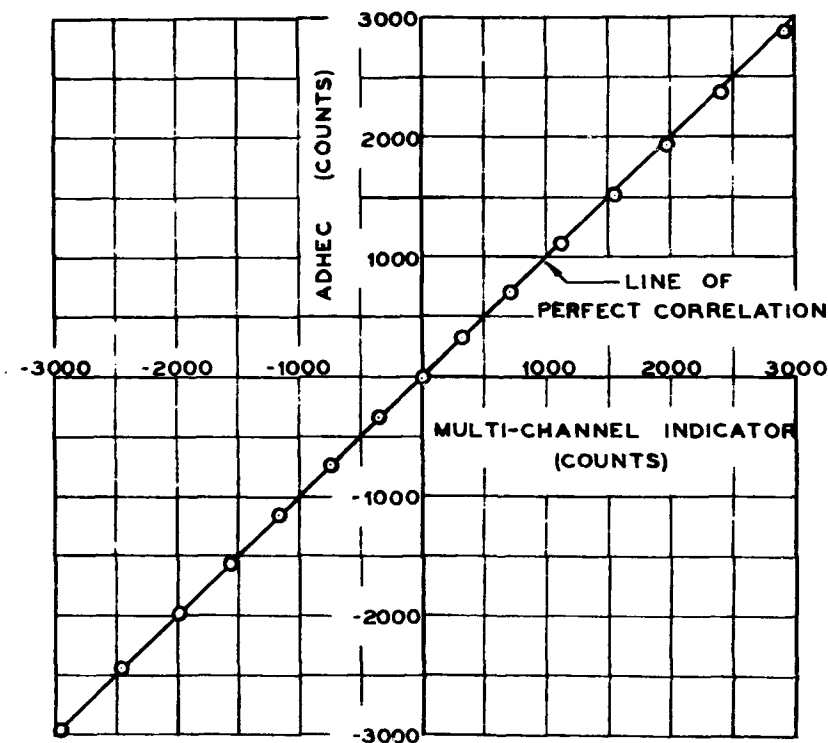


Fig. 3-89. Correlation of ADHEC data with existing indicator data.

Source: OAL

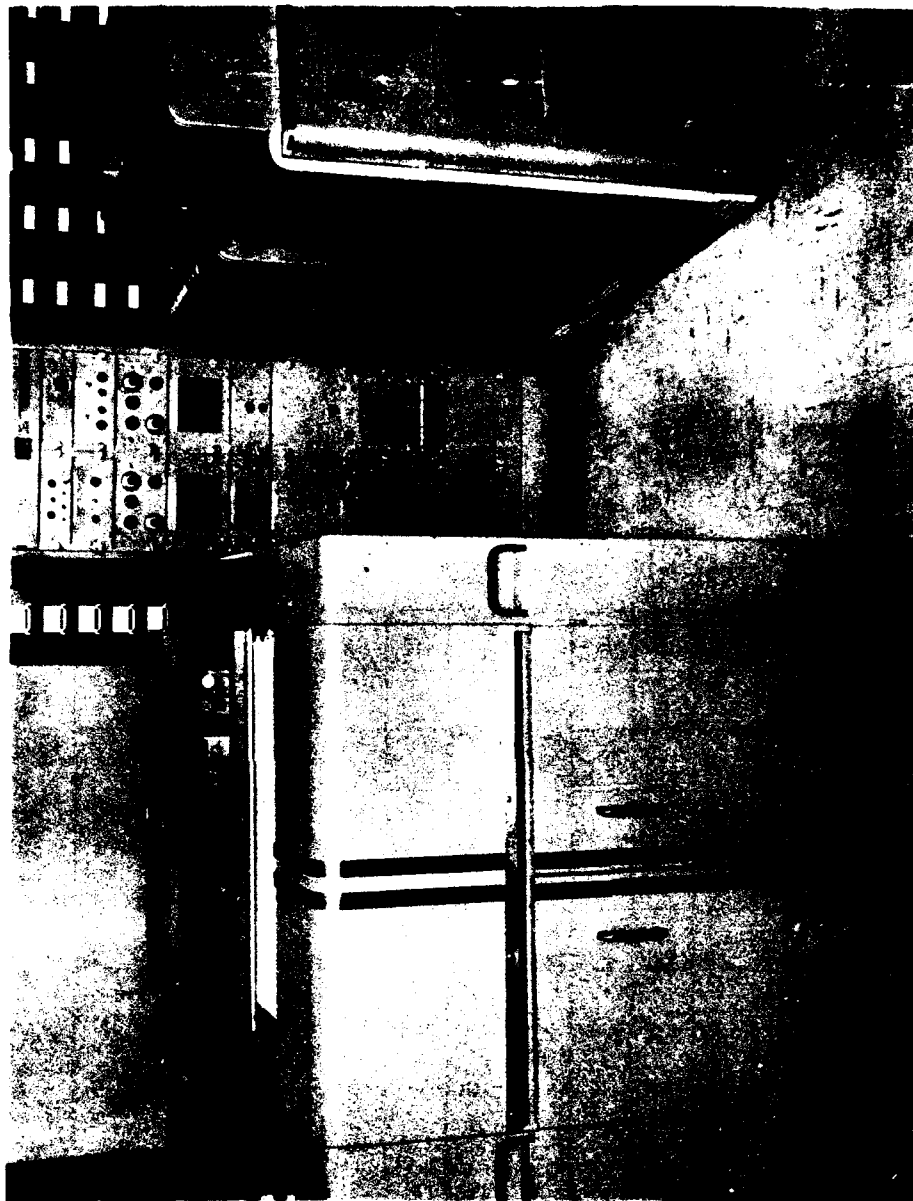


Fig. 3-90. Model 205G vari-plotter and model 17-31A digi-verter.
(Electronics Associates, Inc.)

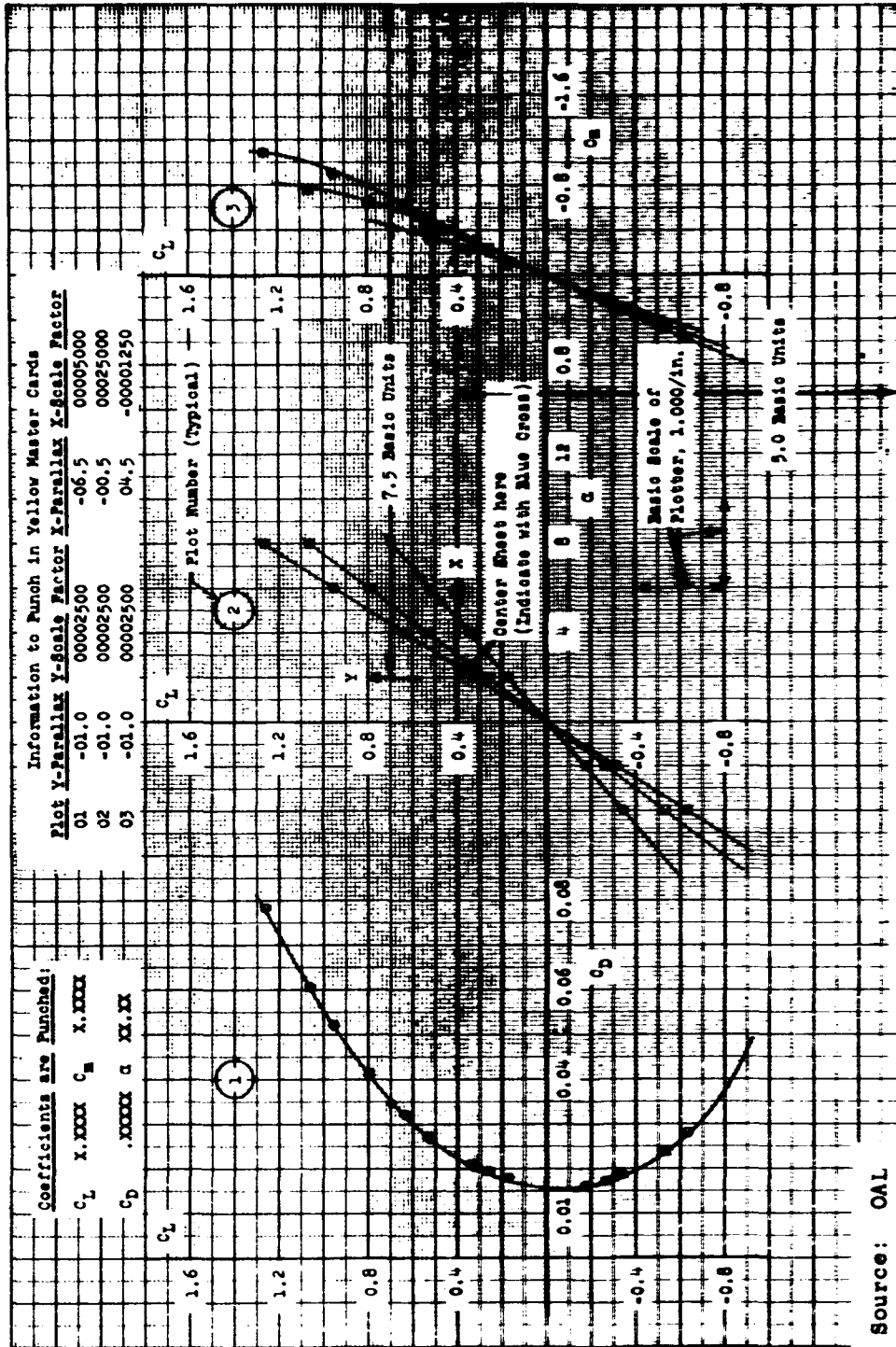


Fig. 3-91. Basic standard scale for conventional three-component data.

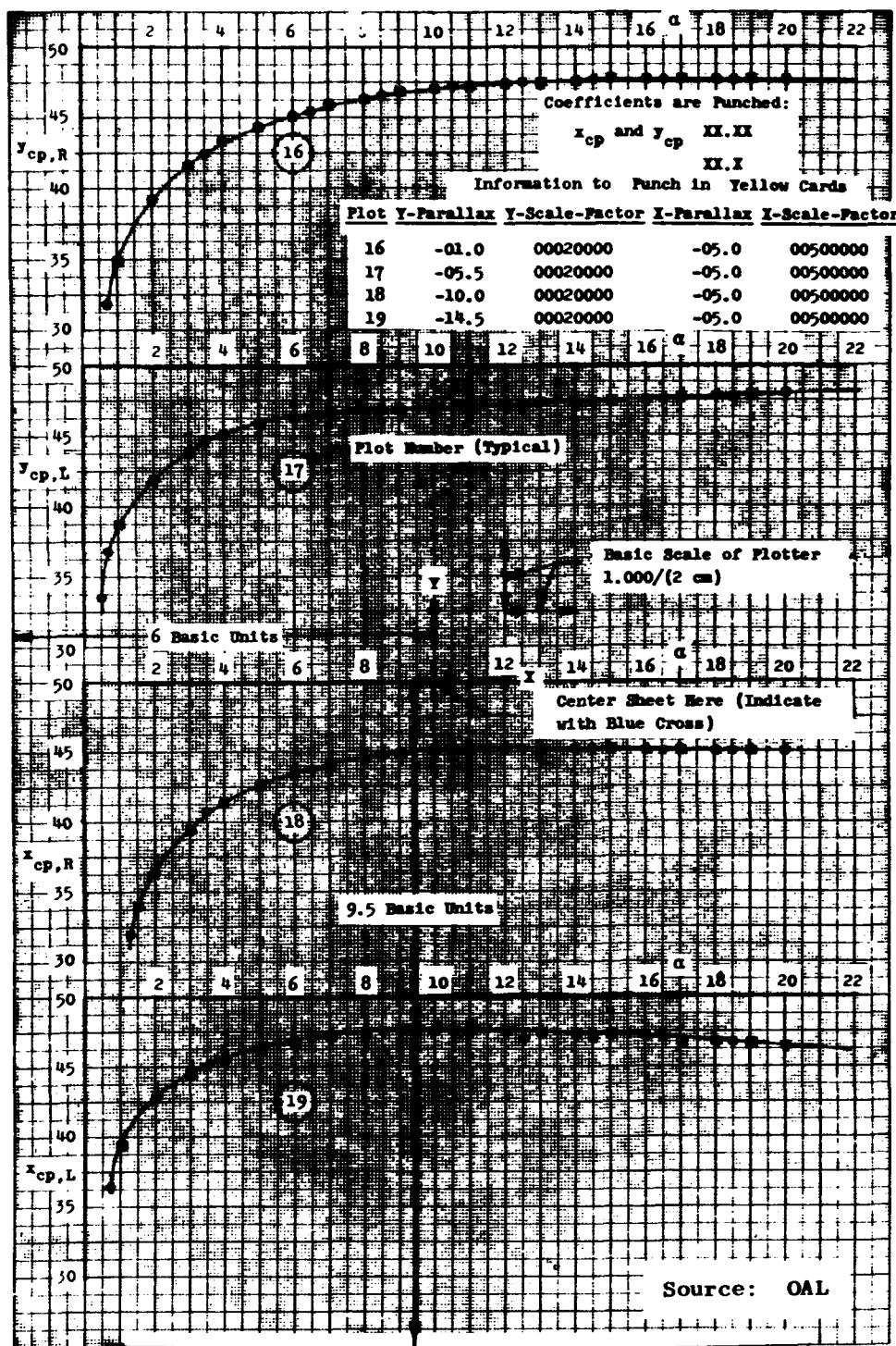


Fig. 3-92. Basic standard scale for other general data.

4. Temperature Measurement

Temperature, a primary variable in many analytical expressions describing the flow of a gas, is one of the fundamental properties of matter. To define completely the state of a perfect gas, it is necessary to determine only two independent properties, of which temperature may be one. No complete theory adequately explains the nature of a body's temperature. However, in dealing with gases, temperature can be visualized as an indication of the kinetic energy level of the molecules in their random translational, rotational, and vibrational modes of motion. Much of the material appearing in this subsection was derived from Refs. 1 and 151 (Section D).

Stream temperature, T_∞ , is frequently referred to as static and is defined as the equilibrium temperature of a particle moving confluent with the stream in the absence of radiation. If the stream velocity is adiabatically reduced to zero, the gas attains its stagnation temperature, T_0 . It is not feasible to measure stream temperature directly because the flow is disturbed by insertion of a probe; a relative velocity always exists between stream and probe, changing the local fluid temperature near the probe. The best that can be done is to design a probe which disturbs the stream in a predictable, consistent manner. With this knowledge it is then possible to calculate the probe temperature, T_p . The relation between probe temperature and stream temperature is usually determined by experiment.

The relation between stream temperature and stagnation temperature is

$$T_0 - T_\infty = \frac{v^2}{2 g c_{ps}} \cdot \frac{c_{ps}}{c_{pa}} \quad (4-1)$$

where

$c_{ps} = c_p$ at standard temperature (540°R) = 0.2398

$c_{pa} = c_p$ at actual temperature

This relation is plotted in Fig. 4-1. Equation 4-1 is only true for relatively small values of $(T_0 - T_\infty)$ where an average value of c_{pa} may be used. For larger differences an integrated value should be found.

The probe temperature, T_p , is usually between T_0 and T_∞ . The difference between T_p and T_0 is caused by shear work in the boundary layer, heat conduction along the probe, and radiation between the probe and its environment. At temperatures of the order of 2000°R caloric imperfections are no longer negligible and at about 5000°R the effects of dissociation and recombination must also be considered (see Ref. 152). When the probe reaches equilibrium conditions with its environment, and no heat flows either into or out of its surface, it is said to be at the adiabatic temperature, T_{pa} .

For adiabatic non-isentropic flow

$$T_{pa} = T_{\infty} + r \frac{v^2}{2g c_{pa}} \quad (4-2)$$

where

r = recovery factor

Combining Eqs. 4-1 and 4-2 gives

$$r = \frac{T_{pa} - T_{\infty}}{T_o - T_{\infty}} \quad (4-3)$$

The magnitude of r in gases will always be above zero and usually less than 1.0

In laminar boundary-layer flow, experience shows the recovery factor to be not only a weak function of Mach number and Reynolds number, but a strong function of Prandtl number and geometry of the probe, where Prandtl number, Pr , is a dimensionless ratio defined by

$$Pr = \frac{c_p \mu}{k} \quad (4-4)$$

and

c_p = local specific heat at constant pressure

μ = local viscosity

k = local coefficient of thermal conductivity

Although each of these parameters varies with temperature as shown in Figs. 4-2 and 4-3, Pr remains approximately constant for gases over a wide range of temperature.

In laminar flow Polhausen has shown that

$$r = (Pr)^{1/2} \quad (4-5)$$

In room-temperature air, $Pr \sim 0.70$, giving $r = 0.835$; however, experiment (Ref. 153a) shows the actual flat-plate laminar recovery factor to be slightly higher than this ($r \sim 0.88$).

In turbulent flow, the situation changes since the effect of boundary-layer momentum transfer must be included in any theoretical analysis. For a flat plate,

$$r \sim (Pr)^{1/3} \quad (4-6)$$

Experiments (Ref. 153a) show the flat-plate recovery factor to be about 0.90 for the turbulent case. During transition from laminar to turbulent conditions, the recovery factor may increase above both the laminar and the turbulent value.

The recovery factor of various geometric shapes has been determined in air and a summary of the existing data (Refs. 153a and 153b) is presented in Table 4-1.

The correction factor for a temperature probe is usually defined as

$$K = \frac{T_p - T_\infty}{T_o - T_\infty} \quad (4-7)$$

This factor includes all effects of stem conduction, radiation, and boundary layer. For an adiabatic probe the first two effects are zero, and K becomes r. The correction factor is usually determined by calibration in flows of known temperature. Though it would theoretically be desirable to design a probe for which $K = 1$, it is in practice more desirable to design one for which K is relatively constant in the range of temperature, stream velocity, and angle of yaw to be explored. Correction factors of the order of 0.99 have been achieved over a Mach number range from 0.2 to 3.0 (Refs. 153c and 153d).

In order to establish thermal equilibrium for a probe, the stem conduction and radiant heat transfer must be balanced by the convective heat transfer through the boundary layer, Q_c . This is expressed by

$$Q_c = hA_p (T_{pa} - T_p) \quad (4-8)$$

where

h = convective heat-transfer coefficient

A_p = wetted area of thermometric device

T_{pa} = adiabatic probe temperature

The heat transfer coefficient, h , is a function of the geometry of the immersed body, the thermal conductivity of the immersing fluid, k , the Prandtl number, the Reynolds number, and the flow regime (i.e., laminar or turbulent).

$$\frac{hD}{k} = \text{constant } Re^m \cdot Pr^n \quad (4-9)$$

where

D = characteristic dimension of the body which also enters in Re .

Both m and n are positive exponents less than unity and depend on the geometry and the direction of the heat flow at the surface.

The non-dimensional quantity, $\frac{hD}{k}$, is known as the Nusselt number, Nu . Another useful parameter in heat transfer calculations is the Stanton number, St , which is defined as a coefficient of heat transfer and may be expressed as $\frac{Nu}{Re \times Pr}$.

In the most efficient temperature probes the sensing element is near the stagnation point where the flow is laminar. In such air flows, whose Pr may be represented by 0.74, Eq. 4-9 may be approximated (Ref. 156) by

$$\frac{hD}{k} = 0.02 (Re)^{0.8} \quad (4-10)$$

In supersonic flow the detached bow wave reduces the stream velocity to a subsonic value at the nose of the probe, increasing the stream temperature but not affecting the stagnation temperature. The Reynolds number, the heat transfer coefficient, and the correction factor, K , should all be related to the subsonic flow characteristics.

4.1 Effect of Stem Conduction on Probe Temperatures

The term "stem conduction" refers to heat conduction from the sensing element of the probe to cooler parts of the supporting structure. The error in probe temperature due to stem conduction, $(\Delta T_p)_c$, is given (in Ref. 151) as

$$(\Delta T_p)_c = \frac{T_p - T_w}{\cosh \left(\sqrt{\frac{hA_p}{kA_c}} \cdot L \right)} \quad (4-11)$$

where

T_w = temperature of coolest part of structure

L = depth of immersion

k = effective thermal conductivity of the support material

A_c = effective cross-sectional area presented to the heat flow

The stem of a probe is usually composed of thermocouple leads, an insulator, and a metallic sheath. These materials must all be considered when calculating k . The heat of conduction may be minimized by increasing the wetted area of the probe, by using fine lead wires, and also by utilizing materials of low conductivity for the supporting stem. For a more detailed analysis of stem conduction see Refs. 151, 157, 158, and 159.

4.2 Effect of Radiant Heat Transfer on Probe Temperature

In a total temperature probe the sensing element at the stagnation point will radiate heat to its environment and thus reduce the

indicated temperature. In order to minimize radiation effects the thermocouple junction should be as small as is consistent with structural integrity and life considerations.

The sensing element of the probe should be surrounded by a radiation shield made of material whose heat conductivity and surface emissivity are both low. Since the temperature of the shield will in general be lower than that of the probe, the temperature reading will be affected by its physical properties. The error in reading due to radiation, $(\Delta T_p)_r$, may be calculated (Ref. 151) from

$$(\Delta T_p)_r = \frac{\sigma \epsilon}{h} \left[\left(\frac{T_p}{100} \right)^4 - \left(\frac{T_r}{100} \right)^4 \right] \quad (4-12)$$

where

σ = Stefan-Boltzmann constant

ϵ = emissivity of the temperature-sensing element

T_r = temperature of the radiation shield

In order to minimize the radiation error, h should be as large as possible, and the temperature difference between the sensing element and the shield should be as small as possible. It is difficult to predict, or to maintain constant, the emissivity of base-metal probes whose surfaces oxidize in the presence of high-temperature gases. Emissivity values of 0.85 for black oxide films and 0.57 to 0.72 for initially polished stainless steel are suggested (Ref. 159). The emissivity of base-metal thermocouples with oxidized surfaces can be substantially reduced by using materials (such as gold and silver, with an emissivity of 0.03 to 0.05, or platinum, with an emissivity of 0.12 to 0.18) which are not subject to oxidation and therefore will retain their effectiveness as radiation shields at all temperatures below their melting points. In special cases the radiation error may be eliminated by electrically heating the radiation shield to the temperature of the probe. This scheme is complicated, time consuming, and costly except for laboratory experiments.

Figure 4-4 shows the effect of radiation on simple thermocouples, both with and without shield. The radiation effects decrease rapidly as the velocity, and hence h , increases.

4.3 Effect of Turbulence, Secondary Flow, and Non-Steady Measurement on Probe Temperatures

Little is presently known about the effect of unsteady flow on the reading of a stagnation-temperature probe. Since variation in stream velocity and angle of attack are largely damped out by the normal shock that is characteristic of the diffuser-type probe, it can be expected that such an instrument will not be greatly influenced by unsteady flows. However, if the stream disturbances become large, they could stall the diffuser and change the internal flow pattern considerably.

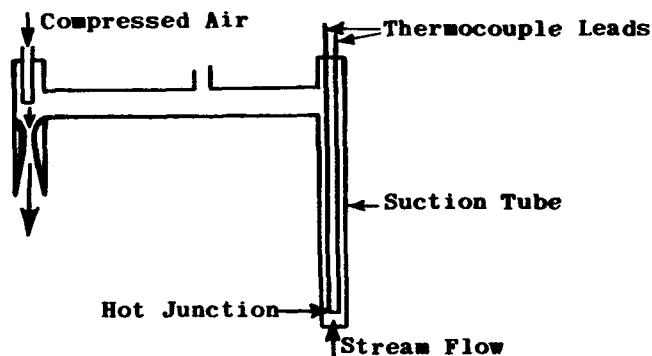
When the Reynolds number (based on probe diameter) becomes less than about 100, viscous effects may give rise to recovery factors greater than 1.0. These effects are significant only in the flow of rarefied gases and when extremely small probes are used (Ref. 160).

4.4 Design of Temperature Probes

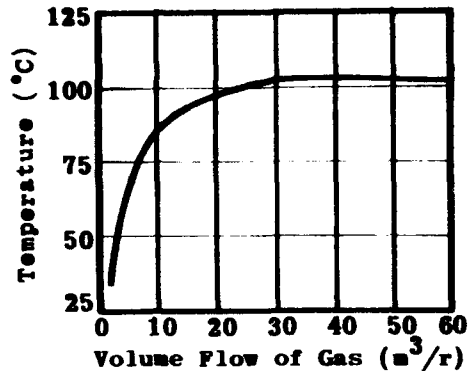
The design of a probe will generally be satisfactory only for the specific purpose for which the probe is intended, since it is so greatly affected by such characteristics as stream velocity, Reynolds number, and range of temperatures. Of these characteristics, the stream velocity is perhaps the most critical. This is particularly true in the wind-tunnel field, where low velocities are usually closely allied with moderate temperatures and small temperature differences. In this regime stem conduction effects predominate. Temperatures become more extreme as the Mach number of the flow increases and the limiting values of the static and stagnation temperatures differ as the square of the velocity (Eq. 4-1). In this flow regime radiation effects predominate.

For very low velocities with small temperature differences radiation effects are small, and temperatures may be measured by means of mercury thermometers or bare thermocouples with appropriate correction factors. Frequent calibration is necessary with bare thermocouples since the recovery factor varies from 0.6 to 0.8, depending on the type of weld and the alignment of the junction with the flow. Radiation effects may be reduced somewhat by plating the sensitive section with gold, silver, or platinum, thus lowering the emissivity. At the same time, however, the film coefficient is also reduced and part of the benefit cancelled. This technique should only be used in flows which are dust free. To ensure accuracy within 1°F, proper caution must be exercised in the mounting and correction of thermocouples and mercury thermometers for stem conduction. Specifications for the use of mercury thermometers are detailed in Refs. 161, 162, and 165. The necessary considerations include sufficient immersion of the bulb and the application of a correction factor based on average stem temperature. Similar precautions in the use of thermocouples, bare or in wells, are discussed in Refs. 164 and 165.

Where the velocity of the flow is too low to provide sufficient convective heat to balance the conductive and radiative heats, it may be increased by the use of an aspirator. Such a probe, shown below, is described in detail in Ref. 166.



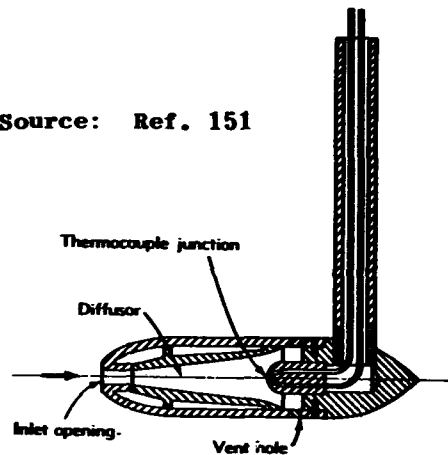
The compressed air velocity may be regulated until a temperature equilibrium is reached. The suction tube also acts as a radiation shield. The effect of mass flow of air on the indicated temperature of such a probe (Ref. 166) is shown below.



In combustion experiments, where there are high temperatures and low velocities, the suction tube may be packed with refractory tubes which surround the hot junction.

Where the stream velocity is high (transonic or supersonic), it must be decelerated to some optimum value dictated by the heat balance between the convective, conductive, and radiative heat contributions. This critical velocity will be dependent upon the total temperature, the temperature difference, and the Reynolds number (based on probe diameter) as well as on the probe material and configuration. The deceleration is usually accomplished by means of a diffuser or stagnation chamber. A typical probe of this type is the Franz probe shown below.

Source: Ref. 151

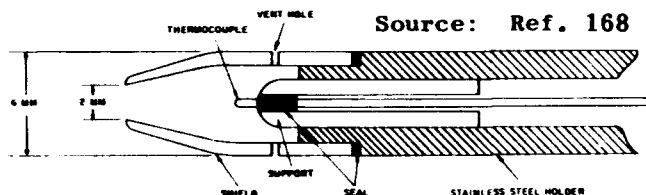


Vent holes allow the gas to escape before it has been cooled by the outer surface. The size and number of the vent holes behind the sensing junction determine the mass flow rate of the air and the heat transfer coefficient of the probe surface. The stagnation chamber is also the radiation shield. Such an instrument is insensitive to angles of yaw up to the stall angle of the diffuser. Franz determined the recovery factor to be 1.0 up to 650 ft/sec air velocity. A similar probe

designed by Eckert (Ref. 167) had a recovery factor of 0.99 up to 980 ft/sec.

A simple probe, easily manufactured and rugged enough to withstand the severe vibrations encountered in supercharger testing, was developed by Pratt and Whitney. Its outer diameter is only 0.1 in., but at high temperatures it should be surrounded by one or more radiation shields. The probe design and its recovery factor as a function of both air-flow speed and angle of attack are shown in Fig. 4-5.

In high Mach number tunnels it is necessary to have elevated stagnation temperatures in order to avoid condensation effects in the test section. Since the temperature gradient is high the sampling area should be minimized; this requires probe entrances of the order of 1 mm. Reference 168 gives details of the design and calibration of several such probes which were used at Mach numbers from 1.5 to 7.6 at temperatures up to 800°K. All the probes were of the same basic design shown below.



The shield is made of low conducting silica coated with platinum to reduce conduction losses. It is cemented to the stainless steel holder by means of a thermally insulating cement.

The thermocouple is 30 or 38 gage iron-constantan wire, fiberglass insulated and sealed in a silica support by means of thermally insulating cement. The exposed surface of the support is platinum plated. Three elements were varied, the ratio of the area of the vent holes to the entrance area, the shield design, and the exposed length of the thermocouple. The probes were calibrated at several Mach numbers and under a range of stagnation temperatures. The correction factor, K (also often called the recovery factor, r), is shown as a function of Reynolds number, Mach number, stagnation temperature, vent-to-entrance-area ratio, and length-to-diameter ratio in Figs. 4-6 to 4-9. For a complete understanding of these figures and the many parameters involved in them one should read Ref. 168. A brief examination of the figures however, will point up several facts, the most important of which is the need to calibrate a temperature probe over the full range of parameters that will be involved in a test. Such calibration may require much ingenuity in providing flows of known parameters in the given range. The correction factor (or recovery factor) becomes constant beyond a critical value of most of the parameters, but below this value it is well defined. It is possible to determine an optimum ratio for the vent-to-entrance areas and also for the length-to-diameter ratio and thus minimize the change in correction factor due to the unavoidable parameter ranges imposed by test conditions. Under the conditions of the tests described in Ref. 168, the conduction error is much greater than the radiation error. This is reflected in the fact that increasing the length of exposed thermocouple wires reduces the total error by increasing the area over which convective heat transfer takes place. The balance between the three types of heat transfer is critically dependent on the probe construction and the environment in which it is used.

4.5 Thermo-Electric Thermometry

The most versatile method of measuring the solid-body temperature of a probe utilizes the thermo-electric power of a bimetallic thermocouple circuit. This technique is most common, since it offers precision, low cost, and simplicity of operation.

Although a thermal emf is developed when the junctions of any two dissimilar metals are maintained at different temperatures, only certain combinations of metals are suitable for use as thermocouples. The combinations most extensively used are given in Table 4-2 together with their pertinent characteristics. For the measurement of temperatures up to 5800°F thermocouples are made of tungsten and tungsten-molybdenum (Ref. 169); for temperatures up to 3800°F, iridium with an iridium-ruthenium alloy (Ref. 170). Much additional information on other metallic combinations is readily available in the literature (e.g., Refs. 171 to 178).

The life of a chromel-alumel or an iron-constantan thermocouple is approximately 1000 hr when used at atmospheric pressure within its normal temperature range (Table 4-2).

Thermocouples are formed by welding, soldering, or brazing together the appropriate wire secured from a reputable manufacturer. Procedures and precautions in the manufacture of junctions are detailed in Refs. 165 and 172. The recovery (or correction) factor of a thermocouple is dependent upon the type of junction, i.e., whether it is a butt weld, a twisted weld, or a ball weld, and also upon the orientation of the wire to the fluid flow.

Clean air appears to be the best protective atmosphere for thermocouples at high temperatures. Reducing and corrosive gases will quickly deteriorate most thermocouple metals, resulting in large fixed errors which are difficult to detect. Such applications require elaborate, gas-tight shielding of the junction. Cold working of thermocouple wire will result in errors; therefore care should be exercised to avoid kinks or sharp bends.

Steep temperature gradients may cause large errors with otherwise "homogeneous" wire. Installations should be insulated to reduce temperature gradients along the thermocouple wire.

The method usually followed to connect thermocouple circuits requires that all intermediate junctions, switch gear, and instruments be maintained at room temperature, appropriately shielded from drafts, radiation, and stray electric fields (Ref. 179). The low-temperature junctions are usually maintained in an ice bath contained in a thermos bottle. In low-precision work the room temperature indicated by a mercury thermometer is often used as a reference; the "cold" junction is frequently in the instrument.

The uncertainty interval to be expected with new thermocouple wire, using the manufacturer's published data, can be secured from each supplier. An example of such data (Ref. 176) is presented in Table 4-2.

4.5.1 Indicating Instruments for Use with Thermocouples

The "direct-deflection" and "null-reading" methods are commonly employed to provide a visual reading of the resultant emf existing in a thermocouple circuit. A typical thermocouple will produce an emf of 30 $\mu\text{v}/^\circ\text{F}$ temperature difference between the junctions. The accurate measurement of such minute potentials requires precision instruments and careful circuit construction.

The direct deflection method usually employs a millivoltmeter to indicate the emf. The less sensitive instruments are often supplied with scales, reading temperature in degrees Fahrenheit or Centigrade for some specific combination of thermocouple metals. Higher accuracy is obtained through the use of a sensitive instrument which is calibrated for each specific thermocouple at appropriate "fixed points" on the absolute temperature scale.

Circuit resistance will introduce an error in the direct deflection measurement because current is flowing in the circuit during the reading. Hence, with this method, great care must be exercised in establishing contacts and junctions.

The null method uses some form of potentiometer which is initially balanced against a standard cell. Many forms of these instruments are available, the best giving accuracy to about 0.0001 mv or about 1/300 $^\circ\text{F}$ for iron-constantan couples. No current flows when the galvanometer is balanced, and circuit resistance therefore introduces no error in the measurement, although it does decrease the instrument sensitivity.

Factors to be considered in the selection of the indicating instrument are accuracy, cost, and ease of operation. Simple direct-deflection instruments are commonly used in routine testing since they are inexpensive and easy to operate. However, they are accurate only to about 5 $^\circ\text{F}$. Direct deflection instruments (Refs. 165, 172, 180, and 181) are also available for high-precision laboratory work; however, they are expensive and lack the ruggedness of the industrial equipment. Most instruments may be used for automatic recording.

Null reading potentiometers (Refs. 148, 165, 172, 180, and 182 to 185) can be obtained in a wide price range, depending upon their accuracy.

All high-precision instruments of either type require a complex setup and delicate handling for the highest accuracy.

4.6 Supplementary Techniques for Measuring Gas Temperature

The insertion of any instrument into a flowing gas will often cause disturbances of the stream which so alter the flow that readings are meaningless. This situation occurs in very high velocity flows and during measurement in small passages. The problem is particularly serious in the presence of severe radiation, since shielded probes are usually quite large. Such difficulty occurs in the measurement of high-velocity, high-temperature streams. If an instrument cannot be inserted into the flow, it is difficult to measure temperatures at a point.

Other methods usually secure only average values, which may be of little use in flows possessing steep temperature gradients.

Spectrographic and absorption techniques may also be used to measure gas temperature. The gas density may be measured with the interferometer, stream pressure with a stream-pressure tap, and the stream temperature calculated from the perfect gas law. A modified D-line reversal technique of temperature measurement is described in Ref. 150. The radiation intensity of a temperature-calibrated continuous spectrum emitter (tungsten ribbon filament lamp) is compared with the temperature-dependent radiation intensity of the sodium D-line emitted by the sodium atoms added to the flow. When the continuous source is beamed through the flow, the sodium D-lines will stand out against the background if the flow is hotter than the source; but if the flow is cooler the D-lines will appear reversed (dark). The background temperature is varied by the operator until the radiation intensities match. Then, ideally, the flow temperature is equal to the known background temperature.

Since the velocity of sound in a perfect gas is proportional to the square root of the absolute temperature, the latter may be calculated from a measurement of the former. This method is attractive because calibration is not necessary and the flow is not disturbed. However, it is essential to determine the stream velocity accurately since the relative acoustic speed must be known in order to calculate the temperature. Several methods of generating weak waves or pulses are given in Ref. 151, Sections C and D. The temperature obtained in this way is an average over the distance that the wave travels. Errors may be incurred where the presence of a thick boundary layer is not taken into account. Turbulence in the free stream also makes these techniques unreliable.

Another technique having limited applicability utilizes the flow of a gas through an orifice. If the mass flow through an orifice is known, the time required is proportional to the square root of the temperature. With this method the gas is passed through two orifices consecutively, and the gas temperature at one of the orifices must be known. The pressure drop across each orifice is measured and the unknown temperature then calculated, since the pressure drop across an orifice is proportional to the absolute temperature (Refs. 43 and 186 to 190). Since stagnation-pressure measurement is unaffected by radiant heat transfer, this technique has obvious advantages when severe radiation is present. Corrections must be made for conduction losses in the mass-flow measuring devices.

4.7 Application of Temperature-Measuring Techniques

The increasing use of temperature-measuring techniques in supersonic wind tunnels is devoted for the most part to the study of heat-transfer characteristics of solid bodies immersed in a moving air stream or to the study of the temperature distribution through the boundary layer. Hypersonic tunnels, or at least the small ones as indicated in Ref. 191, are designed primarily for the investigation of heat-transfer phenomena. These investigations are concerned with the study of steady-state heat transfer, the study of transient heat-transfer effects, and the development of required instrumentation.

4.7.1 Steady-State Heat Transfer

The study of steady-state heat transfer often requires a continuous flow of coolant for the model, and employs a model shell that is thick enough to allow an accurately measurable temperature differential between the outer and inner surfaces of the shell. This differential is generally measured with thermocouples. Usually a one-dimensional heat flow through the shell is assumed. However, when surface temperature gradients are high, this assumption may lead to noticeable error. Insulated plugs of small diameter are therefore inserted into the surface so that the physical reality and one-dimensional theory may be approximated as closely as possible. The centerlines of these plugs, which are of the same material as the model, are normal to the model surface, and their ends are flush with the outer and inner surfaces of the shell. Thermocouples are attached to both ends of the plugs or at known distances from the ends. Since the heat flow is constant after equilibrium conditions are established, the sensing instruments can be relatively simple.

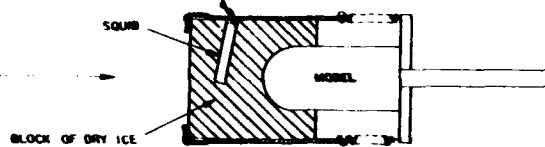
When pairs of thermocouples are used to measure the temperature gradient in a thick shell, the differential millivolt output is usually quite low, unless the two thermocouples are spaced reasonably far apart (i.e., when the shell is thick). Since the heat flux in a solid is generally three dimensional, the ambiguity in determining the normal temperature gradient between two widely separated points may be as large as 50% to 100% of the measured values. A device constructed to avoid these difficulties (Ref. 192) allows the distance between the thermocouple pair to be greatly reduced while the required millivolt output for a given heat flow is maintained. This heat transducer or heat meter is really a thermopile on a miniature scale, with the meter wiring wound on a glass core 0.007 by 1/16 by 1/8 in. Fifty turns of 0.0001-in. constantan wire spaced 0.001 in. apart are wound on the core. To plate one-half of the loop, the long edge of the meter is immersed in a silver-plating solution. Thus an effective silver-constantan junction is formed on each loop at the center of the two flat sides of the meter. To prevent shifting or damage to the wires, a thin coat of high-temperature cement, such as Adweld for medium temperatures (500°F) or Sauerisen for high temperatures (1000°F), is applied. The finished meter is about 0.010 in. thick. For areas of high heat transfer such as the stagnation point, only 25 turns are needed, so that the meter measures only 1/16 by 1/16 by 0.010 in.

4.7.2 Transient Heat Transfer

A different technique is required for the study of transient heating effects. Here the model must have a very thin skin to minimize surface conduction in the presence of thermal gradients. The outer and inner surfaces of the skin are at essentially the same temperature. Only one thermocouple, however, is required at each point where a temperature measurement is desired. Since the thin skin has low thermal capacity, the thermocouples and their sensing instruments must have very fast response times. The heat-transfer characteristics are determined from the rate of change of temperature with time. The model should be cooled initially and then suddenly exposed to the air flow. Since an appreciable time is required for even an intermittent tunnel to reach operating pressure and temperature, some method is required for shielding the model until operating conditions are reached.

One method, used both for cooling the model and for initial shielding, employs a dry-ice (solid carbon-dioxide) cap of sufficient thickness to shield the model during the stabilization time of the tunnel. The dry ice sublimates until it weakens, and the aerodynamic forces then break it off and expose the model to the air flow.

In a typical test (Ref. 193) a cap of dry ice was put on the model just before the wind was turned on, as shown below.



Two clips and springs held the cap in place. The cap was made by heating a solid steel replica of the model to red heat and pressing it into the dry ice. The final outside shape was cut on a saw. The model used was a 4-1/2-in. diameter hemisphere made of a dielectric, such as glass. The skin was 0.2 in. thick and was instrumented with thermocouples. Forty-gage copper-constantan thermocouples were run along lines of constant temperature for about 30 wire diameters on each side of the thermocouple junction before being brought inside the model. Conduction errors were thus minimized. The results were recorded on Bristol wide-strip recorders capable of traversing full scale in two-thirds of a second. Unfortunately, holes frequently develop in the cap before it breaks away, so that only about one run in three is successful. The squib shown is a suggested solution to this problem.

Another method (Ref. 194) employs a retractable shield, which is also designed to carry the coolant to the model. The advantage of this technique is that lower model-surface temperatures can be obtained. Low temperatures approximating 140°F have been attained by use of liquid nitrogen as the coolant. Some fast-response heat-transfer measurement devices for use in shock tubes are reported by Cornell Aeronautical Laboratory (Ref. 195).

4.7.3 Temperature Distribution in the Boundary Layer

The transition from laminar to turbulent boundary layer on a model may be found by surface temperature measurements, since turbulent heat transfer is greater than laminar. The traversing pitot thermocouple (Ref. 196) shown in Fig. 4-10 is used to measure temperature distribution in the boundary layer. For temperature measurement in a boundary layer on a flat plate, this instrument requires sufficient mass air flow over the thermocouple to give a high recovery factor. Its pitot head, moreover, must be of small diameter because the boundary layer is very thin. (During the tests discussed in Ref. 196 it was only of the order of 0.2 in. even at the end of the plate.) The temperature and pressure readings must be taken at the same time and at the same point in the boundary layer, i.e., by means of a single instrument. A copper-constantan couple produces one microvolt for a temperature difference of the order of 0.025°C. Readings are therefore obtainable to within 0.01°C, but accuracy under test conditions is nearer $\pm 0.05^\circ\text{C}$ due to flow fluctuations.

The thermo-junction wires of this pitot thermocouple are of 0.002-in. diameter and the pitot head is between 0.005 and 0.010 in.

o.d. The wires are threaded through the supporting inner glass and quartz tubes to insulate them from the steel supporting tubes. It should be pointed out that the wires are themselves insulated with a shellac-type coat and covered with silk, but the inner glass and quartz tubes help in assembly and are an added insulating medium. To counter any possibility that the wires will rub and cause a short circuit in the support tube, the couple is threaded into the quartz pitot head and the head is then inserted into the 1.5-mm tube. Extreme care must be taken to ensure that the couple remains near the tip of the head and that the small couple wires do not snap, which is particularly difficult when 0.002-in. wires are used.

The seal is made by coating the quartz with platinum (by a liquid platinum process), copper plating this coat, and then soft soldering the joint. This method has proved very successful, and if reasonable care is taken an airtight joint should be obtained. At the other end of the support tube the wires and the manometer lead are fused into glass which also contains a lead to the manometer.

A T-piece is inserted between the lead and the manometer, and a connection made to a vacuum pump. When this by-pass is open, air flows over the thermocouple wires and through the by-pass, ensuring a consistent recovery factor for the thermocouple. When this by-pass is closed, the pressure in the traversing tube rises to give the total head. By this means it is possible to obtain readings of temperature and pressure at the same position and almost at the same time.

Typical temperature recovery factors obtained with different sizes of pitot head and by use of the traversing gear shown in Fig. 4-11 are tabulated below.

Pitot Head Tip (o.d., in.)	0.075	0.040	0.020	0.0085	0.005
Recovery Factor	0.995	0.970	0.960	0.920	0.898

The majority of the measurements were made with tips of 0.020 in. diameter and less. The tabulated recovery factors were measured in the free stream, and it had to be assumed that they would remain constant through the boundary layer. At the time these tests were undertaken the radiation effects were checked by mounting a vertical, steam-heated copper plate and a pitot thermocouple in an evacuated flask. There was no rise in thermocouple temperature until it was only a few thousandths of an inch from the plate. By directing a small air jet at the pitot head this rise could be delayed until the shield was touching the plate.

Another method for detecting temperature differences utilizes the Evaporograph, an instrument developed by Baird Associates, Inc. This instrument employs a thin film of oil whose evaporation rate is proportional to the amount of infrared radiation to which it is exposed. The variation in oil film thickness induced by the infrared radiation forms an image which is readily translatable to temperature differences. To transmit the infrared radiation from its source outside the wind tunnel, however, a special material such as silver chloride, germanium, rock salt, or sapphire must be used. The Evaporograph has been used with some success at AEDC (Ref. 191) to detect boundary-layer transition.

Table 4-1

Recovery factors measured under various conditions

Type of Flow	Model	Mach Number	$Re \times 10^{-6}$	Recovery Factor	Source
Laminar	Cone	2.0	2.7	0.855 ± 0.008	Wimbrow, 1949
Laminar	Cones ($10^\circ - 80^\circ$)	0.88 - 4.65	$6 (\times 10^{-3})$	0.845 ± 0.008	Eber, 1952
Laminar	Cone-Cylinders	0.88 - 4.65	$5 (\times 10^{-1})$	0.845 ± 0.008	Eber, 1952
Laminar	Cone	2.18	0.1 - 1.3	0.851 ± 0.007	des Clerc and Sternberg, 1952
Laminar	Cone	2.0	0.2 - 1.3	0.845	Stine and Scherrer, 1952
Laminar	Flat Plate	2.4	0.2 - 1	0.881 ± 0.007	Stalder, Rubesin, & Tendeland, 1950
Laminar	Flat Plate	2.4	0.15 - 3	0.884 ± 0.006	Slack, 1952
Laminar	Paraboloid	1.5	4.8	0.845 ± 0.008	Wimbrow, 1949
Laminar	Paraboloid	2.0	4.8	0.855 ± 0.008	Wimbrow, 1949
Laminar	Parabolic Body of Revolution*	2.0 - 2.2		$0.848 - 0.860$	Wimbrow, 1949
Transition	Flat Plate	2.4		$0.881 - 0.897$	Stalder, Rubesin, & Tendeland, 1950
Turbulent	Cone**	2.0	2.7	0.855 ± 0.008	Wimbrow, 1949
Turbulent	Cone and Cone Cylinder	2.0 - 3.4	7	0.882 ± 0.007	des Clerc and Sternberg, 1952
Turbulent	10° Cone	1.97 - 3.77	0.4 - 4	0.882 ± 0.008	Stine and Scherrer, 1952
Turbulent	40° Cone-Cylinder	3.10 - 3.77	0.3 - 1	0.885 ± 0.011	Stine and Scherrer, 1952
Turbulent	Cones and Cone-Cylinder	2.87	1	0.92	Eber, 1952
Turbulent	Cones and Cone-Cylinder	4.25	0.25	0.97	Eber, 1952
Turbulent	Flat Plate	2.4	0.2 - 1	$0.884 - 0.897$	Stalder, Rubesin, & Tendeland, 1950
Turbulent	Flat Plate	2.4	3	0.906	Slack, 1952
Turbulent	Flat Plate	2.0	10	0.880 ± 0.004	Hilton, 1951
Turbulent	Flat Plate	1.75		$0.898 - 0.915$	Eckert
Turbulent	Paraboloid	2.0		0.845 ± 0.008	Wimbrow, 1949
Turbulent	Paraboloid	1.5	4.8	0.845 ± 0.008	Wimbrow, 1949
Turbulent	Cylinder Parallel to Flow	1.86 - 4.38		$0.910 - 0.979$	Wimbrow

*With variation of surface roughness

**Artificially tripped boundary layer

Table 4-2

Temperature limits and uncertainty intervals for
Leeds and Northrup thermocouples

Temperature Limits (°F)

Material	Couple Condition	B and S Gauge					
		8	14	16	20	24	30
Platinum and Platinum-Rhodium	Bare	---	---	---	---	---	---
	Protected	---	---	---	2800	2700	2400
Chromel and Alumel	Bare	2000	1700	1700	1600	1400	1300
	Protected	2300	2000	2000	1800	1600	1500
Iron and Constantan	Bare	1200	900	900	800	650	600
	Protected	1400	1100	1100	900	700	700
Copper and Constantan	Bare	---	600	500	400	400	400
	Protected	---	700	600	500	400	400

Uncertainty intervals

Type of Thermocouple	Temperature Range (°F)	Standard Limits of Error
Platinum, Platinum-Rhodium	0 to 1000	+5°F
	1000 to 2700	±0.5%
Chromel and Alumel	0 to 530	+4°F
	530 to 2300	±3/4%
Iron and Constantan	0 to 530	+4°F
	530 to 1400	±3/4%
Copper and Constantan	-300 to - 75	+2%
	- 75 to +200	±1-1/2°F
	200 to 700	±3/4%

Source: Ref. 1

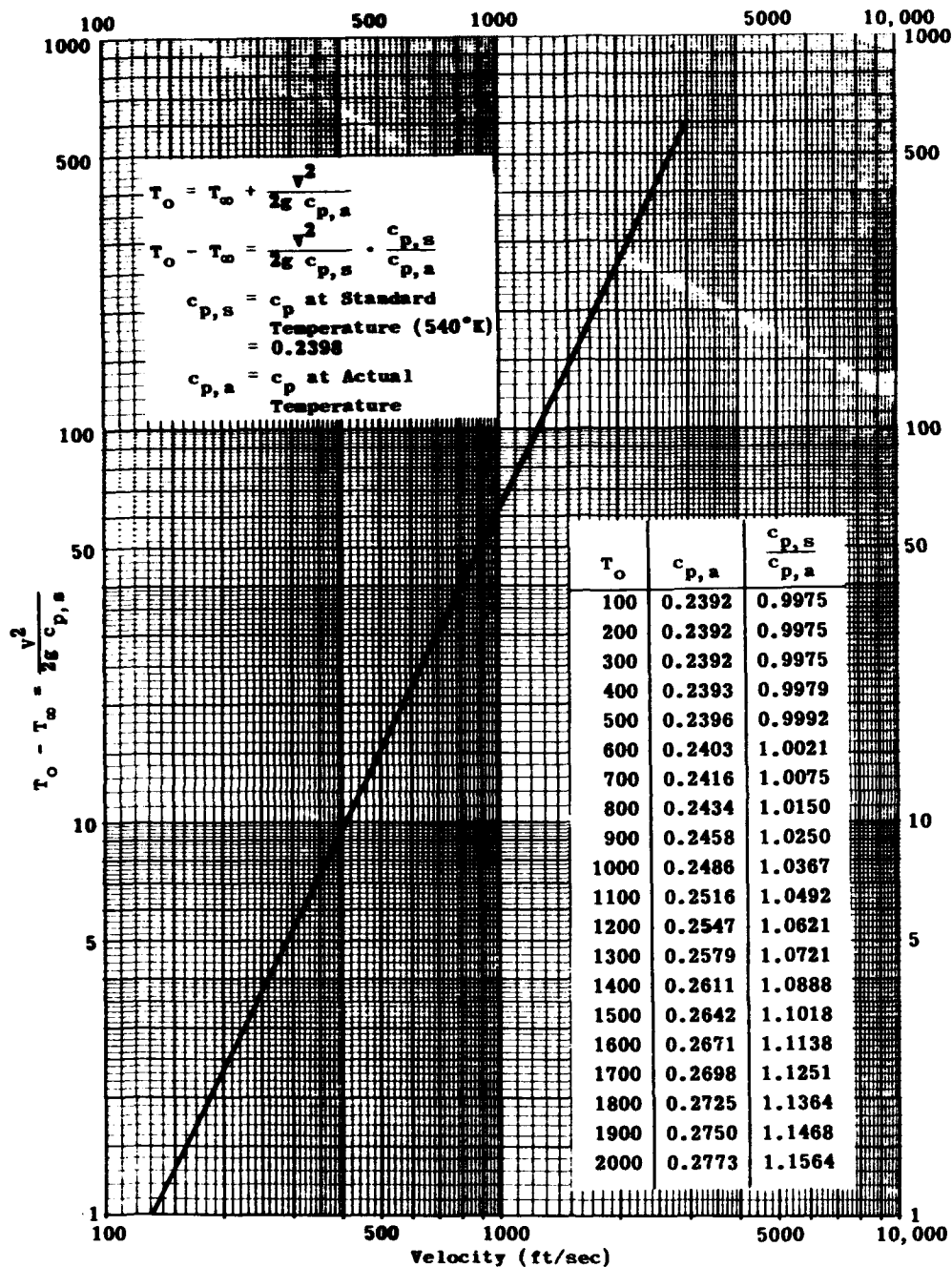


Fig. 4-1. Difference between stagnation temperature and stream temperature vs velocity for air at atmospheric pressure.

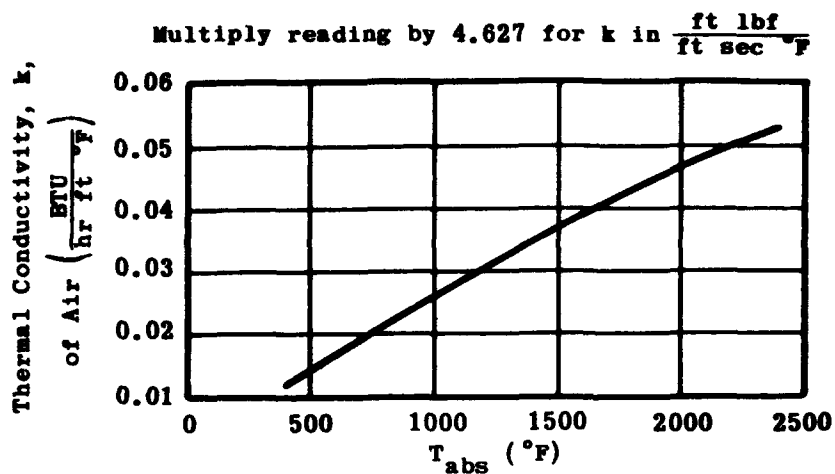


Fig. 4-2. Thermal conductivity of air vs temperature.

Divide reading by $g = 32.17 \frac{\text{lbm ft}}{\text{lbf sec}}$ for μ in $\frac{\text{lbf sec}}{\text{ft}^2}$

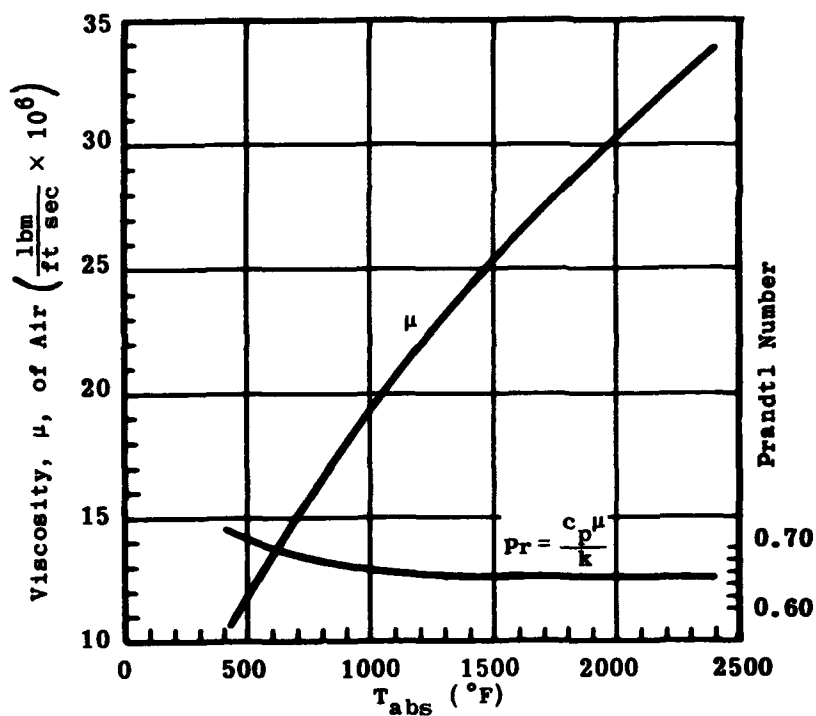


Fig. 4-3. Viscosity and Prandtl number of air vs temperature.

$$a, b \begin{cases} T_o - T_w = 400^\circ R \\ T_{ave} = 1460^\circ R \end{cases}$$

- a = 5 Shield, Radiation
 b = Bare Thermocouple, Radiation
 c = Bare Thermocouple, No Radiation
 d = Mercury Thermometer, No Radiation

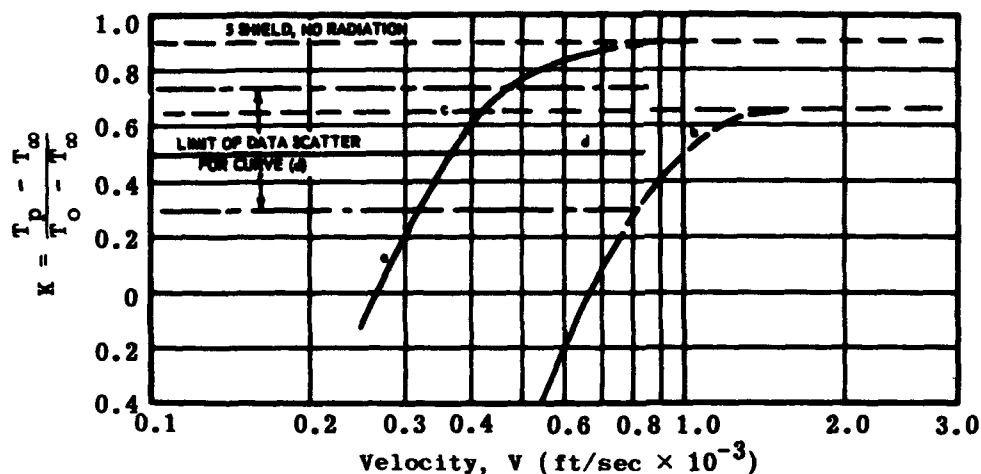


Fig. 4-4. Effect of radiant heat transfer on shielded and bare thermocouples.

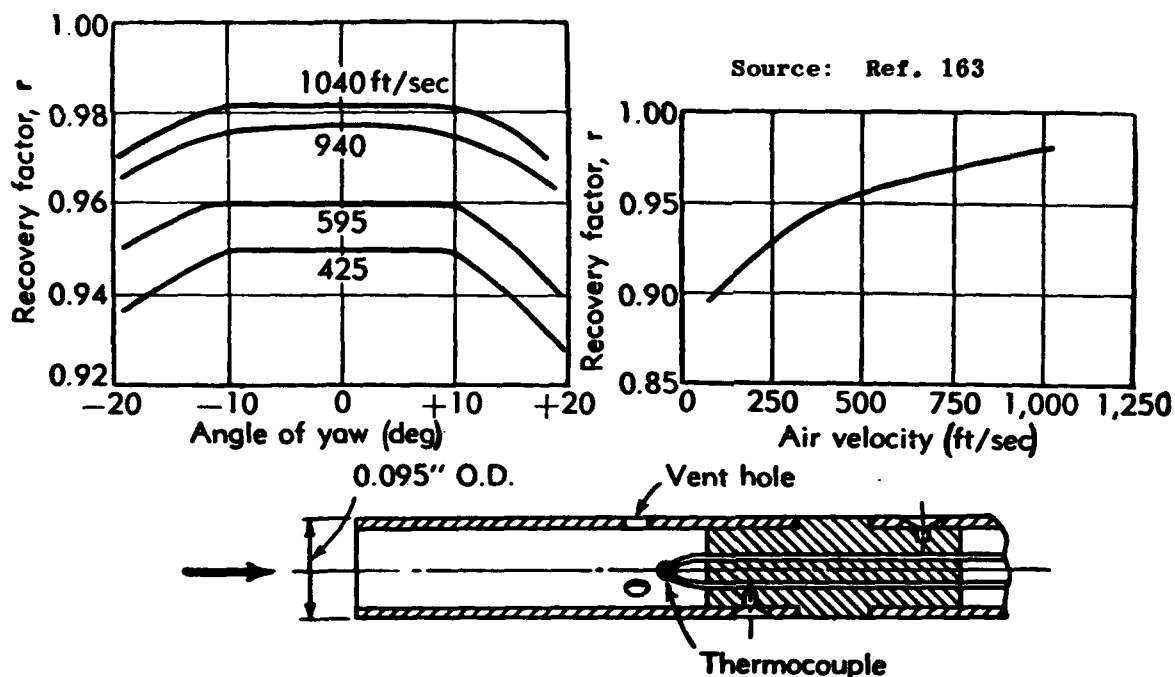


Fig. 4-5. Sensitivity and recovery factor of Pratt and Whitney probe.

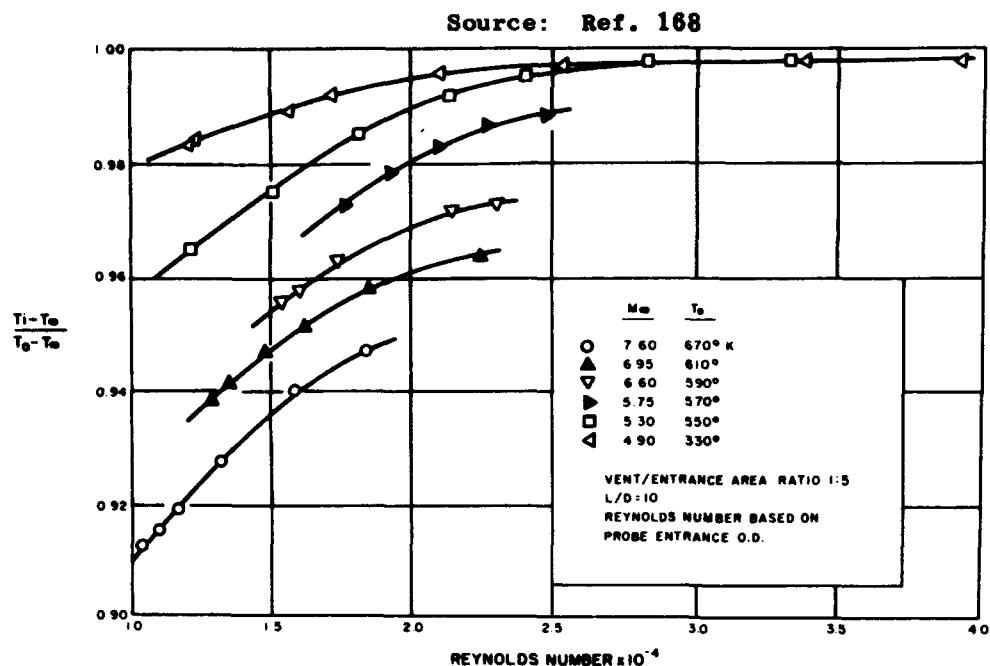


Fig. 4-6. Variation of probe temperature recovery factor with free-stream Reynolds number at various free-stream Mach numbers.

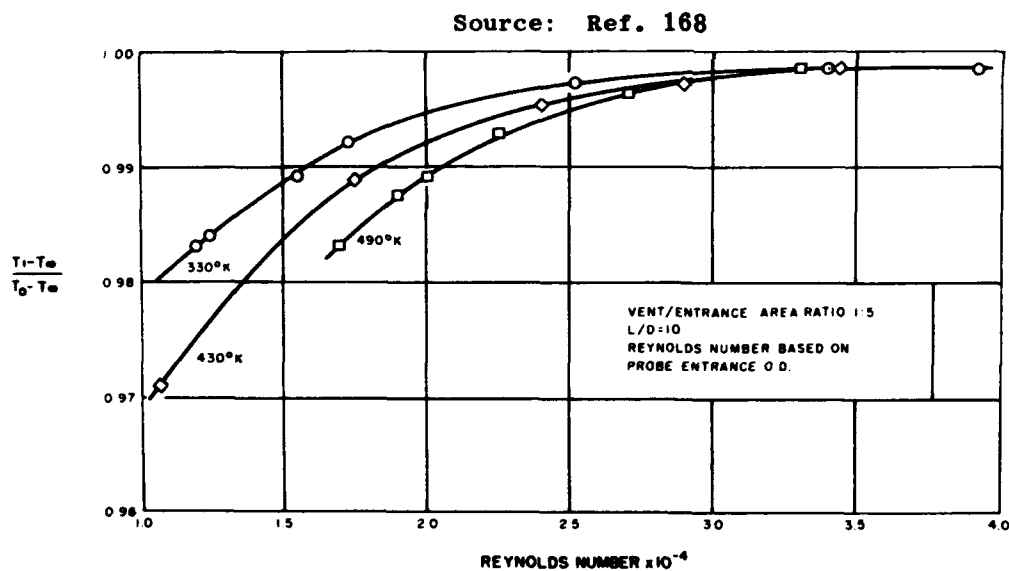


Fig. 4-7. Variation of probe temperature recovery factor with free-stream Reynolds number at three different stagnation temperatures for a free-stream Mach number of 4.90.

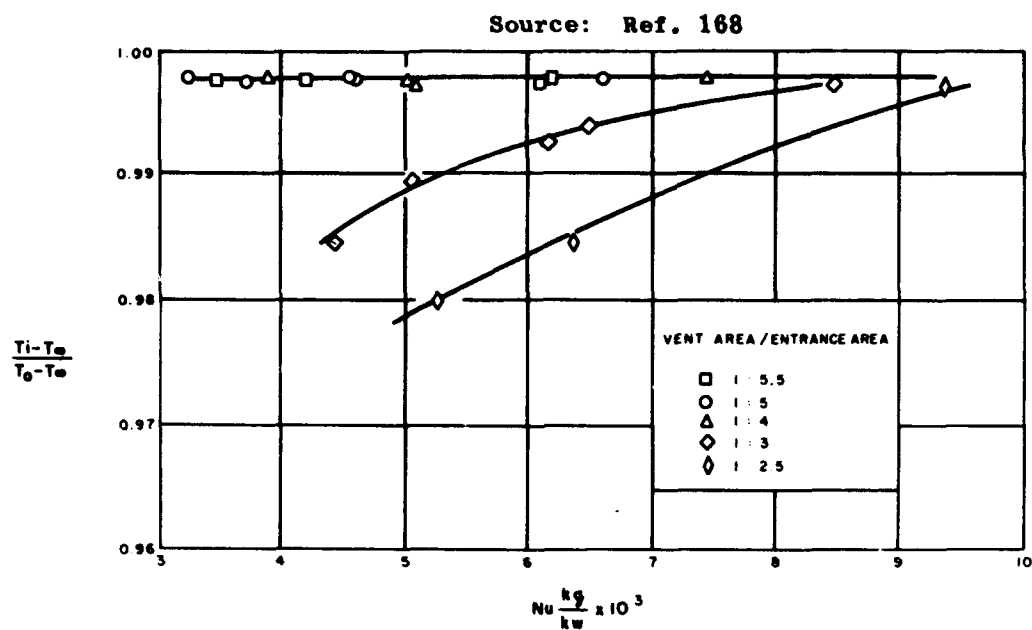


Fig. 4-8. Variation of probe performance with vent-to-entrance-area ratio.

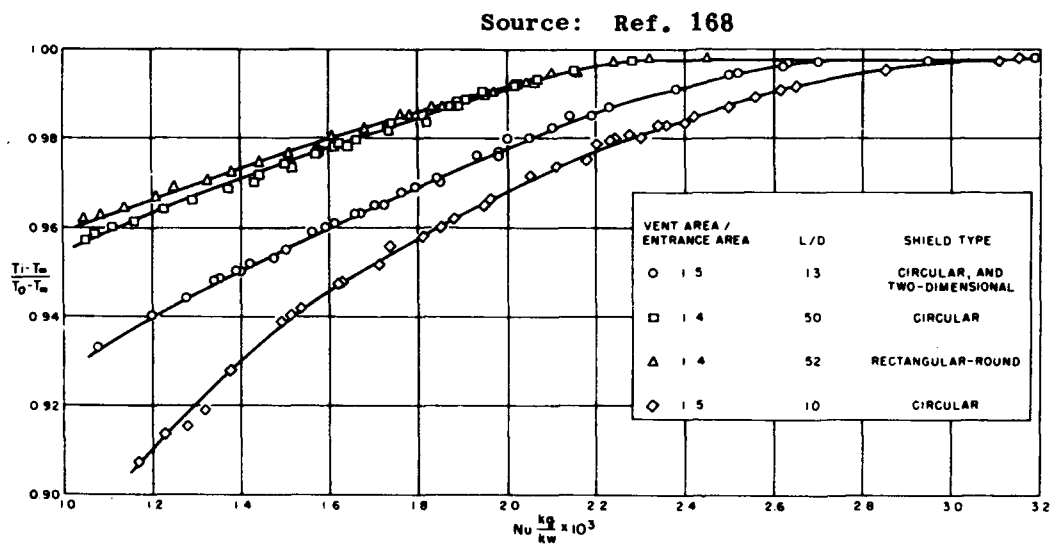


Fig. 4-9. Summary of calibration data for five probes.

Source: Ref. 266

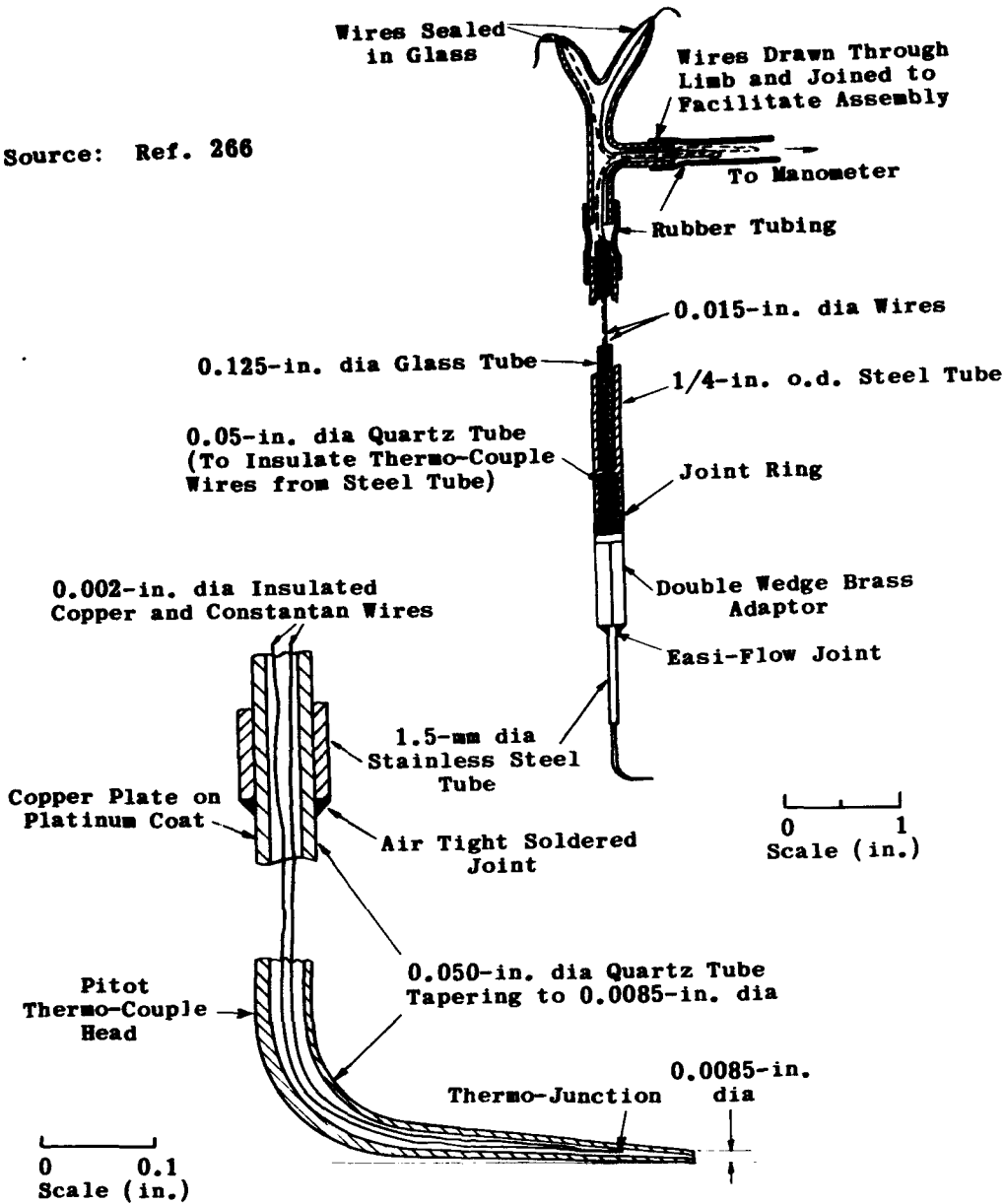


Fig. 4-10. Typical traversing pitot thermocouple.

Source: Ref. 266

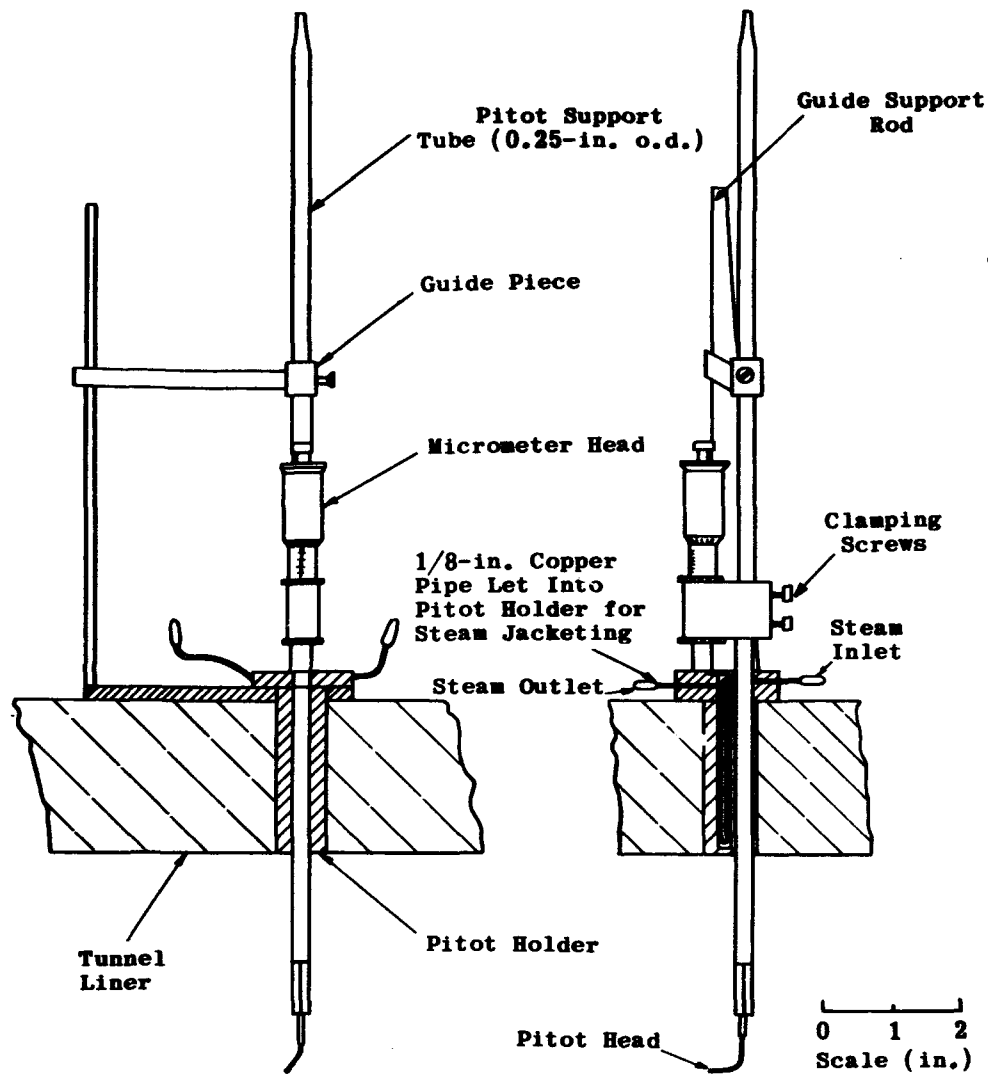
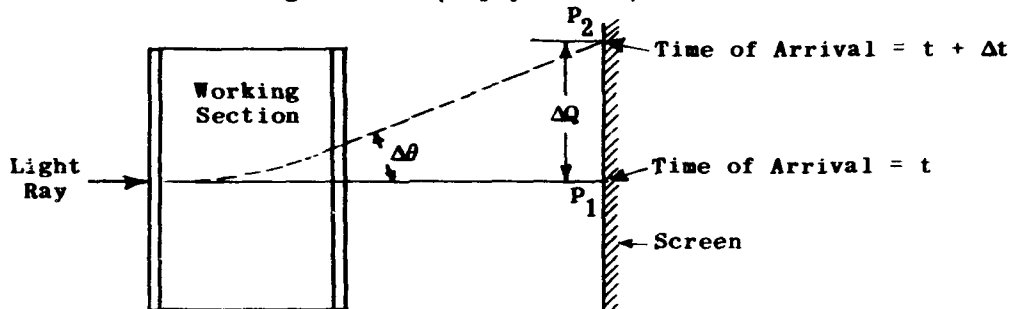


Fig. 4-11. Details of pitot-tube traversing gear.

5. Flow Visualization

Among the methods commonly used to determine the characteristics of compressible flow are those optical techniques known as flow visualization (Refs. 1 and 151), a term normally applied to conventional shadowgraph, schlieren, and interferometer techniques. These techniques are extremely valuable because they provide information about the flow without disturbing it. Their high sensitivity provides qualitative as well as quantitative checks on the many current flow theories as well as their underlying assumptions. The flow visualization material appearing in this subsection has been expanded to include electrical discharge, afterglow, vapor screen, and the various means of determining the boundary-layer state.

Basic to most optical methods of analyzing fluid flow is the fact that variations of density imply variations in the index of refraction. These variations affect the direction of light rays traversing the fluid. The application of this principle is illustrated in the sketch below, in which a ray of light passes through the undisturbed stream in the working section (empty tunnel) and strikes the screen at P_1 .



When a fluid is flowing through a test section in which a model is also present, the resultant density gradient perpendicular to the light ray causes a change in the optical path. As shown in the sketch, the ray is deflected at angle $\Delta\theta$ (characterized by three direction-cosines) and strikes the screen at P_2 , a distance ΔQ from P_1 , which requires additional time, Δt , to traverse the new path. Observations may be made of ΔQ , and $\Delta\theta$, but Δt is determined indirectly from the change in path length. The effects of ΔQ , $\Delta\theta$, and Δt are often inseparably combined.

In practice ΔQ is observed with a direct-shadow arrangement, $\Delta\theta$ with the schlieren, and the increased path length with the interferometer. It may be shown with reasonable accuracy that Δt (given by the interferometer) is a function of density, $\Delta\theta$ (by schlieren) is a function of the density gradient normal to the light path (actually $1/\rho \partial\rho/\partial x$), and ΔQ (by direct shadowgraph) is a function of the rate of change of the density gradient (see Ref. 197). These methods are therefore complementary rather than alternative. Moreover, since the indication given by each method depends on a different derivative of the refractive index, the required quality of the optical components differs for each. For example, wind-tunnel windows which are satisfactory for qualitative schlieren work may not be suitable for interferometry. For quantitative analyses the windows should always be optically perfect and free of striae.

Since the shadowgraph indicates the second derivative of the density, it is particularly useful for showing rapid changes in density, i.e., shock waves, discontinuities, and turbulence. The schlieren system, which indicates density gradients, is at least an order of magnitude more sensitive than the shadowgraph; it is suitable for smaller changes in density and near sonic shocks and weak rarefaction fans, which are hard to locate on an interferogram. The interferogram, however, since it indicates density changes, gives an interpretable picture from which a density distribution may be evaluated.

The characteristics and advantages of the three viewing systems are demonstrated by the three studies of jet mixing shown in Fig. 5-1. This figure also reveals the advantages derived from the use of all three systems on a single problem, since each accentuates particular features of the flow. The shadowgraph and interferogram show CO₂ mixing with air, and the schlieren shows mixing of two other fluids (Ref. 1). Figure 5-2 is a typical schlieren of a hemispherical-nosed cylinder at Mach 1.25 taken with the setup shown in Fig. 5-3. The Mach lines (weak shock waves) caused by tunnel flow irregularities appear quite strong when compared with some of the shock disturbances from the model. These disturbances are caused by ± 0.01 variations in Mach number and are magnified because they extend across the 19.0-in. tunnel width. The faintly visible elliptical patterns are caused by pouring rings in the three-inch thick borosilicate windows and are not indicative of flow phenomena.

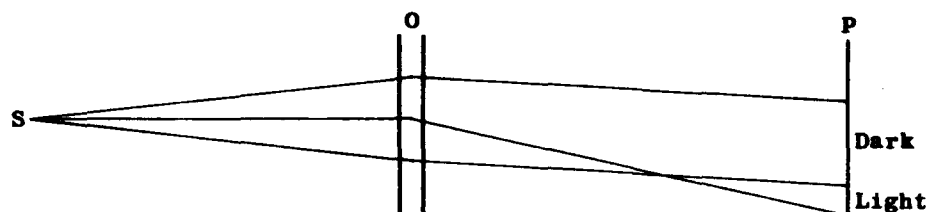
Since optical methods are primarily applicable to compressible flow only, they are often considered as limited to the supersonic regime. It should be noted, however, that all real flows are more or less compressible. Both quantitative and qualitative results have been obtained with the interferometer and with schlieren apparatus, respectively, at airspeeds below 200 fps.

The principal objection to these optical methods is that all density changes in the light paths are integrated across the depth of the field and therefore should be restricted theoretically to two-dimensional flows. In practice, however, they give very satisfactory qualitative results for axis-symmetrical flow and in many cases may even be reduced quantitatively. Serious errors also may arise from phenomena occurring at flow boundaries, such as the ends of a wing, where strict two-dimensionality is destroyed. The integrated density gradients will also be seriously in error where the boundary layer on the test section windows is an appreciable fraction of the test-section depth. The effects of vibration and temperature fluctuations create additional difficulties.

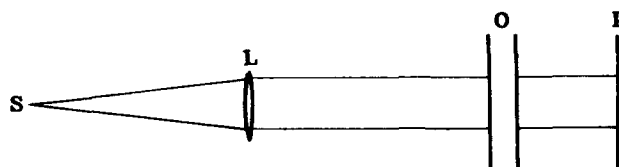
Optical methods of flow visualization are treated fully in Refs. 1, 151, and 198. These references themselves contain excellent bibliographies, and the one from Ref. 1 is presented in Appendix A.

5.1 Shadowgraph

The elementary essentials of the shadowgraph technique are a point source of light, S, and a surface, P, upon which the image of the object, O, may be cast. These characteristics are illustrated in the next sketch.



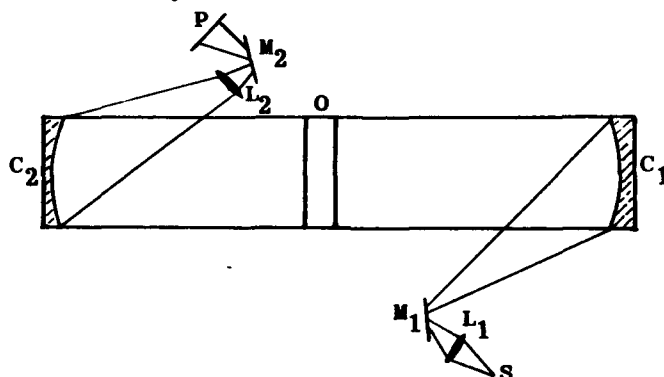
If the density gradient is constant in O , then all the rays will be refracted by the same amount and the intensity of illumination on P will not vary. Where the density gradient is increasing, i.e., where the second derivative of the density is positive, the rays are bent further away from the normal and produce an increased intensity of light in the new position. The place from which they have moved will appear darker. Thus a shock wave will be indicated by adjacent dark and light bands. Despite its simple apparatus, the shadowgraph gives excellent results for such phenomena as shock waves and wake flows. On the other hand, it gives a distorted picture of extended objects, since the magnification varies with position in the field. To overcome this variable magnification the light from a point source, S , may be converted as shown below to a parallel beam by means of a collimating lens, L .



From the point of view of quantitative analysis the shadowgraph also suffers from the lack of 1-to-1 correspondence between the object and the image. The closer the plate is to the field the more nearly this correspondence is approached. Usually photographs are made with the plate at two carefully measured distances from the window, and the width and intensity of specific bands are compared.

In the typical arrangement the lens is 5 to 10 ft from the test section, with the screen or photographic plate 1 to 2 ft from the opposite side. The sensitivity of the system is proportional to the distance between the test section and the plate. The distances obviously are very critical, especially for turbulence studies. If the distance is too great the image lacks definition.

A more useful system, consisting of two lens, L_1 and L_2 , two front face mirrors, M_1 and M_2 , and two concave mirrors, C_1 and C_2 , is shown in the sketch below.

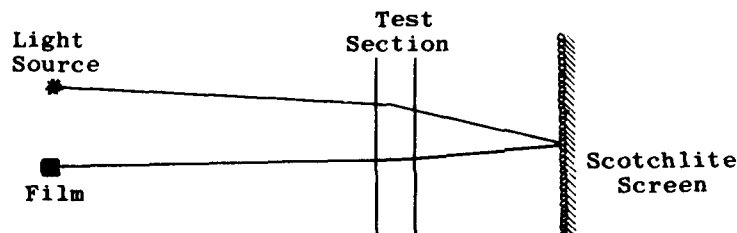


In this system the object and the screen are conjugate planes, and 1-to-1 correspondence is achieved, leaving no ambiguity in the image. If the mirrors are off-axis parabolas the problems of astigmatism, coma, and spherical aberration are also solved.

To obtain the shadow effects, the system is first adjusted so that the object and the image on the plate are in conjugate planes and then the plate is moved slightly to throw it out of focus. All optical surfaces should be of the finest quality and adjusted so that the beam is perpendicular to the windows, and the light source and the image form equal angles with the parallel beam.

Since the intensity of light on the screen or plate is proportional to the second derivative of the density, a double integration is needed to obtain a density distribution. This involves a considerable amount of measurement and computation. The shadowgraph is used, consequently, for qualitative rather than quantitative analyses.

A novel technique for making shadowgraphs of shock waves is described in Ref. 202. An opaque non-specular reflecting surface is used behind the shocks and the shadow image photographed. The high directional reflectivity of a Scotchlite screen reduces the adverse effects of ambient light and enables a satisfactory picture to be obtained with a minimum of artificial light. (Scotchlite is the registered trade mark of a reflective sheeting, made by Minnesota Mining and Manufacturing Co., that is composed of many spherical resin microlenses embedded in the surface.) This technique is illustrated below.



5.1.1 Light Source for Shadowgraph System

Three basic characteristics are associated with the shadowgraph system's light source. The first of these is brilliance, which is of greater concern than the total light output. For continuous observation a Western Electric concentrated-arc lamp is ideally suited. The second requirement is a high-speed light flash. Since one of the advantages of the shadowgraph system is that it gives a clear indication of turbulent effects, the capability for instantaneously "stopping" and photographing the rapidly fluctuating flow is highly desirable. This capability requires either a light source of short duration or a fast-action light shutter. For this second requirement a rotating mirror is sometimes placed at M_2 . A good highly polished steel mirror can be rotated with sufficient speed to give light flashes of the order of 10^{-10} sec. The third requirement of the shadowgraph system is that it should give clear, well-defined images. The diameter of the circle of confusion, d_c , of each point imaged on the screen is given by

$$d_c = \frac{d_s \text{ (distance from object to screen)}}{\text{focal length of lens}} \quad (5-1)$$

where

d_s = diameter of the light source

From this it may be seen that d_s should be as small as possible. A value of $d_c \leq 0.01$ in. is desirable.

A simple spark is entirely adequate for a shadowgraph. Though its total light output is small, its intrinsic brilliance is extremely high. Such a spark, powered by a 0.024- μ f capacitor and firing in the neighborhood of 15,000 v, provides a 2- μ sec exposure that is adequate for a plate or film 4 or 5 ft away from it.

The shadowgraph light source used in the system shown in Fig. 5-3 consists of a GE Pyranol condenser powering a conventional Libessart high-pressure gap (0.125 in.) and rated at 0.12 μ f at 15,000 v. The light source produces a peak light intensity within 0.25 μ sec, with a gradual decay to zero at 3 μ sec at 10,000 v. The sharpest definition of axi-symmetric boundary-layer transition was obtained using the shadowgraph technique, with the light source located between 25 and 50 in. from the test section window and the film placed against the opposite window. A better definition of the boundary-layer flow resulted from further development of this light source, which employed a Sprague Vitamin-Q condenser rated at 0.3 μ f and 15,000 v. However, no adequate measure of the light duration with the Sprague condenser was obtained. Kodak Linagraph Ortho film developed in Kodak D-19 solution for 3.5 min and Kodak Contrast Process Ortho film developed in 1-to-1 and 3-to-1 solutions of D-19 for 5 and 6.5 min have been used successfully.

If the energy in watt-seconds supplied to the source is known, the following equation (Ref. 1) may be used to determine the allowable distance, r , in feet between the source and the film.

$$r^2 = \frac{(\text{watt-sec}) (W.R.)}{96\pi} \quad (5-2)$$

where

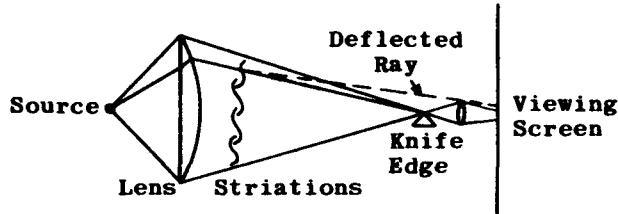
W.R. = Weston rating of the film

This relation is highly approximate and valid only for an order of magnitude. Actually there is great flexibility in the setting of the source. Probably the best method of determining an adequate setting is simply to expose some film until the results are satisfactory.

5.2 Schlieren Systems

In schlieren systems the ambiguity of the shadow (shown by the shadowgraph) is eliminated by the insertion of a lens into the light beam, which produces an image which may have 1-to-1 correspondence with the disturbance. The light intensity on the screen is then a function of the deflection of the rays, which in turn is a function of the density gradient normal to the beam. Although the schlieren system has been widely used in wind-tunnel work to give a qualitative analysis of

the form and position of shock waves, expansions, and flow separations, it does not lend itself readily to the quantitative determination of density since it requires an integration of the observed gradients. With a schlieren picture, however, the quantitative determination of density is simpler than is that of the shadowgraph which requires a double integration. Satisfactory visualizations of strong shocks or steep density gradients may be achieved with comparatively simple systems having optical components which are not of excessively high quality. However, weak shock patterns and quantitative evaluations require high quality components and fine adjustments. Both two-dimensional and axially symmetric flows may be projected with reasonable accuracy.



The above sketch shows a schlieren system of the simplest type, consisting of a small rectangular source of light, a lens, a knife edge, and a focussing lens to image the schlieren on a viewing screen. Light from the source is converged to an image by the lens. If a knife edge is placed at the image so that it just covers the slit of light, the viewing screen remains dark. If a striation located anywhere between the knife edge and the point source deflects a ray of light passing through it in such a way that it will pass over the knife edge, it will continue to the viewing screen. In this manner a pattern of bright areas corresponding in shape to the pattern of the striations is produced on the viewing screen.

To bring out the regions where the rays are deflected both upward and downward, the knife edge is customarily adjusted to cut off the major part of the source image rather than all of it. To view the regions which deflect rays to the right or left, the knife edge and the source slit are rotated through 90 deg. The amount of light coming over the knife edge is a function of a deflection angle which is measured perpendicular to the knife edge. If the light source is a rectangle with its long dimension parallel to the knife edge, the brightness of the image on the viewing screen will be directly proportional to the deflection angle. In cases where the density gradients are of equal interest in all directions, a circular source may be used with either a circular hole in place of the knife edge or an opaque circular stop which cuts off the circular image of the source. Since the image is the result of the super-position of all the images produced by light from each point in the field of striations, a quantitative determination of the density gradient is very complex.

In the adjusted schlieren system the plane of the striae and the photographic plate or screen are conjugate planes. For a finite depth of field it follows that only one plane can be sharply in focus. This blurring of the image may be diminished by using a mirror of longer focal length and adjusting the knife edge so that less light passes over it.

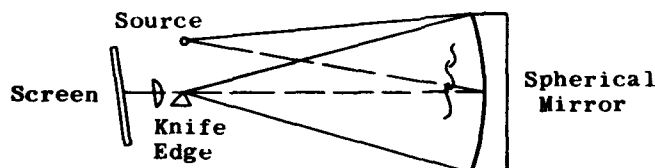
5.2.1 Variations of the Simple Schlieren System

As with the shadowgraph, many modified schlieren systems have been devised. Some have special optical properties, such as a depth of field effect; some are designed to make optimum use of a particular optical element, such as a parabolic mirror; and some are planned to reduce costs. The simple schlieren system has been modified not only for the purpose of accentuating the shadowgraph effect, but also to suppress it.

The simple system described in Subsec. 5.2 has several inherent limitations: Its viewing field is limited by the lens diameter, and its sensitivity is inversely proportional to the focal length of the lens. To minimize these disadvantages or otherwise enhance the system's capabilities, it is necessary to use concave mirrors or lenses of larger diameter. Large lenses of long focal length, however, are very expensive and also subject to both chromatic and spherical aberration if they are not of high quality. Concave mirrors of large diameter and long focal length are much easier to grind and correct than are lenses, and consequently are more economical. The internal quality of the glass from which the mirror is made is not usually of critical importance unless a highly accurate surface contour is required. Moreover, a mirror has only one surface to be ground. A mirror has no inherent chromatic aberration and, if properly designed, no spherical aberration. The thickness of a mirror should be at least one-fifth of its diameter, and the glass should be annealed with great care. The surface of the mirror is usually sputtered with metallic aluminum, which is generally considered preferable to silver since its oxide is transparent and the surface more durable.

5.2.1.1 Single-Mirror Schlieren System

The single-mirror system shown below is similar in operation to the single-lens system except that each ray of light passes twice through the field of striations, thus increasing the sensitivity.



Theoretically, this system should be twice as sensitive as a single coincidence system of similar dimensions. It should be noted, however, that light does not pass through exactly the same point in the field going to and coming from the mirror. Because of this, powerful striations of narrow dimensions (such as shock waves) may appear as double lines. Multiple coincidence systems other than the single mirror are seldom used, though many have been devised.

For the single-mirror system, a spherical mirror is used with the source and the knife edge close together and at the center of curvature of the mirror. Since the source and knife edge cannot occupy exactly the same point, each must be displaced slightly from the optical axis. This displacement results in a slight astigmatism, which tends to spread the image of a point into a line in the direction of displacement. If the displacement and the consequent spreading are along the

knife edge, this effect is not serious. But if the displacement is across the knife edge, the source image becomes fuzzy in the direction in which the deflection angles are to be measured, and the field appears to be unevenly illuminated.

5.2.1.2 Double-Mirror Schlieren System

In the modified schlieren system shown in Fig. 5-3, the two field lenses have been replaced by the two front-surfaced mirrors. Ideally, these mirrors should be off-axis paraboloids to compensate for the fact that both the light source and the knife edge must be placed slightly off the optical axis of the system. However, such mirrors are expensive. In practice an axially figured parabolic mirror may be used provided that the f-ratio (focal length/aperture) exceeds ten. Spherical mirrors are easier to fabricate and are satisfactory for many of the uses of the ordinary schlieren system.

To minimize the aberrations which result with an axially figured mirror, the source and knife edge should be located as close as possible to the parallel light path between the two mirrors and on opposite sides of the axis of the two mirrors. Minimizing the angle through which the light rays must be turned minimizes the effects of astigmatism, and placement of the source and knife edge on opposite sides minimizes the effects of coma. The angle between the source and the optical axis should be equal to that between the knife edge and the optical axis. It is also desirable to arrange the apparatus so that astigmatism distorts the image only in a direction parallel to the knife edge. This may be achieved by placing the knife edge in the same plane as the source and the optical axis between the mirrors. The distance between the mirrors should generally be minimized, since all disturbances between them may appear on the screen, whether they are in the tunnel or not. The mirrors are usually two focal lengths apart, but this distance may vary with the depth of the field being investigated.

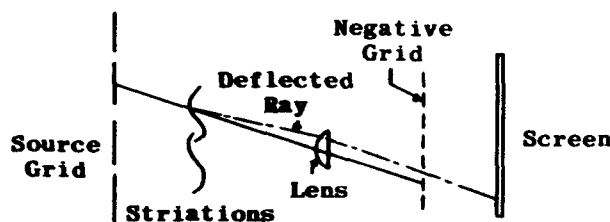
The source must be located accurately at the focus of the first mirror. This may be achieved either by reflecting an image of the source back on to a screen held close to the source (by placing a plane mirror between the concave mirrors) or by measuring the diameter of the beam at different positions along its length between the two concave mirrors. Similarly the knife edge must be located accurately at the focus of the second mirror by adjusting its position until the screen darkens uniformly as the knife edge is moved across the image of the source.

Finally the camera must be focused on the median plane of the tunnel. This may be done by focusing on a grid of fine wires held for the purpose in the middle of the working section. The knife edge should then be adjusted while the tunnel is running, because a lens-like effect of the air flowing through the test section usually causes a bodily shift of the source's image position.

The most popular type of schlieren system in use at the present time employs two ordinary parabolic mirrors, with parallel light passing through the field between them. This system, shown in Fig. 5-4, is quite versatile.

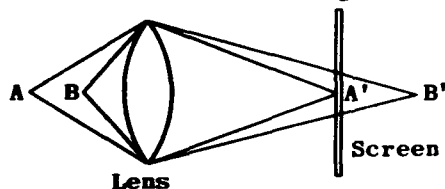
5.2.1.3 Multiple-Source Schlieren System

A modified schlieren system having unique properties is the multiple-source system shown below.



The light source consists of a grid of pinholes or lines, which when illuminated from behind becomes a uniform field of discrete sources of light. In the plane where the lens forms an image of this grid, a negative grid is placed so that the image of each source falls upon an opaque spot surrounded by a transparent area. Under these conditions no light passes to the viewing screen. When a striation appears in the plane that is in focus with the viewing screen, light is deflected so as to pass on to the screen and form an image of the striation. It can be seen (above) that the field size is not limited by the size but by the design of the lens and the size of the easily constructed grid. The lens may be a small, highly corrected camera lens giving an aberration-free rendition of the source-image on the negative grid.

Another property peculiar to this system is the depth-of-field effect. This phenomenon may be best understood if the grid is considered to act as a diffused light source in all areas except its own immediate neighborhood and that of the negative grid. It can be seen below that point A is in focus with the viewing screen, while B cannot focus somewhere behind the viewing screen.



Any light deflected by A will be concentrated at A' on the viewing screen, but light deflected by B will be spread over an area, with a consequent loss of intensity. The depth-of-field effect cannot be obtained in other schlieren systems, and any striation between the source and knife edge, including those in the lenses and mirrors, appears sharply on the viewing screen. (This statement is not absolutely true because a system using a line source has some definite focusing properties, but these are never as pronounced as those of the multiple-source schlieren.)

Another advantage of the multiple-source schlieren is that the light source does not have to approach a point in size. Hence, the choice of the type of light source is not as limited. In fact, several lamps can be placed behind the screen if necessary. This is a very important advantage in some applications.

The focusing effect of the multiple-source schlieren is demonstrated by the two photographs (Ref. 199) presented in Fig. 5-5. Both photographs show an air jet exhausting into still air from a 1/4-in. o.d. tube. Where the jet is in focus, the jet nodes are clearly visible; where the jet is 1 in. out of focus, it is barely visible. Multiple-source schlieren systems are planned for several large modern supersonic wind tunnels (Ref. 200).

Intermediate between the two-field-element system and the multiple-source system is an apparatus that employs two field elements, but with grids for the source and the knife edge. This system is considered intermediate because its field is limited to the size of the field elements, essentially parallel light passes through the subject, and pronounced focusing properties are apparent. The chief justification for this system, which seems to sacrifice the principal advantage of the large field multiple-source system, is that a large light source of relatively low intrinsic brilliance can be used without a loss in photographic speed.

5.2.1.4 Grating-Screen Method

A system which can sometimes be used to obtain an absolute measurement of deflection angles is the Gitterblende or grating-screen method (Ref. 201). In this system the knife edge is replaced by a grating of slits. If this grating is set so that the light from the field at rest falls on an opaque bar, a small deflection will cause light to pass over the bar and a greater deflection will move the image from behind that bar. Since the grating parameter is known accurately, the number of dark lines between two points on the pattern indicates the difference, in terms of number of grating units, in deflection between the two points. This effect is inherent in the multiple-source schlieren system when the grating parameter is small.

Since there is nothing to indicate the direction of the deflection, the problem of distinguishing between two patterns is similar to that in the use of the interferometer. The use of an ordinary schlieren photograph as a guide removes this difficulty. The grating-screen method, though not popular, is by far the most elegant quantitative schlieren method.

5.2.2 Components of the Schlieren System

The discussions preceding this subsection treated the problems of schlieren photography in a general manner. In the material that follows attention will be centered on the separate components of the schlieren apparatus, especially those required for the parallel-light schlieren system shown in Fig. 5-3.

5.2.2.1 Light Source

Mercury vapor lamps such as the Bol lamp are frequently used for schlieren photography because they provide a high-intensity light source which can be made monochromatic by the use of a suitable filter. A Bol lamp operates at high voltages and must be cooled by a forced draft or a water jacket. The General Electric BH-6, an air-cooled Bol lamp, gives monochromatic light of approximately 0.5461 micron wave

length when used with a Wratten 77A filter. This lamp can be used continuously or for single flashes, but must always be mounted in a horizontal position.

Because they are responsive to the fluctuations of alternating current, arc lights are not suitable for use with motion pictures. The BH-6 lamp, however, can be powered by direct current. Recommended circuits for this lamp, including a circuit for single-flash operation, can be obtained from the General Electric Company. When the BH-6 is used for single flashes, a 4-watt-sec rating should never be exceeded because the tube will explode at 8 watt-sec. Special precautions must also be exercised for the eyes. One must never look directly into a schlieren system which employs a continuously operating high-pressure mercury arc because its powerful ultraviolet light can injure the eye.

Although the tungsten ribbon-filament lamp is a satisfactory source for many purposes, it is not suitable for monochromatic work. Its intrinsic brilliance is only approximately one-hundredth that of the Bol lamp.

The Western Electric concentrated-arc lamp is about 2.5 times as bright as a tungsten filament, and the smallest model serves as a source 0.085 mm in diameter. This kind of source is well suited to the "grating-screen" type of measurement. Neither the concentrated arc nor the tungsten lamp is suited for high-speed flash photography.

In addition to the light sources mentioned there are many others suitable for this kind of system (Ref. 151). Among these are xenon flash tubes and various types of spark gaps. With continuous sources which cannot be flashed, electro-optic shutters such as the Kerr cell may be used.

5.2.2.2 Condenser Lens

Because the source is neither uniform in illumination nor sharply bounded, a condenser lens is needed in conjunction with the source. The condenser lens projects an image of the source upon a mask or slit which is of such size and shape that only the light from the uniform portions passes through. The functional "source" for the schlieren system is the condenser slit.

The dimensions of the source slit have been the subject of considerable study. A width of approximately one millimeter is satisfactory except for the measurement of large deflections, but the length of the source is harder to define. If the source is of finite length, it can be shown that the field will not be evenly illuminated and that only a certain part of it, even if the source were infinitely long, would be effective in the center of the field and even less at the edges. The effective length, l , of the infinite source in the focal plane of the first field lens which will just illuminate the second field lens is given by

$$l = \frac{f_1 d_1}{\sigma} \quad (5-3)$$

where

σ = separation of the two field lenses

f_1 = focal length of the field lens nearest the source

d_1 = diameter of the first field lens (or mirror)

For uniformity of field illumination it is sometimes wise to use some fraction of f . A finite source cannot be confined entirely to the optical axis. Consequently it produces astigmatism, which increases with the slit length.

5.2.2.3 Field Mirrors

A factor governing the choice of field mirrors is the f ratio, which is defined as the ratio of focal length to diameter. If this ratio is small, diffraction effects which distort the outlines of the source image are reduced, but effects of astigmatism and aberration become accentuated. An f ratio of about 8 represents a typical choice. The two field mirrors should be identical in order to cancel coma. When off-axis parabolic mirrors are used there is neither coma nor astigmatism.

The on-axis parabolic mirrors shown in Fig. 5-3 may be made from cast pyrex glass blanks. Their specifications require a diameter of 30 in.; focal length of 180 in.; an aluminized front surface; and a parabolic shape, which is ground, polished, and figured (shaped) to within one-tenth of a wave length of sodium light.

5.2.2.4 Test-Section Windows

Suitable wind-tunnel windows of large size are difficult to obtain and maintain because glass is not commercially available in the thickness required to withstand the stresses produced even at nominal temperatures for windows whose diameter approaches 20 in. The use of tempered glass (Herculite) windows that were 28.5 in. in diameter and 1-1/4 in. thick proved satisfactory from the stress standpoint, but the distortion due to tempering gave them poor optical qualities and also made a flush fit of the glass and frame virtually impossible.

Experience at OAL indicates that the best windows are made of borosilicate crown glass cast in one piece and 2-7/8 in. thick. Figure 5-2 shows several stress rings or pouring circles in such a window. It is difficult to mount the glass blank in the frames for a flush fit and to eliminate creep. The glass and frame should be flush to about ± 0.001 in. in order to minimize flow disturbances in the test section.

The OAL windows (borosilicate crown optical glass, Type 517-645, or crown optical glass, Type 523-586) were fine annealed to strain bi-refrindex of 10 μ or less per centimeter of light path, then ground and polished to within one-half wave length of sodium light as determined by the Newton fringe test using an optical flat. The opposite faces of all windows should be parallel in all places to within ± 0.002 in. Suitability of such glass for schlieren photography can be judged by the Foucault pin-hole, knife-edge test.

5.2.2.5 Camera

A lens placed behind the knife edge brings the plane of striations into sharp focus on the film. Assuming the focal length of the camera lens is small relative to that of the field lens, the ratio of the diameter of the image on the film to the diameter of the subject (Subsec. 5.7) is

$$\frac{d_{\text{image}}}{d_{\text{field}}} = \frac{f_3 f_2}{f_2^2 + f_3 (\mu - f_2)} \quad (5-4)$$

Here, f_2 is the focal length of the second field lens or mirror, f_3 is the focal length of the camera lens, and μ is the distance from the field to the second field lens. This assumes that the camera lens immediately follows the knife edge.

The second expression gives the apparent distance to the subject from the camera. This assumes that the subject-to-second-field-element distance, μ , is less than f_2 .

$$\frac{f_2 \mu}{\mu - f_2} + f_2 = \text{Apparent Distance} \quad (5-5)$$

If an ordinary still or motion-picture camera is used, this distance is the one which should be set on its focusing scale. If the camera lens opening is larger than the source image on the knife edge, then all of the light transmitted across the knife edge is received on the film. The choice of the relative sizes of the image at the knife edge and the image on the screen fixes the speed (focal length/diameter) of the camera lens. This lens always de-magnifies the image, which is necessary not only for good photography but also to keep the length of the system within suitable limits.

Film size is also important because films smaller than 4 × 5 in. will usually lose detail when they are enlarged. The 4 × 5-in. size, or larger, is therefore preferred. Nevertheless, the 35-mm film should be considered for marginal illumination situations. When used carefully it can also yield good enlargements. For viewing purposes, however, such images are somewhat small, and occasionally it will be necessary to use a magnifying glass to observe small details. Although it may require two camera lenses and a folding mirror or 45-deg prism, a large viewing image is desirable if the schlieren system is to be used frequently. For a 4-ft tunnel, a 10 to 12-in. viewing image appears reasonable.

For the OAL schlieren system the photographic exposure time, using a 4 × 5-in. Speed Graphic camera, was determined by the discharge rate of a rectifier-condenser storage system which flashes the BH-6 bulb with its discharge pulse. This exposure time of about 5 μsec results in some loss of detail due to motion of the flow during this time. A shorter pulse and faster film would give a sharper picture and greater capability for "stopping" disturbances such as vortices, wakes, and boundary layers. Super-Pan Press cut film, developed in a D-10 developer, can be used for such pictures.

5.2.3 Sensitivity of the Schlieren System

The sensitivity of a schlieren system is usually defined as

$$\frac{\Delta I}{I} = \frac{\alpha b}{a} \quad (5-6)$$

where

I = light intensity

α = smallest deflection which is visible

b = distance from the field to the knife edge

a = unobscured width of the image in the undeflected case

It would appear that the sensitivity could be increased by cutting down the light at the knife edge and removing the knife edge further from the field. Actually, if the long focal length of the field elements is increased without increasing the diameter, the sensitivity of the system is reduced because of the increase in diffraction effects when the f ratio is raised.

The sensitivity of a schlieren apparatus is difficult to determine because it is difficult to measure α exactly. This difficulty is due in part to the smallness of α and in part to the time element involved. For example, the weakest striation that can be recorded when the exposure is a short duration flash is different from that which can be recorded with a very long time exposure. Vibration, light scatter from dust on the elements, diffraction, difficulty of setting the cut-off precisely, and many other "secondary" factors influence sensitivity.

For both a film and the eye, the just-noticeable increase in intensity of light is proportional to the background intensity. Thus the deflection required to produce a noticeable effect under heavy background illumination must be stronger than that required under weak illumination. Consequently, the most sensitive schlieren is that having full cutoff. As previously pointed out, if this were done with an ordinary knife edge, deflections in only one direction could be recorded. If the knife edge were replaced by a bar just covering the source image, deflections in opposite directions normal to the bar could be read. If the bar were replaced by a circular disc and a circular source employed, then the absolute value of deflections in all directions could be read. Despite this sacrifice in information concerning the direction of the deflection, it is the most sensitive screen of all. Since the diffraction effect causes some light always to pass around the circular stop, the sensitivity goes up whenever the deflection can be increased without an increase in this diffraction. For the more common, single knife-edge system, the sensitivity of the system can be considered good if the weak Mach waves normally found in most supersonic wind-tunnel nozzles are barely visible in the background, as shown in Fig. 5-2. This particular system is very sensitive and suitable for studies of small gradients. However, for strong shock waves the system is overdriven, and considerable detail is lost in strong disturbances. The sensitivity is always a compromise, biased by the type of studies for which the system will be used.

When exposure time is critical, one should concentrate on finding the minimum deflection from behind the knife edge which will expose the film adequately. Assuming that both field elements are identical and using the linear deflection of the source image equation, the light per unit area arriving at the film for this system is given by

$$\text{Exposure} = \frac{(IB) \theta}{16 f_1} \left(\frac{d_1 l_{\text{source}}}{A_{\text{film}}} \right) \alpha \quad (5-7)$$

where

IB = intrinsic brilliance of the source

θ = exposure time

f_1 = f ratio of the field lens

d_1 = diameter of this lens

A_{film} = area of the field image on the film

l_{source} = length of the source

Actually there are absorptions in all of the elements, and the rating of the source is dependent upon the color sensitivity of the film. However, this equation shows the relative importance of the major design variables in the system. If a condenser is used, the IB of the apparent source will not be that of the actual source but will be dependent upon the f ratio of the condenser lens. With the standard knife edge, which gives information concerning the direction of the deflection, some light always illuminates the background. The amount of light allowed to pass over the screen should be just sufficient to record the maximum deflection into the knife edge to be measured.

For this case the average illumination on the film will be given by Eq. 5-7, but α will be replaced by $a/(f_1 d_1)$, where a is the width of the portion of the source image not cut off.

For the case of the grating-screen, the angular deflection may be measured in units of the grid spacing. The sensitivity is determined by diffraction effects rather than the spacing. For detailed studies it is desirable to use a larger number of closely spaced bars. However, the diffraction effects increase with the fineness of the spacing and impair the image. As a guide to the lower limit of the spacing it is wise to choose a grating parameter at least an order of magnitude greater than $2f_1\lambda$, where λ is the wave length of the light.

Much additional information on the design and operation of schlieren systems and the analysis of schlieren photographs is available in the literature. In addition to the references already cited, see Refs. 64, 154, and 203 to 212 for more details.

5.2.4 Color Schlieren

The black-and-white schlieren may be converted to color by mounting a prism as shown in Figs. 5-6 and 5-7 to make the light source adjustable. With this arrangement a single color band of the light spectrum may be selected to illumine the screen when the density in the field is uniform. When a density gradient in some part of the test section develops, the corresponding part of the image on the screen changes color. Since the eye is more sensitive to changes in hue than to changes in illumination (Ref. 213), the color-system has obvious advantages over the black-and-white system.

The NAA color schlieren system (Ref. 214) is typical of systems now in operation. In this system the mercury-arc lamp is replaced by a lamp whose white light source is concentrated into a narrow slit and used as a rectangular source. A prism breaks up the narrow beam of light into the colors of the visible spectrum. A double knife-edge at the camera is adjusted to form a narrow slit so that one band of the spectrum, which is an image of the source slit, can be selected as a background color.

The component parts of the complete system (identified by number for the following discussion) are shown in Fig. 5-6. In operation, white light from the source (1) is collected by a double convex lens (2) and focused at plane (3). At this plane, which coincides with the focal plane of the parabolic mirror (6), a narrow vertical slit (4) is introduced to form an effective sharp-edged light source of finite size. This slit passes the white light in a narrow, divergent beam to the constant-deviation prism (5), which performs the dual function of breaking up the light into its constituent spectral colors and turning the beam 90 deg to direct it toward the parabolic mirror (6). All of the divergent, overlapping bands of colored light which emerge from the prism fall on the face of the mirror, so that each of the colors covers the entire face. The mirror then reflects each of these colors in wide overlapping beams through the test section windows (7) and (9) to the second parabolic mirror (10). Although each of these beams is composed of parallel rays, the beams themselves are not parallel to each other, since the original beam emitted from the effective source, slit (4), is divergent and the emergent overlapping beams from the prism are at different angles due to the different index of refraction for each color. Thus each beam strikes the mirror at a different angle and is reflected at a different angle from its overlapping neighbor (see Fig. 5-7). It is necessary that each color beam be of sufficient width to cover the entire test-section window (7) as it passes through. At parabolic mirror (1) each of the beams is collected and re-focused into an image of the effective source, slit (4), at plane (11). The net result is a spectrum in which the slit (4) is duplicated in each of the visible colors. A double knife-edge in the form of a slit (12) is introduced into the image at this plane with its edges parallel to the bands of the spectrum. The edges are then adjusted so that, as indicated above, only one selected color band is allowed to pass through into the schlieren camera to illuminate uniformly the ground-glass viewing screen. Because all of the light rays deflected from the mirror (10) are coincident at plane (11) a uniform darkening or lightening of the screen occurs as the slit is closed or opened, respectively.

When air at supersonic speed is flowing into the tunnel, the rays of light which pass through the density gradients in the shock-wave pattern around the model (8) are deflected from their original

paths. Rays of light passing through a density gradient in air are deflected toward the regions of higher density because they travel more slowly as the density increases. Thus the whole portion of the spectrum which passes through the shock-wave pattern goes through a slight composite shift so that rays of different colors occupy the paths formerly occupied by another color in the emergent light beam. The amount of this shift or refraction for each of the light rays is dependent upon the wave length of each color and the strength and characteristics of the density gradients throughout the shock-wave pattern through which each of the rays pass. The relative position of the spectral image in respect to the slit (12) also shifts, and light rays of colors different from the selected background color pass through the slit, while the rays of the background color which they have replaced are blocked on the edges of the slit. Therefore, the shock-wave pattern is illuminated on the viewing screen in a varied color pattern, the colors of which represent the density gradients created in the air flow by the presence of the model. The visible portion of the test section which is undisturbed by density gradients retains the color of the selected background band.

5.2.4.1 Light Source

For best color results, a tungsten-filament light source (Refs. 214 and 215) is preferable to the mercury-arc BH-6 lamp, which has a predominantly greenish-blue spectrum with a narrow band of red at one extremity. However, the much greater light intensity from the BH-6 bulb allows exposures of a few milliseconds, as compared to exposure times in the order of 1/10 sec for a 300-w GE PS-22 photo-micrograph lamp, and therefore "stops" the flow much more effectively. With the BH-6 light source, high-speed motion pictures of less than 1000 frames/sec have been successfully taken.

Another light source (Ref. 216) utilizes a high-pressure spark consisting of two, steel, conical electrodes separated by a lucite spacer. Maximum light was obtained by using a 3/32-in. orifice in one electrode and a 3/32-in. hole through the lucite spacer. The discharge of a 0.25- μ f oil-filled condenser, charged to approximately 15 kv, across the spark gave a satisfactory film exposure in about 1 μ sec.

5.2.4.2 Sensitivity Control Slit

The sensitivity is maximized when the deflected rays of light (see Fig. 5-6) are exactly perpendicular to the edges of the slit (12), and it decreases as the component of ray deflection perpendicular to the edges decreases. Therefore, this slit should be introduced into the spectral image plane (11) with its longest dimension perpendicular to the direction in which the density gradient to be observed is likely to occur (i.e., a vertical slit for normal or near-normal shocks, and a horizontal slit for observing boundary-layer density gradients and conical shocks at high Mach numbers where the half angle θ_s is less than 45 deg). Whenever the angular position of the slit is changed, the prism and the light entering it from the source must also be changed so that the color spectrum passing through the test section, and consequently the spectral image at focal plane (11), are always situated with the bands parallel to the long side of the slit (12). Since the slit (12) is introduced into the focal plane of the spectral image at (11), a uniform darkening of the screen occurs as the slit is made narrower. This

function is frequently misunderstood because it is often confused with the effect obtained when an obstruction is inserted in the plane of the test section, where a shadow of the obstruction would then appear on the screen. A shadow of the edges of the slit does not appear on the screen because the slit is introduced into the image plane where the rays of light from the second parabolic mirror (10) are coincident, forming a new image of the effective source (4). There is a limit in this narrowing process beyond which sharpness of the model image on the screen is decreased. Thus the width of the slit is governed by three factors:

1. Width of the desired background color band in the spectral image
2. Required illumination or color tone
3. Sharpness of detail in the model silhouette.

5.2.4.3 Effective Light Source

To obtain high sensitivity for a fixed lamp wattage, the light source must be very narrow (see Fig. 5-6) in the direction perpendicular to the edges of the slit (12). It may be long in the direction parallel to this slit because this dimension has no effect on the sensitivity. It must be of sufficient length so that the incident beam at the prism covers its full height and the divergent beam emerging from the prism fills the first parabolic mirror (6) in that dimension. Therefore, the optimum shape of the source is a very narrow rectangle. Because it is difficult to obtain a high-power white-source lamp having a filament of the exact desired dimensions, a mask is necessary. This mask in the form of a slit (4) is introduced into the intense spot image (3) of the real light source formed by the condenser lens (2). It affords a convenient control on the dimensions of the source and may be used to select the most intense portion of the real light source image and thus eliminate the color fringe that is created by the chromatic aberration of the condenser lens. In order to obtain a very pure spectrum it is also necessary to set this slit (4) as narrow as the required illumination on the screen will allow. This reduces overlapping of the color bands of the spectrum to a minimum, so that the spectral image at slit (12) is as narrow as possible and the color purity of each band is then at the maximum obtainable within the limits of illumination. With the test equipment described (Ref. 214) it has been found that the best width for this slit is 0.05 in. With improved illumination and optics, it should be possible to reduce this width and obtain increased purity in the spectrum.

5.2.4.4 Condenser Lens

Since this lens serves to gather the light from the lamp and focus it into an intense image of small area, it is desirable to use a lens of larger diameter and shorter focal length than the one shown in Fig. 5-6 in order to gather more of the available light into a more intense image of smaller size. A 2-in. diameter lens with a focal length of 0.75 in. would be more satisfactory and, in conjunction with a good parabolic reflector behind the lamp, should greatly increase the illumination on the viewing screen.

5.2.4.5 Photographic Film

Several commercially available films can be used to produce color transparencies. They are high-speed Ektachrome, Super Anscochrome, and Kodachrome, each of which is available in both daylight and indoor balance. Experience indicates that the indoor-type film, with its greater blue sensitivity, gives the desired results without concomitant darkening and degradation of the blues in the picture. Ektachrome sheet film, which can be processed immediately in the available darkroom, shows a very long scale with good graduations of color and fairly wide latitude, and has been used successfully.

Because color film is not constant in response from one batch to another, it is advantageous to purchase enough film of the same emulsion number to complete a series of photographs. Variation is also caused by the fact that the spark does not deliver a constant output from day to day or from picture to picture, due partly to atmospheric conditions. Within a particular sequence, however, the variations are usually not great enough to ruin the set. Nevertheless, it is good practice to make several test exposures after a regular series is completed. These exposures may then be developed for the varying times suggested in the instruction leaflets given with the film, and from these results the best developing time can be determined for the test set. With a good deal of experience, a skilled operator may be able to judge proper timing from the density of the negative image just before re-exposure. However, the determination of final color balance cannot be made this way. Once a satisfactory black and white negative has been obtained, the remainder of the color developing procedure is normal.

Even with the greater exposure inherent in the longer duration BH-6 mercury-vapor light source, it is almost necessary for the investigator to control the film development process in his own darkroom, instead of having it processed commercially. A slight under-exposure with a corresponding over-development in the first developer tends to enhance the reds in the Ektachrome film.

5.2.4.6 Simple Color Schlieren System

Acceptable colored schlieren pictures can be obtained with a simple and inexpensive modification to an existing black-and-white schlieren system. Strips cut about 1/16 in. wide from a number of vari-colored Wratten gelatin filters are mounted in a suitable holder with the sides of the strips parallel and close enough to prevent light from passing between them. This "artificial spectrum" replaces the conventional knife edge. A device for raising and lowering the spectrum provides the means for varying the background color. Rotation of the spectrum corresponds to orientation of the knife edge.

This simple system, credited to WADC, is not affected by the type of light source and may employ any type of spectrum. All that is required is brilliance. Unlike the prism system the colors do not depend upon the type of light source. The system is very economical and the results are good.

The spectrum used at WADC was a true color spectrum obtained with a prism and exposed on a sheet of film. It is virtually impossible to obtain the proper exposure simultaneously for the bright and dark

colors in this manner; hence, the vari-colored strip technique is recommended for better results.

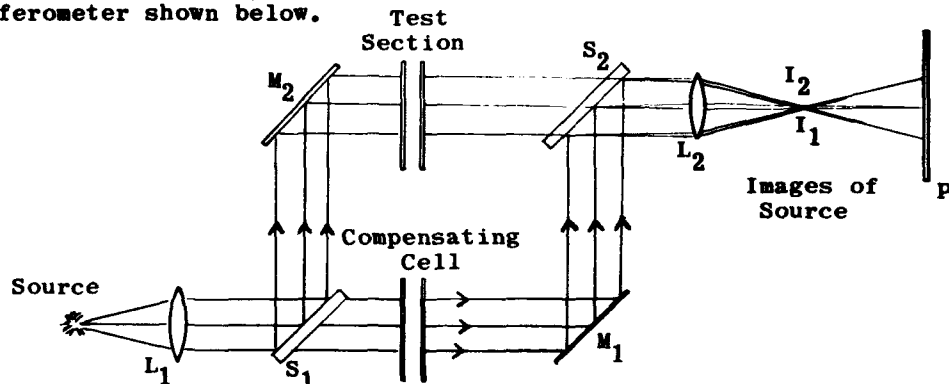
Because of the high cost of color prints, it is advisable to use a $2\frac{1}{4} \times 2\frac{1}{4}$ -in. camera for color photography in order to get negatives which may be mounted directly in standard $4 \times 3\frac{1}{4}$ -in. glass slides.

5.3 Interferometry

Of the three best known methods of flow visualization, the interferometer is the most suitable for quantitative measurements of density because it permits a direct measure of the change in refractive index to be made. Shadowgraph and schlieren operation is based on changes in the refractive index for the bending of light rays. The interferometer, on the other hand, depends upon the fact that the transit time varies with the refractive index. The interferometer has been widely developed and used for a wide range of flow problems.

5.3.1 Mach-Zehnder Interferometer

The basic principle of interferometry is best explained by a description and analysis of a simplified form of the Mach-Zehnder interferometer shown below.



Note: Flow in test section is perpendicular to the page.

Light from a monochromatic source passes through the collimating lens, L_1 , and the parallel beam is divided by the splitter plate, S_1 . Part of the beam is reflected to the mirror, M_2 , where it is again reflected and transmitted to the second splitter plate, S_2 , through the lens, L_2 , to form an image on the photographic plate, P . The second part of the original beam is transmitted by S_1 , reflected by both M_1 and S_2 , and transmitted by L_2 to P . If S_1 , S_2 , M_1 , and M_2 are all parallel and the lengths of the two light paths are equal, the illumination on the screen will be uniform. If S_2 (or any other element) is rotated very slightly, the two wave-fronts will be inclined at an angle to one another, and a phase shift will be shown by a uniform fringe pattern on the plate. When a density disturbance is introduced into one beam, the speed of light in that beam will be changed proportionately and the fringes will

move either up or down. A comparison of the distorted with the undistorted position of the fringes will allow the evaluation of the change in refractive index and hence of the density. It is possible to evaluate a variable density disturbance by following the same basic principle as that of a step change in density.

5.3.2 Design of an Interferometer

The practical design of an interferometer differs in several respects from the idealized one. Adjustments have to be made for the realities of the finite size of the light source and the appreciable thickness of the plates. The whole apparatus must be mounted on a readily movable stand which is also shock and vibration proof. It must be possible to view the striations by eye as well as by means of photographic processes.

5.3.2.1 Light Source

The first requirement of the light source is that it should be monochromatic. This condition is always far from being realized. The presence of a spectral band width in the light beam limits the number of fringes that can be obtained. This is of particular importance in the study of regions of high density gradient where a large number of narrow fringes are necessary to give an accurate measurement. The total number of useful fringes, N , is given by

$$N = \lambda / \Delta\lambda \quad (5-8)$$

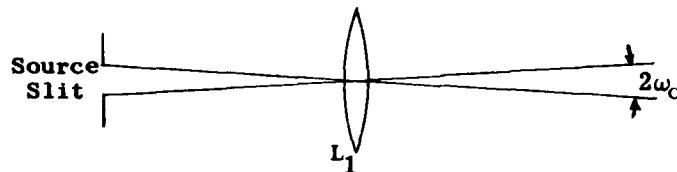
where

λ and $(\lambda + \Delta\lambda)$ = two wave lengths present in the beam

The second requirement of the light source is that it should be a point source. Equation 5-8 shows the effect of the number of fringes when the light is not monochromatic. The effect of the finite size of the light source on the number of useful fringes that may be obtained has been shown (Ref. 151) to be

$$N \leq \frac{1}{2\omega_0} \quad (5-9)$$

where $2\omega_0$, the aperture of the light beam, is defined below.



One frequently used light source employs a capacitance of about 2 μf charged to 2000 v and discharged through a GE high-pressure mercury-vapor capillary-arc BH-6. The light can be made sufficiently

monochromatic to give 200 usable fringes by passing through a Kodak Wratten No. 77A filter. A mask with a small hole should be used to reduce the size of the light source. The BH-6 lamp may be used for short flashes or for the continuous burning required during adjustment of the interferometer.

Another suitable light source uses a 2 μ f capacitance charged to about 16,000 v and discharged in air between magnesium electrodes. The light from this cannot be made monochromatic by means of a simple filter but requires a monochromator, construction details of which may be obtained in Ref. 198.

A rotating mirror and camera lens combination may be used to reduce the effective duration of the light source. This is particularly helpful in studies of the air density around high-speed projectiles.

5.3.2.2 Splitter Plates, Mirrors, Windows, and Compensating Cell

When an interferometer is used in conjunction with a wind tunnel, the field to be studied is nearly always contained between glass windows of considerable thickness to withstand stress. In order to compensate for the increase in optical path of the beam by the windows, a cell composed of two similar windows is placed in the other half of the light path as shown in the sketch in Subsec. 5.3.1. All the plates, mirrors, and windows should be made of good optical glass free of striae and polished flat to 0.1 wave-length of light or better. The thickness of each matched pair should be true to 10 wave-lengths of light. Suitable quality glass is BSC1 or BSC2 (Bausch and Lomb notation). It is difficult, however, to make circular glass windows having a diameter greater than 15 in. which conform to the above specifications. The diameter of most splitter plates and mirrors is therefore of the order of 9 in. Slight variations in refractive index in the glass of the windows may sometimes be mitigated by rotating the windows both with respect to each other and to the sides of the compensating cell. Moreover, the compensating cell may also be adjusted slightly to accommodate the small variations in thickness of the test-section windows.

Ideally, the coating of the splitter plates should transmit and reflect light in equal proportions, while absorbing as little as possible. Since the effectiveness of the coating is closely related to the wave length of the light and its angle of incidence, it may be necessary to use different coatings for different purposes. Reference 198 suggests zinc sulphide as a satisfactory coating. In many cases the reflecting side is coated with TiO_2 , which reflects 35% of the incident light. The non-reflecting side is coated with MgF_2 , which reflects about 4% of the incident light. Since the plates come in matched pairs, they are able to compensate each other.

The mirrors are best when coated with aluminum of such thickness that at least 90% of the light is reflected. They should transmit at least 1% of the light if they are used to adjust the system.

5.3.2.3 Mounting the Interferometer

The interferometer is extremely sensitive to both vibration and temperature. To assure a precise adjustment at all times, it must

be mounted on a very stable base, which should have a low coefficient of thermal expansion and a large heat capacity. Moreover, if the optical surfaces are mounted too tightly, they may produce strains in the glass. Reference 217 gives details of successful methods of mounting.

All the plates should be capable of rotation in both the horizontal and vertical planes, with one axis in the reflecting surfaces. The controls, which require both fine and coarse adjustment, may be hand operated or motor driven. In the latter case the motors should be geared down to give very low speeds in order to allow time to adjust to the desired fringe widths and changes of width. One plate, usually the second splitter plate, should also be capable of translation in order to vary the path distance.

The 10-in. Mach Zehnder interferometer used at WADC (Ref. 218) is illustrated in Fig. 5-8. A unique feature of this particular instrument, whose field of view is a 6 x 9-in. ellipse, is that a schlieren system and interferometer are combined in a single framework.

5.3.3 Adjustment of the Interferometer

Since it is a sensitive instrument, initial adjustment of the interferometer to obtain fringes may involve a long and tedious procedure. The details of this adjusting process may vary from one system to another, depending upon the techniques used and the auxiliary equipment that is available. Since details of several methods may be readily found (Refs. 1, 151, and 198), only the outline is given here.

The first step requires either an exact parallelism between the mirrors and the splitter plates or some equivalent positioning of the four surfaces to provide equal lengths for the two light paths in the system. This may be accomplished by means of a simple continuous light source and a pentaprism on an optical bench, by means of known horizontal and vertical reflecting surfaces, or by means of two sets of cross hairs. If the two sets of cross hairs are employed, one set is mounted near the light source and the other near the first splitter plate. Two screens are set up on opposite sides of the interferometer in such positions that a lens placed behind the second splitter plate focuses one set of cross hairs on each screen. Each set of cross hairs will then produce two images on each screen, one from each light path. The splitter plates must be adjusted until both images on each screen are coincident. This adjustment must be very precise.

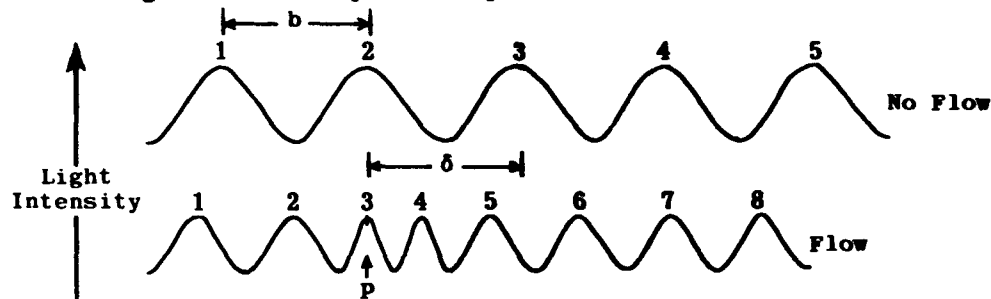
The second step is to produce the fringes. Since the number of fringes obtainable is an inverse function of the bandwidth of the light, it is advisable to have the source as close to monochromatic as possible; if there are relatively few fringes they will be harder to locate on the screen. For this purpose the GE, BH-6 mercury lamp, operating at approximately 60 v under rated voltage, is a satisfactory light source. A slight rotation of either of the plates should produce fringes. If the fringes do not appear, the previous adjustment was not sufficiently accurate.

For the final and most difficult step, the fringes must be centered in the test section focused clearly, and then given the correct orientation, usually either horizontal or vertical. When properly adjusted the fringes are correctly spaced, and the white light fringes

coincide with a pre-determined position in the test section. Since the greatest contrast always occurs near the white light fringes it is advisable to place them in such a position in the field that, in the disturbed state, they will move into the region where the density gradient is of greatest interest, thereby providing the fringes of greatest contrast in that region.

5.3.4 Evaluation of Interferograms

The density distribution in a flow field may be determined by comparing the interferogram of the field with one taken without flow, all other conditions being maintained. The shift of the fringe at any point on the visualization represents the change in the optical path length due to the time average of the density changes experienced by a ray passing through the point. Thus, in two-dimensional fields, the interferogram has a simple interpretation.



As shown above, the light intensity is measured along a line perpendicular to the fringes. The distance from one bright (or dark) band to the next in the no-flow case is called the fringe width, b . For a point, P , on the line in question the displacement, δ , of the fringe from its no-flow position may be measured. The density change between the two field conditions, flow and no-flow, at the point, P , is given by

$$\rho_2 - \rho_1 = \frac{\delta}{b} \cdot \frac{\lambda_0}{KL} \quad (5-10)$$

where

ρ_2 and ρ_1 = densities with flow and no flow

λ_0 = wave length of the light in vacuum

K = Gladstone-Dale constant = $\frac{\eta-1}{\rho}$, where η = index of refraction

L = length traversed in the flow field

Equation 5-10 assumes that the same gas occupies the compensating cell as flows through the test section. Without this assumption the equation becomes more complex (Ref. 201).

The quantity $\frac{\lambda_0}{KL}$ may be computed or measured. In the latter case it is found by measuring the fringe shifts across known density changes such as those across a shock wave of known strength.

If it is to be computed, the values of K and λ must be known. (These values for air, oxygen, nitrogen, and argon can be found in Table 7.2-1 of Ref. 219.) The reference field need not always be the no-flow case; it may be some portion of the field whose density is constant and known, e.g., the undisturbed uniform flow in front of a bow shock wave. In other cases the use of a white light gives sufficiently few fringes to enable one to determine the zero-order fringe from which the fringes may be numbered accurately.

A visualization or a plot of constant-density contours may easily be obtained by superimposing the negatives of flow and no-flow interferograms. Where the fringes are 180 deg out of phase, the intersection of two bright fringes shows up clearly (Fig. 5-9). Lines joining such points are lines of constant density. By displacing the no-flow negative a fraction of a bandwidth, a second set of contours may be obtained. With good negatives it is possible to locate such lines to within one-twentieth of a fringe width. This method is not satisfactory where the two sets of fringes are nearly parallel or where they vary widely in spacing.

In axially symmetric or three-dimensional flows the quantitative analysis is more difficult because the density changes must be integrated across a ray. This is a tedious and time consuming procedure, requiring a great deal of computation. Tables and graphs for use in these computations may be found in Ref. 220.

5.3.4.1 Accuracy of Density Calculations

Precision methods and a good optical system allow displacements in an interferogram to be read to 0.1 fringe width. Using this value and a constant reference density, Eq. 5-10 can be utilized to obtain

$$\frac{\partial \rho}{\rho} = \frac{0.1 \lambda}{KL\rho} \quad (5-11)$$

Since λ , K , and L will be either constant or relatively constant, the accuracy in density measurements will depend on the density itself. For low supersonic flow from atmospheric temperature and pressure the error may be a few per cent; at $M \sim 6$ it will be 40%. This latter value will be rapidly reduced as the stagnation temperature and pressure are increased. The accuracy is also dependent on the density variation in the field. At Mach number 4, the determination of density gradient through a normal shock is four times as accurate as that through the bow shock on a wedge of 10-deg half-angle (Ref. 151). Where the density gradient is high, the path of the rays is curved, the deviation from the straight path being a function of the distance, L , which the light traverses and of the density gradient along the path. This introduces an upper limit on the useful test-section width. DeFrate (Ref. 153), who studied a boundary layer in an 8-in. wide tunnel, finds that the products of maximum density gradient in the boundary layer and tunnel width ($L \, d\rho/dy$) should not exceed about $1.5 \, \text{lb/ft}^3$. If this product is exceeded, the interference bands become indistinguishable in the region of high density gradient. Thus, there is an optimum tunnel width for a given density gradient. If the tunnel is narrower than this optimum, the accuracy decreases; if the tunnel is larger, the bands cannot be seen in the region of high density gradient.

The most basic problem in determining the accuracy of measurements is that the fringe displacement gives the integrated value of an unknown distribution of densities along the light path. This is most particularly a problem when the boundary layer on the windows is relatively thick compared with the distance across the test section.

5.3.5 Interferometric Photography

Since the integrated density change across the test section is determined from an interferogram, the full depth of the test section must be in focus on the film. The relationship that may be derived (Ref. 1) between the parameters involved is

$$d_c = \frac{w}{f_1} \cdot \frac{D_i}{D_o} \cdot \frac{L}{2} \quad (5-12)$$

where, as before,

d_c = diameter of circle of confusion

w = dimension of light source

f_1 = focal length of collimating lens

D_i = diameter of image of field on screen

D_o = diameter of field

L = depth of test section

For a limiting value of the circle of confusion and for any test section, the parameter $\frac{w}{f_1}$ must be adjusted such that all density changes across the test section will be represented in the image on the screen. This effect is shown in Fig. 5-10.

While the relative sharpness of the image is not affected by the image size, the light intensity on the film and the ratio of emulsion grain size to image size are strongly dependent upon the image size. A choice of smaller image size permits correct exposure of a lower-speed film, but at the same time the effects due to emulsion graininess and resolving power become greater and may overshadow those due to lack of depth of field. In general, slower speed films have smaller grain and greater resolving power.

A satisfactory emulsion must have a suitable combination of speed (actual speed will depend upon the spectrum emitted by the source) and resolving power. The choice of emulsion and developer should result in an image of high contrast, since the center of the bands is more sharply defined in a high-contrast emulsion. Plates should be used to eliminate distortion during developing.

As shown in Eq. 5-12 a small w/f_1 ratio should be employed (using either a small source or a long focal-length collimating lens).

Also, the image projected on the screen should be large enough for easy viewing. Analysis indicates that the fast emulsion required for a large picture gives a sharper picture than does a slow emulsion, even if the image size is reduced and the source is increased to give the corresponding optimum conditions.

5.3.6 Applications of Interferometry

The interferometer has been used successfully for the study of axially symmetric, supersonic air jets and the flow which surrounds objects in the air jets whose properties are known. Some of this work is described in Refs. 220 to 223. Interferometry has been utilized to investigate the simpler two-dimensional flow of the usual form of wind tunnel and has proved particularly invaluable in boundary-layer investigations (see Refs. 153, and 224 to 228). The flow around free-flight projectiles in both pressurized and unpressurized ranges has been studied by means of both the interferometer and the shadowgraph method (Refs. 229, 230, and 231). The Mach Zehnder interferometer (Refs. 232 to 235) has been successfully applied to shock-tube studies.

5.4 Electrical Discharge and Afterglow Methods of Flow Visualization

In the field of rarefied gas dynamics, the conventional flow visualization techniques which utilize the density dependence of the refractive index of the gas are inadequate. Although these techniques have been refined such that extremely small differences in gas density can be detected, they are generally inadequate at pressures below a few millimeters of mercury.

The staff at the University of California's low-density supersonic wind tunnel has been the leading contributor to the development of the glow flow-visualization technique in the 0.1-mm Hg free-stream pressure range. Specific details of this technique, which is highly specialized, can be found in Refs. 151 and 236. Only a brief description, with some of the limitations, is given here.

Two distinct phenomena lend themselves to this technique. The first is the relatively strong absorption by molecular oxygen of ultra-violet light whose wave length is approximately 1400 Angstrom units. The noticeable attenuation of a monochromatic light beam of 1470 Angstroms (from a xenon lamp) by a few inches of path length of air at a pressure of 0.1 mm Hg has been shown to be feasible and is described in detail in Ref. 237. The second phenomenon is the emission of light accompanying certain gaseous reactions, particularly those involving oxygen and nitrogen under suitable conditions and those involving argon or helium under a somewhat more limited range of conditions. The intensity of such emission at a gas pressure of 0.1 mm Hg and a thickness of one inch can be sufficient to be clearly visible to the dark-adapted eye. Application of this second phenomenon is discussed below.

Somewhere upstream of the point where the flow is to be visualized, the working medium (dry air, nitrogen, helium, or argon) is passed through an excitation region where an electrical discharge is maintained. In principle, any type of discharge can be used. However, it should be noted that higher power does not always result in a higher yield of afterglow. The optimum electrical conditions vary with dynamic conditions of the fluid.

A wind tunnel operating at 0.1-mm Hg test-section pressure must have a jet diameter of at least several inches. Otherwise the length of the mean free path (and hence, the boundary-layer thickness) is so large that the edge effects tend to distort the free-stream phenomena.

The system in use at the University of California is shown in Fig. 5-11. A high-frequency electrodeless discharge in a 6-in. diameter glass pipe was found most suitable for stagnation chamber pressures up to 10 mm Hg and flow rates of 0.2 to 15 g/sec up to Mach 3, with lower flow rates up to Mach 4. For higher stagnation pressures, a pulsed condenser discharge with water-cooled electrodes was employed. Steady a-c or d-c discharges using metal electrodes in the stagnation chamber proved too erratic and less efficient. Even if an intense condensed discharge were used close to the nozzle throat, it is doubtful that the glow flow-visualization would be effective at flows beyond Mach 5 or 6 and static pressures near 0.1 mm Hg. At much lower static pressures the Mach number range may be extended somewhat.

At Mach 4 an adequate intensity was obtained only by addition of nitric oxide gas to the excited air stream immediately upstream of the nozzle entrance (frequently referred to as an enriched air after-glow). A sample photograph of typical results obtainable with this technique is shown in Fig. 5-12.

At test-section densities corresponding to test-section pressures above 1 mm Hg and relatively low Mach numbers, the purely optical techniques discussed earlier are considered superior.

When electrical sparks are being discharged within an airflow at a sufficiently high repetition rate (some thousands per second) they usually follow the same ionized path established by the first spark of a series. This ionized path is carried along with the flow. When photographed, the sparks appear in a pattern from which conclusions can be drawn concerning the magnitude of the velocities at corresponding points. The velocities can be calculated by dividing the measured spatial distance on the photographs by the electronically known time interval of two succeeding sparks.

This principle has been verified by experiment only at low speeds (Ref. 238), and more experimentation is required before definite conclusions can be reached concerning its application to quantitative routine measurements in wind tunnels.

Other spectral absorption and X-ray techniques are discussed in Ref. 151.

5.5 Vapor Screen Method of Flow Visualization

Some of the earliest developmental work on the vapor-screen flow visualization technique was done at NACA and subsequently adapted to the OAL supersonic wind tunnel (Ref. 91). The material appearing in this subsection is derived from the work done at the latter facility.

The vapor-screen technique of flow visualization requires an intense source of light that is completely shielded except for a slit

which allows a narrow beam of light to pass across the test section and a moisture-laden airstream. When the moisture is added to the airflow, minute droplets of water condense as the air passes through the test section. This fog of condensed water vapor disperses the light passing across the test section, thus producing a white screen. Initially the screen is transparent, with low relative moisture content, but it becomes more opaque as the moisture content is increased. (However, the moisture content should not be increased to such an extent that the flow characteristics are appreciably affected.) Disturbances in the air stream, such as a vortex, are made visible by upsetting the uniform distribution of the water droplets, thus producing light and dark areas on the vapor screen as shown in Fig. 5-13. A reduction in the number of water droplets thins the vapor screen and appears black, while a concentration of water droplets intensifies the white areas.

The apparatus for making vapor screen observations and photographs is shown schematically in Figs. 5-14 and 5-15. The periscope shown in Fig. 5-15 utilizes a right-triangular prism whose 45-deg surface is silvered. The prism is mounted in an aluminum alloy box and its exposed face is covered with a sheet of Herculite plate glass to resist erosion. The periscope is mounted in the wind-tunnel diffuser wall so that the vapor screen can be photographed from downstream of the model.

During the early work at NACA, a 16-mm motion-picture gun camera having an f 2.5 wide-angle (Morton Widar) lens looking upstream was fastened to the sting support aft of the model. The camera was operated at the low camera speed of 4 frames/sec, which was obtained by varying the voltage to the electric-motor camera drive. However, even with five GE BH-6 lamps (operating on a-c) placed right against the wind-tunnel window in a vertical line behind a slit, it was necessary to use "shellburst" film (Weston blue-sky rating 200, white-sky 160) to obtain sufficient exposure.

To prevent excessive erosion of the camera lens, the air flowing through the test section must be free of contamination. If contamination exists, the periscope approach shown in Fig. 5-15 should be used.

5.5.1 Light Sources for Vapor Screen

Two intensely brilliant light sources have been developed for the purpose of making visual observations of vortices, wakes, and shock waves in a flow field of moderately high dew point. In each unit, the light is emitted uniformly from a narrow slit in a completely shielded box. The large light source shown in Fig. 5-16 contains three GE BH-6 mercury-vapor lamps. A number of plane mirrors are used behind the light source to increase the intensity of illumination and to give a uniform light distribution. The slit is approximately 30-in high, so that the entire cross-section of the tunnel can be illuminated. The slit width is variable from 0 to 1-13/16 in.; however, the best flow field definition has been obtained with a 1/8-in. slit. Since the light is not parallel, the thickness of the light screen at the tunnel centerline is about twice the slit width set on the box. In normal use, the light screen is perpendicular to the direction of flow, but it has also been used successfully when horizontal or parallel to the flow.

The portable light source shown in Fig. 5-17 contains one GE BH-6 mercury lamp and employs a shroud of 6-1/2-in. diameter and 18-in.

length that weighs approximately 9 lb. The slit width is variable from 0 to 1/4 in. The unit can be used for exploratory surveys and for getting angle views through the top and bottom windows as well as the side windows of the test section.

5.5.2 Dew Point for Vapor Screen

The amount of moisture required for good vapor screen visualization is not very critical. The following values of dew point are given as the approximate range for which good vapor-screen images have been obtained in the OAL tunnel, which operates at a stagnation temperature of 150°F.

Mach Number	Dew-Point Range (°F, 1 atm)
1.25	40 to 50
1.50	29 to 40
2.00	21 to 33

The vapor screen flow visualization technique has proved to be of great value for certain types of qualitative wind-tunnel studies (Ref. 239).

5.6 Visualization of Boundary-Layer Transition

Various methods (Ref. 64) are available for determining the velocity distribution in the boundary layer. In many experimental applications, however, it is necessary to know the nature of the boundary layer, the position of transition from the laminar to turbulent state, and the location of separation if this takes place. This is particularly true for evaluating drag forces on scale models in the wind tunnel (see Subsec. 3.3.1.2). A number of valuable methods have been developed. A general review of early work is given in Ref. 240.

The use of a smoke filament is suitable only for speeds below about 200 fps. Although the conventional optical techniques (Subsecs. 5.1, 5.2, and 5.3) may be used for some boundary-layer characteristics, the three most practical techniques for this purpose are the china-clay, luminescent lacquer, and azobenzene techniques.

5.6.1 Optical Methods of Showing Boundary-Layer Transition

The use of photographs to study boundary-layer transition on axially symmetric, three-dimensional models, though simple and convenient, is limited to the phenomena on the upper and lower model surface only. The advantage of the shadowgraph and schlieren systems is that the absence of instrumentation in the proximity of the transition region eliminates the possibility of induced interference. In addition, a time history of transition-point fluctuation may readily be established by taking an appropriate number of short-duration spark photographs.

Three types of photographs are used to determine transition in model boundary layers. These are shadowgraph, conventional black-and-white schlieren, and colored schlieren. A colored schlieren photograph

can be obtained with a simple modification of the conventional schlieren system (Subsec. 5.2.4). Proper adjustment of such a system results in a photograph that plainly shows a difference in color between a laminar and turbulent boundary layer. Much better color contrast is obtained if the negative is viewed directly through a magnifying lens. One schlieren light source used is a 1000-w mercury arc (GE BH-6) with a total spark duration of 4 μ sec. Peak light intensity is reached in a somewhat shorter time.

The best definition in the model boundary layer by optical means has been obtained from spark shadowgraphs with the spark source located in front of a test-section window and the film placed against the opposite window. In routine applications the light source is positioned on a permanent mount and its light is directed to a parabolic mirror which reflects collimated light through the tunnel test section. The resulting shadowgraphs show the major disturbances existing in the air stream.

The shadowgraph light source is comprised of a conventional Libessart high-pressure gap (0.125 in.) powered by a Sprague Vitamin-Q condenser rated at 0.3 μ f at 15,000 v. An adequate measure of the light duration has not been obtained with this light source.

5.6.2 China Clay Method of Showing Boundary-Layer Transition

When this procedure is utilized, the surface under investigation is given an over-all coating with china clay (kaolin), a crystalline solid having a refractive index of 1.56 and a white appearance when dry (Ref. 64). The china clay deposit is then sprayed with a volatile liquid of approximately the same refractive index, so that the resultant deposit becomes transparent. Because the rate of evaporation is greater in the turbulent region than in the laminar region of the boundary layer, the white deposit of dry china clay appears first behind the transition point.

The china clay is best applied by spraying, as a suspension in some liquid. A suitable suspension is formed by diluting 100 ml of colorless Frigilene with 100 ml of butyl acetate, 100 ml of butyl alcohol, and 50 ml of xylene and then wet-grinding with 100 g of china clay until the mixture is smooth. The mixture should then be transferred to a bottle, thoroughly shaken and allowed to stand so that large undispersed agglomerates may separate. After deposition (about 10% of the original weight of clay usually separates) the supernatant solution should be poured off. When the solution dries, the lacquer can be rubbed down with fine emery paper to remove any irregularities which may be present. The size of the china clay particles should be very small in order to achieve a sufficiently smooth surface. The volatile liquid of "developer" that is chosen must be such that the indication of transition is produced in a reasonable time under the test conditions. On the other hand, the indication must not be too rapid, or spurious effects may occur because of movements of the transition point during the period in which the tunnel is brought up to speed. Some suitable volatile oils are compared on the following page. It may be seen that because of their relatively high boiling points and rapid rates of evaporation, Iso-safrole and Eugenol are usually selected for supersonic testing.

Liquid	Boiling Point ($^{\circ}$ C)	Refractive Index	Relative Rate of Evaporation
Ethyl Benzoate	213	1.506	1.0
Methyl Salicylate (Oil of Wintergreen)	223	1.538	1.1
Ethyl Salicylate	231.5	1.523	2.1
Safrole	231	1.538	2.3
Iso-safrole	252	1.578	5.4
Eugenol	254	1.544	about 14

After use, the china clay deposit may be re-sprayed with the developer in preparation for another run. The china clay remains permanently on the surface throughout a whole series of tests. After some time, however, the deposit may erode around the leading edges; if the transition is to be indicated here, the deposit may have to be replaced periodically. On large models it is usually possible to prevent the blockage of surface pressure holes during spraying.

The china clay technique is difficult to accomplish in practice if the time required to install the model and start the tunnel is excessive (order of several minutes) or if the operating stagnation temperature is high (order of 150° F).

5.6.3 Liquid-Film Methods of Visualizing Boundary-Layer Transition

A liquid film (Ref. 64) is easier to apply than the china clay but gives much less contrast in the indication. Nevertheless, the indication is clearly visible to the eye without special lighting arrangements. Visualization is made clear if the surface is dusted with french chalk after the indication is complete.

For this method a volatile oil is applied evenly to the surface with a spray or swab. During the run this oil film evaporates more rapidly in the turbulent region than in the laminar region of the boundary layer, so that the film soon disappears behind the transition front. Very thin films may be used so that the surface roughness is neither increased or reduced (in some cases the china clay deposit may affect the surface roughness). The best contrast is obtained if the surface of the model is painted black before the experiment. (Care must be taken that the paint does not dissolve in the liquid used for transition indication.) Surface pressure holes are free as soon as the liquid film has evaporated. This method, with a suitable liquid, has been used up to high Mach numbers.

Another technique of this same type which has been used successfully in supersonic wind tunnels with ambient stagnation temperatures involves the use of a thin coating of luminescent lacquer. The critical requirement for successful operation with this medium is a very uniform coating over the entire specimen. For three-dimensional bodies this can be accomplished by turning the model in a lathe at a reasonably high rate while making one smooth pass with a spray gun set for a fine mist. Best visual effects are obtained by bathing the model with ultraviolet light and photographing with a red filter over the camera lens.

A third technique depends on the different rates of sublimation of a solid deposit from the surface in the laminar and turbulent regions of the boundary layer, the increased rate of diffusion in the turbulent layer leading to a more rapid rate of sublimation. The solid is dissolved in some convenient liquid and applied to the surface by spraying. The solvent is then allowed to evaporate from the surface before the experiment is begun. Suitable solid substances are camphor, borneol, and azobenzene; and suitable solvents are benzene, xylene, and acetone.

Azobenzene, a sublimating solid, was first used by the British in 1945 and later extended to free-flight and supersonic wind-tunnel applications. This material appears to be the most suitable for the supply temperature and pressure range of contemporary continuous-flow supersonic wind tunnels.

An experimental program was run at JPL to determine if the azobenzene affected the boundary layer and indicated transition, and what controlling parameters govern the time factor for indication of transition. The results indicated in all cases that the azobenzene does not affect boundary-layer transition. Azobenzene is dissolved in a carrier of acetone (requiring a ventilation system to draw off the fumes when spraying). Even when laid on heavily, it quickly erodes to a smooth coating, and the pattern which finally develops is the same as that for the smoothest, thinnest coating.

Previous testing of instrumented flat plates at JPL showed that transition denoted by a schlieren photograph corresponded approximately to the first peak of the thermocouple reading. Using this definition it was observed at three Mach numbers that the azobenzene does indicate properly the pattern of boundary-layer transition.

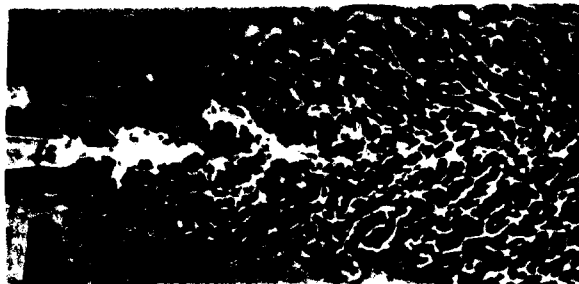
The tests at JPL showed that Mach number and pressure level had a relatively minor effect on pattern development time compared to the effect of tunnel stagnation temperature. The strong dependence on tunnel temperature was determined. As a fully operational technique the tunnel stagnation temperature must be 130°F or warmer. There is a factor of 5 to 10 in the sublimation time required for a laminar boundary layer as opposed to that for a turbulent boundary layer. At this temperature the pattern develops in 5 or 10 min (50 to 120 min at 70°F) and will remain unchanged for 30 min or more in the airstream. Therefore, it is unnecessary to stop the flow at a precise time in order to photograph the pattern quickly. The models can be removed from the tunnel for photographing. A general procedure at JPL is to mount the model on a remotely-rolled sting, which simplifies the complete spraying job and allows the model to be photographed from all sides with a single camera in both color and black and white, using a red filter.

The azobenzene technique was also adapted to the OAL supersonic wind tunnel (150°F stagnation temperature). At this facility the azobenzene acetone mixture, 9 parts by weight acetone to 1 part azobenzene, was applied with a conventional paint spray gun. The acetone, used as a carrying agent, was completely evaporated before the azobenzene mist reached the model. Prior to spraying, the model was cleaned with acetone to remove oil and dust. Better photographic results were obtained with a darkened model, i.e., gun metal blueing on steel models and blue Dykem sprayed evenly on aluminum models. (If the sprayed surface appears extremely lumpy, the mixture has been sprayed

on too thick; if the metal is visible, the coat is too thin. Best results were obtained when the spray gun was moved slowly back and forth for an even coat approximately four to eight inches from the model. Acetone was used to clean the spray nozzle when it became clogged.) Good photographic results were obtained with a 4 x 5 Speed Graphic camera and an "A" red filter with black-and-white film or with Ektachrome color film without a filter. Regions of laminar boundary layer will be indicated by a white or light color in black-and-white photos and by a yellowish-brown color in color film. Superior prints resulted when the model was photographed in a booth lighted by a diffused light source rather than in the wind tunnel with the window removed.

The sublimating solid method of flow visualization using azobenzene proved to be the best and most practical method of boundary-layer transition determination yet encountered in supersonic flow.

Source: Ref. 1



Shadowgraph, showing fine structure of turbulence.



Schlieren, showing density as relief map illuminated from side.



Interferogram, showing concentration as contour map.

Fig. 5-1. Comparison of shadowgraph, schlieren, and interferometer optical techniques.

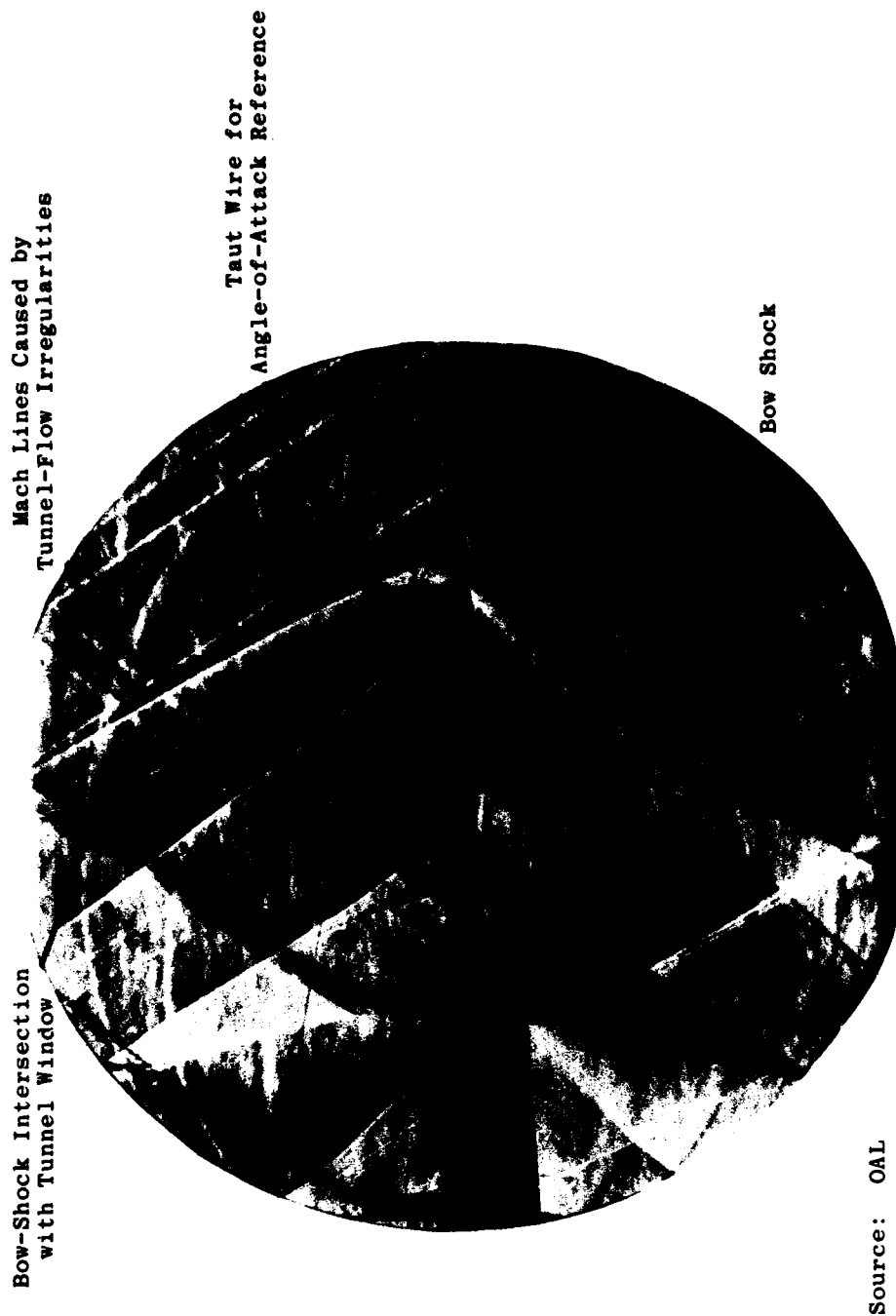


Fig. 5-2. Typical schlieren of a sting-mounted, hemispherical-nosed cylinder; Mach number 1.25, 6-deg angle of attack.

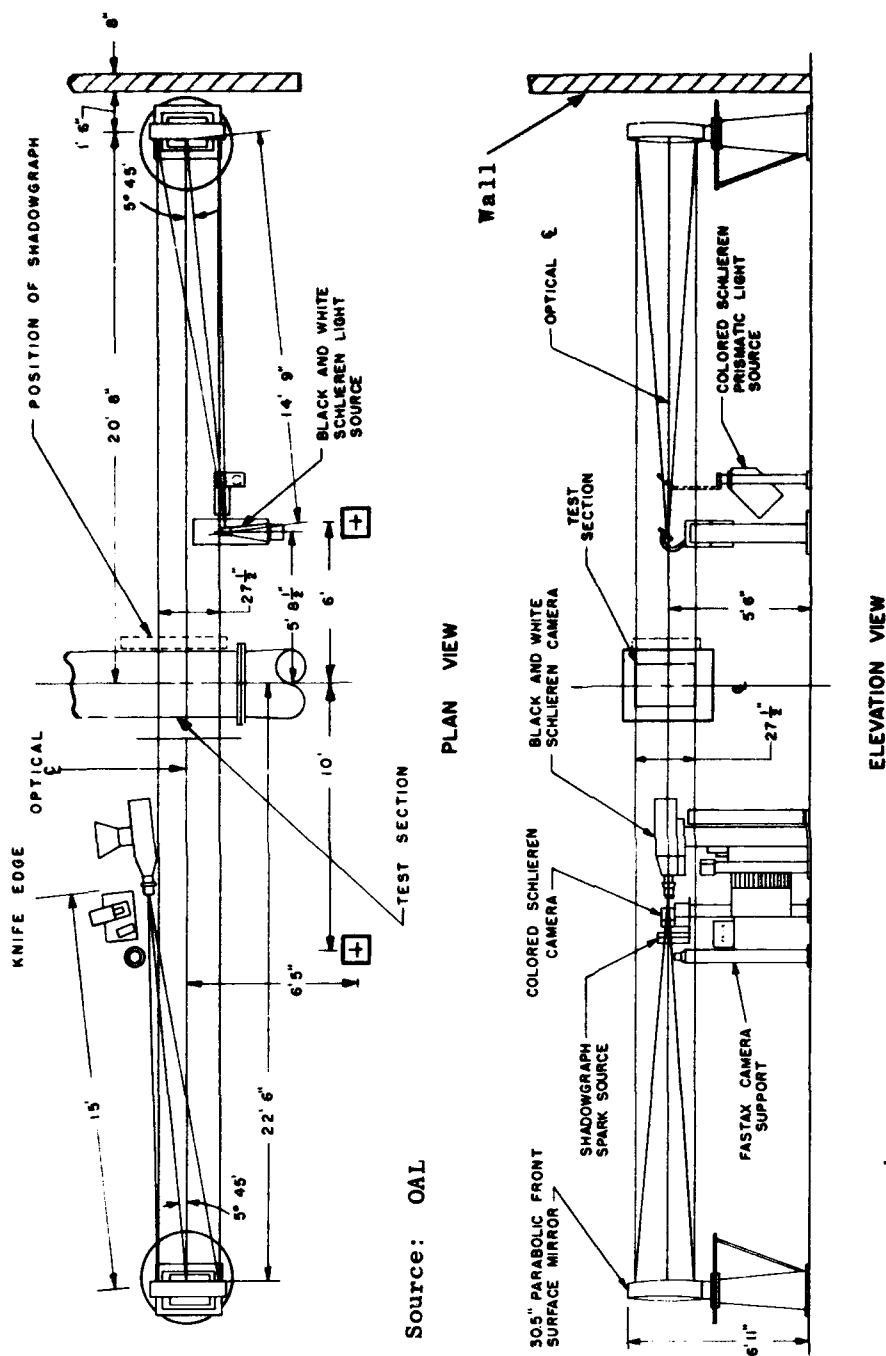


Fig. 5-3. OAL optical system.

Source: OAL



Jet in focus



Jet 1 in. out of focus

Fig. 5-5. Focusing effect of multiple-source schlieren.

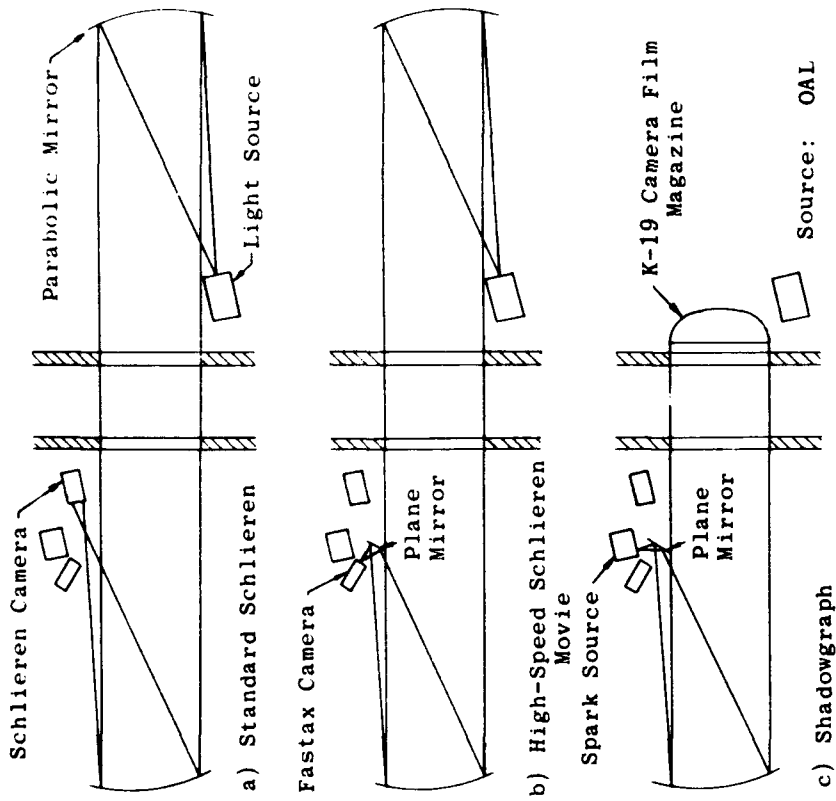
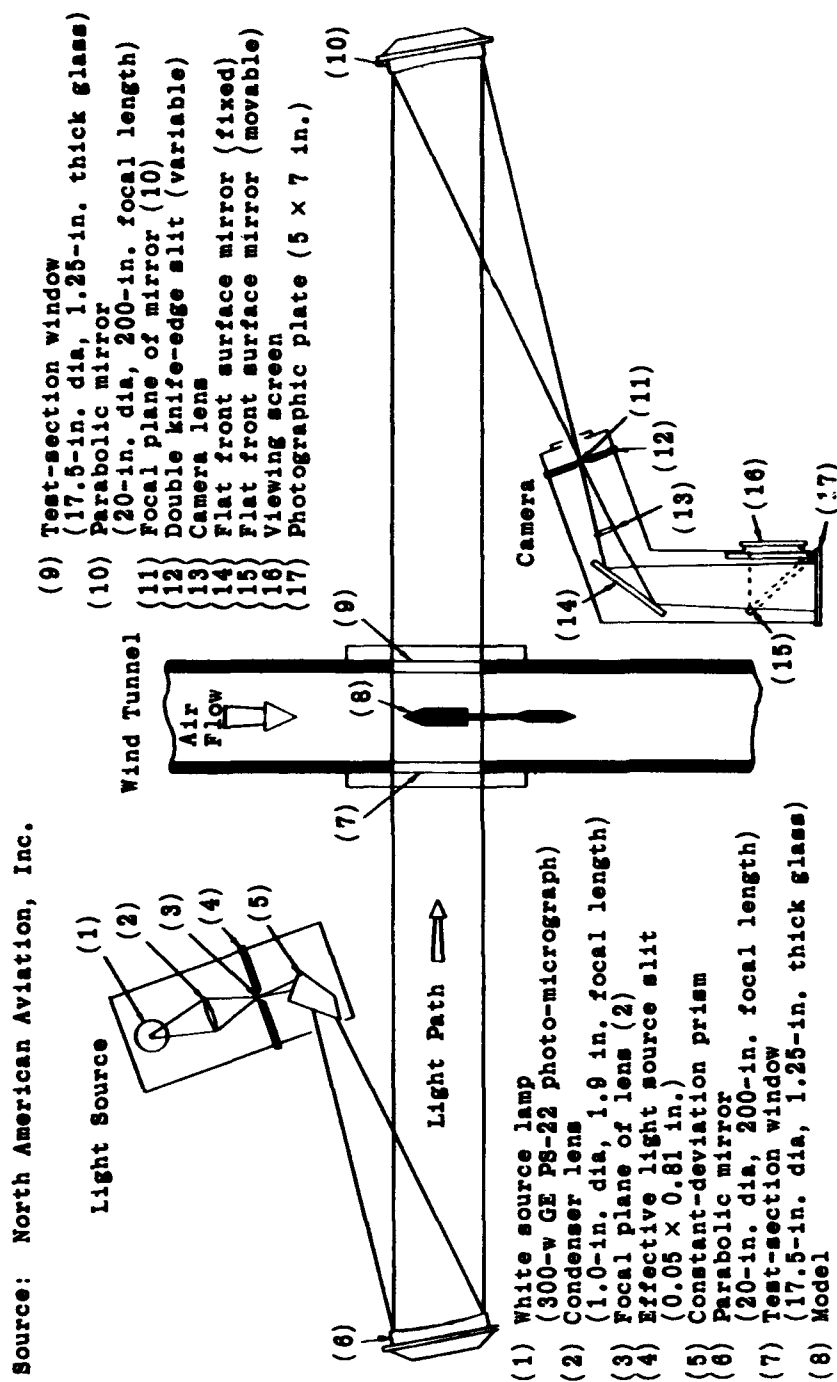


Fig. 5-4. Three-way optical system designed for maximum flexibility.



Note: Light source and camera are offset 4 deg.

Fig. 5-6. Optical system for NAA color schlieren.

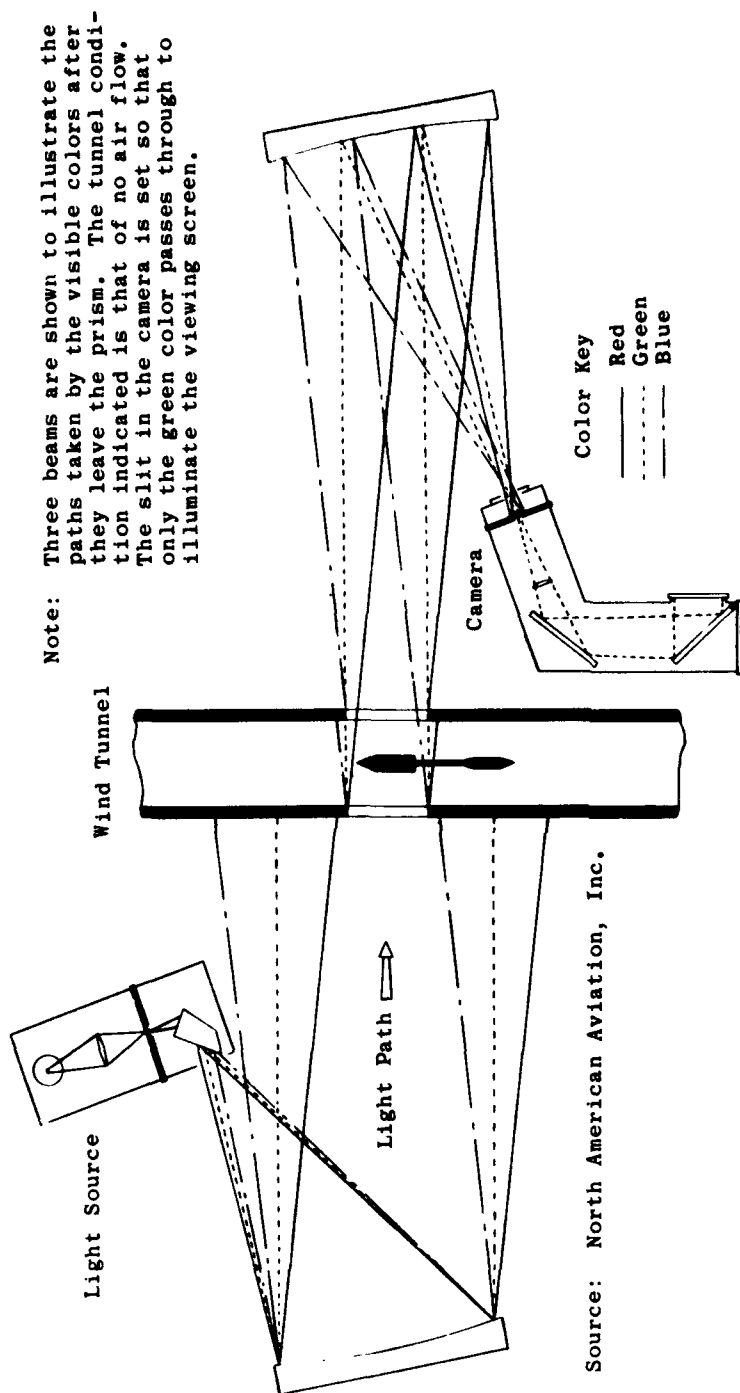


Fig. 5-7. Effect of prism on light path.

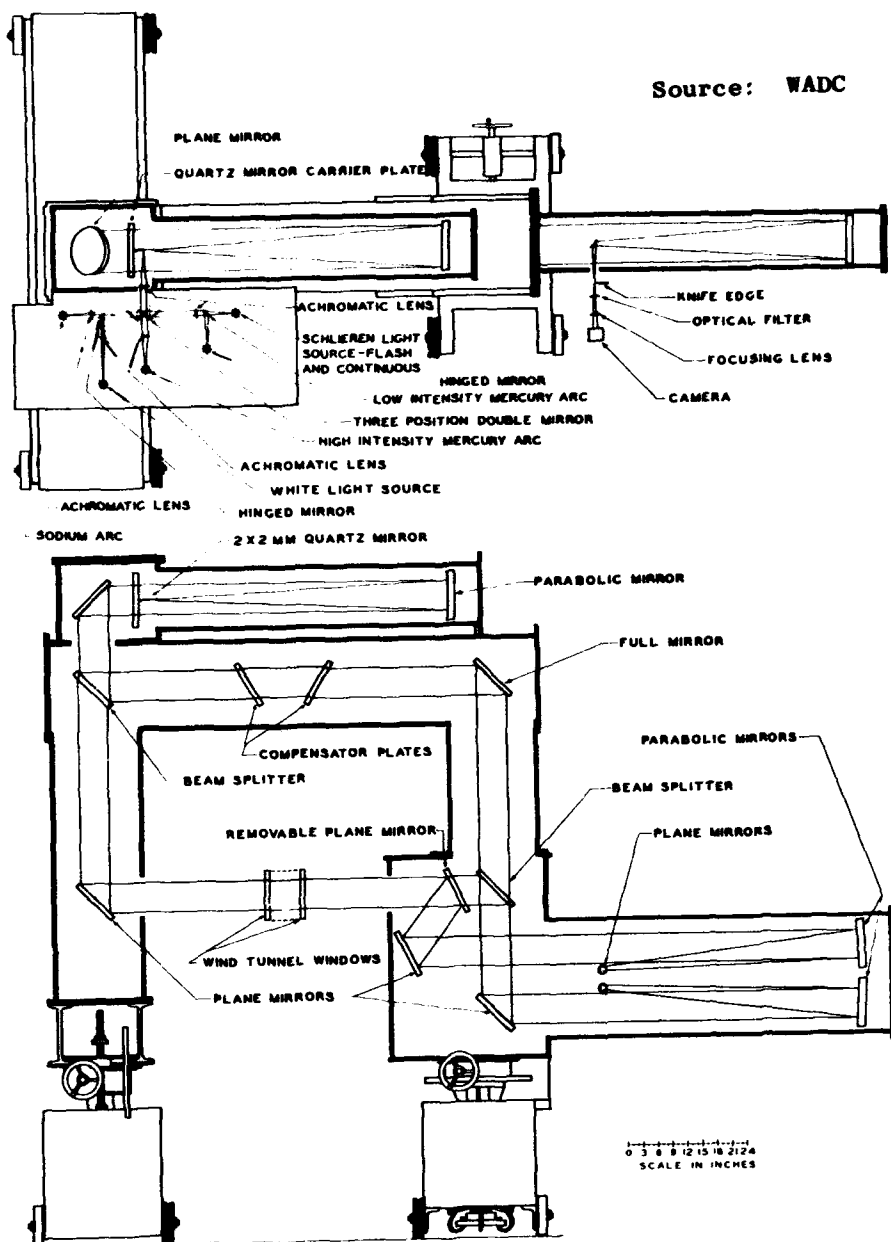
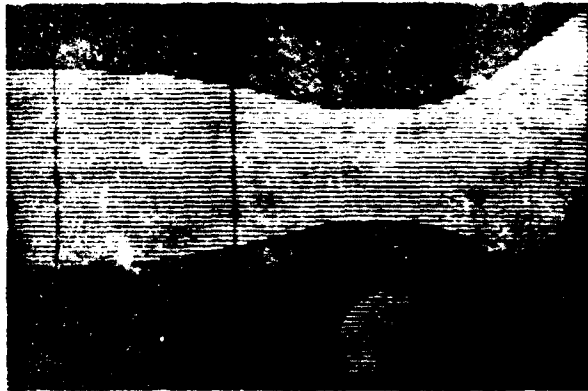
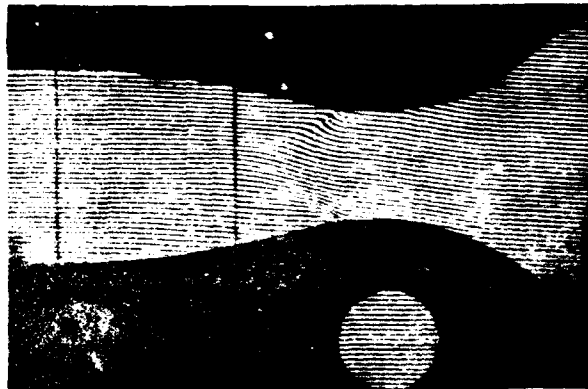


Fig. 5-8. Ten-inch Mach-Zehnder interferometer and schlieren system for WADC 6 × 6-in. supersonic wind tunnel.

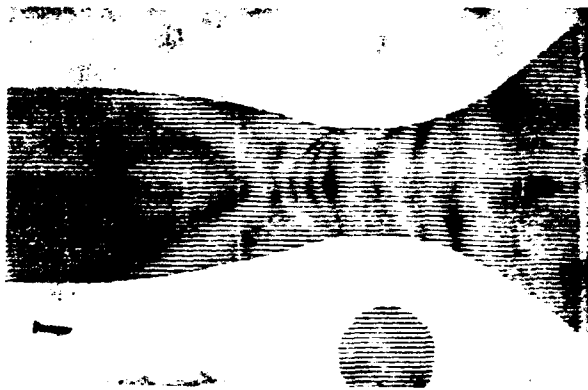
Source: Ref. 1



(a) No flow



(b) Flow



(c) Superimposed flow and no-flow negatives

Fig. 5-9. Interferograms illustrating superposition for evaluating band displacement.

Source: Ref. 1



(a) $f_1 = 24$ in., $w = 0.25$ in. or 1 in., $\frac{w}{f_1} = 0.01$ or 0.04



(b) $f_1 = 4.5$ in., $w = 0.12$ in., $\frac{w}{f_1} = 0.027$



(c) $f_1 = 24$ in., $w = 0.12$ in., $\frac{w}{f_1} = 0.005$

Note: The numbers are one inch apart along the light path, and the prints are of the same magnification.

Fig. 5-10. Dependence of depth of field on ratio w/f_1 .

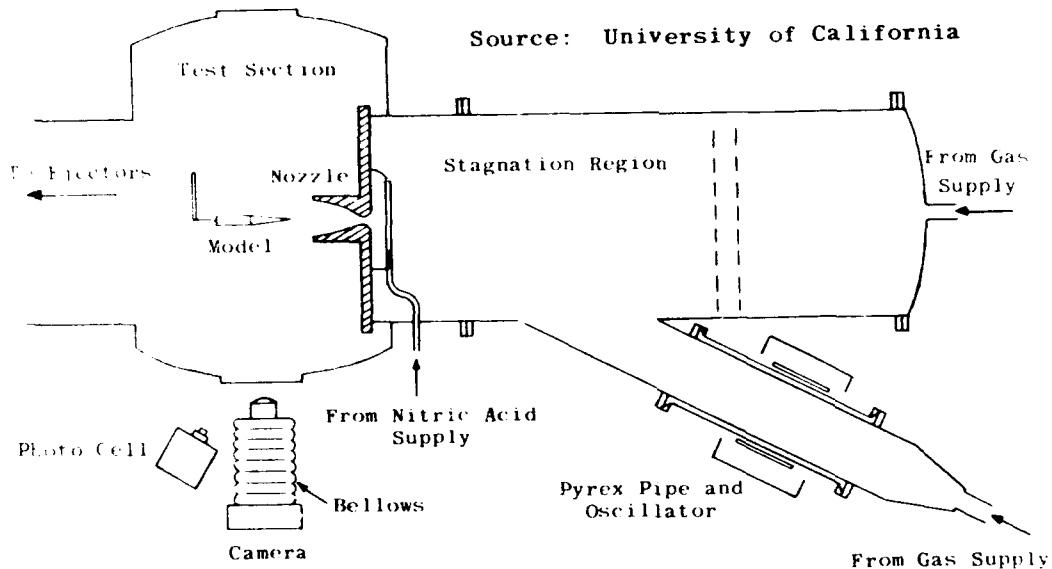


Fig. 5-11. Glow-flow visualization system.

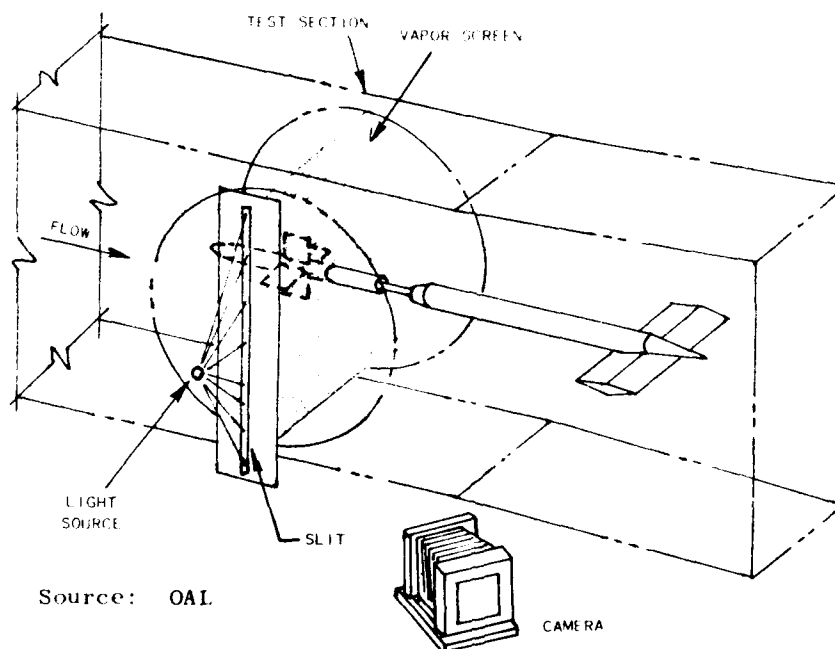


Fig. 5-12. Typical air afterglow of two shocks and boundary layers. Each shock wave static pressure 1.5×10^{-4} atm.

Source: OAL



Fig. 5-13. Flow pattern, vapor-screen technique.



Source: OAL

Fig. 5-14. Isometric sketch of vapor-screen technique.

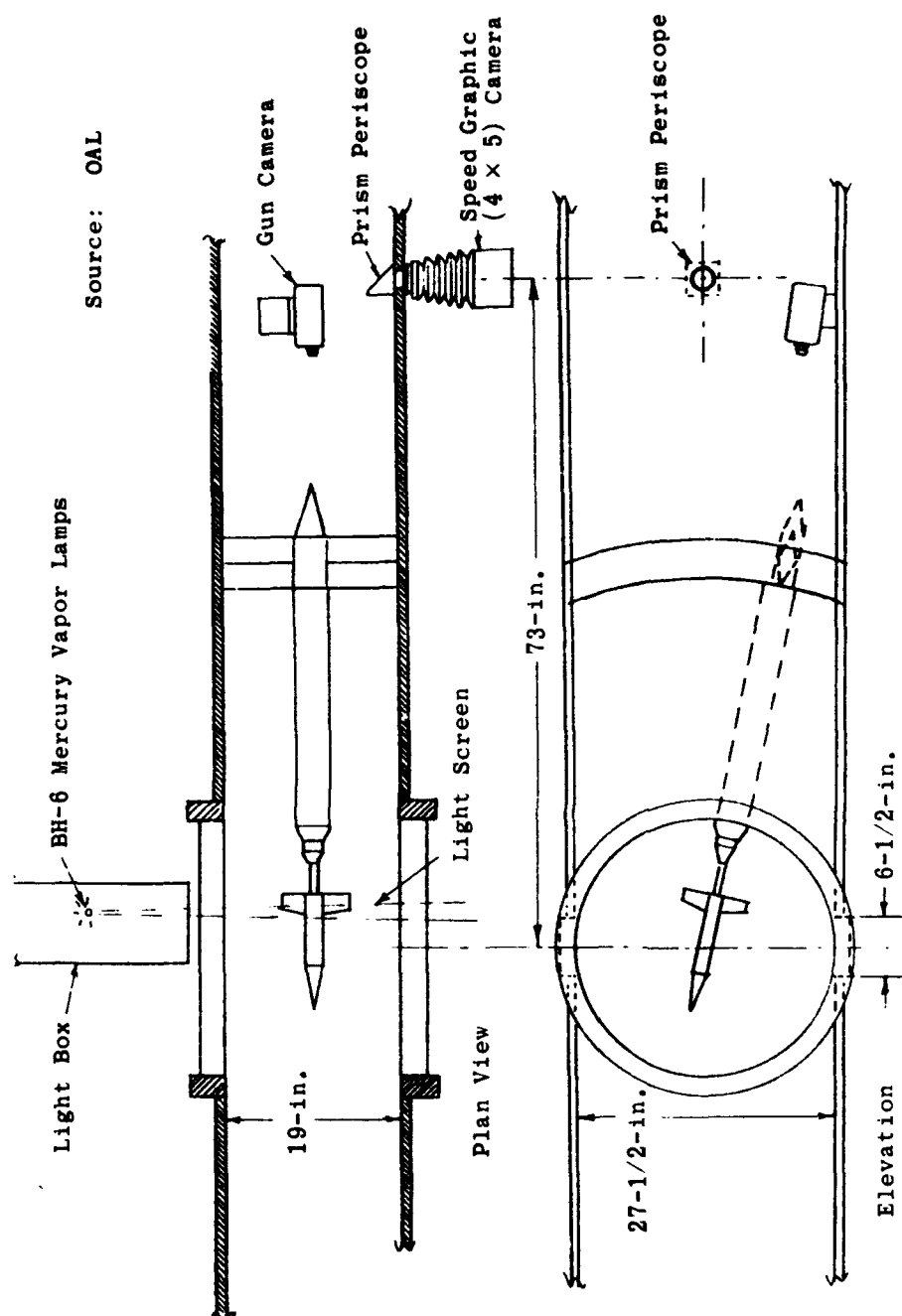


Fig. 5-15. OAL vapor screen technique.

Source: OAL

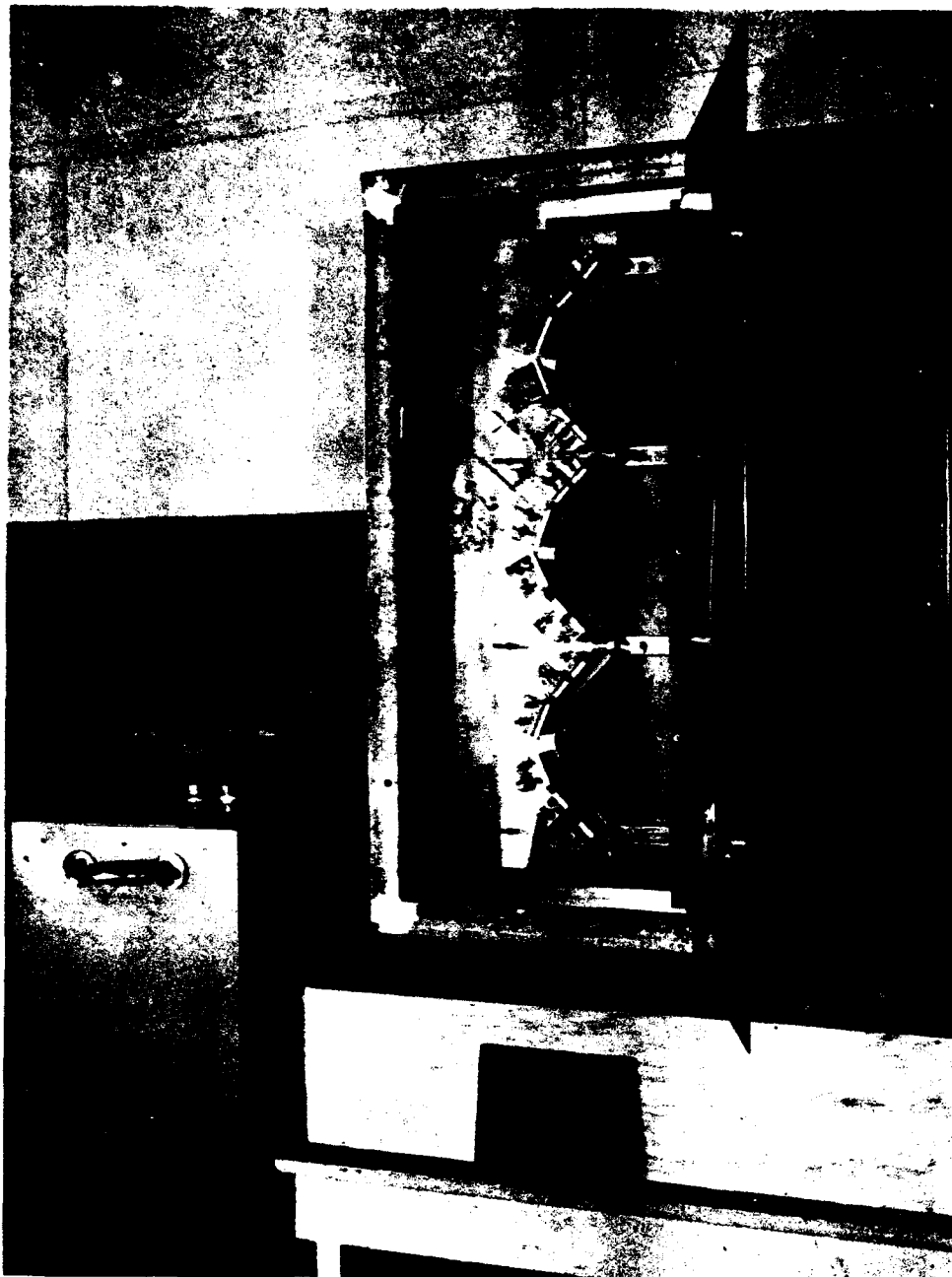


Fig. 5-16. Light source with inspection door open.

Source: OAL

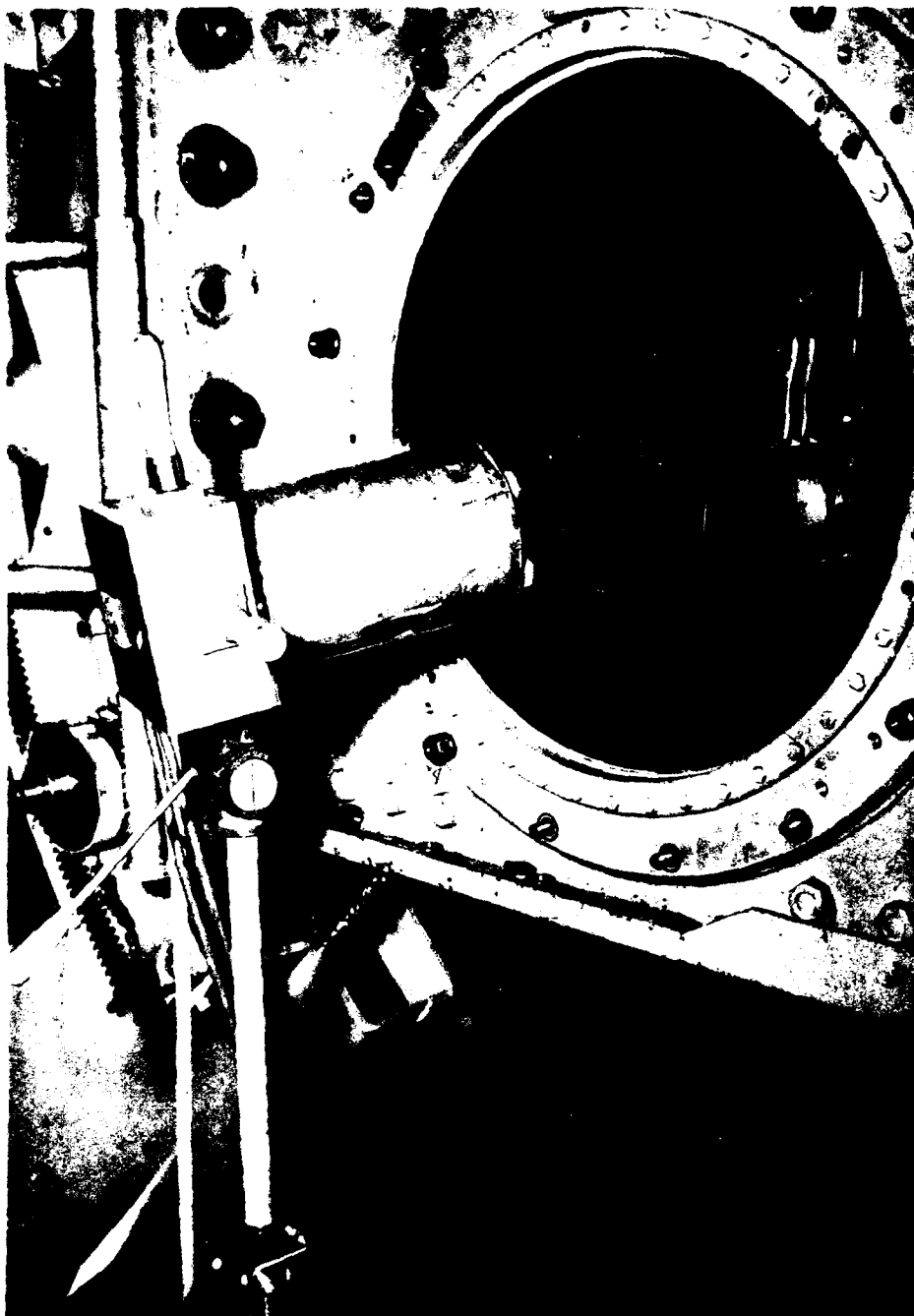


Fig. 5-17. Portable vapor-screen light source mounted on tripod.

6. Turbulence

The relative magnitude of velocity fluctuations is an important variable in wind-tunnel measurements. It determines the degree to which measurements performed on a model may be applied to the full-scale structure as well as how the measurements on similar models in different tunnels can be compared.

The degree or intensity of turbulence is defined as

$$\frac{\sqrt{\frac{u^2 + v^2 + w^2}{3}}}{U} \quad (6-1)$$

where

u, v, and w = turbulent velocities in the three coordinate directions

U = free-stream velocity

In isotropic turbulence the mean velocity fluctuations are equal to one another, and the intensity is given by

$$\frac{\sqrt{u^2}}{U} \quad \text{or} \quad \frac{u'}{U}$$

A second characteristic of turbulence is the magnitude of the eddies, known as the scale of turbulence. The characteristic length, L, of the turbulent eddies may be calculated from

$$L = \int_0^\infty \frac{u_1 u_2}{\sqrt{u_1^2} \sqrt{u_2^2}} \cdot dy \quad (6-2)$$

where subscripts 1 and 2 denote values taken at points 1 and 2, distance y apart.

6.1 Effect of Turbulence on Wind-Tunnel Measurements

To the wind-tunnel operator the most significant feature of turbulence is its effect on the boundary layer. The Reynolds number at which transition occurs is directly related to the intensity of turbulence. But the stability derivatives of simple flight vehicles fortunately are virtually insensitive to the intensity of wind-tunnel turbulence and to moderate changes in Reynolds number. An example of this insensitivity is shown in Fig. 6-1, which gives the stability characteristics measured at two distinct turbulence levels. In each case the Reynolds number of the free stream is 6.6×10^6 /ft of characteristic

length, but the transition Reynolds number is approximately 1.45×10^6 for one case and 3.8×10^6 for the other (see Fig. 6-3). On the other hand, the state of the boundary layer may have significant effect on the skin friction drag of a configuration. It also affects the wake flow and, consequently, the base drag. Turbulence and boundary-layer transition are closely allied to flow separation, and therefore the change in location of separated regions may have appreciable effect on control surfaces. Figure 6-1 compares the axial force for a typical cruciform missile configuration measured at the same two turbulence intensities noted above and shows clearly the effect of turbulence.

The axial force coefficient, C_A , of a simple vehicle with control surfaces at zero angle of attack is in general nearly independent of angle of attack. (Figure 6-1 is a typical example of the magnitude of the dependence.) It should be noted, however, that Fig. 6-2 (from Ref. 125) shows C_A to be strongly dependent on angle of attack.

In this latter case, optical techniques (see Subsec. 5.6) indicated that boundary-layer transition occurred about one body diameter from the model base at zero angle of attack. Agreement between axial-force measurement and calculated drag with laminar skin-friction confirmed this observation. At 2-deg angle of attack it was established that transition had moved forward to about one diameter from the model nose.

The calculated axial force based on the observed variation of transition point with angle of attack is shown in Fig. 6-2 as the dotted curve. The trend of the experimental data agrees with the calculated values. In this test the change of transition location on the body is caused by a change in angle of attack. If the transition region is moved forward by changes in the turbulent intensity, similar increases in skin friction could be expected.

6.2 Measurement of Turbulence

The purpose of a great many wind-tunnel tests is to obtain data pertaining to flight vehicles. It is therefore desirable that the tunnel's turbulence characteristics should be equivalent to those of the atmosphere, or else that these characteristics should be defined clearly enough to allow corrections to be made to the data in order to account for the difference in the location of the boundary-layer transition. Compared to the boundary-layer thickness, the scale of turbulence in the atmosphere is large and produces no appreciable aerodynamic effects. Hence, its intensity of turbulence may be regarded as zero. Although wind-tunnel values may be as low as 0.1% they are usually much higher.

Two general methods of measuring turbulence are currently used. The first, an indirect method, is based upon a comparison of the location of the transition on a standard model tested under various conditions of turbulence. With the second, a more difficult method, the actual velocity fluctuation is measured from point to point.

6.2.1 Indirect Method of Measuring Turbulence

To compare the turbulence level in wind tunnels at many facilities, a standard model, the NOL 5-deg cone, is tested through a wide

range of Mach and Reynolds numbers. This 20-in. cone has a 0.002-in. tip radius, is polished to an 8- μ in. finish, and is joined to a cylinder 10 in. long and 1.75 in. in diameter. The model is instrumented with a single copper-constantan thermocouple to verify that equilibrium temperature is obtained before measurements are made. The boundary-layer transition is determined photographically.

This model was used to obtain the transition Reynolds number in the test section at OAL, NOL, and JPL. Enough shadowgraph pictures were taken during the test to assure that a reasonable and statistically average value of transition Reynolds number would be obtained. All of the measurements were averaged because the values obtained on the top of the model did not always agree with those obtained on the bottom. In addition, the cone was tested at two axial locations in most of the nozzles to minimize the effect of local tunnel disturbances on the results. The test results are shown in Fig. 6-3. From the curves of transition Reynolds number which are presented, comparative values of the turbulent intensity in the test section may be obtained.

An absolute measure (Subsec. 6.2.2) of the intensity, u'/U , was made in the supply chamber of the NOL and JPL tunnels, and the values obtained were 1.0% and 0.3%, respectively. When screens were installed in the supply chamber of the NOL tunnel, the intensity was reduced to 0.3%. To determine the effect of this reduced value the 5-deg cone tests were repeated. It may be noted from Fig. 6-3 that the decrease in turbulent intensity in the supply section of the NOL tunnel significantly increases the transition Reynolds number at Mach numbers below three. However, it may also be seen that for the two tunnels whose supply section turbulent intensity is 0.3%, there is a wide difference in transition Reynolds number, the difference decreasing as the Mach number approaches three. These two effects suggest that though the test-section turbulence is closely related to that of the supply section, other factors also enter into the relationship (see Subsec. 6.3).

A second standard cone model was used to determine the transition Reynolds number in several of the NACA tunnels. This model was a 10-deg cone instrumented with surface thermocouples whose readings indicated the transition region. The results of these measurements are also shown in Fig. 6-3.

An increase in transition Reynolds number was observed in the Mach 1.73 nozzle at OAL when four damping screens were installed in the supply section (see Subsec. 6.3 and Fig. 6-3).

6.2.2 Measurement of Turbulent Velocity Fluctuations

Fluctuating velocities may be measured directly by means of a hot-wire anemometer or a corona anemometer. The advantage with these instruments is that the observations may be recorded and analyzed automatically. In the hot-wire anemometer the magnitude of velocity is obtained from its effect upon the heat-transfer characteristics of a small, fine, electrically heated wire. In the corona anemometer the fluctuations of velocity are determined as a measure of the distribution and path of ions carried by the stream.

Neither of these methods has been used extensively for determining the turbulent intensity of wind tunnels commonly used as test facilities. One probable reason is that the schlieren and shadowgraph photography employed in nearly all test programs, in addition to other techniques (Subsec. 5.6), enable the transition region on a model to be well defined. Another reason is that dirt particles quickly destroy the fine wire of hot-wire anemometers, thus prohibiting their use in practically all but special experimental tunnels.

6.2.2.1 Hot-Wire Anemometer

The hot-wire anemometer has been used for many years to measure the fluctuating flow of gases. The working element for this instrument is an electrically heated wire whose temperature varies in response to rapid changes in the instantaneous flow velocity. If a constant heating current is maintained, the flow-velocity fluctuations can be expressed as a function of the intensity of the resulting voltage fluctuations. The voltage, which can be amplified and measured, depends upon the electrical resistance of the wire, the resistance is determined by the temperature of the wire, and the temperature in turn is affected by the cooling effect of the airstream. Since the wire is small, the response to fluctuations in air velocity is very rapid. For average velocities the time-average voltage across the hot wire can be measured with a potentiometer, and the corresponding velocity then obtained from a calibration curve. Extremely fine wires whose diameter runs from 0.00005 to 0.0005 in. are commonly employed in order to reduce the thermal lag and thus improve the frequency-response characteristics of the sensing element. The wire should have a high temperature coefficient of resistivity and should be capable of prolonged operation at high temperatures without oxidation or loss of mechanical strength.

The hot-wire itself is usually made of tungsten, platinum, platinum-iridium, or platinum-rhodium alloys and is soldered or welded at each end to supporting needles. Soldering makes a better electrical connection and therefore is preferred, unless the probe is to be used at temperatures higher than the melting point of the solder. If the wire is to be soldered, its two ends must first be electroplated with copper. To prevent it from sagging when heated or aerodynamically loaded, the wire must be mounted under tension, an operation that requires the use of a microscope. Considerable care must be exercised to assure that the end joints are properly tapered and the central portion of the wire is not damaged by the mounting process.

The hot-wire anemometer utilizes either a "constant current" or a "constant temperature" circuit. With the constant-current circuit a constant heating current is maintained (usually by placing a very large fixed resistor in series with the hot wire) so that the voltage across the hot wire can be recorded. The hot wire's response to a velocity fluctuation is modified by its own internal heat capacity, the effect of which increases with the frequency of the fluctuations. It is therefore necessary when examining velocity fluctuations in the constant-current type of instrument to include a compensating circuit in the amplifier to correct automatically for this internal heat capacity. The appropriate setting of the compensation circuit depends upon the operating conditions of the hot wire and is usually determined by the "square-wave calibration circuit" method. In this method, when a small square-wave current is superimposed on the steady heating current of the hot wire, the amplifier output appearing on an oscilloscope will

reproduce this square-wave pattern only when the compensation control is correctly set. A useful frequency range of 100,000 cps or more can be achieved in this way.

The constant temperature of the hot wire in the second type of instrument is dependent upon a constant resistance which is maintained by a feedback circuit. The energy input to the hot wire is absorbed by the air stream. Thus the internal heat capacity of the hot wire becomes unimportant since its temperature is constant; consequently, this energy input (proportional to the square of the current) is a measure of the instantaneous air velocity.

Despite its theoretical advantages, this constant-temperature system is subject to some serious design limitations. The upper frequency limit of its feedback amplifier must be more than twice the useful frequency range of the instrument. To match the performance of the best constant-current systems therefore requires excessively high frequency operation, which introduces problems of stability. Noise levels are generally higher, and drift in the high-gain d-c amplifier must be carefully controlled. High-capacity power supplies must be regulated to better than 0.001%, which implies obvious expense and bulk. Operationally, while the constant-current system requires a compensation set, the constant-temperature system requires an amplifier null.

The constant-current instrument has an additional advantage. When the square-wave method has been used to set the compensation circuit correctly, the size of the square-wave signal at the amplifier output (as presented on an oscilloscope, or measured on an rms meter) automatically determines the proportionality between velocity fluctuations and signal output. As a consequence, quantitative work with constant-current equipment is usually easier than it is with constant-temperature equipment.

Several electrical circuits for hot-wire anemometers that have been used successfully are illustrated in the literature (Refs. 241 to 244).

Since basic equations relating to the theory of hot-wire anemometry are readily available (Refs. 151, 242, and 245), only the simplified final form will be given here. The constant-current hot-wire relationship with the wire axis perpendicular to the flow direction is

$$\frac{R}{R - R_a} = D + F \sqrt{U} \quad (6-3)$$

where

R = mean resistance of hot wire at mean temperature of wire, ohms

R_a = resistance of wire at adiabatic temperature, ohms

U = local mean velocity at any point, fps

D and F = constants

In calibration (R/R_a) is plotted versus \sqrt{U} , giving a straight line of slope F and intercept D . A measurement in still air together with one measurement at a known velocity is theoretically enough to establish the line. (The velocity at the point under consideration must be ascertained by means of a pitot-static tube.) Two or three additional points should be found as a check.

The turbulence intensity may be calculated (Ref. 245) from

$$\frac{u'}{U} = \frac{2R_a (B/G)}{i F \sqrt{U} (R - R_a)^2} \quad (6-4)$$

where

u' = root-mean-square velocity fluctuation

B = thermocouple milliammeter reading

G = amplifier gain

i = current

The measured intensity, u'/U , may be corrected for the effects of the scale of the turbulence, L , by an interpolation from the following values (Ref. 246).

l/L	Correction Factor
0	1.000
3.2	1.512

For the length of wire, l , ordinarily used this correction is less than 0.5%.

If the turbulence is not isotropic it is necessary to find v' and w' separately. Methods for doing so are given in the references previously cited.

6.2.2.2 Corona Anemometer

This anemometer employs a corona discharge as a source of positive ions which are carried downstream by the air flow and transported across the stream by the electric field between the corona electrode and the outer electrode. Since fluctuations in the velocity (turbulence) will cause the point of arrival of the ions on the outer electrodes to fluctuate, the outer electrodes may be divided into segments, and the current received by each segment will be a measure of the turbulence. The motion of the ions is also affected by the variations of density in the fluid. A means exists for separating the components of velocity fluctuation parallel and transverse to the flow, as well as simultaneously distinguishing density effects.

Measurements (at the Rosemount Laboratory, University of Minnesota) indicate that the corona anemometer can be effectively operated for frequency responses beyond 100 kc in supersonic flow. Except for relatively large probe size, the lower density limit for operation of a corona anemometer is presently in the vicinity of 0.1 to 0.25 times room density. Although the corona anemometer has been sufficiently developed for many uses, experience under a wide range of operating conditions has yet to be accumulated. Its background noise in supersonic flow is comparable to the hot-wire anemometer, and for many purposes its interpretation is simpler.

6.3 Minimizing Turbulence Effects

Though all the causes of turbulence in a wind tunnel are not clearly understood, a few methods of decreasing it have been found. The best known is perhaps that of placing fine screens or meshes in the low-velocity supply chamber. Under certain flow conditions these screens cause no eddies of their own. When successive screens are used they should be far enough apart to cause the turbulence created by the first to decay before the next screen is reached. Suitable size of mesh and gage of wire are given as a function of flow Reynolds number in Ref. 64. The effect of screens in the OAL tunnel at Mach 1.75 may be seen in Fig. 6-3.

The contraction ratio between the tunnel throat and the stilling chamber also affects the intensity of turbulence. This is a problem of tunnel design rather than tunnel instrumentation. Reference 247 shows that the longitudinal component of the turbulent velocity decreases in absolute magnitude and the lateral component increases as the flow accelerates through the contraction. However, elementary considerations show that in supersonic nozzles the increase in mean velocity and the decrease in density are both beneficial in reducing the flow irregularities and restoring the isotropy.

The smoothness of the flow-channel walls of a tunnel may also affect the turbulence. It is suggested that the increase in critical Reynolds number in the OAL Mach 2.77 nozzle (Fig. 6-3) is due to the smoother finish of the walls of that particular nozzle.

Where it is impossible to change the turbulence level of a test section it may to some extent be compensated for by fixing the transition from laminar to turbulent boundary layer at some specified position which would correspond to a fixed turbulence level. Methods by which this may be achieved are discussed in the next subsection.

6.4 Fixing Boundary-Layer Transition on Models

Since supersonic wind tunnels are limited in size and tunnel stagnation pressure by power requirements, most model tests are made at Reynolds numbers much lower than those of the full-scale aircraft. As a result, the boundary layer may be laminar over a large part or all of the model surface instead of turbulent, as it frequently is at the higher Reynolds numbers of flight. This difference affects the skin-friction drag, the rate of growth of the boundary layer, the conditions under which the boundary layer separates, its behavior after separation, and the effectiveness of control surfaces that are partially immersed in the boundary layer.

To reduce or eliminate these scale effects, it is often desirable to fix transition to turbulent boundary layer by some artificial method. This requirement presents the problem of choosing a mechanism which will promote transition with minimum collateral effect on the flow. The methods which have been used (Ref. 248) to fix transition include 1) the use of carborundum grit, single or multiple wires, or ridges on the model surface; 2) cutting multiple grooves into the surface; and 3) injecting air into the boundary layer.

The use of grit or wires appears most practical for use in supersonic wind tunnels. Multiple wires may prove more satisfactory in some situations since their size can be smaller than that of a single wire; consequently, the production of less severe disturbances in the free stream can be expected. Grooves transverse to the airstream have proved less satisfactory than ridges on the model. Air injection has been used satisfactorily on flat plates, but its application to complex models is limited because of the increased complexity of the models. The disadvantage of carborundum grit is that it tends to erode. In low-speed tests, however, it may have a possible advantage. Results show that it provides less distortion of the boundary-layer velocity profile than other methods do.

A typical plot of drag coefficient versus roughness height at Mach 4.09 obtained in experiments at JPL is shown in Fig. 6-4. The models used were bodies of revolution composed of conical noses and cylindrical afterbodies joined by tangent circular ogives. The bodies had included-angle cones of 12, 20, and 30 deg and an over-all fineness ratio of 10.6. Additional data on all the models were obtained over a Mach number range of 1.63 to 4.09 and are shown in Fig. 6-5. However, the quantitative results will apply in general only to the JPL 20-in. supersonic wind tunnel, where the investigation was made. The critical roughness will be a function of wind-tunnel turbulence, temperature, and model geometry.

It may be concluded, for the ranges of variables tested, that both the single-element and the distributed roughnesses can be used satisfactorily to fix transition, with negligible effect on drag due to the roughness itself (apart from that attributed to movement of the transition point). It is believed that further increase in roughness size may have an effect on the wave drag, especially at lower Mach numbers.

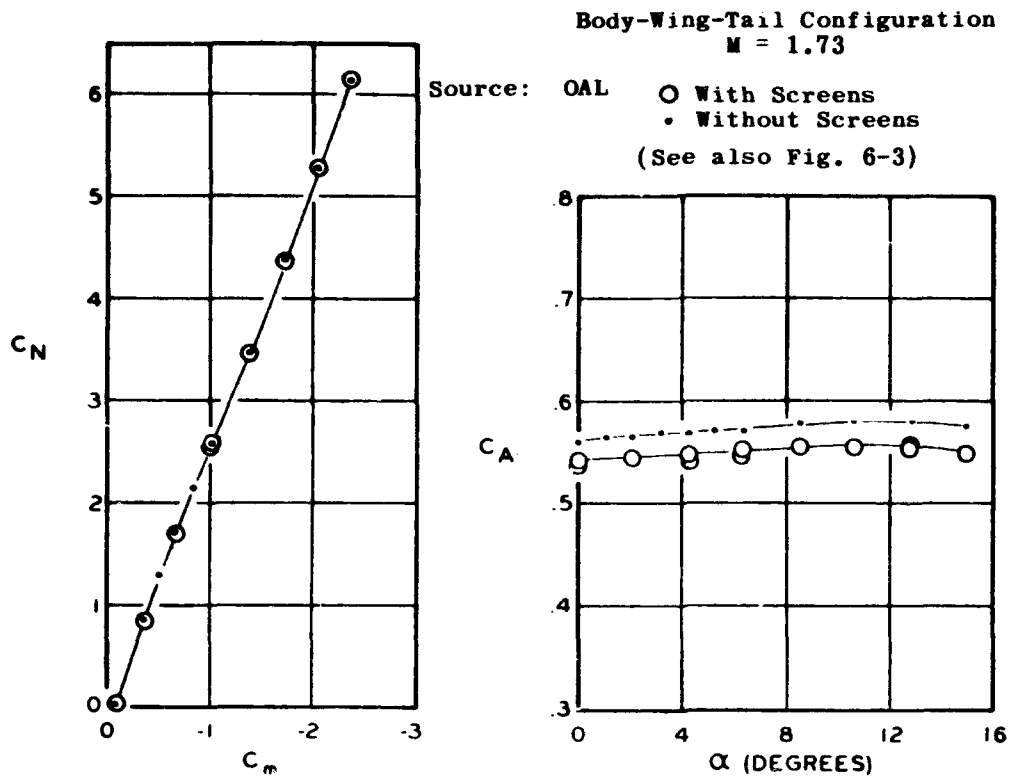


Fig. 6-1. Effect of stilling chamber screens on model stability and axial force characteristics in the OAL Mach 1.73 nozzle.

Source: OAL

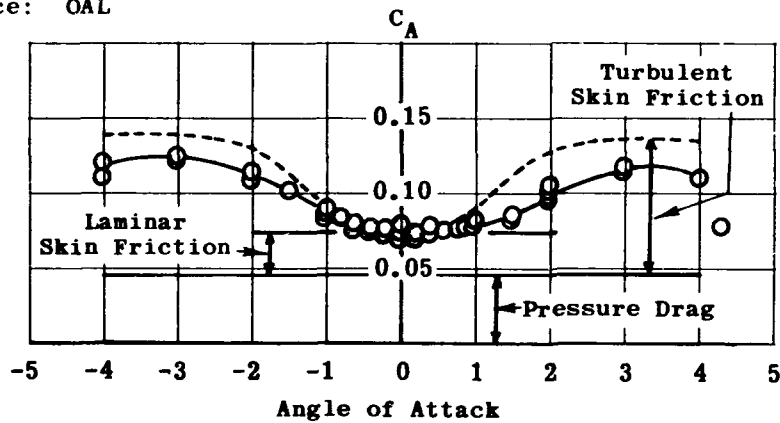


Fig. 6-2. Variation of body-alone (RM-10) axial force coefficient with angle of attack; Mach number 1.73, Reynolds number 6.66×10^{-6} .

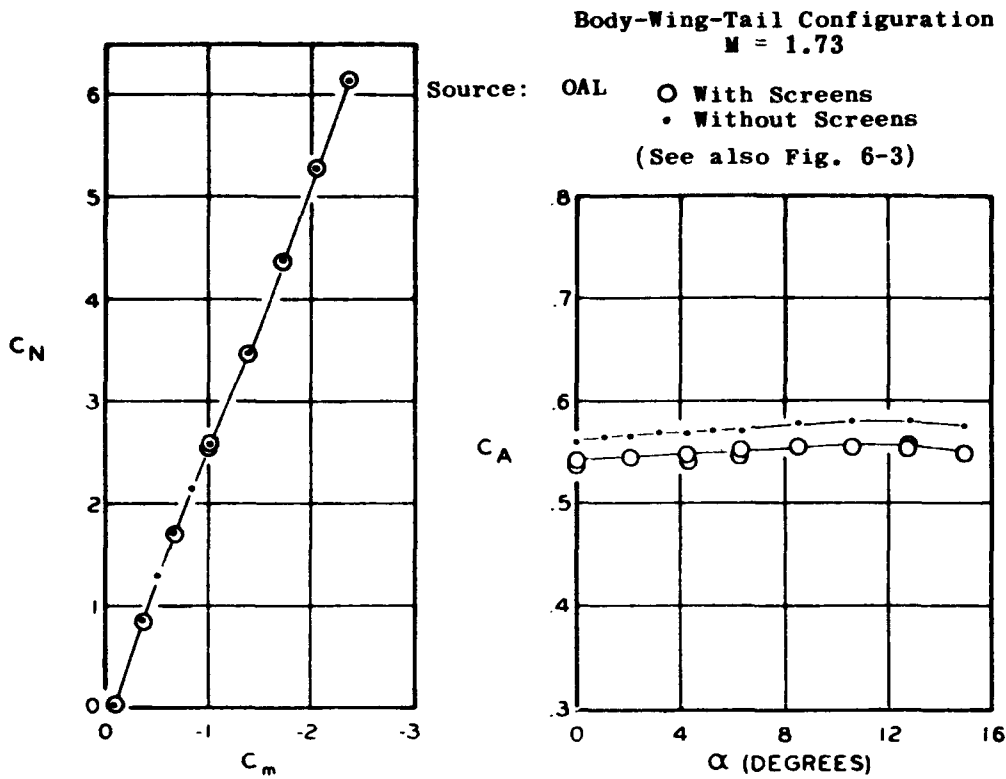


Fig. 6-1. Effect of stilling chamber screens on model stability and axial force characteristics in the OAL Mach 1.73 nozzle.

Source: OAL

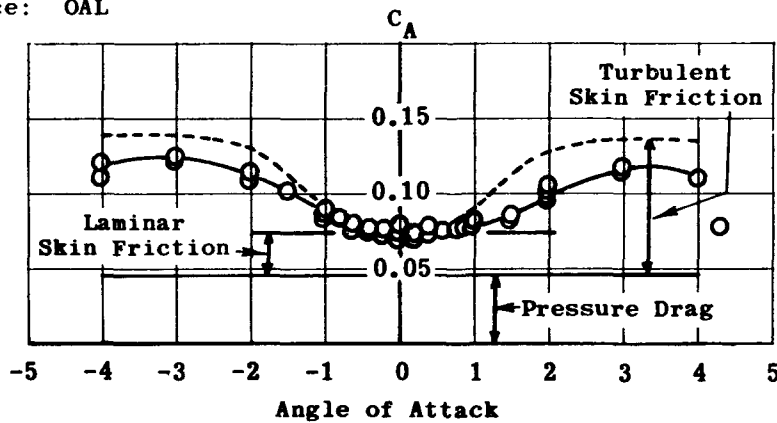


Fig. 6-2. Variation of body-alone (RM-10) axial force coefficient with angle of attack; Mach number 1.73, Reynolds number 6.66×10^{-6} .

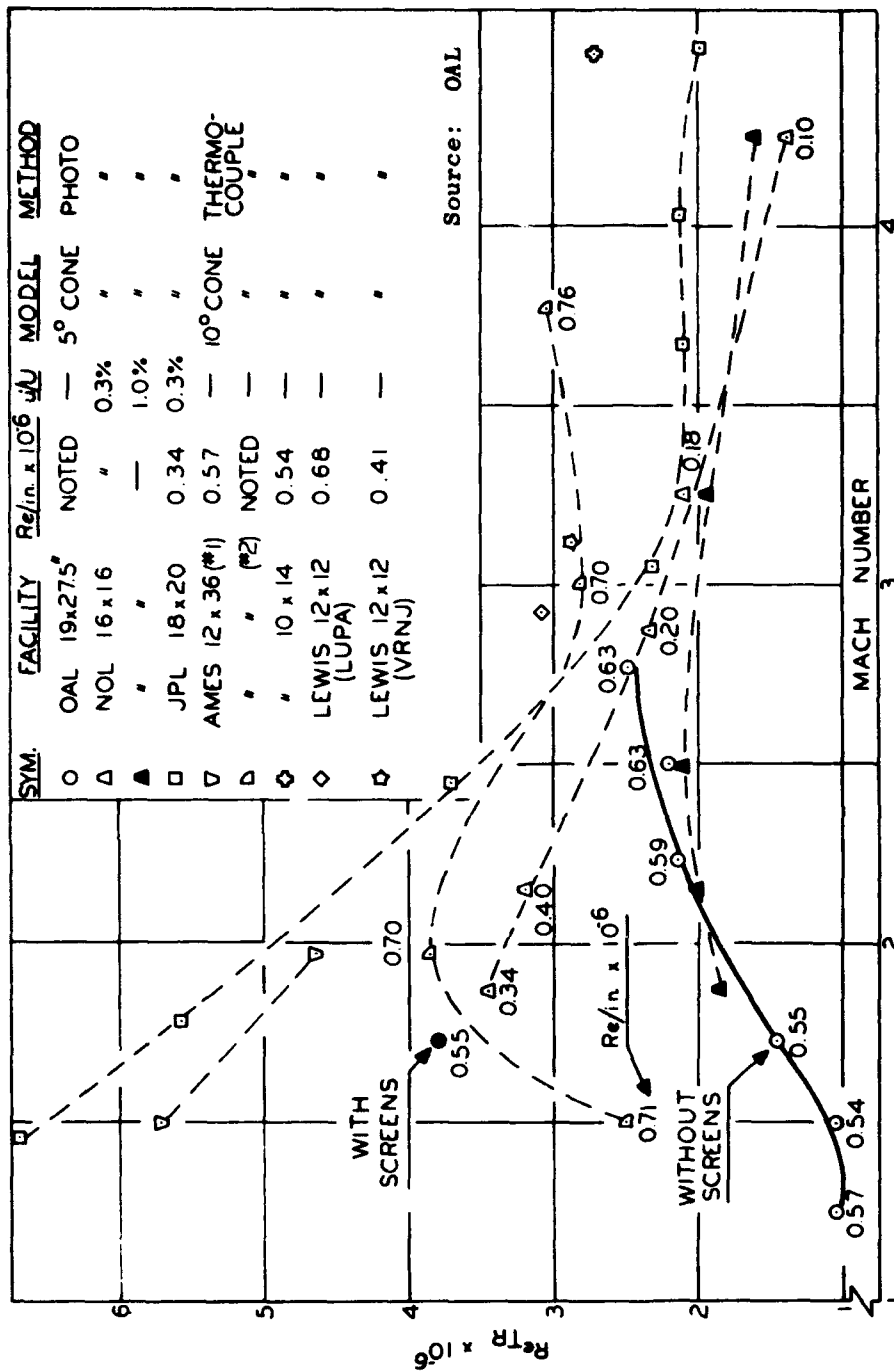


Fig. 6-3. Comparison of transition Reynolds number on 5- and 10-deg cones observed at several facilities.

Source: Ref. 248

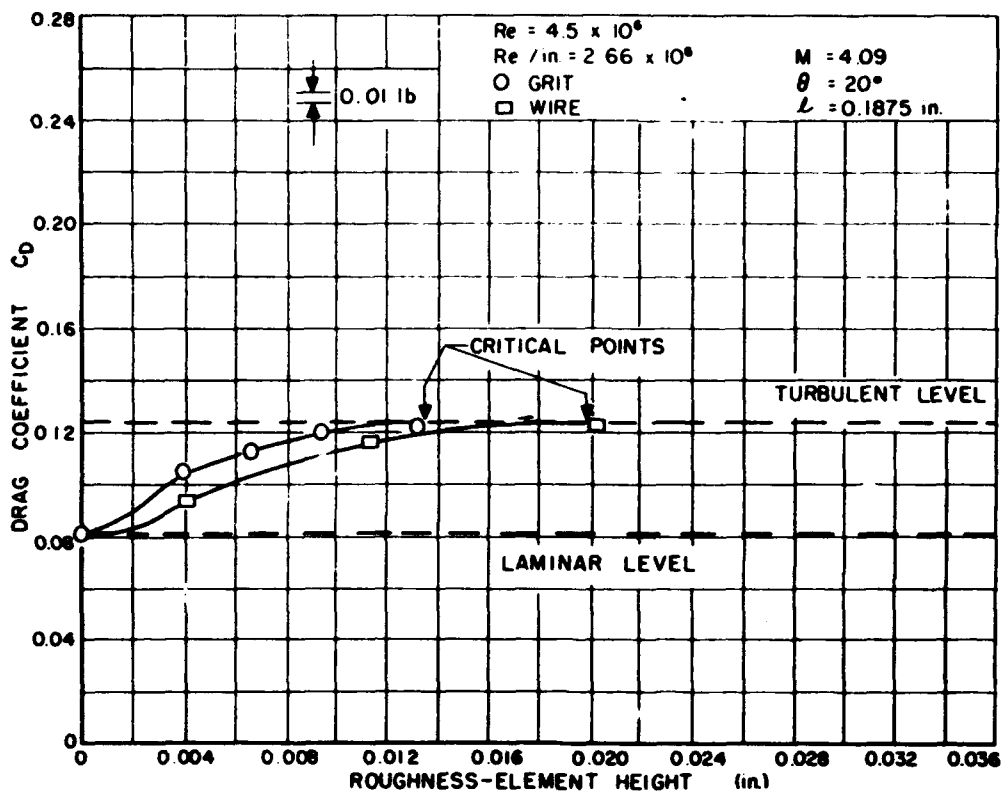


Fig. 6-4. Typical plot of drag coefficient vs roughness height.

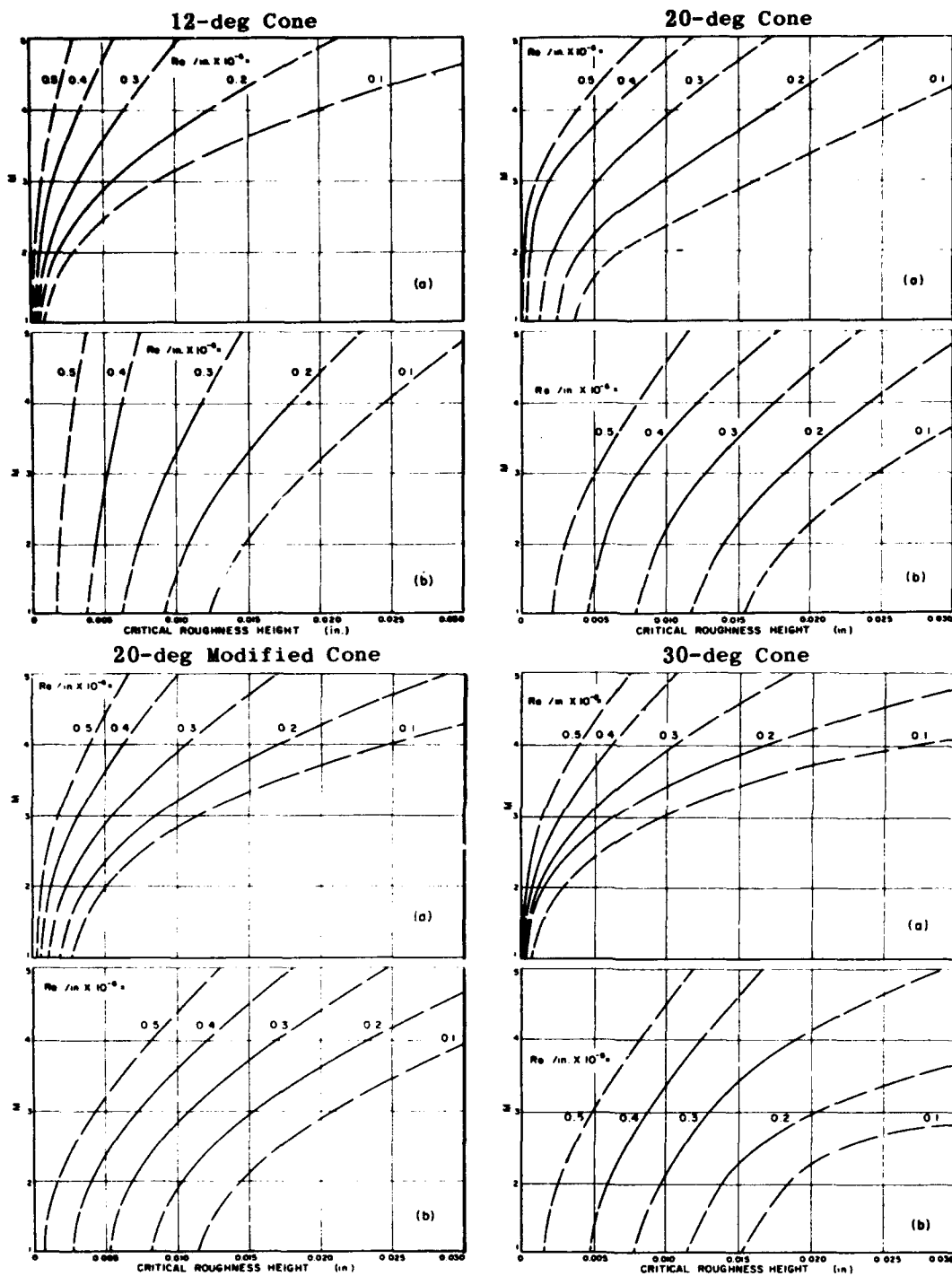


Fig. 6-5. Effect of Mach number on critical roughness height.

7. Tunnel Blockage

When supersonic flow cannot be established in the wind-tunnel test section, the resultant condition is known as a "blocked tunnel." This condition is caused primarily by 1) insufficient compression ratio, 2) excessive moisture (or condensed gas) in the airstream, or 3) too large a model.

7.1 Inadequate Compression Ratio

Figure 7-1 presents a broad range of experimentally determined minimum compression ratios as a function of Mach number, together with minimum theoretical value, which is the pressure ratio through a normal shock. In general, this evidence shows that the classical normal shock pressure ratio is insufficient to start an empty tunnel since it does not account for pressure losses in the system. Considerable refinement in diffuser design has made it possible to start empty tunnels with near-normal shock pressure ratios. However, the addition of a typical model and support system usually increases the required minimum compression ratio so that it approximates the dotted curve in Fig. 7-1.

7.2 Excessive Humidity

Operation of a supersonic wind tunnel at a dew point high enough to allow water vapor to condense in the test section can introduce "condensation shocks" and, hence, variations from the desired Mach number. Water vapor in excessive quantities can also prevent the establishment of supersonic flow in the test section. It is therefore necessary to monitor the test section dew point during operation to assure that there are no undesirable humidity effects.

Figure 7-2 is a handy chart for converting dew point in degrees Fahrenheit to specific humidity in pounds of water vapor per pound of air as a function of absolute pressure. The dew point is quoted at atmospheric pressure (the dotted line in Fig. 7-2). The presence of condensation shocks causes errors in pressure readings. To keep these errors within allowable limits the air must be dried to the dew points indicated in Fig. 7-3. These dew points are given as a function of free-stream Mach number for two stagnation temperatures (100°F and 500°F). The calculations are based on the methods presented in Ref. 249.

7.2.1 Humidity Indicating Instruments

A survey of the methods of measuring humidity, calibrating instruments, and producing atmospheres of controlled humidity, as well as a list of available literature, including manufacturers' catalogs, appears in Ref. 250. (It is suggested that Ref. 250 be examined before the first step is taken to select a humidity indicator. No attempt will be made here to describe the many instruments that are available.)

Two techniques (Ref. 1) which depend upon the appearance of visible water droplets at the dew point are in common use. A classic and reliable method, often used as a primary standard, involves visual

or photo-electric indication of a water (or ice) film appearing and disappearing on a metallic mirror as it is heated and cooled. The mirror surface temperature is equal to the dew point when clouding first appears, and it is best measured by surface thermocouples. With this method the instruments are fitted with an automatic control which maintains the mirror at the dew point. Various types of such indicators are commercially available, some with a reported accuracy of $\pm 1\%$ of the water-vapor pressure.

A more dependable and less complicated type of instrument (Alnor Dewpoint Indicator, Illinois Testing Laboratories) produces a cloud of fine water drops or ice particles when the temperature drop of an adiabatic expansion reaches the dew point. The cloud is illuminated by a lamp and observed visually or photo-electrically. An initial pressure is built up in the air sample by means of a hand pump and then allowed to expand. The correct initial pressure, which just reaches the dew point after expansion, is determined by trial and error. This indicator is used widely to measure dew points as low as -40 to -70°F during supersonic wind-tunnel operation.

The most frequently made error in obtaining dew points is caused by inadvertent contamination of the gas sample. Water or condensation in the sampling line between the gas to be sampled and the instrument will markedly affect the true dew point.

7.3 Model Size

It is usually desirable to utilize a model of the maximum size in order to realize the greatest aerodynamic forces and minimize instrumentation errors. An added advantage is that the larger the model the more nearly the Reynolds number approaches that of free flight. However, the size of any test configuration is limited by the blocking factor. (See also Subsec. 8.1.)

One-dimensional flow theory generally defines an absolute upper limit for the cross-sectional area of any model to be tested in the wind tunnel. It is the condition at which a normal shock would occur and would initiate subsonic flow in the test section. This upper limit does not take into account any other losses than those incurred at the normal shock; hence the practical area limitation will be considerably below this upper theoretical limit. The absolute magnitude of the limiting condition or the degree of reduction from the one-dimensional theory for actual testing of particular models is poorly defined. Due to this insufficient knowledge concerning the relative choking properties of different test configurations, many theoretical blocking limitation curves have included a notation to the effect that the theoretical values should be reduced by some arbitrary percentage to guarantee a margin for safe testing. Such design methods have frequently resulted in the needless curtailment of the size of many test configurations, particularly those having streamlined nose sections, because of the fear that a choked condition would result in the wind tunnel.

A series of disks of varying diameters and a dual series of axially symmetric cones with included angles of 20 and 60 deg were tested in the WADC 6-in. supersonic wind tunnel in order to determine more accurately the limiting size of future test configurations. Data were obtained at nominal Mach numbers of 1.50 , 1.75 , 2.00 , 2.25 , and

2.50, and at a Reynolds-number-per-foot value of 4.68×10^6 . The ratio of cross-sectional model area, A_M , to test-section area, A_T , above which the flow within the tunnel was completely choked is shown in the following table. A strong shock wave existed across the channel ahead of the model, and the flow within the immediate region of the model was largely subsonic.

Ratio of A_M to A_T

Mach No.	Theory	Disk	60-deg Cone	20-deg Cone
1.50	0.086	0.025	0.040	0.070
1.75	0.136	0.053	0.076	---
2.00	0.178	0.077	0.100	---
2.25	0.213	0.099	0.116	---
2.50	0.240	0.117	0.122	---

At the time this data was gathered the 20-deg cones had been tested only at Mach 1.50. However, the results suggest that the limit for the one-dimensional theory can be closely approached with conical noses of low included angle. These data and the theoretical limiting area ratio are shown in Fig. 7-4.

The flow characteristics along the length of the model should be considered if an extensive afterbody is present. The flow conditions at the nose of the model would present no problems; however, as the critical area ratio for blockage is approached, the shock interference tends to move upstream from the subsonic diffuser toward the rear of the model. A shock wave interference could then exist on the afterbody.

Since the initial investigation was concerned solely with the nose effects of axially symmetric bodies upon the relative blockage, no effort was made to determine the effect of the body length of an afterbody. Because of the boundary-layer growth along the length of a body, an additional blockage effect can be expected.

Figure 7-4 also presents some experimental results obtained at OAL in the lower supersonic Mach number range. It should be noted that such test installations as transverse rods can block the tunnel even though larger cross-sectional area configurations allowed the flow to be established.

Probably the most fundamental approach to this problem is being taken at JPL. Preliminary results of JPL's study show that tunnel blocking can be predicted if the bow-shock-wave intensity at the wind-tunnel wall is great enough to exceed the critical pressure required to separate the tunnel boundary layer from the wall.

Facility	Test Section Size (in.)	Operation	Nozzle	Diffuser
○ AEDC	9 × 12	Intermittent	Flexible	Fixed
△ ATD-Mugu	17 × 21	Continuous	Fixed	Fixed
□ BRL	15 × 20	Continuous	Flexible	Variable
▽ DTMB	18 × 18	Intermittent	Fixed	Fixed
◇ JPL	18 × 20	Continuous	Flexible	Variable
○ NAA	16 × 16	Intermittent	Fixed	Variable
○ NAA	3.5 × 3.5	Intermittent	Fixed	Variable
○ NSL-MIT	18 × 24	Continuous	Fixed	Fixed
○ OAL	19 × 27.5	Continuous	Fixed	Fixed
▽ Redstone	7 × 7	Intermittent	Fixed	Variable
◇ Univ. Mich	4 × 4	Intermittent	Variable	Variable
◇ Univ. Mich	8 × 13	Intermittent	Fixed	Variable
▽ WADC*	6 × 6	Continuous	Fixed	Fixed

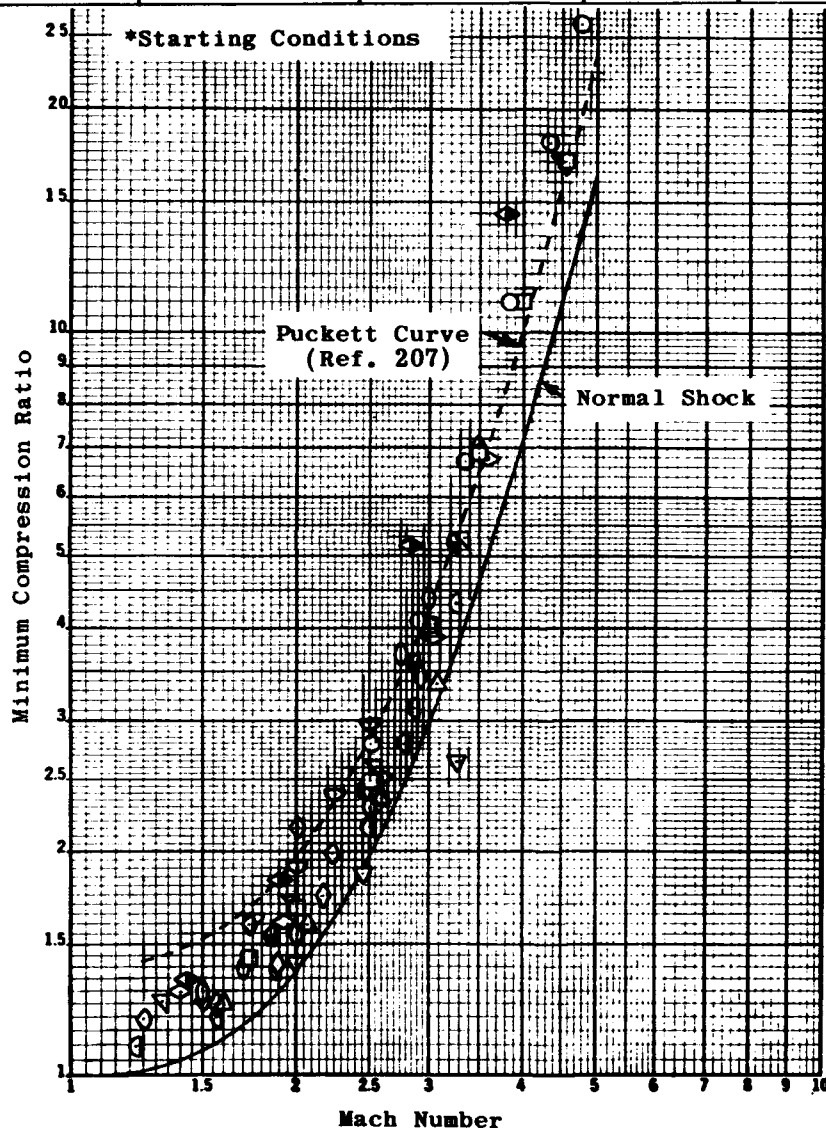


Fig. 7-1. Minimum operating compression ratio for supersonic wind tunnels.

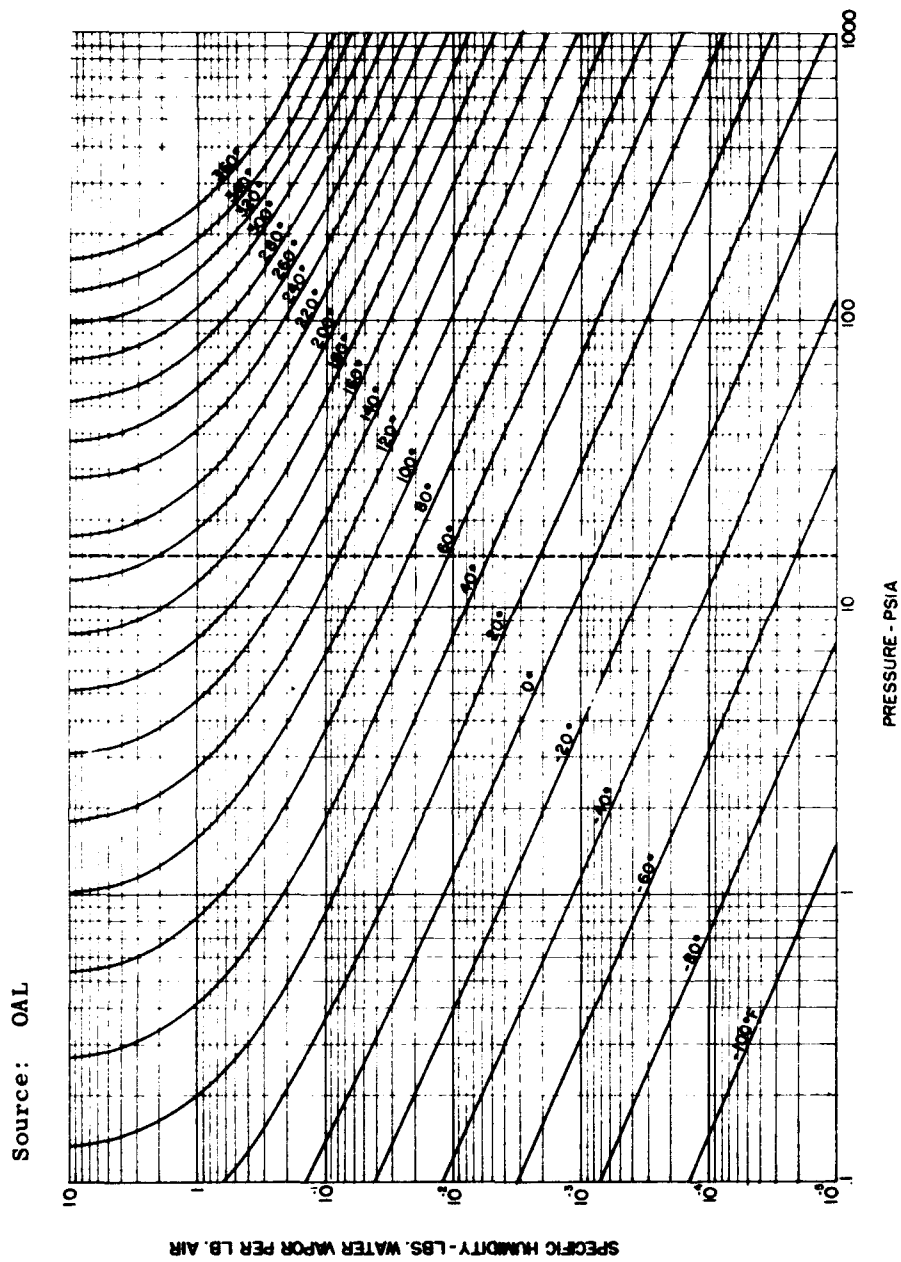


Fig. 7-2. Saturation weight of water vapor in air.

Source: Ref. 249

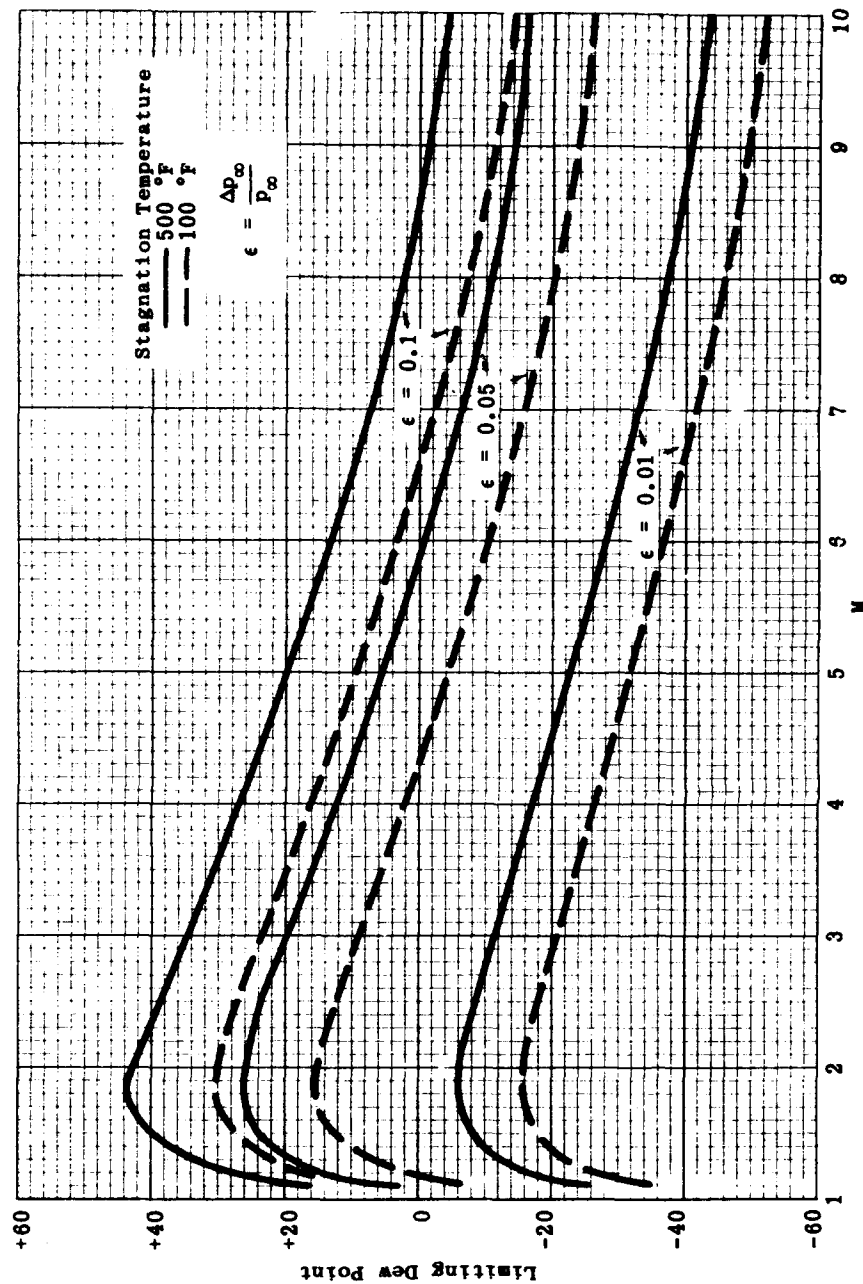


Fig. 7-3. Lower limit of dew point as a function of Mach number for various errors in static pressure; $T_0 = 500^\circ\text{F}$ and 100°F .

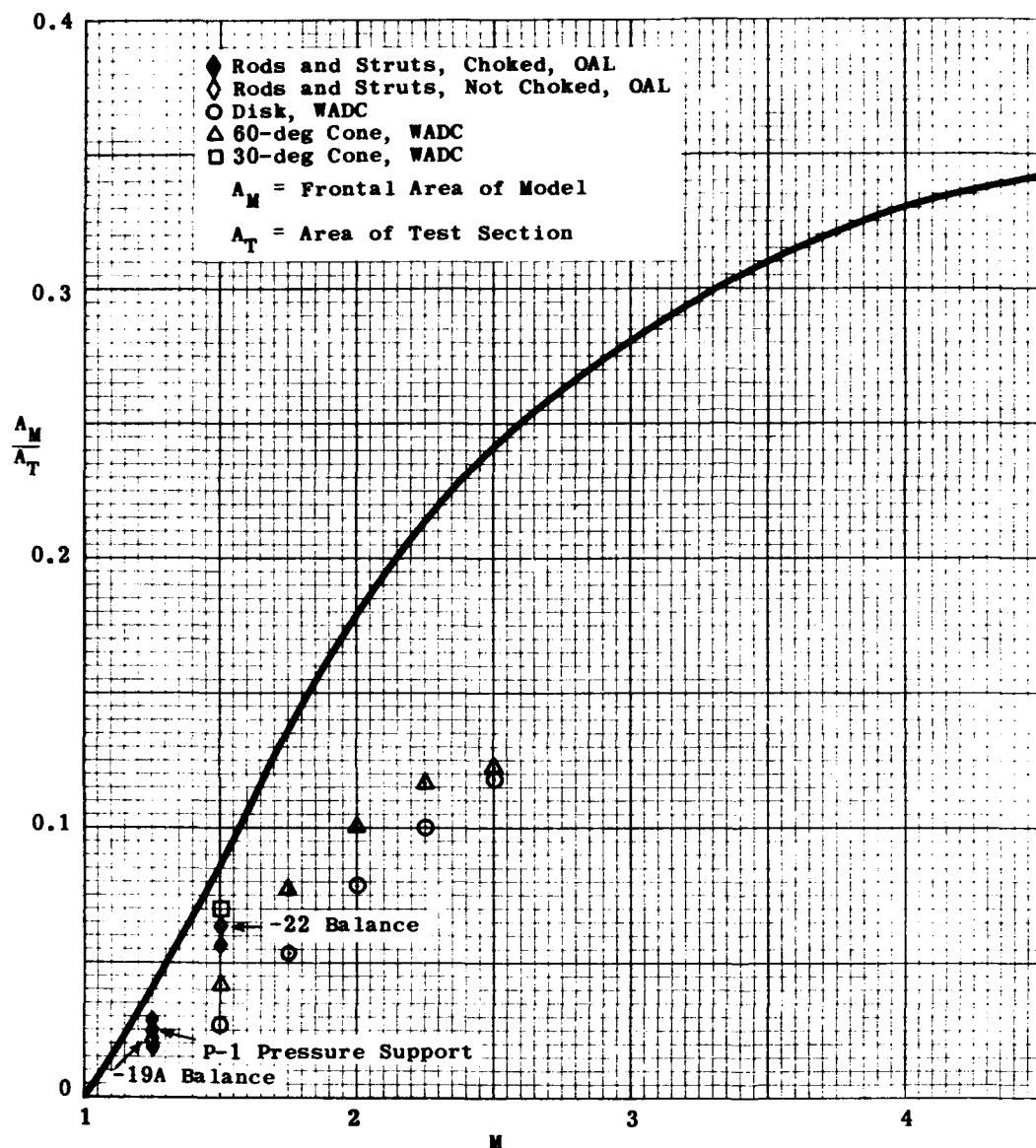


Fig. 7-4. Upper limit of model area to test section area as a function of Mach number.

8. Model Design

It is generally desirable to make a wind-tunnel model as large as possible in order to maximize air loads and thus increase the accuracy of measurements. The larger size also provides a more realistic Reynolds number. Moreover, as the model size is increased the problems of design and fabrication become less difficult. Several factors limit the maximum model size for any given facility, and these are:

1. Tunnel blocking, which governs maximum frontal area
2. Reflected shock-wave interference, which governs model length
3. Limitations on the aerodynamic loads, including the dynamic effects of starting and stopping the wind tunnel.

The first of these has been discussed in Subsec. 7.3, and the limiting area is defined in terms of the nose geometry and the free-stream Mach number.

8.1 Shock-Wave Reflection

Shock waves from models in a supersonic wind tunnel may produce two undesirable effects not found in free flight.

First, behind normal shocks and some low supersonic Mach number shocks there exists a region of subsonic flow. This region tapers away to nothing at some distance from its origin; but should it strike a wall of the wind tunnel before vanishing, pressure disturbances at the wall can propagate back through this subsonic region and influence the flow properties over the model. This possibility may generally be ignored even at very low supersonic speeds, since tunnel blocking considerations for solid walled nozzles will usually impose a more serious restriction on allowable model size.

Second, when a bow wave from a model strikes a wall of the tunnel it is reflected into the stream and may impinge on the afterbody of the model. The same kind of effect may be produced by the reflection of an expansion wave on a free jet boundary. If this occurs, the pressures on the model in the vicinity of the reflected shock impingement will no longer be representative of free-flight conditions. Therefore, the model length should be chosen such that the reflected shock intersects the tunnel axis well aft of the model base. This requirement seriously limits the model length for tests at low supersonic Mach numbers, but becomes less significant as the Mach number increases. The limiting length of the model is also strongly dependent on the width of the test section.

A study of shock-wave photographs from tests (Ref. 91) of models with various nose shapes has resulted in an approximate method for rapidly locating the position of reflected shocks from conical, ogival, hemispherical, and ducted-nose (without duct flow) flow-waves. The results of this study are presented in Figs. 8-1, 8-2, and 8-3. Whitfield (AEDC GDF) has measured shock reflection characteristics for hemispherical and conical noses for angles of attack of 0, 15, and 30 deg at Mach numbers 1.5, 2.0, 2.5, 3.0, 4.0, and 5.0, and the results are presented in Figs. 8-4 to 8-21. These charts provide a

graphical method for locating within ± 1 in. the position of the reflected shock wave from various shaped noses for various angles of attack. The charts may be used directly for conical and hemispherical noses. If the nose shape is ogival it may be replaced by an effective cone whose vertex angle is 80% of the ogive vertex angle. The ogive vertex half-angle, θ_s , is given by

$$\theta_s = 2 \arctan \frac{1}{2 \sqrt{(C - 0.25)D}} \quad (8-1)$$

where

C = caliber of the model tangent ogive

D = maximum diameter of ogive

The chart for ducted, no-flow models may be used for either conical or ogival cowls. In a tunnel where the height is considerably greater than the width, the reflection from the side walls will always be critical. However, this is not the case if the test section is square and the model is at an angle of attack.

To use the charts (Figs. 8-4 to 8-21) it is necessary to employ the following procedure.

1. Determine the effective distance, Y/D , from the side wall to the tunnel centerline. The effective wall is assumed to be displaced inward from the physical wall by one-fourth of the boundary-layer thickness.
2. Find the intersection of Y/D with the effective nose angle.
3. From this point draw the reflected shock, making the angles of reflection and incidence equal.

The point of intersection of the reflected ray and the tunnel centerline will give an indication of the limiting length of a model.

8.2 Aerodynamic Loads Imposed by Starting and Stopping Flow

Methods such as those which utilize simplified linear theories for calculating the steady-state air loads on surfaces and bodies are readily available in the literature and supported by an abundance of wind-tunnel test data. However, in selecting a model scale such that the air loads will not exceed the capacity of the supporting structure it is necessary to take into account the additional loads incurred during the starting and stopping of the air flow. In wind tunnels whose dynamic pressure is high this increase in load is very great.

Figures 8-22 and 8-23 (Ref. 252) present typical examples of the starting and stopping loads encountered in tests on a generalized cruciform model in a continuous closed-return wind tunnel. The tests employed wing-alone, body-alone, and wing-body configurations. Pitching moment, normal force, and axial force data were recorded on an oscillograph. The frequency and duration of loading were also documented.

Values presented are the maximums encountered during several starts and stops of the same configuration. These multiple readings are necessary because the starting phenomena are random, and sufficient measurements must be made to assure a statistically reliable answer.

The models were set at zero angle of attack during starting and stopping, but the measured normal forces compared with the steady-state values at 10-deg angle of attack, the highest anticipated value for the particular setup. Figure 8-22 shows that the transient loads not only increase with Mach number but also may increase many fold. The axial forces shown in Fig. 8-22 are in both cases based on the zero lift value. Although the starting and stopping load factor for the axial force has increased much more than it has in the case of the normal force, the absolute value of the axial force is very much smaller than that of the normal force.

In the OAL tunnel the stopping loads appear to be approximately 20% higher than the starting loads. This difference results from the fact that the entire circuit is at ambient pressure just prior to starting the tunnel. However, during operation the pressure in the return line of the tunnel is above atmospheric, thus increasing the stagnation pressure in the circuit during shutdown.

The foregoing data were compared with similar data obtained on wind-tunnel models of typical airplane configurations in the same OAL tunnel, and it was found that reasonable agreement existed between these data and that from all three configurations tested. In the latter tests, it was noted that the side loads for a cruciform model were in the same order of magnitude as the normal loads during the starting and stopping phases.

The following expression (Ref. 253) is used to predict the starting normal force, N , experienced by an airplane-type model in the AEDC GDF E-1 tunnel.

$$\frac{N}{p_o S} = \frac{7(M^2 - 1)}{6(1 + 0.2M^2)^{3.5}} \quad (8-2)$$

where

p_o = instantaneous total pressure that exists when the tunnel starts

S = total planform area of the wing

This expression is based on the assumption that supersonic flow exists over the top surface of the wing and body, with a normal shock standing below the leading edge and followed by subsonic flow over the lower surface of wing and body. Experimental results (Ref. 253) show good agreement with this rather arbitrary physical picture.

Another loading problem connected with starting and stopping is that of model oscillation. The natural frequency of the model-balance system should damp rapidly to the steady state, a prime consideration in blowdown tunnels since it effectively curtails the run-time.

An experiment at United Aircraft's 4.5 by 4.5-in. tunnel, utilizing a single dynamic pressure pickup which measured the pressure difference between the top and bottom surfaces of a rigidly mounted wing at zero angle of attack, indicated that the pressure difference during the starting process oscillated at frequencies of several hundred cycles per second and had a maximum value equal to the pressure ratio across a normal shock wave at the tunnel Mach number. Experimental values were always less than this value because of the dynamic effects related to the frequency of the oscillating loads and the natural frequency (86 cps) of the model in pitch.

The duration of the increased loading is governed largely by the time required for closing the by-pass valve, which may vary from a few milliseconds to several seconds. In a series of starts with valve opening times of 8.5, 35, and 500 msec, the starting loads in the UAC tunnel were essentially the same at the two lower values, but two or three times higher for the slowest valve opening.

However, experiments in BRL's Tunnel No. 3 do not corroborate this. Tests with the continuous-flow, closed-circuit, variable-density tunnel having a starting time of 1.5 min showed that the loads are greatest during the period of 3 to 6 sec, when the transition shock system passes over the model. Quick-operating valves which opened within a second were tried, and it was found that the maximum loads were of the same order as those with the regular valving.

8.3 Model Construction Techniques

Models are usually constructed of steel, aluminum, or brass. The body is generally made of SAE 4140 steel, heat-treated to 125,000 psi. Highly stressed parts such as aerodynamic surfaces require a material that exhibits good machining properties at a high degree of heat treatment. For this purpose SAE 6150 steel or an equivalent is used. Heat treatment for strength prior to machining should not exceed a hardness of Rockwell C-40 or 180,000 psi. It is difficult to machine steel that exceeds this hardness.

The selection of material used to construct flare housings, model fairings, antennae, etc., is usually governed by the method of fabrication. Aluminum and brass are not easily eroded and have been used successfully for these parts.

Highly stressed parts should be designed for a minimum amount of deflection as well as for load carrying capability. Abrupt changes in cross section should be accompanied by generous fillets. To avoid fatigue failures file marks should be polished out of fillets which will be exposed to high stress concentrations. Holes should not be drilled in a changing cross-section, i.e., through a radius, unless absolutely necessary. Information relating to techniques and ideas of proven value can be found in Ref. 91.

Although structural defects and unpredictable loading conditions cannot be anticipated before a model is designed, some provisions must be made to allow for these factors. Otherwise valuable tunnel time can be lost. Since it is impractical to make spares for each model part, the spare parts to be constructed should be selected with care. Moreover, practical considerations require immediate access to an adjacent machine shop during wind-tunnel test.

8.3.1 Joining Body Sections

Sections that require no rotational orientation to each other can be fastened together by means of a screw joint as shown in Fig. 8-24. The joint should be turned tightly to avoid loosening under continuous vibration. With this type of jointure a strap wrench is usually required.

Sections that require an exact rotational position relative to each other may be connected by a slip joint which is locked in place with hardened steel set screws. Aligning pins are used as shown in Fig. 8-24 to ensure exact and repeatable orientation of the body sections. The set screws in this type of joint must be frequently tightened or locked in place because vibration may loosen them. Moreover, the location of the screw holes must be carefully selected to obviate as much as possible the need for filling unnecessary holes, which is a time-consuming task.

A tight, aerodynamically clean joint which utilizes a left and right hand thread on the inside diameter is shown in Fig. 8-25. As the inside sleeve is rotated, the sections move together and are aligned by a pin which is concealed upon assembly. A special tool is needed to install and remove this sleeve. This type of joint may be used where the model wall is too thin to allow the use of set screws.

Another frequently used joint utilizes a tie rod to apply an axial force on the slip joints as shown in Fig. 8-26. This tie rod also may be used to seat the model on the internal balance taper. The body sections can be oriented relative to each other by use of aligning pins which are concealed when the joint is assembled and which will ensure accurately repeatable orientation of the body sections.

Most model bodies are built in three sections, with a joint ahead of the wings and a joint between the wings and tails. The taper in the model that mates with the taper in the internal balance is normally machined in the mid-body section. Therefore, varying configurations should be designed around this mid-body section so that the model need not be removed from the internal-balance assembly when a configuration change is necessary. In this way valuable running time may be saved.

8.3.2 Mounting Aerodynamic Surfaces

Aerodynamic surfaces fall into two categories, fixed incidence and variable incidence. The fixed-incidence surface normally has an island at its base, as shown in Fig. 8-27, which mates with a groove in the body and is held in place by one of several methods. The variable-incidence surface utilizes interchangeable incidence pins or interchangeable surfaces.

With the incidence pin design, the surface (Fig. 8-28) has a slot machined in the surface hub which mates with an incidence pin as shown in Fig. 8-29. The desired incidence angles are machine-ground on the incidence pins; after assembly this ground surface mates with a similar surface on the hub, thus forcing the surface to the desired incidence angle. A separate incidence pin is required for each angle. For a wing-control model, the incidence pins should be placed in such a manner

that the heads will be exposed when the nose section is removed. In a tail-control model, shown in Figs. 3-59 and 8-28, the incidence pins should be installed in the base of the model if the model planform permits. If this cannot be done, the pins should be installed ahead of the tail surfaces so that they are exposed when the aft body joint is broken.

When interchangeable surfaces are used to vary the incidence on wings or tails, a surface integral with the island is made for each desired incidence angle. Figure 8-29 shows a typical example of this design for wings, and Fig. 8-30 shows one for tail surfaces. The model nose is used to lock the wing surfaces in place, while a retaining ring is used for the tail surfaces.

8.3.3 Surfacers and Fillers

Screw holes and discontinuities in fairings which appear on models can produce undesirable flow disturbances. Several commercial putties and surfacers are available to fill in the holes and to fair in the discontinuities in body lines. The results obtained with these materials will depend on the manner in which the model is prepared and on the care exercised during application and finishing. Some of the commercial products which have been used for this purpose are Met-L-It, Duratite, and New Metal. Of these, Duratite seems to be the most workable and requires least application time. All of these products will dry slowly if they are applied too thickly. To save time any holes may be temporarily plugged with wooden plugs, cotton, etc., and smoothed over with a putty or surfacers.

Soft solder can be used as a permanent fill for holes and nicks. Beeswax, sometimes used as a temporary fill, is not satisfactory because it becomes plastic at elevated temperatures. A mixture of chalk dust and household cement, mixed to form a paste, has also been used. To date, no filler has been found which will meet all of the strict requirements of the model designer. However, in many tests such as force measurements, the effect on the flow of unfilled holes may be within the accuracy of the measurements.

Source: OAL

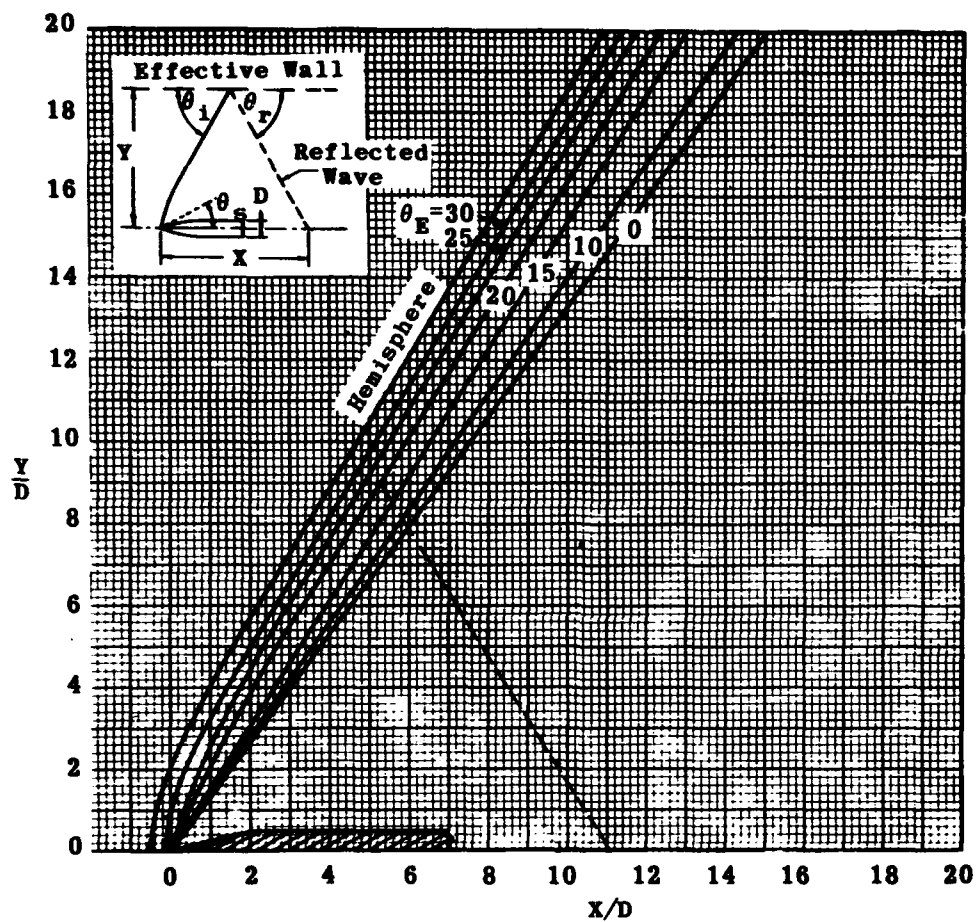


Fig. 8-1. Bow waves from conical and hemispherical noses,
Mach number 1.25.

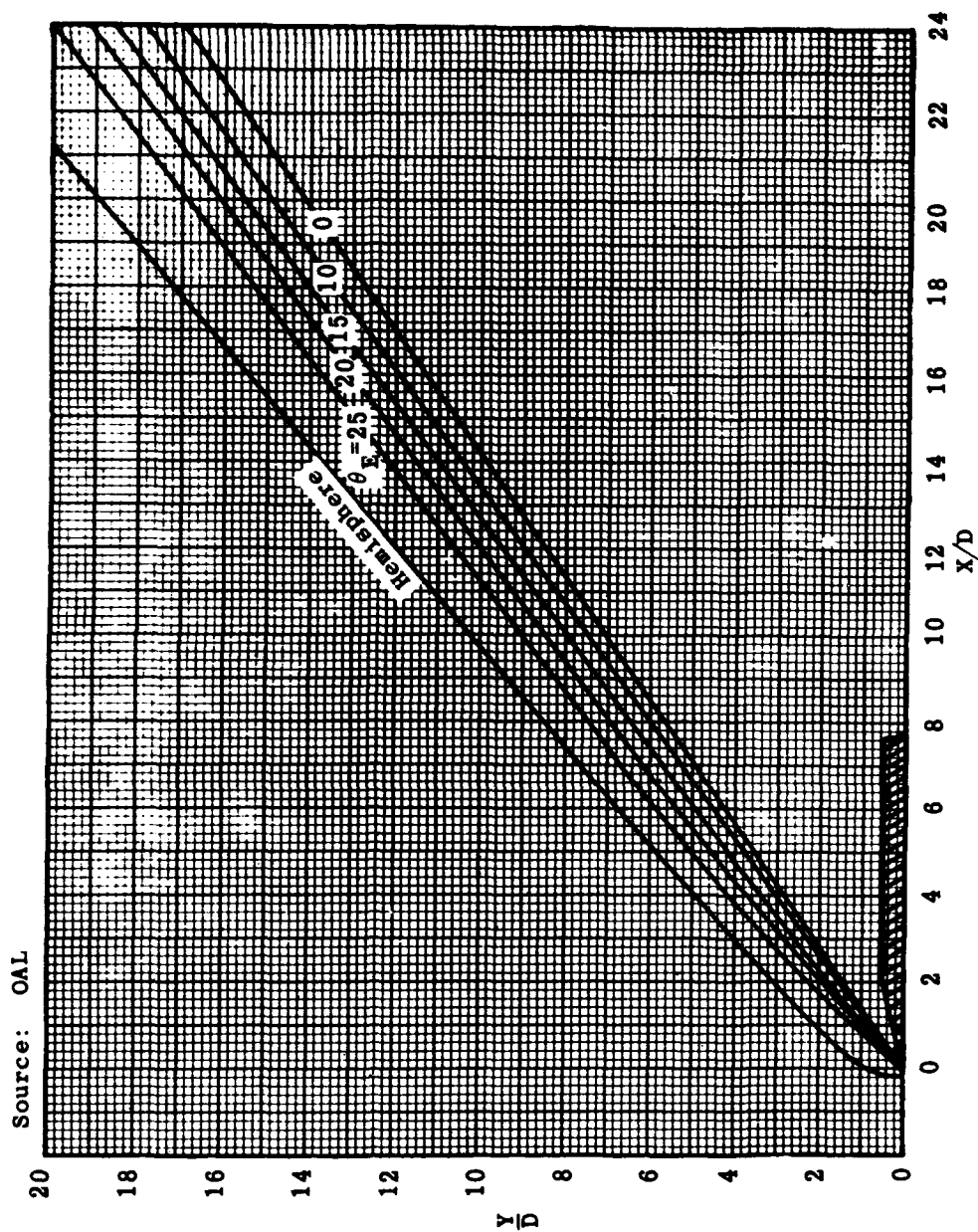


Fig. 8-2. Bow waves from conical and hemispherical noses, Mach number 1.73.

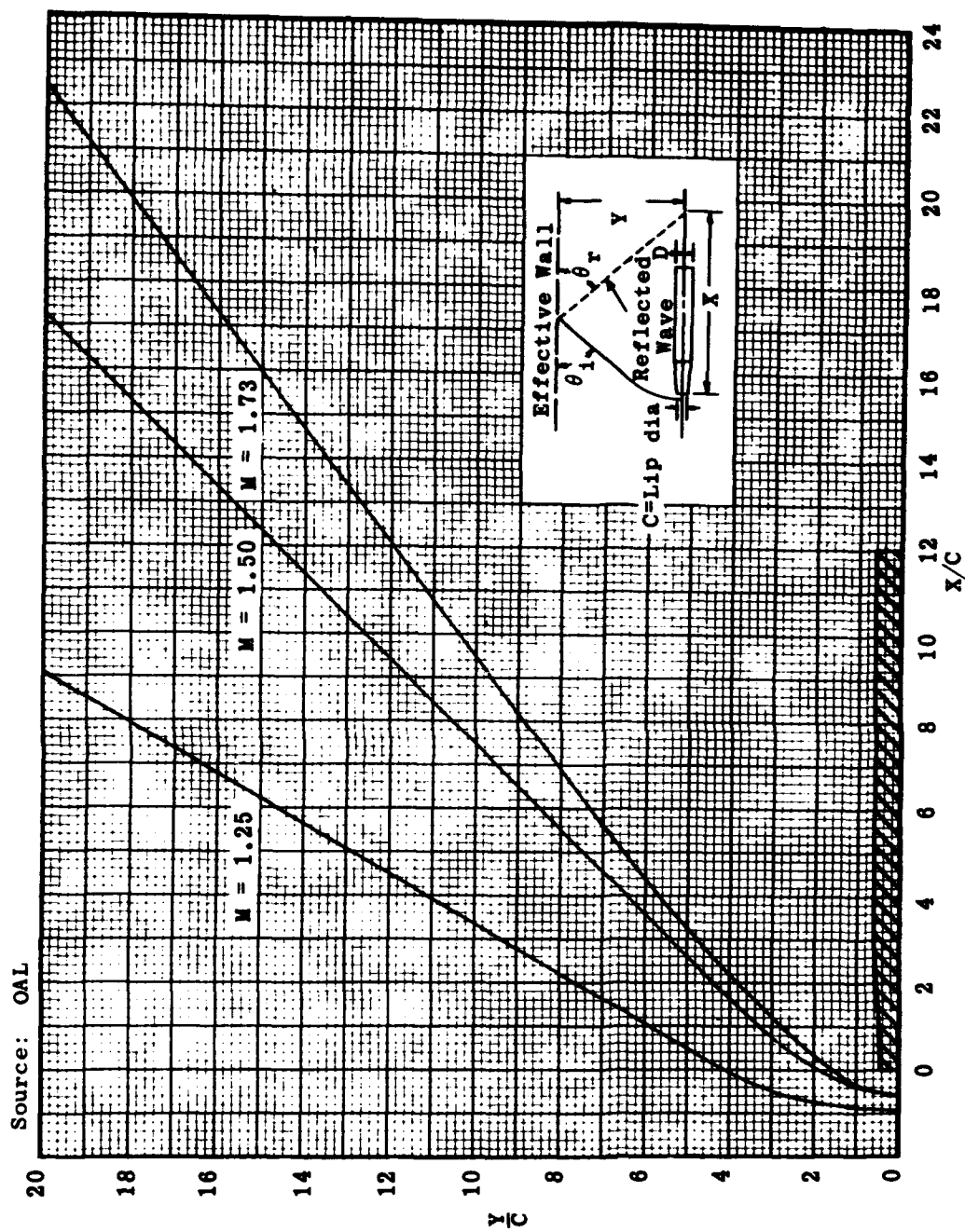


Fig. 8-3. Bow waves from ducted model inlet with no flow through duct.

Source: AEDC

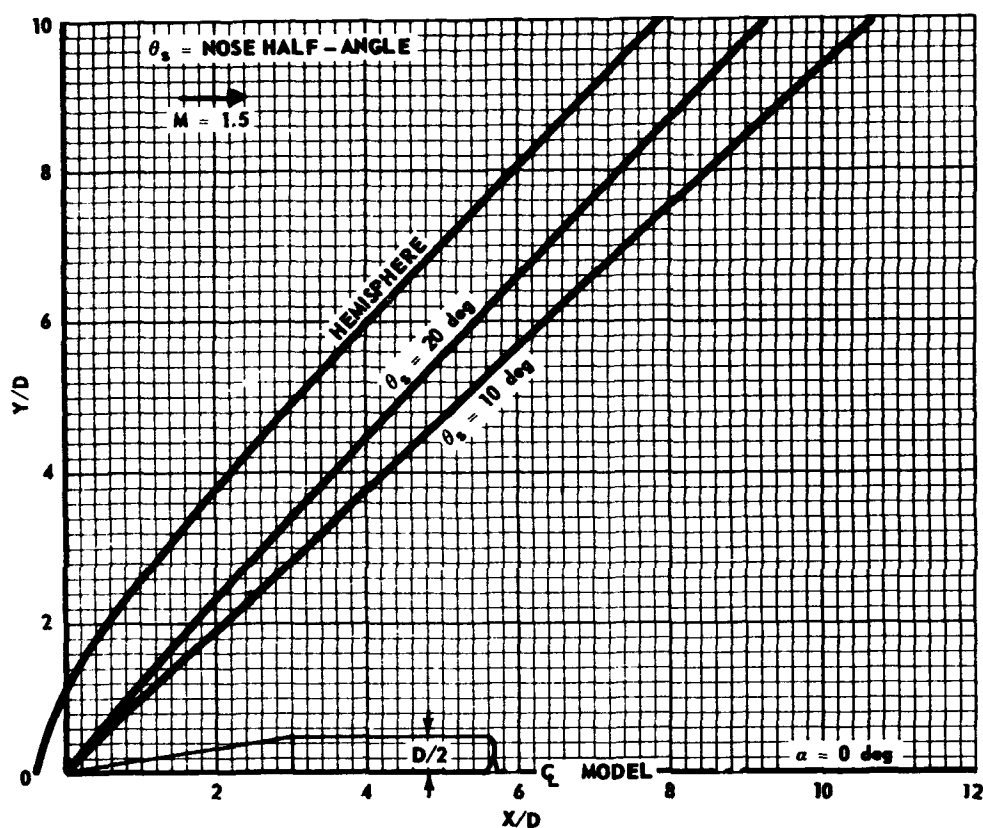


Fig. 8-4. Bow waves from conical and hemispherical noses; Mach number 1.5, $\alpha = 0 \text{ deg}$.

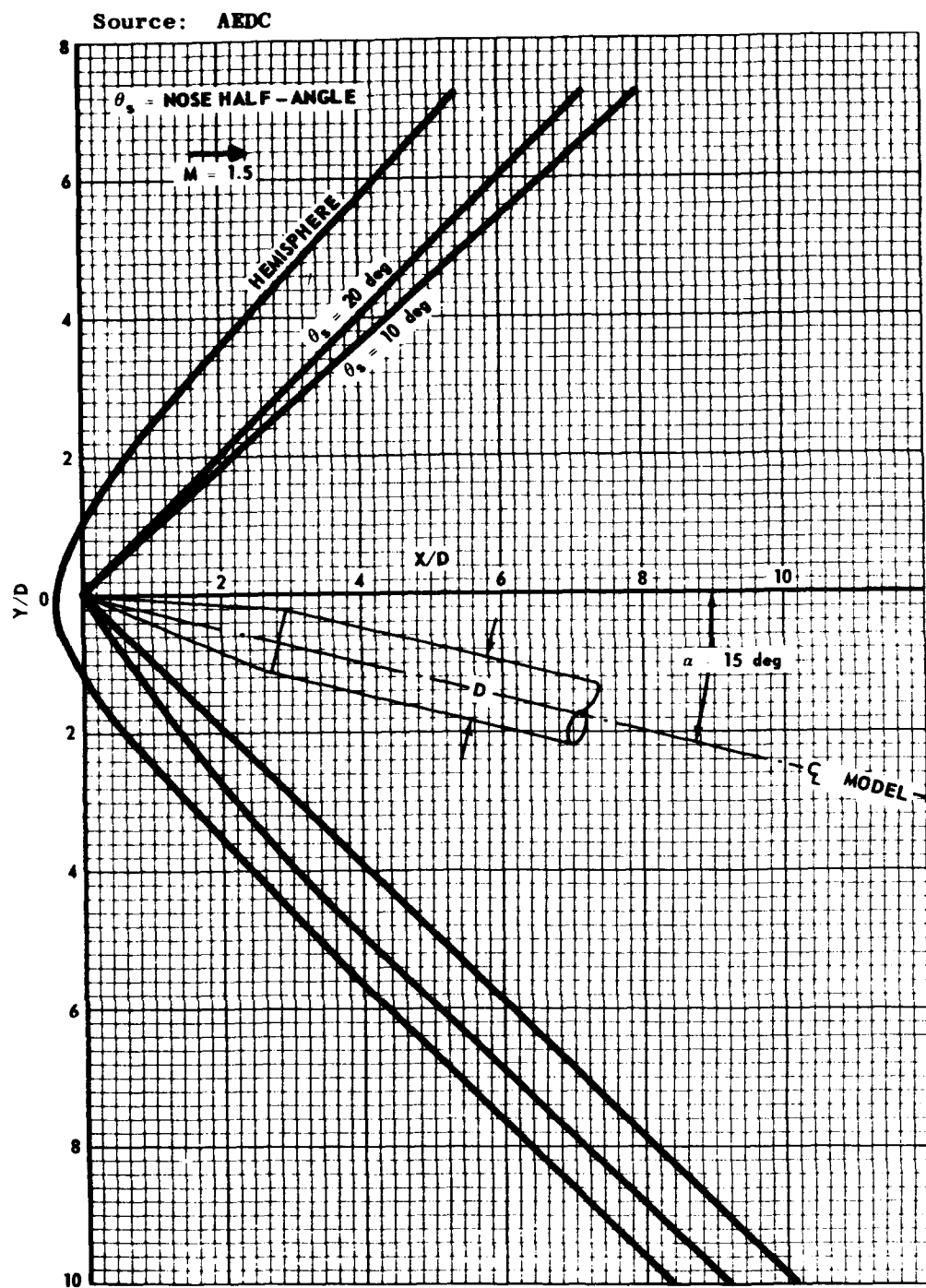


Fig. 8-5. Bow waves from conical and hemispherical noses; Mach number 1.5, $\alpha = 15 \text{ deg}$.

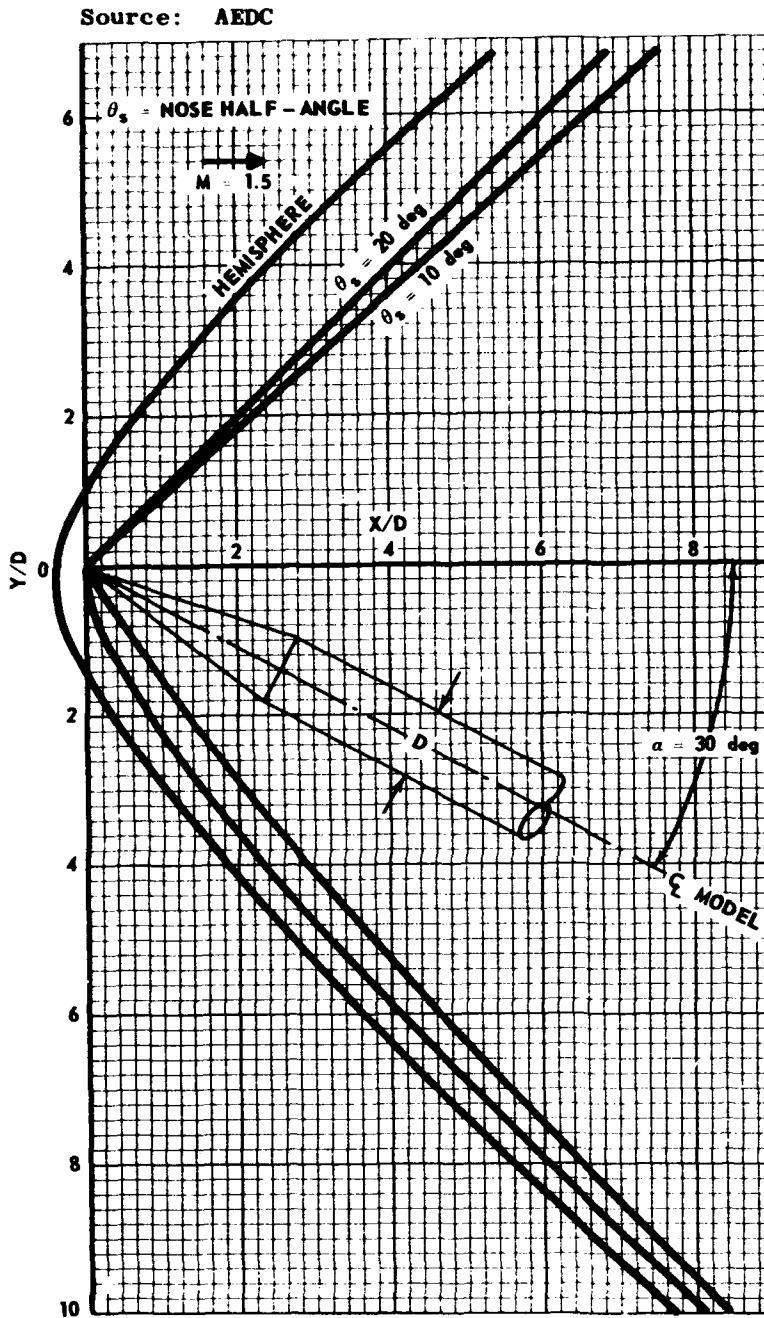


Fig. 8-6. Bow waves from conical and hemispherical noses; Mach number 1.5, $\alpha = 30 \text{ deg}$.



Fig. 8-7. Bow waves from conical and hemispherical noses; Mach number 2.0, $\alpha = 0 \text{ deg}$.

Source: AEDC

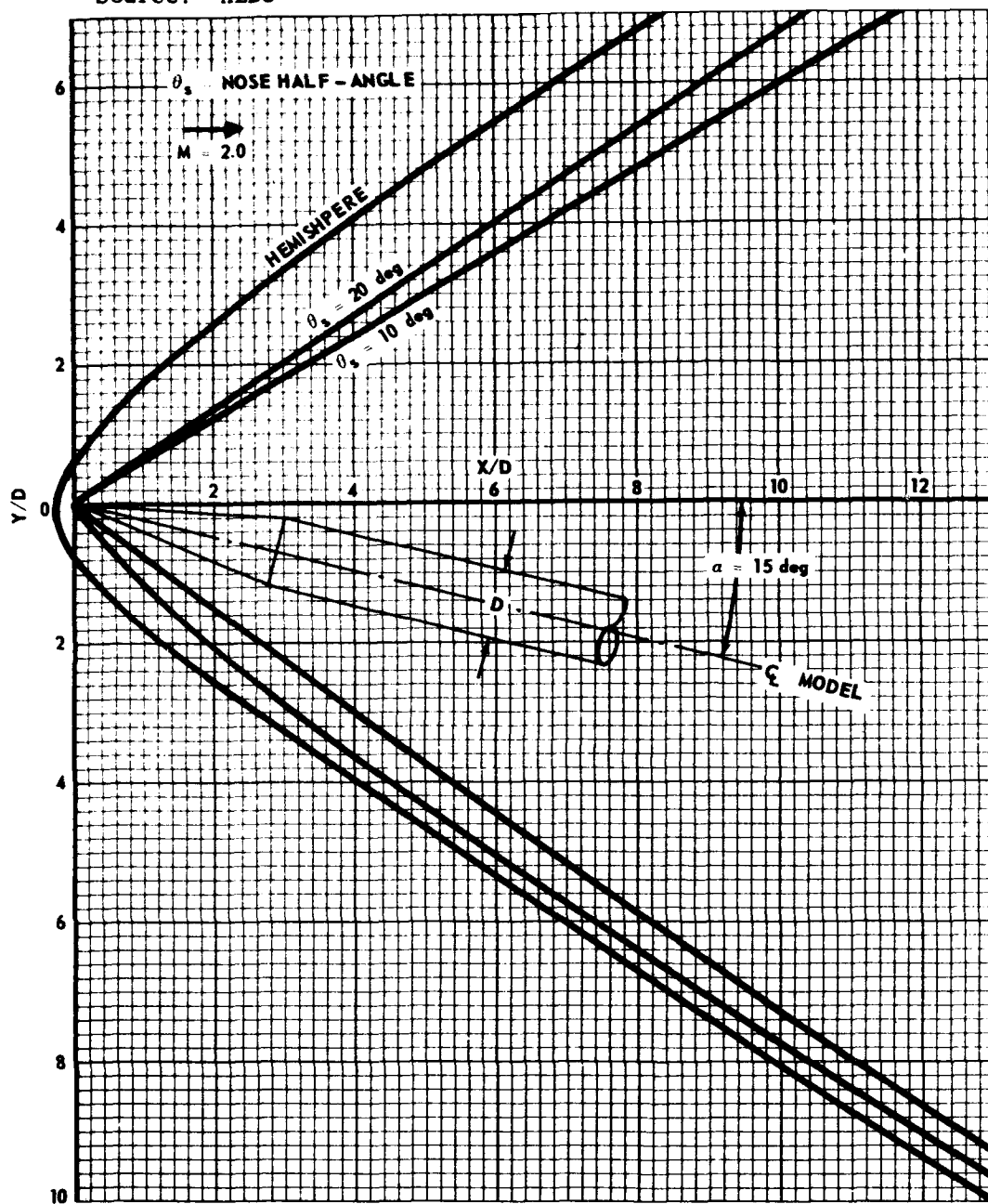


Fig. 8-8. Bow waves from conical and hemispherical noses; Mach number 2.0, $\alpha = 15$ deg.

Source: AEDC

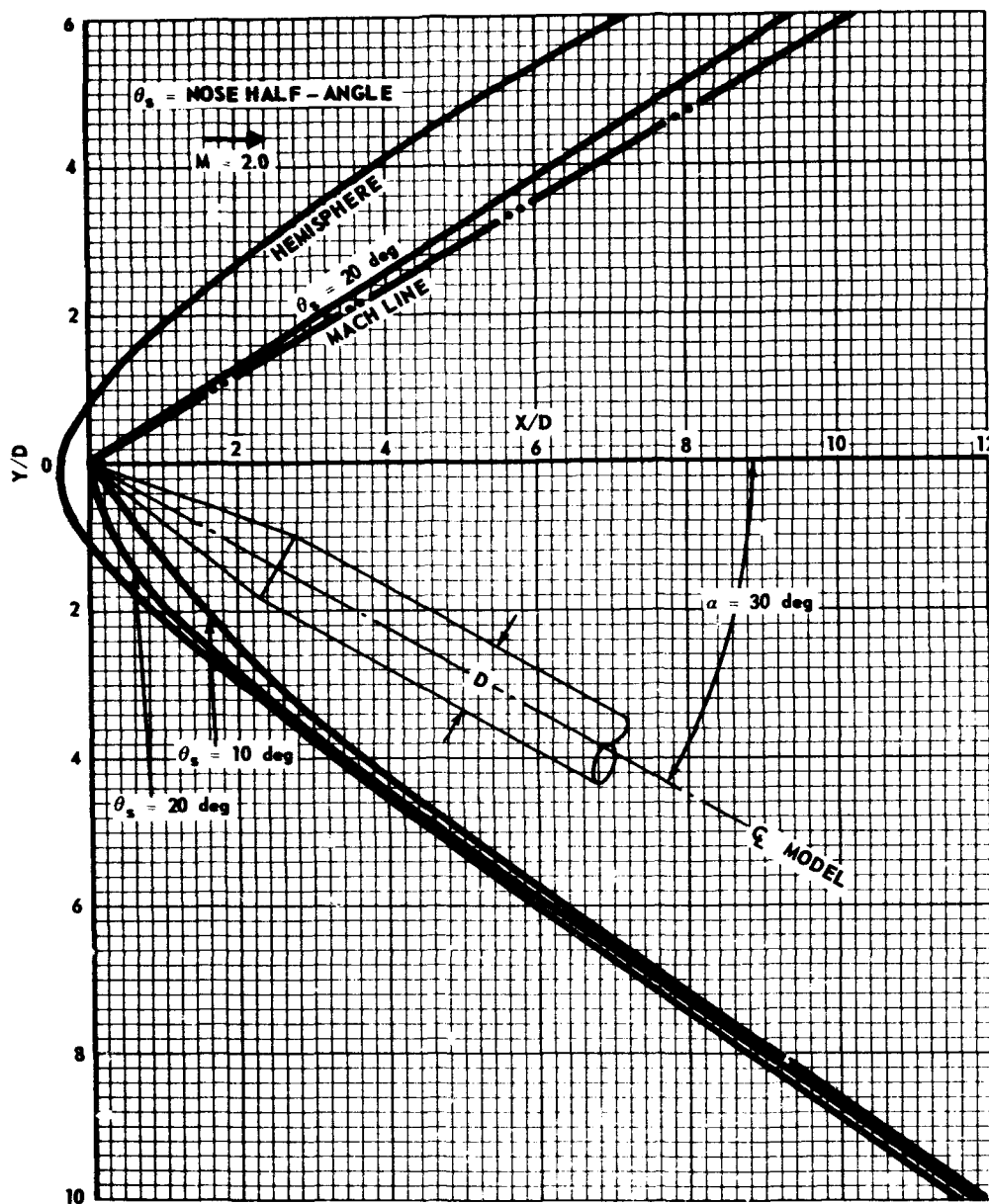
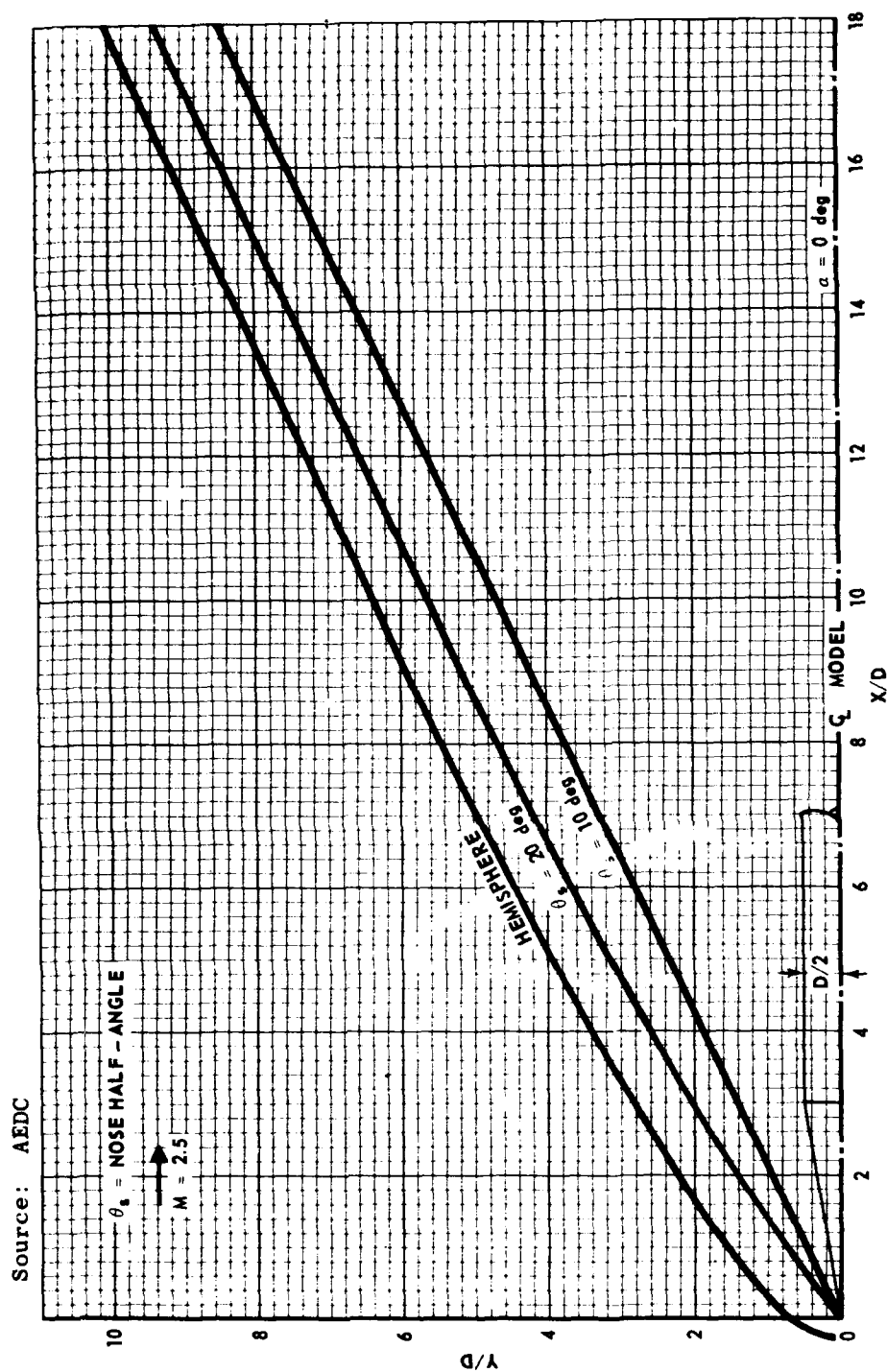


Fig. 8-9. Bow waves from conical and hemispherical noses; Mach number 2.0, $\alpha = 30^\circ$.

Fig. 8-10. Bow waves from conical and hemispherical noses; Mach number 2.5, $\alpha = 0 \text{ deg}$.

Source: AEDC

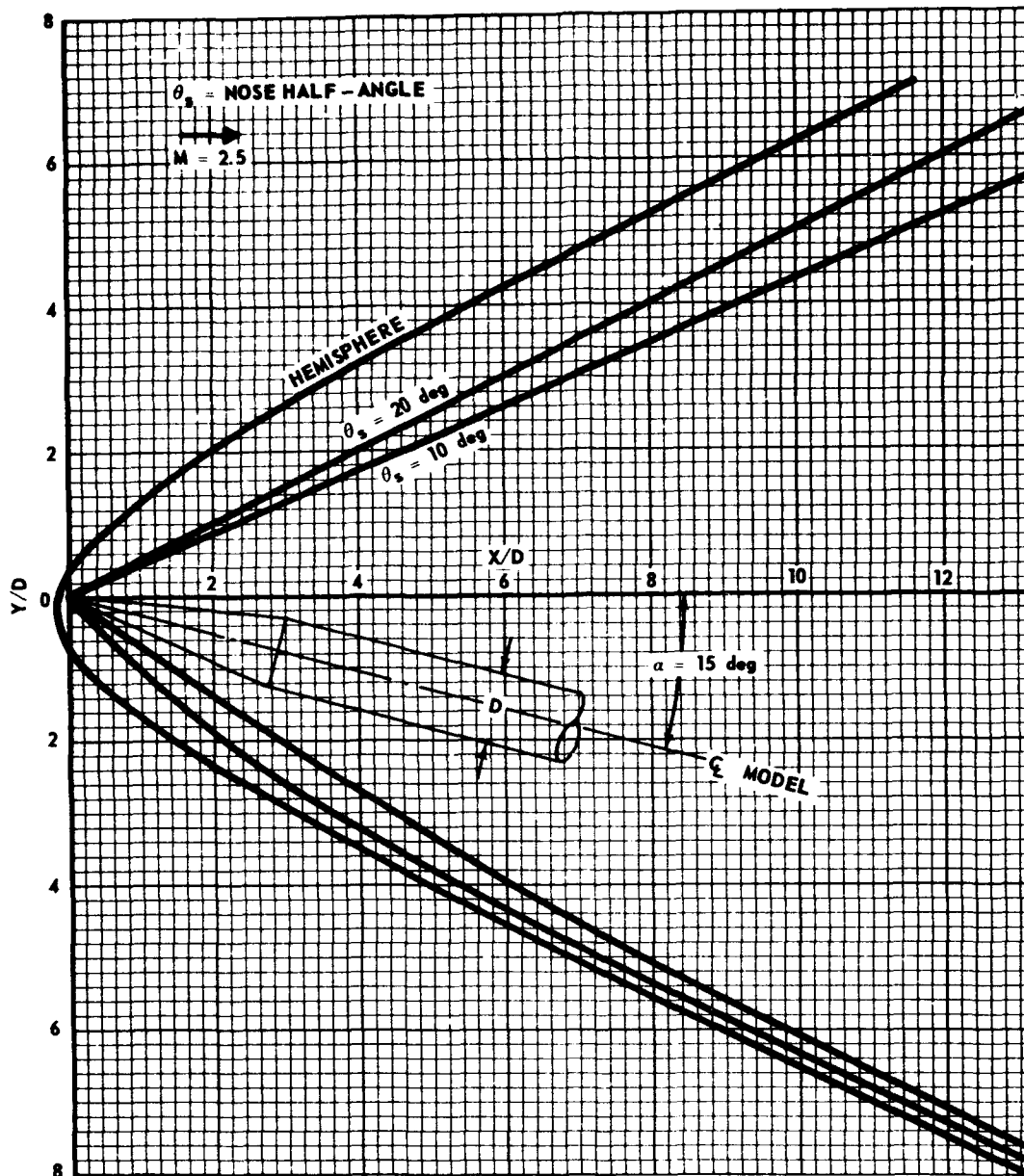


Fig. 8-11. Bow waves from conical and hemispherical noses; Mach number 2.5, $\alpha = 15^\circ$.

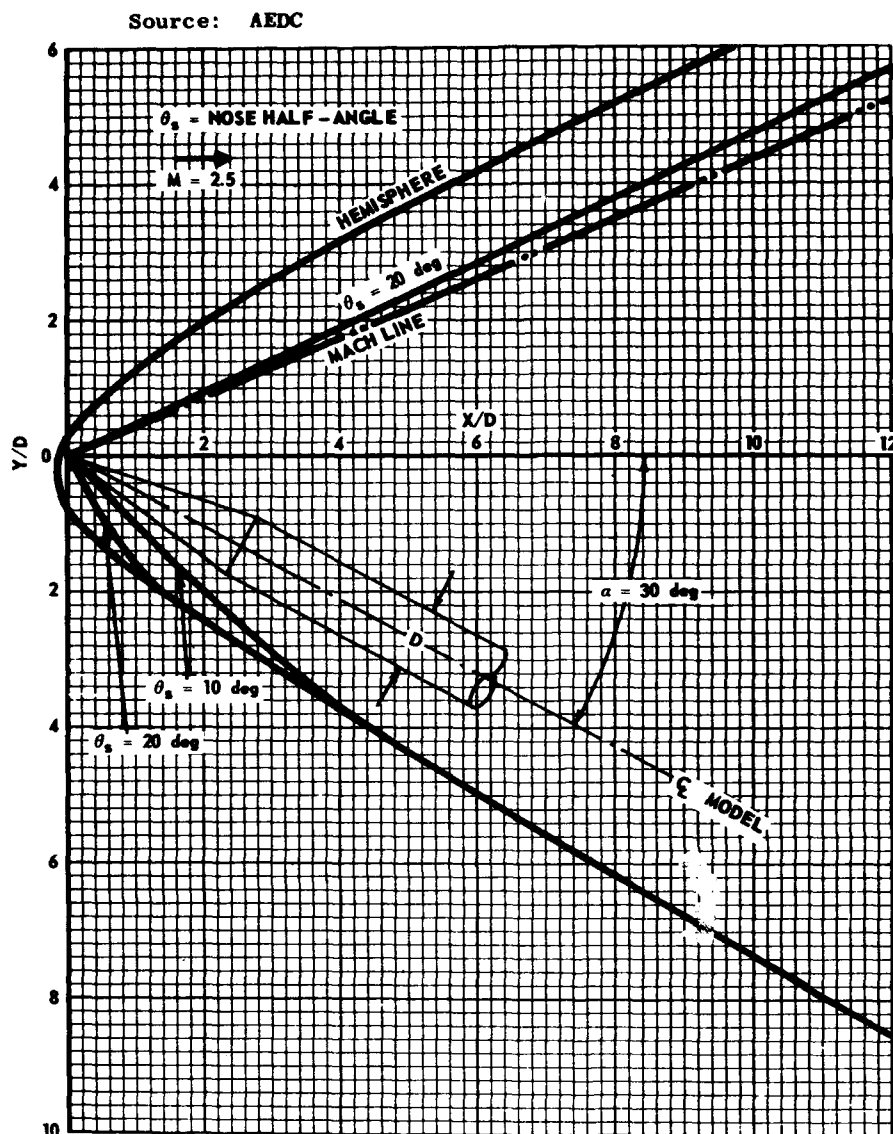
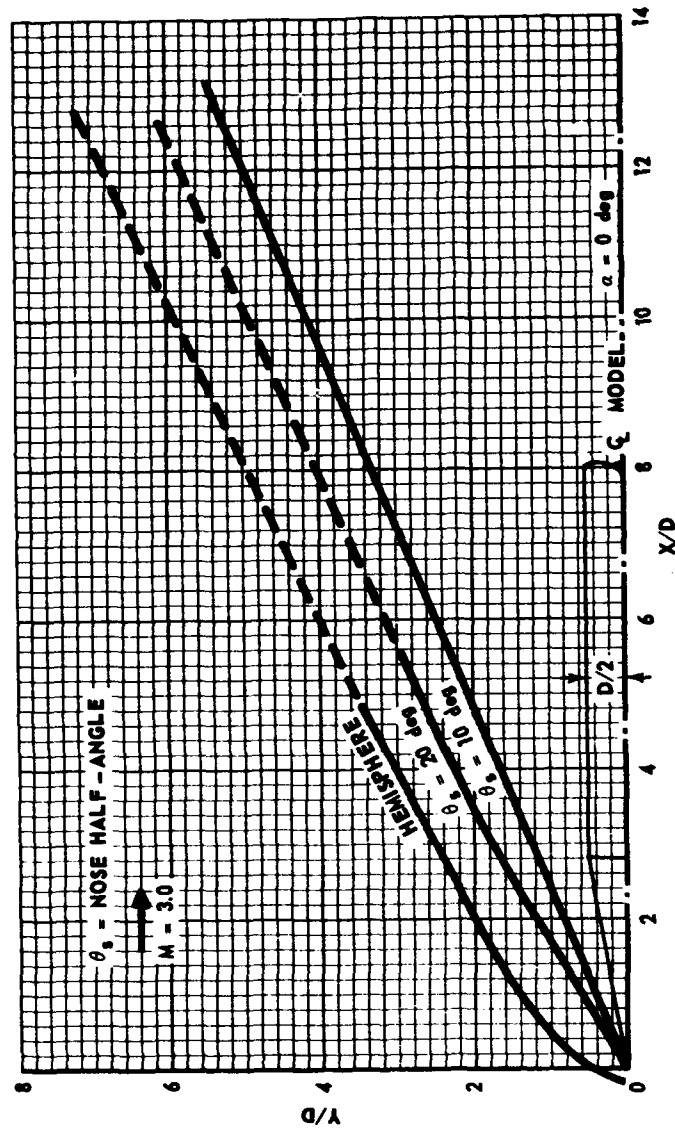


Fig. 8-12. Bow waves from conical and hemispherical noses; Mach number 2.5, $\alpha = 30^\circ$.

Source: AEDC

Fig. 8-13. Bow waves from conical and hemispherical noses; Mach number 3.0, $\alpha = 0^\circ$.

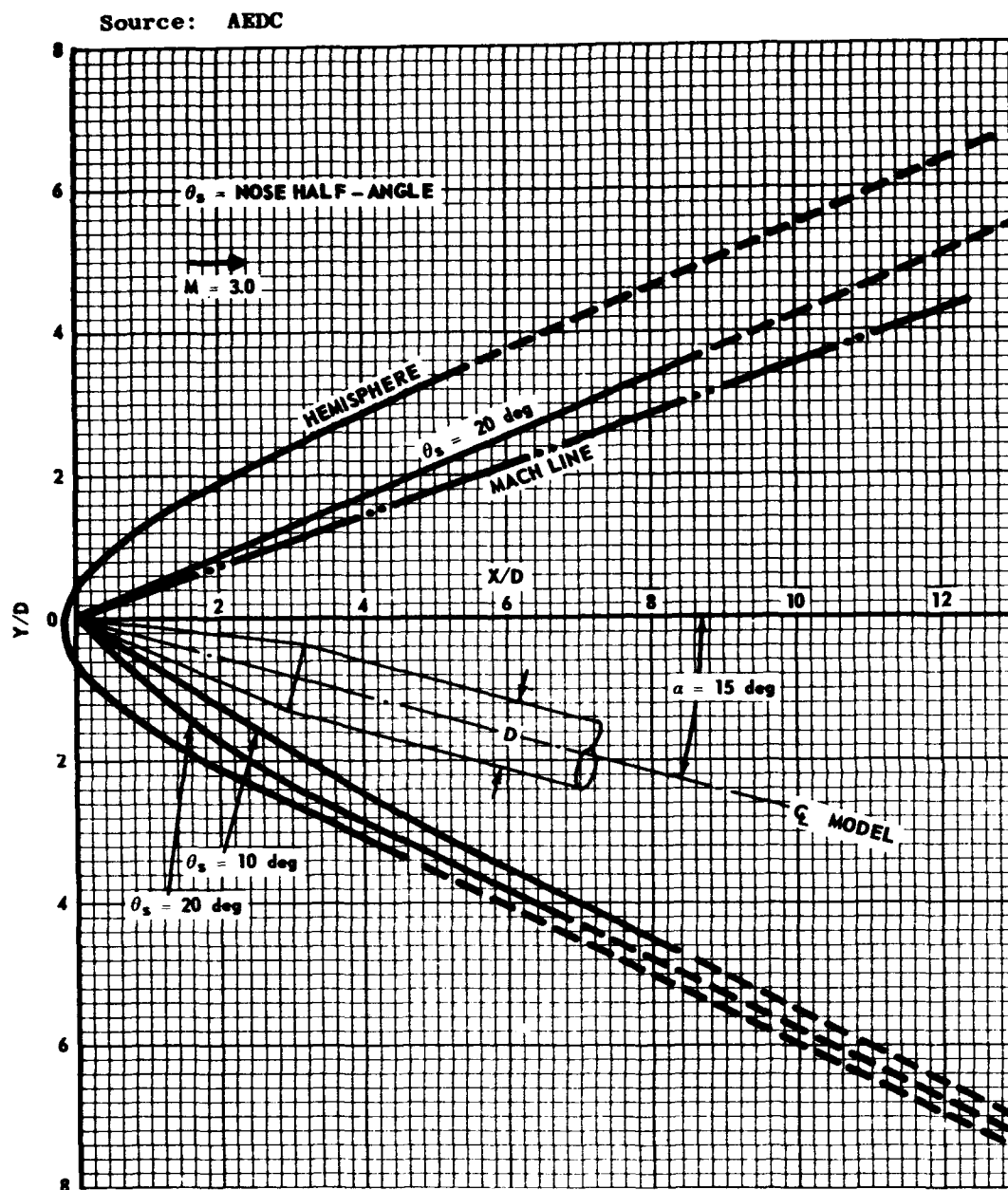


Fig. 8-14. Bow waves from conical and hemispherical noses; Mach number 3.0, $\alpha = 15$ deg.

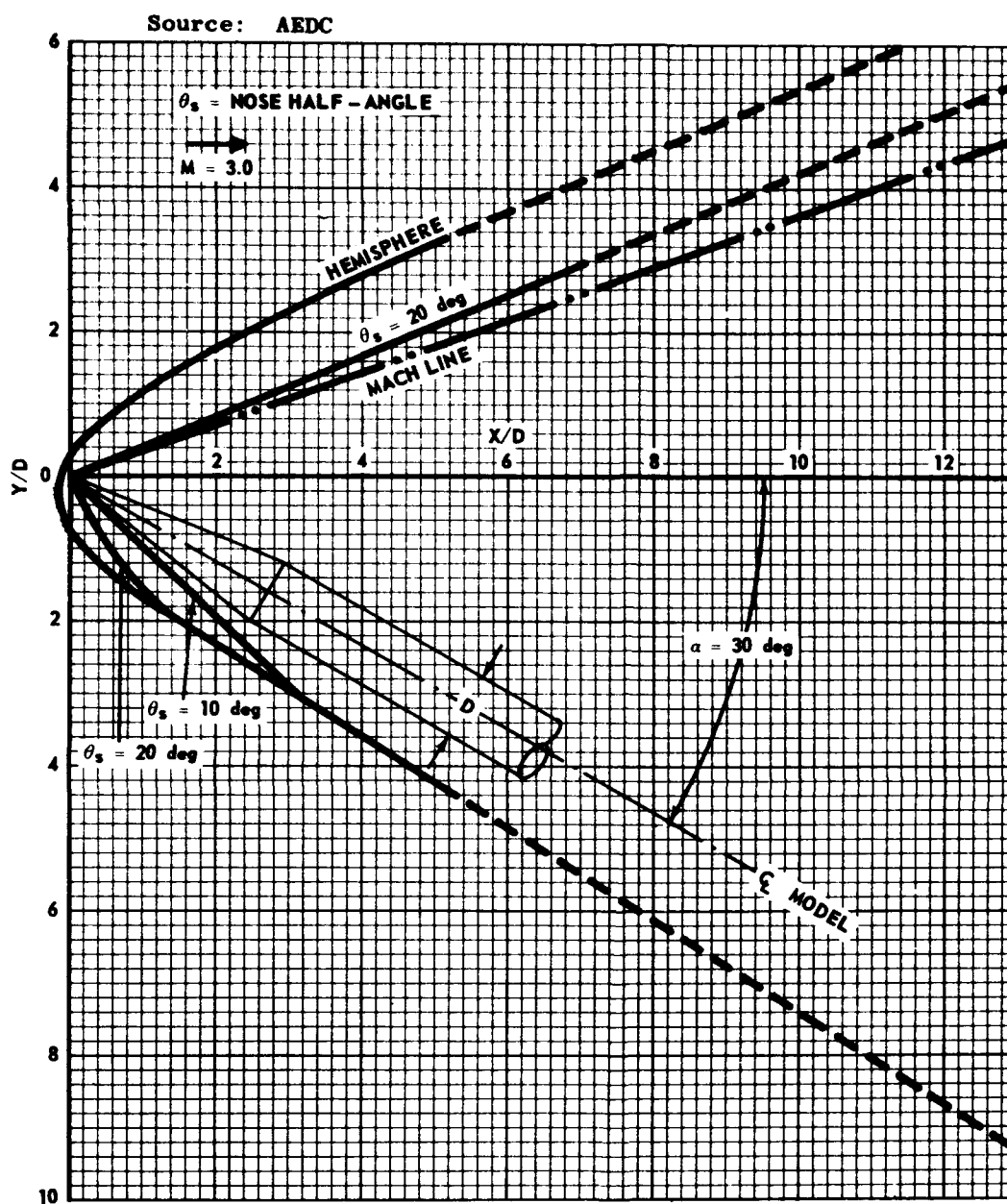
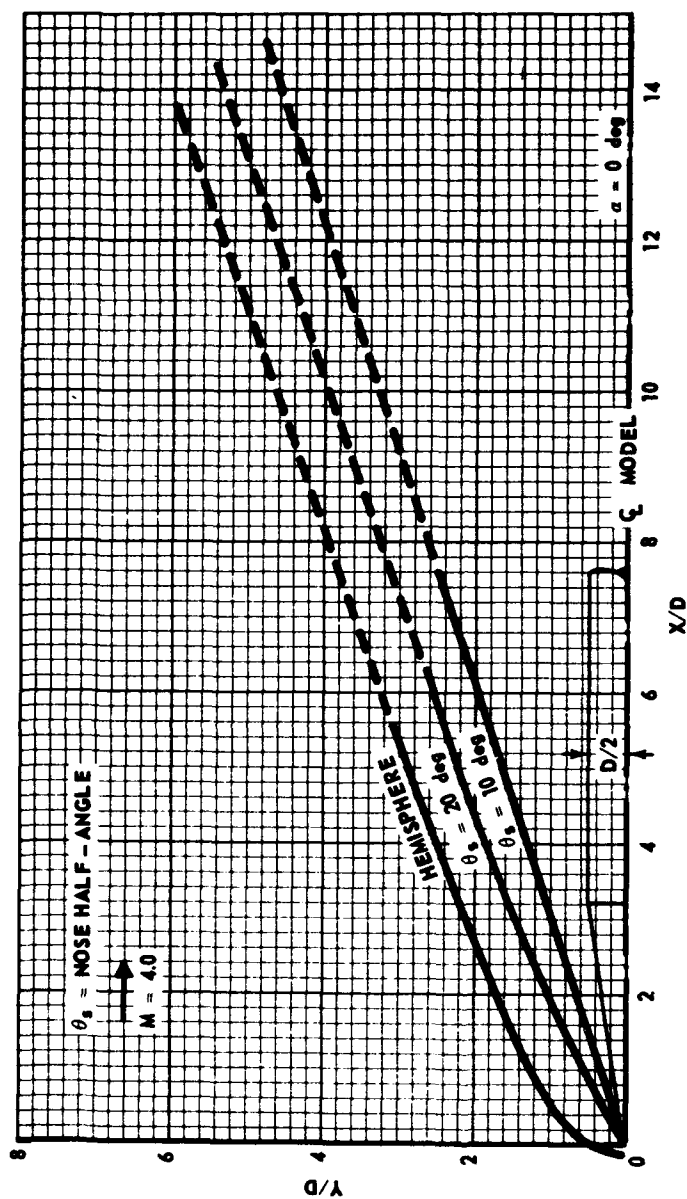


Fig. 8-15. Bow waves from conical and hemispherical noses; Mach number 3.0, $\alpha = 30^\circ$.

Source: AEDC

Fig. 8-16. Bow waves from conical and hemispherical noses; Mach number 4.0, $\alpha = 0^\circ$.

Source: AEDC

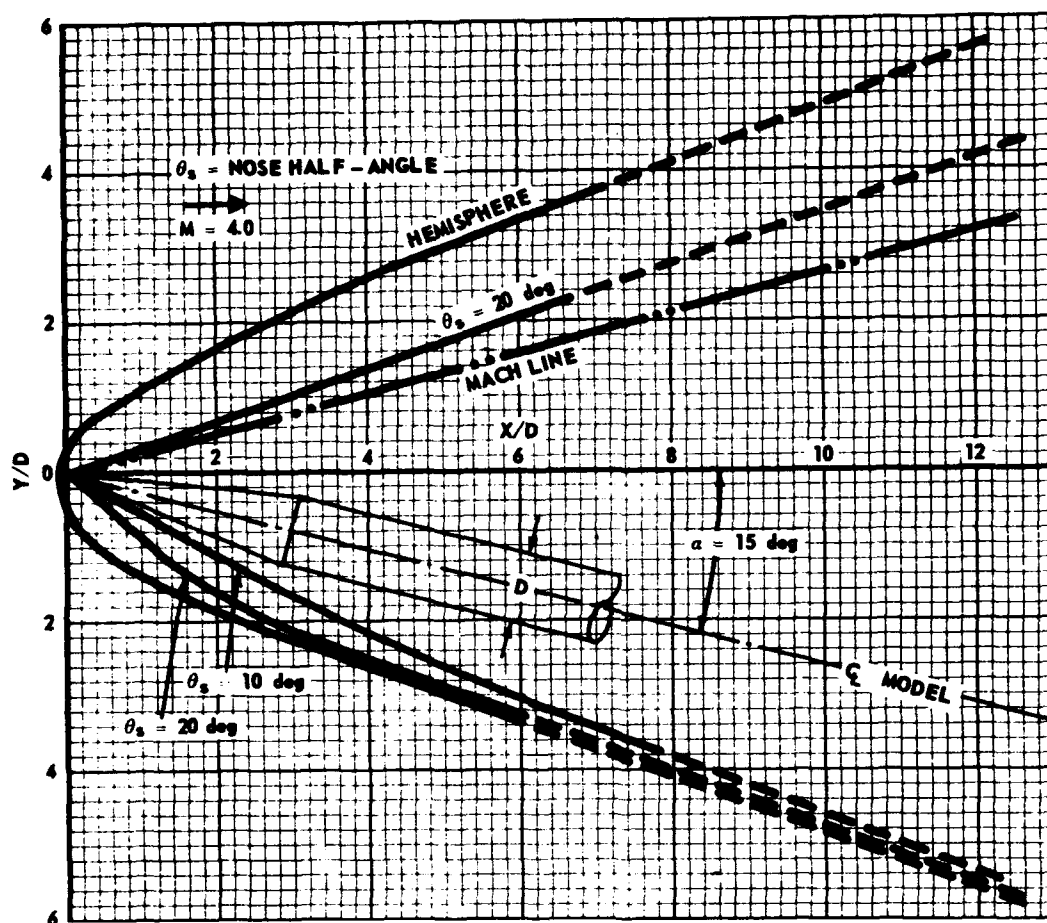


Fig. 8-17. Bow waves from conical and hemispherical noses; Mach number 4.0, $\alpha = 15^\circ$.

Source: AEDC

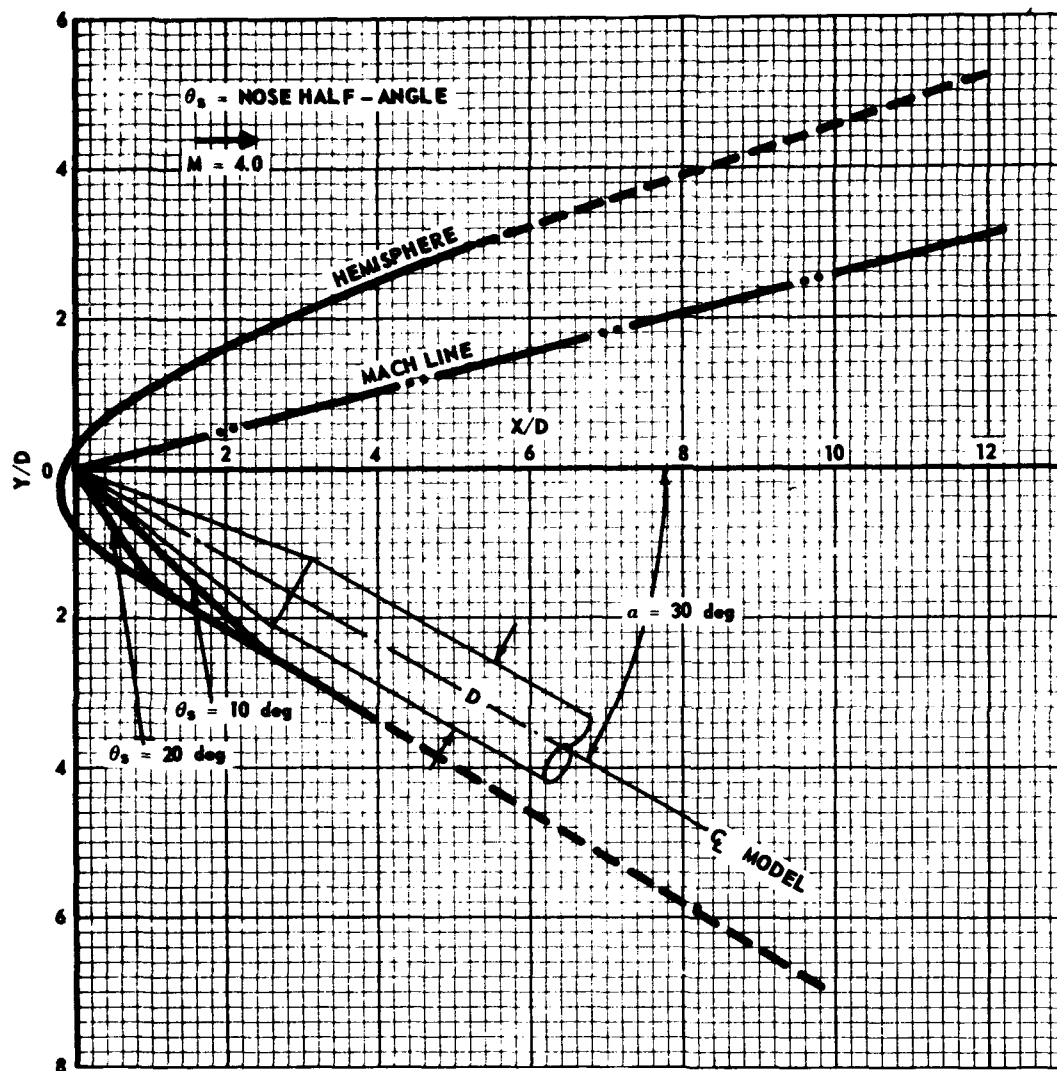
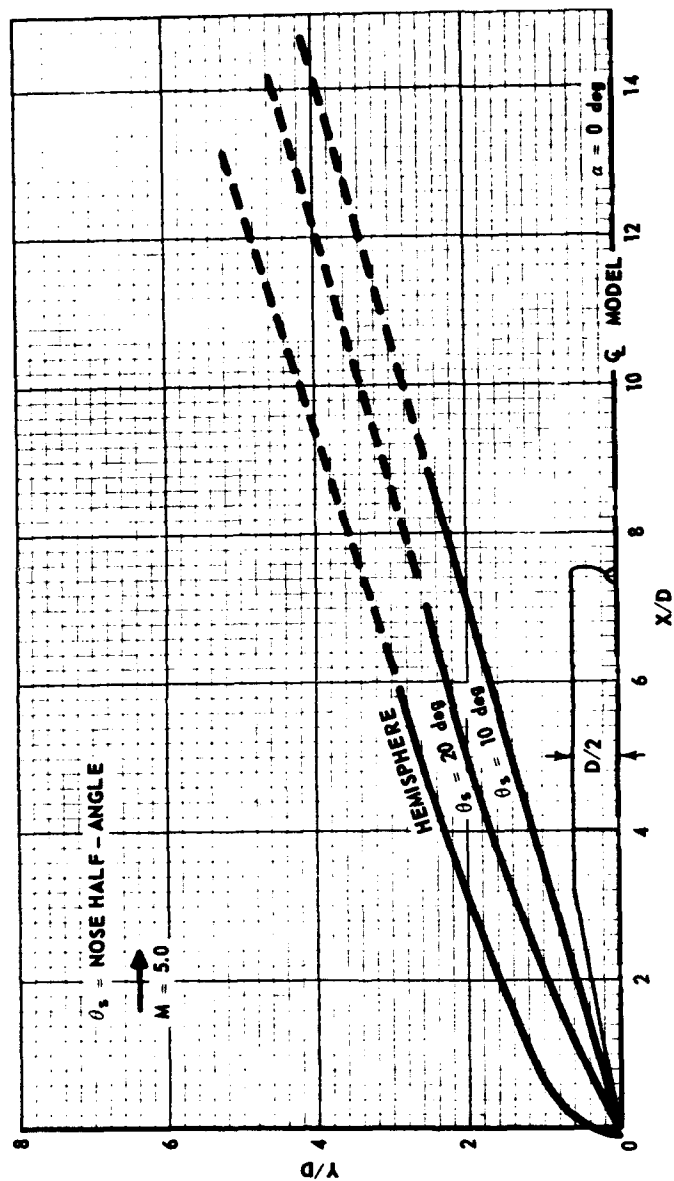


Fig. 8-18. Bow waves from conical and hemispherical noses; Mach number 4.0, $\alpha = 30 \text{ deg}$.

Source: AEDC

Fig. 8-19. Bow waves from conical and hemispherical noses; Mach number 5.0, $\alpha = 0^\circ$.

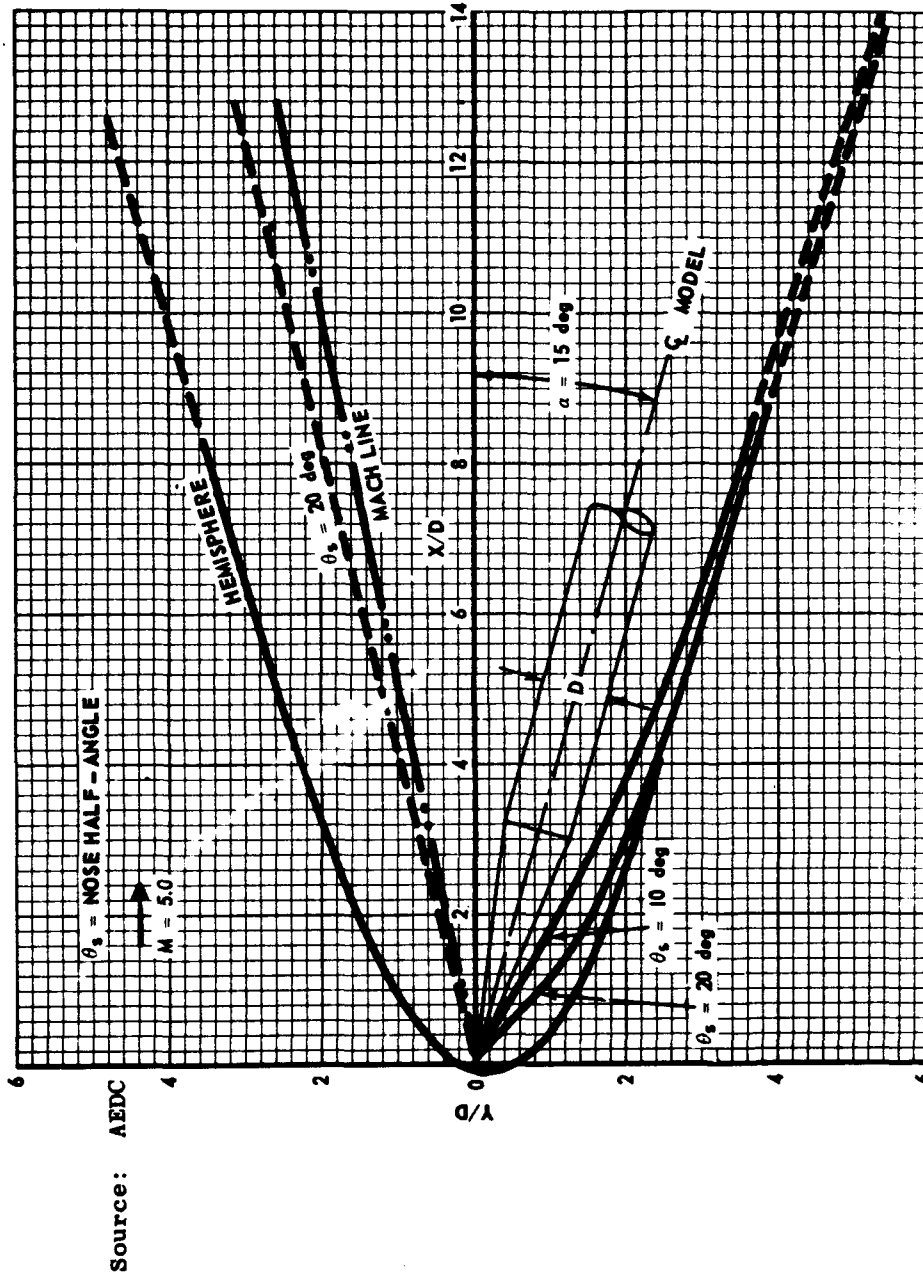


Fig. 8-20. Bow waves from conical and hemispherical noses; Mach number 5.0, $\alpha = 15 \text{ deg}$.

Source: AEDC

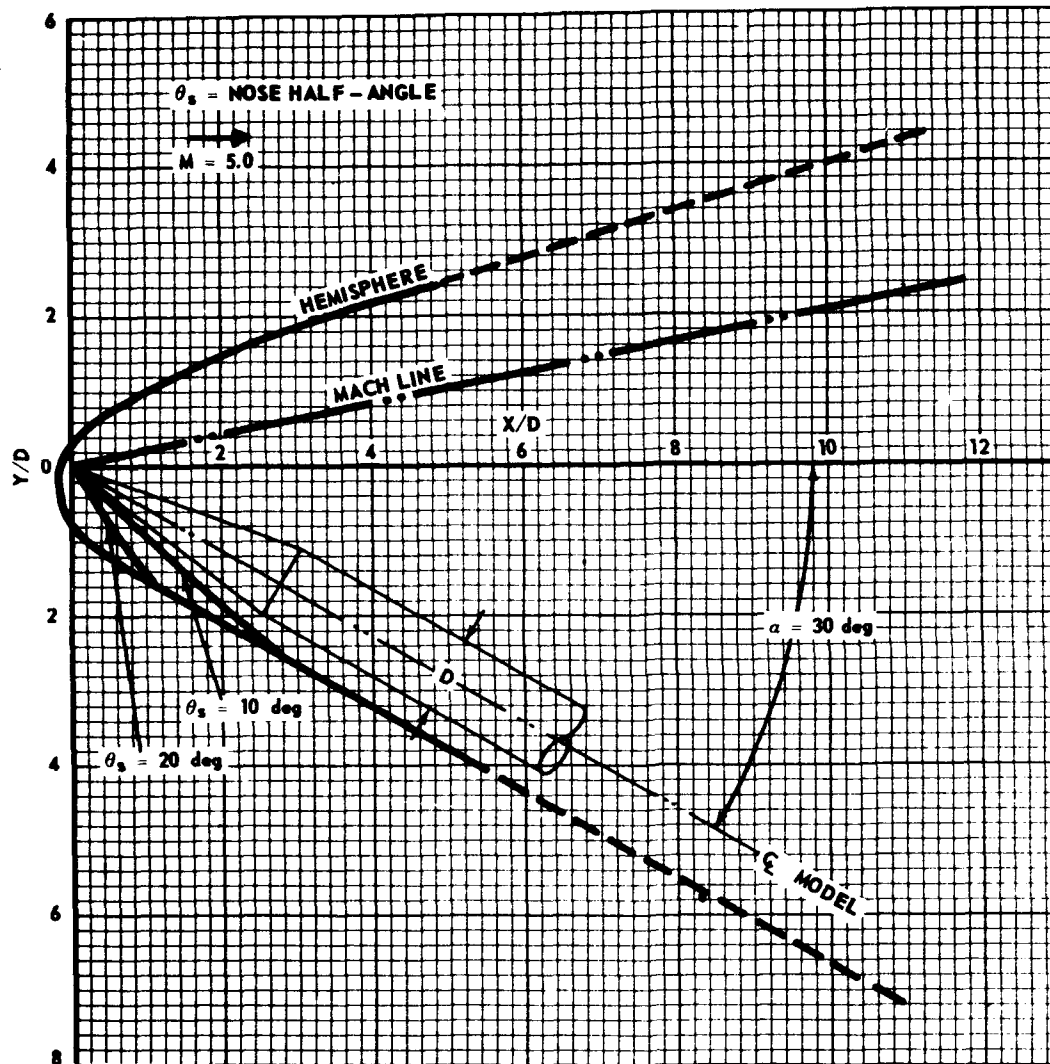


Fig. 8-21. Bow waves from conical and hemispherical noses; Mach number 5.0, $\alpha = 30^\circ$.

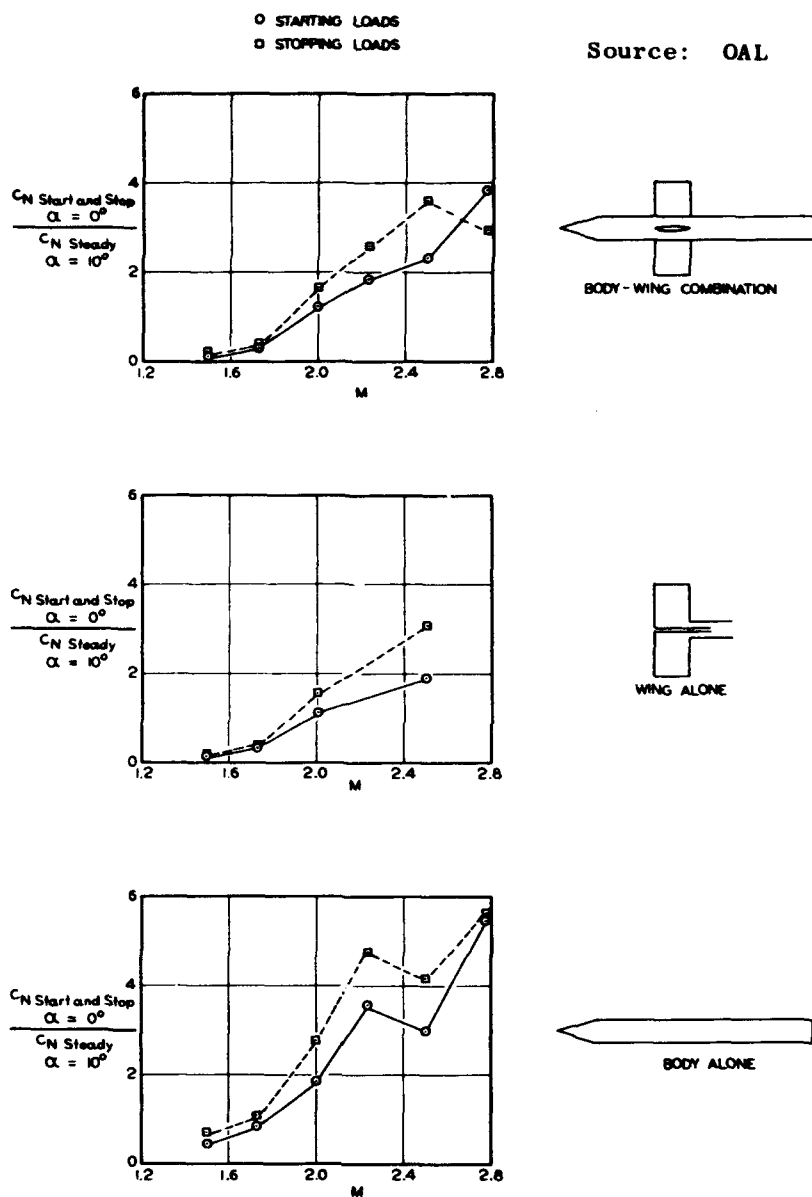


Fig. 8-22. Maximum normal force loads experienced during wind-tunnel starting and stopping.

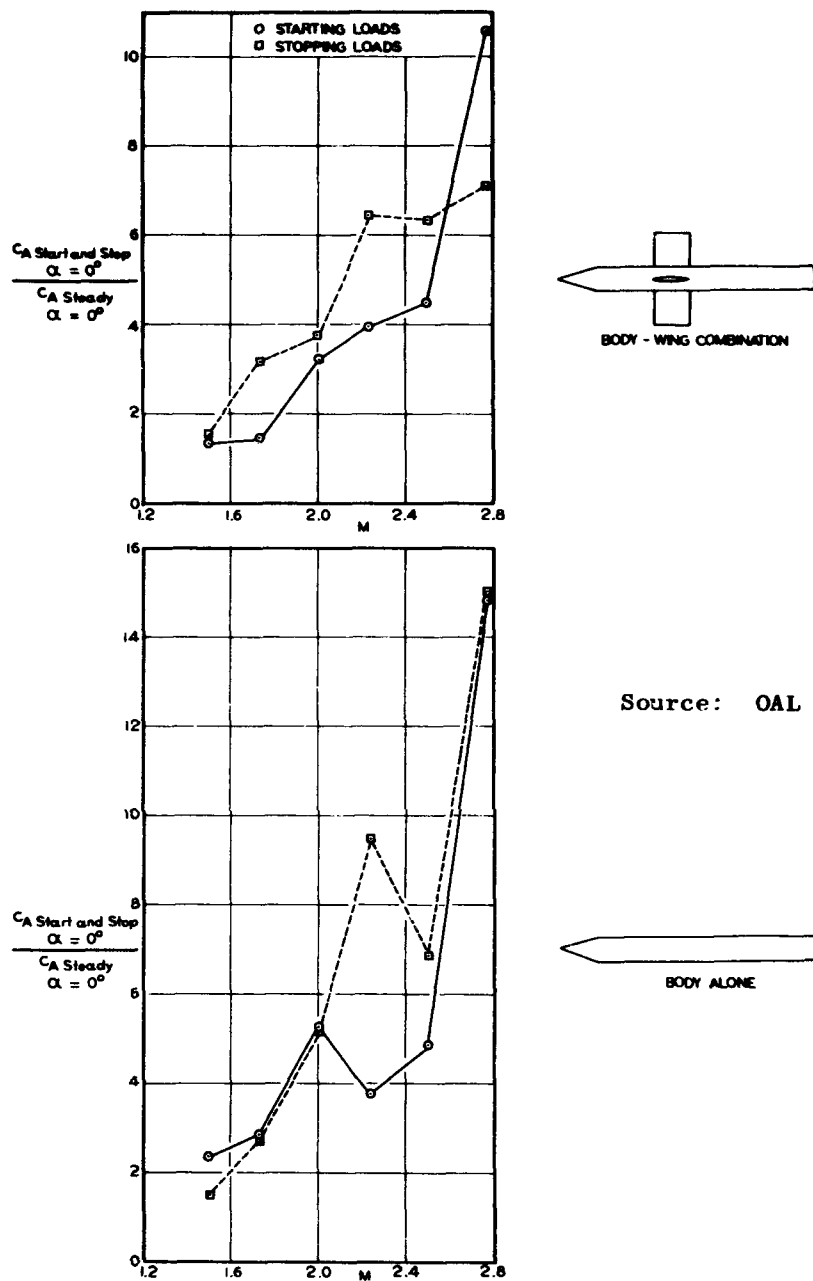
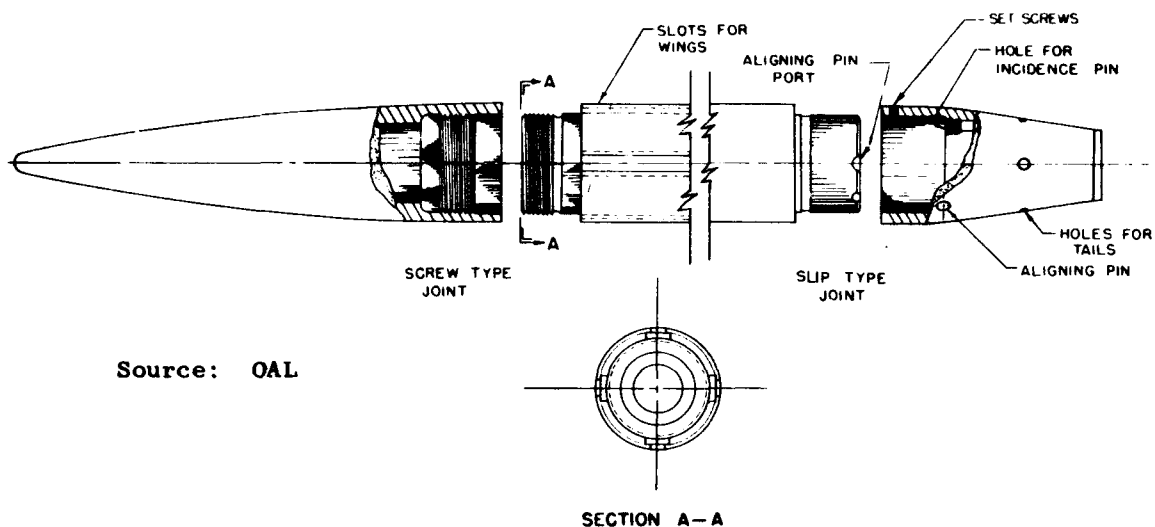


Fig. 8-23. Maximum axial force loads experienced during wind-tunnel starting and stopping.



Source: OAL

Fig. 8-24. Details of screw-joint and slip-joint methods for joining model sections.

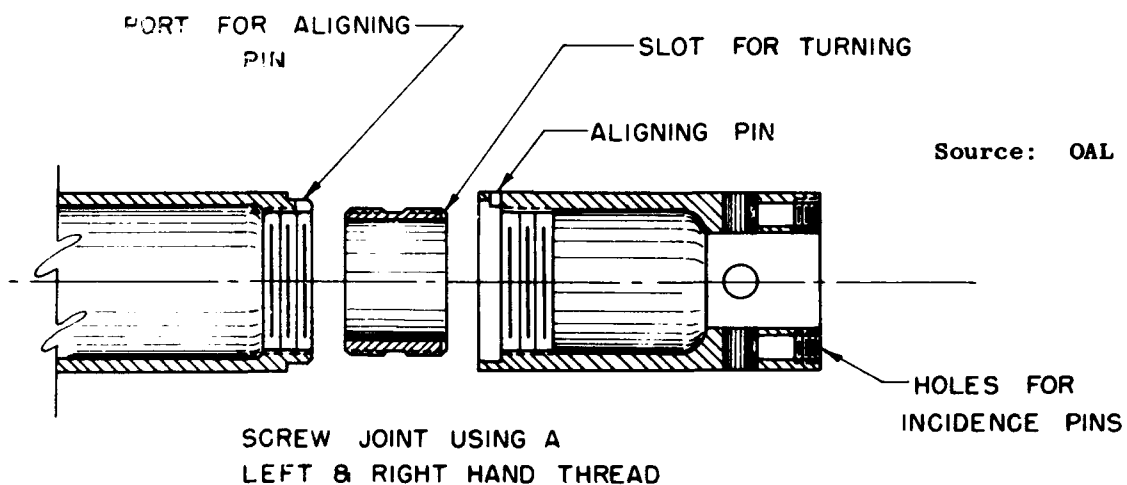


Fig. 8-25. Details of left and right-hand thread in screw-type joint.

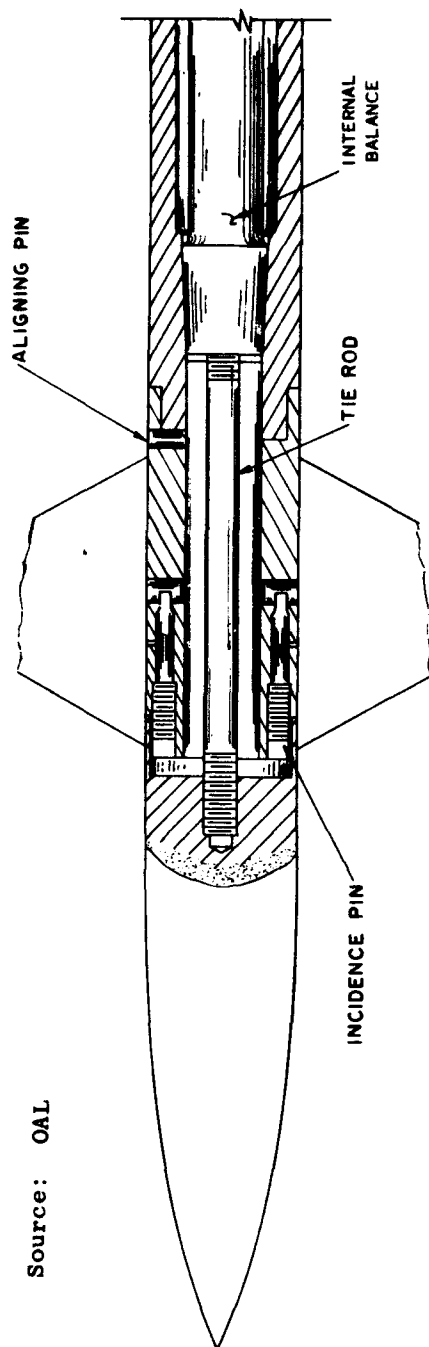
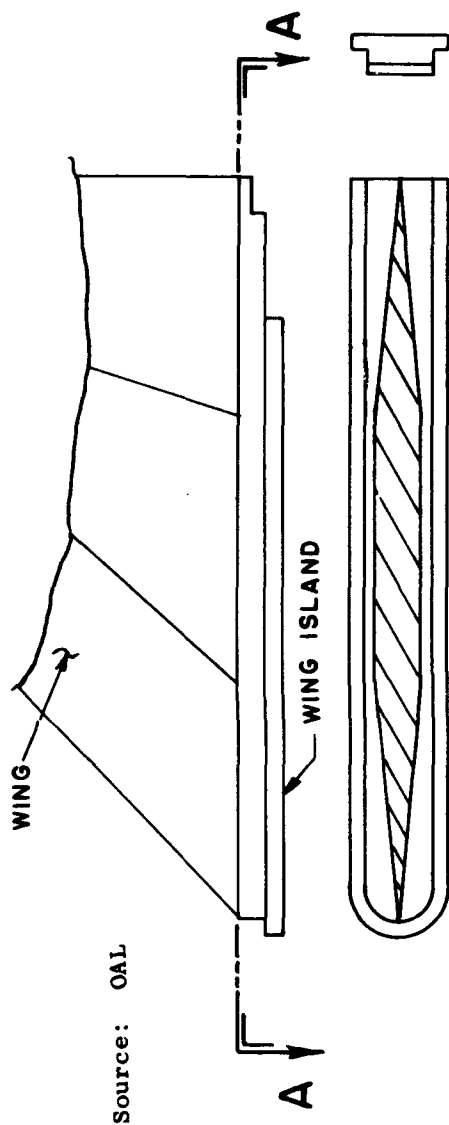
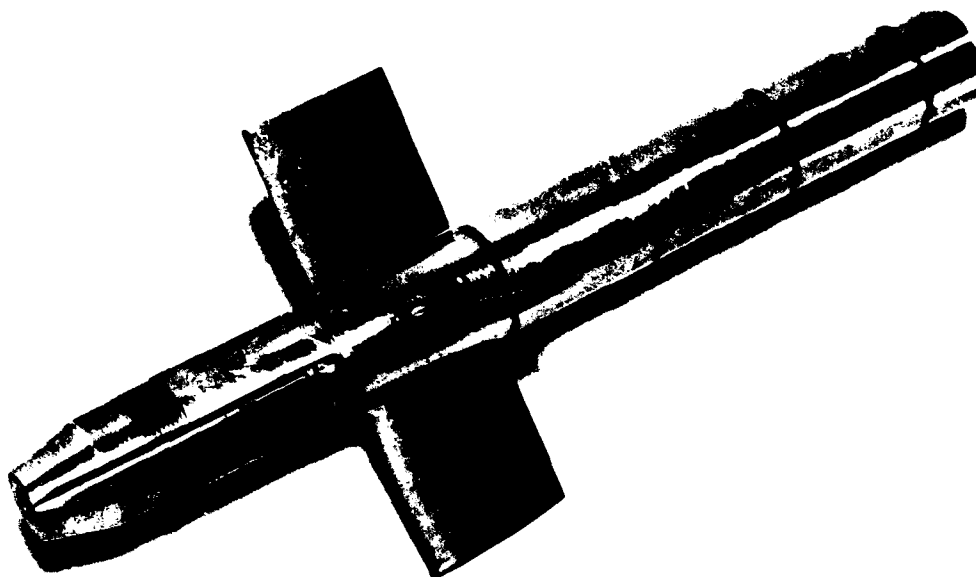


Fig. 8-26. Model sections joined by means of a tie rod.



SECTION A-A

Fig. 8-27. Details of base for surface with fixed attitude.



Source: OAL

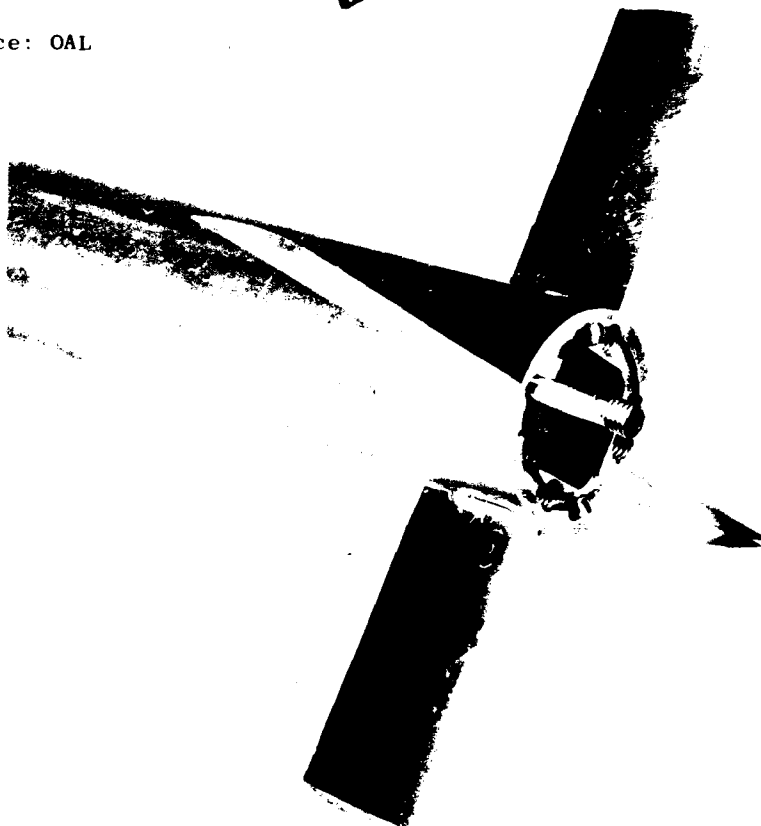
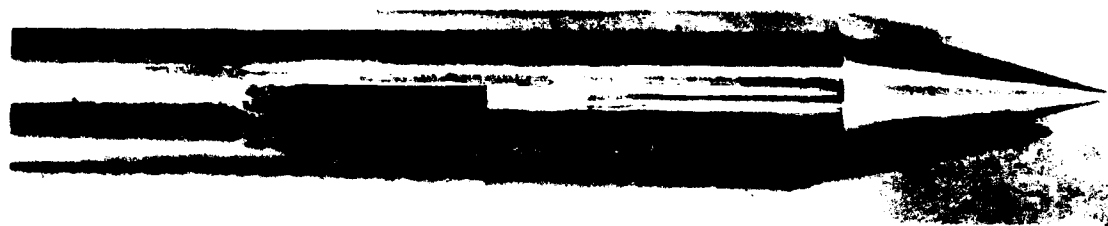


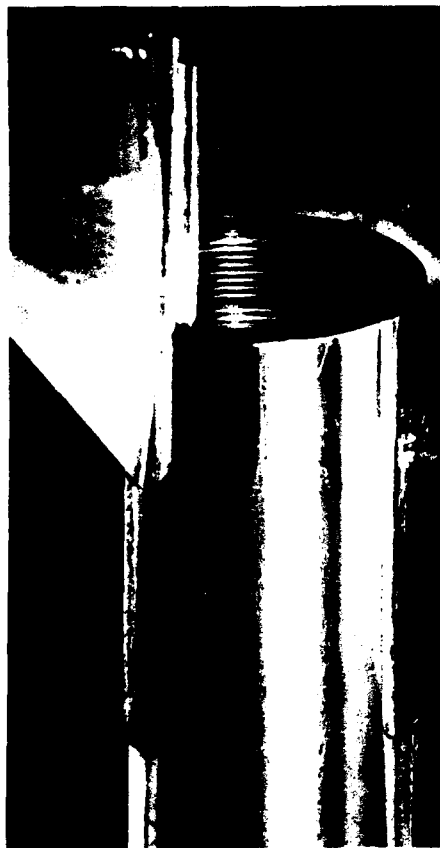
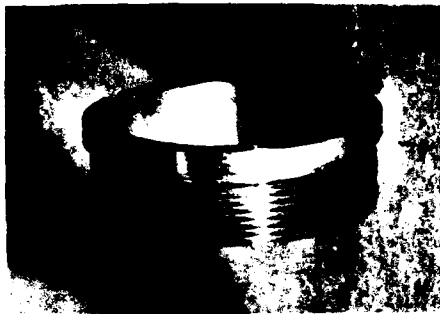
Fig. 8-28. Model with incidence pins installed.



Source: OAL



Fig. 8-29. Methods for setting incidence on surfaces.



Source: OAL

Fig. 8-30. Fixed incidence tail and retaining ring.

9. Force Measuring Systems

Research and development in the field of supersonic aerodynamics demands the immediate availability of large quantities of wind-tunnel data upon completion of a test. Prototype design decisions and accuracy of existing theory depend heavily on these data. The demand is particularly pressing when a crisis of aerodynamic origin develops in a flight-test program. The only immediate economical solution is a crash program of wind-tunnel testing to determine the aerodynamic effects of various configuration modifications. The mere accumulation of large amounts of wind-tunnel data is, in itself, useless unless the data can be quickly converted to the necessary aerodynamic parameters. Wind-tunnel facilities have met this demand with improvements in instrumentation and testing techniques which have resulted in significant advances in total output and operational efficiency.

The efficiency of a tunnel is a direct function of the skill and ingenuity with which the various components of a wind-tunnel measuring system are knit together into an over-all system. The user demands speed, accuracy, low cost, and versatility; the operator would like simplicity of action, easy maintenance, low initial cost, and low overhead. Advances in the design of equipment are being made at such a rapid rate that what is efficient today is obsolete tomorrow. Hence, the description of any one system as typical is not too informative since it is only typical of a particular stage of development. A discussion of the phases of operation such as data taking, converting, reducing, and plotting is more appropriate. What seem to be the most efficient techniques at the present time are discussed below, with emphasis on method rather than on mechanism.

Prospective users of presently available wind tunnel facilities may always obtain more detailed information on the individual systems than it is possible to include in the limited space available here. Such systems are constantly being made more efficient by the addition of new equipment.

Prospective designers of wind tunnel data systems would look to the future rather than the past or the present and seek the advice of established firms whose experience would enable them to design and integrate a system most ideally suited to the type of testing anticipated.

9.1 Data Taking, Reduction, and Plotting Techniques

The most efficient speed for taking force data and the optimum amount of data that should be taken are closely related to the accuracy required in the end results and the capability of the on-line components of the system. The time required in the data-taking process is some times more limited by the physical changes required in model orientation and configuration changes than it is by the actual taking and processing of the data. To expedite data taking an automatic control timer has been used in one facility to program the angle-of-attack drive and roll-positioning motor in the model support (Refs. 91, 254, and 255). The sequence time is variable over a range of 1-1/4 to 6 sec, though the time is usually set to give increments of 1 deg in angle of attack and 5 deg in roll attitude at 4.5-sec intervals. The analog-to-digital converter samples, converts, and stores strain-gage signals once during each cycle. This cycle is automatically repeated until data have been obtained over a pre-set range of model angle of attack

or roll angle, and is then stopped manually.

At another facility a similar operation takes 8 sec per cycle, the difference in time being that required by the flexowriter to tabulate the data. This raises one of the issues that has to be resolved in the design philosophy of a system. In the complete "on-line" system the data is plotted as it is taken. The data at the maximum value of the angle of attack is taken first so that the scale factors may be checked and sensitivity settings adjusted if necessary. The static zero readings are plotted before and after the run. Since the data are plotted while the test is in progress, all computations are based on the initial zero readings and have no way of allowing for zero shifts that may occur during the run. From the on-line data plots the test engineer is able to decide whether additional check points need be run. This decision can thus be made before the model is touched and thus may effect not only a saving of time but also ensure an identical set-up for any necessary re-runs.

In off-line data reduction systems the final plot is not available for a period of several minutes to one-half hour after the run is finished. Small corrections derived from a comparison of the initial and final static zeroes are incorporated. Time is available for the investigation of any irregularities in the data. It is argued that computers geared to keep up with on-line data reduction lie idle during model changes or that the data-taking process is slowed down to the capacity of the computer. Plots of raw data are useful for on-the-spot decisions.

The length of time that the tunnel can run continuously and the interval between runs may be factors in the solution of the on-line versus off-line problem for any particular facility. An example of such a timing problem is given by a 4×4 -ft blowdown tunnel where the run time is less than 30 sec (Ref. 256). A typical run would consist of pitching the model through a complete angle-of-attack range during this time. Normally, data are taken at every degree to the maximum positive allowable angle, which is generally around 20 deg. It was determined that the maximum usable steady-state pitching rate was about 5 deg/sec combined with a high-speed return-to-zero rate of 20 deg/sec. During a high-speed pitching run it is necessary to sample the 20 data channels at a high rate in order to "freeze" the model at discrete angles of attack. An optimum system would sample these 20 channels 5 times/sec.

When samples are taken at a rate of 400 samples/sec, each channel will be sampled $2\frac{1}{2}$ msec later than the preceding one. During this time, the model has pitched through an "error" angle of $2\frac{1}{2}$ msec times the pitching rate. Each succeeding channel has a proportionally greater error with respect to the angle of attack. The effect could be compensated in the data reduction process, but the computation machinery requirements would be considerably increased. If the channels which vary most slowly are sampled last for each angle of attack, the accuracy of the recorded data will be satisfactory without an angle-of-attack correction. To provide some on-line data, the output from 10 of the 20 channels is reduced and plotted in five types of plots during the course of the run, giving sufficient information for rapid decisions on necessary re-runs. Apart from these on-line plots, all data is accumulated during a day's operation and reduced to final form in about 15 min the same evening.

At OAL it is standard practice to take data in 1-deg increments of angle-of-attack and approximately 5-deg increments of roll. The closely spaced data 1) eliminate the need for re-running observed bad points, since enough valid data remain to define the curve adequately; 2) eliminate the fairing of curves; and 3) define local aerodynamic phenomena which large-increment data would be likely to miss. Aerodynamic data are usually presented in the form of plotted curves, examples of which are shown in Figs. 9-1 and 9-2. The plotting may be performed by a vari-plotter (Subsec. 3.8) which can handle up to 3000 points an hour. For the case of on-line data reduction it is often customary to add a final zero angle-of-attack check point and to print the final static zero reading on the plot so that any necessary corrections can be made to account for zero drift.

The data are often stored on punched cards or on magnetic tapes from which they may easily be transferred to punch cards for use on such computers as the IBM 704. The data may also be stored on punched tape.

The performance characteristics and estimated accuracy of one high-speed force-measuring system are summarized below.

Performance Characteristics
(Ref. 256)

High-Speed Data Channels	20
Channel Signal Level	+5 to +30 mv, full scale
Maximum Signal Variation	1/3 full scale/sec
Electrical Filtering	Variable frequency cutoff down to 5 cps
Switching Rate	200 to 1000 samples/sec
Scanning Rate	Manual to 5 scans/sec
High-Speed Switching	Electronic, diodes at 100-v level
Analog-to-Digital Converter	Successive approximation system
Data Storage	Magnetic tape, playback to IBM cards
Computation Time	Overnight, IBM 701 or 704 to data cards
Data Plotting	5 flat-plate plotters
On-Line Data	Simplified 10-channel general-purpose analog computer

Estimated Accuracy (Ref. 256)

Model Pitch Angle for	
Maximum Loads	15 deg
Maximum Rate of Pitching	5 deg/sec
Rate of Signal Change	1/3 full scale/sec
System Component Accuracy	1/10%
Over-All System Accuracy	1/3%
Probable System Error	
(Minimum Signal from Drag)	+4%
Accuracy of Analog Computer	+3 to +5%
Repeatability of Analog	
Computer	+1/2%
Quoted Accuracy of Plotter	+1/4%
Maximum Trace Speed of	
Plotter	20 in./sec

9.1.1 Damping Device (developed at WADC)

Under certain testing conditions, the model and balance may vibrate in a manner determined by the resonant frequency of the model-balance-support system and the aerodynamic characteristics of the model. These vibrations cause corresponding a-c voltages to be superimposed on the d-c output of the strain gages, which in turn cause the self-balancing potentiometers to oscillate about their average values. An effective device to damp these oscillations consists of a drag-cup generator circuit and a filter or tuned amplifier circuit.

The drag-cup generator is a special device which generates a voltage proportional to shaft angular velocity having a frequency equal to the field frequency and independent of angular velocity. This generator is connected to the self-balancing potentiometer dial by a friction drive, and consequently it generates a voltage which is proportional to a velocity when the instrument is moving. The generator field and potentiometer drive motor are both supplied with 60-cps excitation. Since the phase of the generator is adjusted to oppose the driving voltage present in the potentiometer amplifier, the addition of the generator voltage to the amplifier voltage tends to reduce or cancel the latter and reduce the motor-drive torque. This reduction of torque is, in effect, a damping of the oscillations of the instrument. This section of the damping unit is effective for oscillations of the order of 1 or 2 cps.

An RC filter which is tuned to 60 cycles and has an approximate band width of one-half cycle attenuates the oscillations whose frequencies are greater than 2 cps.

9.1.2 Measuring Bridges

In the discussion of measuring bridges for strain-gage signals, presented in Subsecs. 3.1 and 3.2, it was pointed out that an a-c bridge is preferred for both strain-gage and pressure transducer signals. The use of an a-c carrier for the signal eliminates errors from thermo-electric and contact potential. In addition, if the strain-gage bridges are fed from the same transformer which supplies measuring bridge voltages, no regulation is needed on the voltages. Figure 9-3 shows an a-c bridge circuit, whose parts are identified, and Fig. 9-4 shows the basic circuit for d-c measurements. The d-c measuring bridges are used for measuring voltages from thermocouples, electromagnetic potentiometers, and pressure transducers.

9.2 Analog-to-Digital Conversion

The major difference in the many force-measuring systems presently in use is in the analog-to-digital conversion features.

At the OAL facility the high-speed, analog-to-digital, electronic converter (ADHEC) described in Subsec. 3.7.2 is employed. This is a null-balance converter which measures a 60-cycle analog voltage output from a bridge circuit. This voltage may be in the range of 0-15 to 0-75 r for a full scale reading of 10,000 units. A four-digit output from the ADHEC is fed directly to an IBM lister and card punch and indicated on a bank of neon lighted numerals. A typical (OAL) force-measuring system is shown in Fig. 9-6.

At the WADC facility the digital converter takes the reading from a standard, precise, self-balancing potentiometer and transmits it to a standard punch card machine and also to a plotter if the latter is desired. In principle, this converter (Fig. 9-5) simulates a four-wheel mechanical counter and converts shaft position into electrical contact settings. Contact arms are attached to the counter wheels and are normally out of engagement with the stationary contact plates. At readout, a rotary solenoid is energized so that a star wheel is positioned to align the rotating contact arms, and after alignment the contact plates are moved to close with the rotating contact arms. The circuitry can be arranged so that current flows through the contacts only after closure and is cut off prior to opening. This arrangement results in a greatly extended life and low driving torque, less than 1/8 inch-ounce.

At the BRL facility an analog digitizer and memory system are shared by two tunnels which have their own data input, output, and control systems. The electrical input signals from the tunnel using the equipment are taken to the converter room where they are converted to shaft rotations. Three uses are made of the shaft angular positions: 1) They are repeated in the tunnel control room by means of synchro repeaters. 2) They operate the analog-to-digital converters. 3) They drive the plotters.

The analog-to-digital converters include a relay memory, so that when the "read" button is pushed, the digital counts in all eight channels are stored simultaneously in the eight memory units. They are then read out in sequence from the memory units to the flexowriter, which prints one line of data. Solenoid brakes halt the signal servos during the fraction of a second needed for the system to fill the memory units.

Figure 9-7 is a photograph of one channel in which the various parts are identified. The wiring diagram of the analog-to-digital converter is shown in Fig. 9-8. The input shaft rotation drives the slider of a helipot with a single center tap. This results in a resistance proportional to the absolute value of the shaft rotation from mid-position.

Assuming that the signal-measuring potentiometer and this center-tapped input potentiometer are linear, the result is an input resistance proportional to the absolute value of the electrical input signal. The analog-to-digital converter is simply a Wheatstone bridge, which balances this input resistance by shorting out some of a set of 16 resistors in the measuring arm of the Wheatstone bridge. These 16 measuring resistors are precision resistors having ratios of 1, 2, 4, 8; 10, 20, 40, 80; 100, 200, 400, 800; 1000, 2000, 4000, 8000. Thus the readout consists of noting which resistors are not shorted after the balance is obtained. The readout occurs in binary-decimal form. A completed reading is made in about 7.5 sec, so that readings can be taken at 8-sec intervals.

This system operates successfully and has materially shortened the running time required for each test at BRL. It requires only one or two operators and thereby allows the rest of the tunnel crew to prepare for the next model change.

One modern system (Ref. 256) scans automatically and switches each channel electronically into an analog-to-digital converter which operates at rates up to 2000 samples per second. The output is a 12-digit binary-coded decimal number and sign. This information is impressed on an electronic shift register which transfers it to a magnetic tape and then to punched cards. The system is depicted in Fig. 9-9.

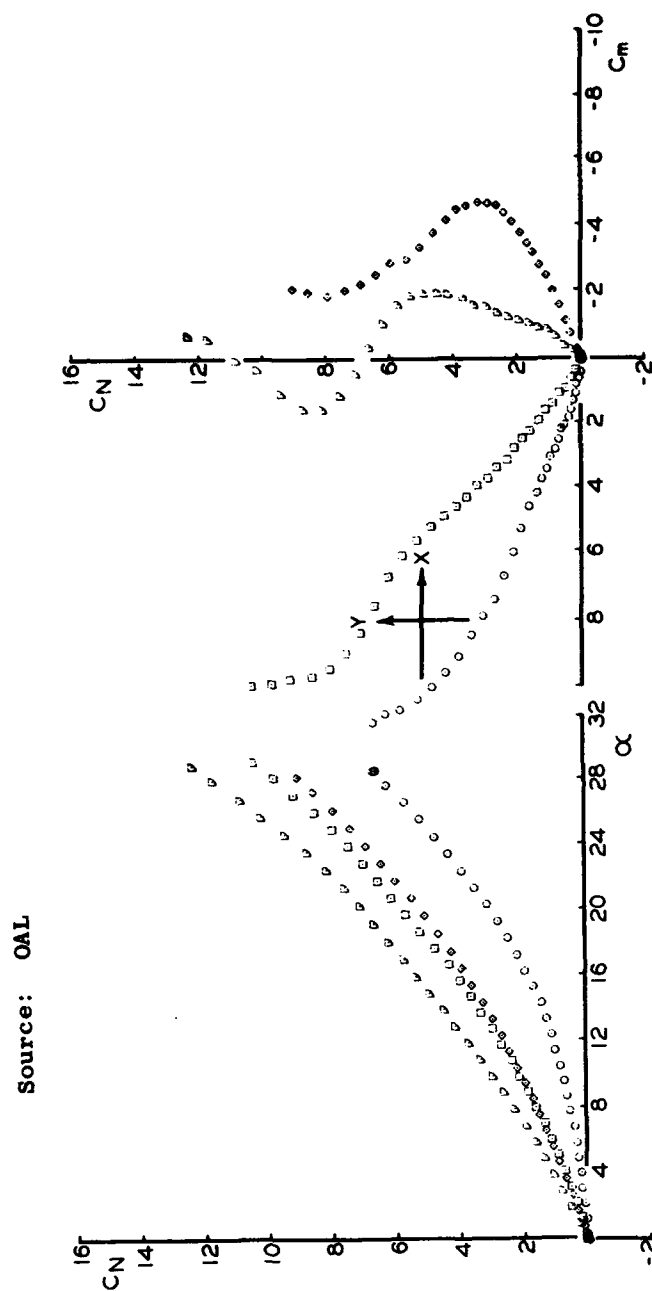


Fig. 9-1. Typical stability data at constant roll attitude.

Source: OAL

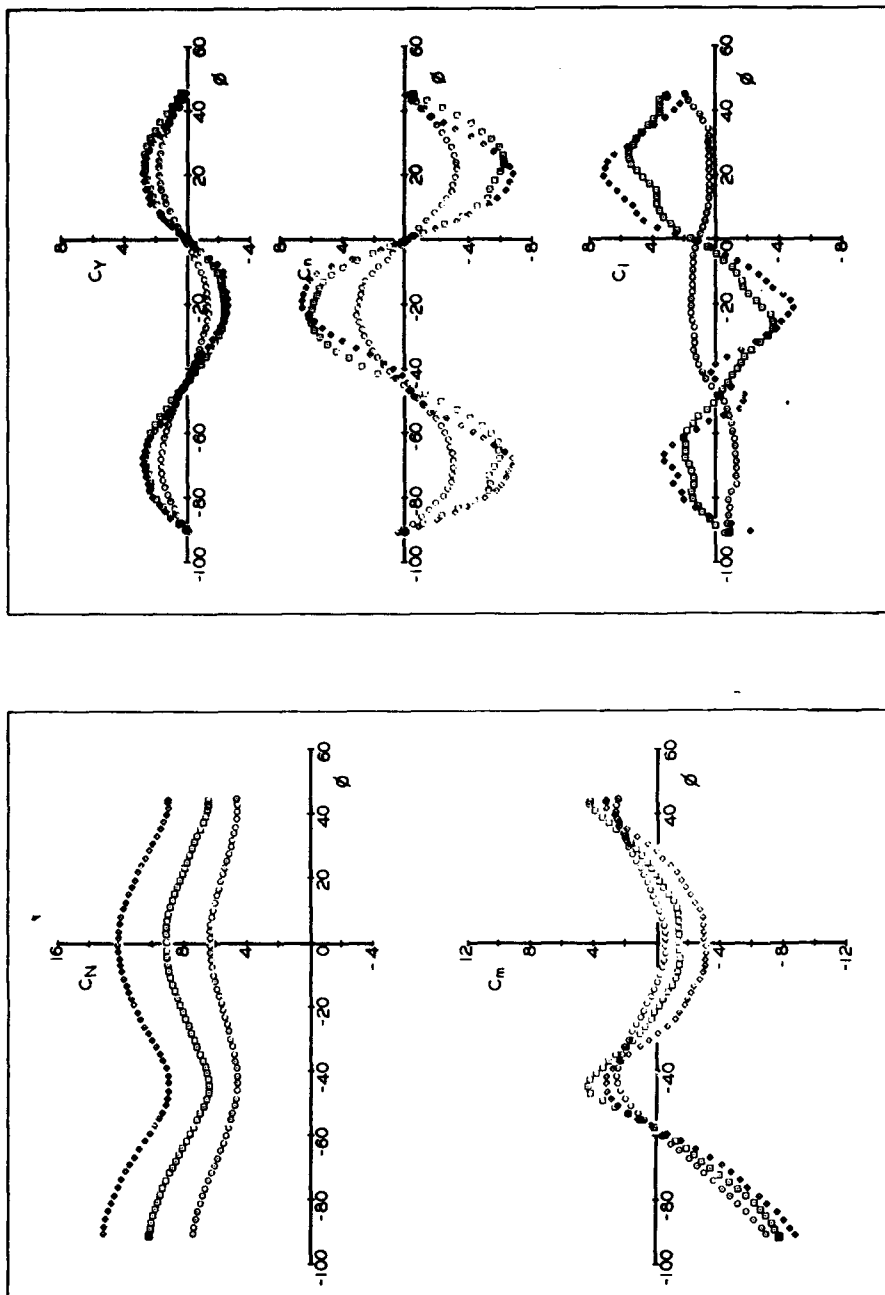


Fig. 9-2. Typical force data for various constant angles of attack.

- A Zeroing Helipot (to compensate for transducer unbalance)
- B Helipot (for zeroing servo-system)
- C Low-Gain Brown Servo Amplifier
- D Brown Servo Motor
- E Six Volt Strain-Gage Power Supply (with ground point through symmetric resistors; prevents drawing of excessive current if strain-gage lead grounds out)
- F Winding of 0.2 v (to supply bridge)
- G Plug-in Calibration Resistor (normally set to give 30 mv across bridge, allowing for signal levels to ± 15 mv)
- H Measuring Helipot (15 turns of smooth single wire to give infinite resolution)
- J Signal Transformer (feeds high-gain (40X) Brown servo-amplifier)
- K Servo Amplifier
- L Brown Servo-Motor (drives measuring Helipot)
- T Transformer (with 6 or 7-v secondary and 8 single or 2 turn secondaries for measuring bridge supplies)

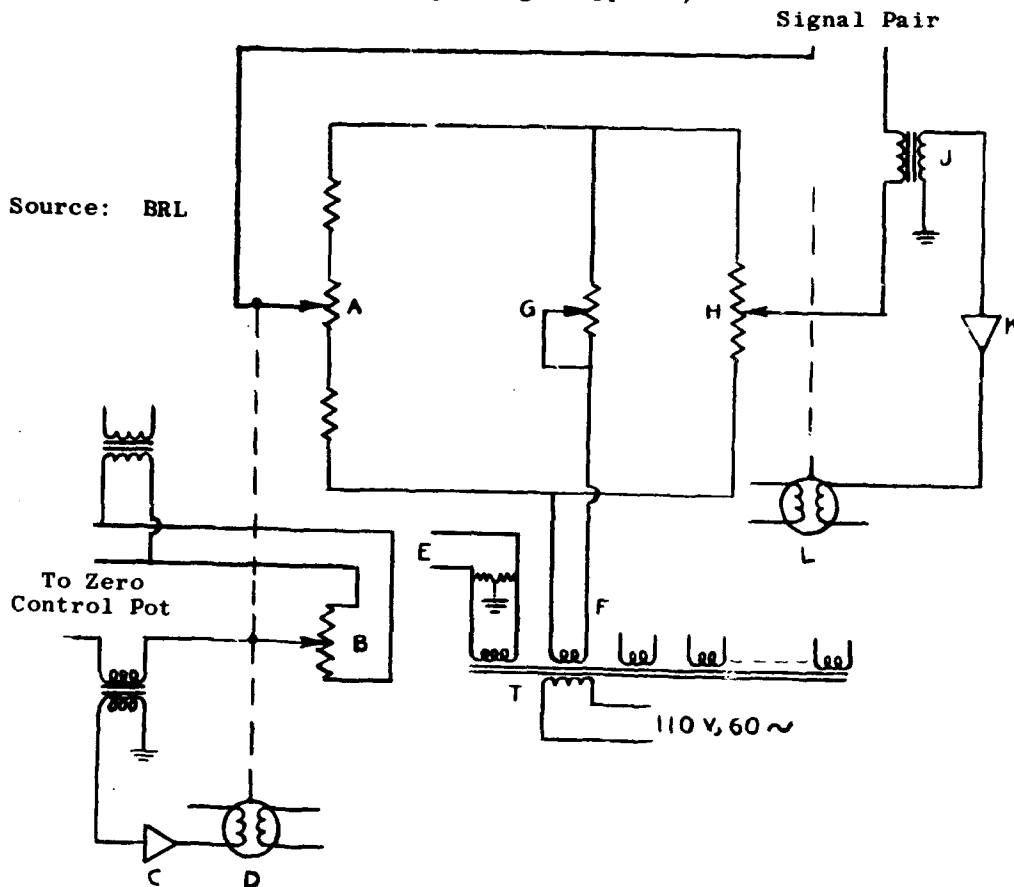


Fig. 9-3. Wiring diagram of a-c bridge.

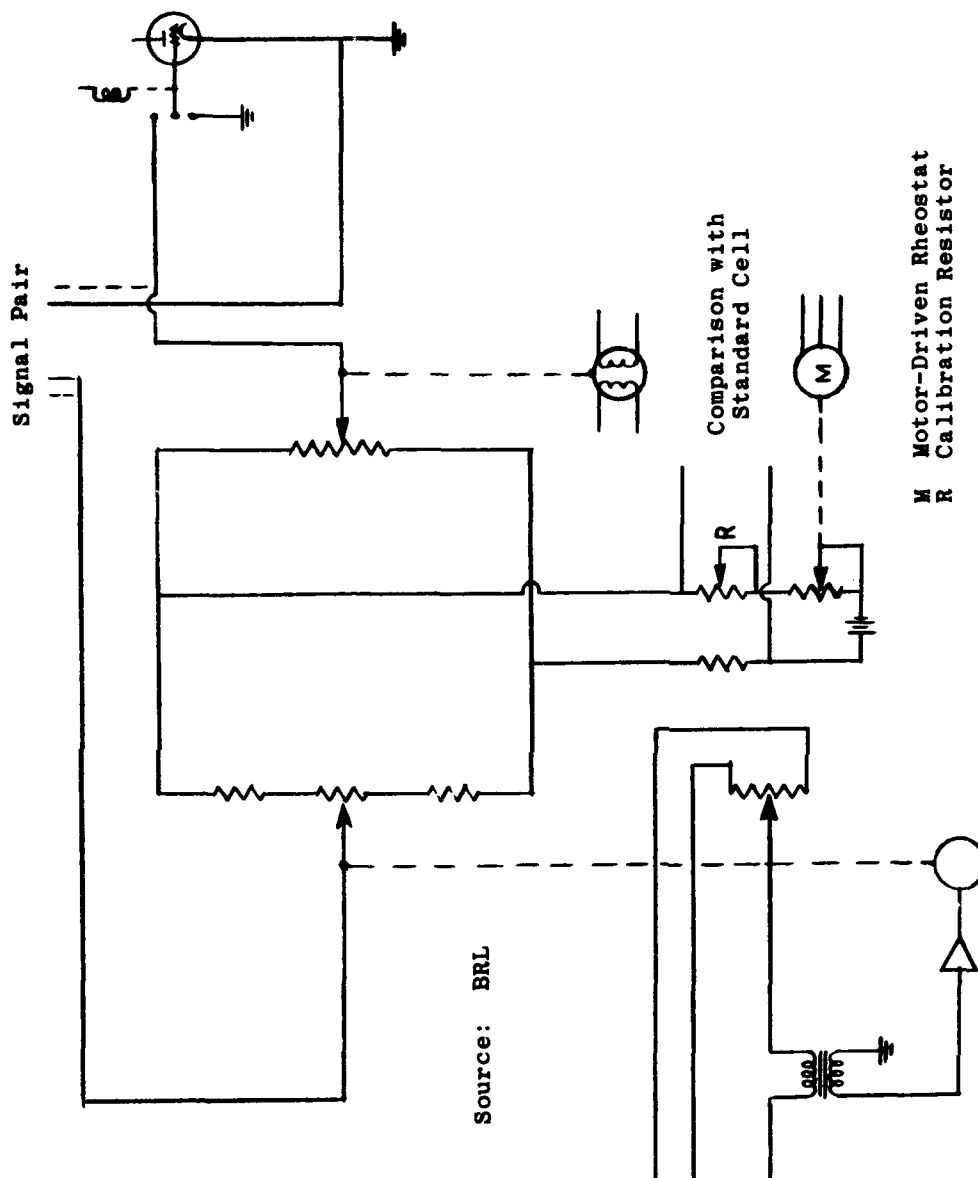


Fig. 9-4. Wiring diagram of d-c bridge.

Source: WADC

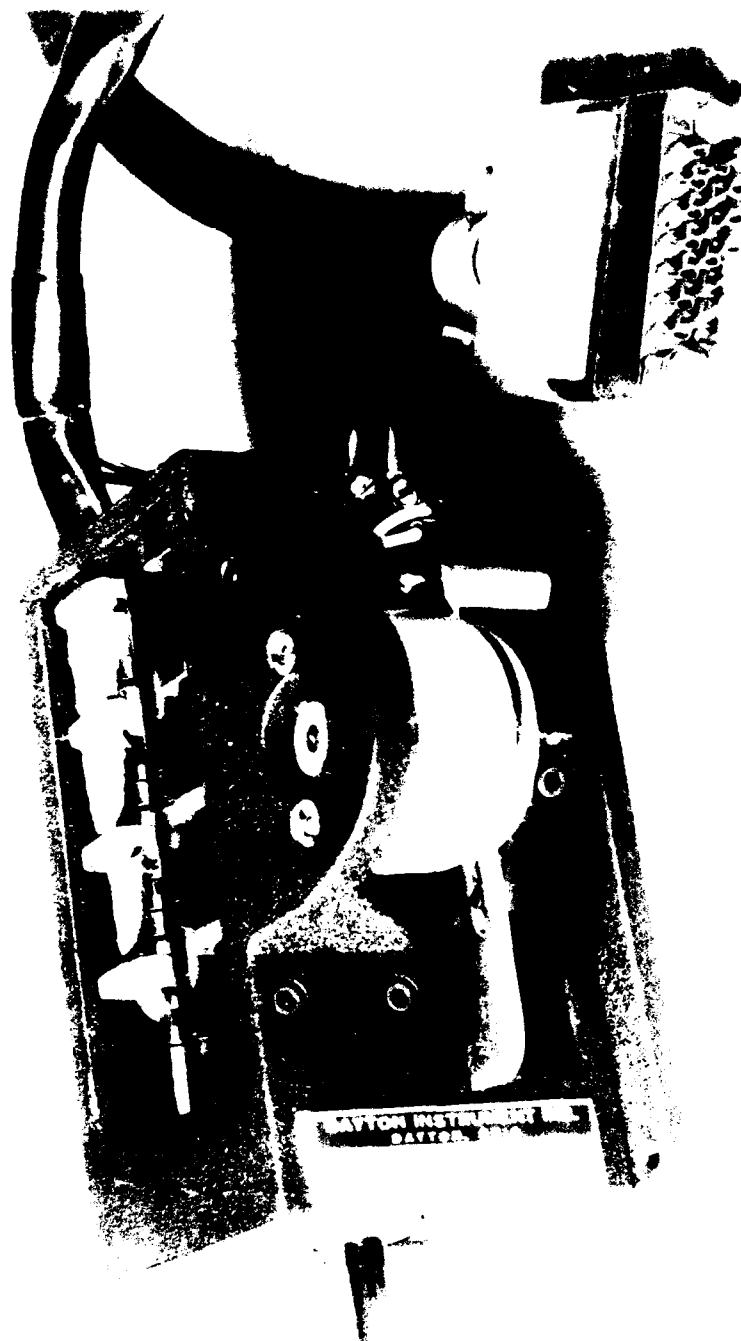


Fig. 9-5. Digital converter (Dayton Instrument Model No. D1-4-54).

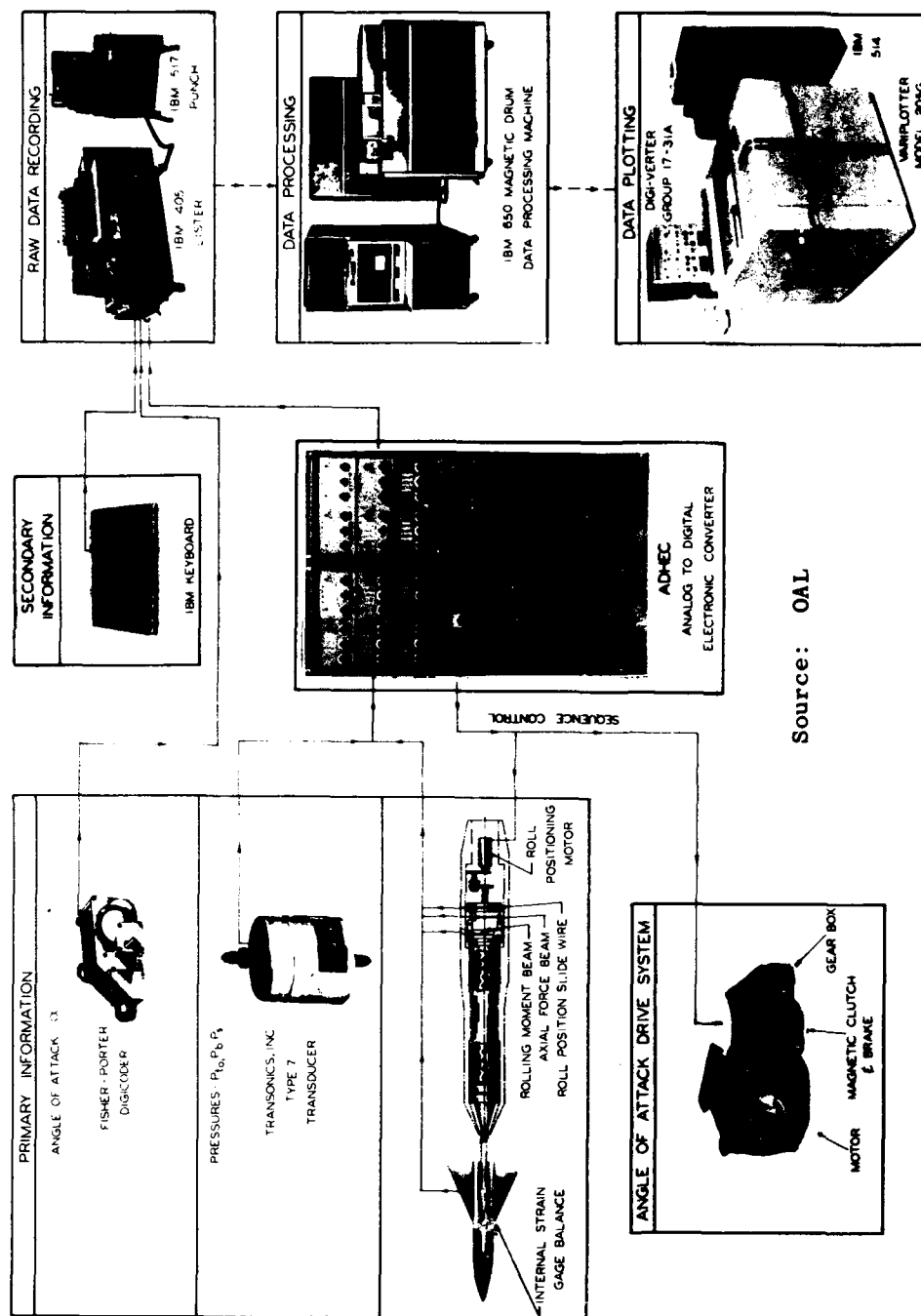


Fig. 9-6. OAL automatic data system.

Source: BRL

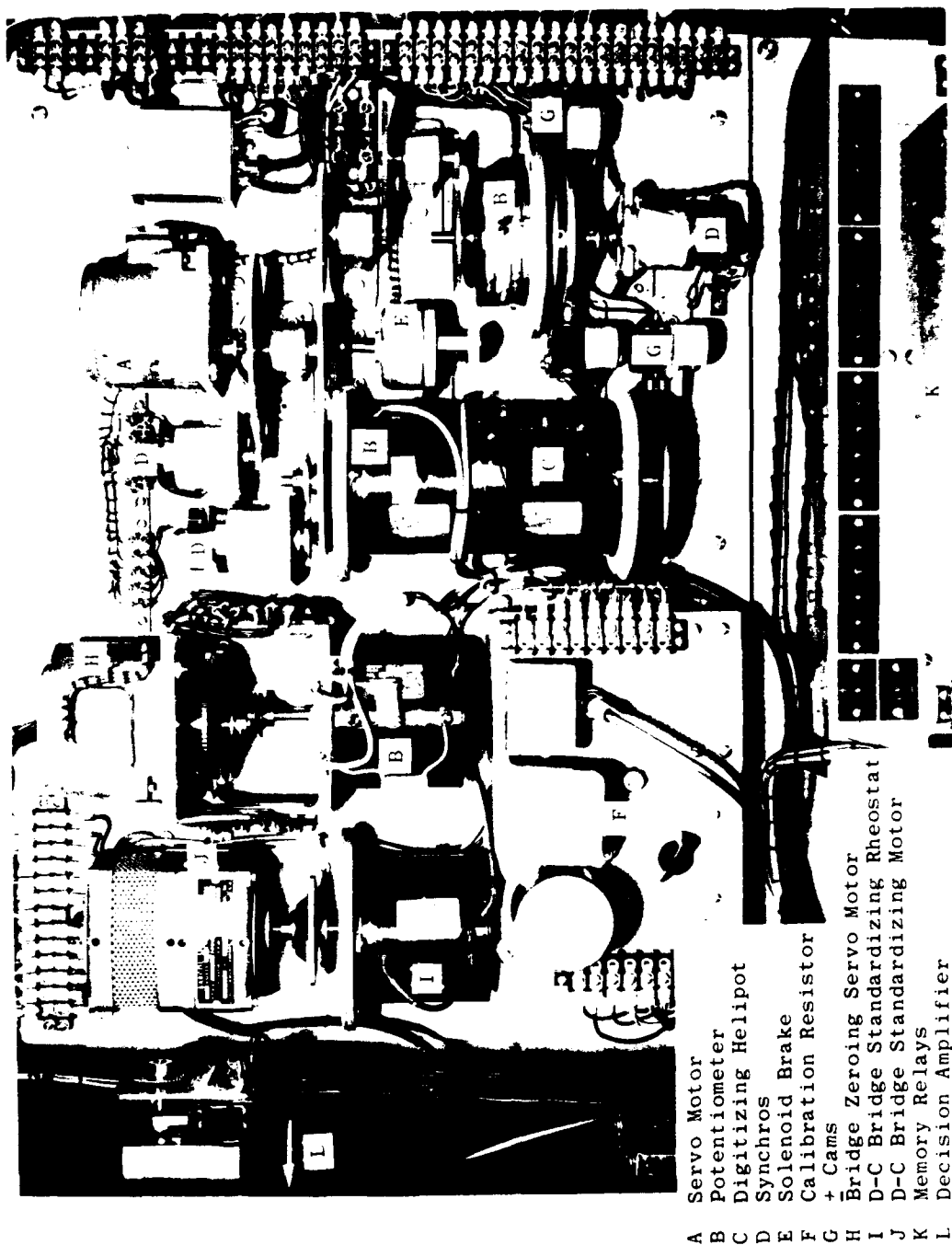


Fig. 9-7. One channel of BRL converter servo system.

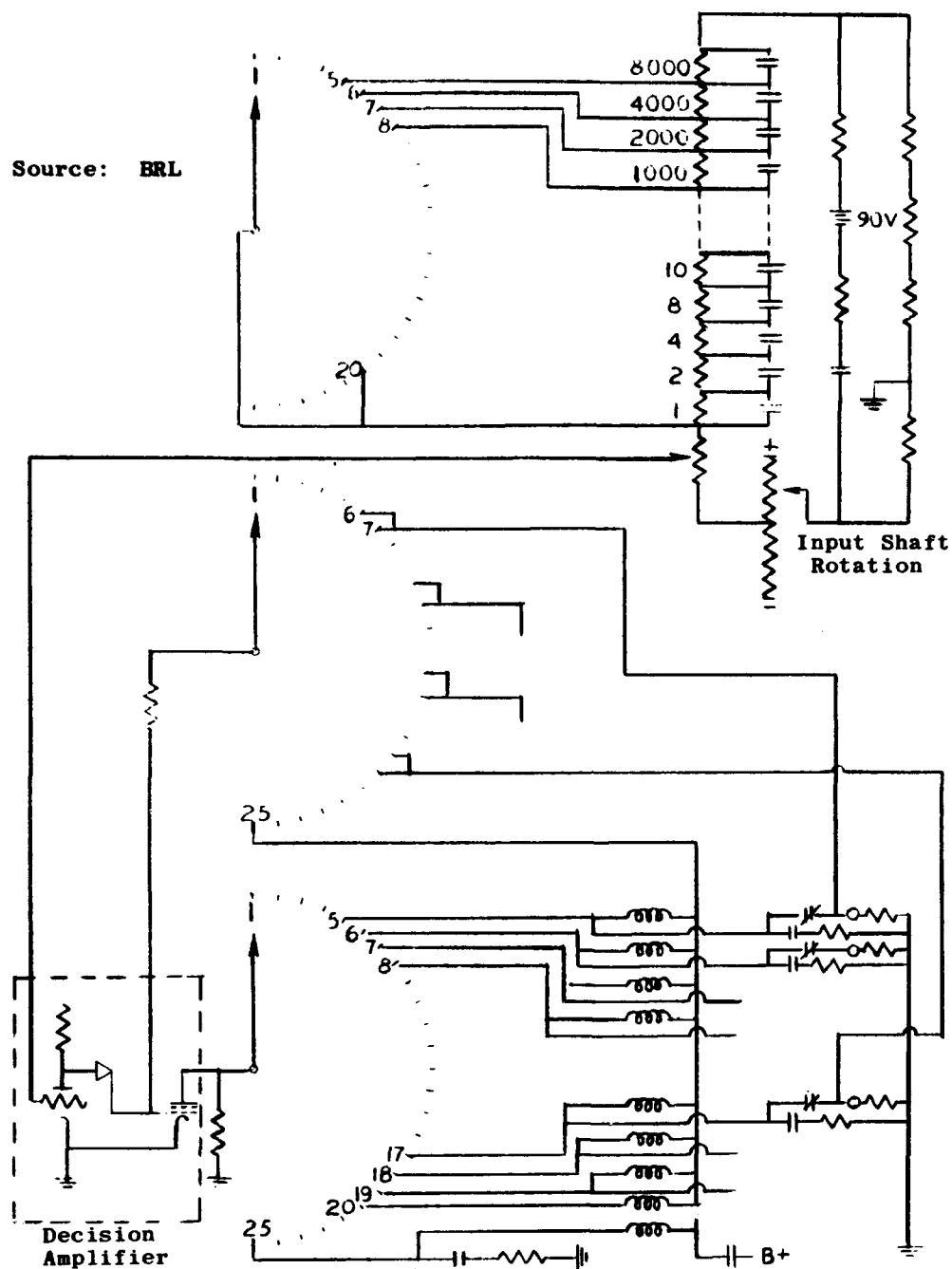


Fig. 9-8. Schematic of BRL analog-to-digital converter.

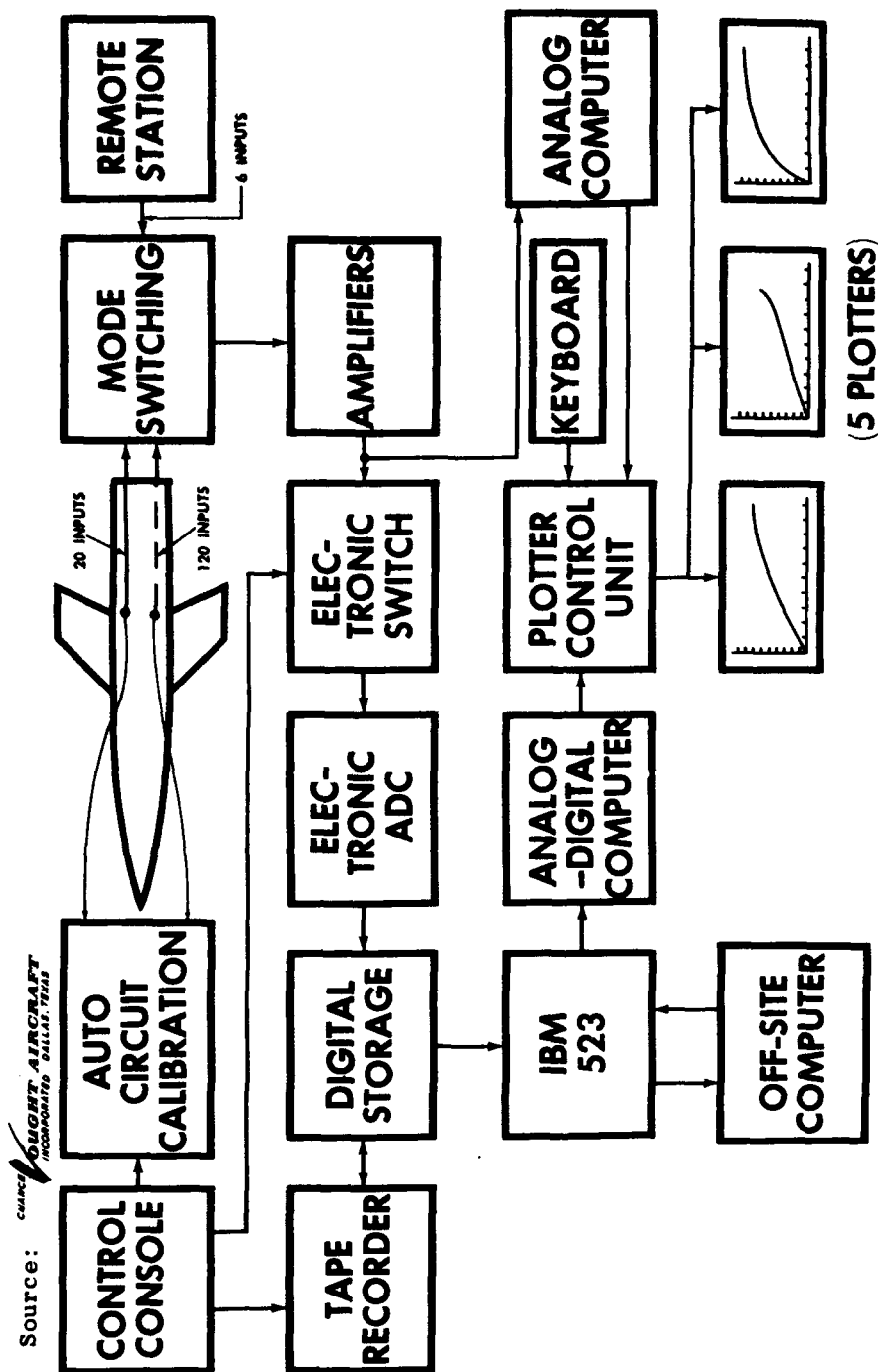


Fig. 9-9. Block diagram of high-speed wind-tunnel data system.

10. Pressure Measuring Systems

Pressure measurements are essential for nozzle calibration, tunnel operation, and pressure ratio or pressure coefficient data for research and development tests of external and internal aerodynamics. Extensive pressure measurements, however, usually require the expenditure of much time and labor. Many man-hours are needed, for example, to attach all leads and then to test them for leaks. This time is further increased if manometers have to be read visually or even photographed at each setting. Automatic pressure-measuring systems are therefore needed to avoid excessive time delays between test and evaluation, to reduce human errors, and to make pressure testing as efficient as force testing with respect to time.

Regardless of the method utilized to record pressures the entire pressure-measuring system, from orifice to pressure recorder, must be designed as an optimum system with respect to response lags (Subsec. 2.3.6). This design should minimize leakage and should enable the maximum number of pressures to be recorded and reduced in a minimum time. In most modern wind tunnels the automatic pressure reducing system is developed around a pressure transducer and pressure switch. However, a fully automatic device coupled to a mercury manometer system has been shown to be very efficient. A pressure scanning valve has also found wide application. Some of the best characteristics of pressure-measuring systems that have been developed up to the present time are treated briefly herein.

10.1 Pressure Transducer Systems

The pressure transducer (Subsec. 2.3.3) lends itself readily to incorporation in a fully automatic pressure measuring system. The transducer output is stable and linear and also exhibits minimum hysteresis effects. The system itself permits the rapid collection of large quantities of pressure data with minimum effort and in a form suitable for machine computation. A transducer system is compact and may be readily housed in a few standard relay racks.

There are many ways in which a system may be designed. It can utilize a single transducer for each pressure, or a multiple switch in combination with a transducer to allow it to sample many pressures in one cycle. By means of an electrical switch, one channel may sample many such transducer systems in a single cycle. Details of several proven systems may be found in Refs. 255 and 258 to 263. Only a generalized description of such systems can be presented herein, since the quantitative element selected for a system, and hence the design of any system, is usually determined by the use for which it is intended.

A typical transducer system is shown in Fig. 10-1. Each transducer in this system, one of which is shown, consists of a beryllium copper bellows attached to a steel frame, with a hardened steel cone on the free end. The cone engages a conical depression in the end of a cantilever which is equipped with strain gages. At assembly the bellows is compressed by the cantilever to the equivalent of about 35 in. Hg. This initial compression allows the transducer to be used for measurement of vacuum as well as pressure. The pressure range of the 18 transducers in the system is 0 to 100 in. Hg abs. Each of the transducers is connected to a channel of an analog-to-digital converter which converts

the strain-gage signal to digital form. A pressure switching system allows the measurement of four model pressures and a reference pressure on each of 17 transducers, with the eighteenth being used to measure the test-section stagnation pressure for reference.

The operation of another pressure transducer system is illustrated in Figs. 10-2 and 10-3. Each transducer in this system consists of a 240-ohm bonded strain-gage element developed from a cylinder and enclosing a stainless steel bellows (see Subsec. 2.3.3.1 and Fig. 2-22). The strain-gage flexures are designed for 10,000 psi (a stress considerably lower than usual in strain-gage practice) in order to reduce hysteresis and to avoid nonlinearity by limiting the bellows extension to 0.002 in. at full design pressure. Each transducer is connected to its own measuring servo which consists of a self-balancing a-c potentiometer having two measuring ranges, 5 and 10 mv. Outputs of the servo go to a four-digit visual counter and to a four-wheel, decimal, shaft, analog-to-digital converter shown in Fig. 9-5 and described in Subsec. 9.2.

Figure 10-2 shows the flow diagram for the 98-channel pressure data system and indicates the principal control circuits and the IBM readout circuits. The system is divided into 7 groups of 14 channels each. When readout is initiated, the servo freeze control is activated and opens one phase of each of the 98 balancing servo-motors, thus stopping all the servos and storing the data. A change in test conditions may be started at this point without altering the stored data. The control unit next energizes the first of the 7 group control lines, closes the readout contacts on the first group of 14 digital converters, and signals the IBM summary punch to read. The punch records a 9-digit test-condition identification number, a single-digit group identification number, and 14 four-digit-plus-sign items of data, thus completely filling the 80-digit IBM card. Upon completion of the first card, the summary punch signals the control unit which drops out the first group control circuit, energizes the second, and signals the punch unit to read another card. This process is repeated for 7 cards in approximately 10 sec. The control circuits are arranged such that any group or groups may be omitted if desired.

The system depicted in Fig. 10-3 is housed in four standard 19-in. relay racks. Two complete servo units are mounted in each rack panel such that each of three bays contains 28 servos, any pair of which may be removed for servicing. The fourth bay contains one group of 14 servos plus the control unit. The transducer bank and its associated three-way solenoid valves is contained in a temperature-controlled steel box mounted within the pressure cabin atop the plenum chamber of the wind tunnel. Pneumatic connections between the transducers and the model orifices can thus be made with reasonable lengths of tubing (Subsec. 2.3.6).

10.1.1 Switches Used in Conjunction with Pressure Transducers

The number of pressures that may be sampled in any given transducer system may be multiplied many fold by using either electrical switching or pressure switching. In the first case a transducer is provided for each pressure and several transducers in sequence are connected electrically to each converter. In the second case several pressures are introduced sequentially to the transducer. The electrical switching system would represent a saving of time since one pressure

stabilization period would be required for each sequence. This system, however, would be more costly since transducers are expensive and a great many more would be required. In most systems in operation at present a combination of both types of switching is employed.

The simplest pressure switching system consists of pneumatic clamps applied to the leads by means of solenoid valves. Operation of the clamps in the desired sequence is controlled by an automatic programmer. In conjunction with the programmer, a manual switching arrangement can be used to calibrate or alter the sensitivity of the analog-to-digital converter for each test. A schematic of the system is shown in Fig. 10-4.

A commercial pressure scanning valve available (from General Design Co., San Diego, Cal.) with many modifications has been widely used in wind-tunnel pressure tests. This valve is shown, both assembled and disassembled, in Fig. 10-5. The assembly consists of a wafer with 12 input taps and 1 output tap located around the periphery, a slotted rotor, a spring washer, and a hold-down ring. An annular groove in the wafer is connected to the output tap only. The slot in the rotor connects any single input tap to this annular groove. The mated surfaces of the wafer and the rotor are lapped to provide good sealing surfaces. The spring washer and the hold-down ring provide a positive pressure against the rotor to prevent air leakage between the mated surfaces. This small slot in the lapped surface of the scanning disk (wafer) plus space adjacent to the transducer diaphragm represents a very slight increase in the volume occurring for each tube selection that is made (in some cases as little as 0.0006 cu in.). This affords an extremely rapid response and an insignificant error due to the residual pressure in the slot.

Figure 10-6 shows a pressure selector switch assembly with three wafers installed. Three standard 12-position wafer switches are used to position the three rotors, supply electrical information, and switch in connecting devices. A 12-position Ledex rotary actuator selects the desired pressure. With this valve system it should be pointed out that the metal-to-metal seal between the rotor and the wafer may leak air at high pressures. It is therefore unwise to use the switch for any application where pressures greater than 10 psig are encountered unless pressure is applied to one side of the pressure scanning disk.

The valve unit which is employed for the CAL pressure measuring system is 1-1/4 in. in diameter and 1-3/4 in. long. This unit measures 48 pressures with the use of one transducer. Six of these units are geared together and actuated by a common rotary solenoid stepping motor. The pressures are switched by means of two lapped surfaces in the valve, one of which contains a slot which connects each of the pressures in turn to the integral flush transducer. Total volume in the scanning chamber is less than 0.002 cu in.

10.1.2 Performance Characteristics of Pressure Transducer Systems

The accuracy of any system is determined principally by the accuracy of the individual transducers. For one system (Fig. 10-2) in which all transducers were carefully calibrated the total average error was below 0.1% of the reading down to 10% of the full-scale value.

Below 10% of full scale the error becomes too difficult to determine. The measuring servo is usually accurate to within $\pm 0.03\%$ of full scale.

If the pressure transducers are subject to temperature drifts it is advisable to enclose them in steel cans to keep them at a constant temperature. At one facility the transducers and switches are contained in an oven which maintains the temperature constant to within a few degrees.

A comparison of data for a pressure test between readings on a multi-tube manometer and the transducer system (Fig. 10-1) for 1065 individual pressures gave an average over-all absolute difference of 0.17 in. Hg. During the test, the complete cycle time was run at 75, 55, and 38 sec, and only small differences were due to the changes in the lead systems. The time required to record a cycle of pressures depends to a great extent upon the time required for the individual pressures to stabilize. In many cases while one pressure in a scanning valve is being sampled the next is already stabilizing. In one typical system having 100 leads, for example, the punch cycle is 0.6 sec, of which 0.5 sec is available for pressure stabilization. Where the pressures are much lower or the changes greater, the stabilization time may be of the order of several seconds.

Depending on the choice of transducer element, systems may be used with a high degree of accuracy for the measurement of pressures from a few millimeters (Ref. 261) to several atmospheres. At ABMA hysteresis effects in low-pressure measurements were minimized for the Wiancko 5-psia gage by maintaining the pressure measurement level for about 30 min prior to use. The differential pressure and therefore the leakage may be greatly reduced by enclosing the system in the wind-tunnel structure and venting the enclosure to test-section static pressure.

10.1.3 Unique Features in Pressure Transducer Systems

Many facilities employ unique design features in their systems in order to make them more versatile, to suit special circumstances, or to obviate certain general or specific problems. These features, whose details may be found in Refs. 255 and 258 to 263, are worthy of special note.

10.1.3.1 Automatic Zero Balancing

At the WADC transonic tunnel a solenoid clutch and associated circuits are provided in order that the entire system may be automatically zero-balanced with a single push button command without reducing the tunnel speed to zero. Each transducer is connected to a three-way solenoid-operated valve such that the active sides of the transducers may be vented to the reference pressure on command, thus establishing zero differential pressure across each transducer. The same balancing command operates the solenoid clutch in each servo and also removes the measuring potentiometer from the signal circuit. The servos then drive the balancing potentiometers to null the zero-pressure output signals from the transducers. If the solenoid valve circuit is interrupted, the zero-balance command can be used to suppress the system to zero output at the pressure level existing when the zero-balance command is

initiated. However, the 1000-count electrical zero-suppression is usually employed for reading pressures which may be both positive and negative during a run. The schematic of the system incorporating this device is shown in Fig. 10-2.

10.1.3.2 Cathode-Ray Manometer Simulator

A cathode-ray tube has been used to provide a visual picture of pressure distribution over any desired portion of the model or wind-tunnel test section. The cathode-ray tube displays the analogs from some of the servos in the form of pulses which simulate the appearance of a manometer bank. Each of the 98 measuring servos in this system is equipped with an analog generating potentiometer which, when connected to a stable d-c voltage source, will provide a voltage for display as a pulse on a 21-in. cathode-ray indicator. A telemetering type commutating switch connects any 60 of the analog voltages in sequence to the vertical deflection circuit of the indicator and also provides a synchronizing pulse at the start of each scan such that the 60 pulses appear on the screen with heights proportional to the 60 pressures. The pressures may be selected for display in any order by means of a patch panel in the control unit, and rapid change-over from one display to another may be effected by removing a wired 60-pin cannon connector and replacing it with a connector wired for a different display. The schematic of the system incorporating this useful device is shown in Fig. 10-3.

10.1.3.3 Internal Manometer

An internal automatic pressure measuring system developed at CAL has units of three transducers housed within a 3-in. long, 2-7/8-in. cylinder. Each unit measures 100 pressures by use of pressure switches (Fig. 10-6). By placing these units inside the model, very short lengths of tubing may be connected to the orifices. Very small switched volumes will then give pneumatic stabilization times of the order of 100 msec. The system uses a high-speed data readout system, reading data into IBM cards at the punch machine speed of 100 cards/min.

Complete leak and lag checks are made prior to tunnel installation. Once the model is "buttoned up," it is unnecessary to disturb the pressure tubing. This greatly decreases the possibility of a malfunction. The sting interference and simultaneous force and pressure data problems are eased, since only a few electrical leads are brought from the model.

Although the transducers being used (CEC-4-312) experience a zero shift (due to gravity effects) as their attitude is changed, the output for a 30-deg change in attitude about the most sensitive axis is less than 1%. However, no difficulties are expected due to model vibrations. To minimize zero shifts and changes in transducer sensitivity with temperature, the units are placed within temperature-controlled jackets.

10.2 Automatic Digital Recording Manometers

The Automatic Digital Recording Manometer (ADRMAN) was developed (Ref. 264) to meet the need for a rapid means of reading pressures and converting them into a suitable form for high-speed data

reduction. The device automatically reads the level of the liquid in a conventional manometer and records it on IBM cards.

The basic unit of the manometer reader, the meniscus-transducer shown in Fig. 10-8, is a miniature photoelectric cell, with associated light source and optical system, which travels up and down to scan the level of the liquid in the tube. The components of each transducer are mounted in a small aluminum block which conforms to the shape of the manometer tube. When the transducer reaches the meniscus during a scanning operation, the light passes through the empty manometer tube, energizing the photoelectric cell to produce a triggering pulse which determines the relative position of the meniscus. A bank of as many as 20, 100-in. tubes may be read simultaneously by employing as many transducers, the actual number being limited by the number of available spaces on the IBM punch cards and the physical size of the cross arm on which the transducers are mounted. A schematic of the model is shown in Fig. 10-7.

In addition to any number of meniscus-transducers which might be employed, a counting head and its associated light source and optical system (Fig. 10-9) is incorporated into each bank of tubes. This photoelectric cell reads the specific increment of travel on a perforated steel tape extending the full length of the manometer board. The cross arm upon which the units are mounted travels at 20 in./sec, and as it does so the counting-head cell is alternately sensitized and desensitized by the perforations in the tape. Each half-cycle of the resultant sine wave output, whose frequency is 200 cps, is a counting pulse and is equal to 0.050-in. Hg or unity oil. As the manometer bank is scanned, the movement of the cross arm is recorded by a binary counter; and when the meniscus of a tube is passed by its related transducer, the reading of the binary counter is set into a binary converter. The scanning cycle for one bank of 20 tubes is 6 sec. The scanning head is activated by use of cables attached to air cylinders.

The output of the photoelectric cell of the counting head is amplified as shown in Fig. 10-10 and used to drive a frequency-doubler which in turn drives a shaper circuit whose output is a 400-cps square wave. The output signal of the shaper is fed to a circuit which discriminates between a usable signal and stray pulses that may derive from the preceding stage. The discriminator output is fed to the binary counter and also through a signal inverter to gate tubes which serve the manometer-tube units.

The counting system consists of an electronic counter, which is capable of counting to 999, and decoupling networks. The output of the counter is fed to as many individual decouplers as there are manometer tubes, and these outputs in turn are fed to individual relays in the binary converter unit.

The outputs of the meniscus-transducers are amplified, and each is used to pulse one of the control grids of as many gate-tube circuits as there are manometer tubes. These gating circuits are also controlled by the output pulses of the discriminator. When a meniscus is reached, a pulse from the discriminator appears in the output circuit of the involved gate tube as a negative square wave and drives a signal-inverter and trigger stage. The output signal of the trigger is differentiated and the resultant pulse is fed to all the relay control tubes in the binary converter unit.

When the control grid of any relay control tube of the converter is pulsed by the binary counter while being pulsed by the trigger, a relay in the plate circuit of that tube closes to permit the IBM to read out. With the proper selection of contacts on the relays, it is possible to set up closed circuits for all digits required, i.e., zero to nine.

When the ADRMAN is used in conjunction with a force and pressure balance (Subsec. 2.6.1), the necessary computations for each point are completed in approximately 30 sec, using an IBM CPC for on-line data reduction, thus enabling the test engineer to make any necessary modifications in the parameter ranges.

It is sometimes desirable to have a single manometer to measure a pressure which differs widely from the remaining pressures in a test or which cannot be included in the transducer system for reason of its location. Those pressures which may be read on a manometer include supply pressure, model base pressure, or diffuser pressure. A remote reading manometer devised at JPL for such a purpose employs a servo-driven photo-cell which follows the mercury meniscus and remotely operates a counter by means of a second servo. The pressure may be directly digitized from the drum that drives the photo-cell up and down the tube.

Source: OAL

Pressure Lead Connections

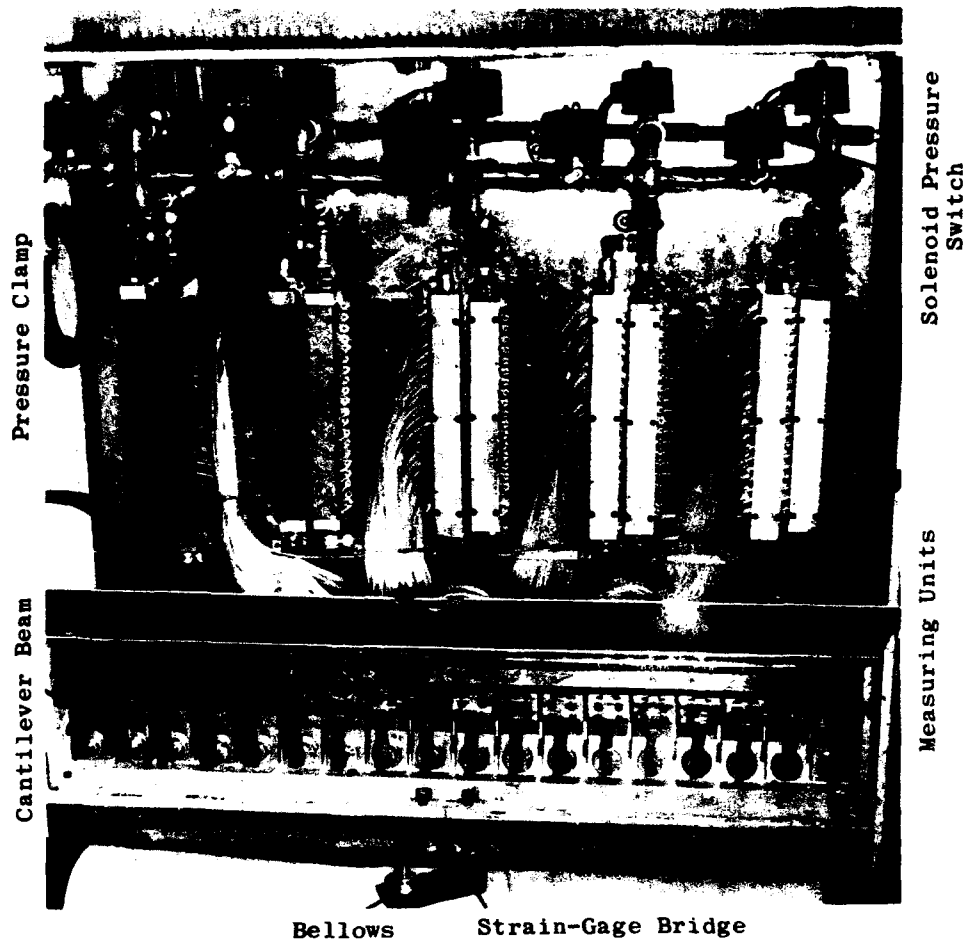
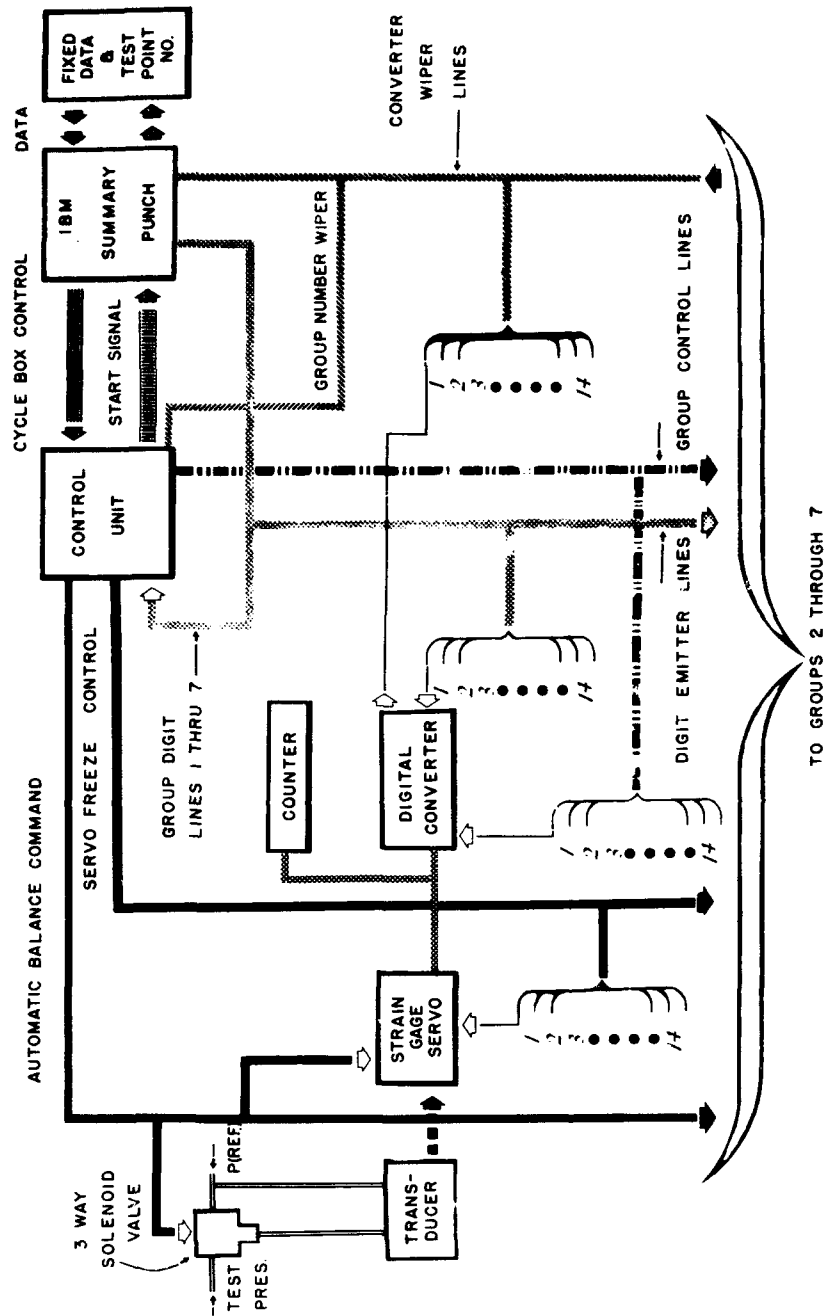


Fig. 10-1. OAL pressure transducer console.

Source: WADC



F g. 10-2. Flow diagram of WADC 98-channel pressure recording system.

Source: WADC

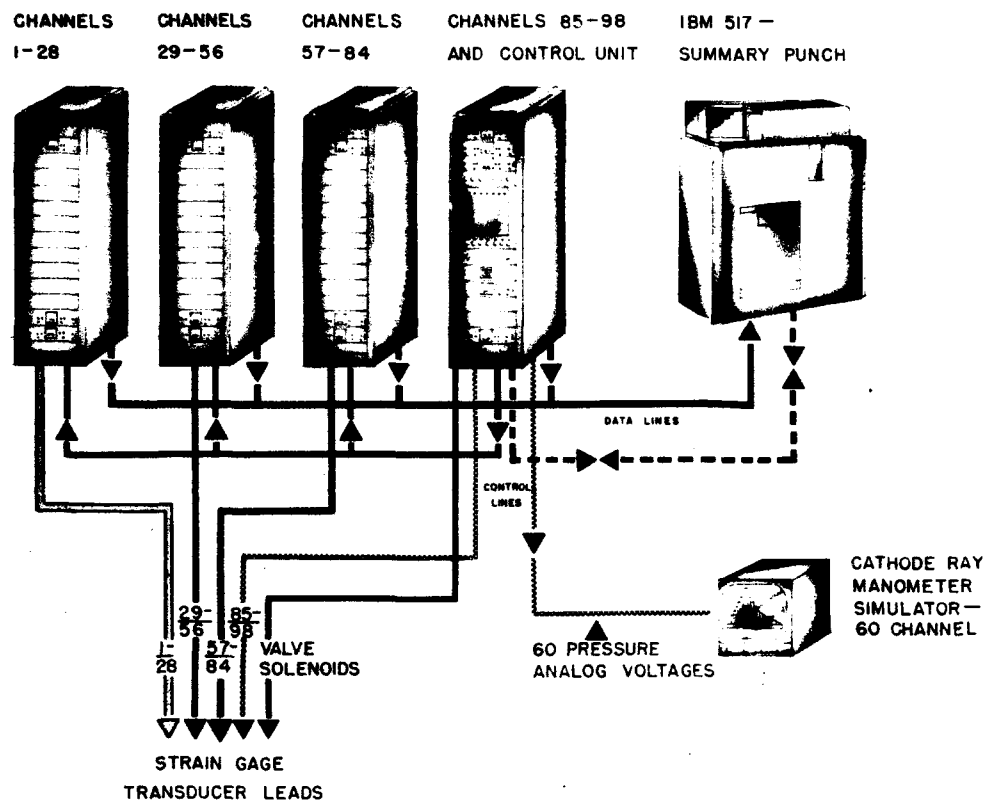


Fig. 10-3. WADC 98-channel automatic pressure recording system.

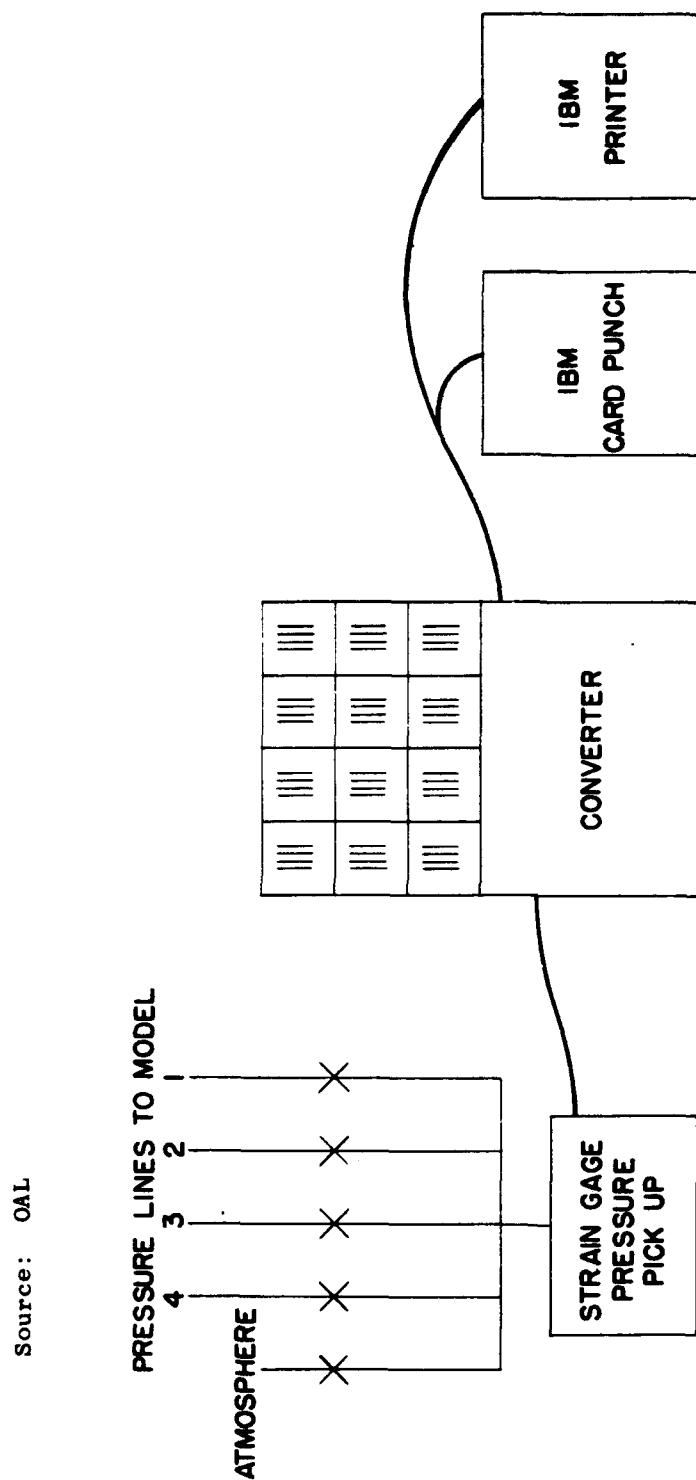


Fig. 10-4. OAL pressure data recording system.

Source: Boeing Aircraft Co.

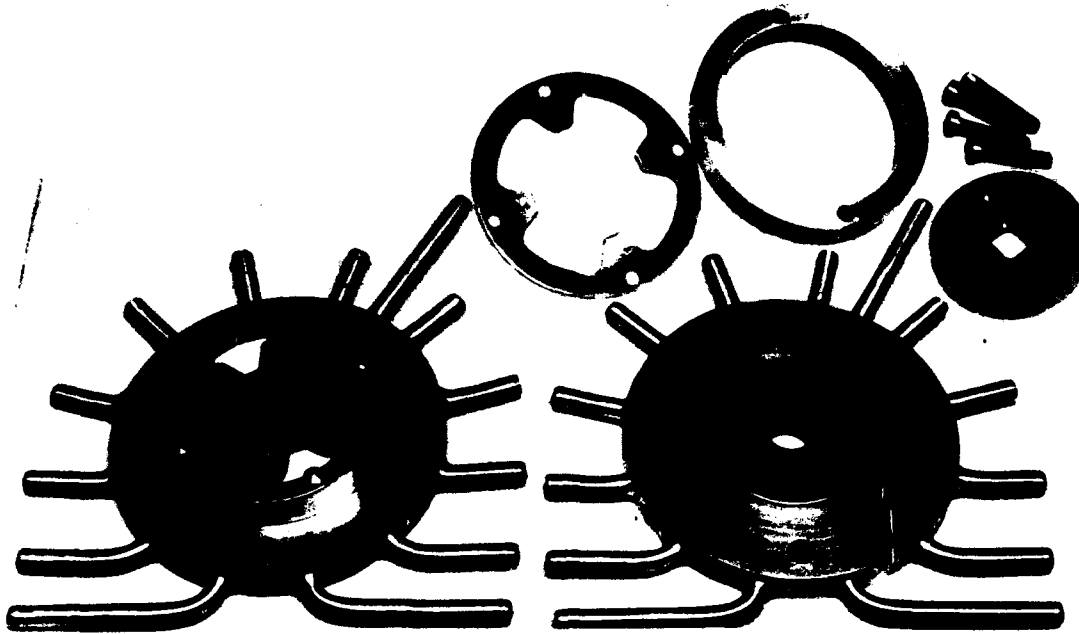


Fig. 10-5. Boeing 12-point pressure selector valve wafer assembly.

Source: Boeing Aircraft Co.

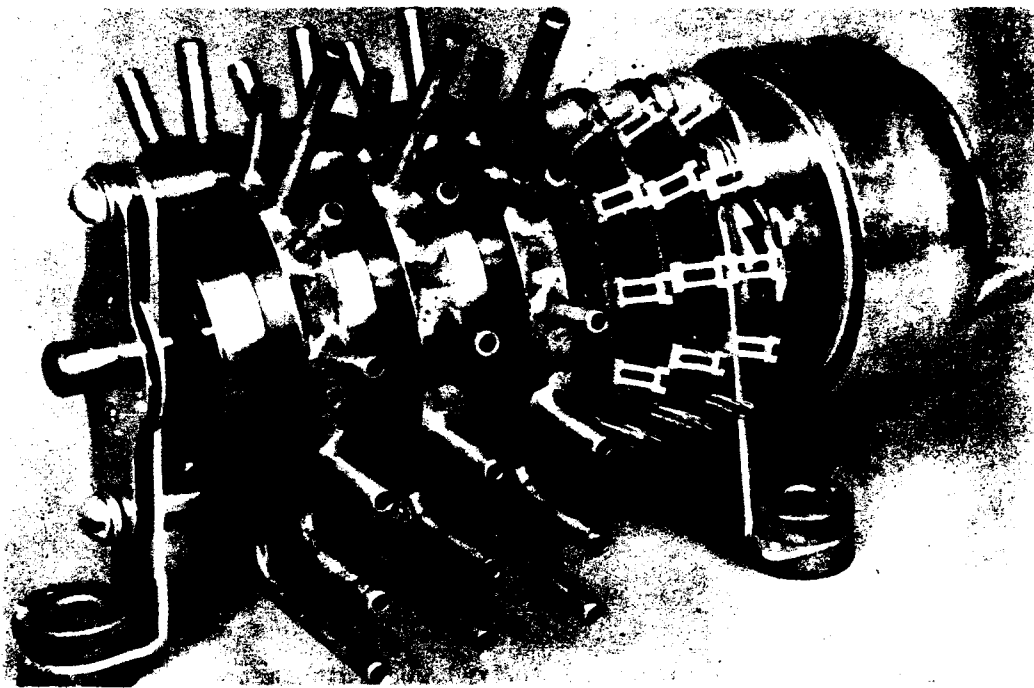


Fig. 10-6. Boeing 12-point pressure selector switch assembly.

Source: OAL

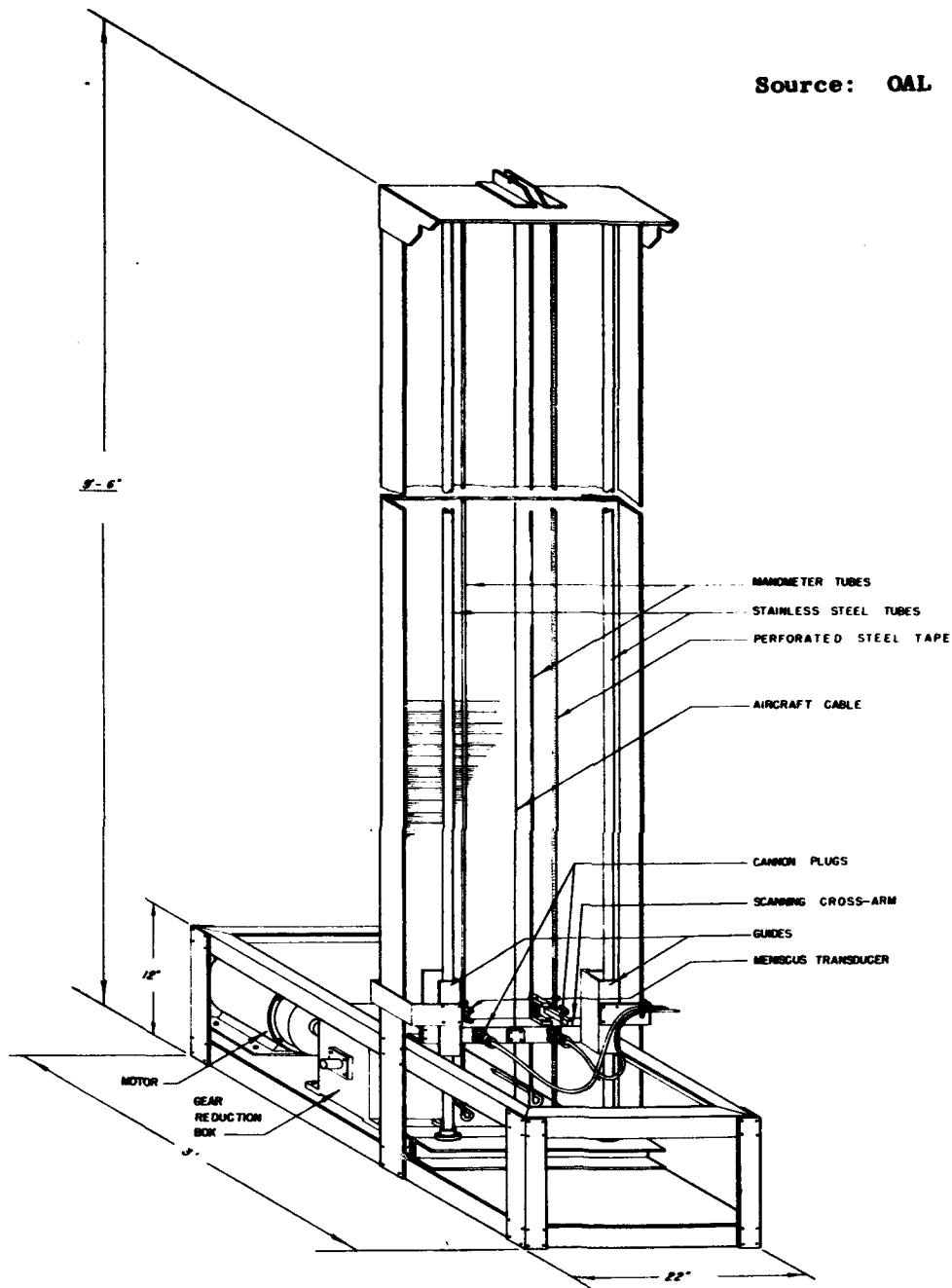


Fig. 10-7. Two-tube automatic digital recording manometer (ADRMAN).

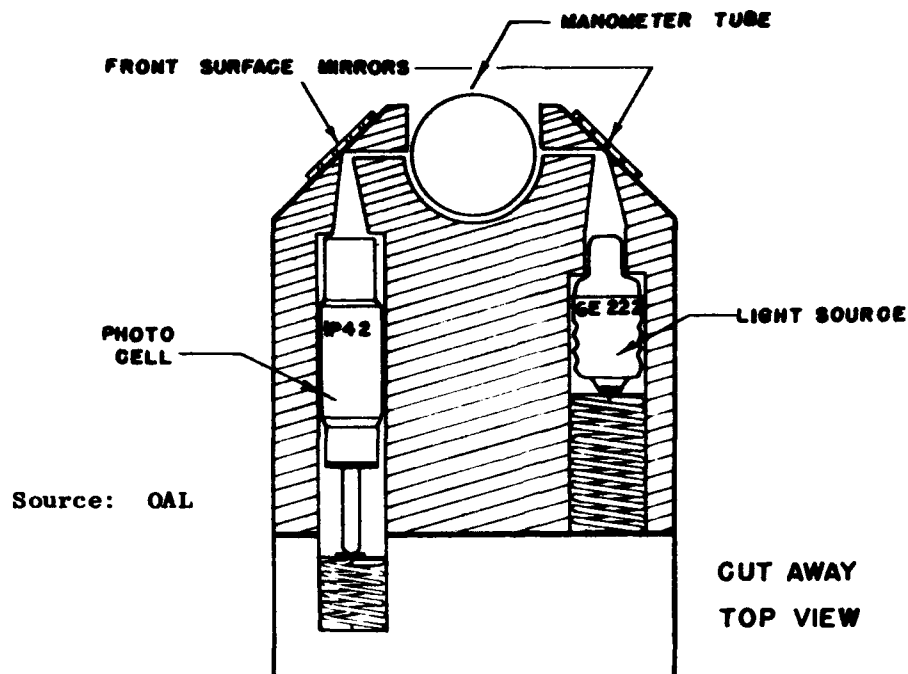


Fig. 10-8. ADRMAN meniscus transducer.

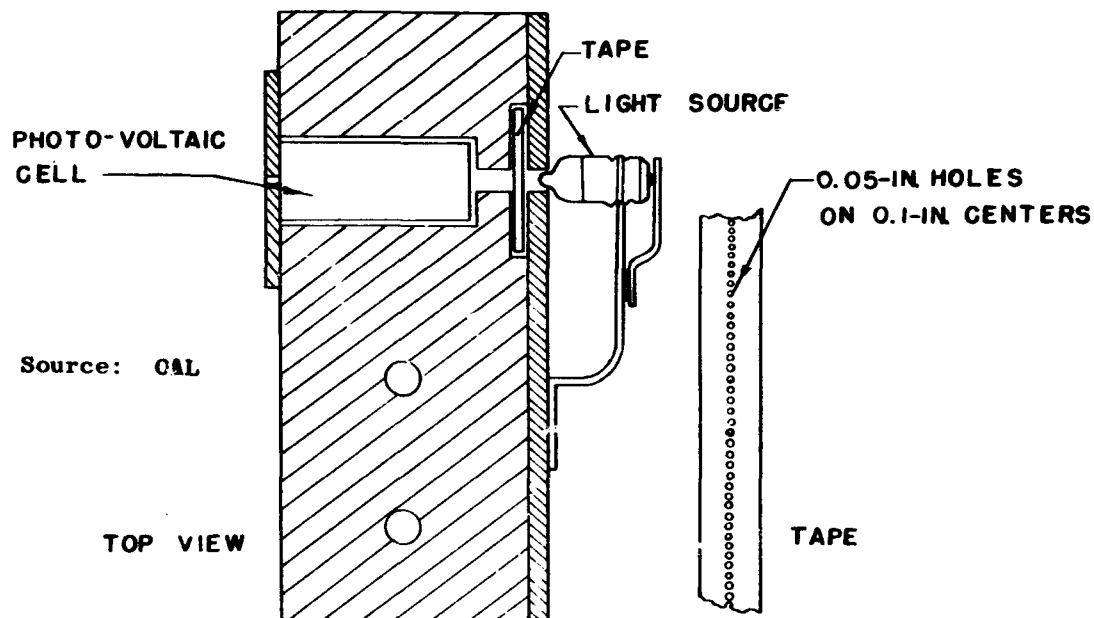


Fig. 10-9. ADRMAN counting head.

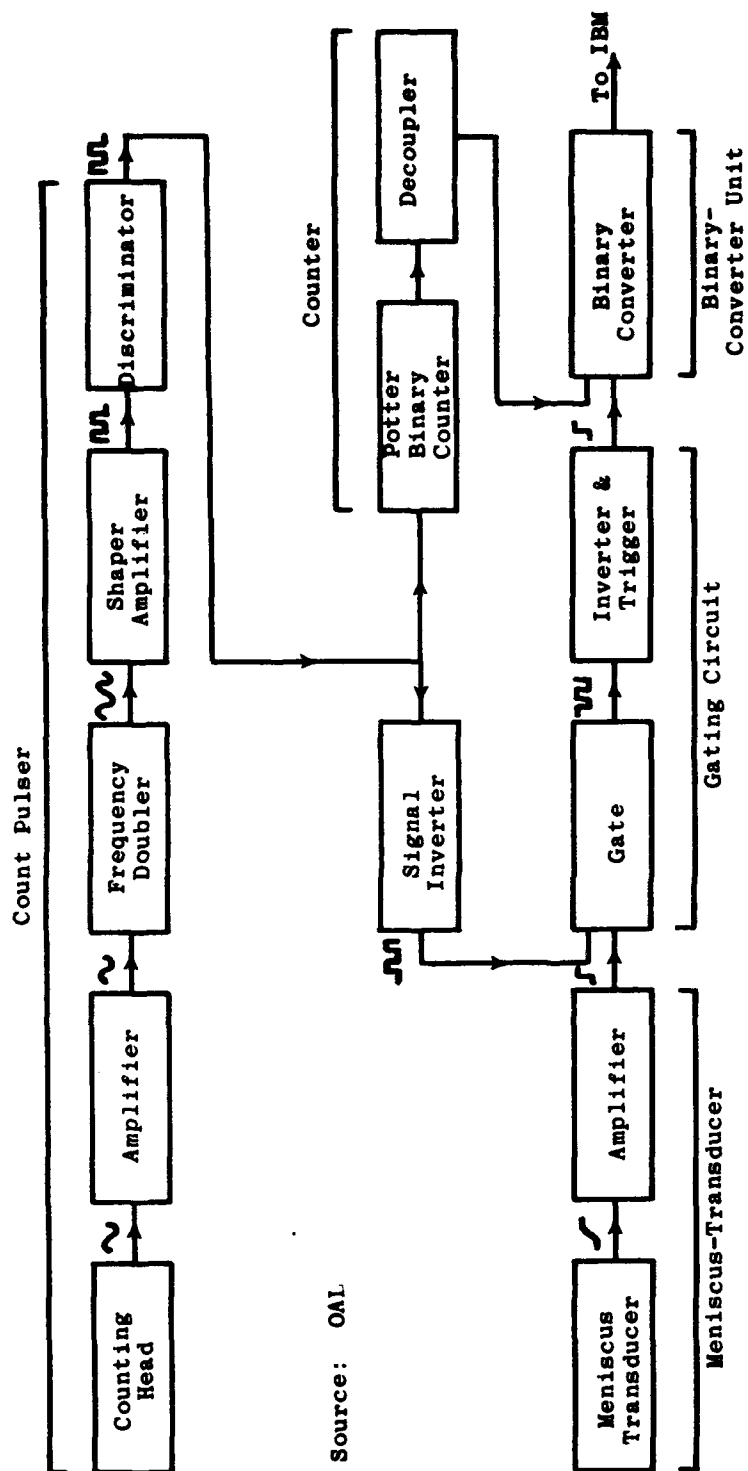


Fig. 10-10. Block diagram of digital recording manometer.

REFERENCES

1. Dean, R. C. Jr., et al. Aerodynamic Measurements. Fifth Printing, Gas Turbine Laboratory, Massachusetts Institute of Technology. Boston and New York: Eagle Enterprises, 1958.
2. Ower, E. and Johanson, F. C. The Design of Pitot-Static Tubes. ARC R and M 981, Aeronautical Research Council, August 1925.
3. Angus, R. W. "Errors in Pressure Readings Due to Wrong Gauge Connections," J. Am. Wat. W. Assn. (1937).
4. Fuhrmann, G. "Theoretische und Experimentelle Untersuchungen on Ballon Modellen," Dissertation Gottingen, 1912, Jahrb. Motorluft, Vol. 5 (1911-1912), p. 63.
5. Mills, H. F. "Experiments Upon Piezometers Used in Hydraulic Investigations," Proc. Am. Acad. Arts Sci. (1878).
6. Schuster, P. "Mitteilungen uber Forschungsarbeiten," Ver. deut. Ing. Forschungsheft, 82 (1905).
7. Allen and Hooper. "Piezometer Investigation," Trans. ASME, Vol. 54, 1932.
8. Rayle, R. E. An Investigation of the Influence of Orifice Geometry on Static Pressure Measurements. M.S. Thesis, Department of Mechanical Engineering, Massachusetts Institute of Technology, 1949.
9. Walchner, O. The Effect of Compressibility on the Pressure Reading of a Prandtl Pitot Tube at Subsonic Flow Velocity. NACA TM 917, November 1939.
10. Mollo-Christensen, Landahl, and Martuccelli. "A Short Static-Pressure Probe Independent of Mach Number," J. Aeronaut Sci. (August 1957), p. 625.
11. Goldstein, S. "A Note on the Measurement of Total Head and Static Pressure in a Turbulent Stream," Proc. Roy. Soc. London, Series A, Vol. 155, No. 886 (July 1936), pp. 570-575.
12. Fage, A. "On the Static-Pressure in Fully-Developed Turbulent Flow," Proc. Roy. Soc. London, Series A, Vol. 155 (July 1936), pp. 577-596.
13. Fage, A. "Turbulence in the Wake of a Body," ARC R and M 1510, Aeronautical Research Council, September 1932.

14. Towend, H. C. H. "Statistical Measurement of Turbulence in the Flow of Air Through a Pipe," Proc. Roy. Soc. London, Series A, Vol. 145 (1934), p. 180.
15. Applied Physics Laboratory, The Johns Hopkins University. Handbook of Supersonic Aerodynamics, NAVORD Report 1488, Vol. 5, Sec. 16, "Mechanics of Rarefied Gases," 1959.
16. Morkovin, M. V. "Design of a Device for Measurement of Free Stream Static Pressure at Supersonic Speeds," Aeronaut. Eng. Rev., Vol. 9 (December 1950), pp. 25-28.
17. Gettelman, C. C. and Krause, L. N. Characteristics of a Wedge with Various Holder Configurations for Static Pressure Measurements in Subsonic Gas Stream. NACA RM E51G09, September 1951.
18. Baker, V. D. Characteristics of a 3-Hole Yaw Probe. PWA-618, Pratt and Whitney Aircraft Co., July 1946.
19. Instrumentation Catalog. Flow Corporation, Arlington, Mass., November 1957.
20. Mollo-Christensen, E. and Lewis, S. "Measurement of Pressure Distribution on Oscillating Wings in Supersonic Flow. 1 -- Experimental Methods," Aeronaut. Eng. Rev. (August 1956), p. 138 (M.I.T. ASRL TR 57-1, December 1955).
21. Folsom. Summary of Pertinent Information for Designer and User. Review of the Pitot Tube. Report 142, Industry Program, University of Michigan, November 1955.
22. Gracey, W. Wind-Tunnel Investigation of a Number of Total-Pressure Tubes at High Angles of Attack. Subsonic, Transonic, and Supersonic Speeds. NACA TR 1303 (Supersedes TN 3641), 1957.
- 22a. Rogers, E. W. E. and Berry, C. J. Tests on the Effect of Incidence on Some Pressure Heads at High Subsonic Speeds. ARC CP41 (ARC 13,263) Aeronautical Research Council, July 1950.
23. Gracey, W., Coletti, D. E., and Russell, W. R. Wind Tunnel Investigations of a Number of Total-Pressure Tubes at High Angles of Attack. Supersonic Speeds. NACA TN 2261, January 1951.
24. Gracey, W., Letko, W., and Russell, W. R. Wind Tunnel Investigations of a Number of Total-Pressure Tubes at High Angles of Attack. Subsonic Speeds. NACA TN 2331, April 1951.
25. Humphreys, M. D. Effects of Compressibility and Large Angles of Yaw on Pressure Indicated by a Total Pressure Tube. NACA WR L-77, 1945.
26. Bennett, M. D. Calibration Test of a Full-Scale Pitot Probe for the Tartar Missile at Mach Number 1.50. OAL Report 510, September 1956.

27. Kiel, G. Total Head Meter with Small Sensitivity to Yaw. NACA TN 775, August 1935 (from Luftfahrt, May 1935, pp. 75-79).
28. Moffatt, M. Report on Kiel Probes. PWA-576, Pratt and Whitney Aircraft, October 1945.
29. Russell, W. R., Gracey, W., Letko, W., and Fournier, P. G. Wind Tunnel Investigations of Six Shielded Total-Pressure Tubes at High Angles of Attack. NACA TN 2530, November 1951.
- 29a. Gracey, W. and Scheithauer, E. F. Flight Investigation of the Variation of Static-Pressure Error of a Static-Pressure Tube with Distance Ahead of a Wing and a Fuselage. NACA TN 2311, March 1951.
30. Barker, M. "On the Use of Very Small Pitot Tubes for Measuring Wind Velocity," Proc. Roy. Soc. London, Series A, Vol. 101 (1922), p. 435.
- 30a. Hurd, C. W., Chesky, K. P., and Shapiro, A. H. "Influence of Viscous Effects on Impact Tubes," J. Appl. Mech. (Trans. ASME), Vol. 75 (June 1953), p. 253.
31. Chambre, P. L. The Theory of the Impact Tube in a Viscous Compressible Gas. Report HE-150-50, Engineering Research Project, University of California, 1948.
32. Gerdes, H. A., Brooks, D. M., and Kalina, J. F. "The Effect of Reynolds Number on Impact Tube Calibration." Naval Arch. Thesis, Massachusetts Institute of Technology, 1950.
33. Homann, F. "Einfluss Grosser Zahigkeit Bei Stromugun Zylinder," Forsch. Gebiete Ing., Vol. 7 (1936), pp. 1-10.
34. Hurd, C. W. and Chesky, K. P. "Experimental Investigation of the Effect of Viscous Forces Upon Pitot Tube Readings." Naval Engr. Thesis, Massachusetts Institute of Technology, 1951.
35. Lee, V. A. "Interference Effects from Total-Pressure Rakes in Supersonic Flow." M.S. Thesis, University of Texas, August 1955.
36. Bradfield, W. S. and Yale, G. E. "Small Pitot Tubes with Fast Pressure Response Time," J. Aeronaut. Sci., Vol. 18 (October 1951), pp. 697-698.
37. Gezilius, E. J. E. "Making Small Metal Tubes by Electrodeposition on Nylon Fibers," Rev. Sci. Instr., Vol. 21 (October 1950).
38. Young, A. D. and Maas, J. N. The Behavior of a Pitot-Tube in a Transverse Pressure Gradient. ARC R and M 1770, Aeronautical Research Council, September 1936.

39. Stanton, T. E., Marshall, D., and Bryant, C. N. "On the Conditions at the Boundary of a Fluid in Turbulent Motion," Proc. Roy. Soc. London, Series A, No. 97 (1920).
40. Page, A. and Faulkner, V. M. "An Experimental Determination of the Intensity of Friction on the Surface of an Airfoil," Proc. Roy. Soc. London, Series A, Vol. 129 (1930), pp. 378-410.
41. Dryden, H. L. Air Flow in the Boundary Layer Near a Plate. NACA TR 562, 1936.
42. Heenan, H. and Gilbert, W. "The Design and Testing of Centrifugal Fans," Proc. Inst. Civil Engs., Vol. 123 (1893-6), p. 272.
43. Coles, D. "Measurements in the Boundary Layer on a Smooth Flat Plate in Supersonic Flow." Ph.D Thesis, California Institute of Technology, 1953.
44. Bradfield, W. S. and Yale, G. E. Small Pitot Tubes with Fast Pressure Response Time. Memo. No. 1, Rosemount Engineering Laboratory, University of Minnesota.
45. Kumbruch, H. Pitot-Static Tubes for Determining the Velocity of Air. NACA TM 303, 1925 (from Forsch. Auf. Dem Gebiete Des Ing., No. 240, 1921).
46. Birdwell, J. M. Application of the von Karman Momentum Theorem to Turbulent Boundary Layers. NACA TN 2571, December 1951.
47. Johnson, R. C. Averaging of Periodic Pressure Pulsations by a Total Pressure Probe. NACA TN 3568, October 1955.
48. Tsien, H. S. "Notes on Aerodynamics of Compressible Fluids," Aeronautical Engineering Department, Massachusetts Institute of Technology, 1949.
49. Chambre, P. L. and Schaaf, S. A. "The Theory of the Impact Tube at Low Pressures," J. Aeronaut. Sci., Vol. 15 (December 1948), pp. 735-737.
50. Kane, E. D. and Maslach, G. J. Impact-Pressure Interpretation in a Rarefied Gas at Supersonic Speeds. NACA TN 2210, October 1950.
51. Lin, T. C. and Schaaf, S. A. Effect of Slip on Flow Near a Stagnation Point and in a Boundary Layer. NACA TN 2568, December 1951.
52. Sherman, F. S. New Experiments on Impact-Pressure Interpretation in Supersonic and Subsonic Rarefied Air Streams. NACA TN 2995, September 1953.
53. Talbot, L. Viscosity Corrections to Cone Probes in Rarefied Supersonic Flow at a Nominal Mach Number of 4. NACA TN 3219, November 1954.

54. High Speed Aerodynamics and Jet Propulsion, Vol. IX, Physical Measurements in Gas Dynamics and Combustion (edited by R. W. Ladenburg). Princeton: Princeton University Press, 1954.
55. Schaaf, S. A. and Cyr, R. R. "Time Constants for Vacuum Gage Systems," J. Appl. Phys., Vol. 20 (1949), pp. 860-863.
56. Maslach, G. J. "A Precision Differential Manometer," Rev. Sci. Instr., Vol. 23 (1952), pp. 367-369.
57. Pearcey, H. H. The Effect of the Condensation of Atmospheric Water Vapor on Total Head and the Measurements in the NPL High Speed Tunnels. ARC R and M 2249, Aeronautical Research Council, February 1944.
58. Taylor, G. I. Pitot Pressure in Moist Air. ARC R and M 2248, Aeronautical Research Council, January 1945.
59. Hansen, C. F. and Nothwang, G. J. Condensation of Air in Supersonic Wind Tunnels and its Effects on Flow About Models. NACA TN 2690, April 1952.
60. Cawthon, J. A. Water Vapor Condensation Effects in the Ordnance Aerophysics Laboratory Supersonic Wind Tunnel. OAL Report 340-1 (CM 872), August 1956.
61. Thomson, T. A. A Multi-Tube Manometer for an Intermittent Supersonic Wind Tunnel. Australian Note A.R.L. 56, October 1955.
62. OAL Handbook for Testing in the Jet Engine Test Facilities. Convair, Daingerfield, Texas.
63. Kaye, G. W. C. and Laby, T. H. Tables of Physical and Chemical Constants. Tenth Edition. New York: Longmans, Green and Co., 1948.
64. Pankhurst, R. C. and Holder, D. W. Wind Tunnel Technique. London: Pitman and Sons, 1952.
65. Shaw, H. Note on the Conversion of an Electric Plug and Socket into a Multitube Pneumatic Connection. ARC R and M 9561, Aeronautical Research Council, 1946.
66. Ower, E. Measurement of Air Flow. London: Chapman and Hall, 1949.
67. Maslach, G. J. and Sherman, F. S. Design and Testing of an Axisymmetric Hypersonic Nozzle for a Low Density Wind Tunnel. WADC TR 56-341, 1957.

68. Sherman, F. S. New Experiments on Impact Pressure Interpretation in Supersonic and Subsonic Rarefied Air Streams. NACA TN 2995, September 1953.
69. Maslach, G. J. "A Precision Differential Manometer." Rev. Sci. Instr., Vol. 23, No. 7 (July 1952), pp. 367-369.
70. Kavanau, L. L. Base Pressure Studies in Rarefied Supersonic Flows. Report HE-150-125, Engineering Project, University of California, November 1954.
71. Schaaf, S. A. and Cyr, R. R. "Time Constants for Vacuum Gage Systems." J. Appl. Phys., Vol. 20, No. 9 (September 1949), pp. 860-863.
72. Larson, H. "Accurate Measurement of Small Pressure Differences Using the Foxboro Micromanometer." B.S. Thesis, Department of Mechanical Engineering, Massachusetts Institute of Technology, May 1952.
73. Eichhorn, R. and Irvine, T. F., Jr. "Description of Sensitive Micromanometer," Rev. Sci. Instr., Vol. 29, No. 1 (January 1958), pp. 23-27.
74. Poggi, L. "Un Nuovo Tipo Di Micromanometro Differenziale," Rivista Misure e Regolazioni, Vol. 5 (September-October 1955). (Also Publication XVI, No. 752 of the Facolta d'Ingeneria di Pisa).
75. Mason, H. L. "Sensitivity and Life Data on Bourdon Tubes," Trans. ASME, Vol. 78 (January 1956), p. 65.
76. Church, R. J. "Pressure Gage Elements," Instrumentation, Vol. 10, No. 6 (November-December 1957), pp. 21-24.
77. Pressure Transducers. TN 4. Colvin Laboratories, Inc., East Orange, N. J., June 1955.
78. Statham Instruments. Statham Laboratories, Inc., Los Angeles, California.
79. Laurmann, J. A. Experimental Investigation of the Flow About the Leading Edge of a Flat Plate. Engineering Report HE-150-126, University of California, October 1954.
80. Liccini, L. L. NOL Hypersonic Tunnel No. 4 Results -- VII. Development and Calibration of Mass Flow Probes in Hypersonic Flow. NAVORD Report 4078, November 1955.
81. Sinclair, A. R. and Robins, A. W. A Method for the Determination of the Time Lag in Pressure Measuring Systems Incorporating Capillaries. NACA TN 2793, September 1952.

82. Ducoffe, A. L. "Pressure Response in Supersonic Wind Tunnel Instrumentation," J. Appl. Phys., Vol. 24, No. 11 (1953), pp. 1343-1354.
83. David, W. T. Lag in Pressure Systems at Extremely Low Pressures. NACA TN 4334, September 1958.
84. Aldrich, J. F. L. and Tripoli, S. "Error in Non-Equilibrium Pressure Measurements Following Step and Ramp Pressure Changes." SAE Engineering Paper 587, Douglas Aircraft Company, March 1958.
85. Bauer, R. C. A Method of Calculating the Response Time of Pressure Measuring Systems. AEDC TR 56-7 (ASTIA No. AD-98978), November 1956.
86. Kopal, Z., et al. Tables of Supersonic Flow of Air Around Cones, M.I.T. TR No. 1, Massachusetts Institute of Technology, 1947.
87. Centolanzi, F. J. Characteristics of a 40° Cone for Measuring Mach Number, Total Pressure, and Flow Angles at Supersonic Speeds. NACA TN 3967, May 1957.
88. van der Bouwhuysen, J. Standard Conical Probes. NAA FDL No. 53-3, North American Aviation, January 1953.
89. Cawthon, J. A. Wind Tunnel Investigation of a Five-Orifice Truncated-Cone Probe Designed for Use as a Nozzle Calibration Instrument. OAL Report 340-5, November 1957.
90. Moeckel, W. E. and Connors, J. F. Charts for the Determination of Supersonic Airflow Against Inclined Planes and Axially Symmetric Cones. NACA TN 1373, July 1947.
91. Schueler, C. J., Jr. Handbook for Testing at the OAL Supersonic Wind Tunnel. APL TG-54, Rev. 4 (OAL Report 46), October 1956.
92. Covey, R. E. Calibration of the 20 Inch Supersonic Wind Tunnel at the Jet Propulsion Laboratory. Reports SWT 12-C15 and 12-C-16, Jet Propulsion Laboratory.
93. Willmarth, W. W. "On the Measurement of Surface Pressure with a Static Probe," J. Aeronaut. Sci., Vol. 20 (June 1953), pp. 438-439.
94. Ormsby, R. B. Jr. An Angle-of-Attack and Angle-of-Yaw Indicator Using a Direct Reading Simple Strain Gage Circuit on Sting Balances, DTMB Aero 855 (also DTMB 885). David Taylor Model Basin, February 1954.
95. Murray, W. N. and Stein, P. K. Strain Gage Techniques. Parts 1 and 2. Special Summer Program Notes, Massachusetts Institute of Technology, 1956.

96. Perry, C. C. and Lissner, H. R. The Strain Gage Primer. New York: McGraw-Hill Book Co., 1955.
97. SR-4 Strain Gages for Stress Analysis. Bulletin 4452, Baldwin-Lima-Hamilton Corporation, 1955.
98. Kuczynski, G. C. "A Note on the Remarkable Stability of the Alloy Used in SR-4 Gages," Testing Topics, Vol. 9, No. 3, Baldwin-Lima-Hamilton Corporation, 1954.
99. How to Apply SR-4 Strain Gages. Bulletin 279-B, Testing Equipment Department, Baldwin-Lima-Hamilton Corporation, 1951.
100. Tarbox, J. "Strain Gages," CEC Recordings, Vol. 9, Nos. 2 and 3, 1955.
101. Peirce, G. R. Practical Considerations in Designing AC and DC Bridges. ISA Preprint No. 53-7-1, Instrument Society of America.
102. Koch, J. J., Boiten, R. G., et al. Strain Gauges--Theory and Application. Phillips Technical Library. New York: Elsevier Press, Inc., 1952.
103. Hetenyi, M. Handbook of Experimental Stress Analysis. New York: John Wiley and Sons, Inc., 1950.
104. McFarland, K. H. and Dimeff, J. Problems Involved in Precision Measurements with Resistance Strain Gages. AGARD Report 12, February 1956.
105. Westkaemper, J. C. Some Sources and Magnitudes of Strain Gage Errors. OAL Memo 130, June 1953.
106. Campbell, W. R. Errors in Indicated Strain for a Typical Wire Strain Gage Caused by Prestraining, Temperature Changes and Weathering. NACA TN 1011, April 1946.
107. Campbell, W. R. Performance Tests of Wire Strain Gages. VI-Effect of Temperatures on Calibration Factor and Gage Resistance. NACA TN 1456, January 1948.
108. Campbell, W. R. Tests of Six Types of Bakelite-Bonded Wire Strain Gages. NACA TN 1656, July 1948.
109. Symposium on Elevated Temperature Strain Gages. ASTM Special Tech. Publ. No. 230. American Society for Testing Materials, 1958.
110. Westkaemper, J. C. Some Notes on Using Wire to Temperature Compensate Strain Gage Bridges. OAL Memo 131, June 1953.
111. Methods for the Improvement of Results Obtainable with Commercial Type Bonded Strain Gages. Southern California Co-operative Wind Tunnel, California Institute of Technology, 1952.

112. Tonkin, G. P. Elevated Stagnation Temperature and Strain Gauge Balances in the Instrumentation of a Supersonic Wind Tunnel. AGARD Report 15, February 1956.
113. Wolko, H. S. and Carpenter, J. E. Final Report on Development of a High Temperature Strain Gauge. Report 1G-800-S-11, Cornell Aeronautical Laboratory, December 1953.
114. Lightfoot, J. R. and White, C. E. Special Application of Strain Gauge Balances Used in Supersonic and Hypersonic Wind Tunnels at the U.S. Naval Ordnance Laboratory. NATO AGARD Report 8, February 1956.
115. Liccini, L. L. NOL Hypersonic Tunnel No. 4 Results -- IX. The Development of a Water-Cooled Strain-Gage Balance (Including Sting Effects) and its Application to a Study of Normal Force and Pitching Moments of a Cone and Cone-Cylinder at Mach Numbers 5 to 8. NAVORD Report 4334, August 1956.
116. Burkheimer, G. E. Design of Strain Gauge Systems for Wind Tunnel Balances. OAL Memo 133, 1951.
117. Anderson, J. R. Strain Gauge Balances for Wind Tunnels: An Outline of Practice in the United Kingdom. AGARD Report 5 (RAE TN Aero. 2434), February 1956.
118. Rebuffet, P. Some Strain Gauge Balances Used in French Wind Tunnels. AGARD Report 6-T, February 1956.
119. Smith, T. L. Special Types of Internal Strain Gauge Balances. AGARD Report 7, February 1956.
120. Hansen, R. M. Mechanical Design and Fabrication of Strain-Gage Balances. AGARD Report 9, February 1956.
121. Shantz, I., Gilbert, B. T., and White, C. E. NOL Wind-Tunnel Internal Strain-Gage Balance System. NAVORD Report 2972, September 1953.
122. Ormsby, R. B., Jr. Notes on the Design, Calibration, Instrumentation and Maintenance of Strain-Gage Balances. DTMB Aero Report 854, November 1953.
123. Wilson, E. R. Aluminum as a Material for Strain Gauge Beams. OAL Memo 122, June 1955.
124. Gordon, C. C. The Effect of Internal Balance Section Size and Indicator Sensitivity on Data Repeatability (Unpublished OAL Report).
125. Tate, R. E. and Taylor, A. L. An Investigation of the Axial-Force Characteristics of a Parabolic Body of Revolution (NACA RM-10) at Various Reynolds Numbers and Mach Numbers 1.50, 1.73, 2.00, 2.23, and 2.50. OAL Report 375, May 1955.

126. Schueler, C. J. and Strike, W. T. An Investigation of the Lift, Drag, and Pitching Moment Characteristics of AGARD Calibration Models A and B. AEDC TN 55-34, February 1956.
127. Fixing Boundary-Layer Transition on Supersonic Wind Tunnel Models. JPL Progress Report 20-256, California Institute of Technology, August 1955.
128. Turner, R. L. Analytical and Experimental Methods for the Determination of the Proper Axial Station for Attachment of an Internal Balance Within a Model to Prevent Grounding of the Model and Balance Under Load. OAL Memo 115, February 1957.
129. Hansen, R. W. "Evaluation and Calibration of Wire-Strain-Gage Wind Tunnel Balances Under Load." NACA-LMAL paper presented at AGARD Wind Tunnel and Model Test Panel in Rome, February 1956.
130. Tate, R. E. A Proposed Method for Measuring Deflection of any Model with Only One Moment Bridge in Each Plane. OAL TM-50, January 1955.
131. Bruman, J. R. Equations for Wind-Tunnel Force Data Reduction. Publication No. 58. Jet Propulsion Laboratory, California Institute of Technology, December 1955.
132. van der Blik, J. A. The Zero Lift Drag of Full and Half Models of a Body of Revolution. NAE Report LR-139, National Aeronautical Establishment, Ottawa, Canada, 1955.
133. Patterson, R. T. An Investigation of the Use of Spacers in the Boundary Layer of a Supersonic Air Stream for Testing Semi-Bodies of Revolution. DTMB Aero Report 817, May 1952.
134. Patterson, R. T. Balance Number 69 (1-Inch Wall Balance); Description, Instructions and Corrections. DTMB Aero Memo 49, May 1956.
135. Eley, H. O. Proposal for Six-Component Force and Pressure Balance (-34 Balance). OAL Memo Report 56, November 1952.
136. Eley, H. O. Fundamental Operational Principles of the OAL-34 Balance Proposal. OAL Memo Report 59, January 1953.
137. Latz, R. N. Design of a Two Component Micro-Balance for Low Density Wind Tunnels. Engineering Project Report HE-150-124, University of California, August 1954.
138. Orlik-Ruckemann, K. Methods of Measurement of Aircraft Dynamic Stability Derivatives. NAE Report 1957-4 (Quarterly Bulletin), National Aeronautical Establishment, Canada, October-December 1957.

139. Radt, H. S. and Bicknell, J. Apparatus for Measurement of Damping-in-Pitch Derivatives in a Transonic Wind Tunnel. TACP Report 13, Aeronautical Engineering Department, Massachusetts Institute of Technology, December 1954.
140. Beam, B. H. Wind Tunnel Test Technique for Measuring the Dynamic Rotary Stability Derivatives Including the Cross Derivatives at High Mach Numbers. NACA TN 3347, January 1955.
141. Lessing, H. C., Fryer, T. B., and Mead, M. H. A System for Measuring the Dynamic Lateral Stability Derivatives in High-Speed Wind Tunnels. NACA TN 3384, 1954.
142. Oltronix Dampometer. Brochure DM-6, Oltronix Electronic Instrument Designers and Suppliers, Atlanta, Ga., January 1959.
143. Bower, C. W. Survey of Analogue-to-Digital Converters. NBS Report 2755, National Bureau of Standards, July 1953 (also J. Instr. Am., December 1954).
144. Webb, E. E., Talley, J. W., and Martin, C. G. ADHEC Analog-to-Digital High-Speed Electronic Converter. OAL Memo 97, September 1957.
145. Gordon, C. C. Linearity of ADHEC Units. OAL Memo 117, July 1957.
146. Jackson, C. E. and Hansen, A. T. W. Automatic Plotting of Wind Tunnel Test Data. OAL Memo 82, June 1955.
147. Hollitch, R. S. and Hawkes, A. K. A Catalog of Devices Useful in Automatic Data Reduction. WADC TR 54-519, Part II, First Revision (Supersedes Part II, dated November 1954), July 1956.
148. Operative Principles of Brown Electronic Continuous Balance Potentiometer Pyrometers. Bulletin No. 15-6, Brown Instrument Company (Minneapolis-Honeywell Regulator Co., Philadelphia, Pa.), 1943.
149. Bialer, M. and Crow, T. T. Precision Potentiometers Approaching Infinite Resolution. WADC TN 56-61, February 1956.
150. Heidmann, M. F. and Priein, R. J. "A Modified Sodium-Line Reversal Technique for the Measurement of Combustion Temperatures in Rocket Engines," J. Am. Rocket Soc. (July-August 1953).
151. High Speed Aerodynamics and Jet Propulsion, Vol. IX. Physical Measurements in Gas Dynamics and Combustion (edited by R. W. Ladenburg). Princeton: Princeton University Press, 1954.
152. Ames Research Staff. Equations, Tables, and Charts for Compressible Flows. NACA Report 1135, 1953.

153. DeFrate, L. A. "Application of the Interferometer to the Study of Boundary Layers." Sc.D Thesis, Massachusetts Institute of Technology, 1950.
- 153a. Stalder, J. R., Rubesin, M. W., and Tendeland, T. A Determination of the Laminar-Transitional and Turbulent Boundary Layer Temperature Recovery Factor on a Flat Plate in Supersonic Flow. NACA TN 2077, June 1950.
- 153b. Kaye, J. "Survey of Friction Coefficients, Recovery Factor, and Heat Transfer Coefficients for Supersonic Flow," J. Aeronaut. Sci. (February 1954), pp. 117-129.
- 153c. Scadron, M. D., Gettelman, C. C., and Pack, G. J. Performance of Three High Recovery Factor Thermocouple Probes for Room Temperature Operation. NACA RM E50129, December 1950.
- 153d. Goldstein, D. L. and Scherrer, R. Design and Calibration of a Total-Temperature Probe for Use at Supersonic Speeds. NACA TN 1885, May 1949.
154. Burton, R. A. "Notes on the Multiple Source Schlieren System," J. Opt. Soc. Am., Vol. 41 (November 1951), pp. 858-859.
155. Ladenburg, R., Van Voorhis, C. C. and Winckler, J. Interferometric Study of Supersonic Phenomena. Part II: The Gas Flow Around Various Objects in a Free Homogeneous Supersonic Air Stream. Report 93-46. Inyokern, Calif.: U. S. Naval Ordnance Test Station, September 1946.
156. McAdams, W. H. Heat Transmission. New York and London: McGraw-Hill Book Company, Inc., 1942.
157. Moffatt, E. M. "Errors in High Temperature Probes for Gases," ASME Preprint No. 48-A-52, 1948.
158. Moffatt, E. M. "Multiple Shielded High Temperature Probes--Comparison of Experimental and Calculated Errors," SAE Preprint No. T13, January 1952. Also in SAE Quart. Trans., Vol. 6 (October 1952).
159. Moffatt, E. M. Calibration Report No. 5. The Airflo Instrument Co., Glastonbury, Conn., November 1949.
160. Mack, S. F. and Schaaf, S. A. Viscous Effects on Stagnation-Point Temperatures. Report No. HF-150-96, Institute of Engineering Research, University of California, November 1951.
161. Diederichs and Andrae. Experimental Mechanical Engineering, Vol. 1. New York: John Wiley and Sons, 1946.
162. Busse, J. "Liquid in Glass Thermometers." Temperature - Its Measurement and Control in Science and Industry. New York: Reinhold Company, 1941, pp. 228-256.

163. Hottel, H. C. and Kalitinski, A. "Temperature Measurements in High Velocity Air Streams," J. Appl. Mech., Vol. 12 (1945).
164. Buckland, B. O. and Stack, S. S. "Thermocouples for Testing Steam Turbines." Temperature - Its Measurement and Control in Science and Industry. New York: Reinhold Company, 1941, pp. 884-897.
165. Baker, H. D. Manual on Thermometry. Pratt and Whitney Aircraft, 1950.
166. Mullikin, H. F. "Gas Temperature Measurement and the High-Velocity Thermocouple." Temperature - Its Measurement and Control in Science and Industry. New York: Reinhold Company, 1941, pp. 775-804.
167. Eckert, E. Temperature Recording in High Speed Gases. NACA TM 983, 1941.
168. Winkler, E. M. Stagnation Temperature Probes for Use at High Supersonic Speeds and Elevated Temperatures. NAVORD Report 3834, October 1954.
169. Pirani, M. and von Wagenheimer, G. "Ein Thermoelement fur Hochste Temperaturen," Zeitschrift fur Technische Physik., Vol. 6, No. 7A (1925), pp. 358-359.
170. Weber, R. L. Heat and Temperature Measurements. New York: Prentice Hall, 1950.
171. Dike, P. H. Thermoelectric Thermometry. Tech. Publication EN-33a(1). Leeds and Northrup Company, Philadelphia, Pa., September 1954.
172. Roeser, W. F. "Thermoelectric Thermometry." Temperature - Its Measurement and Control in Science and Industry. New York: Reinhold Company, 1941, pp. 180-205.
173. Dahl, A. I. "The Stability of Bare-Metal Thermocouples in Air from 800 - 2200°F." Temperature - Its Measurement and Control in Science and Industry. New York: Reinhold Company, 1941, pp. 1238-1266.
174. Homewood, C. F. "Factors Affecting the Life of Platinum Thermocouples." Temperature - Its Measurement and Control in Science and Industry. New York: Reinhold Company, 1941, pp. 1272-1280.
175. Thermocouples, Assemblies, Parts and Accessories. Catalogue EN-S2, Leeds and Northrup Company, Philadelphia, Pa., 1952.
176. Standard Conversion Tables for Leeds and Northrup Thermocouples. Catalogue No. 31031, Leeds and Northrup Company, Philadelphia, Pa.

177. Schulze, A. "Metallic Materials for Thermocouples," Symposium on Gas Temperature Measurements, J. Inst. Fuels, Vol. 12 (March 1939).
178. Anderson, A. R. and MacKenzie, D. G. Materials for High (2500°-4000°) Gas Engine Temperature Measurements. SAE Preprint No. 158B. New York: Society of Automotive Engineers, April 1960.
179. White, W. P. "Leakage Control by Shielding." Temperature - Its Measurement and Control in Science and Industry. New York: Reinhold Company, 1941.
180. Electrical Measuring Instruments for Research, Teaching and Testing. Catalogue E, Leeds and Northrup Company, Philadelphia, Pa., 1940.
181. Galvanometers. Bulletin No. 320, Rubicon Instruments Div., Minneapolis-Honeywell Regulator Co., Philadelphia, Pa.
182. Type K Potentiometers and Accessories. Catalogue E-50B, Leeds and Northrup Company, Philadelphia, Pa.
183. Potentiometers. Bulletin No. 270, Rubicon Instrument Div., Minneapolis-Honeywell Regulator Company, Philadelphia, Pa.
184. Potentiometer Pyrometers. Catalogue No. 1105, Brown Instrument Company, Minneapolis-Honeywell Regulator Company, Philadelphia, Pa., 1944.
185. White, W. P. "Sensitive Moving Coil Galvanometers," Phys. Rev., Vol. 19 (November 1904).
186. Blackshear, P. L. Sonic Flow Orifice Temperature Probes for High Gas-Temperature Measurements. NACA TN 2167, September 1950.
187. Cesaro, R. S., Koenig, R. J., and Pack, G. J. Experimental Analysis of a Pressure Sensitive System for Sensing Gas Temperature. NACA TN 2043, 1950.
188. Clark, J. A. and Rohsenow, W. M. A New Method for Determining the Static Temperature of High-Velocity Gas Streams. ASME Preprint No. 51-SA-33, 1951. Also in Mech. Engr., Vol. 73 (1951), p. 750.
189. Moffatt, E. M. Report on Cylindrical Total Temperature Probes. PWA 599, Pratt and Whitney Aircraft Company, May 1945.
190. Wildhack, W. A. "A Versatile Pneumatic Instrument Based on Critical Flow," Rev. Sci. Inst., Vol. 21, No. 1 (January 1950), p. 25.
191. Smelt, R. and Sivells, J. C. Design and Operation of Hypersonic Wind Tunnels. AGARD Report 135, July 1957.

192. Hartwig, F. W., Bartsch, C. A., and McDonald, H. "Miniaturized Heat Meter for Steady-State Aerodynamic Heat Transfer Measurements," J. Aeronaut. Sci., Vol. 24 (March 1957).
193. Durgin, F. H. "The Measurement of Heat Transfer Using a Step Function in Velocity (MIT)," The Readers Forum, J. Aeronaut. Sci. (July 1956).
194. Jack, J. R. and Diaconis, N. S. Heat-Transfer Measurement on Two Bodies of Revolution at a Mach Number of 3.12. NACA TN 3776, October 1956.
195. "Cornell Instruments for Shock Tubes," Aviation Week (October 1956), p. 51.
196. Monaghan, R. J. and Cooke, J. R. The Measurement of Heat Transfer and Skin Friction at Supersonic Speeds. Part III--Measurements of Overall Heat Transfer and of the Associated Boundary Layers on a Flat Plate at $M = 2.43$. ARC TR CP 139 (TN Aero 2129), Aeronautical Research Council, December 1951.
197. Hilton, W. F. High Speed Aerodynamics. New York: Longmans, Green and Company, 1951, p. 464.
198. Woods, G. P. Optical Methods for Examining the Flow in High-Speed Wind Tunnels. Part II, Interferometer Methods. AGARD 23, November 1956.
199. Westkaemper, J. C. An Investigation of Focusing and Stereoscopic Schlieren Systems for Use in the OAL Wind Tunnel. OAL Memo 57, November 1952.
200. "New System Improves Shock Wave Pictures," Aviation Week (October 1957), p. 64.
201. Schardin, H. Toepler's Schlieren Method: Basic Principles for Its Use and Quantitative Evaluation. DTMB Translation 156, July 1947 (translated by F. A. Raven from Forschung auf dem Gebiete des Ing., 367, Vol. 5, July-August 1934).
202. McLanahan, C. Shock Wave Photography Using Scotchlite Reflective Sheeting. NAVORD Report 6760, June 1960.
203. Holder, D. W. and North, R. J. The Toepler Schlieren Apparatus. ARC R and M 2780, Aeronautical Research Council, April 1950.
204. Speak, G. S. and Walter, D. J. Optical Considerations and Limitations of the Schlieren Method. RAE TN IAP 968, Aeronautical Research Council, January 1950.
205. Mair, W. A. "The Sensitivity and Range Required in a Toepler Schlieren Apparatus for Photography of Supersonic Flow," Aeronaut. Quart., Vol. 4 (August 1952).

206. Burton, R. A. "The Application of Schlieren Photography to Fluid Flow and Heat Transfer Analysis." M.S. Thesis, The University of Texas, 1951.
207. Liepmann, H. W. and Puckett, A. E. Introduction to Aerodynamics of a Compressible Fluid. New York: John Wiley and Sons, 1947.
208. Schardin, H. "Die Schlierenverfahren und Ihre Anwendungen," Ergeb. Exakt. Naturw., Vol. 20 (1942), pp. 310-314.
209. Schmidt, E. "Schlierenaufnahmen des Temperaturfeldes" (Schlieren Photographs of the Temperature Field), Forschung auf dem Gebiete des Ing., Vol. 3 (1932), p. 181.
210. Schaeffer, H. J. "Physical Optic Analysis of Image Quality in Schlieren Photography," J. Soc. Motion Picture Engrs. (October 1949).
211. Kantrowitz, A. and Trimpi, R. L. "A Sharp-Focusing Schlieren System," J. Aeronaut. Sci. (May 1950).
212. Mortensen, J. E. "An Improved Schlieren Apparatus Employing Multiple Slit Gratings," Rev. Sci. Inst., Vol. 21, No. 1 (1950).
213. Holder, D. W. and North, R. J. "Color in the Wind Tunnel," The Aeroplane, Vol. LXXXII, No. 2111 (January 1952), p. 16.
214. Mardin, H. R. The Color Schlieren System. Report AL-2052, North American Aviation, September 1954.
215. Westkaemper, J. C. Supersonic Flow Visualization in Color. OAL Memo 67, January 1954.
216. Bogdonoff, S. M., Keppler, C. E., and Sanlorenzo, E. A Study of Shock Wave Turbulent Boundary Layer Interaction at $M = 3$. Report No. 222, Department of Aeronautical Engineering, Princeton University, July 1953.
217. Steegmaier, K. Fundamentals of Construction and Application of Interferometers. Report LF 226, Ministry of Supply, 1943.
218. Buckley, A. B. Notes on the WADC 6-Inch x 6-Inch Supersonic Wind Tunnel. WADC, July 1955.
219. Applied Physics Laboratory, The Johns Hopkins University. Handbook of Supersonic Aerodynamics, NAVORD Report 1488, Vol. 6, Sec. 18, "Shock Tubes," 1960.
220. Gooderum, P. B. and Wood, G. P. Density Fields Around a Sphere at Mach Numbers 1.30 and 1.62. NACA TN 2173, August 1950.

221. Ladenburg, R., Van Voorhis, C. C., and Winckler, J. A Supersonic Air Jet at 60 lb/in² Tank Pressure. NAVORD Report 69-46, 1946.
222. Ladenburg, R., Van Voorhis, C. C., and Winckler, J. "Interferometric Studies of Faster Than Sound Phenomena," Phys. Rev., Vol. 73 (1948), pp. 1359-1377.
223. Gooderum, P. B., Wood, G. P., and Brevoort, M. J. Investigation with an Interferometer of the Turbulent Mixing of a Free Supersonic Jet. NACA TN 1857, 1949 (NACA TN 963, 1950).
224. Bershader, D. "An Interferometric Study of Supersonic Channel Flow," Rev. Sci. Instr., Vol. 20 (1949), pp. 260-275.
225. Zobel, T. Flow Measurement by Means of Light Interference. NACA TM 1253, 1949.
226. Ladenburg, R. "Application of Interferometry to the Study of Supersonic Flow," Proceedings of the Seventh International Congress on Applied Mechanics, Vol. 2 (1948), pp. 388-397.
227. Ladenburg, R. and Bershader, D. Interferometric Studies on Laminar and Turbulent Boundary Layers Along a Plane Surface at Supersonic Velocities. NAVORD Report 1133, 1949.
228. Blue, R. E. Interferometric Corrections and Measurements of Laminar Boundary Layers in Supersonic Stream. NACA TN 2110, 1950.
229. Giese, J. H., Bennett, F. D., and Bergdolt, V. E. "A Simple Interferometric Test for Conical Flow," J. Appl. Phys., Vol. 21 (1950), pp. 1226-1231.
230. Bennett, F. D., Carter, W. C., and Bergdolt, V. E. "Interferometric Analysis of Air Flow About Projectiles in Free Light," J. Appl. Phys., Vol. 23 (1952), pp. 453-468.
231. Giese, J. H. and Bergdolt, V. E. Interferometric Studies of Supersonic Flow About Truncated Cones. BRL Report 830, 1952.
232. Bleakney, W., Weimer, D. K., and Fletcher, C. H. "The Shock Tube: A Facility for Investigations in Fluid Dynamics," Rev. Sci. Instr., Vol. 20 (1949), pp. 807-815.
233. Bleakney, W. and Taub, A. H. "Interaction of Shock Waves," Revs. Mod. Phys., Vol. 21 (1949), pp. 584-605.
234. Bleakney, W., Fletcher, C. H., and Weimer, D. K. "The Density Field in Mach Reflection of Shock Waves," Phys. Rev., Vol. 76 (1949), pp. 323-324.

235. Bleakney, W., White, D. R., and Griffith, W. C. "Measurements of Diffraction of Shock Waves and Resulting Loading of Structures," J. Appl. Mech., Vol. 17 (1950), pp. 439-445.
236. Kunkel, W. B. and Hurlbut, F. C. Luminescent Gas Flow Visualization in a Low Density Supersonic Wind Tunnel. Report HE-150-135, University of California, September 1956.
237. Sherman, P. M. Visualization of Low-Density Flows by Means of Oxygen Absorption of Ultraviolet Radiation. Engr. Project Report HE-150-130, University of California, August 1955.
238. Bomelburg, H. C. A Method for Measurement of the Flow of Air by Means of Series of Electrical Sparks. TN BN-68, Institute for Fluid Dynamics and Applied Mathematics, University of Maryland, 1956.
239. Cawthon, J. A. Vapor Screen Photographs of a Generalized Missile Model at Mach Numbers 1.50 and 2.00 (OAL Tests 289-8 and -9). OAL Memo 66, December 1953.
240. Preston, J. H. Visualization of Boundary Layer Flow. ARC R and M 2267, Aeronautical Research Council, 1946.
241. Dryden, H. L. and Kuethe, A. M. Effect of Turbulence in Wind Tunnel Measurements. NACA TR 342, 1929.
242. Dryden, H. L. and Kuethe, A. M. The Measurement of Fluctuation of Air Speed by the Hot-Wire Anemometer. NACA TR 320, 1929.
243. Mock, W. C., Jr. Alternating Current Equipment for the Measurement of Fluctuations of Air Speed in Turbulent Flow. NACA TR 598, 1937.
244. Mock, W. C., Jr. and Dryden, H. L. Improved Apparatus for the Measurement of Fluctuations of Air Speed in Turbulence. NACA TR 448, 1932.
245. Schubauer, G. B. and Klebanoff, P. S. Theory and Application of Hot-Wire Instruments in the Investigation of Turbulent Boundary Layers. NACA WR W-86 (originally NACA ACR 5K27, March 1946).
246. Dryden, H. L., et al. Measurements of Intensity and Scale of Wind-Tunnel Turbulence and Their Relation to the Critical Reynolds Number of Spheres. NACA TR 581, 1937.
247. Uberoi, M. S. "Effect of Wind-Tunnel Contraction on Free Stream Turbulence," J. Aeronaut. Sci., Vol. 23 (1956), pp. 754-764.
248. Luther, M. "Fixing Boundary-Layer Transition on Supersonic Wind Tunnel Models," J. Aeronaut. Sci., Vol. 24 (August 1957), pp. 579-586.

249. Faro, I. D. V. Condensation Effects in Supersonic Blowdown Tunnels. CF 1020, Applied Physics Laboratory, The Johns Hopkins University, 1948.
250. Methods of Measuring Humidity. NBS Circular 512, National Bureau of Standards, 1951.
251. Brown, Dinardo, Cheng, and Sherwood. "The Flow of Gases in Pipes at Low Pressures," J. Appl. Phys., Vol. 17 (October 1946), p. 802.
252. Roye, H. D. Starting and Stopping Loads in the 19.0 x 27.5-Inch Supersonic Wind Tunnel. OAL Report 109-9, September 1957.
253. Kinsolving, S. L. and Jackson, R. Starting Loads in an Intermittent Wind Tunnel. AEDC TN-55-6 (AD 208691), January 1959.
254. Webb, E. E. Remote Control of Model Attitude in the OAL Wind Tunnel. OAL Memo 113, October 1957.
255. Lobrecht, D. L. Summary of Operational Performance of the Ordnance Aerophysics Laboratory Supersonic Wind Tunnel thru December 1956. OAL Memo 51-1, August 1957.
256. McWherter, R. C. Design and Operational Characteristics of a High-Speed Electronic Data System. Chance Vought Aircraft, Inc.
257. Specifications for the Boeing Wind Tunnel Data System. Document No. D-16601, Boeing Airplane Company, Seattle, Washington.
258. Goin, K. L. Proposed Revision of Automatic Pressure Recording System. OAL Memo (to R. J. Volluz), February 1957.
259. McCleskey, H. W. A 132-Channel Automatic Pressure Recorder. OAL Memo 110, September 1957.
260. Bain, M. and Bowersox, R. B. A Multi-Pressure Measuring System. Progress Report 20-301, California Institute of Technology June 1956.
261. Clark, J. W. Pressure Measuring System for 7 x 7-Inch Wind Tunnel. ABMA Note WT1-2, September 1955.
262. Frederick, C. L. Automatic Pressure Measuring Systems Used with High-Speed Wind Tunnels. AGARDograph No. 10, June 1955.
263. Doyle, J. P., Jr. Instrumentation and Data Handling Methods for Determining Load Distribution on Wind Tunnel Models by Pressure Distribution Measurements. AGARD Report 114, April-March 1957.
264. Wade, M. G. Reduction of Experimental Data Concurrent with Wind Tunnel Operation. OAL Memo 68, September 1953.

265. "Automatic-Control Terminology" (Compiled by Committee on Terminology of Industrial Instruments and Regulators Division, ASME), Mechanical Engineering, June 1952, p. 486.
266. Monaghan, R. J. and Cooke, J. R. The Measurement of Heat Transfer and Skin Friction at Supersonic Speeds. Part III: Measurements of Overall Heat Transfer and of the Associated Boundary Layers on a Flat Plate at $M = 2.43$. ARC TR CP139 (TN Aero 2129), Aeronautical Research Council, December 1951.

INDEX

- aberration, spherical, 310
- accuracy
 - of angle of attack, 87
 - of conical probes, 50
 - definition of, 117
 - of external balances, 174
 - of force measurements, 144ff
 - of interferometric evaluation, 326
 - of simple manometers, 27ff, 32ff, 36
 - of stagnation pressure measurement, 11ff
 - of static pressure measurement, 4ff, 32
 - of strain gages, 130ff
 - in thermometry, 282ff
- afterglow, 329
- analog computers, 202
- analog digitizer, 409
- analog-to-digital converters, 196ff, 405, 408ff, 421
- anemometer
 - corona, 356
 - hot wire, 354
 - calibration of, 356
 - principles of the, 352
- angle of attack, determination of, 67, 167
 - high, supports for, 181
 - for pressure models, 67
- astigmatism (single-mirror schlieren), 309
- axial force, 136, 147, 149, 163, 173ff, 352
- azobenzene, use of, 335
- balance, 135ff
 - accuracy, 174, 180
 - Boeing-636, 149
 - calibration, 157ff
 - design, 141ff
 - external, 172ff
 - advantages of, 173
 - flexure pivot, 177
 - performance of, 174
 - sidewall, 177
 - force and pressure, 182ff
 - hinge moment, 178
 - calibration of, 180
 - sting mounting, 179
 - internal, 135ff
 - calibration of, 157ff
 - disadvantages of, 157
 - micro-balance, 183
 - model mounting, 145
 - requirements of, 136
 - skin friction, 184
 - special purpose, 180ff
 - two-moment, basic system, 137
 - use of, 138, 144ff, 147
 - windshield "buzz," 156
- barn-gate micro-pressure gage, 35
- base pressure, 150, 173
- beam, cantilever, 143, 146
 - deflection of, 143
- blockage, causes of, 363ff
- Boeing pressure valve, 22, 422
- Bol lamp, 312
- boundary layer
 - effect of, 15, 154ff, 175
 - laminar, 280
 - sublayer, 16
 - measurement of, 10, 15ff, 184
 - spacers for half-model testing, 175ff
 - temperature distribution, 291
 - transition, 332ff
 - artificial, 151, 358
 - axisymmetric (shadowgraph), 307
 - fixing, 357
 - turbulence effects on, 351
 - visualization of, 333ff
 - turbulent, 17, 155, 280
 - velocity gradients, steep,
 - effect of, 13
 - visualization of, 332ff
 - china clay, 333
 - liquid film, 334
 - optical, 332
- Bourdon pressure gage, 21, 35
- bridge
 - balance, 118
 - composite, 140
 - definition of, 117
 - measuring, 408
 - temperature compensation, 126
 - unequal expansions, 133
 - Wheatstone, 123, 409
- brilliance (light source), 306
- bursting pressures (German soda glass), 24
- buzz
 - diffuser, 62
 - windshield, 156
- calibration
 - hinge-moment balance, 157
 - internal balance, 157
 - manometer, 27
 - nozzle, 55
 - roll orientation, 170
 - stagnation probe, 15
 - static probe, 9
- cannon plugs, 25, 143
- capillarity, 28, 44
- carrier systems (in strain-gage circuits), 129
- cathode-ray manometer simulator, 425
- cements
 - bonding, 131
 - high temperature, 290
- china clay method of flow visualization, 333
- circle of confusion, 306

AD-A298 224

HANDBOOK OF SUPERSONIC AERODYNAMICS SECTION 28 WIND
TUNNEL INSTRUMENTATION AND OPERATION(U) BUREAU OF NAVAL
WEAPONS WASHINGTON DC R J VOLLUZ JAN 61

676

UNCLASSIFIED

NAVORD-1488-VOL-6 XB-NAVORD

NL

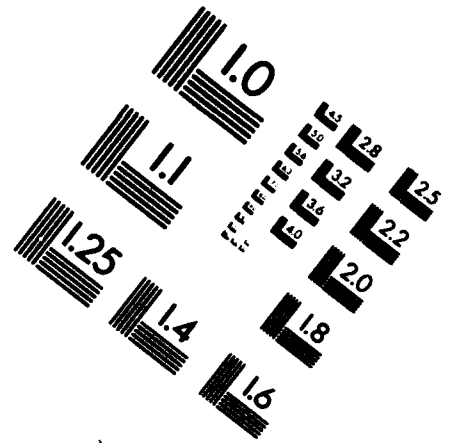
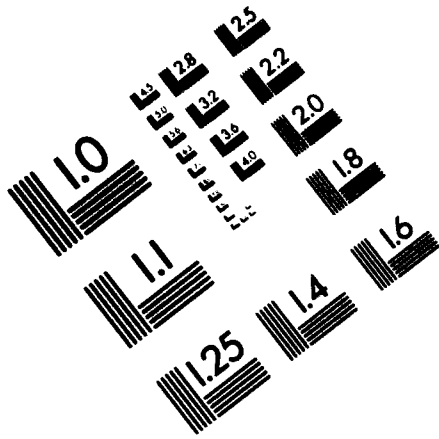
END
FILMED
DTIC



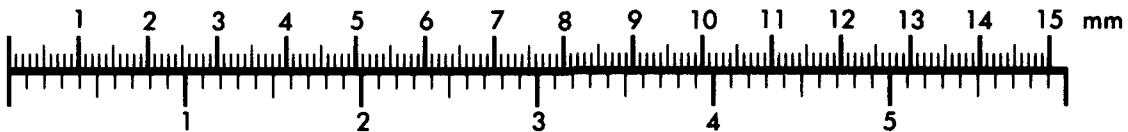
AIMM

Association for Information and Image Management

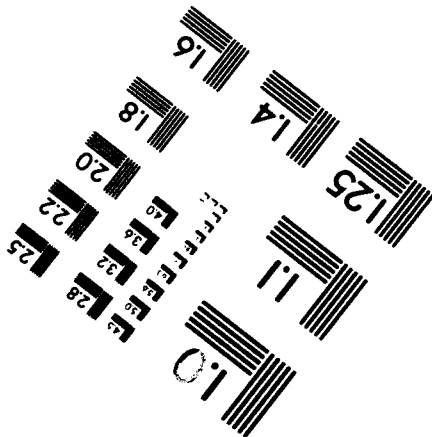
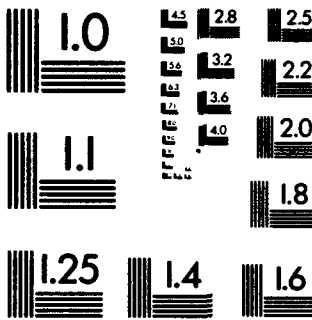
1100 Wayne Avenue, Suite 1100
Silver Spring, Maryland 20910
301/587-8202



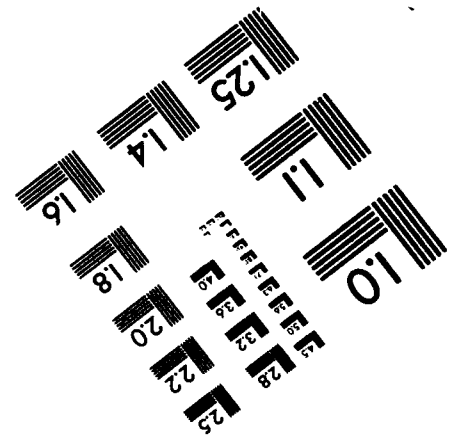
Centimeter



Inches



MANUFACTURED TO AIMM STANDARDS
BY APPLIED IMAGE, INC.



- comp, 310
- compensating cell, 322, 324
- compression ratio, 363
- computer
 - analog, 202
 - digital (data plotting), 201
 - IBM-650, 51
 - IBM-704, 407
 - for wind-tunnel data reduction, 406ff
- condensation, 332, 363ff
- condenser lens, 313, 320
- conduction, probe stem, 282
- cone pressures, machine computation of, 51
- converters, analog-to-digital, 196ff, 405, 408ff, 421
 - advantages of, 200
 - components, description of, 198
 - electro-mechanical, 196
 - electronic, 197
 - principles of, 197
- correction factor, temperature probe, 281
- counter, Veeder-Root, 32
- creep, strain gage, 134
- damping devices, 408
- dampometer, Oltronix, 195
- data taking, reduction, and plotting, 200, 405
 - automatic, 200ff
 - flexowriter, 407
 - off-line reduction, 406
 - on-line reduction, 406, 424
 - variplotter (data plotter), 407
- dead band, definition of, 117
- definitions, basic, 117ff
- density
 - determination of, 327
 - gradients in manometers, 29
 - stagnation pressure measurement, effects of, 201
- design of
 - actuator, linear, 55
 - balances
 - external, 171ff
 - internal, 135ff
 - strain-gage, 135ff
 - extensions, support, 181ff
 - interferometer, 323
 - manometers, 21ff
 - models, 371ff
 - probes
 - pitot-static, 53
 - stagnation, 12ff
 - static, 5ff
 - temperature, 284
 - supports
 - force, 58
 - pressure, 58, 67ff
 - transducers, 37ff
 - windshields, 155
- dewpoint, 332, 364
- drag-cup generator, 408
- dynamic stability, 184
 - pitch, 190
 - roll, 191
- electrical discharge, 329
- electro-mechanical converters, 196
- electronic converters, 197
- emissivity, 283
- error
 - definition of, 117
 - manometer, 27
 - bore non-uniformity, 28
 - density gradients, 29
 - meniscus-capillary, 28
 - stagnation probe measurement, 11
 - density, low, 20
 - entrained particles, 20
 - Mach number effect, 11
 - pulsations, 19
 - turbulence, 18
 - velocity gradient, 13
 - viscosity, 12
 - yaw, 12
 - static probe measurement, 4
 - inherent, 4
 - Mach number effect, 6
 - non-steady pressures, 9
 - probe misalignment, 9
 - Reynolds number, 10
 - tap, 5
 - turbulence, 8
 - velocity gradients, 9
 - strain-gage
 - creep, 134
 - mismatch, 134
 - evaporograph, 292
- fillers and surfacers, 376
- floating-element balance, 184
- flow
 - free-molecule, 47
 - slip-flow, 46
- flow visualization, 303ff
 - afterglow, 329
 - comparison of methods, 304
 - electrical discharge, 329
 - interferometry, 322
 - schlieren, 307
 - color, 318, 321
 - double-mirror, 310
 - single-mirror, 309
 - shadowgraph, 304
 - vapor screen, 330
- fluids, manometer, 23ff
- force measurement
 - axial (drag), 136, 147, 149, 163, 173ff, 352
 - Magnus, 194ff
 - measuring systems, 405ff
 - normal (lift), 138, 148, 160, 163, 168, 174, 373
 - side, 163, 174
 - tare, 136
- free-molecule flow, 46
- gage
 - bellows (diaphragm), 36
 - Bourdon, 35
 - factor, 140
 - McLeod, 32
 - Pirani, 33

- strain
 - foil, 120
 - wire, 119ff
- transducer, 36
- voltage, 140
- gas temperature-measuring techniques, 288ff
- Gladstone-Dale constant, 326
- glass tubing, bursting pressures of, 24
- glyptal cement, 184
- grating screen, 312, 317
- half models, 188
- heat transfer
 - through boundary layer, 281
 - coefficient of, 281
 - convective, 284
 - parameters, 282
 - radiant, 282
 - steady-state, 290
 - transient, 290
- hinge moment, 178
- balances, 178
- models, 179
- humidity, 363
- indication of, 363
- inclined manometers, 281
- instruments
 - humidity indicating, 363
 - potentiometers, 203
 - pressure indicating, 21
 - hydrostatic (see also manometers), 21
 - mechanical, 35
 - transducer, 36
 - temperature indicating, 279ff
 - thermocouples, for use with, 258
 - turbulence indicating, 354, 356
- interference
 - aerodynamic, 153
 - sting, 155
 - windshield, 154
- interferometer, 322
 - adjustment of, 325
 - applications of, 329
 - description of, 323
 - evaluation of, 326
 - light source, 323
 - Mach-Zehnder, 322
 - mounting of, 324
 - photography, 328
- Kerr cell, 313
- Kiel probe, 12
- knife edge, 308ff
- Knudsen number, definition of, 41
- lag, response time, 43
- leaks in pressure lines and connections, 26
- light source
 - interferometer, 323
 - multiple source, 311
 - schlieren, 312
 - color, 318 ff
- shadowgraph, 306
- spark, 307
- vapor screen, 331
- loading systems
 - dead weight, 158
 - jack and load cell, 159
 - loads, starting and stopping, 372ff
- Mach number
 - determination by means of
 - conical probes, 50
 - stagnation pressure, 50
 - static pressure, 49
 - visual means, 55
 - wedges, 54
 - effect
 - on stagnation pressure measurement, 11
 - on static pressure measurement, 6
- Mach-Zehnder interferometer, 322ff
- Magnus forces, 194ff
- manometer (see also micromanometer), 21ff
 - accuracy of, 27
 - automatic digital recording, 425
 - cathode ray simulator, 425
 - errors, simple system (see also error, manometer), 27ff
 - fittings, 23ff
 - fluids, 23ff
 - inclined, 22
 - internal, 425
 - leads, 25
 - leaks, 26
 - scales, 30
 - servicing, 30
 - tubing, 24
- McLeod pressure gage, 32
- meniscus-capillary errors, 28
- meniscus transducer, 426
- mercury-vapor light source, 312
- Merriam Unity oil, 24
- micro-balance, 183
- micromanometer, 31ff
 - barn-gate, 35
 - Cole's low pressure (multimanometer), 31
 - concentric tube (multimanometer), 34
 - Flow Corporation, 33
 - Foxboro, 34
 - McLeod, 32
 - NACA, 33
 - precision mercury, 32
 - precision oil, 32
 - precision thermistor, 33
 - single-tube, 35
 - spherical float, 34
- mirror
 - interferometer, 324
 - schlieren, 314
- model
 - aerodynamic surfaces, mounting of, 375
 - body sections, joining of, 375
 - construction techniques, 374
 - design, 371
 - half, 188

- materials, 374
- NACA (RM-10), 148
- size limitations, 364
- spares, requirements for, 374
- supports, 67
- surfacers and fillers, 376
- modulus, section, definition of, 140
- moment
 - bending, 144, 178
 - hinge, 178ff
 - pitching, 149, 161, 163, 174, 190
 - rolling, 145, 163, 174, 191
 - yawing, 149, 163, 174
- normal force, 148, 160, 163, 168, 174, 373
- nozzle
 - calibration equipment, 55
 - flexible, 56
 - linear actuators, 55ff
- Nusselt number, 282
- off-line data taking, 406
- oil
 - Merriam unity, 24
 - volatile, 334
- Oltronix dampometer, 135
- on-line data taking, 406, 424
- orifices, pressure, 6, 13, 14, 45, 53, 85, 376
- perfect gas, 3
 - constant, R, 3
 - equation of state, 3
- photography, 315, 317, 321, 328, 331
- Pirani pressure gage, 33
- pitch, dynamic, 188
 - half-model technique, 188
 - three-dimensional model, 190
- plug, cannon, 143
- Poisson's ratio, 119
- Polhausen (recovery factor in laminar flow), 282
- potentiometer, 140, 203, 408
- Prandtl number, 280
- precision, definition of, 117
- precision manometers (see micro-manometer)
- pressure
 - base, 150, 173
 - indicators
 - hydrostatic (see also manometer), 21
 - mechanical (see also gages), 35
 - transducers, 36
 - measurement of, 2, 4, 421
 - automatic, 421
 - definition of, 3
 - non-steady, 9
 - ratio through a shock wave, 6
 - measuring systems, 421ff
 - manometer (see manometer and micromanometer)
 - transducer
 - automatic zero-balancing, 424
 - cathode-ray manometer simulator, 425
 - internal manometer, 425
 - stagnation, 11ff
 - definition of, 11
 - entrained particles, 20
 - errors, 4
 - indicating instruments, 21
 - Mach number, supersonic, 11
 - measurement of, 11
 - at low density, 20
 - near a wall, 15
 - probe, shrouded, 12
 - pulsations, periodic, 19
 - turbulence, 18
 - velocity gradients, 13
 - viscosity, 12
 - yaw, 12
 - static, 4, 56
 - definition of, 3
 - effect of Mach number, 6
 - errors, 5
 - surveys
 - bodies of revolution, 65
 - thin surfaces, 66
 - transducers, 21, 36, 408
- probe
 - free-molecule, 41
 - mass-flow, 42
 - misalignment, 5, 9
 - pitot-static, 50, 53
 - positioning, 64
 - response time, 43
 - spacing, 3, 12
 - stagnation pressure, 12ff
 - fast response, 17
 - Kiel, 12
 - shrouded, 11, 12
 - Stanton, 15
 - static pressure, 4ff
 - conical, 50
 - NPL, 5
 - Prandtl, 5
 - spherical, 10
 - wedge-shaped, 10
 - temperature, 279ff
 - design of, 284ff
 - Franz, 285
 - Pratt-Whitney, 286
 - radiation effect on, 282
 - Winkler (NOL), 286
- Rayleigh formula, 11
- recorders, Bristol wide-strip, 291
- recovery factor, 292ff
 - definition of, 280
 - in laminar flow, 280
 - in turbulent flow, 280
- reflection plane technique, 175
- resolution sensitivity, definition of, 117
- response time, 43
 - criteria for minimum, 45
 - limitations, 45
 - of probes, 43, 46ff
- Reynolds number effect
 - on boundary-layer transition, 351
 - on static pressure, 10
 - on turbulence, 352ff
- roll, measurement of dynamic, 191ff

- Saurisen high-temperature cement, 290
- scales, manometer, 30
- Schaevitz transformer, 184
 - for axial force measurement, 149
 - for skin friction balance, 184
- schlieren system, 307
 - camera, 315
 - color, 318, 321
 - double mirror, 310
 - grating screen, 312
 - lens, condenser, 313
 - light source, 312
 - mirrors, field, 313
 - multiple-source, 310ff
 - sensitivity of, 316
 - control slit, 319
 - single mirror, 309ff
 - variations of, 309
 - windows, test section, 314
- Scotch-lite screen, 306
- shadowgraph, 304ff
- shock wave
 - effect on stagnation pressure, 11
 - reflection, 371
- side force, 163, 174
- size, model, 364
- skin-friction balance, 184
- slip flow, 46
- spark source, 307
- splitter plate, 375
- Sprague-Vitamin Q condenser, 333
- stability, dynamic, measurements of, 184ff
 - for fixed model, 187
 - for moving model, 185
- stagnation pressure measurement (see also pressure), 11ff
- Stanton number, 282
 - experiment, 116
 - probe, 15
- static pressure measurement (see also pressure), 4ff
- steady-flow equation, 3
- Stefan-Boltzmann constant, 283
- stem conduction, 282
- sting interference, 155
- Stokes flow
 - creeping, 15
 - sphere, about a, 13
- strain gage, 119ff
 - application, 122
 - balance (see balance)
 - cements, 131
 - circuits, typical, 129
 - creep, 134
 - errors (see also error, strain gage), 130
 - hysteresis in, 121
 - instrumentation, 123
 - manufacturers, 121
 - materials, 120
 - moisture-proofing, 122
 - resistive type, 119
 - temperature compensated, 130
 - testing, 123
 - tolerances, manufacturing, 134
 - use at high temperature, 135
- stream pressure, indicated, 8
- supports
 - drag, 181
 - force and pressure, 58ff
 - pressure model, 67
 - remote roll indexing, 181
- surfacers and fillers, 376
- tap error, static measurement, 5
- Taylor-Maccoll cone theory, 54
- temperature
 - adiabatic, 279
 - drift, 424
 - measurement of, 288
 - probe, 279, 281
 - stagnation, 279
 - static, 279
- thermocouple, 286ff
 - instrumentation, 288
- thermometers, 284
- thermometry, thermo-electric, 287
- thermopile, 290
- transducer
 - meniscus, 426
 - pressure, 21, 36, 408
 - accuracy of, 421
 - calibration of, 39
 - Hagan, 40
 - manufacturers of, 37
 - OSU, 40
 - use of, 37ff, 41
 - WADC, 37ff
- tubing, glass, 24
- tunnel blockage, 363
- turbulence
 - effects
 - on measurement, 351
 - on probe temperatures, 283
 - on stagnation pressure, 18
 - on static pressure, 6, 8
 - intensity of, 351
 - measurement of, 352
 - minimum, methods for, 357
 - scale of, 351
 - screens, 357
- valve scanning, 421
 - Boeing pressure, 22, 423
 - solenoid, 423
- vapor screen technique, 330ff
- Variplotter, 407
- Veeder-Root counter, 32
- velocity gradient, effect on static pressure, 9, 11, 13
- velocity-measuring devices
 - corona anemometer, 356
 - hot-wire anemometer, 354
- viscosity effect on stagnation pressure measurement, 12
- Wheatstone bridge, 123, 409
- windshield interference, 154
- wind tunnel
 - design, 155
 - testing requirements for strain-gage design, 135
- windows, 314, 325

yaw effect on stagnation pressure
measurement, 12

zero balancing, 424
zero shift, transducer, 425

APPENDIX A

Supplemental Bibliography

(General References Reprinted from Ref. 1)

- 001 A.S.M.E. Power Test Codes "Instruments and Apparatus."
Part I, General Considerations, 1935.
Part II, Temperature Measurements, Chapt. 1, General, 1931.
Part III, Temperature Measurements, Chapt. 3, Thermocouple, Thermometers or Pyrometers, 1940.
- 002 Diederiche and Andrae, Experimental Mechanical Engineering Vol. I, New York: John Wiley and Sons, 1946.
- 003 Den Hartog, J. P., Mechanics, New York: McGraw-Hill Book Company, Inc., 1948.
- 004 Den Hartog, J. P., Mechanical Vibrations, New York: McGraw-Hill Book Company, Inc., 1948.
- 005 Goldstein, S., Modern Developments in Fluid Dynamics, Vol. I and Vol. II, Oxford: Clarendon Press, 1938.
- 006 Hunsaker, J. C., and Rightmire, B. G., Engineering Applications of Fluid Mechanics, New York: McGraw-Hill Book Company, Inc., 1947.
- 007 Jean, Sir James, Kinetic Theory of Gases, Cambridge: University Press, 1946.
- 008 Keenan, J. H., Thermodynamics, New York: John Wiley and Sons, Inc., 1941.
- 009 Keenan, J. H. and Kay, E., Gas Table, New York: John Wiley and Sons, Inc., 1948.
- 010 Keenan, J. H. and Keyes, F. G., Thermodynamic Properties of Steam, New York: John Wiley and Sons, Inc., 1949.
- 011 Liepmann, H. W. and Puckett, A. E., Introduction to Aerodynamics of a Compressible Fluid, New York: John Wiley and Sons, Inc., 1947.
- 012 McAdams, W. H., Heat Transmission, New York and London: McGraw-Hill Book Company, Inc., 1942.
- 013 Ower, E., Measurement of Air Flow, London: Chapman and Hall, 1949.
- 014 Prandtl, L. and Tietjens, O. G., Applied Hydro and Aero Mechanics, New York: McGraw-Hill Book Co., Inc., 1934.
- 015 Sears, F. W., Optics, Cambridge: Addison-Wesley Press, 1946.
- 016 Shapiro, A. H., Lecture Notes, 2.491--Flow of Compressible Fluids, Department of Mechanical Engineering, M. I. T.
- 017 Airflow Instruments, The Airflow Instrument Co., Glastonbury, Conn.

- 018 Statham Instruments, Statham Laboratories, Inc.
- 019 Aerodynamic Precision Instruments, Division of Engineering, Brown University, June 1952.
- 020 Gorton, R. E. and Miller, B. E., "Instrumentation for Aircraft Gas Turbine Development." SAE No. 730, Jan. 1952.
- 021 Shapiro, A. H., Hawthorne, W. R. and Edelman, G. M., "The Mechanics and Thermodynamics of Steady One-Dimensional Gas Flow with Tables for Numerical Solutions," M. I. T. Meteor Report No. 14, Dec. 1947.
- 022 Meyer, C. A. and Benedict, R. P., "Instrumentation for Axial-Flow-Compressor Research," ASME Paper No. 52-SA-18, June 1952.
- 023 Brunot, A. W. and Fulton, R. O., "A Clearanceometer for Determining Blade-Clearances of Axial-Flow-Compressors," ASME Paper No. 52-SA-16, June 1952.
- 024 Aircraft Instruments, Aug. 1943, General Electric Company, Schenectady, New York.
- 025 General Catalog of Foxboro Industrial Instrumentation, Bull. 450.
- 026 Theoretical Aerodynamics, L. M. Milne--Thompson, D. Van Nostrand Company, Incorporated, New York, 1952.
- 027 Specialized Testing and Measuring Equipment Catalog, General Electric Company.
- 028 Chemical Rubber Company, Handbook of Chemistry and Physics, 1944.

Errors and Presentation of Data

- 101 Deming, W. E., "Some Notes on Least Squares," Mimeographed Notes, the Graduate School, Dept. of Agriculture, ..., 1938.
- 102 Hoel, P. G., Introduction to Mathematical Statistics, New York: Wiley and Sons, 1947.
- 103 Deming and Birge, "On the Statistical Theory of Errors," Review of Modern Physics, 6, pp. 119-161, July 1934.
- 104 Deming, W. E., Statistical Adjustment of Data, New York: Wiley and Sons, 1938.
- 105 Fisher, R. A., Statistical Methods for Research Workers, Edinburgh: Oliver and Boyd, 10th Ed., 1948.
- 106 Schultz, H., Jou. Amer. Statistical Assoc., Vol. 25, pp. 138-185, 1930.
- 107 Scarborough, Numerical Mathematical Analysis, Johns Hopkins Press, 2nd Edit., 1950.
- 108 American Standard Assoc., "Engineering and Scientific Graphs for Publications, American Standards, ASA Z 15:3," published by ASME 1943, reaffirmed 1947.

- 109 Lieblein, J., "Properties of Certain Statistics Involving the Closest Pair in a Sample of Three Observations," Jour. of Research, Nat. Bur. of Std., Vol. 48, No. 3, p. 255, March 1952.
- 110 "Estimation of Experimental Uncertainty," Wilson, 2:68 Notes, Mass. Inst. of Tech.
- 111 Wernimont, G., "Precision and Accuracy of Test Methods," Symposium on Applications of Statistics, ASTM, San Francisco, October 11, 1949.
- 112 Tuemmler, F. D., Discussion to above, Symposium on Applications of Statistics, ASTM San Francisco, October 11, 1949.
- 113 Kline, S. J. and McClintock, F. A., "Describing Uncertainties in Single-Sample Experiments," ASME Spring Meeting, Columbus, Ohio, April 28-30, 1953. Published in Mechanical Engineering, January 1953.

Temperature Measurements

(References 201 to 215 are taken from "Temperature - Its Measurement and Control in Science and Industry," American Inst. of Physics, 1941.)

- 201 Wensel, H. T., "Temperature."
- 202 Worthing, A. G., "Is Temperature a Basic Concept."
- 203 Mueller, E. F., "Precision Resistance Thermometry."
- 204 Roeser, W. F., "Thermoelectric Thermometry," (pp. 180-205).
- 205 Busse, Johanna, "Liquid in Glass Thermometers."
- 206 White, W. P., "Potentiometers for Thermoelectric Measurements."
- 207 Roeser, W. F., Wensel, H. T., "Methods of Testing Thermocouple and Thermocouple Materials."
- 208 Kennard, R. B., "Temperature Distribution and Heat Flux in Air by Interferometry," (pp. 685-706).
- 209 Suits, C. G., "High Temperature Gas Measurements in Air."
- 210 Mullikin, H. F., "Gas Temperature Measurement and the High-Velocity Thermocouple."
- 211 Mullikin, H. F. and Osborne, W. F., "Accuracy Tests of the High Velocity Thermocouple."
- 212 Whitesel, H. A., "Temperature Measurements in Air Conditioning."
- 213 Buckland, B. O. and Stack, S. S., "Thermocouples for Testing Steam Turbines."
- 214 Dahl, A. I., "The Stability of Bare-Metal Thermocouples in Air from 800 - 2200°F."

- 215 Homewood, C. F., "Factors Effecting the Life of Platinum Thermocouples."
- 216 "Steels for Elevated Temperature Service," United States Steel Co., 1949.
- 217 "Resume of High Temperature Investigations 1948 - 1950," Timken Roller Bearing Co.

(References 218 to 224 are from Leeds and Northrup Co.)

- 218 "Thermocouples, Assemblies, Parts and Accessories," Catalogue EN-S2, 1952
- 219 "Standard Conversion Tables for Leeds and Northrup Thermocouples," Catal. No. 31031.
- 220 "Apparatus for Checking Thermocouple Pyrometers in Plant and Laboratory," Catal. E-33A-503, 1940.
- 221 "Electrical Measuring Instruments for Research, Teaching and Testing," Catal. E, 1940.
- 222 "Notes on Moving Coil Galvanometers," Notebook Ed (1), 1943.
- 223 "Type K Potentiometers and Accessories," Catal. E-50B.
- 224 "Wenner Thermocouple Potentiometers," Catal. E-33-A(1), 1944.
- 225 "Potentiometers," Bulletin No. 270. Rubicon Co.
- 226 "Galvanometers," Bulletin No. 320. Rubicon Co.
- 227 "Operation Principles of Brown Electronik Continuous Balance Potentiometer Pyrometers," Bulletin No. 15-6, 1943, Brown Instrument Co.
- 228 "Potentiometer Pyrometers," Catal. No. 1105, 1944, Brown Instrument Co.
- 229 Baker, H. Dean, "Manual on Thermometry," Pratt and Whitney Aircraft, 1950.
- 230 Beede, H. M. and Droms, C. R., "A Simplified Thermocouple for Temperature Measurements in High Velocity Gas Streams," Instruments, Vol. 24, No. 3, p. 338, March 1951.
- 231 Brooks, H. B., "Sensitivity of a Galvanometer as a Function of its Resistance," Jour. of Research of the Nat. Bur. of Standards Vol. 4, pp. 297-312, Feb. 1930.
- 232 Blackshear, Perry L., "Sonic Flow Orifice Temperature Probes for High Gas-Temperature Measurements," NACA - TN 2167, Sept. 1950.
- 233 Cesaro, R. S., Koenig, R. J. and Pack, G. J., "Experimental Analysis of a Pressure Sensitive System for Sensing Gas Temperature," NACA - TN 2043, 1950.

- 234 Cesaro, R. S. and Matz, N., "Pressure Sensitive System for Gas Temperature Control," NACA - RM E8C04.
- 235 Clark, F. W., "Characteristics of Stagnation-Temperature Probes for High-Velocity Gas Streams," Pratt and Whitney Aircraft Report PWA 549, Apr. 20, 1945.
- 236 Clark, J. A. and Rohsenow, W. M., "A New Method for Determining the Static Temperature of High-Velocity Gas Streams," ASME Paper No. 51-SA-33, 1951.
- 237 Grocco, Luigi, "Transmission of Heat From a Flat Plate to a Fluid Flowing at High Velocity," NACA - TM 690, Oct. 1932.
- 238 Drake, R. M. and Becker, G. H., "Heat Transfer from Spheres in Supersonic Flow to a Rarefied Gas," Univ. of Cal., Institute of Engr. Research, Rept. No. HE-150-78, Feb. 15, 1951.
- 239 Eckert, E., "Temperature Recordings in High Speed Gases," NACA - TM 983, Aug. 1941.
- 240 Eckert, E. and Weise, W., "The Temperature of Unheated Bodies in High-Speed Gas Streams," NACA - TM 1000, Dec. 1941.
- 241 Emmons, H. W. and Brainerd, J. G., "Temperature Effects in a Laminar Compressible Fluid Boundary Layer Along a Flat Plate," Trans. ASME. Vol. 63, pp. A-105 to A-110, 1941.
- 242 Fiock, E. F., "Thirteenth Monthly Report of Progress on the Development of Thermocouples, Pyrometers for Gas Turbines," Nat. Bur. of Standards, Jan. 21, 1947.
- 243 Fiock, E. F. and Dahl, A. J., "The Use of Thermocouples in High-Velocity-Gas Streams," J. Am. Soc. Naval Engrs. 60: 139, 1948.
- 244 Fishenden, M. and Saunders, O. A., "The Error in Gas Temperature Measurements and their Calculations," Jour. of the Inst. Fuel (British), Vol. XII, No. 64, March 1939, pp. S5-15, S82-107.
- 245 Fitzgerald, A. E., Basic Electrical Engineering, (Potentiometers, p. 386), New York: McGraw-Hill Book Co., Inc., 1945.
- 246 Franz, A., "Pressure and Temperature Measurements in Supercharger Investigations," NACA - TM 953, 1940.
- 247 Garbett, C. R., "The Determination of Heat Transfer Coefficients by the Transient Method for High Velocity Flow," Stanford Univ. Tech. Rept. No. HS-1, 1949.
- 248 Goldstein, D. L. and Scherrer, R., "Design and Calibration of a Total-Temperature Probe for Use at Supersonic Speeds," NACA - TN 1885, May 1949.
- 249 Hottel, H. C. and Kalitinsky, A., "Temperature Measurements in High-Velocity Air Streams," Jour. of App. Mech., pp. A25-A32, March 1945.
- 250 Huston, W. B., "Accuracy of Air Speed Measurements and Flight Calibration Procedures," NACA - Rept. 919, 1948.

- 251 Kalhman, L. E., "Heat Transmission in the Boundary Layer," NACA - TM 1229, April 1949.
- 252 King, W. J., "Measurement of High Temperatures in High Velocity Gas Streams," Trans. ASME, Vol. 65, pp. 421-423, 1943.
- 253 Letsch, E. R. and King, W. J., "Methods of Measuring High Temperatures in Gas Streams," ASME 51-A-143, Nov. 1951.
- 254 Lindsey, W. F., "Calibration of Three Temperature Probes and a Pressure Probe at High Speeds," NACA - WR 1-273, April 1942.
- 255 Mack, S. F. and Schaaf, S. A., "Viscous Effects on Stagnation-Point Temperatures," Univ. of Cal., Inst. of Engr. Research, Rept. No. HF-150-96, Nov. 29, 1951.
- 256 Markowski, S. J. and Moffatt, E. M., "Instrumentation for Development of Aircraft Powerplant Components Involving Fluid Flow," SAE--Quarterly Transactions, Vol. 2, No. 1, pp. 104-116, Jan. 1948.
- 257 Moffatt, E. M., "Errors in High Temperature Probes for Gases," ASME 48-A-52, 1948.
- 258 Moffatt, E. M., "Multiple Shielded High Temperature Probes--Comparison of Experimental and Calculated Errors," SAE T13, Jan. 1952.
- 259 Moffatt, E. M., "Calibration Report No. 5," The Airflow Instrument Co., Nov. 1949.
- 260 Moffatt, E. M., "Report on Cylindrical Total Temperature Probes," Pratt and Whitney Aircraft Company, PWA 559, May 1945.
- 261 Moore, D. W., Jr., "A Pneumatic Method for Measuring High-Temperature Gases," Aeronautical Engineering Review, Vol. 7, No. 5, May 1948.
- 262 Moss, S. A., "The Impact Tube," Trans. ASME, Vol. 38, pp. 761-797, 1916.
- 263 Pirani, M. and von Wagenheimer, G., "Ein Thermoelement fur Hochste Temperaturen," Zeitschrift fur Technische Physik, Vol. 6 (No. 7A - 1925), pp. 358 - 359.
- 264 Pohlhausen, E., "Der Warmearstausch Zwischen Festern Korpern und Flussigkeiten mit Kleiner Reibung und Kleiner Wärmeleitung," Zeitschrift fur Angewandte Math. und. Mech., Vol. 1, 1921, pp. 115 - 121.
- 265 Probert, R. P. and Singham, J. R., "The Measurement of Gas Temperatures in Turbine Engines," Jour. of Scientific Instruments, Vol. 23, No. 4, pp. 72 - 77, April 1946.
- 266 Rohsenow, W. M., "A Graphical Determination of Unshielded Thermocouple Thermal Corrections," Trans. ASME. V. 68, No. 3, p. 195, April 1946.
- 267 Rohsenow, W. M. and Hunsaker, J. P., "Determination of the Thermal Correction for a Single Shielded Thermocouple," Trans. ASME, Vol. 69, No. 6, p. 699, Aug. 1947.

- 268 Scadron, M. D., Gettelman, C. C. and Pack, G. J., "Performance of Three High-Recovery Factor Thermocouple Probes for Room Temperature Operation," NACA - RM E50129, Dec. 1950.
- 269 Schulze, A., "Metallic Materials for Thermocouples," Symposium on Gas Temperature Measurements, Jour. of the Institute of Fuels, Vol. 12, March 1939.
- 270 Scherrer, R., "The Effects of Aerodynamic Heating and Heat Transfer on the Surface Temperature of a Body of Revolution in Steady Supersonic Flight," NACA - TN 1300, July 1947.
- 271 Shoulberg, R. H., Kendall, R. E., Rivas, M., "Test of Stagnation Temperature Probes," Mass. Inst. of Tech., Dept. of Mech. Engr., HT-3, March 1, 1952.
- 272 Smith, Otto J. M., "Thermistors," Part I and II, Rev. of Scientific Inst., April 1950.
- 273 Stalder, J. R., Rubesin, M. W. and Tendeland, T., "A Determination of the Laminar-Transitional and Turbulent Boundary Layer Temperature Recovery Factor on a Flat Plate in Supersonic Flow," NACA - TN 2077, June 1950.
- 274 Tarr, Philip R., "Methods for Connection of Revolving Thermocouples," NACA - RM E50J23a, Jan. 1951.
- 275 Tucker, M. and Maslen, S. H., "Turbulent Boundary Layer Temperature Recovery Factors in Two-Dimensional Flow," NACA - TN 2296, Feb. 1951.
- 276 Van der Maas and Wynia, S., "Corrections in the Thermometer Reading in an Air Stream," NACA - TM No. 956, Oct. 1940.
- 277 Vounegnt, B., "Vortex Thermometer for Measuring True Air Temperature and True Air Speeds in Flight," Rev. of Scientific Inst., p. 653, July 1950.
- 278 Weber, R. L., Heat and Temperature Measurements, New York: Prentice Hall, 1950.
- 279 White, W. P., "Leakage Control by Shielding," American Inst. of Physics, op. cit. "Temperature," 1941.
- 280 White, W. P., "Sensitive Moving Coil Galvanometers," Physical Review, Vol. 19, Nov. 1904.
- 281 White, W. P., "Everyday Problems of the Moving Coil Galvanometer," Physical Review, Vol. 22, Nov. 1906.
- 282 Wildhack, W. A., "A Versatile Pneumatic Instrument Based on Critical Flow," Review of Scientific Instruments, Vol. 21, No. 1, p. 25, Jan. 1950.
- 283 Wimbrow, W. R., "Experimental Investigation of Temperature Recovery Factors of Bodies of Revolution at Supersonic Speeds," NACA - TN 1975, Oct. 1949.
- 284 Wimmer, W., "Stagnation Temperature Recordings," NACA - TM 967, 1941.

- 285 Freeze, P. D., "Bibliography on the Measurement of Gas Temperature," National Bureau of Standards, Circular 513, Aug. 20, 1951.
- 286 Alford, J. S. and Helsing, C. R., "Fast Thermocouples as Control System Elements Sensing Exhaust Gas Temperatures in Aircraft Gas Turbines," ASME Paper No. 52-SA-35, June 1952.
- 287 "Narrow Span Electronic Potentiometers," Instr. Data Sheet No. 10. 0-8, 1952, Brown Instrument Company.
- 288 "Speedomax--Type G Instruments," Catalog ND46(1), 1952, Leeds and Northrup Company.
- 289 "Measuring Techniques for Fluid Flow," Bull. No. DF51 GT 366, Dec. 15, 1951, General Electric Company.
- 290 Moffat, M. E., "Minimizing Errors in the Measurement of High Temperature in Gases," Instruments, Vol. 22, Feb. 1949, No. 2.
- 291 "Batt-Welded Thermocouple Element Construction," Specif. Sheet 206, Honeywell.
- 292 "Velocity of Sound in Hot Gases," Reports on Research M. I. T. Vol. 3, No. 7, May 1952.
- 293 "Temperature Measurements," Reports on Research, M. I. T., June 1952, Vol. 3, No. 8.
- 294 "Thermocouple Lead Wires," Wire Section 30-1, Thermo Electric Company, Inc., 1949.
- 295 "Heat and Airflow Instruments," Revere Corp. of America, Wallingford, Connecticut.
- 296 Introducing Honeywell's New Insulated Thermocouple Wires, Bull. 5600, Honeywell.
- 297 Notes on Temperature Measuring Instruments, Mech. Engrg. Lab., ME 122.
- 298 Dewpoint Recorder, General Electric Special Products Digest (G.E.), Vol. X, No. 5, Sept. 1952.
- 299 A Device for Determining the Stagnation or Total Temperature of a Gas, J. A. Clark.
- 2000 Strain Gage Catalogs, Baldwin.
- 2001 Rubicon Notes No. 1; Rubicon Company.
- 2002 The Measurement of Air Temperatures in High-Speed Flight. E. Eckert and W. Weise.

Pressure Measurements

- 301 Angus, "Errors in Pressure Readings Due to Wrong Gauge Connections," J. Am. Wat. W. Assn., 1937.

- 302 Bairstow, Fower, Hartree, "The Pressure Distribution on the Head of Shell Moving at High Velocities," Proc. Royal Society, A, Vol. 97, 1920.
- 303 Barker, M., "On the Use of Very Small Pitot Tubes for Measuring Wind Velocity," Proc. of Royal Soc., Series A, Vol. 101, p. 435, 1922.
- 304 Beavan, J. A. and Manwell, A. R., "Tables for Use in the Determination of Profile Drag at High Speeds by the Pitot Traverse Method," A.R.C., R and M No. 2233, Sept. 1941.
- 305 Birdwell, J. M., "Application of the von Karman Momentum Theorem to Turbulent Boundary Layers," NACA - TN 2571, Dec. 1951.
- 306 Bradfield, W. S., "Measure of Shearing Stress on a Body of Revolution," Catal. AF33(038)12918, AMC Project Rept., Oct. 1 - Dec. 1, 1950.
- 307 Bradfield, W. S. and Yale, G. E., "Small Pitot Tubes with Fast Response Time," Jour. of Aero. Sci., Vol. 18, No. 10, pp. 697-8, Oct. 1951.
- 308 Bramwell, F. H., Relf, E. F. and Fage, A., "On a Determination of the Whirling Arm of the Pressure Velocity Constant for a Pitot (Velocity Head and Static Pressure) Tube; and on the Absolute Measurement of Velocity in Aeronautical Work," A.R.C. R and M 71, 1912.
- 309 Brinich, P. F., "Boundary Layer Measurement in 3.84 - by 10 inch Supersonic Channel," NACA - TN 2203, Oct. 1950.
- 310 Brombacher, W. G., "Some Problems in the Precise Measurement of Pressure," Instruments 22, 358, 1949.
- 311 Buckingham, E., "The Theory of the Pitot and Venturi Tubes," NACA Rept. No. 2, Part 2, 1915.
- 312 Chambre, P. L., "The Theory of the Impact Tube in a Viscous Compressible Gas," Un. Cal. Eng. Research Project Report HE-150-50, 1948.
- 313 Chambre, P. L. and Schaaf, S. A., "The Theory of the Impact Tube at Low Pressures," Jour. Aero. Sci., Vol. 15, No. 12, pp. 735-7, Dec. 1948.
- 314 Fage, A., "On the Static-Pressure in Fully-Developed Turbulent Flow," Proc. Roy. Soc., Ser. A., Vol. 155, No. 886, pp. 577-596, July 1, 1936.
- 315 Fage, A., "Turbulent Flow in a Circular Pipe," Philosophical Mag., Vol. 21, p. 80, 1936.
- 316 Fage, A., "Turbulence in the Wake of a Body," A.R.C. R and M 1510, Sept. 1932.
- 317 Fage, A. and Faulkner, V. M., "An Experimental Determination of the Intensity of Friction on the Surface of an Airfoil," Proc. Roy. Soc., Ser. A, Vol. 129, pp. 378-410, 1930.

- 319 Faulkner, V. M., "A Modified Chattock Gauge of High Sensitivity," A.R.C. R and M 1589, Jan. 1934.
- 320 Fowle, A. A., "Measurement of Nonstationary Pressure with a Pitot Probe," M. I. T. S.M. Thesis, Mech. Eng., May 1949.
- 321 Fuhrmann, G., "Theoretische und Experimentelle Untersuchungen on Ballon Modellen," Dissertation Gottingen 1912, Jahrb Motorluft, Vol. 5, p. 63, 1911 - 1912.
- 322 Gerdes, H. A., Brooks, D. M., and Kalina, J. F., "The Effect of Reynolds Number on Impact Tube Calibration," M. I. T. Naval Arch. Thesis, 1950.
- 323 Gettelman, C. C. and Krause, L. N., "Characteristics of a Wedge with Various Holder Configuration for Static Pressure Measurements in Subsonic Gas Streams," NACA - RM E51G09, Sept. 5, 1951.
- 324 Gezilius, E. J. E., "Making Small Metal Tubes by Electrodeposition on Nylon Fibers," Review of Sci. Instruments, Vol. 21, No. 10, Oct. 1950.
- 325 Goldstein, S., "A Note on the Measurement of Total Head and Static Pressure in a Turbulent Stream," Proc. Roy. Soc., Ser. A, Vol. 155, No. 886, pp. 570-75, July 1, 1936.
- 326 Gracey, W., Coletti, D. E. and Russell, W. R., "Wind Tunnel Investigations of a Number of Total-Pressure Tubes at High Angles of Attack. Supersonic Speeds," NACA - TN 2261, Jan. 1951.
- 327 Gracey, W., Letko, W., and Russell, W. R., "Wind Tunnel Investigations of a Number of Total-Pressure Tubes at High Angles of Attack. Subsonic Speeds," NACA - TN 2331, April 1951.
- 328 Gracey, W. and Scheithauer, E. F., "Flight Investigation of the Variation of Static-Pressure Error of a Static-Pressure Tube with Distance ahead of a Wing and a Fuselage," NACA - TN 2311, March 1951.
- 329 Henke, P. E., "Influence of the Orifice on Measured Pressure," NACA - TN 250, Nov. 1926.
- 330 Hensley, R. V., "Calibrations of Pitot-Static Tubes at High Speeds," NACA - WR L-396 (Orig. ACR July 1942).
- 331 Herschel, W. H., "The Pitot Tube and Other Anemometer for Aeroplanes," NACA Rept. No. 2, Part I, 1915.
- 332 Hodgson, Proc. Inst. Marine Eng. 36, p. 487, 1924.
- 333 Homann, F., "Einfluss Grossen Zahigkeit Bei Stromugum Zylinder," Forsch. Ingwes, Vol. 7. pp. 1 - 10, 1936.
- 334 Hooper-Allen, "Piezometer Investigation," A.S.M.E. Trans., Vol. 54, 1932.
- 335 Humphreys, M. D., "Effects of Compressibility and Large Angles of Yaw on Pressure Indicated by a Total Pressure Tube," NACA - WR L-77 (Orig. RB L5C30, 1945).

- 336 Heenan and Gilbert Proc. Inst. Civil Engineers, 123, p. 272, 1893-6.
- 337 Hurd, C. W. and Chesky, K. P., "Experimental Investigation of the Effect of Viscous Forces upon Pitot Tube Readings," M. I. T. Naval Engr. Thesis, 1951.
- 338 Hurd, C. W., Chesky, K. P., and Shapiro, A. H., "Influence of Viscous Effects on Impact Tubes," to be published in Jour. of Applied Mechanics.
- 339 Keenan, J., and Neuman, E. P., "Measurement of Friction in a Pipe for Subsonic and Supersonic Flow of Air," Jour. App. Mech., June 1946.
- 340 Kendall, J. M., "Time Lag Due to Compressible Poiseuille Flow Resistance in Pressure Measuring Systems," Naval Ordnance Laboratory Memorandum 10677.
- 341 Kiel, G., "Total Head Meter with Small Sensitivity to Yaw," NACA - TM 775, Aug. 1935 (from Luftfahrt, May 16, 1935, pp. 75-79).
- 342 Kumbruch, H., "Pitot-Static Tubes for Determining the Velocity of Air," NACA - TM 303, 1925, (from Forsch. Auf. Dem Gebiete Des Ing. 1921, No. 240).
- 343 Krisam, F., "Speed and Pressure Recording in Three-Dimensional Flow," NACA - TM 688, Oct. 1932.
- 344 Letko, W., "Investigations of the Fuselage Interference on a Pitot-Static Tube Extending Forward from the Nose of the Fuselage," NACA - TN 1496, Dec. 1947.
- 345 Lindsey, W. F., "Calibration of Service Pitot Tubes in the Langley 24 inch High Speed Tunnel," NACA - MR L6A08 (WRL-580), Feb. 1946.
- 346 Lindsey, W. F., "Effect of Mach Numbers on Position Error as Applied to a Pitot-Static Tube Located 0.55 Chord Ahead of an Airplane Wing," NACA - CB L4E 29 (WR L-75), May 1944.
- 347 Lock, C. N. H. and Hilton, W. F., "Calibration of Standard Pitot-Static Heads in the High Speed Tunnel," A.R.C. R and M No. 1752, 1936.
- 348 Lock, C. N. H., Knowles, H. E. and Percy, H. H., "The Effect of Compressibility on Static Heads," A.R.C. R and M 2386, Jan. 1941.
- 349 Lord, W. T. and Beastall, D., "On the Errors Involved in Measuring Supersonic Mach Numbers," R.A.E. Tech. Note, Aero. 2100.
- 350 Merriam, K. G. and Spaulding, E. R., "Comparative Tests of Pitot-Static Tubes," NACA - TN 546, Nov. 1935.
- 351 Mills, H. F., "Experiments Upon Piezometers Used in Hydraulic Investigations," Proc. Am. Acad. Arts and Sci., 1878.
- 352 Moffatt, M., "Report on Kiel Probes," PWA-576, Pratt and Whitney Aircraft, Oct. 1945.

- 353 Morkovin, M. V., "Design of a Device for Measurement of Free Stream Static Pressure at Supersonic Speeds," Aero. Eng. Rev. 9, 12, pp. 25-28, Dec. 1950.
- 354 Ower, Trans. Inst. of Chem. Eng. 18, p. 87, 1940.
- 355 Ower, E. and Johanson, F. C., "The Design of Pitot-Static Tubes," A.R.C. R and M 981, Aug. 1925.
- 356 Ower, E. and Johanson, F. C., "Pitot-Static Tube Factor at Low Reynolds Numbers," A.R.C. R and M 1437, 1932.
- 357 Ower, E. and Johanson, F. C., "On the Determination of the Pitot Static Tube Factor at Low Reynolds Numbers with Special Reference to Measurement of Low Air Speeds," Proc. Roy. Soc., Ser. A, Vol. 136, p. 153, 1932.
- 358 Patterson, J. L., "A Miniature Electrical Pressure Gage Utilizing a Stretched Flat Diaphragm," NACA - TN 2659, April 1952.
- 359 Pearcey, H. H., "The Effect of the Condensation of Atmos. Water Vapor on Total Head and the Measurements in the NPL High Speed Tunnels," A.R.C. R and M No. 2249, Feb. 1944.
- 360 Rayle, R. E., "An Investigation of the Influence of Orifice Geometry on Static Pressure Measurements," M. I. T. S.M. Thesis, Dept. of Mech. Eng., 1949.
- 361 Rayleigh, Lord, "Aerial Plane Waves of Finite Amplitude," Proc. Roy. Soc., Ser. A, No. 8A, pp. 247-284, 1910.
- 362 Reynolds, O., "On the Dynamical Theory of Incompressible Viscous Fluids and the Determination of a Criterion," Phil. Trans. Roy Soc., Ser. A, Vol. 186, pp. 123 - 164, 1895.
- 363 Rogers, E. W. E. and Berry, C. J., "Tests on the Effect of Incidence on Some Pressure Heads at High Subsonic Speeds," ARC, CP41, Arc. 13,263, July 21, 1950.
- 364 Rolfe, E., "The Study of Mass Transfer by Profile Measurements in the Boundary Layer," M. I. T. Master's Thesis, Chem. Eng. Dept., 1951.
- 365 Rosenhead, L. and Schwabe, M., "An Experimental Investigation of the Flow behind Circular Cylinders in Channels of Different Breadths," Proc. Roy. Soc., Ser. A, Vol. 79, p. 115, 1930.
- 366 Ross, Richard, M. I. T. ScD Thesis, Dept. Chem. Eng., 1952.
- 367 Rowse, W. C., "Pitot Tubes for Gas Measurement," Trans. ASME, Vol. 35, 1913.
- 368 Russell, W. R., Gracey, W., Letko, W. and Fournier, P. G., "Wind Tunnel Investigations of Six Shielded Total-Pressure Tubes at High Angles of Attack," NACA - TN 2530, Nov. 1951.
- 369 Schaaf, S. A., "Theory of Minimum Response Time for Vacuum," Univ. of Cal. Rept. No. HE-150-21.
- 370 Schlichting, H., "Uber Das Ebene Windshatten Problem," Ingenieur Archiv., Vol. 1, p. 533, 1929-1930.

- 371 Schuster, P., "Mitteilungen uber Forschungsarbeiten," Verein Deutscher Ingenieure Heft 82, 1905.
- 372 Shapiro, A. H. and Smith, R. D., "Friction Coefficients in the Inlet Length of Smooth Round Tubes," NACA - TN 1785, Nov. 1948.
- 373 Spivack, H. M., "Experiments in the Turbulent Boundary Layer of a Supersonic Flow," North American Aviation, Inc., Aerophysics Lab., Project Bumblebee, Rept. CM-615, Jan. 16, 1950.
- 374 Stanton, T. E., Marshall, D. and Bryant, C. N., "On the Conditions at the Boundary of a Fluid in Turbulent Motion," Proc. Roy. Soc., Series A, No. 97,413, 1920.
- 375 Stivers, L. C., Jr. and Adams, C. N., Jr., "High Speed Wind-Tunnel Investigations of the Effects of Compressibility of a Pitot-Static Tube," NACA - RM A7F12, Aug. 1947.
- 376 Taback, I., "The Response of Pressure Measuring Systems to Oscillating Pressures," NACA - TN 1819, Feb. 1949.
- 377 Taylor, G. I., "Pitot Pressure in Moist Air," A.R.C. R and M No. 2248, Jan. 1945.
- 378 Towend, H. C. H., "Statistical Measurement of Turbulence in the Flow of Air Through a Pipe," Proc. Roy. Soc., Ser. A, Vol. 145, p. 180, 1934.
- 379 Tsien, H. S., "Notes on Aerodynamics of Compressible Fluids," M. I. T. Aero. Eng. Dept., 1949.
- 380 Turner, A. L. and Ratherst, G. A., Jr., "Pressure Lag in Tubing used in Flight Research," NACA - RB 5F15, July 1945.
- 381 Werner, F. D., "An Investigation of the Possible Use of the Flow Discharge as a Means for Measuring Air Flow Characteristics," Rev. of Scientific Inst., Vol. 21, No. 1, Jan. 1950.
- 382 Weidemann, Hans, "Inertia of Dynamic Pressure Arrays," NACA - TM 998, Dec. 1941.
- 383 Young, A. D., "Notes on a Method of Measuring Profile Drag by means of an Intergrating Comb," A.R.C. R and M No. 2257, 1948.
- 384 Young, A. D. and Maas, J. N., "The Behavior of a Pitot-Tube in a Transverse Pressure Gradient," A.R.C. R and M 1770.
- 385 Zahm, A. F., "Pressure of Air on Coming to Rest from Various Speeds," NACA - Rept. 247, 1926.
- 386 Zahm, A. F. and Smith, R. H., "Comparison of United States and British Standard Pitot-Static Tubes," NACA Rept. 81, 1920.
- 387 Zalovcik, J. A. and Daum, F. L., "Flight Investigation at High Mach Numbers of Several Methods of Measuring Static Pressure on an Airplane Wing," NACA - RB L4H 10a (WR L 20), Nov. 1944.
- 388 Allen and Hooper, "Piezometer Investigation," ASME Trans., Vol. 54, 1932.

- 389 Walchner, O., "The Effect of Compressibility on the Pressure Reading of a Prandtl Pitot Tube at Subsonic Flow Velocity," NACA - TM 917, Nov. 1939.
- 390 Li, Y. T., "Design of Strain Gage Pressure Indicators," to be presented to the Institute of the Aeronautical Sciences, Sept. 10, 1952.
- 391 Li, Y. T., "Crystal Press Pickups," M. I. T. Aeronautical Eng. Dept. Acct. 2004 Progress Report, Aug. 1952.
- 392 Draper, C. S. and Li, Y. T., "A New High-Performance Engine Indicator of the Strain-Gage Type," Jour. of the Aeronautical Sciences, Vol. 16, No. 10, Oct. 1949.
- 393 Larson, H., "Accurate Measurement of Small Pressure Differences Using the Foxboro Micromanometer," M.I.T. S.B. Thesis, Dept. of Mech. Eng., May 1952.
- 394 Design Manual for Air and Gas Flow Measurement Probes, Vol. 1, Data Folder No. DF 51 GT 379, General Electric, New York.
- 395 Hodgson, Journal of Scientific Instruments 6, 1929.
- 396 "Model P81 Subminiature Pressure Transducer," Statham Scientific Instruments. Bull. No. 3.4.
- 397 "Avionics Tiny Pick-up Aids Convair Study" by Bill Chan. Reprinted from Aviation Week, Jan. 7, 1952.
- 398 Brunot, A. W. and Fulton, R. O., "A Clearanceometer for Determining Blade-Tip Clearances of Axial-Flow Compressors." Paper No. 52-SA-16, Trans. of the ASME.
- 399 Meyer, C. A and Benedict, R. P., "Instrumentation for Axial-Flow Compressor Research." Trans. of the ASME.
- 3001 "A diaphragm-Type Magnetic Pressure Gage," W. C. Johnson and D. J. Montgomery, Princeton University.
- 3002 "Crystal Type Total Pressure Probe" by Edward Dytko.

Velocity and Mach Number Measurements

- 401 Cooley, W. C., "Measurement of Supersonic Velocities by Ion Transit-Time Methods," M.I.T. ScD. Thesis, 1951.
- 402 Fage, A. and Towend, H. C. H., "An Examination of Turbulent Flow with an Ultra-Microscope," Proc. Roy. Soc., Ser. A, Vol. 135, 1932.
- 403 Huber, P. W. and Kantrowitz, A., "A Device for Measuring Sonic Velocity and Compressor Mach Number," NACA - TN 1664, July 1948.
- 404 Hilton, High-Speed Aerodynamics, New York: Longmans, Green and Co., 1951.

Stream Direction Measurements

- 501 Baker, V. D., "Characteristics of a 3-Hole Yaw Probe," Pratt and Whitney Aircraft Co., Rept. PWA-618, July 1946.
- 502 Cooper, Morton and Webster, "The Use of an Uncalibrated Cone for Determination of Flow Angles and Mach Numbers at Supersonic Speeds," NACA -TN 2190, March 1951.
- 503 Eckert, B., "Experiences with Flow-Direction Instruments," NACA - TM 969, March 1941.
- 504 Eichenberger, H. P., "The Shear Flow in Bends," M.I.T. ScD. Thesis, Dept. of Mech. Engr., 1952.
- 505 Emmons, H., "Preliminary Report on the Theory, Calibration and Use of a 5-Hole Axial Yaw Probe," Rept. No. 110, Harvard Rept. to Pratt and Whitney.
- 506 Evans, R. A., "Flow Visualization at Low Pressures," Univ. of Cal. Dept. Eng. Rept. No. HE-150-21, 1947.
- 507 Fusfeld, R. D., "A Probe for Measuring Flow Inclination in a Supersonic Air Stream," Jour. Aero. Sci., Vol. 18, No. 5, p. 356, May 1951.
- 508 Golden, J., "The Effect of Large Angles of Yaw on the Accuracy of Wing-Tip Yawmeters," NACA - RB, Sept. 1942.
- 509 Jegorow, G., "Measurement of Direction, Velocity and Pressure in a Three Dimensional Current," R. T. P. Translation No. 2498, Durand Reprinting Comm., Cal. Inst. of Technology.
- 510 Keast, F. H., "High Speed Cascade Testing Technique," Trans. ASME, Vol. 74, No. 5, p. 685, July 1952.
- 511 Kronauer, R. E., "Secondary Flow in Fluid Dynamics," Harvard PhD. Thesis, 1951.
- 512 Lavender, T., "A Direction and Velocity Meter for Use in Wind Tunnel Work etc.," A.R.C. R and M 844, Jan. 1923.
- 513 Ling, A. T. A., "Study of Secondary Flow Effect on Single Symmetric Airfoil," M.I.T. S.M. Thesis, Feb. 1952.
- 514 Schulze, Wallace M., Ashby, George C. Jr., and Ermin, John R., "Several Combination Probes for Surveying Static and Total Pressure and Flow Direction," NACA TN 2830.

The Hot-Wire

- 601 Bailey, A., "A Directional Hot-Wire Anemometer," A.R.C. R and M No. 777, Jan. 1922.
- 602 Betchov, R., "Non-Linear Theory of a Hot-Wire Anemometer," NACA - TM 1346, July 1952.
- 603 Betchov, R. and Welling, W., "Some Experiences Regarding the Non-linearity of Hot-Wires," NACA - TM 1223, June 1952.

- 604 Corrsin, S., "Extended Applications of the Hot-Wire Anemometer," NACA - TN 1864, April 1949.
- 605 Dryden, H. L., "Turbulence Investigations at the National Bureau of Standards," Proc. 5th Int. Cong. Appl. Mech., pp. 362-368, Cambridge, Mass., 1938.
- 606 Dryden, H. L., "Isotropic Turbulence in Theory and Experiment," Appl. Mech. Theodore von Karman Anniversary Volume, pp. 85-102, May 11, 1941.
- 607 Dryden, H. L., "Air Flow in the Boundary Layer Near a Plate," NACA - Rept. 562, 1936.
- 608 Dryden, H. L. and Keuthe, A. M., "The Measurement of Fluctuation of Air Speed by the Hot-Wire Anemometer," NACA - Rept. No. 320, 1929.
- 609 Dryden, H. L., Schubauer, G. B., Mock, W. C., Jr. and Skramstadt, H. K., "Measurements of Intensity and Scale of Wind-Tunnel Turbulence and Their Relation to the Critical Reynolds Number of Spheres," NACA Rept. 581, 1937.
- 610 Page, A., "A Description of a Hot-Wire Anemometer which is Sensitive over a Large Range of Wind Speeds," A.R.C. R and M 556, Nov. 1918.
- 611 Ferrari, C., "Electrical Equipment for the Experimental Study of the Dynamics of Fluids" (Translation), NACA - TM 1006, March 1942.
- 612 Gerdien, H., "The Anemoklinograph, an Apparatus for the Investigation of the Structure of the Wind" (German), Jahrb wiss. Gesellsch. Flugtech, Vol. 2, 1913-1914.
- 613 Hall, A. A., "Measurements of the Intensity and Scale of Turbulence" A.R.C. R and M 1842.
- 614 Hukille, W. V., "Characteristics of Thermocouple Anemometers," ibid, American Inst. of Physics, 1941, pp. 666-672.
- 615 King, L. V., "On the Convection of Heat from Small Cylinders in a Stream of Fluid: Determination of the Convection Constants of Small Platinum Wires with Application to Hot-Wire Anemometry," Phil. Trans. Roy. Soc., Ser. A., Vol. 214, pp. 373-432, 1914.
- 616 King, R. O., "The Measurement of Air Flow," Engineering, Vol. 117, pp. 136-249, 1924.
- 617 King, L. V., "Precision Measurement of Air Velocity by Means of the Linear Hot-Wire Anemometer," Phil. Mag., Vol. 29, 1915.
- 618 Knoblock, F. D., "A Hot-Wire Anemometer Developed for Full-Scale Airship Measurements," The Daniel Guggenheim Airship Inst., pp. 58-61, 1935.
- 619 Kovasznay, L., "Calibration and Measurement in Turbulence Research by the Hot-Wire Method," NACA - TM 1130, June 1947.

- 620 Laufer, J., "Investigations of Turbulent Flow in a Two Dimensional Channel," NACA - TN 2123, July 1950.
- 621 Levine, R. S., "Construction and Use of a Hot-Wire Turbulence Measuring Device," M.I.T. Internal Report No. 5, M.I.T. Guided Missiles Program Meteor, Dec. 1947.
- 622 Lowell, H. H., "Design and Applications of Hot-Wire Anemometers for Steady State Measurements at Transonic and Supersonic Air-Speeds," NACA - TN 2117, July 1950.
- 623 MacGregor, Morris J. T., "The Electrical Measurement of Wind Velocity," Engineering, Vol. 94, No. 26, pp. 892-894, Dec. 27, 1912.
- 624 Mock, W. C., Jr., "Alternating Current Equipment for the Measurement of Fluctuations of Air Speed in Turbulent Flow," NACA Rept. 598, 1937.
- 625 Mock, W. C., Jr. and Dryden, H. L., "Improved Apparatus for the Measurement of Fluctuations of Air Speed in Turbulence," NACA Rept. 448, 1932.
- 626 Rynyan, R. A. and Jeffries, R. J., "Empirical Methods for Frequency Compensation of the Hot-Wire Anemometer," NACA - TN 1331, June 1947.
- 627 Schlichting, H., "Lecture Series Boundary Layer Theory - Part 1, Laminar Flow," NACA - TM 1217, April 1949.
- 628 Schlichting, H., "Turbulent Flow," Part II, NACA - TM 1218, April 1949.
- 629 Schubauer, G. B., "A Turbulence Indicator Utilizing the Diffusion of Heat," NACA Rept. 524, 1935.
- 630 Schubauer, G. B., "Effect of Humidity in Hot-Wire Anemometry," Nat. Bur. of Stds. Journal, Res. Vol. 15, No. 6, pp. 575-578, Dec. 1935.
- 631 Schubauer, G. B. and Klebanoff, P. S., "Theory and Application of Hot-Wire Instruments in the Investigation of Turbulent Boundary Layers," ACR 5K27 (WR W-86), March 1946.
- 632 Simmons, L. F. G., "Note on Errors Arising in Measurement of Turbulence," A.R.C. R and M No. 1919.
- 633 Simmons, L. F. G. and Bailey, A., "Note on a Hot-Wire Speed and Direction Meter," A.R.C. R and M 1019, Feb. 1926.
- 634 Simmons, L. F. G. and Bevan, J. A., "Hot-Wire Type of Instrument for Recording Gusts," A.R.C. R and M 1615, Feb. 1934.
- 635 Simmons, L. F. G. and Salter, C., "Exp. Investigation and Analysis of the Velocity Variation in Turbulent Flow," Proc. Roy. Soc., Ser. A, 145, 212, 1934.
- 636 Simmons, L. F. G. and Salter, C., "An Experimental Determination of the Spectrum of Turbulence," M. A. Proc. Roy. Soc. (A), Vol. 165, 1938.

- 637 Taylor, C. F., "A Suggested Method for Measuring Turbulence," NACA - TN 380, 1931.
- 638 Thomas, J. S. G., "Hot-Wire Anemometry: Its Principals and Applications," Jour. Soc. Chem. Ind. Trans., Vol. 37, pp. 165T-168T, Discussion pp. 169T-170T, June 15, 1948.
- 639 Thomas, J. S. G., "Hot-Wire Anemometry," Phil. Mag., Vol. 39, 1920.
- 640 Tsien, H. S., "Wind Tunnel Testing Problems in Super Aerodynamics," Jour. Aero. Sci., Vol. 15, No. 10, pp. 573-580, Oct. 1948.
- 641 von Doenhoff, A. E. and Tetervin, N., "Determination of General Relations for the Behavior of Turbulent Boundary Layers," NACA ACR No. 3G13, 1943.
- 642 Weske, J. R., "Methods of Measurement of High Air Velocities by the Hot-Wire Method," NACA - TN 880, Feb. 1943.
- 643 Weske, J. R., "A Hot-Wire Circuit With Very Small Time Lag," NACA - TN 881, Feb. 1943.
- 644 Weske, J. R., "Measurement of the Arithmetic Mean Velocity of a Pulsating Flow of High Velocity by the Hot-Wire Method," NACA - TN 990, April 1946.
- 645 Willis, J. B., "Review of Hot-Wire Anemometry," Rep. ACA-190, Australian Council Aero., Oct. 1945.
- 646 Catalogue of Baker and Co., Inc., Newark, New Jersey.
- 647 "Apparatus for Measuring Flow Turbulence" by G. Daetwyler.
- 648 Lawrence, J. C. and Landes, L. G., "Auxiliary Equipment and Techniques for Adapting the Constant-Temperature Hot-Wire Anemometer to Specific Problems in Air-Flow Measurements," NACA TN 2843.

Mass Flow Measurements

- 701 Anon, "Standards for Discharge Measurement with Standardized Nozzles and Orifices. German Industrial Standard 1952," NACA - TM 952, Sept. 1940.
- 702 ASME, "Fluid Meters, Their Theory and Application," ASME Research Publication, Fourth Edition, 1937.
- 703 Li, Y. T. and Lee, S., "A Fast Response True-Mass-Rate Flowmeter," to be presented to A.S.M.E., Dec. 1952.
- 704 Li, Y. T., "Principles of a True Mass Rate Flow Meter," M.I.T., Cambridge, Mass., March 24, 1952.
- 705 Westmoreland, J. C., "A Meter for Timing the Flow of Very Small Volumes of a Gas," NACA - RM 52109.

Humidity Measurements

- 801 National Bureau of Standards, "Methods of Measuring Humidity," NBS Circular 512, 1951.
- 802 Wadleigh, K. R., "An Experimental Investigation of a Small Scale Aerothermopressor," M.I.T. Doctor's Thesis, 1953.
- 803 Illinois Testing Laboratories Dewpoint Indicator. Instruments 19, 1946.
- 804 Western Precipitation Bulletin, Western Co., Los Angeles, Calif.
- 805 Sinclair, David, "Light Scattering by Spherical Particles," Reprint from Journal of the Optical Society of America, Vol. 37, No. 6, 475-480, June 1947.
- 806 Sinclair, David and LaMer, V. K., "Light Scattering as a Measure of Particle Size in Aerosols--The Production of Particle Size in Aerosols."
- 807 " H_2SO_4 Mist Droplet Size Determination," F. D. C.
- 808 Johnstone, H. F., "High Velocity Impactor for Sampling Aerosols," Univ. of Illinois.

Optical Instruments

- 901 Burton, R. A., "Schlieren Photography," 1951.
- 902 Burton, R. A., "The Application of Schlieren Photography to Fluid Flow and Heat Transfer Analysis," Master's Thesis, The University of Texas, Austin, Texas, 1951.
- 903 Burton, R. A., "Notes on the Multiple Sonic Schlieren System," J. Opt. Soc., Amerc., Nov. 1950.
- 904 Kantrowitz, Arthur and Trimpi, R. L., "A Sharp-Focusing Schlieren System," J. of Aero. Sciences, May 1950.
- 905 Liepmann, R. W. and Puckett, A. E., "Introduction to Aerodynamics of a Compressible Fluid," New York: John Wiley and Sons, Inc., 1947.
- 906 Mortensen, J. E., "An Improved Schlieren Apparatus Employing Multiple Slit Gratings," Review of Scientific Instruments, 21, No. 1, 1950.
- 907 Schardin, H., "Das Toeplersche Schlieren Verfahren," V.D.I. Forschungheft 366, 1934.
- 908 Schardin, H., "Die Schlieren Verfahren and Ihic Anwendungen," Erget der Exakten., Naturweisser schafter, 20, Berlin: Springer 1942, 310-314.
- 909 Schmidt, E., Forschung auf den Gietete des Irg. 3.

- 910 Schaeffer, H. J., "Physical Optic Analysis of Image Quality in Schlieren Photography." Society of Motion Picture Engineers, Oct. 1949.
- 911 Bijchele, D. R. and Day, P. B., "Interferometer with Large Working Field Utilizing Schlieren Optics," NACA - RM E50127, Jan. 1951.
- 912 Blue, R. E., "Interferometer Corrections and Measurements of Laminar Boundary Layer in a Supersonic Stream," NACA - TN 2110.
- 913 Faulders, C. R., "An Interferometric Investigation of the Flow Through a Cascade of Turbine Nozzle Blades," ASME 52-SA-36, June 1952.
- 914 Gooderum, P. B., Wood, G. P. and Brevoort, M. J., "Investigations with an Interferometer of the Turbulent Mixing of a Free Supersonic Jet," NACA - TN 1857, April 1949.
- 915 Gooderum, P. B., Wood, G. P. and Brevoort, M. J., "Investigation with an Interferometer of the Turbulent Mixing of a Free Supersonic Jet," NACA - Rept. 963, 1950.
- 916 Hahner, C. H. and Gardner, I. C., "Research and Development in Applied Optics and Optical Glass at the Nat. Bur. of Std.," NBS M194, Sept. 1949.
- 917 Tilton, L. W., "Optical Glass of Interferometer and Schlieren Quality for Wind Tunnel Optics," NBS RP 1969, May 1949.
- 918 Zobel, T. H., "Development and Construction of an Interferometer for Optical Measurement of Density Field," NACA - TM 1184, Sept. 1947.
- 919 Photographs of Interferometer Cascade, (American Optical Co.).
- 920 Edelman, G. M. and Bright, M. H., "The Specific Refractivity of Gases for Various Wave-Lengths of Light," Report No. 6, M.I.T.
- 921 Giese, J. H. and Bergdolt, V. E., "Interferometric Studies of Supersonic Flows About Truncated Cones," Ballistic Research Laboratories, Report No. 830.
- 922 Norton, J. L., "Design of a Mach-Type Optical Interferometer for Measurement of Density in Supersonic Wind Tunnels." Thesis (S.M.) M.I.T., June 1947.
- 923 Ladenburg, R., Van Voorhis, C. C. and Winckler, J., "Interferometric Study of Supersonic Phenomena. Part II: The Gas Flow Around Various Objects in a Free Homogeneous Supersonic Air Stream," Report 93-46. Inyokern, Calif.: U. S. Naval Ordnance Test Station, September 2, 1946.
- 924 Winkler, E. H., "Analytical Studies of the Mach-Zehnder Interferometer," Report No. 1077. White Oak, Silver Spring, Md.: U. S. Naval Ordnance Laboratory, Dec. 5, 1947.
- 925 Landolt-Bornstein, "Physikalisch - Chemische Tabellen;" erster Ergänzungsband. Berlin: Julius Springer, 1927, p. 525.

- 926 Landolt-Bornstein, "Physikalisch - Chemische Tabellen;" zweiter Ergänzungsband, zweiter Teil. Berlin: Julius Springer, 1931, pp. 814-815.
- 927 Landolt-Bornstein, "Physikalisch - Chemische Tabellen;" dritter Ergänzungsband, zweiter Teil. Berlin: Julius Springer, 1935, pp. 1677-1679.
- 928 Hodgman, C. D., ed., "Handbook of Chemistry and Physics;" 30th ed. Cleveland, Ohio: Chemical Rubber Publishing Co., 1947.
- 929 Edelman, G. M., and Bright, M. H., "The Specific Refractivity of Gases for Various Wavelengths of Light," Gas Turbine Laboratory Report No. 6, Cambridge, Mass.: M.I.T., May, 1948.
- 930 DeFrate, L. A., "Application of the Interferometer to the Study of Boundary Layers." Thesis (Sc.D) M.I.T., 1950.
- 931 Edelman, G. M., "The Design, Development, and Testing of Two-Dimensional Sharp-Cornered Supersonic Nozzles," Meteor Report No. 22, Cambridge, Mass.: M.I.T., May 1, 1948. (This report is a portion of the author's thesis (S.M.) of the same title, M.I.T., Mechanical Engineering Department, 1948.)
- 932 Bergdolt, V. E., "A New Interferometer with a Large Working Field," Report No. 692. Aberdeen Proving Grounds, Md.: Ballistic Research Laboratories, Jan. 11, 1949.
- 933 Eckert, E. R. G., Drake, R. M., Jr., and Soehngen, E., "Manufacture of a Zehnder-Mach Interferometer," Technical Report No. 5721. Dayton, Ohio: U. S. Air Force, Air Material Command, Wright-Patterson Air Force Base, Aug. 31, 1948.
- 934 Ladenburg, R., and Bershader, D., "On Laminar and Turbulent Boundary Layer in Supersonic Flow," Reviews of Modern Physics, Vol. 21, No. 3: pp. 510-515, July 1949.
- 935 Barry, F. W., Shapiro, A. H., and Neumann, E. P., "The Interaction of Shock Waves with Boundary Layers on a Flat Plate," Meteor Report No. 52. Cambridge, Mass.: M.I.T., March, 1950.

High Speed Photography

- 936 Edgerton, H. E., "Stroboscopic and Slow-Motion Pictures by Means of Intermittent Light," Jour. Soc. of Motion Picture Engineers, Vol. XVIII, No. 3, pp. 356-364, Nov. 1932.
- 937 Edgerton, H. E., "Stroboscopic Moving Pictures," Electrical Engineering, 50, pp. 327-329, May 1931.
- 938 Edgerton, H. E., "Light Meter for Electric Flash Lamps," Electronics, pp. 78-81, June 1948.
- 939 Edgerton, H. E. and Germeshausen, K. J., "Stroboscopic-Light High-Speed Motion Pictures," Jour. Soc. of Motion Picture Engineers, Vol. XXIII, No. 5, pp. 284-298, Nov. 1934.

- 940 Edgerton, H. E. and Wyckoff, C. W. "A Rapid Action Shutter with No Moving Parts," Journal of Society of Motion Picture and Television Engineers, Inc.
- 941 Germeshausen, K. L., "New High-Speed Stroboscope for High-Speed Motion Pictures," Jour. Soc. of Motion Picture Engineers, 52, Part II, pp. 24-34, March 1949.
- 942 Edgerton, H. E., "Theory of Electronic-Flash Lighting Equipment," M.I.T. Notes.
- 943 Bibliography--Electronic Flash Tubes and Spark Photo. See Bibliography on Hi-speed Photo. in Journal of Soc. of Motion Picture and Telev. Engr., Jan. 1951.
- 944 Barstow, F. E., "Infrared Photography with Electric-Flash," Jour. of the SMP and TE, Vol. 55, Nov. 1950.
- 945 Flashtubes, G. E. Co., Edgerton, Germeshausen and Grier, Inc., Anglo Corp., Sylvania Elec. Prods. Inc., Westinghouse Elec. Corp., Kewlite Labs.
- 946 Kodak Films, Kodak Data Book, 5th Edition, Eastman Kodak Co.
- 947 Stroboscopes, General Radio Corporation.

Miscellaneous

- 948 "Flight Tests with the Paincare--Farman Torque Meter by Jacques Salez (Translation).
- 949 "Torque Meter for Power-Driven Aircraft Models in the Wind Tunnel," by R. Siber and A. Oudart (Translation) (Bull. des Services Techniques, No. 84).
- 950 "An Electrical Torque Meter Without Slip Rings for Measurements at Very High RPM's," W. Golilke (Report of the Hermann Goering Aero. Research Inst., Braunschwerz).

The Fundamental Principles of Dynamic Measurement

- 1001 Instrument Engineering; Draper, McKay and Lees, McGraw Hill, 1952-3, Vol. I, II.
- 1002 Functions of a Complex Variable; E. G. Phillips, Oliver and Boyd, 1946.
- 1003 Transients in Linear Systems; Vol. I, Gardner and Barnes, John Wiley and Sons, 1942.
- 1004 Aerodynamic Stability and Automatic Control: W. Bollay; Inst. of Aero. Sciences, Vol. 18, p. 569, 1951.
- 1005 Principles of Servomechanisms; Brown and Campbell, John Wiley and Sons, Inc.

- 1006 Theory of Servomechanisms; James, Nichols, and Phillips; Radiation Laboratory Series No. 25, McGraw Hill Book Company, Inc.
- 1007 Design Factors Controlling the Dynamic Performance of Instruments; Draper and Bentley, Trans. ASME, 1940.
- 1008 General Principles of Instrument Analysis; C. S. Draper and G. V. Schiestett, Instruments, 1939.
- 1009 Servomechanism Analysis; Thaler and Brown, McGraw Hill, 1953.
- 1010 Graphical Analysis of Control Systems; W. R. Evans, Trans. AIEE, 1948.
- 1011 Control System Synthesis by Root Locus Method; W. R. Evans, Trans. AIEE, 1950.
- 1012 Principles of Industrial Process Control; D. P. Eckmann, John Wiley and Sons.
- 1013 Modern Operational Mathematics in Engineering; R. V. Churchill, McGraw Hill Company, 1944.
- 1014 Dimensionless Analysis of Servomechanisms by Electrical Analogy; McCann and Herwald, AIEE, 1946, 1947.
- 1015 The Effect of Pole and Zero Locations on the Transient Response of Linear Dynamic Systems; J. H. Mulligan, Jr., Proc. I.R.E., May 1949.
- 1016 The Electronic Control Handbook; Ralph R. Batcher and William Moulic, Caldwell-Clements, Inc.
- 1017 A New High-Performance Engine Indicator of the Strain Gage Type; C. S. Draper and Y. T. Li, J.A.S., Oct. 1949.
- 1018 A Mass Rate Flowmeter with Fast Response; Y. T. Li and S. Y. Lee, ASME Trans. July 1953.
- 1019 Servomechanisms and Regulator Systems Design, Vol. 1, Chestnut and Meyer, John Wiley and Sons, 1951.